

Special Issue Vol. XLI No 1

Warszawa 2000

ISSN 0324-8313

Indeks 362123

DELO QUARTY LITERSKID 4
20000913 068

Journal of Technical Physics

Copyright (c) 1999 by Institute of Fundamental Technological Research,
Polish Academy of Sciences, Warsaw, Poland

Aims and Scope

Journal of Technical Physics (formerly Proceedings of Vibration Problems) is a refereed international journal founded in 1959. The journal is devoted to the application of the phenomenological and continuum physics idea in: mechanics, thermodynamics, electrodynamics, coupled mechanical, electromagnetic and thermal fields, plasma physics, superconductivity and many others. Papers published in the Journal of Technical Physics are original contributions of the authors, or survey articles dealing with theoretical and experimental aspects of physical problems listed above.

Occasionally special issues of the journal may be devoted to publication of all, or selected papers presented at international conferences or other scientific meetings. However, all papers intended for such an issue are subjected to the usual reviewing and acceptance procedure.

FOUNDER

S. KALISKI

INTERNATIONAL COMMITTEE

Chairman WŁADYSŁAW FISZDON

Members: J.B. ALBLAS (Netherlands), A.U. ERDEN (Turkey),
A.C. ERINGEN (USA), E. INFELD (Poland), O.N. KROKHIN (Russia),
F.M. LESLIE (UK), V.G. MAKHANKOV (Russia), I. MALECKI (Poland),
G.A. MAUGIN (France), K. MIYA (Japan), B. NYROLES (France),
B. PASZKOWSKI (Poland), D. ROGULA (Poland), J. STEFANIAK (Poland),
M. SUFFCZYŃSKI (Poland), H.F. TIERSTEN (USA), E. WŁODARCZYK (Poland),
J. ZAGRODZIŃSKI (Poland), R. ŻELAZNY (Poland)

EDITORIAL COMMITTEE

CZ. RYMARZ-Editor-in-Chief, Z. PERADZYŃSKI - Associate Editor
E. DANICKI, J. DEPUTAT, Z. DŻYGADŁO, K. JACH, A. KRAWCZYK, A. ROGALSKI,
J. SŁAWIANOWSKI, A. TURSKI, J. WOŁOWSKI, J. ŻMIJA
Z. KRAWCZYK - Managing Editor

Address of the Editorial Office:
Journal of Technical Physics
Institute of Fundamental Technological Research
Świętokrzyska 21
PL 00-049 Warsaw, Poland

Tel.: (48-22) 826 60 22, Fax: (48-22) 826 98 15,
E-mail: publikac@ippt.gov.pl

REPORT DOCUMENTATION PAGE

Form Approved OMB No. 0704-0188

Public reporting burden for this collection of information is estimated to average 1 hour per response, including the time for reviewing instructions, searching existing data sources, gathering and maintaining the data needed, and completing and reviewing the collection of information. Send comments regarding this burden estimate or any other aspect of this collection of information, including suggestions for reducing this burden to Washington Headquarters Services, Directorate for Information Operations and Reports, 1215 Jefferson Davis Highway, Suite 1204, Arlington, VA 22202-4302, and to the Office of Management and Budget, Paperwork Reduction Project (0704-0188), Washington, DC 20503.

1. AGENCY USE ONLY (Leave blank)		2. REPORT DATE 11 August 2000		3. REPORT TYPE AND DATES COVERED Conference Proceedings	
4. TITLE AND SUBTITLE XXIV International Conference on Phenomena in Ionized Gases				5. FUNDING NUMBERS F61775-99-WF025	
6. AUTHOR(S) Conference Committee					
7. PERFORMING ORGANIZATION NAME(S) AND ADDRESS(ES) Laser-Produced Plasma Physics Dept., Institute of Plasma Physics and Laser Microfusion 23 Hery St., PO Box 49 Warsaw 00-908 Poland				8. PERFORMING ORGANIZATION REPORT NUMBER N/A	
9. SPONSORING/MONITORING AGENCY NAME(S) AND ADDRESS(ES) EOARD PSC 802 BOX 14 FPO 09499-0200				10. SPONSORING/MONITORING AGENCY REPORT NUMBER CSP 99-5025	
11. SUPPLEMENTARY NOTES					
12a. DISTRIBUTION/AVAILABILITY STATEMENT Approved for public release; distribution is unlimited.				12b. DISTRIBUTION CODE A	
13. ABSTRACT (Maximum 200 words) The Final Proceedings for XXIV International Conference on Phenomena in Ionized Gases, 11 July 1999 - 16 July 1999 This is an interdisciplinary conference. Topics include elementary processes, low-pressure glows, arcs, surface discharges and high pressure glows, diagnostics, non-idea plasmas, numerical modeling, high-current discharges, waves and instabilities, and other topics.					
14. SUBJECT TERMS EOARD, Plasma Physics, Ionospheric Heating, Laser Beam-Plasma Interaction, Plasma Surface Interaction, Low Density Plasma, Laser plasmas				15. NUMBER OF PAGES 605	
				16. PRICE CODE N/A	
17. SECURITY CLASSIFICATION OF REPORT UNCLASSIFIED	18. SECURITY CLASSIFICATION OF THIS PAGE UNCLASSIFIED	19. SECURITY CLASSIFICATION OF ABSTRACT UNCLASSIFIED	20. LIMITATION OF ABSTRACT UL		

NSN 7540-01-280-5500

Standard Form 298 (Rev. 2-89)
Prescribed by ANSI Std. Z39-18
298-102

Contract F61775-99-WF025
CSP 99-5025

POLISH
ACADEMY
OF SCIENCES

INSTITUTE
OF FUNDAMENTAL
TECHNOLOGICAL
RESEARCH

MILITARY
UNIVERSITY
OF TECHNOLOGY

Journal of Technical Physics

Special Issue Vol. XLI No 1

Warszawa 2000

ISSN 0324-8313

Indeks 362123

INTERNATIONAL CONFERENCE ON PHENOMENA IN
IONIZED GASES

Warsaw, 11 - 16 July, 1999

INVITED LECTURES

Editors: TADEUSZ PISARCZYK (IPPLM, POLAND)
JERZY WOŁOWSKI (IPPLM, POLAND)
PAWEŁ PISARCZYK (IPPLM, POLAND)

AQ F00-12-3867

Organizer

Institute of Plasma Physics and Laser Microfusion, Warsaw, Poland

Professor Andrzej Wiszniewski, President of the State Committee for Scientific Research of the Polish Government was an Honorary Patron of XXIV ICPIG

International Scientific Committee

J.E. ALLEN	United Kingdom	R. MORROW	Australia
M. CAPITELLI	Italy	G. MUSA	Romania
E. DESOPPERE	Belgium	A.H. OIEN	Norway
T. GOTO	Japan	L.C. PITCHFORD	France
E.E. KUNHARDT	USA	A.A. RUKHADZE (chairman)	Russia
J. MENTEL	Germany	Z. ZAKRZEWSKI	Poland

Local Organizing Committee

A. GALKOWSKI	IPPLM	T. PISARCZYK (secretary)	IPPLM
E. INFELD	SINS, Warsaw	M. SADOWSKI	SINS, Warsaw
Z. KŁOS	SRC PAS, Warsaw	M. SCHOLZ	IPPLM
J. MIZERACZYK	IFFM PAS, Gdańsk	Z. SKŁADANOWSKI	IPPLM
J. MUSIELOK	Opole Univ., Opole	J. WOŁOWSKI (chairman)	IPPLM
K. MUSIOL	Jagiellon. Univ., Cracow	Z. ZAKRZEWSKI	IFFM PAS, Gdańsk
Z. PERADZYŃSKI	IFTR PAS, Warsaw		

Sponsors

- State Committee for Scientific Research of the Polish Government
- National Atomic Energy Agency of the Polish Government
- Institute of Plasma Physics and Laser Microfusion, Warsaw
- International Union of Pure and Applied Physics (IUPAP)
- US Air Force through the EOARD

IUPAP sponsorship

"To secure sponsorship, the organizers have provided assurance that the XXIV ICPIG will be conducted in accordance with IUPAP principles as stated in the ICSU-Document "Universality of Science" (sixth edition, 1989) regarding the free circulation of scientists for international purposes. In particular, no bona fide scientist will be excluded from participation on the grounds of national origin, nationality, or political considerations unrelated to science."

**The conference organizers acknowledge financial support
from all the sponsors.**

Printed and bounded by

PRINTING DIVISION

SPACE RESEARCH CENTRE, POLISH ACADEMY OF SCIENCES

18A BARTYCKA ST., 00-716 WARSAW, POLAND

Preface

This special issue of the Journal of Technical Physics contains the manuscripts of invited lectures presented at the XXIV International Conference on Phenomena in Ionized Gases which was held in Warsaw, Poland, from 11 to 16 July, 1999. Out of 8 general and 32 topical invited lectures selected by the International Scientific Committee of the ICPIG and presented at the conference, all general ones and 22 topical papers are published in this issue. One invited lecturer did not submit a manuscript. The papers are ordered alphabetically within a group of general invited lectures and a group of topical lectures, according to the presenting author's name.

A short article on Hans von Engel and the ICPIG conference (written by Prof. R. Franklin), a lecture given by Prof. R. Balescu the winner of the first von Engel Prize and the Summary of the XXIV ICPIG are placed at the beginning of this volume.

In addition, three papers submitted by the Conference Workshop speakers and three late contributed papers are included in the Appendix.

All the invited papers included in this volume have followed the current procedure in scientific journals. The manuscripts were reviewed twice: first by members of the International Scientific Committee and then by referees selected by the ISC members and agreed by the chairman of the Local Organizing Committee representing the Guest Editors of this issue.

The contributed papers presented in the poster sessions during the conference were published in the five volume set of the Proceedings of Contributed Papers and distributed to all conference participants.

The additional copies of the Proceedings are available through the IPPLM in Warsaw.

The Guest Editors want to express their acknowledgement to the authors for their hard work in preparing the manuscripts and to all the referees for their time and effort devoted to revision the invited papers.

We are grateful to the Editorial Committee of the Journal of Technical Physics for dedicating this Special Issue to the XXIV ICPIG conference.

Finally, we also want to thank the Publisher for their perfect cooperation.

Guest Editors: Tadeusz Pisarczyk
Jerzy Wołowski
Paweł Pisarczyk

Preceding Page's Blank

SUMMARY
of the XXIV International Conference on Phenomena
in Ionized Gases
11 - 16 July, Warsaw, Poland

1. General

The XXIV International Conference on Phenomena in Ionized Gases is a subsequent conference in the series of meetings being organized biennially with participation of 400-500 attendees, the last having been held in Toulouse, France, in 1997.

The ICPIG is the only international conference comprising a full range of low-temperature plasma which, produced by various methods, has some common physical properties. For a long time such a plasma has found very broad applications (e.g., in lighting engineering, processing of metals, plasma engines, etc.) which are still being improved thanks to investigations. New sensational possibilities of employment of such a plasma are still emerging (e.g., plasma sources of ions, electrons, and X-rays used in material technology, equipment applied in environment protection, plasma displays, etc.).

The scientific program of the ICPIG conferences, selection of the invited lectures and guidance for the Local Organizing Committee (LOC) are the responsibility of the **International Scientific Committee (ISC)**.

The ICPIG conferences are an important forum for promotion of investigations and applications of plasma in developing countries. The ICPIG has traditionally been the principal forum for scientific exchange between researchers in plasma physics and technology in Eastern and Western European countries.

The XXIVth International Conference on Phenomena in Ionized Gases was held in **Warsaw centre at the campus of the Warsaw University**, from 11th to 16th July 1999.

The local arrangements for the conference were made by the **LOC** in co-operation with the **Institute of Plasma Physics and Laser Microfusion (IPPLM)** in Warsaw.

2. Scientific program

Subject areas. The XXIV ICPIG subject areas presented in **Table 1**, were updated by the ISC in April, 1998. As previously, the scientific program of the conference was completed with additional topics related to important applications of plasma. Two topics which had previously been proposed for the XXIII ICPIG in Toulouse, in 1997, were included in the fixed topical set as topics No. 19 and 20 in the subject areas. As topic 21, the special topic was included in the subject areas according to the suggestion given by the LOC. This topic relates to plasma generated in Z-pinches and plasma-focus devices. These plasmas find various applications e.g. in material technologies and development of protections against neutrons and X-rays.

Invited papers. The ISC invited scientists from 21 countries to give lectures devoted solely to the proposed topic of the lecture and the research output of the lecturer. The ISC approved of the list of **8 general lectures** (containing reviews of broad fields of interest) and **24 topical lectures** (presenting specialized reviews of topics included in the conference). One topical lecture was cancelled (due to the illness of the speaker). The invited papers were refereed twice: first by an ISC member and next by a referee appointed by the ISC member in agreement with the chairman of the LOC representing the Guest Editors of the Special Issue of the Journal of Technical Physics (this volume).

Contributed papers. A total of **468 contributed papers** (including 6 "very late" papers not printed in the proceedings) had been reviewed and accepted by the LOC for poster presentation. The presenter was one of the co-authors registered as a conference participant.

Table 1 shows the number of posters divided according to subject areas.

A five volume set of the **Proceedings of Contributed Papers (462 works)** was printed before the conference and distributed during the conference. This set consisted of one volume for each of four days when poster sessions were held. The fifth volume contains the "late" contributed papers.

The additional sets of the Proceedings are available for sale (US\$ 60) at the address of the IPPLM in Warsaw.

3. Conference Workshop

The ICPIG conferences traditionally unite cognitive and applicable aspects. Also the XXIV ICPIG was of the same character. The applicable aspect was manifested among the others, by organizing the Conference Workshop on industrial applications of low-temperature plasma physics. The Workshop topics and their speakers invited by the LOC were as follows:

1. Pseudospark discharge: physics and applications, *W. Hartmann (Siemens, Erlangen, Germany)*
2. Industrial applications of e-beam plasma to air pollution control (electric plant "Pomorzany"), *A. G. Chmielewski (INCT, Warsaw, Poland)*
3. Supersonic plasma jets and their influence on aerodynamics of flight, *A. A. Alexandrov, (M.S.Univ, Moscow, Russia)*
4. Studies and applications of dense magnetized plasmas for isotope separation in plasmas, *A. I. Karchevsky (M.P.I., RRC Kurchatov Inst., Moscow, Russia)*
5. Table-top plasma for industrial and domestic applications, *J. van der Mullen (Tech.Univ., Eindhoven, The Netherlands)*
6. Magnetron sputtering of materials based on nanocomposite coatings, *J. Musil (Univ. West Bohemia, Plzen, Czech Republic)*

About **250 people** participated in the Conference Workshop.

Table 1. Number of poster divided among the different topics.

Topics	Number of posters
1. Kinetics, thermodynamics and transport phenomena	18
2. Elementary processes	23
3. Low-pressure glows	40
4. Coronas, sparks, surface discharges and high-pressure glows	31
5. Arcs	31
6. High-frequency discharges	46
7. Ionospheric, magnetospheric, and astrophysical plasmas	6
8. Plasma diagnostic methods	36
9. Plasma wall interactions, electrode and surface effects	18
10. Physical aspects of plasma chemistry, plasma processing of surfaces and thin film technology	47
11. Generation and dynamics of plasma flows	8
12. Non-ideal plasmas. Clusters and dusty plasmas	21
13. Waves and instabilities, including shock waves	17
14. Nonlinear phenomena, self-organization and chaos	10
15. Particle and laser beam interaction with plasmas	24
16. Plasma sources of radiation	24
17. Numerical modelling	36
18. Plasmas for environmental issues	12
19. Highly ionized, low-pressure plasmas (plasma thrusters, ion sources and surface treatment)	8
20. High-pressure, non-thermal plasmas	1
21. Special topic to be emphasized (at the XXIV ICPIG): high-current discharges (Z-pinches, plasma-focus, plasma X-ray sources, etc.)	11
Total	468

4. Von Engel Prize and prizes for the best posters

The "Von Engel Prize" was established in 1998 in place of the Penning Prize awarded during the previous ICPIG conferences. This prize is sponsored by the "Hans von Engel and Gordon Francis Fund" and is administered by the University of Oxford. The prize, comprising of US\$ 1000 and a certificate, will be awarded every two years to an individual for the achievements in the field of physics and technology of plasmas and ionized gases, as covered by ICPIG meetings.

The first von Engel Prize was awarded during the XXIV ICPIG to Prof. R. Balescu who presented a special lecture: "Some reflections about transport in plasmas".

The ISC awarded three prizes for the best posters relating to an experimental work, a theoretical work and to work on numerical simulation. Apart from substantial and graphical quality of the poster its compliance with the corresponding paper were taken into account. The winners were as follows:

- for the experimental work - "Dust as a sheath diagnostic" prepared by *D. A. Law, E. B. Tomme, W.H. Steel, B. M. Annaratone, and J. E. Allen (United Kingdom)*,
- for the theoretical work - "Formation of oscillatory sheath structure in electronegative plasmas" prepared by *A. Kono (Japan)*,
- for the work on numerical simulations - "Two-temperature, two-dimensional modelling of cathode-plasma interaction electric arcs" prepared by *J. Wendelstoft (Germany)*.

5. Participation

A total of 411 scientists coming from 42 countries (see Table 2) were registered as the participants at the XXIV ICPIG. There were also about 40 registered accompanying persons. The conference fee was waived for about 90 participants. More than 100 participants had paid a reduced conference fee. A partial financial assistance for local expenses was also given to some participants from poorer countries.

6. Conference program

The conference program comprised **oral and poster presentations**. 8 general lectures were given in plenary sessions. 23 topical lectures were delivered in two parallel sessions covering different subjects. There were three lectures on similar subjects in each topical session. The invited lectures were not in parallel with poster sessions.

The contributed papers (accepted by the LOC) were presented during 7 poster sessions, each 2.5 hour long (including coffee breaks).

The **Conference Workshop** on industrial application of plasma physics (open to all registered participants) was held on Sunday afternoon, 11 July and comprised six lectures.

The **von Engel Prize award and lecture** were delivered before the Closing Ceremony on Friday morning, 16 July. The diplomas and gifts were handed to the authors of the best posters before the von Engel Prize award.

7. Social events

A welcome reception for all participants and accompanying persons was held on Monday evening, 12 July. The conference banquet for the persons who had purchased the banquet tickets and the persons invited by the LOC was held on Thursday evening, 15 July. During the conference there were six excursions for

the accompanying persons and two excursions for the participants (on Wednesday afternoon, July 14).

Table 2. Number of participants coming from different countries.

Country	Number of participants	Country	Number of participants
1. Algeria	1	22. Italy	10
2. Argentina	1	23. Japan	66
3. Australia	3	24. Korea South	1
4. Austria	3	25. Mexico	3
5. Belarus	4	26. Moldova	1
6. Belgium	4	27. Norway	2
7. Brazil	1	28. Poland	50
8. Bulgaria	3	29. Portugal	7
9. Canada	1	30. Romania	1
10. China	1	31. Russia	51
11. Croatia	2	32. Slovakia	2
12. Czech R.	26	33. Slovenia	2
13. Egypt	3	34. Spain	3
14. Estonia	3	35. Sweden	3
15. France	39	36. Switzerland	3
16. Germany	33	37. Syria	2
17. Hungary	3	38. The Netherlands	6
18. India	2	39. Ukraine	7
19. Iran	1	40. UK	2
20. Ireland	2	41. USA	20
21. Israel	2	42. Yugoslavia	3
		Total	411

On behalf of the Local Organizing Committee:

Chairman of XXIV ICPIG
Jerzy Wołowski

Secretary of XXIV ICPIG
Tadeusz Pisarczyk

The next XXV ICPIG conference will be held in Nagoya,
Japan, July, 2001.

CONTENTS¹

- 003 *Preface*
- 005 *Summary of the XXIV ICPIG*
- 013 R. FRANKLIN, *Hans von Engel and the ICPIG conference*
- 015 **Lecture presented by the von Engel Prize winner:**
R. BALESCU, *Some reflections about transport in plasmas*

General invited lectures

- 023 A. DALGARNO, *Atomic and molecular processes in astrophysical plasmas*
- 035 O. JOUBERT, P. SCHIAVONE, L. VALLIER, D. FUART, L. DESVOIVRES, P. SCHIAVONE, C. MONGET, P. GOURAUD and P. CZUPRYNSKI, *Trends in plasma processing for ultra large scale integration technology*
- 051 T. LETARDI, F. FLORA, C. E. ZHENG, P. DI LAZZARO and S. BOLLANTI, *Soft X-ray generation by laser interaction with matter*
- 073 A. D. R. PHELPS, *Novel relativistic electron beam experiments providing new microwave sources*
- 089 K. U. RIEMANN, *Theory of the plasma-sheath transition*
- 123 M. SADOWSKI, *Studies and applications of dense magnetized plasmas*
- 147 M. ŠKORIĆ, T. SATO, A. MALUCKOV and M. JOVANOVIĆ, *Complexity in laser plasma instabilities*
- 165 S. TORVÉN, *Electron beam-plasma interaction in laboratory and space*

Topical invited lectures

- 183 A. BOGAERTS and R. GIJBELS, *Modeling of radio-frequency and direct current glow discharges in argon*
- 203 G. COLONNA, I. ARMENISE, M. CATELLA and M. CAPITELLI, *Non equilibrium effects in plasma expansion flows*
- 215 S. ELIEZER, *The inverse Faraday effect in plasmas and its possible applications*
- 227 M. T. C. FANG, J. D. YAN, and R. E. BLUNDELL, *Recent progress in our understanding of the physical processes in arcs in gas flow*
- 239 P. J. M. BADIE and PH. BERTRAND and G. FLAMANT, *Complete temperature monitoring in a pilot transferred-arc plasma furnace*
- 257 J. HAIDAR, *Metal droplet formation in gas metal arc welding*
- 273 E. J. M. VAN HEESCH, A. J. M. PEMEN, K. YAN, P. P. M. BLOM, P. A. H. J. HUIJBRECHTS and P. C. T. VAN DER LAAN, *Pulsed corona for sustainable technology*
- 293 V. I. KARAS', V. A. BALAKIREV, YA. B. FAINBERG, I. V. KARAS', E. A. KORNILOV, V. D. LEVCHENKO, YU. S. SIGOV and G. V. SOTNIKOV, *Nonlinear phenomena and self-organization structures in plasmas*
- 307 T. KLINGER, N. O. KRAHNSTÖVER, T. MAUSBACH and A. PIEL, *Taming instabilities in plasma discharges*

¹Underlined names correspond to authors who presented orally the lecture.

- 325 U. KORTSHAGEN and B. HEIL, *Kinetic modeling and experimental studies of large-scale low-pressure RF discharges*
- 345 T. MAKABE, *Modeling and diagnostics of two-frequency pulsed CCP and related charging in the microstructure of SiO₂ trench*
- 361 K. MORAWETZ, V. ŠPIČKA and P. LIPAŤSKÝ, *Nonlocal transport and correlations in strongly interacting Fermi systems*
- 377 T. NEGER, *Advanced techniques of plasma diagnostics using coherent optics*
- 391 H. L. PÉCSELI, S. H. HØYMØRK, B. LYBEKK, J. TRULSEN and A. ERIKSON, *Solitary waves in the earth's upper ionosphere*
- 401 A. M. POINTU and G. MODREANU, M. GANCIU, N. B. MANDACHE, M. NISTOR and I. IOVITZ POPESCU, *Electron beams generated in hollow cathode low pressure transient discharges*
- 421 G. POPA and V. ANITA, *Transitory phenomena in reactive magnetron discharge*
- 439 N. SATO and S. IIZUKA, *Plasma control for next-stage plasma processing*
- 449 J. SKALNY, *The role of electronegative impurities in ozone generation by high pressure discharges*
- 469 P. S. STRELKOV, *Plasma high-power microwave sources driven by relativistic electron beams*
- 485 A. L. VIKHAREV, *Gas discharge produced by strong microwaves of nanosecond duration*
- 505 Y. WATANABE, M. SHIRATANI, T. FUKUZAWA and K. KOGA, *Growth processes of particles up to nanometer in high-frequency SiH₄ plasmas*
- 521 E. WORYNA, J. KRÁSA, L. LÁSKA, K. MAŠEK, P. PARYS, K. ROHLENA and J. WOŁOWSKI, *Laser-produced plasma as an effective source of multicharged ions*

Appendix

Lectures presented at the Conference Workshop

- 533 A. F. ALEXANDROV, N. V. ARDELYAN, S. N. CHUVASHEV, A. P. ERSHOV, A. A. RUKHADZE, I. B. TIMOFEEV, B. I. TIMOFEEV and V. M. SHIBKOV, *Supersonic plasma flows and their influence on aerodynamics of flight*
- 551 A. G. CHMIELEWSKI, Z. ZIMEK, E. ILLER, B. TYMIŃSKI and J. LICKI, *Industrial applications of e-beam plasma to air pollution control*
- 573 D. A. DOLGOLENKO, N. M. GORSHUNOV, A. I. KARCHEVSKY, V. S. LAZKO, Yu. A. MUROMKIN, V. G. PASHKOVSKY, A. T. PESHKOV, E. P. POTANIN and G. E. ZOTIN, *A review of experimental and theoretical investigations of stable isotope separation by plasma methods*

Late contributed papers

- 589 E. ABU ASSALI, *On the theory of non-reciprocal surface electromagnetic waves in semi-bounded magnetized electron plasma*
- 593 D. N. GERASIMOV, O. A. SINKEVICH and V. F. CHINNOV, *Periodic structures in thermal dusty plasmas*
- 597 D. GRONDONA, H. KELLY, A. MÁRQUEZ and F. MINOTTI, *Electrostatic probe measurements in the outer region of a nitrogen operated pulsed low pressure arc*
- 603 **Author Index**

HANS VON ENGEL AND THE ICPIG CONFERENCE¹

R. FRANKLIN

THE OPEN UNIVERSITY

Fox Combe Hall Boars Hill Oxford, UK

In 1953 a conference on ionization phenomena in gases was held in Oxford organized essentially by Hans von Engel and Gordon Francis as Chairman and Secretary respectively.

There was some national support in Britain but the Physical Society was of the opinion that 'it was doubtful if there was sufficient demand for there to be a regular international conference in the subject area'.

However, such interest and enthusiasm was generated that a second conference was held in Delft in 1955 and a third in Venice in 1957.

The fourth in Uppsala in 1959 marked a coming to maturity with the conference proceedings being published in proper book form and since then they have formed part of the scientific literature.

During the 1961 conference in Munich the Berlin Wall went up to the dismay of many, including participants of the conference.

Von Engel was sensitive to the position in Europe and what it meant for scientists. He had survived two crises in his life. The first was when he turned his back on his Austro-Hungarian family estate (he was entitled to call himself Baron) and became a practising scientist. The second occurred in 1939 when he left his post at Siemens and a fruitful collaboration with Steenbeck over several years which gave rise to the two volume work which was the standard textbook *Elektrische Gasentladungen*.

And so for a number of years the conference, which had by then acquired its present title, alternated between countries in the Eastern and Western blocs. This had its effect on attendance but even those whose travel was restricted could attend every other conference and almost inevitably a country's representation was strongest when it was host.

In 1971 the Conference was again in Oxford with von Engel again Chairman but this time I was one of the Secretaries. During that meeting a constitution

¹The speech delivered by Prof. R. Franklin before awarding Prof. R. Balescu with the von Engel Prize.

was developed giving the conference and its International Scientific Committee continuity and a standing with bodies such as IUPAP.

The 1971 meeting was a financial success and the profits were used to establish the Gordon Francis Fund which over the years since then has enabled a significant number of younger scientists from Oxford to attend the Conference.

Hans von Engel was himself a regular attender at the conferences and in particular enjoyed his television interview in Berlin in 1977 when he informed his interviewer that "organizing a conference was rather like having a baby". Since he was male and had no children of his own I wondered what the basis was for his simile, the interviewer was at a loss for words.

In the fulness of time there came the idea of a prize to recognize achievement in the field and contribution to the conference. The Philips Company sponsored the prize for four successive awards. Fittingly Hans von Engel was the first recipient of the Penning Prize in 1991. But unfortunately his health did not allow him to travel to Barga to receive it and he died a few months later.

When it was learned that Philips were withdrawing their support there was dismay amongst regular attenders but also a palpable desire to continue the concept of a prize. That has been achieved through a private benefaction augmenting the Gordon Francis Fund so that it is now the Gordon Francis and von Hans Engel Fund with a primary purpose of ensuring continuity of the von Engel Prize for so long as the conference continues to flourish. This also provides a way of remembering a remarkable individual who overcame several setbacks in his own life *and yet* assisted many young people to fulfilling scientific careers. I count myself privileged to be one of them.

Let me end with the story of how he came to write *Ionized Gases*. On a visit to the United States he learned from the (so-called) Department of Justice that during the Second World War they had seized the copyright to *Elektrische Gasentladungen*. His reply was "I will write another book which will be so different, your copyright will be worthless". That reply is typical of the man and his book is well known to most, if not all, present today. If he were still alive this would be his one hundredth year and yet he would be surprised by the success of what he started.

Lecture presented by von Engel Prize winner

SOME REFLECTIONS ABOUT TRANSPORT IN PLASMAS

R. BALESCU

ASSOCIATION EURATOM-ETAT BELGE, UNIVERSITÉ LIBRE DE BRUXELLES, CP 231

Campus Plaine ULB, Bd. du Triomphe 1050 Bruxelles, Belgium

I should like to say, in the first place, how happy and honoured I feel upon receiving the first von Engel prize. It has been a wonderful surprise! I wish to express my deep gratitude to the International Scientific Committee of the International Conference on Phenomena in Ionized Gases and the von Engel Foundation for this honour bestowed to me.

Hans von Engel was one of the earliest pioneers of the physics of ionized gases. Upon re-reading his first 2-volume treatise (written in collaboration with M. Steenbeck) "*Elektrische Gasentladungen: ihre Physik und Technik*" [1] one cannot but be impressed by the amount of information accumulated at the time, and especially by the clarity and the modernity of the text. The book can be read today as easily as a contemporaneous one, without any feeling of archaism. Together with a large amount of experimental (and technical) data, a simple, but accurate and meticulous theoretical explanation of the phenomena is provided. The remarkable fact is that with such simple tools a consistent overall picture emerges for the extraordinarily complex superposition of processes taking place in a gas discharge.

Von Engel used in 1932 the term "*plasma*" (originally due to Langmuir) in the very special meaning of a fully ionized gas, and studied some of its properties (in particular, the plasma oscillations)¹; but at that time it seems that such a state of matter was still considered as rather exceptional. The omnipresence of plasma in the universe was not realized at that time: a typical statement from the book (vol. 2, §13) is: "Da nun in Wirklichkeit niemals - vielleicht mit Ausnahme von Nebelsternen - ein Plasma ohne äußere Störung sich selbst

¹Note that the title of von Engel's last book is "*Electric Plasmas: their nature and uses*" [2]: here the term "plasma" is given its modern meaning, covering both fully and partially ionized gases.

überlassen bleibt, sondern da zur Erhaltung des Plasmas irgendeine elektrische Entladung notwendig ist...²"

One fact appears clearly in von Engel's 1932 book: the crucial importance of *transport phenomena* in understanding the behavior of plasmas. Diffusion, heat conduction and electrical currents are the basic ingredients necessary for understanding what happens in any system out of equilibrium. In such a system the density, the temperature and the electric potential are spatially inhomogeneous. The system then tends to equalize these quantities: this produces fluxes of particles, heat and electric charge. But the detailed transport mechanisms can be incredibly complex; their study may involve contributions from most fields of physics.

The simplest situation occurs in neutral gases. It was known since Boltzmann (1872) that the diffusive fluxes were determined by a competition between free motion of the molecules and their mutual elastic collisions. Whenever a sufficiently strong electric field is applied, the situation changes radically. The competition is now between free motion of neutrals and accelerated motion of charged particles on one hand, and on the other hand elastic and inelastic collisions of all kinds (excitations and de-excitations, ionizations and recombinations, chemical transformations,...). von Engel was a master in constructing a consistent picture of these extremely complex processes by using very elementary descriptions of the collision processes. The input for a complete explanation requires the (experimental or theoretical) knowledge of cross-sections for all these collision processes, a formidable task which is far from being exhausted in the present time.

The picture sketched above is valid for weakly ionized gases. When we consider a fully ionized plasma the picture is again quite different. The difficulties due to the atomic processes are no longer present, but another difficulty creeps in. von Engel was quite conscious of this in 1932: the interactions between charged particles could no longer be described by the simple concept of *collisions* of the same kind as in a neutral gas. This is due to the long range of the Coulomb force. Von Engel's description went as follows: The entire space is filled with an electric field produced by the charged particles; it depends on the instantaneous positions of the particles and is therefore wildly changing in space and time. He called this the *microfield*. A description of the transport processes in the plasma required a statistical study of the microfield.

At the time of the publication of the von Engel-Steenbeck treatise, there existed a very successful theory of electrolyte solutions due to Debye and Hückel in 1923. It had introduced the important concept of a self-consistent average field which described the dominant collective effects in a system of charged particles (in equilibrium). It is very strange to note that this development (in physical chemistry) had no immediate impact on the theory of gas discharges. Even the fundamental concept of Debye length is not mentioned by von Engel and

²Since in reality - perhaps with the exception of nebular stars - a plasma cannot be self-sustained without an external factor; for the conservation of a plasma some electrical discharge is necessary...

Steenbeck. The average field is bypassed by the authors³ and only the much more complicated field fluctuations are treated, necessarily in a very primitive way. It was only in 1938 that Vlasov derived an equation for the evolution of the plasma distribution function under the action of a self-consistent average field, much in the spirit of the Debye-Hückel theory. This equation was promised to an extremely wide success for the description of certain properties of plasmas, especially in the very high temperature regime, where the collision frequency is quite small, and which became crucial when fusion research started to develop.

The problem of the fluctuating microfield posed by von Engel remained, however, open. In 1936 a first important approach was attempted by Landau. Instead of focussing on the microfield statistics, he turned to the statistics of its sources, i.e., the particles: this was an important step. In order to describe Coulomb collisions, he retained the idea that, because of the long range of the electric forces, the particles influence each other even at large distance, when the intensity of the interactions is small. As a result, he expanded the Boltzmann kinetic equation and obtained a limiting kinetic equation which bears a superficial resemblance to the Fokker-Planck equation of Brownian motion theory. This equation, combined with the Vlasov equation, is still used in our days as a simple approximation for the Coulomb collisions. It appeared, however, immediately that the Landau equation missed its target. The integral defining its coefficients diverge, both at small distance and at large distance. The reason for the former divergence is obvious (at small range the weak coupling condition breaks down), but the large distance divergence was quite disturbing. It clearly meant that the Landau weak coupling approximation did not capture the whole specificity of the Coulomb interactions.

By the time when I was working on my PhD thesis (late fifties) enormous progress had been reached in nonequilibrium statistical mechanics. Several approaches (Kirkwood, Bogolyubov, Prigogine) - which later proved to be equivalent - led to rigorous derivations of the "classical" kinetic equations (Boltzmann, Landau) from first principles, by using perturbation expansions in some small parameter, such as the electric charge e for the Landau equation. This progress was due, in particular, to the impact of the methods developed in quantum field theory. At the same time, Joseph Mayer had obtained a remarkable derivation of the *equilibrium* Debye-Hückel theory by using orthodox methods of statistical mechanics (the virial series). The striking feature of his theory is the fact that an *infinite subseries* of contributions to the virial series, defined by a precise criterion, had to be summed in order to obtain the equilibrium Debye theory.

Given that "environment", it was pretty straightforward to try combining these various approaches for obtaining a transport theory for plasmas. Nonequilibrium statistical mechanics provided the "raw material", i.e., a systematic rule for constructing all possible contributions to the perturbation series (in powers of the charge) for the time-dependent distribution function of charged particles. This produces, however, an enormously intricate forest of terms, each of which can be identified visually by a diagram, that is in one-to-one correspondence

³The only (implicit) use of the average field appears in the very short chapter on plasma oscillations, where the electron plasma frequency ω_{pe} is derived.

with the mathematical expression. In order to create a path through this forest I needed an additional criterion, which came from the Debye equilibrium theory. The screened Debye potential is well-known:

$$(1) \quad V_D(r) = \frac{e^2}{r} \exp(-\kappa r), \quad \kappa = \left(\frac{4\pi e^2 n}{T} \right)^{1/2},$$

where e is the charge, n the particle density and T the temperature (in energy units). Remarkably, the charge appears in two forms: once as a prefactor of the potential, and also within the inverse Debye length κ which enters the argument of the exponential. In order to obtain a theory consistent with Debye's, and in which the plasma is considered weakly coupled, one should keep in the perturbation series the dominant contributions in the "bare" charge e^2 , but simultaneously retain the combination $e^2 n$ to all powers. The diagram technique allows the easy identification of all the terms fulfilling this criterion. From here on mathematics did its job. Fortunately, it turned out that the infinite series could be summed exactly in closed form. The result is a kinetic equation for the evolution of the distribution function of a weakly non-ideal, fully ionized plasma [3, 4]. It has the general form of the Landau equation, but the Coulomb interaction potential is replaced by an effective potential that is self-consistently defined in terms of the unknown distribution function. This potential changes synchronously with the evolution of the distribution function. As a result, the equation is very strongly nonlinear (which makes its solution very difficult). This nonlinearity expresses the *collective character of the collision process*, which could be described as a superposition of two-body, three-body, four-body,... collisions. Seen from another perspective, the collision process involves the whole plasma environment, which is permeated by the fluctuating "microfield" defined by von Engel.⁴

This kinetic equation thus solved the problem of the definition of the Coulomb collisions in a plasma. This does not imply by any means that it solved the problem of transport in plasmas! The collective nature of the plasma phenomena shows up not only in the fluctuations of the microfield at atomic length scales, but also as waves at all intermediate scales up to macroscopic ones. The creation, mixture and annihilation of these waves gives rise to an enormously complex *turbulent state* of the plasma which is by no means exceptional, but is rather the common state of a real high-temperature magnetically confined plasma. It appeared quite soon that the measured values of the transport coefficients (e.g., the diffusion coefficient) of the electrons in a tokamak plasma exceed by two to three orders of magnitude the values computed from the "classical" kinetic equations.

⁴When this work was finished and sent to publication in 1961, I obtained from my friend Melville Green a preprint of a paper which was sent simultaneously to another journal: I was amazed to find out that A. Lenard had obtained exactly the same equation, quite independently and by a different method [5]. (I first met Lenard twenty years later at a Conference in Vienna commemorating Boltzmann's kinetic equation!) A little later, I learned that R.L. Guernsey also obtained the same kinetic equation (but published it only as an internal report). Thus, the same ideas popped up simultaneously at locations separated by thousands of kilometers!

The collisions become very rare at the high temperatures of the fusion plasmas. The transport phenomena are then mainly controlled by wave-particle and wave-wave interactions. Their description requires a "second level" of statistics. The particle distribution functions no longer obey deterministic kinetic equations, but must be considered as random quantities because of the presence of turbulent field fluctuations. The determination of the so-called *anomalous transport coefficients* is a problem presenting enormous difficulties: it is still open at the present time, in spite of enormous theoretical and computational efforts in view of its solution.

The influence of turbulence on transport is not only a quantitative one. It is well-known that the "classical" theory of transport is governed by Onsager's symmetry principle⁵. The transport matrix relating linearly the vector \mathbf{J} of the fluxes (particle flux Γ , heat flux \mathbf{q} , electric current \mathbf{j}) to the corresponding vector of thermodynamic forces (pressure gradient ∇P , temperature gradient ∇T , electric field \mathbf{E}) is symmetric. This is a direct consequence of a deep property of the collision operator (self-adjointness). In presence of turbulence, the transport coefficients may be represented as sums of a classical part and an anomalous part. (Note that this decomposition is made solely for theoretical convenience; the two parts cannot be determined separately.) The transport equations are then written as:

$$(2) \quad \mathbf{J} = (\mathbf{T}_{cl} + \mathbf{T}_{an}) \cdot \mathbf{X}.$$

Onsager's principle tells us that the classical matrix equals its transpose: $\mathbf{T}_{cl} = \mathbf{T}_{cl}^T$. It can be shown from rather general arguments that the symmetry breaks down for the anomalous transport matrix [6]: $\mathbf{T}_{an} \neq \mathbf{T}_{an}^T$. This is because some of the basic assumptions of the Onsager theorem break down in turbulent systems.⁶

The effect of turbulence on transport can be even deeper. Consider, for simplicity, the diffusion flux, defined by the transport equation: $\Gamma = D(-\nabla n)$, where D is the diffusion coefficient. Combined with the continuity equation, it yields the well-known diffusion equation for the density profile $n(x, t)$: $\partial_t n = D \nabla^2 n$. It is well known that the latter equation can be understood stochastically. $n(x, t)$ is then interpreted as the probability distribution of an ensemble of particles undergoing a random walk under the action of collisions and/or field fluctuations. Let $x(t)$ be the instantaneous position of a particle starting at the origin. It is easily shown [7] that, if the diffusion equation is valid, the *mean square deviation* is a linear function of time (at least in the limit of long time):

⁵The forthcoming statements are oversimplified. We consider systems in absence of magnetic field, and make no distinction between electron and ion temperatures. The results are, however, easily generalized.

⁶This point gave rise to some polemic discussions in the literature. Let me just mention here that the authors who claim to have obtained a symmetric transport matrix are using different sets of forces and fluxes for the classical and the anomalous part of the matrix. The symmetry in the new set of variables does not, in general, imply the symmetry in the original (physical) representation.

$$(3) \quad \langle x^2(t) \rangle \equiv N^{-1} \int dx x^2 n(x, t) = 2D t.$$

Such a *diffusive behavior* is, however, not guaranteed in a turbulent plasma. Rather, all possibilities of the following type are, *a priori*, possible:

$$(4) \quad \langle x^2(t) \rangle = B t^\alpha.$$

The real number α is called the *diffusion exponent*. Whenever $\alpha \neq 1$ we deal with *strange transport*⁷. Two cases are distinguished:

$$\begin{aligned} \alpha &> 1 : \text{Superdiffusion,} \\ \alpha &< 1 : \text{Subdiffusion.} \end{aligned}$$

The subdiffusive case is particularly interesting for plasmas in presence of a fluctuating magnetic field. The reason is that particles (or guiding centers) tend to stick to the field lines. When collisions are rare, the transport across the magnetic field is controlled by the field fluctuations and gives rise to a subdiffusive process with $\alpha = \frac{1}{2}$ [8], [9]. This process is connected to a *continuous time random walk*. Instead of a diffusion equation, the density profile obeys a *non-markovian diffusion equation* of the form:

$$(5) \quad \partial_t n(x, t) = \int_0^t d\tau H(\tau) \nabla^2 n(x, t - \tau).$$

Another interesting case is provided by the magnetic field structure in a tokamak or a stellarator. It is well-known that in presence of spatial perturbations (due to external and/or internal sources) the regular structure of nested toroidal magnetic surfaces is deformed. In the neighborhood of rational surfaces there appear magnetic *islands* lined with chaotic layers and separated from each other by undestroyed (KAM) surfaces. Upon increasing the amplitude of the fluctuations the thickness of the chaotic regions increases, more surfaces are destroyed and eventually the chaotic region invades the whole plasma. The physically useful case (because it corresponds to confinement) is the former case of incomplete chaos; it also poses, however, the most difficult mathematical problem. It has been shown, semi-numerically, that a magnetic line starting in a chaotic layer progressively fills the latter by undergoing a typical subdiffusive behavior [9, 10]. Its motion is again slowed down because of its sticking to the island surface.

⁷Physicists working in the field of dynamical systems use the term *anomalous transport* for this phenomenon. We prefer the present terminology in order to make a distinction with the "anomalous transport" introduced above (a name currently used in plasma physics), which is diffusive, but non-collisional, hence controlled by the turbulent fluctuation spectrum.

These few examples should suffice to suggest that the field of *plasma transport theory*, brilliantly started by the pioneers of plasma physics, in particular by Hans von Engel seventy years ago, is more active than ever, appealing to almost all fields of physics. Its importance is crucial in numerous applications. Among others we may quote gas discharges, fusion physics, geophysics, astrophysics, not forgetting its quantum version appearing in condensed matter physics. As some problems are solved, new ones appear at the horizon. The younger generations will still be active for decades to come.

References

1. A. von ENGEL and M. STEENBECK, *Elektrische Gasentladungen: ihre Physik und Technik*, 2 vols., Springer, Berlin, 1932, 1934.
2. A. von ENGEL, *Electric Plasmas: their nature and uses*, Taylor and Francis, London, 1983.
3. R. BALESCU, Phys. Fluids, **3**, 52, 1960.
4. R. BALESCU, *Statistical Mechanics of Charged Particles*, Interscience, New York, 1963.
5. A. LENARD, Ann. Phys. NY, **3**, 390, 1960.
6. R. BALESCU, Phys. Fluids, **B 3**, 564, 1991.
7. R. BALESCU, *Statistical Dynamics: Matter out of Equilibrium*, Imperial Coll. Press, London, 1997.
8. R. BALESCU, Phys. Rev., **E 51**, 4807, 1995.
9. R. BALESCU, Trans. Fusion Technol., **33** (2T), 192, 1998.
10. R. BALESCU, Phys. Rev., **E 55**, 2465, 1997.

**General
invited lectures**

ATOMIC AND MOLECULAR PROCESSES IN ASTROPHYSICAL PLASMAS

A. DALGARNO

HARVARD-SMITHSONIAN CENTER FOR ASTROPHYSICS
Cambridge, MA 02138, USA

A brief survey is presented of the sources of ionization in the Universe and a description is given of the physical atomic and molecular processes that determine the characteristics of the resulting plasmas.

1. Introduction

The Universe offers a broad range of plasmas, varying in density, temperature and degree of ionization, produced by a diversity of ionization sources. Atomic and molecular processes are central to the characterization of the responses of the matter to the ionization and exercise a substantial influence on the evolution of astronomical objects. They also provide diagnostic probes of the physical conditions in their creation of photons which collected by telescopes are our major source of information about the Universe. I present here an account of some of the sources of ionization in the Universe and discuss the atomic and molecular processes that occur.

2. Early Universe

According to the standard cosmology, the big bang cosmology, the Universe expanded from a singularity. It was very hot, too hot for any composite particle to exist except as a transient species quickly destroyed by the intense radiation field and by energetic collisions. The Universe was a plasma, a gluon plasma, in which the main constituent consisted of quarks. The expansion was adiabatic and the Universe cooled rapidly to a temperature at which quarks could combine and remain combined in the form of protons. The protons captured electrons to form neutrons and after about 200 seconds a brief period of nucleosynthesis ensued in which ^4He nuclei were created together with trace amount of ^3He , ^2H and ^7Li nuclei.

The temperature was about 10^9 K and the Universe was a fully-ionized electron plasma with no bound electrons, irradiated by photons. Radiation and matter were closely coupled by Thompson scattering of photons and electrons and shared a common temperature.

The Universe then coasted for about 100,000 years, gradually getting colder and less dense. Any recombination of electrons and charged nuclei that occurred was immediately reversed by photoionization and by electron impact ionization. Eventually though the temperature fell to about 4000 K, the supply of photons and electrons energetic enough to cause ionization diminished, and recombination took effect.

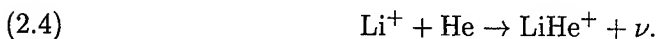
In this recombination era, the Universe was transformed from a fully-ionized plasma to an almost neutral gas. Thermal contact between electrons and photons was lost and radiation and matter subsequently evolved independently. The loss of contact permitted the formation of density enhancements in the matter which were later to be enlarged by gravitational accumulation to create the first distinct cosmological objects.

The recombination was radiative recombination. It was not a sudden event. It occurred sequentially in the order of the ionization potentials, beginning with the recombination of Li^{3+} ,



followed by the conversion of Li^{2+} to Li^+ , He^{2+} to He^+ to He and H^+ to H. The lithium was left mostly singly ionized because by the time photoionization and electron impact ionization of lithium which has an ionization potential of 5.4 eV became ineffective recombination of the major constituents of H and He was complete and there were few electrons left with which Li^+ could recombine.

With the formation of a neutral species, the helium atom, the formation of a stable molecular system became possible. The molecular ions HeH^+ , He_2^+ , and LiHe^+ came into existence by radiative association



All were removed by dissociative recombination



The net effect of the formation of molecular ions was a slight acceleration of the recombination of He^+ , H^+ and Li^+ .

With the recombination of H^+ , hydrogen atoms participated in exchange reactions



H_2^+ ions were later produced by radiative association



and the ions underwent charge transfer in collisions with hydrogen atoms



to create the first neutral molecular species, molecular hydrogen. The sequences that formed H_2^+ became effective sources of H_2 when the temperature had fallen so that photodissociation and electron impact dissociation of H_2^+ no longer occurred. Later still, negative ions H^- formed by radiative attachment,

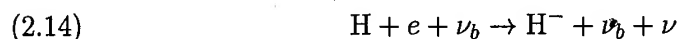
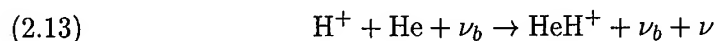


survived to react with H by associative detachment,



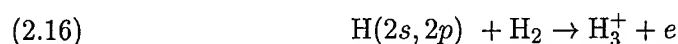
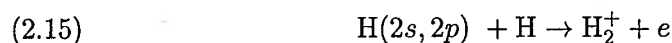
The sequence of (1.11) and (1.12) was the most abundant source of H_2 in the early Universe.

The formation of HeH^+ by radiative association and of H^- by radiative attachment is enhanced by the stimulated emission of photons by the cosmic background radiation field [1, 2].



but the effects on the molecular composition in the recombination era were small.

Associative ionization involving excited hydrogen atoms



played a minor role as sources of ionization.

Detailed accounts of the hydrogen, deuterium, helium and lithium early Universe chemistries and of the evolution of the molecular abundances of the different constituents have been presented [3, 4, 5, 6]. Molecular hydrogen is the most abundant molecular species with a fractional content of about 10^{-6} and relict electrons left after recombination are present at a fraction of about 10^{-4} .

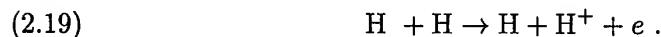
Because of the efficiency of molecules as coolants, the presence of H_2 and of HD, LiH, and LiH^+ had a substantial influence on the masses of the first collapsing objects. As the collapse proceeded and the density increased, molecular abundances were enhanced by three-body association. Pressure gradients built up and shocks developed in which ionization was initiated by associative ionization



polar ionization



and direct impact ionization



The rate coefficients of these reactions are not known. With the re-introduction of electrons, (2.18) being followed by (2.12), electron impacts



superseded (2.17)-(2.19) as a source of ionization.

The collapse ended in the creation of star-like objects in which nuclear energy was converted into electromagnetic radiation. A large supply of ultraviolet and X-ray photons was created that by photodissociating and photoionizing hydrogen molecules may have reversed the collapse and inhibited the collapse of other objects.

In the absence of the cooling due to H_2 the succeeding objects must have been massive. Nuclear reactions in the dense cores of the objects produced heavy elements and photons. Photoionization then caused the re-ionization and re-heating of the Universe, as evidenced by the limited presence of neutral gas in the intergalactic medium. The heavy elements were distributed into the Universe by stellar-like winds and supernova-like explosions and the Universe became complicated. A review of the evolution of the early Universe has been given by Lepp and Stancil [7].

3. Photoionized nebulae

Hot stars are sources of ultraviolet radiation which create around them ionized zones, manifested as extended regions of luminosity. Photoionization also produces visible emission from planetary nebulae, nova shells, starburst galaxies and active galactic nuclei [8]. Photoionization by photons of frequency ν emitted by the central stars



produces positive ions together with electrons of energy $E = h\nu - I_x$ where I_x is the ionization potential of the system X . The fast electrons e_f collide elastically with the ambient electrons e_a



and a Maxwellian velocity distribution is quickly established. For emission nebulae and planetary nebulae, temperatures may range from 5000 K to 15000 K. The hot electrons excite the constituents of the ionized gas and produce characteristic spectra from which the electron densities and temperatures and the element abundances can be inferred [9].

The spectra are recombination spectra produced in the radiative and dielectronic recombination of the ions and electron impact emission spectra produced by collisional excitation. There may be present also emission lines arising from charge transfer recombination of heavy ions which occurs if neutral gas is present in the plasma. An example of charge transfer recombination is the process

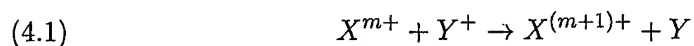


which leads to several emission lines near 300 nm and one at 559.2 nm. All of them have been detected in planetary nebulae [10].

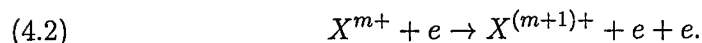
4. Collisionally-ionized gas

Hot gas in which collisions are energetic enough to cause ionization is found in the coronae of stars including the Sun, in young supernova remnants and in the hot phase of the interstellar medium. The ionization by collisions is balanced by radiative and dielectronic recombination. If the plasma is in a steady state, it is said to be in coronal equilibrium. The rates of ionization and recombination are both proportional to the electron density and are both functions of temperature. Thus in coronal equilibrium, the distributions of ionization stages depend only on temperature. The presence of the gas is indicated by emission lines of highly ionized material produced by electron impact excitation and dielectronic recombination and by absorption lines in the direction of hot stars. Thus the supernova remnant Puppis A emits strong lines of O^{7+} and Ne^{8+} [11] and the hot phase of the interstellar medium is suggested by the detection of absorptions at 103.2 nm and 103.8 nm by O^{5+} in the transitions $^2S_{1/2} - ^2P_{3/2}$ and $S_{1/2} - ^2P_{1/2}$ respectively [12]. The hot gas may be the result of overlapping fossil supernova remnants.

If charge transfer recombination of highly-ionized species occurs preferentially into the ground state of the parent, charge transfer ionization



may occur more rapidly than electron impact ionization



Examples are $\text{Si}^+ + \text{H}^+$, $\text{Si}^{2+} + \text{He}^+$ [13] and $\text{Fe}^+ + \text{H}^+$ [14].

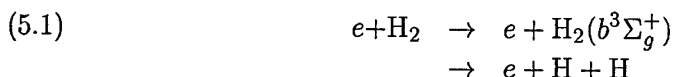
5. Shock wave ionization

Shock waves occur in compressible fluids when the pressure gradients are sufficient to generate supersonic motion. Because information about the pressure disturbance cannot propagate upstream faster than the velocity of sound, the fluid cannot respond before the shock arrives. The shock compresses and heats the fluid. Depending on the shock velocity, the shocked gas may be excited, dissociated and ionized. The subsequent recombinations and emissions produce photons which dissociate and ionize the gas ahead and behind the shock. This precursor radiation modifies the dynamical and thermal evolution of the gas. Any magnetic fields that are present can have a substantial influence. Shocks may be preceded by magnetic precursors, compressing and heating the gas ahead and behind the shock front.

Shocks are ubiquitous in astrophysics. In the interstellar medium, they are driven by supernova explosions, by stellar winds and by outflows from protostellar objects.

Detailed calculations have been carried out of the spectra resulting from the shocked gas in supernova remnants where shocks with velocities of several hundred km s⁻¹ occur and the shocked gas attains temperatures of the order of 10⁶ K. The spectra of the cooling recombining gas can be analyzed to infer the properties of the shocked gas and the velocity of the shock [15].

Slower shocks may be non-dissociative in which the molecules present in the pre-shock gas survive or dissociative, in which case H₂ is destroyed by electron collisions [16]



and other molecules are destroyed by exchange reactions such as



There are substantial differences between dissociative and non-dissociative shocks [17, 18, 19]. In non-dissociative shocks the heated gas enables endothermic reactions to proceed and the ionization structure is profoundly altered. The C⁺ ions that are the major ionization carriers in the diffuse pre-shock gas are converted to CH⁺ ions by the endothermic reaction



providing an additional source of CH⁺ and reducing the electron density because of the rapid removal of CH⁺ by dissociative recombination [19, 21]. In dissociative shocks, substantial abundances of molecular ions OH⁺, SO⁺ and HeH⁺ can be achieved [22]. The SO⁺ ion has been detected in many astrophysical sources [23] but it is also abundant in PDRs [24], which I describe next.

6. PDRs and XDRs

Photon-dominated regions (PDRs), also described as photodissociation regions [25], are regions of interstellar gas subjected to intense ultraviolet radiation. Molecular formation is driven by photoionization and molecular destruction is driven by photodissociation. The enhanced photoionization and photodissociation heats the gas and produces a boundary zone in which the temperature is elevated. The chemistry is then similar to that in the immediate post-shock gas following a non-dissociative shock. The increase in the production of C^+ ions enhances the abundance of CH^+ through the reaction (5.3) and of CO^+ through the sequence



which becomes efficient in warm gas, and



The presence of rotationally-excited CH^+ [26] and of the ion CO^+ [27, 28] are strongly suggestive of PDR's but they are also present in dissociative shocks [22].

XDR's are X-ray dominated regions in which gas is subjected to intense X-ray irradiation [29]. Close to an X-ray source, energetic electrons generated by X-ray absorption destroy molecules and ionize hydrogen and helium. The high-frequency X-rays are preferentially absorbed by heavy elements in inner shell transitions followed by Auger decays. The resulting plasma is hot. It contains highly charged atomic systems mixed with a substantial neutral component of hydrogen and helium. Charge transfer recombination processes are important in determining the distribution of the charge states.

With increasing distance from the source of X-rays, the plasma cools and molecules form in the warm gas by mechanisms similar to those operating in cooling shocked gas [30, 31]. Evidence to support this scenario is provided by the observations of Phillips and Lazio [32] who detected emission from HCO^+ offset from a probable hard X-ray source near the Galactic center. Their interpretation is supported by a detailed model [33].

7. Supernova ejecta

A supernova occurs when the iron core of a massive star collapses and the rebound shock drives an explosion leaving behind a neutron star. Supernova ejecta are powered by the radioactive decay initially of ^{56}Ni to ^{56}Co and ^{56}Co to ^{56}Fe . The ^{56}Co has a half-life of 77 days. For SN 1987A it has been overtaken as an energy source by ^{57}Co , ^{44}Ti and ^{26}Na . Today the main energy source of the continuing luminosity are the positrons from the decay of ^{44}Ti , the γ -rays escaping with little interaction with the now diffuse gas. The radioactive decays emit γ -rays and positrons. The γ -rays Compton scatter with the bound and free electrons and are degraded to X-rays. The X-rays are absorbed by the heavy elements, producing multicharged ions. The plasma is initially hot but it cools

rapidly as the ejecta expand and energy is lost by radiation. Radiative and dielectronic recombination remove the highly charged ions. Once recombination has produced neutral helium, charge transfer recombination occurs producing singly charged ions. The singly charged ions then undergo charge transfer processes such as



resulting in an ionization distribution dominated by ions such as Co^+ and Fe^+ that have low ionization potentials and which are slowly recombining by radiative recombination.

The molecular ion H_3^+ may be present in the envelope. Two emission features at $3.41 \mu\text{m}$ and $3.53 \mu\text{m}$ have been tentatively attributed to H_3^+ [34]. The chemistry is similar again to that of the early Universe but the ionization is provided by γ -rays. A successful model of the chemistry has been constructed [5].

8. Interstellar clouds

Interstellar clouds are concentrations of gas in which the cloud constituents have a common mean velocity. They are classified as diffuse, translucent and dense. A diffuse cloud is a cloud through which the interstellar radiation penetrates and a dense cloud is one in which the radiation is excluded by grains. A translucent cloud shares the characteristics of diffuse and dense clouds and is intermediate in column density.

The ionization in diffuse clouds arises from photoionization and all elements with ionization potentials less than that of atomic hydrogen are fully-ionized. There is additional ionization by cosmic rays. The diatomic molecules CH , CH^+ , CN , C_2 , H_2 , CO and OH have been detected in diffuse clouds. The origin of the CH^+ ions is not yet established but appears to involve local regions of heated gas in which the reaction (5.3) which is endothermic by 0.4 eV can proceed. The characteristic temperature of a diffuse cloud is 70 K.

Dense clouds are ionized by galactic cosmic rays. In dense clouds, the hydrogen is largely in molecular form and ionization is initiated by



followed immediately by

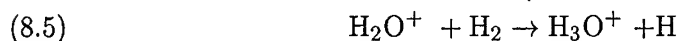
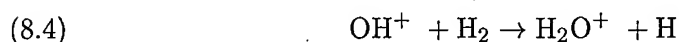


The molecular ion H_3^+ has recently been detected in the interstellar gas by absorption of radiation from stars with strong infrared emission [38, 39, 40].

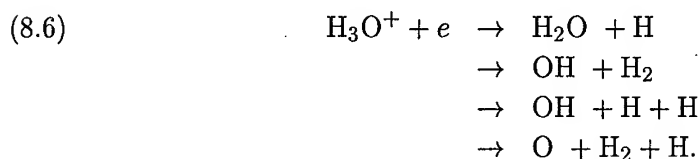
Ion molecule chemistry is initiated by proton transfer reactions such as



followed by abstraction reactions



The ion H_3O^+ does not react with H_2 and instead undergoes dissociative recombination



The branching ratios are crucial ingredients of the chemistry. They have been measured recently using a heavy ion storage ring [36].

Together with contributions from grain chemistry, elaborate models have been constructed but no entirely satisfactory representation of the abundances of the more than one hundred distinct molecular species that have been detected has been obtained [37].

The ion-molecule chemistry of the interstellar gas is based upon positive ions from cosmic rays but recently a detection has been reported of a negative ion C_7^- and it has been proposed that C_7^- and other carbon chain ions may be responsible for the diffuse interstellar absorption bands [41]. The negative ions are made by radiative attachment



and destroyed by photodetachment



associative detachment



and mutual neutralization



where X^+ is any positive ion and the final state C_7 may be dissociated. Calculations suggest that if large molecules are indeed present in abundance in interstellar clouds, a significant fraction of them will be anions. The molecular composition will be modified because mutual neutralization replaces dissociative recombination as the charge removal process [42]. However, no quantitative explanation has yet been advanced for substantial abundances of large neutral molecules [43].

Acknowledgment

This research has been supported by the Astronomy Division of the U.S. National Science Foundation.

References

1. B. ZYGELMAN, P. C. STANCIL and A. DALGARNO, *Stimulated Radiative Association of He and H⁺*, Ap. J., **508**, 131, 1999.
2. P.C. STANCIL and A. DALGARNO, *Chemical Processes in Astrophysical Radiation Fields*, Faraday Discuss., **109**, 61, 1998.
3. E. BOUGLEUX and D. GALLI, *Lithium Hydride in the Early Universe and in Protogalactic Clouds*, MNRAS, **288**, 638, 1997.
4. D. GALLA and F. PALLA, *The Chemistry of the Early Universe*, A&A **335**, 403, 1998.
5. P. C. STANCIL, S. LEPP and A. DALGARNO, *The Lithium Chemistry of the Early Universe*, Ap. J., **458**, 401, 1996.
6. P. C. STANCIL, S. LEPP and A. DALGARNO, *The Deuterium Chemistry of the Early Universe*, Ap. J., **509**, 1, 1998.
7. S. LEPP and P. C. STANCIL, *Molecules in the Early Universe and Primordial Structure Formation in the Molecular Astrophysics of Stars and Galaxies*, (Oxford Science Publications) Eds. T. W. Hartquist and D. A. Williams, pp. 37-52, 1998.
8. A. DALGARNO and S. LEPP, *Applications of Atomic and Molecular Physics to Astrophysics in Atomic, Molecular and Optical Physics Handbook* (American Institute of Physics) Ed. G.W.F. Drake, pp. 919-929, 1996.
9. D. E. OSTERBROCK, *Astrophysics of Gaseous Nebulae and Active Galactic Nuclei* (University Science Books) 1989.
10. X. LIU and J. DANZIGER, *Observations of the Bowen Fluorescence Mechanism and Charge Transfer in Planetary Nebulae-I*, MNRAS, **261**, 465, 1993.
11. F. F. WINKLER, C.R. CANIZARES, G.W. CLARK, T.H. MARKERT, K. KALATA and H. W. SCHNOPPER, *A Survey of X-ray Emission Lines from the Supernova Remnant Puppis A*, Ap. J., **246**, L27, 1981.
12. E.B. JENKINS, *Coronal Gas in the Galaxy. I. A New Survey of Interstellar OVI*, Ap. J., **219**, 845, 1978.
13. S. L. BALIUNAS and S.E. BUTLER, *Silicon Lines and Spectral Diagnostics: The Effect of Charge Transfer*, Ap. J., **235**, 1980.
14. D.A. NEUFELD and A. DALGARNO, *Charge Transfer in Collisions of Doubly-Charged Ions of Iron and Nickel with Hydrogen Atoms*, Phys. Rev., **A 35**, 3142, 1987.
15. M. A. DOPITA, *Optical Emission from Shock Waves. II. Diagnostic Diagrams*, Ap. J. S., **33**, 437, 1977.
16. D. HOLLENBACH and C. F. MCKEE, *Molecular Formation and Infrared Emission in Fast Interstellar Shocks II. Dissociation Speeds for Interstellar Shock Waves*, Ap. J., **241**, 147, 1980.
17. C. F. MCKEE and D.J. HOLLENBACH, *Radio Recombination Lines from Fast Shocks in Molecular Clouds with Applications to Bipolar Flows*, Ap. J., **322**, 275, 1987.
18. B.T. DRAINE, W.E. ROBERGE and A. DALGARNO, *Magnetohydrodynamic Shockwaves in Molecular Clouds*, Ap. J., **246**, 1045, 1983.
19. D.A. NEUFELD and A. DALGARNO, *Fast Molecular Shocks. I. Reformation of Molecules behind a Dissociative Shock*, Ap. J., **340**, 869, 1989.
20. M. ELITZUR and W. D. WATSON, *Formation of CH⁺ in Interstellar Shocks*, Ap. J., **222**, 2141, 1978.

21. D.R. FLOWER, G. PINEAU des Forêts and T.W. HARTQUIST, *Theoretical Studies of Interstellar Molecular Shocks-I. General Formulation and Effects of the Ion-Molecule Chemistry*, MNRAS, **214**, 775, 1985.
22. D.A. NEUFELD and A. DALGARNO, *Fast Molecular Shocks II. Emission from Fast Dissociative Shocks*, Ap. J., **344**, 251, 1989.
23. B.E. TURNER, *Detection of Interstellar SO^+ : A Diagnostic of Dissociative Shock Chemistry*, Ap. J., **396**, L107, 1992.
24. A. STERNBERG and A. DALGARNO, *Chemistry in Dense Photon-Dominated Regions*, Ap. J. S., **99**, 565, 1995.
25. A.G.G.M. TIELENS and D. HOLLENBACH, *Photodissociation Regions. I. Basic Model*, Ap. J., **291**, 747, 1985.
26. J. CERNICHARO, X.-W. LIU, E. GONZALEZ-ALFONSO, P. COX, M.J. BARLOW, T. LIM and B.M. SWINYARD, *Discovery of Far-infrared Rotational Transitions of CH^+ in NGC 7027*, Ap. J., **483**, L65, 1997.
27. W. B. LATTEY, C. R. WELKER and P.R. MALONEY, *Detection of the Carbon Monoxide Ion (CO^+) in the Interstellar Medium and a Planetary Nebula*, Ap. J., **419**, L97, 1993.
28. H. STÖRZER, J. STUTZKI and A. STERNBERG, *CO^+ in the Orion bar, M17 and S140 Star-forming Regions*, A&A **296**, L9, 1995.
29. A. STERNBERG, M. YAN and A. DALGARNO, *Photon-dominated and X-ray Dominated Regions in Molecules in Astrophysics: Probes and Processes*, (IAU Symposium 178) Ed. E.F. van Dishoeck, pp. 141-152, 1997.
30. S. LEPP and A. DALGARNO, *X-ray Induced Chemistry of Interstellar Clouds*, A&A, **306**, L21, 1996.
31. P.R. MALONEY, D.J. HOLLENBACH and A.G.G.M. TIELENS, *X-Ray Irradiated Gas. I. Physical Processes and General Results*, Ap. J., **466**, 561, 1996.
32. J. A. PHILLIPS and T.J.W. LAZIO, *Images of HCO^+ (1-0) Emission in a Molecular Cloud near IE 1740.7-2942*, Ap. J., **442**, L37, 1995.
33. M. YAN and A. DALGARNO, *The Molecular Cloud near the Hard X-ray Source IE 1740-2942*, Ap. J., **481**, 296, 1997.
34. J.S. MILLER, J. TENNYSON, S. LEPP and A. DALGARNO, *Identification of Features due to H_3^+ in the Infrared Spectra of Supernova 1987A*, Nature, **355**, 420, 1992.
35. M. YAN and A. DALGARNO, *H_3^+ in the Ejecta of SN 1987A*, Ap. J., **500**, 1049, 1998.
36. L. VEJBY-CHRISTENSEN, L.H. ANDERSEN, O. HEBER, D. KALLA, H.B. PEDERSEN, H.T. SCHMIDT and D. ZAJFMAN, *Complete Branching Ratios for the Dissociative Recombination of H_3O^+ , H_2O^+ and CH_3^+* , Ap. J., **483**, 531, 1997.
37. E.F. VAN DISHOECK, *The Chemistry of Diffuse and Dark Interstellar Clouds*, in *The Molecular Astrophysics of Stars and Galaxies*, (Oxford University Press) Ed. T.W. Hartquist and D.A. Williams, pp. 53-100, 1999.
38. T.R. GEBALLE and T. OKA, *Detection of H_3^+ in Interstellar Space*, Nature, **384**, 334, 1996.
39. B.J. MCCALL, T.R. GEBALLE, R.H. HINKLE and T. OKA, *Detection of H_3^+ in the Diffuse Interstellar Medium towards Cygnus OB2 No. 12*, Science, **279**, 1910, 1998.
40. T.R. GEBALLE, B.J. MCCALL, R.H. HINKLE and T. OKA, *Detection of H_3^+ in the Diffuse Interstellar Medium: The Galactic Center and Cygnus OB2 Number 12*, Ap. J., **510**, 251, 1999.
41. M. TULEJ, D.A. KIRKWOOD, M. PACHKOV and J.P. MAIER, *Gas-Phase Electron Transitions of Carbon Chain Anions coinciding with Diffuse Interstellar Bands*, Ap. J., **506**, L69, 1999.
42. S. LEPP and A. DALGARNO, *Polycyclic Aromatic Hydrocarbons in Interstellar Chemistry*, Ap. J., **324**, 553, 1988.
43. D. P. RUFFLE, R. P. A. BETTENS, R. TERZIEVA and E. HERBST, *The Abundance of C_7^- in Diffuse Clouds*, Ap. J., **523**, 678, 1999.

TRENDS IN PLASMA PROCESSING FOR ULTRA LARGE SCALE INTEGRATION TECHNOLOGY

O. JOUBERT¹, P. SCHIAVONE¹, L. VALLIER¹, D. FUARD¹, L. DESVOIVRES¹,
P. SCHIAVONE², C. MONGET², P. GOURAUD³, P. CZUPRYNSKI⁴

¹LABORATORIE DES TECHNOLOGIES DE LA MICROELECTRONIQUE
CNRS EP 2073, 17 avenue des Martyrs (CEA-LETI), 38054 Grenoble cedex, France

²FRANCE TELECOM, BRANCHE DEVELOPMENT
CNET-CNS, BP 98, 38243 Meylan cedex, France

³STMICROELECTRONICS
38926 Crolles cedex, France

⁴LETI (CEA TECHNOLOGIES AVANCÉES)
DMEL-CEA/G, 17 rue des Martyrs, 38054 Grenoble Cedex 9, France

A review of plasma processes involved in silicon device fabrication is presented in this paper. An example of plasma-assisted deposition processes for oxynitride thin film elaboration is presented in the first part of the paper. In the second part of the paper, silicon and dielectric etch processes are discussed and emphasis is put on the key issues which need to be solved in the near future. In the last part of the paper, the applications of plasma processes for advanced lithography techniques will also be discussed.

1. Introduction

Approximately 40% of the steps in the fabrication of microelectronic devices use plasma processes. Applications in many new technological areas (surface modification, cleaning, sterilization, sputter coating, and many other areas) are growing based on developments made for the processing of microelectronics materials. Fundamental understanding of plasma processes is still insufficient to have a clear picture of all the phenomena involved in the plasma environment and during its interaction with a substrate.

Plasmas are involved in many key technological steps for device fabrication. In particular, High Density Plasmas (HDP) are very largely used for silicon-based dielectric film deposition and for films of recent interest with lower dielectric constant. High density plasmas are particularly well adapted for Ultra Large Scale Integration Technology (ULSI) due to their capability to fill high aspect ratio topography[1].

Since its introduction in the 1970s, plasma etching has become an integral part of semiconductor integrated-circuit processing. It is now the method of choice for fine-line pattern definition, selective processing over topography and resist stripping. The difficulty of plasma etching processes scales inversely with the dimension of the structures to be defined [2, 3]. When entering in the sub $0.1\ \mu\text{m}$ regime, a number of complex phenomena, brought about by the difference in directionality between electrons and ions in the plasma, become crucial for process optimization.

In this paper we will give a brief overview of plasma processes for thin film deposition, for advanced etching applications and for advanced lithography techniques.

2. New trends in plasma-assisted chemical vapor deposition

Five principal types of silicon-based thermal and plasma chemical vapor deposition (CVD) dielectric materials are currently used in Integrated Circuit (IC) fabrication: silicon dioxide, silicon nitride, silicon oxynitride, phosphorous-doped silicon oxide (PSG) and boron/phosphorous-doped silicon oxide (BPSG). The properties of these films can be adjusted to achieve desirable functions. In this article we will briefly mention the key applications where plasmas can be used in the deposition of dielectric materials in the microelectronic industry and give more details on the deposition of plasma deposited antireflective layers based on oxynitride films for advanced lithographic applications.

For microelectronics applications, the plasma deposition processes of interest are conventional Plasma Enhanced CVD (PECVD) techniques, remote PECVD and High Density Plasma CVD (HDP CVD). A recent review by Lucowsky covers the evolution of low-temperature remote plasma-assisted deposition for device quality silicon dioxide and silicon nitride thin films [4]. Remote PECVD differs from conventional PECVD in that the substrate is not subjected to ion bombardment by the plasma. Process gases can either be introduced into the plasma region or downstream from the plasma, causing substantial differences on the final characteristics of the deposited film.

In plasma CVD, the plasma energy supplied by an external rf source generates species that can react and deposit on substrate surfaces. The excessive heating that occurs during a conventional CVD process can be avoided by using plasma electron kinetic energy instead of thermal energy. Besides this key aspect of generating reactive species at lower processing temperatures, the ion bombardment can be used to tune the film properties. Film properties can be tuned by varying deposition parameters such as temperature, rf power, pressure, reactant gas mixture ratio, and type of reactant.

One new field growing extremely fast is the deposition of SiO_2 using High Density Plasmas (HDP CVD). The first application of HDP CVD SiO_2 is Shallow Trench Isolation (STI) to ensure the isolation between transistors instead of using the traditional Local Oxidation of Silicon (LOCOS)[5]. The HDP CVD technique is particularly well suited for this application, requiring the deposition of very dense oxide in structures with aspect ratios (ratio of the depth to the width

of a structure) as high as 4:1. HDP CVD SiO_2 is also used as an Intermetal Dielectric (IMD) in the fabrication of interconnections. One parameter becoming increasingly important for interconnect fabrication is the dielectric constant (k) of the IMD material. Use of a material having a lower dielectric constant leads to lower total capacitance, decreasing the interconnection delay and power dissipation and thus enhancing performance. The dielectric constant of HDP CVD oxide is typically 4.1 to 4.2. New IMD materials are currently being deposited using the HDP CVD technique, including amorphous carbon and fluorinated carbon films, because of their low dielectric constants (2.1 to 2.3) and thermal stability up to 400°C [6].

Finally, plasma deposited films can be used for advanced lithography applications. Lithography is the critical step that defines the minimum transistor dimensions. These dimensions can be reduced by decreasing the illumination wavelength. However, at shorter wavelengths, increased substrate reflectivity causes undesired light reflections to become critical. During the exposure of a photosensitive resist, light reflection from previously patterned layers is also a source of reflected light. The irregular topography of the substrate causes undesired variations in the exposure energy and consequently in the shape of the photoresist. Antireflective layers (ARLs) are widely used to overcome these problems. Two types of antireflective materials are available, organic and inorganic. The former are easily spin coated, but their planarizing properties (capability of smoothing the topography at the wafer surface) make them difficult to use efficiently. The latter presents the advantage of conformal deposition (same thickness deposited everywhere on the wafer even in the presence of topography) and only thin films are needed because of their high optical absorbance. One of the most promising candidates for inorganic ARL is silicon oxynitride (SiO_xN_y) [7]. One advantage of this material is the low deposition temperature. Its composition can be varied from SiO_2 to $\text{SiO}_{0.2}\text{N}_{0.8}$ to optimize its optical properties with respect to the exposure wavelength and the substrate. High Density Plasmas at low deposition temperature can be used, with SiH_4 and N_2O as gas precursors [8]. Fig. 1 gives an example of the refractive index of the SiO_xN_y films obtained as a function of the $\text{N}_2\text{O}/\text{SiH}_4$ ratio. Several compositions and therefore different gas mixtures can provide films with the required optical constants. Controlling the $\text{N}_2\text{O}/\text{SiH}_4$ ratio is a very simple way of adjusting the composition of the material to meet the requirements of an optimum ARL, depending on the underlying stack of layers. The efficiency of SiO_xN_y layers is illustrated by the Scanning Electron Microscope (SEM) image of Fig. 2. A 0.25 μm line stepping down from a thick oxide area (bottom of the picture) to the active area was printed with 248 nm illumination. The step height is 200 nm with a slope angle of around 45°. The line with no underlying ARL in Fig. 2(a) broadens due to the reflection of light at the resist/substrate interface on the sloped step. In this case, the negative photoresist absorbs increased exposure energy since it receives light coming from above as well as that reflected from the step. The SiO_xN_y film reduces the reflection coefficient to a few percent and thus virtually eliminates the parasitic light reflection from the substrate. The line in Fig. 2 (b) is straight and shows no broadening from local over-exposure of the resist.

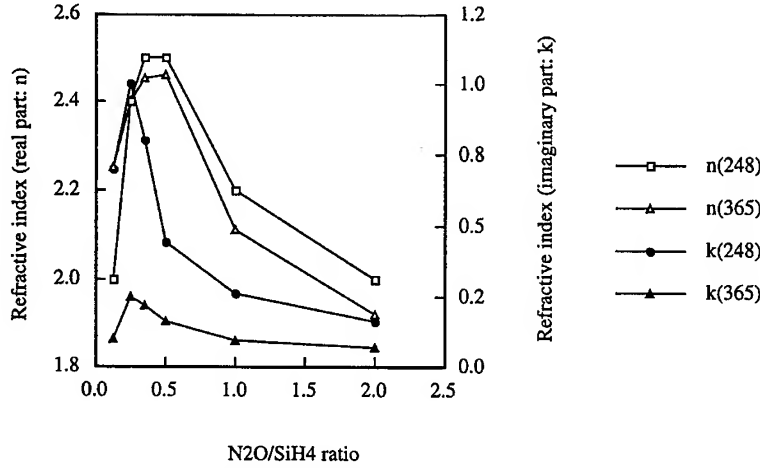


FIG. 1. Refractive index (real and imaginary parts) of SiO_xN_y materials at 248 and 365 nm for different $\text{N}_2\text{O}/\text{SiH}_4$ ratio.

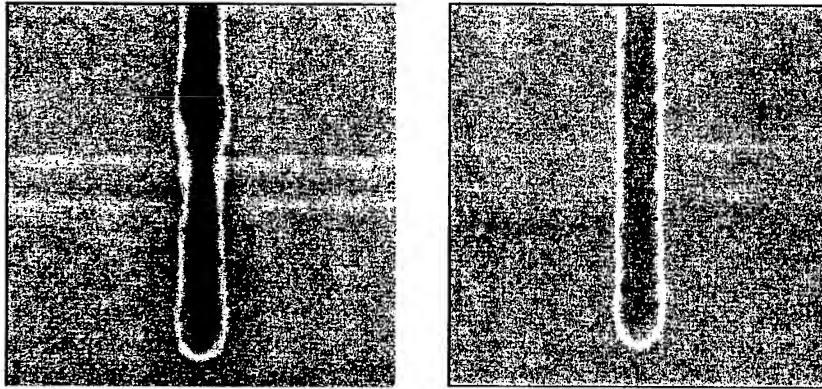


FIG. 2. SEM micrograph of a 25 μm polysilicon gate stepping down from thick isolation oxide to active area. a) without Anti Reflective 1 μm , b) with SiO_xN_y ARL.

3. New trends in plasma etching

Etch requirements depend on the materials and process schemes used to construct the transistors, DRAM memory cells and interconnects that comprise integrated circuits (IC). In semiconductor manufacturing, this concerns three basic categories of materials: polysilicon (including silicides and polycides), dielectrics and metals. In general, the requirements for each of these materials are well defined and predictable for each new IC generation.

In polysilicon etching, the main application is the transistor gate region, which requires etching through a gate stack to stop on a very thin gate SiO_2

layer. The selectivity with respect to the gate oxide is critical and requires the development of complicated recipes to minimize damage to the SiO_2 layer while maintaining the critical dimension (CD) control (the critical dimension is the final dimension targeted including the lithography step and transfer into the polysilicon gate layer).

Dielectric etch applications are the most challenging processes in ULSI technologies, due to the combination of the complexity of structures to be etched and the trade-off between opening high aspect ratio structures and obtaining high etch selectivities between the dielectric, silicon and silicon nitride. Furthermore, a new category of materials with low dielectric constants need to be integrated into standard processes, opening a new field of investigation in plasma etching.

In this section, the etching mechanisms for silicon and dielectrics will be discussed with reference to results and performance obtained in industrial etchers.

3.1. Gate patterning in High Density Plasmas

In polysilicon etching the main application is the formation of the transistor gate region which requires the etching of a silicide/polysilicon sandwich which must stop on a very thin gate oxide. Selectivity to the gate oxide is critical since only minimal amounts of oxide loss can be tolerated. The challenge will continue to be critical dimension (CD) control while maintaining selectivity and integrity of the gate oxide.

Polysilicon gate etching is achieved in high density plasma (HDP) etching tools such as the LAM TCP, the Applied Materials Decoupled Plasma Source (DPS) system or Inductively Coupled Plasma sources excited by Helicon waves [9, 10, 11, 12]. The parameter which has the strongest influence on the design of a gate etch recipe is the thickness of the gate oxide. For $0.25\text{ }\mu\text{m}$ design rules, the gate oxide thickness is between 4 and 5 nm whereas it decreases to 3.5 to 4 nm for $0.18\text{ }\mu\text{m}$ design rules and to 1.5 nm for sub $0.12\text{ }\mu\text{m}$ gates. The development of a polysilicon gate etch process on ultra-thin gate oxide requires the combination of appropriate etch chemistry [9, 10, 11, 12] (usually $\text{HBr}/\text{Cl}_2/\text{O}_2$ gas mixtures), the design of a good recipe (i.e. the combination of several different plasma etching steps) and a precise end point detection method allowing the arrival at the gate oxide to be monitored.

One major issue associated with the design of etching recipes is the "trenching" effect, induced by the reflection of ions by the sidewalls of the features, which induces an increase of the etching rate of polysilicon at the edges of the gate [13]. Trenching causes defects at the edges of the polysilicon gate (see Fig. 3). Transfer of this trenching into the gate oxide can be minimized by decreasing the ion energy, which decreases the amplitude of the trenching, and by adjusting the chemistry to increase the polysilicon/ SiO_2 selectivity [14].

The most critical issue for gate etching is to preserve the thin gate oxide and simultaneously maintain the critical dimension (CD) defined by the lithography step while optimizing an anisotropic etching process. Several studies have already shown that straight polysilicon sidewalls are obtained if a "passivation layer" builds up on the sidewalls as the etching proceeds [12, 14]. The proposed mechanism is that the ion bombardment sputters SiO_x -based products from the

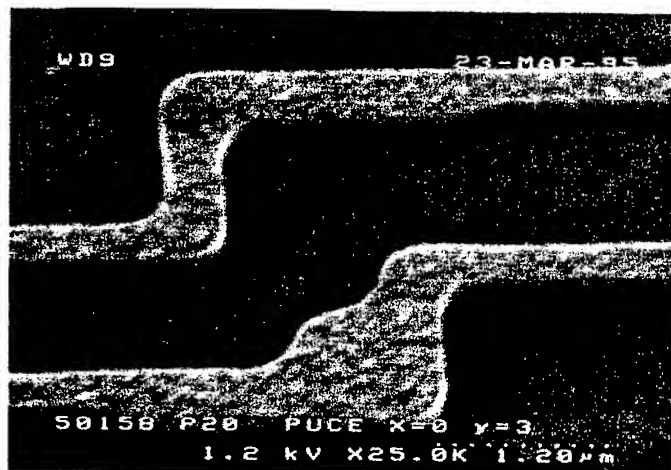


FIG. 3. Damage observed at the edges of polysilicon gates etched using a process developed in a LAM TCP system using $\text{HBr}/\text{Cl}_2/\text{O}_2$ mixtures. SEM observations were made after stripping of the mask and removal of the gate oxide in a HF bath.

bottom of the trench, which are in turn deposited on the sidewalls of the polysilicon gate. The thickness of the sidewall passivation layer is dependent on the O_2 concentration in the gas phase when using $\text{HBr}/\text{Cl}_2/\text{O}_2$ gas mixtures.

3.1.1. Thin gate oxide behavior during plasma treatment

It has also been shown recently that when very thin gate oxides are used, polysilicon etch processes may induce some "damage" of the underlying bulk silicon [15]. When exposed to an HBr/O_2 plasma for example, which is the most popular chemistry used in the microelectronics industry for gate patterning, very thin oxides get thicker. By combining real-time and spectroscopic ellipsometry [16], and quasi in-situ X Ray Photoelectron Spectroscopy analysis (XPS) [17], it has been shown that very thin gate oxide structures are strongly affected during plasma treatment. When the etching process is monitored by real time ellipsometry an unexpected signature of the ellipsometric angle Δ is observed at the end of the process, which indicates that the gate oxide is getting thicker. A procedure based on XPS analyses to determine the SiO_2 thicknesses [17], also confirms that gate oxides are getting thicker during the etching process. This phenomenon has been carefully analyzed by exposing thin blanket oxides with different thicknesses to O_2 and H_2 plasmas and by evaluating the oxide thickness before and after plasma treatment by spectroscopic ellipsometry (SE) and XPS measurements. Fig. 4 shows as an example, the real time ellipsometric recordings of blanket oxides with thicknesses ranging between 18 and 62 Å exposed to a pure O_2 plasma (using operating conditions close to real process conditions). The decrease in Δ observed for oxides thinner than 45 Å indicate that the thin oxide has grown under O_2 plasma exposure. These results show that oxygen species diffuse through thin gate oxides ($< 50\text{Å}$) and induce oxidation of the

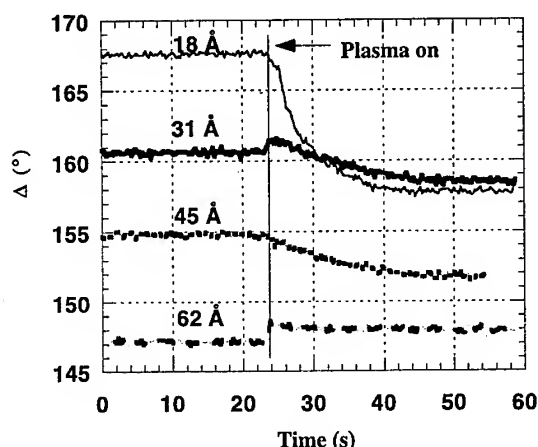


FIG. 4. Kinetic variation of the ellipsometric angle Δ recorded at 1.96 eV on several blanket oxides during oxygen plasma treatment.

bulk Si substrate, leading to the observed increase in gate oxide thickness. The final oxide thickness after O_2 plasma exposure was also measured by SE and XPS. The two measurements are in very good agreement (see Table 1).

Table 1. SiO_2 thickness determined by spectroscopic ellipsometry and X-ray photoelectron spectroscopy before and after oxygen plasma treatment

Before treatment (nm) XPS and SE	After treatment (nm)	
	XPS	SE
1.8	3.8	3.7
3.1	3.8	3.7
4.5	5.3	5.3
6.2	6.6	6.1

Similar results are obtained after exposing thin oxides to a pure hydrogen plasmas. The results indicate that, although the H_2 plasma treatment only slightly modifies the SiO_2 thickness, it strongly affects the bulk Si substrate by inducing partial amorphization. It was found that the thinner the oxide before treatment, the thicker the perturbed layer induced by the H_2 plasma treatment. It has also been suggested that this perturbed layer originates from hydrogen plasma active species penetration, either by implantation or by diffusion, through the thin gate oxide layer.

Experiments carried out at different bias power have indicated that these phenomena are only observed when significant bias power is applied to the wafer. When the wafer is left floating, no gate oxide growth is observed. This highlights the influence of the sheath electric field on the gate oxide perturbation, further indicating that ion implantation may be responsible for the phenomena reported.

3.1.2. Charging effects

A large category of etching anomalies [18, 19] can be related to charging of microstructures. Local electric fields form as a result of microstructure charging brought about by the different directionality of the fluxes of ions and electrons. During the initial stages of the etching, the bottom of the etched features charges up positively while the upper sidewall and resist mask charge up negatively. As the positive potential at the trench bottom increases, ions are deflected towards the sidewall of the trench. The best example of charging induced anomaly is the notching effect, where a narrow groove (the notch) opens in a conductive material at the interface with the underlying insulating material (see Fig. 5). The

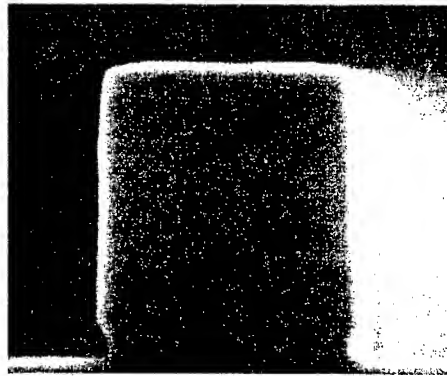


FIG. 5. Polysilicon gate etched in a high density plasma etch tool. The distortion in profile observed at the bottom of the gate is attributed to ions deflected at the bottom of the gate by charging effects.

notch occurs perpendicularly to the normal ion direction and appears mainly during the overetch step in high density plasma tools. Recent simulation studies indicate that notching is due to etching of the poly-Si sidewall foot by energetic ions that get deflected and accelerated towards it [20, 21]. The sidewall foot is precisely the location along the sidewall of the gate where the oxide-like passivation film is the thinnest thereby favouring the notch formation caused by deflected ion bombardment. Recent interesting studies have shown that anomalous sidewall etching can also be suppressed in pulsed-power chlorine inductively coupled plasmas [22, 23].

3.2. Dielectric etching

The construction of advanced multilevel interconnection systems has become the most difficult part of the process integration in Integrated Circuits fabrication. Dielectric etch applications represent the most challenging processes of ULSI technologies. Standard etch applications include conventional structures such as contact and vias holes etched in SiO_2 . In addition, a key requirement is the lowering of the dielectric constant of the film, mandatory in future processes.

3.2.1. Oxide etching

In the microelectronics industry, dielectric etch processes compatible with industrial requirements must be highly selective to various types of underlayers (Si, TiN, TiSi_2) and to the etching mask, while allowing high yields to be achieved. Dielectric etching can be achieved using high density plasma sources (inductively coupled or microwave driven plasmas) [24, 25, 26] or Reactive Ion Etching (RIE) based systems (such as Magnetically Enhanced RIE systems) [27, 28]. The chemistries used for standard SiO_2 dielectric etch are based on fluorocarbon gases such as C_2F_6 , C_3F_8 , C_4F_8 , $\text{C}_2\text{H}_2\text{F}_2$ and others, mixed with additives as CO, O_2 , Ar or H_2 .

The principle of selective etching of SiO_2 versus silicon relies on the fact that, in a first approximation, fluorocarbon gases induce the deposition of a fluorocarbon polymer on silicon surfaces while SiO_2 surfaces remain fluorocarbon free. At the end of a contact hole etch process, when the silicon surface is reached, the fluorocarbon polymer grows on the silicon surface, thereby preventing its consumption. In practice, the situation is more complicated, as there is always a balance to be found between etching and deposition on SiO_2 surfaces. If the chemistry used induces too much gas phase polymerization, the polymer film may also grow on the SiO_2 surface leading to "etch stop" problems. In recent years, a large research effort has been focused on fluorocarbon plasmas to obtain a better understanding of the gas phase chemistry and its impact on plasma processes [29].

Studies performed in commercial high density plasma tools have shown that high aspect ratio contact holes can be opened in thick dielectric layers with minimal consumption of underlayers [30]. In high density plasma sources, fluorocarbon polymer deposition is abundant. Once the silicon surface is reached, the polymer growth starts, its thickness continuously increases as a function of time allowing a good protection of the contacts or vias bottoms. The polymer thickness deposited on the silicon surface at the bottom of contact holes increases with the aspect ratio of contact holes (polymers as thick as 2000 to 3000 Å are deposited in contact holes with an aspect ratio of 3 to 4).

Recently, much work has also been carried out in MERIE systems [31]. Using chemistries such as $\text{C}_4\text{F}_8/\text{CO}/\text{Ar}$ gas mixtures, the SiO_2 etching rates measured on patterned wafers are much lower than in HDP's (around 500 nm/min to be compared to more than 1 $\mu\text{m}/\text{min}$ in HDP's). However, contrary to HDP's, very high aspect ratio contact holes can be opened in thick SiO_2 layers. Fig. 6 shows an example of 0.3 μm contact holes opened in 1.6 μm thick SiO_2 films demonstrating the capabilities of the MERIE source.

The differences in behaviour between HDP's and MERIE systems are related to the ion current densities and energies obtained in both sources and the very different gas mixtures used. The ion density estimated in HDP's is around 10^{12} ions/ cm^3 whereas it is an order of magnitude lower in MERIE systems. The self-bias voltages used are around 200 V and 500 V in the HDP and MERIE, respectively.

In HDP's, the thickness and the F/C ratio of the polymer deposited in contact holes increased with the aspect ratio whereas the flux of deposition precursors



FIG. 6. $0.3\ \mu\text{m}$ contact holes etched in $1.6\ \mu\text{m}$ SiO_2 using an MERIE source under standard process conditions.

is expected to decrease as a function of aspect ratio (due to shadowing effects). This phenomenon is attributed to power density loss [32] at the bottom of the etched features induced by charging effects developed in the structures as the etching proceeds. The ion power density as a function of the aspect ratio of contact holes directly determines the polymerization rate on SiO_2 surfaces at the bottom of contact holes. In HDP's, very high source and bias powers are applied to obtain high ion power density at the bottom of contact holes which keep SiO_2 surfaces fluorocarbon free. However, for high aspect ratio contact holes, in which ion power density loss is important, fluorocarbon deposition may take place, leading to the etch-stop phenomenon. Furthermore, the very high power density used lead to a high resist etching rate leading in some cases to a distortion of the shape of contact holes.

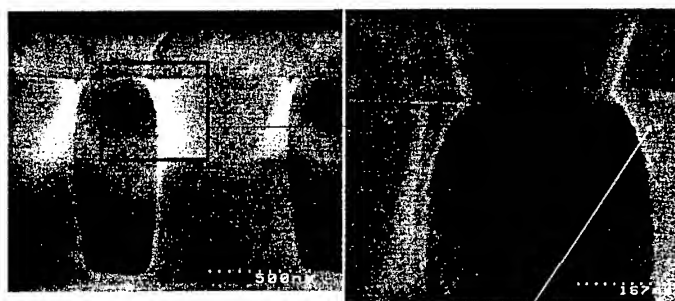
In MERIE sources, the ion power density reaching the etched surfaces is around five times smaller than in the HDP system, which is not high enough to keep SiO_2 surfaces fluorocarbon free at the bottom of high aspect ratio contact holes but, on the other hand favours the minimization of resist erosion. As a consequence, oxygen-based species addition is necessary (O_2 and CO) to keep the SiO_2 surfaces at the bottom of high aspect ratio structures free of fluorocarbon deposition. When the silicon surface is reached at the bottom of contact holes, oxygen-based species of the feed gas stock prevent the growth of a thick fluorocarbon polymer. Nevertheless, a thin fluorocarbon polymer film grows on the silicon surface, mainly formed by the direct reaction of fluorocarbon ions with silicon.

3.2.2. Etching of low dielectric constant materials

The need for materials with low dielectric constants, otherwise known as low- k materials, arises from the simple fact that chip speed is limited by both the resistance of the metal line and by the capacitance of the surrounding insulator [33]. The goal of the push to low- k materials is to reduce capacitance which helps minimize crosstalk between adjacent metal lines.

The dielectric constant of conventional materials (SiO_2 films deposited by a variety of techniques) used in production range between 4 and 4.5. In the longer term, the switch to a totally new type of material, a plastic-like organic polymer with a dielectric constant of around 2 and with thermal stability compatible with Integrated Circuits applications will become necessary. Switching to carbon containing materials will require new masks (hard masks) and new etch chemistries.

Carbon-based low- k dielectric materials are etched using O_2 -based chemistries. As later in the interconnexion fabrication process, the sidewalls of the polymer are in contact with metals, the sidewall must remain fluorine, sulfur and chlorine free to prevent corrosion problems. Very simple chemistries must be used, such as H_2 , N_2 , O_2 . As oxygen containing chemistries are very reactive with respect to carbon-based polymers, the plasma operating conditions and chemistry must induce the formation of a sidewall passivation layer to prevent spontaneous etching reactions between the polymer and the reactive species of the plasma [34]. Recent studies have shown that this passivation layer is only formed under conditions where the polymer surface is "graphitized" during the etch process. The graphitization simply means that the polymer structure is strongly modified by the plasma. The graphitization of the polymer during the process is required to achieve a good profile control as it favors the formation of heavy etch products which are redeposited on the sidewalls of the etched features allowing the sidewall passivation layer to be formed (Fig. 7). Graphitization of



Sidewall
passivation layer

FIG. 7. High aspect ratio contact holes etched in polymers. The sidewall passivation layer formed during the etch process is observed in the higher magnification picture (white arrow).

the polymer is obtained when the physical component of the etch dominates the chemical component of the etch. This is achieved by using oxygen deficient chemistries and high ion energy etch conditions. Fig. 7 shows high aspect ratio contact holes etched using $\text{H}_2/\text{N}_2/\text{O}_2$ gas mixtures. A thick passivation layer has been formed during the etch process from heavy graphitized etch products redeposited on the polymer sidewalls. Despite the passivation layer which prevents spontaneous etch reactions between neutral reactive species of the plasma and the polymer, bowed profiles are observed. As for polysilicon and oxide, the

deformation of the etch profile is attributed to charging effects deflecting high energy ions on the sidewalls. For polymer-based materials with a low chemical sputtering threshold (less than 10 eV), high energy ions impinging at grazing angle on the polymer sidewall may generate the profile deformation observed in Fig. 7. Such profile deformations are also observed in SiO_2 . However, the sputtering threshold of SiO_2 being much higher (around 40 eV), bowed profiles are only observed in very high aspect ratio contact holes where charging effects are more important.

4. Plasma processes for advanced lithography techniques

Besides standard wet resists used for lithography, much research has been focused on alternative approaches to obtain resist patterns suitable for IC fabrication. Various resist schemes use the so-called top surface imaging (TSI) technique where the UV light is confined to a very thin resist layer, and the final image is obtained, after transfer, in a thicker planarizing organic resist [35, 36, 37] (see Fig. 8). Fig. 8 shows a general scheme of TSI schemes. In a first step, the thin

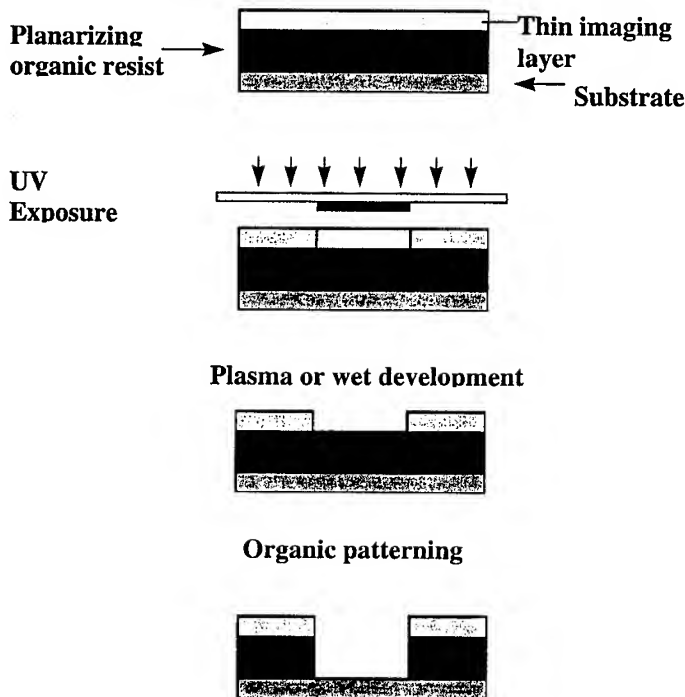


FIG. 8. Top surface imaging schemes for advanced lithography techniques.

imaging layer can be spin coated (bi-layer approach), or obtained using the silylation technique [35] or plasma deposited [36, 37] (CVD resist scheme). After UV exposure, the photosensitive layer is developed (by standard wet approaches or reactive plasmas) and the final pattern is obtained after a so-called dry devel-

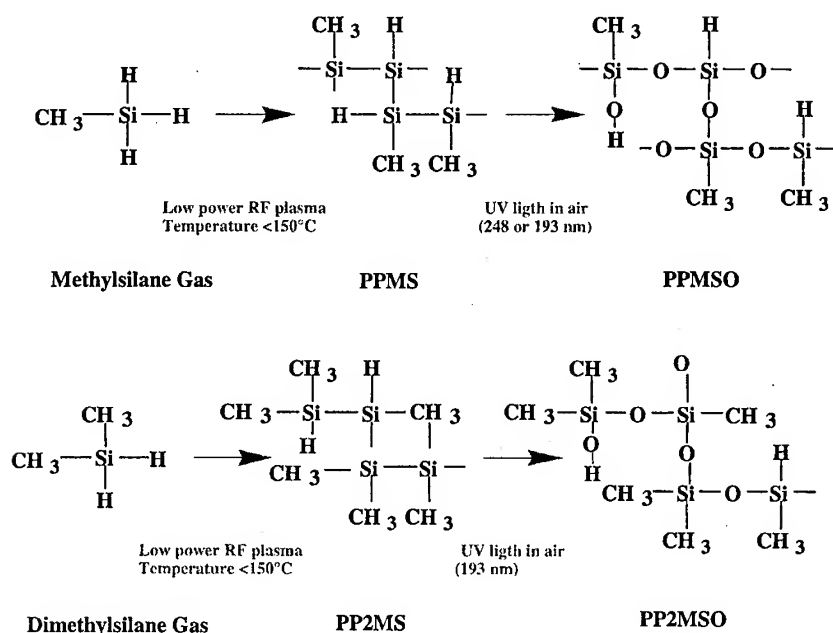


FIG. 9. Schematic view of the chemical composition of an as deposited PPMS and PP2MS, PPMS and PP2MS exposed to UV to form PPMSO and PP2MSO.

opment step usually performed in high density plasmas using mixtures of O_2 or SO_2/O_2 [34]. This last step is common to all the top surface imaging techniques and consists of etching a thick organic resist using a silicon-containing mask. In the following, we will describe in more detail the CVD resist approach.

The CVD resist approach is an all dry chemical vapor deposition (CVD) process based on plasma polymerized methylsilane (PPMS) or plasma polymerized dimethylsilane (PP2MS). This all dry scheme provides a thin conformal and photosensitive layer combined with UV exposure (see Fig. 9). A thin amorphous film of Si-Si bonded material is deposited using plasma enhanced chemical vapor deposition (PECVD) with methylsilane or dimethylsilane as the gas precursor. Upon UV exposure under air at 248 or 193 nm, photo-induced oxidation of the CVD resist occurs, generating a latent image. The image is then developed in a chlorine-based plasma (which removes the unexposed areas), providing a negative tone process. This mask can be used to pattern a thick organic underlayer, this constituting a general bilevel process. The photosensitivity of CVD resist films can be tuned using the deposition temperature, gas pressure (methylsilane or dimethylsilane), gas flow in the chamber and RF power injected in the deposition chamber. Typical deposition temperatures are controlled in the range between 50 and 150°C: a decrease in deposition temperature leads to an increase in PPMS film photosensitivity. The film photosensitivity is also found to be pressure dependent. RF power applied to the chamber primarily affects the uniformity and deposition rate. Industrial reactors developed for dielectric deposition are very well suited for this application. Following exposure, the

development is accomplished in a high density plasma. During this step, the development conditions have to be optimized to remove unexposed and partially exposed areas while maintaining the remaining thickness of PPMSO or PP2MSO as high as possible. Chlorine and Bromine based plasmas can be used for the dry development step of PPMS.

The lithographic performances of PPMS and PP2MS have been evaluated using the new generation 193 nm lithography tools. Fig. 10 shows the ultimate resolution obtained with the all dry PP2MS process. Bi-layer PP2MS patterns are obtained with equal lines and spaces down to a resolution of $0.1\ \mu\text{m}$. Under identical process conditions, $0.08\ \mu\text{m}$ bi-layer lines with spaces of $0.16\ \mu\text{m}$ can also be obtained.

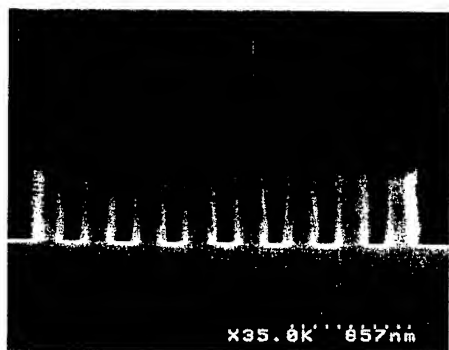


FIG. 10. Scanning electron micrograph cross-section view of $0.1\ \mu\text{m}$ L/S bi-layer PP2MS features exposed at 193 nm under annular illumination conditions.

5. Conclusion

It is hard to imagine a more complex and dynamic environment than that found in plasmas. As integrated circuit dimensions will shrink further and aspect ratios get larger, plasma etch and deposition processes will become even more complicated. The successful development of these processes will depend largely on a better understanding of the plasma itself and on the electrical, physical and chemical phenomena occurring in high aspect ratio structures.

References

1. M.A. LIEBERMAN, A.J. LICHTENBERG, *Principles of plasma discharges and materials processing*, Wiley, New York, 1994.
2. H.F. WINTERS, J.W. COBURN, T.J. CHUANG, *Surface processes in plasma-assisted etching environments*, J. Vac. Sci. Technol B, **1**, 469, 1983.
3. D.L. FLAMM, V.M. DONNELLY, D.E. IBBOTSON, J. Vac. Sci. Technol.B, **1**, 23, 1983.
4. G. LUCOWSKY, *Preparation of device-quality SiO₂ thin films by Remote Plasma Enhanced Chemical Vapor Deposition (PECVD): Applications in Metal-Oxide-Semiconductor (MOS) Devices*, Adv. Mater. Opt.Electron., **6**, 55-72, 1996.

5. S. NAG, G.A. DIXIT, M.K. JAIN, K.J. TAYLOR, S. KRISHNAN, L.M. TING, J.D. LUTTMER, R.H. HAVERMANN, Proceedings of the VMIC conference, 25, 1995.
6. GRILL, V. PATEL, K.L. SAENDER, C. JAHNES, S.A. COHEN, A.G. SCHROTT, D. EDELSTEIN, J.R. PARASZCAK, *Diamondlike carbon Materials as low-k dielectrics for multilevel interconnects in ULSI*, Proceedings of the MRS Symposium on Low-k dielectric constant materials II, 155, Boston, 1996.
7. T. OGAWA, H. NAKANO, T. GOCHO, T. TSUMORI, Proc. SPIE 2197, 722, 1994.
8. F. GAILLARD, P. SCHIAVONE, P. BRAULT, J. Vac. Sci. Technol. A, **15**, 5, 2777, 1997.
9. F.H. BELL, O. JOUBERT, J. Vac. Sci. Technol. B, **15**, 1, 88, 1997.
10. K.V. GUINN and V.M. DONNELLY, J. Appl. Phys., **75**, 4, 2227, 1994.
11. K.V. GUINN, C.C. CHENG and V.M. DONNELLY, J. Vac. Sci. Technol. B, **13**, 2, 214, 1995.
12. TEPPERMEISTER, N. BLAYO, F.P. KLEMENS, D.E. IBBOTSON, R.A. GOTTSCHO, and J.T.C. LEE, H.H. SAWIN, J. Vac. Sci. Technol. B, **12**, 4, 1994.
13. S. VAN NGUYEN, D.DOBUZINSKY, S.R.STIFFLER, G.CHRISMAN, J.Vac.Sci.Technol, **138**, 1112, 1991.
14. O. JOUBERT, F.H. BELL, J. Electrochem. Soc., **144**, 5, 1854, 1997.
15. V.M. DONNELLY, F.P. KLEMENS, T.W. SORSCH, G.L. TIMP and F.H. BAUMANN, Appl. Phys. Lett., **74**, 1260, 1999.
16. S. VALLON, L. VALLIER, *In Process Control, Diagnostics, and Modeling in Semiconductor Manufacturing* editors M. Meyyappan, D. J. Economou and S. W. Butlet, (The Electrochemical Society, Montreal, 1997) pp. 168-175.
17. F.H. BELL and O. JOUBERT, J. Vac. Sci. Technol. B, **14**, 3473, 1996.
18. T. NOZAWA, T. KINOSHITA, T. NISHIZUKA, A. NARAI, T. INOUE, A. NAKAUE, Jpn. J. Appl. Phys., **34**, 2107, 1995.
19. N. FUJIWARA, T. MARUYAMA, M. YONEDA, Jpn. J. Appl. Phys., **34**, 2095, 1995.
20. G.S. HWANG, K.P. GIAPIS, J. Vac. Sci. Technol. B, **15**, 1, 70, 1997.
21. G.S. HWANG, K.P. GIAPIS, Appl. Phys. Lett., **70**, 18, 2377, 1997.
22. T.H. AHN, K. NAKAMURA, H. SUGAI, Plasma Sources Sci. Technol., **5**, 139, 1996.
23. S. SAMUKAWA, K. TERADA, J. Vac. Sci. Technol. B, **12**, 3300, 1994.
24. J. MARKS, K. COLLINS, C.L. YANG, D. GROECHEL, P. KESWICK, C. CUNNINGHAM, M. CARLSON, Proc. SPIE, 1803, 1992.
25. J.H. KELLER, J.C. FORSTER, M.S. BARNES, J. Vac. Sci. Technol., A **11**, 2487, 1993.
26. J. ASMUSSEN, J. Vac. Sci. Technol. A, **7**, 883, 1989.
27. S. SAMUKAWA, Y. SUZUKI, M. SASAKI, Appl. Phys. Lett., **57**, 403, 1990.
28. M. SEKINE, M. NARITA, K. HORIOKA, Y. YOSHIDA, H. OKANO, Jap. J. Appl. Phys., **1**, 34, 6274, 1995.
29. J.P. BOOTH, G. CUNGE, F. NEUILLY, N. SADEGHI, Plasma Sources, Science and Technology, **7**, 423, 1998.
30. O. JOUBERT, P.CZUPRYNSKI, F.H. BELL, P. BERRUYER, R. BLANC, J. Vac. Sci. Technol. B, **15**, 3, 629, 1997.
31. P BERRUYER, Proceedings of Semicon Europa 97, Geneva, Switzerland.
32. O. JOUBERT, G.S. OEHRLEIN, M. SURENDRA, J. Vac. Sci. Technol. A, **12**, 3, 665, 1994.
33. T. GAO, W.D. GRAY, M. VAN HOVE, E. ROSSEEL, H. STRUYF, H. MEYNEN, S.VAN HAELEMEERSCH, K. MAEX, Proceedings of IITC, 53, 1999.
34. M. PONS, J. PELLETIER, O. JOUBERT, J.Appl.Phys., **75**, 9, 4709, 1994.

35. S.C. PALMATEER, R.R. KUNZ, M.W. HORN, A.R. FORTE, M. ROTHSCHILD, Proc. SPIE Advances in Resist Technology and Processing XII (Vol. 2438), 455, 1997.
36. T.W. WEIDMAN, A.M. JOSHI, Appl. Phys. Lett., **62**, 4, 372, 1993.
37. O. JOUBERT, T.W. WEIDMAN, A. JOSHI, R. CIRELLI, S. STEIN, J.T.C. LEE, S. VAIDYA, J. Vac. Sci. Technol. B, **12**, 6, 3909, 1994.

SOFT X-RAY GENERATION BY LASER INTERACTION WITH MATTER

T. LETARDI¹, F. FLORA¹, C. E. ZHENG², P. DI LAZZARO¹, S. BOLLANTI¹

¹ENEA

Frascati-Roma, Italy

²EL-EN

Firenze, Italy

Soft X-ray sources based on laser-generated plasmas are very promising systems, thanks to their compactness, low cost and high efficiency. Applications like microscopy, microlithography and radiobiology have benefited by their development, and some results obtained in these fields are presented. Experimental set-ups for soft X-ray generation will be shown, and their performances will be discussed in terms of dependence on several parameters (i.e. laser intensity and wavelength, target material), together with a spectroscopic analysis and an extensive treatment of the debris problem.

1. Introduction

The exact range of the electromagnetic spectrum that is called "Soft X-rays" is rather questionable. It derives more from technical than from scientific reasons. According to [1] it extends from a wavelength of about 30 nm to about 0.2 nm, that is with photon energies ranging from 40 eV to 6 KeV.

Many fields of science and technology, as astrophysics, plasma physics, biology, and microelectronics, are looking at this electromagnetic spectral region for pure or applied research, encouraging the development of soft X-ray sources.

Laser-plasma sources have recently become competitive with synchrotrons thanks to their compactness and lower cost, and to the capability of achieving high peak brightness with high efficiency. The X-ray emission is obtained by focusing a high-peak-power beam on a target, reaching peak intensities typically ranging from 10^{10} W/cm² to 10^{14} W/cm². A dense plasma is created with diameter of 10 – 100 μ m and a temperature of 10^6 – 10^7 K. The emitted X-ray spectrum and conversion efficiency are heavily dependent on several parameters, as laser wavelength and intensity, and target material, so that laser-plasma sources can be optimized depending on the specific application [2].

This paper will present a review of this field, from the state-of-the-art to future perspectives, ranging from applications to sources description and characterization, with the most encountered problems and possible solutions, concluding with a comparison with other sources.

2. Current and prospective applications

In the case of the microelectronic industry, the trend toward higher DRAM memory content, which requires higher resolution from writing systems, is well known. Table 1 represents a projection, in the future, of the demand in writing density with the correspondent minimum size to be resolved for next years.

Table 1. Trends in microlithography (Revision from data by H. Kinoshita, X-Tech Workshop 96, Berlin)

DRAM (bytes)	Year	Minimum Size (μm)	Exposure Technique
256M	1998	0.25	KrF + Phase Shift
1G	2001	0.18	KrF (ArF) + Phase Shift + Off-axis illumination
4G	2004	0.13	ArF + Phase Shift + Off-axis illum. X-ray Proximity
16G	2007	0.1	X-ray Proximity / EUVL
64G	2010	0.07	EUVL
256G	2013	0.04	EUVL

If we define the key parameters of the writing system of the optical lithography as the wavelength λ of the e.m. radiation, the numerical aperture NA of the optical system, the minimum size (MS) that can be resolved, and the depth of focus DOF , we have the well known relations:

$$(2.1) \quad MS = \frac{K_1 \lambda}{NA}$$

$$(2.2) \quad DOF = \frac{K_2 \lambda}{(NA)^2}$$

We can put, with reasonable approximation, $K_1 = K_2 = 0.6$, and then combining (2.1) and (2.2) we have:

$$(2.3) \quad DOF = \frac{(MS)^2}{(0.6 \cdot \lambda)}$$

In Fig. 1 DOF vs MS , at constant λ , and the line $DOF = MS$ are plotted. Given λ , MS can be changed varying the numerical aperture NA . When $DOF = MS = \lambda$, it is $NA = 1$. Higher values of NA are not technically possible, so that the region below the line $DOF = MS$ is not accessible. Lines numbered 1, 2, 3 refers to the now available excimer lasers with $\lambda = 308$ nm (XeCl), 248 nm (KrF), 193 nm (ArF). It is clear that to achieve the writing density capacity in

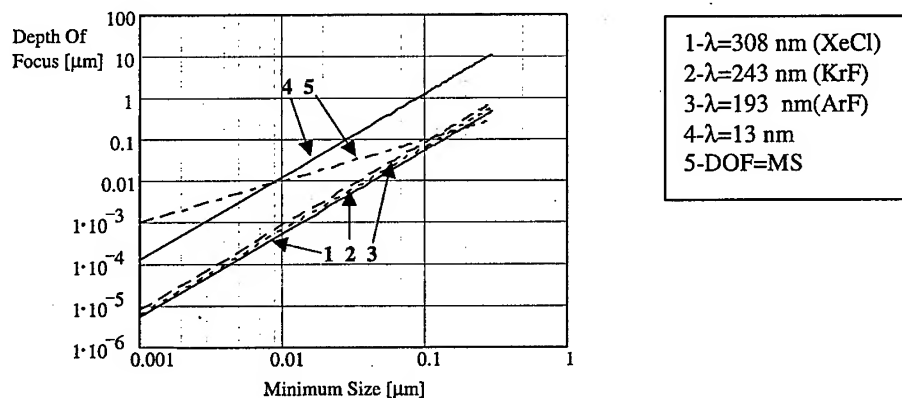


FIG. 1. Depth of focus vs. minimum feature size.

the region of Gbytes, this means with minimum size smaller than $0.15 \mu\text{m}$, new wavelength regions should be explored. The attention is now focussed on two spectral lines, which correspond to two different approaches. The first one has the value of 13 nm (100 eV), which is often mentioned as the EUV approach [3, 4]. In this region, multilayer coatings, with reasonable reflectivity, are now available. An industrial plant requires reflectivity $> 60\%$. According to this proposal, a reflective optic, such as a Schwarzschild objective (see Fig. 2), could be used. In this case, the use of demagnifying optic permits less stringent requirements on the masks, but further development on multilayer coatings is required.

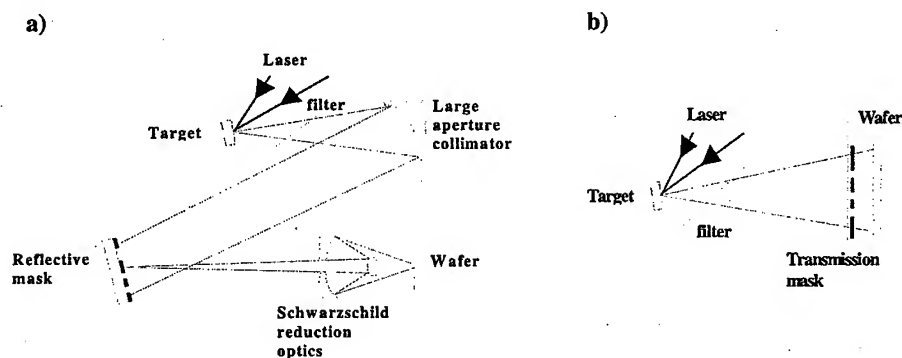


FIG. 2. Apparatus for X-ray projection (a) or proximity (b) lithography.

The second approach [5, 6] considers the wavelength around 1.3 nm (1 keV). In this region, the reflectivity of multilayer coating falls down to few percent [7]. A simple so called contact or proximity lithography (Fig. 2b) is used. The mask is put in close contact (few microns) with the photoresist. A suitable X-ray beam reproduces, in a 1:1 scale, the image of the mask on the photoresist. In Fig. 3a $0.2 \mu\text{m}$ (limited by the master mask) structure obtained with this method using synchrotron radiation ($0.8 - 3.0 \text{ keV}$) is shown.

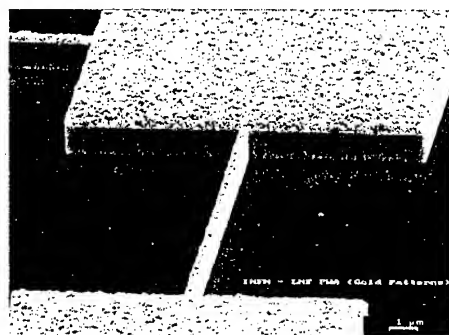


FIG. 3. SEM photograph of a $0.2\ \mu\text{m}$ pattern obtained with contact lithography technique. The synchrotron-radiation-irradiated ($0.8 - 3.0\ \text{keV}$) PN 100 resist has been removed. The resolution is limited by the master mask [8].

This technique imposes more severe constraints on the masks, because optical demagnification is not possible. As for the choice of the photon energy, we must mention that in this region two effects compete for resolution: diffraction, which decreases with increasing photon energy, and diffusion of photoelectrons in the photoresist, which increases with increasing photon energy. The best compromise is reached around $1\ \text{keV}$.

Similar problems are posed by a rapidly increasing technology, which is usually named microtechnology or microfabrication. In essence, it is the fabrication, on micrometric scale, of electro-optical or mechanical devices. The most used method is the so called LIGA one. This method is quite similar to a contact lithography, but the requirement of a photon energy higher than $1\ \text{keV}$ is more stringent, also because the X-rays must have a deep penetration on the photoresist.

In close connection with the writing problems (lithography and microtechnology), is the reading problem, that is the technology of microscopy. The most familiar devices are the optical microscope, the SEM (Scanning Electron Microscope), the TEM (Transmission Electron Microscope), and the AFM (Atomic Force Microscope). In Table 2 are reported the resolution for the different types.

Table 2. Spatial resolution of different types of microscopes

Type	AFM	TEM	SEM	Optical
Resolution	0.1 nm	0.1 nm	5 nm	200 nm

It can be interesting to remind the size of some microscopic objects: bacteria, diameter $0.3 - 2\ \mu\text{m}$, length $0.3 - 100\ \mu\text{m}$; virus, dimension $20 - 300\ \text{nm}$; NaCl reticule, size $0.281\ \text{nm}$.

Moreover, most of the systems mentioned before are essentially limited to the observation of the surface, because the used radiation has small penetration. Only the recently developed confocal microscope, operating in the optical region, has the possibility of observing inside the object, but with resolution and contrast determined by the properties of the e.m. radiation in the optical region.

The penetration of soft X-rays for water and proteins (that is, for samples of biological interest) can arrive up to $50\text{ }\mu\text{m}$ as shown in Fig. 4. The contrast between water and proteins, in the so called water window (2–4 nm) is enhanced as a consequence of strong difference in the absorption coefficient, while in the other region is mainly connected to the Z of the components; the resolution, which is due both to diffraction and to the statistical properties of radiation, can reach 30 nm [9]. Imaging system can be done or through a contact technique [10, 11] (quite similar to the microlithography technique) or using Fresnel zone plates [9, 12].

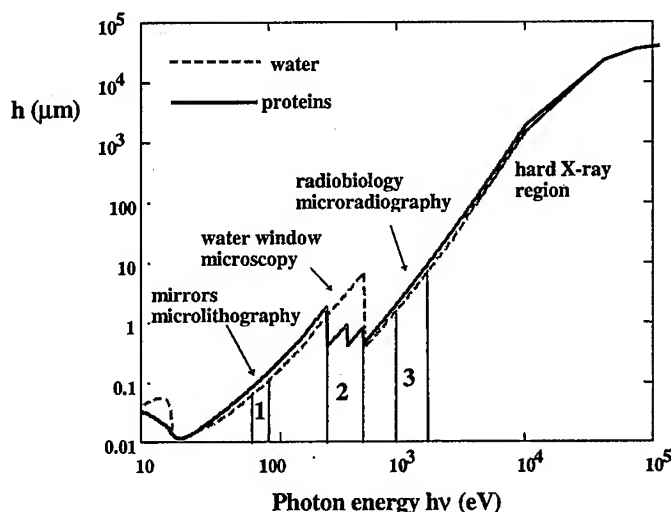


FIG. 4. 50% penetration depth (h) of X-rays in water and in biological material vs. photon energy. Gray spectral intervals correspond to different applications: (1) projection lithography, (2) microscopy and (3) proximity lithography.

It is important to mention the applications in radiobiology [13], because at the typical energies of soft X-rays ($< 8\text{ keV}$) the photons are mainly absorbed by photoelectric effect, this means with emission of an electron which has a very short (few nm) range. Very localized, with a corresponding very high dosage, damages can be studied, also in those structures (DNA) where high resolution is required.

3. Soft X-ray sources

The most common sources of soft X-rays are: the synchrotron light, it is the radiation emitted by accelerated electrons (typically, centrifugal acceleration in circular paths), the radiation emitted by electrons impinging on a target through the bremsstrahlung effect (i.e. vacuum X-ray diodes), and the radiation emitted by matter when heated to a suitable temperature, at which it is highly ionized, so that these sources are called "plasma sources".

One convenient way of heating a solid target is by means of the interaction with a short, focussed, high-peak-power laser pulse. Present technology permits achieving power densities in the order of 10^{20} W/cm² [14]. Under the action of laser radiation, matter is partly vaporized and ionized, so that the solid target is partly screened by a plasma cloud, whose refractive index (N), for e.m. radiation at ω_0 frequency, can be written as:

$$(3.1) \quad N^2 = 1 - \frac{n_e e^2}{m_e \varphi_0 \omega_0^2},$$

where n_e is electron number density, e and m_e are the electric charge and mass of the electron, φ_0 is vacuum dielectric constant. If we define the plasma frequency ω_p as:

$$(3.2) \quad \omega_p = \frac{n_e e^2}{m_e \varphi_0}$$

we can finally write:

$$(3.3) \quad N = \sqrt{1 - \frac{\omega_p^2}{\omega_0^2}}.$$

In conclusion, the e.m. wave can propagate in the plasma only if $\omega_0 > \omega_p$ or, in terms of wavelength λ , if:

$$(3.4) \quad n_e [\text{cm}^{-3}] \leq 1.12 \times 10^{21} \lambda^{-2} [\mu\text{m}]$$

that means that lasers with short λ are better for plasma sources, because they can penetrate in the cloud plasma up to higher electron densities.

The power density radiated by the hot plasma scales as a power of the temperature (fourth power, for ideal black body, lower [15, 16], in the case of a real laser plasma source) and must be balanced by the input power density given by the laser: to achieve high electron temperature T_e , high power density I_L must be realized and it is given by:

$$(3.5) \quad I_L = \frac{(\text{NA})^2}{(M\lambda)^2} \cdot \frac{E}{\Delta t},$$

where NA is the numerical aperture < 1 , E is the laser pulse energy, M is the laser beam quality factor > 1 , Δt is the pulse time duration. High quality ($M = 1$, single transverse mode), short pulse, short wavelength λ , and high energy per pulse are required to achieve high power density, and so high temperatures.

The input energy is shared, according to theoretical simulations [17], among kinetic energy of emitted debris, changes in internal and potential energy, and emitted radiation (about 26% of the input energy, in the specific studied case). In general, only a fraction of the input power is emitted in the form of radiation. Experimental results [18] show a dependence also on the wavelength of the laser, with comparable conversion efficiency, as shown in Fig. 5.

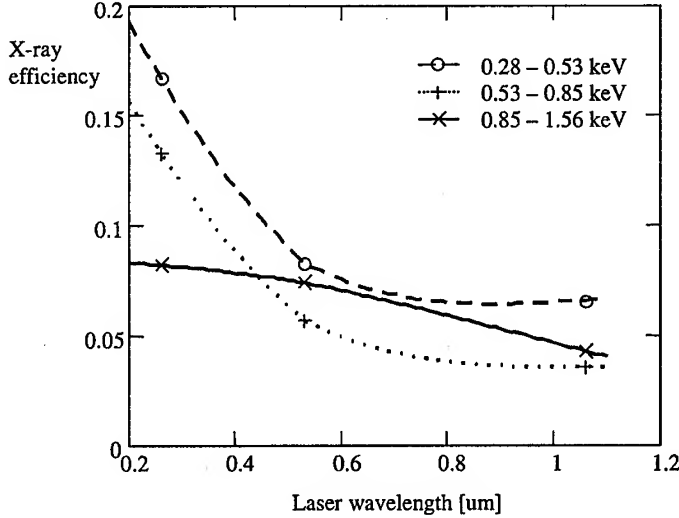


FIG. 5. X-ray conversion efficiency for a gold target vs. laser wavelength at $I_L = 10^{14} \text{ W/cm}^2$, in accordance with Ref.18.

We have mentioned that essentially the laser radiation transfers the energy to the electrons, and then the electrons go in equilibrium with the atoms. The equilibrium time τ , according to [15], goes as:

$$(3.6) \quad n_e \tau = 10^{11 \div 12} [\text{cm}^{-3} \text{s}].$$

If we take, as n_e , the limit electron density at λ , finally we have:

$$(3.7) \quad \tau [\text{ns}] = (0.1 \div 1) \lambda^2 [\mu\text{m}]$$

as the time to achieve equilibrium, when operating at wavelength λ . For u.v. radiation, we are in the region of tens of ps. When irradiating with pulses shorter than the equilibrium time, at a given electron temperature T_e , matter is less heated, and less vaporized, and this can have important consequences also from a technical point of view.

Most part of radiation is emitted in the form of recombination continuum and spectra lines. Even if the source is far from being of black body type, because the emitting plasma is not always in equilibrium, nor it is always fully opaque to the emitted radiation, anyway some considerations can be done on the simple model of a black body. It has been shown both experimentally and theoretically that the electron temperature T_e increases with the increase of the laser power density I_L . On the limit of black body and with an assumption of all the radiated energy being balanced by the incident laser power density, we may write the Stefan-Boltzman law as:

$$(3.8) \quad T_e [\text{eV}] = 0.0559 I_L^{0.25} [\text{W/cm}^2].$$

The more accurate theory of Colombant and Tonon [15] gives:

$$(3.9) \quad T_e[\text{eV}] = 5.2 \times 10^{-6} A^{1/5} \lambda^{6/5} [\mu\text{m}] I_L^{0.6} [\text{W}/\text{cm}^2]$$

(A is the atomic weight), while the experiments obtained for an aluminum target and a KrF laser ($\lambda = 248$ nm) [16] give:

$$(3.10) \quad T_e[\text{eV}] = 1.16 \times 10^{-5} I_L^{0.57} [\text{W}/\text{cm}^2].$$

A comparison between the results from Eqs. (3.8), (3.9) and (3.10) is shown in Fig. 6: the larger power density emitted by an ideal black body reduces its

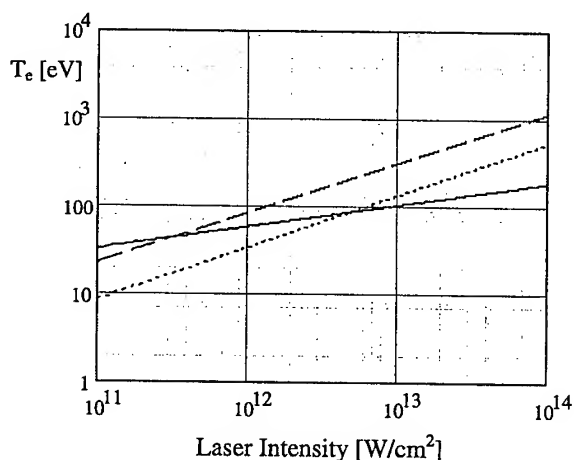


FIG. 6. Plasma temperature vs. laser power density according with a black body equilibrium model (solid line), and according with the experimental (dashed line) [16] or theoretical (dotted line) [15] values obtained for an Al target irradiated by a KrF laser ($\lambda = 248$ nm).

temperature of equilibrium with the laser radiation with respect to a real plasma. It is evident that the laser power density on the target must be changed according to the spectral range in which the maximum emission is required.

4. Typical experimental apparatus and some results

A typical experimental apparatus (Fig. 7) includes a laser source and a chamber in which the laser beam is focussed on a convenient target. In the chamber a vacuum better than few Torr or better than 10^{-2} Torr must be ensured for the propagation of 1 keV or 100 eV X-rays respectively. The target can be in the form of a solid rod or, in order to reduce the debris [19] as explained better in the following, in the form of a thin tape.

The X-ray pulse closely follows the laser pulse only for a time duration shorter than about 10 ns. For longer laser pulses, the situation is more complicated, because the X-ray time duration depends also from the observed spectral range, as shown in Fig. 8 for a 120 ns laser pulse.

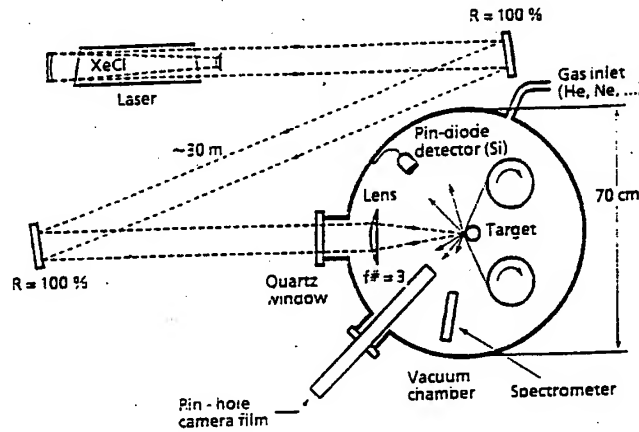


FIG. 7. Experimental set-up for an X-ray plasma source (in this case a XeCl laser is used and the long path between the laser and the vacuum chamber works as a delay line to avoid damages on the laser mirrors by the plasma scattered light) [20].

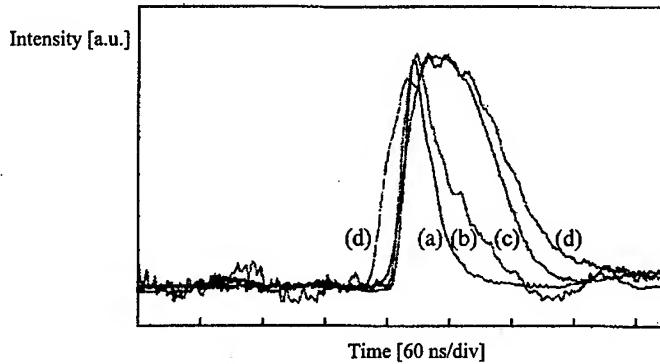


FIG. 8. Time evolution of a 120 ns excimer laser pulse (curve d) and of the X-rays in the S_{70} , S_{ww} and S_{1k} spectral regions (curves a, b and c, respectively). Laser peak power density $= 5 \times 10^{12} \text{ W/cm}^2$ [13].

In the measurements done in our laboratory [13] three spectral regions, corresponding to three important applications, have been measured:

- S_{70} : $40 < h\nu < 70 \text{ eV}$ (for imaging micro-lithography)
- S_{ww} : $300 < h\nu < 500 \text{ eV}$ (for microscopy)
- S_{1k} : $0.8 < h\nu < 1.6 \text{ keV}$ (for radiobiology or contact micro-lithography).

These regions correspond in Fig. 4 to the grey areas 1, 2 and 3, respectively. The X-ray regions have been selected by means of filters, and have been detected by

means of pin diodes. From the results (see Fig. 8) we observe that only in the lower energy range the X-ray pulse closely follows the laser pulse, while for higher energies there is a shortening effect.

Time duration and X-ray conversion efficiency depend also on the laser power density [21]. In Fig. 9 the results of measurements are reported. Power density is changed defocusing the laser beam. Similar measurements, done in our group [13], have been performed measuring peak conversion efficiency vs. laser power density, by means of defocusing, as shown in Fig. 10. Even if many effects, including different ways of plasma expansion according to the different beam size should be considered, a very simple approach according to a black body emission, with a dependence of T_e on I_L given in Fig. 6, shows the correct behavior.

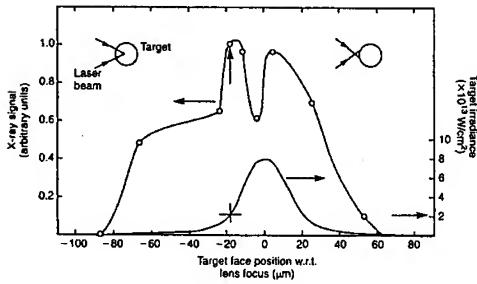


FIG. 9. Experimental behavior of X-ray emission as a function of the laser intensity, according with Ref.8 [21].

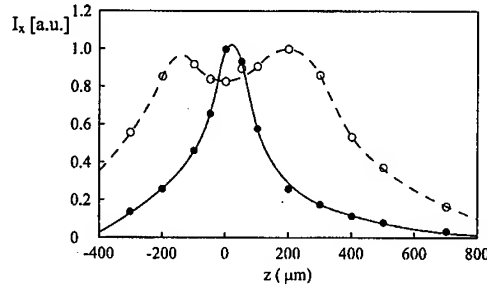


FIG. 10. Experimental behavior of the X-ray emission I_X in the S_w (dashed line) and S_{1k} (solid line) spectral regions vs. target position z with respect to the laser beam waist using a 10 ns excimer laser pulse [13]. Laser peak intensity $= 3 \times 10^{13} \text{ W/cm}^2$.

The X-ray emission peak can be changed, at constant laser power density, changing the target material. This has been treated theoretically in [2] and [22] and experimentally verified in [23]. The measurements refer to two spectral ranges (100 – 750 eV, 750 – 2000 eV), and two wavelengths (1.06 μm and 0.26 μm), as shown in Fig. 11.

As it has been mentioned before, both from theoretical considerations and experimental results, it is clear that not all the impinging laser radiation is re-emitted at shorter wavelengths, because part is reflected, part goes in the ablation processes, part in kinetic energy of liquid droplets. The measurements of the conversion efficiency, that is (total irradiated energy)/(total impinging laser energy), is of primary importance, both for theoretical and practical reasons. In Fig. 12 the results are shown of operation with a laser pulse at $\lambda = 248 \text{ nm}$, 30 ns, 30 J/p, focused on a Cu target [24]. In the very short pulses range, similar results have been obtained with 4 ps pulses, that is a peak conversion efficiency of about 10% [25].

Similar measurements have been done in our group [13], using a XeCl laser in two different operating conditions: 6 J in 120 ns, and 2 J in 10 ns. The X-ray energy has been measured in the three spectral ranges mentioned before.

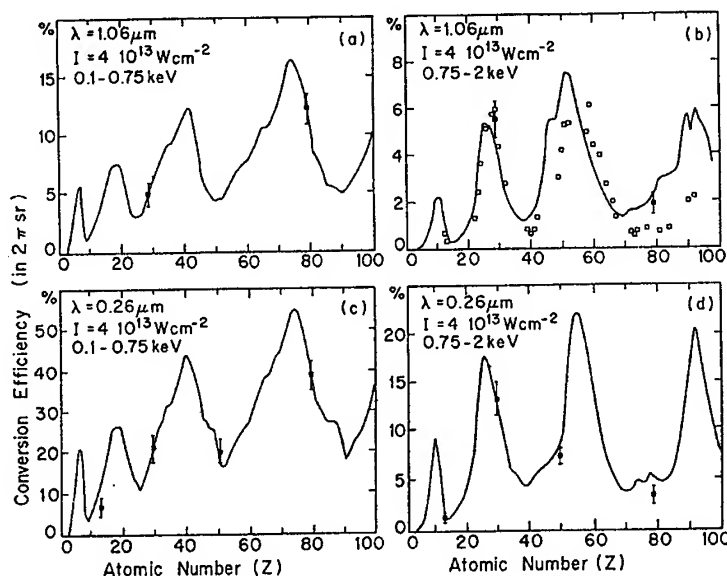


FIG. 11. X-ray conversion efficiency vs. atomic number Z for different spectral regions and laser parameters, from Ref. [23].

The results are reported in Fig. 13 for a Cu target. The conversion efficiency is defined as $\eta = E_X / (0.65 E_L)$, because the beam transport efficiency from the laser source to the target is about 65%. A maximum conversion efficiency of 12%, in the 40 – 70 eV range, has been measured.

5. Debris emission

When a target material is irradiated by a focused laser beam, it is instantaneously liquefied, vaporized and ionized, causing a very high plasma pressure P_p near the laser spot, whose value can reach $P_p = 10^6$ bar for a laser power density of 5×10^{12} W/cm² [26]. With expansion of the hot ionized plasma into the vacuum, a plasma pressure-driven shock wave is formed, penetrating into the target, melting and ablating the target material in a region around the initial focal spot. The matter in the crater is emitted in all directions, having three different species other than electrons [27, 28]: fast ions moving with velocity of up to $10^5 - 10^7$ cm/s [28, 29, 30], neutral atoms following the ions, and hot pieces of material ejected from target as particles of various form and sizes of from sub-up to 100 μ m with a velocity in a range of 10^3 to 10^5 cm/s [27, 31, 32, 34, 35, 36].

The large size debris have been observed to be sharply directed along the target normal for a laser angle of incidence of 45° [37]. A typical spatial distribution of the debris, measured using a XeCl laser of 2 J and pulse duration of 10 ns focused on a Cu target at 10^{13} W/cm², is shown in Fig. 14 [38].

Clearly, the production of plasma debris is more serious for the case of solid target, and it leads to several consequences for some X-ray applications, such as

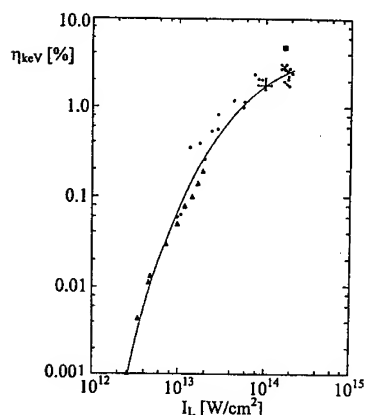


FIG. 12. Conversion efficiency η_{keV} from laser to $1 \text{ keV} < h\nu < 1.4 \text{ keV}$ X-rays vs. laser intensity I_L (from Ref.24).

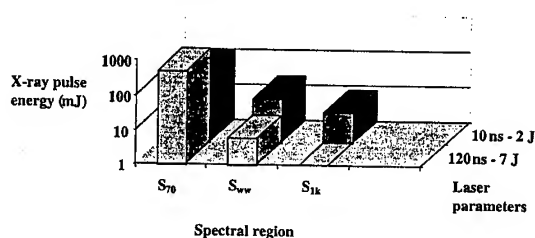


FIG. 13. X-ray pulse energy emitted by a Cu target in different spectral regions and for different duration of the XeCl excimer laser pulse. (spot diameter = $30 \mu\text{m}$ at 86% of power).

(1) the damage of X-ray filters, masks, thin membrane window, (2) the formation of films on the surfaces of optics or other objects; thus, the solution of this problem is of central importance for the use of laser plasma sources.

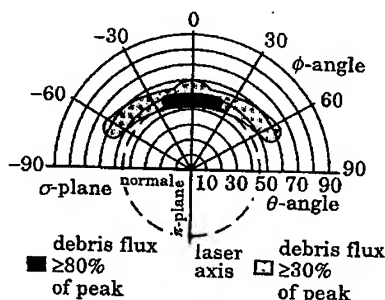
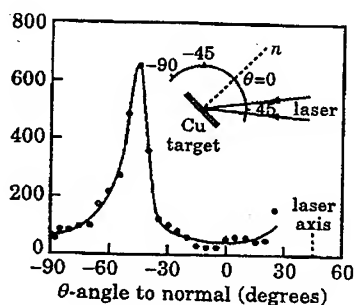


FIG. 14. Spatial distribution of large size ($> 10 \mu\text{m}$) debris emitted by a Cu target at a laser intensity of 10^{13} W/cm^2 (from Ref. [38]).

To control the debris generation, a number of studies were carried in the past. The main techniques used are: (1) filters for stopping the projectile particles; (2) helium buffer gas for reducing the expansion range of the debris [27, 39]; (3) jet gas for slowing down the debris velocity; (4) thin tape target, usually in the order of several $10 \mu\text{m}$, where a hole can be drilled by the laser ablation and plasma shock wave, and the debris will be ejected in the direction of the laser beam [1, 24, 25]; (5) rotating disk shutter, synchronously triggered with the laser pulses through a delay circuit and used as a debris-velocity filter, for removing from the soft X-ray beam the particles with velocities lower than a value of the

order of 10^2 m/s [30, 34]; (6) short laser pulse (in the order of some ps) for reducing the debris production because of the target lattice atoms remaining much colder than electrons [40].

Alternatively, droplet liquid targets [41, 42] or gas jet targets [43] rather than the traditional solid targets have been proposed. Unfortunately, each of these solutions has some drawbacks in terms of complexity of the system and of conversion efficiency in defined spectral intervals, in particular in the 50–200 eV region; this is a consequence of the fact that for such targets the laser parameters, like pulse duration, wavelength and intensity, must be chosen according with the target requirements rather than with the requirement for the highest X-ray production in the spectral interval of interest.

In Fig. 15 the scheme of a droplet target plasma source is shown. A train of ethanol droplets, with about $10\text{ }\mu\text{m}$ diameter, is ejected in a vacuum chamber. A synchronized, frequency doubled, 70 mJ, 100–120 ps Nd:Yag laser pulse heats the droplet.

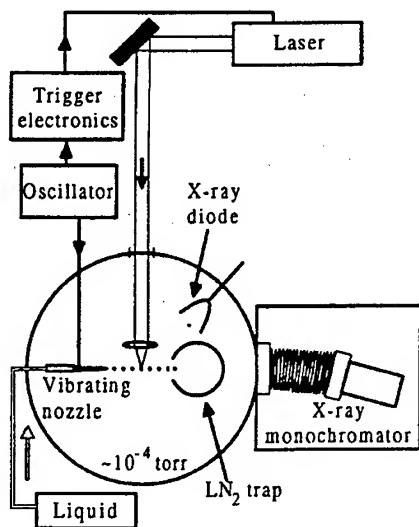


FIG. 15. Experimental apparatus for droplet targets plasma source (from Ref. [42]).

The system achieves some results: the source is practically debris-free, and the optical quality, due also to the small dimensions of the droplet, is good. On the other hand, the formation of the stable droplets is connected to the surface tension, and only few liquids can be explored, the dimensions of the droplets cannot be larger, in order not to load the vacuum system, and the overall efficiency, as reported in [42], is about two orders of magnitude lower than that with solid targets.

For the exploration of gas targets, in [43] a pulsed N_2 gas jet, at pressure higher than 1 bar, has been injected in a vacuum chamber. A 1 ns, 1 to 5 J Nd:glass laser pulse has been used. Soft X-ray emission in the water window has been observed. Again, also in this case the efficiency is very low and, moreover,

due to the diffused nature of the target, the X-ray beam quality could be worst.

Coming back to solid targets, the thin-tape solution has given excellent results only at 1 – 1.5 keV photon energy, that is in the interval of interest for the proximity lithography, while for the liquid and gas target the conversion efficiency is limited by the small size or low density of the target respectively. More recently, good efficiency values in the 1 – 1.5 keV region have been obtained also from cryogenic Xe targets [44]. For the $h\nu = 50 - 200$ eV X-rays region, all non-solid targets potentially present the problem of the high absorption of the target residual vapors which remain in the vacuum chamber.

A completely different approach is now under development in our laboratory [45] for controlling the debris damage in the imaging microlithography application (S_{70} spectral region). As mentioned before, the X-ray production in the above range is increased by an off-focus alignment of the laser beam (down to laser intensities I_L of the order of 10^{10} W/cm²), which decreases the plasma temperature T_p , finally leading to a reduction of the debris velocity. In fact, for the gas phase expansion in vacuum, the maximum particle velocity V_m is expected to scale as $V_m \propto T^{1/2}$ [31, 46], where T is the temperature before expansion. For the laser plasma, we may approximate T with the plasma temperature T_p , which is approximately determined by the laser intensity on the target according to $T_p \propto I_L^{1/2}$ [47]. Finally, we have $V_m \propto I_L^{1/4}$, so that going from $I_L \approx 10^{12} - 10^{13}$ W/cm² down to $\approx 10^{10}$ W/cm², the maximum debris velocity should diminish of a factor 3 – 5.5. This reduced speed value should permit a successful use of mechanical stoppers in order to discriminate the debris from the X-rays.

In Fig. 16 we report two images of debris-emitted light from tantalum target at $I_L = 5 \times 10^{12}$ W/cm² and 10^{10} W/cm², respectively. Since the images have

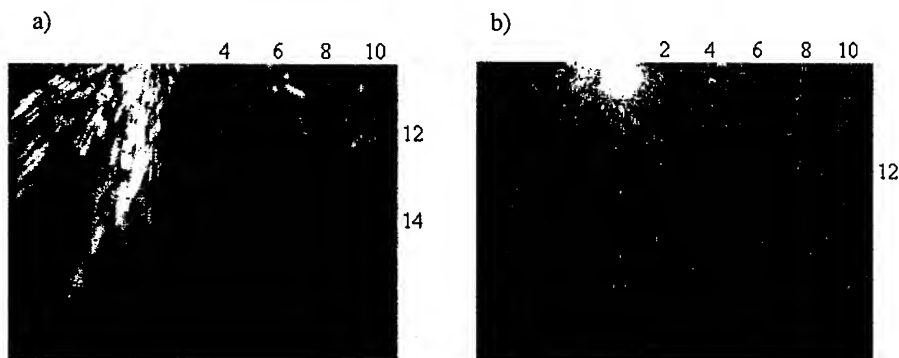


FIG. 16. Photographs of the debris emitted by a Ta target at a laser intensity of (a) $5 \cdot 10^{12}$ W/cm² and (b) 10^{10} W/cm². The photographs are obtained by the observation, through a fast CCD camera (PCO Computer Optics, DICAM-2), of the light emitted by the debris. Dashed lines show the distance from the target (in cm). Laser pulse duration: 120 ns. Exposure time: 50 μ s. Beginning of the exposure: 500 μ s after the plasma generation.

been acquired in the same way (see figure caption), it is evident that in the low intensity case the maximum distance reached by visible debris is reduced

of about a factor 5 with respect to the high intensity irradiation, as expected from the theory. The quite long exposure time confirms the possibility of using mechanical stoppers for these visible debris.

Obviously, not all the debris are visible in the images of Fig. 16: we have estimated a minimum debris diameter of about 1 mm in order to emit sufficient luminous power to be detectable by our CCD camera. Anyway, the small-size, invisible debris, as well as ions, do not represent a serious problem, since they can be arrested just filling the interaction chamber with helium gas at low pressure. In Fig. 17 the mass range R_p of the debris flight (before reaching a complete

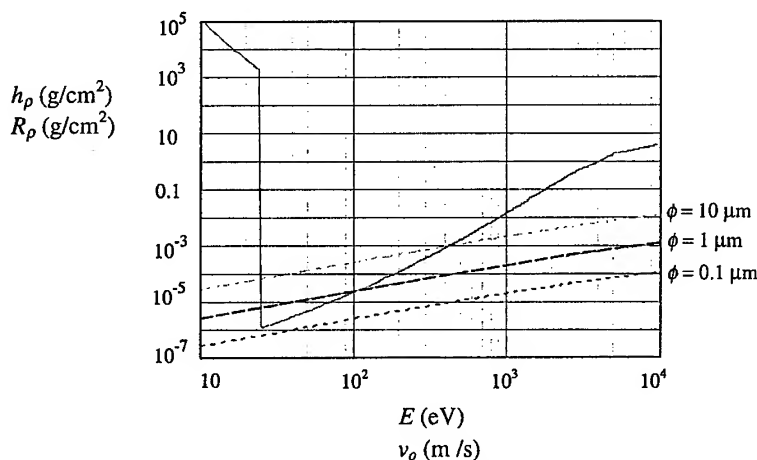


FIG. 17. Mass penetration depth (h_{rho}) of X-rays (solid line) and debris mass flight range (R_p) (dashed lines) vs. photon energy E and vs. initial speed v_0 , respectively, calculated for different debris diameters (ϕ). [48]. Both ordinates are normalized to the helium density ρ . The range is calculated for a helium pressure of 5 Torr (R_p is little depending on the value of ρ) and for spherical copper particles.

stop) versus the initial debris speed V_0 for different debris diameters is reported together with the mass penetration depth h_p of the X-rays in helium versus the photon energy E . Here both R_p and h_p are normalized to the helium gas density ρ and the target material is copper.

Since h_p is the X-ray propagation distance where the intensity decreases to $1/e$ of the initial value, it is possible to know from the figure which particles can be stopped by using helium as buffer gas still maintaining a relevant percentage (36.8%) of the generated radiation, i.e. those having $R_p < h_p$. As it can be seen, in the S_{70} interval the maximum mass penetration depth is around 10^{-5} g/cm². At this "distance" all the debris with diameter $\phi = 0.1$ μ m are stopped if their initial velocity is smaller than 500 m/s, while for $\phi = 1$ μ m the maximum V_0 for a complete arrest is about 40 m/s. On the other hand, from Fig. 16b we can estimate an average visible-debris (i.e. $\phi \geq 1$ μ m) speed of about 60 m/s. This means that $\phi < 1$ μ m debris can be arrested with a helium thickness which can still transmit $1/e = 36.8\%$ of X-rays in the S_{70} spectral window.

For a practical use, the flight range R (in cm) can be expressed through an approximated formula; valid for a spherical particle with diameter ϕ , in helium

(up to a pressure $p[\text{torr}] < 142\phi [\mu\text{m}]$), and up to a particle Reynolds number equal to 1000 [48]:

$$(5.1) \quad R[\text{cm}] = 4.26 \times 10^{10} \phi[\mu\text{m}] \frac{\rho_t}{\rho} (V_0[\text{cm/s}])^{0.95},$$

where ρ_t is the particle density. Hence the range of a particle is (almost) proportional to its diameter.

6. Spectroscopy

The knowledge of the emission spectra of laser plasma sources with high spectral and spatial resolution is of crucial importance for different reasons: first of all, the high resolution X-ray spectroscopy gives a unique possibility to test the correctness of various quantum-electro-dynamical models for high accuracy theoretical calculations of different atomic structures; secondly, the use of laser plasma sources is one of the few possibilities of measuring the ionization potential of multi-charged ions; then, the obtained results can be used in modeling codes to estimate with high accuracy plasma parameters, like electrons and ions density and temperature, number of hot electrons in the plasma, ions ionization distribution; finally, a wide spectroscopic characterization of the plasma source changing the target element and laser parameters is a peerless way to optimize the X-ray emission for a specific application.

In our laboratory we have carried on measurements of high resolution spectroscopy [49]–[59] in cooperation with the NPO VNIIFTRI Institute of Moscow, using particular spectrometers based on spherically bent mica crystals. These spectrometers allow to get simultaneously the spectrum and the one-dimensional imaging of the plasma source, as shown in Fig. 18. A spectral resolution $\lambda/\Delta\lambda$ up to 10^4 can be reached.

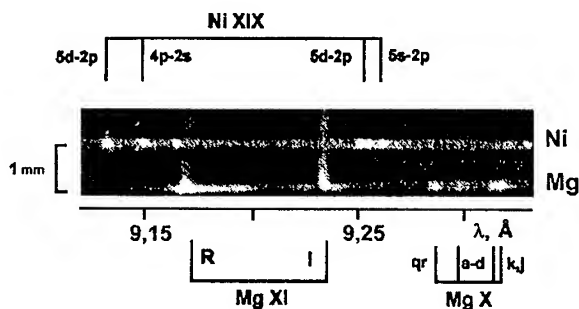


FIG. 18. Magnesium and Nickel spectra obtained using the XeCl excimer laser in the configuration of 10 ns — 2 J. The one-dimensional imaging of the plasma (vertical scale) is in the direction z normal to the target. The two targets have been placed (sequentially) at two different z positions (1 mm apart) so that the two spectra do not overlap (see ref. [51]).

In particular the magnesium XI (i.e. He-like ions) resonant line at $\lambda = 9.1681 \text{ \AA}$ and the inter-combination line at $\lambda = 9.2307 \text{ \AA}$ (corresponding to the

transitions $2^1P_1 - 1^1S_0$ and $2^3P_1 - 1^1S_0$, respectively) can be used as reference points for the determination on the wavelengths of the other lines like the satellite ones of magnesium X. Experimental results have been compared with very precise theoretical calculations performed at LLNL using the atomic code HULLAC, allowing for the first time to identify and measure with record accuracy wavelengths and ionization potentials of different multi-charged ions [49]. Moreover, the increased spectral resolution of the obtained spectra allowed us to develop new methods of plasma diagnostic, based on line intensities caused by transitions from Rydberg auto-ionizing states of multi-charged ions.

7. Comparison with other sources

A parameter that is usually considered for comparison with other X-ray sources is the spectral brightness $B(E)$ which gives the number of photons emitted at a given energy (eV) per second, from 1 mm^2 of emitting source, in one mrad^2 solid angle, in 0.1% of spectral bandwidth. In conclusion, it is :

$$(7.1) \quad B(E) = \frac{\text{Number of photons at energy } E(\text{eV})}{\text{s} \times \text{mm}^2 \times \text{mrad}^2 \times 0.1\% \text{ spectral bandwidth}}$$

If we treat the plasma source in the limit of a black-body radiator (this approximation becomes worse when the plasma temperature goes beyond $\approx 10^2 \text{ eV}$), we can write:

$$(7.2) \quad B(E, T) = 1.57 \times 10^{11} \frac{E^3}{\exp(E/T) - 1},$$

where E and T are the photon energy and plasma temperature in eV units. If, given the spectral energy E , we optimize T in order to have the maximum of the emission at E (optimized black-body, i.e. $T = E/2.82$), then we finally obtain:

$$(7.3) \quad B_{\text{MAX}}(E) = 1.57 \times 10^{11} \frac{E^3}{\exp(2.82) - 1}.$$

In Fig. 19 we have reported the plot of the peak brightness of some most common sources and compared it with B_{MAX} .

As a matter of fact, the comparison based on $B(E)$ as defined in (7.2) is meaningful only for applications where a narrow bandwidth ($\Delta E/E \approx 10^{-3}$) is required, like scanning or projection microscopy (where zone plates are used), or material studies (for example, absorption spectroscopy). In the case of radiobiology, X-ray contact microscopy, contact and projection microlithography the useful bandwidth can be of the order of 10%, so that plasma sources become very competitive with respect to the narrow-spectral-width radiation from synchrotron+undulator (SU) systems. In the same way, for a very important application like the projection microlithography a low ($\text{mm}^2 \times \text{mrad}^2$) product like in SU is not necessary.

Then, in Fig. 20 we compare the average number of photons emitted per second in 10% of spectral bandwidth from a plasma source having a laser driver

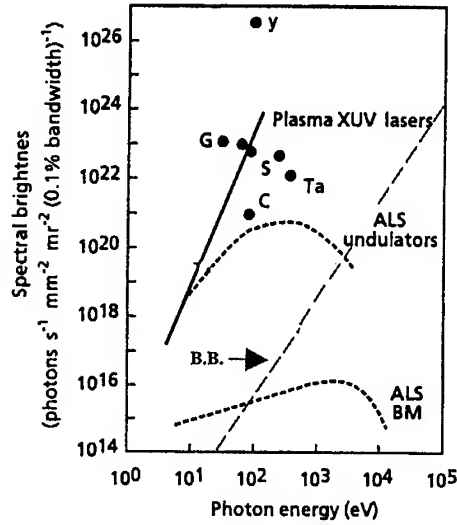


FIG. 19. Peak spectral brightness of some X-ray sources and of an ideal optimized black-body.

of 300 W average power (considering a conversion efficiency of 40%) with those radiated by an undulator of 40 steps with $K = 2$ in a storage ring with 100 mA of circulating current, into the full emission bandwidth ($\approx 1\%$).

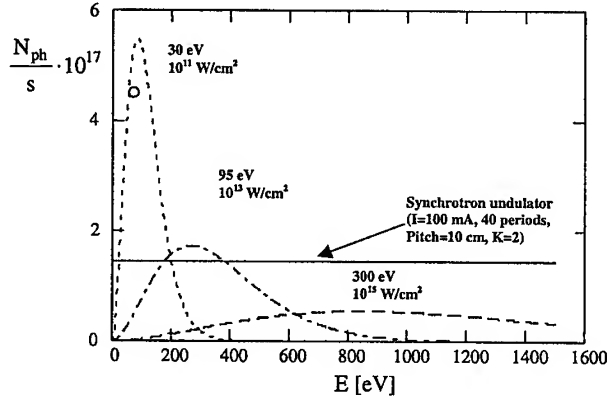


FIG. 20. Number of photons N_{ph} emitted per second into a 10% bandwidth by a 40%-efficiency plasma source with a 300 W-average-power driving laser at different values of the plasma temperature T , calculated in the black-body approximation, and by a synchrotron undulator into the full emission bandwidth ($\approx 1\%$, see text). The values of laser pulse duration Δt and of the source diameter ϕ reported in parenthesis are examples on how to obtain different laser intensities and, consequently, different T values. The circle represents a particular measurement of the emission in a narrow spectral range by the Hercules laser plasma source [13] extrapolated to 50 Hz repetition rate.

The emission peak in the SU is moved changing the energy of the electrons, while the temperature of the plasma source is changed by means of the focussed

diameter and the pulse length, at constant average power of the driving laser. As we can see from the results (Fig. 20), at low photon energy (that is, around 100 eV), the plasma source is very competitive.

References

1. Flugge, *Encyclopedia of Physics*, vol. XXX, p. 94, 247, 1957.
2. F. O'NEILL, *Laser-plasma X-UV Sources*, in *Laser-Plasma Interactions 4*, p.285, M.P.Hooper Ed., SUSSP Publ., Edinburgh, 1988.
3. F. BIJKERK and A.P. SHEVELKO, *Soft X-ray radiation from excimer-driven laser-plasma sources: application to submicron lithography*, in *Excimer lasers*, pp. 339-353, L.D. Laude Ed., Kluwer Academic Publishers, 1994.
4. I.A. ARTYUKOV et al., *Soft X-ray submicron imaging experiments with nanosecond exposure*, *Optics Comm.*, **102**, 401-406, 1993.
5. J. R. MALDONADO, *Prospects for granular X-ray lithography sources*, in *Applications of Laser Plasma Radiation II*, M.C. Richardson, G.A. Kyrala Eds., *Proc. SPIE*, **2523**, 2-22, 1995.
6. H. SHIELDS, M. POWERS, I.C.E. TURCU et al., *High power excimer laser-generated plasma source for X-ray microlithography*, in *Applications of Laser Plasma Radiation II*, M.C. Richardson, G.A. Kyrala Eds., *Proc. SPIE*, **2523**, 122-128, 1995.
7. I.V. KOZHEVNIKOV et al., *Synthesis and measurement of normal incidence X-ray multilayer mirrors optimized for a photon energy of 390 eV*, *Nuclear Inst. & methods in Phys. Research A*, **354**, 594-603, 1994.
8. K. SHIXIU, A. GRILLI, A. RACO, *X-ray mask copying based on negative resist RAY-PN*, *Micro-electronic Engineering*, **23**, 231-234, 1994.
9. R. MEDENWALDT, J. ABRAHAM-PESKIR and E. UGGERHFJ, *X-ray microscopy in Aarhus with 30 nm resolution*, *Sunch. Rad. News*, **11**, 4, 1998.
10. P. ALBERTANO et al., *X-ray contact microscopy using an excimer laser plasma source with different target materials and laser pulse durations*, *J. of Microscopy*, **187**, (Pt.2), 96-103, 1997.
11. A.D. STEAD et al., *A comparison of soft X-ray contact microscopy with light and electron microscopy for the study of algal cell ultrastructure*, *J. Microscopy*, **149**, 207-216, 1988.
12. G. SCHNEIDER and B. NIEMANN, *Cryo X-ray microscopy experiments*, *Int. Conf. on X-ray Microscopy and spectromicroscopy*, Wurzburg, 19-23 Aug., 1996, ed. by Jurgen Thieme et al., I-25 - I-34, 1996.
13. S. BOLLANTI et al., *Soft X-ray plasma source for atmospheric pressure microscopy, radiobiology and other applications*, *Il Nuovo Cimento*, **D20**, 1685-1701, 1998.
14. P. GALLANT et al., *Sub-picosecond time resolved X-ray spectroscopy of plasmas produced by high intensity ultrashort laser pulses*, in *Applications of X-Rays Generated from Lasers and Other Bright Sources*, G.A. Kyrala, J.J. Gauthier Eds., *Proc. SPIE*, **3157**, 44-51, 1997.
15. D. COLOMBANT and G. TONON, *X-ray emission in laser produced plasmas*, *J. Appl. Phys.*, **44**, 8, 3524-3537, 1973.
16. P.D. GUPTA, R. POPIL, R. FEDOSEJEVS, A. OFFEMBERGER, D. SALZMANN and C.E. CAPJACK, *Temperature and X-ray intensity scaling in KrF laser plasma interactions*, *Appl. Phys. Lett.*, **48**, 2, 103-5, 1986.
17. D. DUSTO, R.W. CLARK, J. DAVIS, J. APRUZESE, *Radiation energetics of a laser produced plasma*, *Phys.Rev.*, **A27**, 1441-1460, 1983.
18. R. KODAMA et al., *J. Appl. Phys.*, **59**, 3050, 1986.
19. I.C.E. TURCU and J.B. DANCE, *X-rays from laser plasmas*, p.215 and following, John Wiley & Sons, 1999.

20. S. BOLLANTI et al., *Long duration soft X-ray pulses by XeCl laser driven plasmas and applications*, Journal of X-ray science and technology, **5**, 261-277, 1995.
21. E. TURCU, G. DAVIS, M.C. GOWER, F.O'NEILL, M. LAWLESS, *X-ray lithography using a KrF Laser Plasma source at $h\nu$ 1 keV*, Microelectronic Engineering, **6**, 287-92, 1987.
22. A.V. VINOGRADOV and V.N. SHLYAPTSEV, *Characteristics of a laser plasma x-ray source (review)*, Sov. J. Quantum Electron., **17**, 1, 1, 1987.
23. M. CHAKER, H. PEPIN, V. BAREAU, B. LAFONTAINE, *Laser plasma sources for microlithography*, J. Appl. Phys., **63**, 3, 892, 1988.
24. G.M. DAVIS, M.C. GOWER, F. O'NEILL, I.C.E. TURCU, *Plasma X-ray source for lithography generated by $a = 30$ J, 30 ns KrF laser*, Appl. Phys. Lett., **53**, 1583-1585, 1988.
25. I.C.E. TURCU, I.N. ROSS, G.J. TALLENTS, *Efficient keV X-ray emission from plasma generated with 4 ps KrF laser pulses*, Appl. Phys. Lett., **63**, 3046-3048, 1993.
26. V.G. BAKAEV, V.Yu. KOROL', I.G. LEBO, N.N. MEL'NIK, G.E. METREVELI, A.G. MOLCHANOV, V.V. NIKISHIN, V.B. ROZANOV, G.V. SYCHUGOV, V.F. TISHKIN and V.D. ZVORYKIN, *Laser-Target interactions at KrF GARPUN facility*, Reprint No. 69 of Lebedev Physical Inst., Russian Academy of Sciences, Moscow, 1997.
27. R. BOBKOWSKI and R. FEDOSEJEVS, J. Vac. Sci. Technol., **A14**, 4, 1973, 1996.
28. M. RICHARDSON, W.T. SILFVAST, H.A. BENDER, A. HANZO, V.P. YANOVSKY, F. JIN, and J. THORPE, Appl. Opt., **32**, 6901, 1993.
29. P.L.G. VENTZEK, R.M. GILGENBACH, C.H. CHING, and R.A. LINDLEY, J. Appl. Phys., **72**, 1696, 1992.
30. H.A. BENDER, D. O'CONNEL, W.T. SILFVAST, *Velocity characterization of particulate debris from laser-produced plasmas used for extreme-ultraviolet lithography*, Appl. Opt., **34**, 28, 6513-6521, 1995.
31. R.M. GILGENBACH and P.L.G. VENTZEK, *Dynamics of excimer laser-ablated neutral atom plume measured by dye laser resonance absorption photography*, Appl. Phys. Lett., **58**, 15, 1597-1599, 1991.
32. M.S. SCHULZ, A.G. MICHETTE, and R.E. BURGE, *A Study of X-Ray Microscopy with a Laser Plasma Source*, in X-Ray Microscopy III (Proc. of the 3-rd Int. Conf., London, Sept. 3-7, 1990), Springer-Verlag, Berlin, p. 58, 1991.
33. H. DUPENDANT, J.P. GAVIGAN, D. GIVORD, A. LIENARD, and J.P. REBOUILLAT, Appl. Surf. Sci., **43**, 369, 1989.
34. D. LUBBEN, S.A. BARNETT, K. SUZUKI, S. GORBATKIN, and J.E. GREENE, J. Vac. Sci. Technol., **B3**, 4, 968-974, 1985.
35. W. MARINE, J.M.S. D'ANIELLO, and J. MARFAING, Appl. Surf. Sci., **46**, 239, 1990.
36. T. TOMIE, K. KOYAMA, N. ATODA, S. KOMEJI, Y. MATSUMOTO, A. YAOITA, I. MATSUSHIMA, and M. YANO, Proc. SPIE, **831**, 224, 1987.
37. L. LYNDY and B.R. WEINBERGER, Mater. Res. Soc. Symp. Proc., **191**, 3, 1990.
38. S. BOLLANTI et al., *Development and characterisation of an XeCl excimer laser-generated soft-X-ray plasma source and its applications*, Il Nuovo Cimento, **D18**, 1241-1255, 1996.
39. F. BIJKERK, E. LOUIS, L. SHMAENOK, H.J. VOORNA, J. HARM, M.J. WIEL, I. C. TURCU, and G.J. TALLENTS, Proc. SPIE, **1848**, 516, 1992.
40. F.O. NEILL, I. C. E. TURCU, D. XENAKIS and M. H. R. HUTCHINSON, *X-ray emission from plasmas generated by an XeCl laser picosecond pulse train*, Appl. Phys. Lett., **55**, 2603-2604, 1989.
41. L. RYMELL and H.M. HERTZ, *Droplet target for low debris laser-plasma soft X-ray generation*, Optics Comm., **103**, 105, 1993.

42. H.M. HERTZ, L. RYMELL, M. BERGLUND and L. MALMQVIST, *Debris free soft X-ray generation using a liquid droplet laser-plasma target*, in Applications of Laser Plasma Radiation II, M.C. Richardson, G.A. Kyrala Eds., Proc. SPIE, **2523**, 88-93, 1995.
43. H. FIEDOROWICZ, A. BARTNIK, R. JAROCKI, M. SZCZUREK and T. WILHEIN, *X-ray emission in the water-window from a nitrogen gas puff target irradiated with a nanosecond Nd:glass laser pulse*, Appl. Phys., **B67**, 391-393, 1998.
44. P. CELLIERS, L.B. DA SILVA et al., *Optimization of X-ray sources for proximity lithography produced by a high average power Nd: glass laser*, J. Appl. Phys., **79**, 11, 8258-8268, 1996.
45. S. BOLLANTI et al., : *High average power and debris free soft X-ray source for microlithography pumped by a long pulse excimer laser*, in EUV, X-Ray, and Neutron Optics and Sources, Proc. SPIE 3767, 1999, (to be published).
46. Y.B. ZEL'DOVICH and Yu.P. RAIZER, *Physics of Shock Waves and High Temperature Hydrodynamic Phenomena* (Academic, New York, vol. 1, 1964),.
47. F. O'NEILL, *Laser-plasma X-UV Sources*, in Laser-Plasma Interactions 4, p.300, M.P.Hooper Ed., SUSSP Publ., Edinburgh, 1988.
48. T. LETARDI and C.E. ZHENG, *Particle range in a laser-plasma generated soft X-rays chamber*, ENEA Technical Report, unpublished.
49. S. BOLLANTI et al., *Na-like autoionization states of copper ions in plasma, heated by excimer laser*, Physica Scripta, **51**, 326-329, 1995.
50. G.A. VERGUNOVA et al., *Features of plasma Produced by excimer laser at low intensities*, Physica Scripta, **55**, 483-490, 1997.
51. A.I. MAGUNOV et al., *Precision measurement of the ionization energy of the ground state and the wavelength of the $nl-2l'$ ($n=4-15$) spectral lines of Ne-like ion Ni XIX.*, JEPT, **83**, 267-273, 1996.
52. A.Ya. FAENOV et al., *Characteristics of plasma heating by short-wavelength excimer laser radiation*, Quantum Electronics, **26**, 701-705, 1996.
53. A.I. MAGUNOV et al., *Formation of the X-ray line emission spectrum of excimer-laser-produced plasmas*, Physica Scripta, **55**, 478-482, 1997.
54. F.B. ROSMEJ et al., *Dominant role of dielectronic satellites in the radiation spectra of a laser plasma near the target surface*, JEPT Lett., **65**, 9, 708-713, 1997.
55. F.B. ROSMEJ et al., *Inner-shell satellite transitions in dense short pulse plasmas*, Journal Quant. Spectr. Rad. Trans., **58**, 4-6, 859-878, 1997.
56. A.E. STEPANOV et al., *Modeling of the He-like magnesium spectral lines radiation from the plasma created by XeCl and Nd-glass lasers*, Journal Quant. Spectr. Rad. Trans., **58**, 4-6, 937-952, 1997.
57. A. MAGUNOV et al., *Formation of X-ray spectrum of excimer laser-produced plasmas*, Laser and Particle Beams, **16**, 1, 61-70, 1998.
58. F.B. ROSMEJ et al., *Line formation of high intensity HeB-Rydberg Dielectronic Satellites $1s3lnl'$ in dense laser produced plasmas*, J. Phys. B: At. Mol. Opt. Phys., **31**, L921-L931, 1998.
59. B.K.F. YOUNG et al., *High resolution X-ray spectrometer based on spherically bent crystals for investigations of femtosecond laser plasmas*, Rev. Sci. Instrum., **69**, 4049-4053, 1998.

NOVEL RELATIVISTIC ELECTRON BEAM EXPERIMENTS PROVIDING NEW MICROWAVE SOURCES

A. D. R. PHELPS

DEPARTMENT OF PHYSICS AND APPLIED PHYSICS, UNIVERSITY OF STRATHCLYDE
Glasgow G4 0NG, Scotland, UK

Both electron beams and microwave sources have a long history and yet in recent years there have been new advances made in electron beam production, propagation and interaction that have provided new microwave sources and developments to existing ones. Electron beams produced by cold cathodes, plasma cathodes, field emission array cathodes and pseudospark cathodes are compared with those produced by conventional thermionic cathodes. The electron beam propagation can be influenced by the accelerating electrode geometry and any imposed magnetic fields. A range of different electron beam electromagnetic wave interactions have been studied including electron cyclotron maser, free electron laser and Cherenkov maser.

1. Introduction

One of the uses of low temperature plasmas is as a copious source of electrons. Solid-state emitters of electrons have current density and peak power handling limitations that plasmas can readily exceed. In the steady state the average electron current extracted from the plasma usually equals the average electron current extracted from the solid state cathode substrate that ultimately connects the plasma to the external circuitry. One of the advantages of the plasma is in providing a lower effective work function source for the extraction of the electrons. Another advantage that applies in some cases, such as the pseudospark cathode, is that the cross-sectional area of the electron extraction surface in the plasma is very much smaller than the surface area of the solid-state conductor that provides the connection to the external circuitry and hence the current density is higher and the electron beam is brighter. For time-dependent transient plasma cathodes the peak electron current extracted from the plasma cathode can become very large when very short duration pulsed large electric fields are applied.

For many years plasmas, in various configurations, have been employed as cathodes. In sections 2 and 3 below two different types of plasma cathode are described which have both been successfully exploited as high current electron

beam sources which in turn have been used to drive high power microwave generators. A general bibliography covering high power microwave sources and charged particle beams is given [1 - 13]. In contrast to the plasma cathodes and for some specialised applications microscopic field emitters can be fabricated using conventional silicon wafer plasma processing technology. This exploits plasmas in the manufacturing process rather than in the device itself. When such emitters consisting of tens of thousands of individual emitters are fabricated into an array the potential of field emission array (FEA) cathodes [14, 22] can be realised. A collaborative project with industry which culminated in the first FEA driven gyrotron is described in section 4.

The science of intense electron beams can be regarded as a branch of plasma physics particularly at high frequencies where only the dynamics of the electrons are important. The subject is sometimes known as "non-neutral plasma physics". Although the directed energy in such beams can be large the actual plasma temperatures of these beams can be comparable with those of the low temperature technological plasmas. The theory of waves in plasmas provides an excellent vehicle for the study of high frequency waves on these intense electron beams. The invention, design and development of some new sources of electromagnetic radiation, discussed in section 5, have depended on analyses of the interactions between modes of the electron beams and modes of a range of waveguiding structures using frequency versus wavenumber diagrams in an identical way to their use in studies of plasma waves. Research results from a variety of different microwave sources are given in the later references [14 - 35]. A brief review of recent experimental studies of phenomena associated with superradiative behaviour in microwave sources is presented in section 6.

2. Plasma cathodes

When a fast rising high voltage pulse is applied to a cold cathode vacuum diode, within nanoseconds the cathode surface becomes covered with a low temperature plasma. The mechanism for this is that the field emission from fine whiskers on the surface supplies an initial current which then heats and explodes the whiskers and forms a low work function plasma from which electrons are readily extracted. An alternative to the whisker theory is that impurities included in the surface can act as the initial current source. The nature of this plasma depends upon the material and the construction of the cathode. Typical cathode materials are stainless steel and graphite. Velvet cloth forms a particularly effective material with which to cover the cathode surface. The plasma that rapidly covers the surface acts as a copious source of electrons and currents of high voltage electrons can typically be drawn for times as long as 100 ns up to 1 microsecond. Currents are typically in the kA range and this type of cathode is extremely robust.

3. Pseudospark cathodes

A novel type of cathode, namely the pseudospark discharge, has been used as the electron source for a Cherenkov maser amplifier experiment [35]. The Cherenkov

free electron maser interaction region in this case consists of a dielectric-lined, cylindrical waveguide. The pseudospark discharge offers the possibility of producing electron beams of high current density $> 10^4 \text{ A cm}^{-2}$, high brightness up to $10^{12} \text{ A m}^{-2} \text{ rad}^{-2}$, narrow beam diameter ($> 4 \text{ mm}$), very low emittance (tens of mm mrad) and variable duration (tens of ns to hundreds of ns). It is therefore very attractive as an electron beam source for high power sources of microwave radiation, such as free electron lasers (FELs), cyclotron autoresonance masers (CARMs) and Cherenkov masers. Numerical simulations and some experimental results from a Cherenkov maser amplifier based on a multi-gap pseudospark discharge have been presented [35]. The one-dimensional model of the Cherenkov maser amplifier takes into account effects due to electron velocity spread and resonant space charge forces and can predict non-linear effects such as saturation. The experimental results include electron beam voltage, current and brightness from this pseudospark cathode and microwave frequency, power and mode pattern measurements from the Cherenkov maser output. The simulations and experimental results agree and the desirable properties of the pseudospark cathode are confirmed.

A pseudospark discharge is a low pressure, transient hollow cathode gas discharge which occurs in a special geometry in different kinds of gases, i.e., nitrogen, oxygen and hydrogen, etc. The background gas pressure is such that pd , the product of the gas pressure p and the distance d between the front faces of the cathode and anode, is on the left-hand side of the Paschen curve between the Paschen minimum and vacuum breakdown. We here present the experimental details and results of pseudospark-based electron beam production.

The pseudospark experimental setup for the electron beam production is shown in Fig. 1. The discharge chamber consists of a planar anode, a planar cathode with an adjustable cylindrical hollow cavity, and several sets of Perspex insulators and interelectrodes of 6.5 mm thickness. Both the anode and cathode have an on-axis hole of 3 mm diameter. The centre of the cathode was designed to be an interchangeable structure, which allowed different sizes of cathode core and different kinds of cathode materials to be studied. The hollow cathode cavity made of stainless steel of outer and inner diameters of 63 and 50 mm respectively was length-adjustable through an adjuster. Gas pressure was measured by a digital, active Pirani gauge. The cathode side of the chamber was charged up to 30 kV through a $30 \text{ M}\Omega$ charging resistor and the charging voltage was measured by a capacitive voltage probe. The discharge current was monitored by a 0.066Ω current viewing resistor (CVR). The beam current was measured by a Rogowski coil located 6 cm away from the anode and the beam brightness was measured with a 6 cm long cylindrical collimator connected to the anode as shown in Fig. 1.

The basic investigations of electron beam production were first carried out on a single-gap pseudospark system for a wide range parameters, including cathode cavity length, cathode hole size, applied voltage, external capacitance and the inductance in the discharge circuit. The experiments showed that the pseudospark discharge phenomenon appeared when the ratio between the cathode cavity length to the cathode hole diameter was greater than 1. The discharge

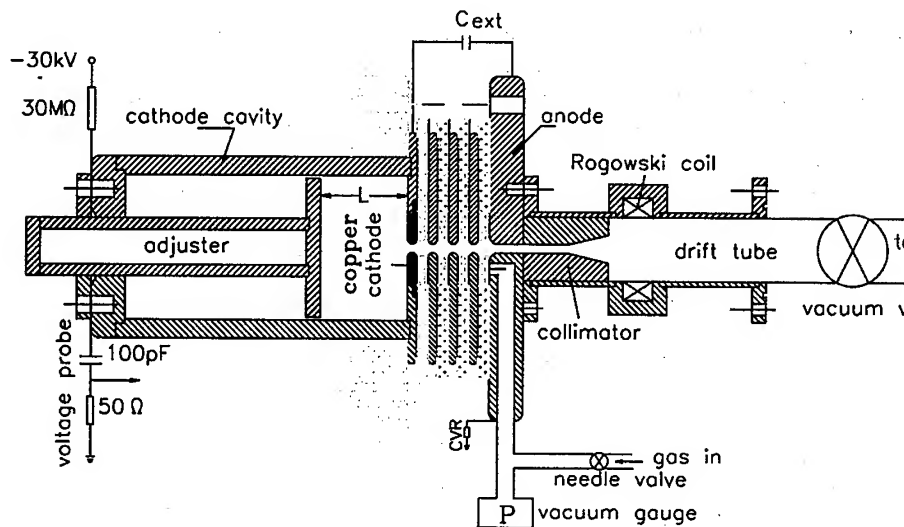


FIG. 1. The pseudospark cathode experimental configuration.

current approximately obeyed the relation $I_{\text{discharge}} = V_0(C_{\text{ext}}/L)^{1/2}$, where C_{ext} is the external capacitance, V_0 the applied voltage and L the total inductance in the discharge circuit. The beam current however had a saturation value when changing the external capacitance. To get maximum beam current the inductance in the discharge circuit should be minimized. The optimum beam current from the single-gap pseudospark discharge chamber was 100 A at 10 kV with $C_{\text{ext}} = 500$ pF.

Higher energy electron beam production was then studied from 3-gap pseudospark systems. Fig. 2 shows the voltage, diode current and beam current

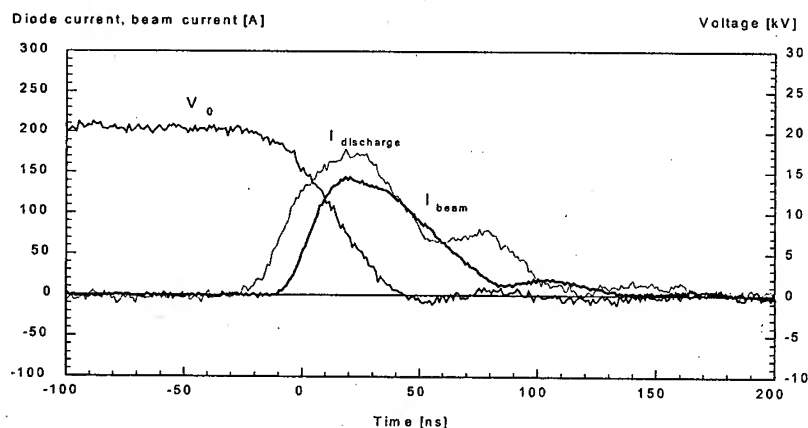


FIG. 2. The voltage, diode current and beam current from the 3-gap pseudospark experiment.

from the 3-gap pseudospark system. The beam brightness was measured to be $\geq 10^{11} \text{ Am}^{-2}\text{rad}^{-2}$ with a 6 cm long collimator in contact with the anode. For the 4-gap pseudospark system, a beam of up to 260 A was measured after the collimator with the Rogowski coil.

Following investigations of the electron beam produced by the pseudospark cathode a Cherenkov maser amplifier experiment has been designed and constructed at the University of Strathclyde. The main aim of the experiment was to demonstrate the suitability of the pseudospark cathode as an electron source for high power microwave generation. In this experiment, an electron beam generated by an 8-gap pseudospark cathode was passed through a section of cylindrical waveguide lined with a layer of dielectric (alumina). The presence of the dielectric allowed a resonant interaction to occur between a TM or HE waveguide mode and the electron beam.

A one-dimensional model of the Cherenkov maser amplifier has been developed in an attempt to predict the behaviour of this device both in the linear and nonlinear regime of operation. The model takes into account effects due to electron velocity spread and resonant space charge forces. A typical example of the results produced by this model is that for the TM_{01} mode, the mode power at saturation is $\approx 220 \text{ kW}$, corresponding to an interaction efficiency of $\approx 11\%$. These computer simulations, showed that the Cherenkov maser amplifier to be a promising device for verifying the effectiveness of the electron beam produced by the pseudospark cathode in applications to high power microwave generation.

To confirm this an experimental demonstration of microwave Cherenkov maser amplifier based upon the electron beam extracted from a pseudospark cathode has been successfully achieved. In these experiments, which were reported in reference [35], a gain of $29 \pm 3 \text{ dB}$ was measured in the frequency range 25.5 - 28.6 GHz.

4. Field-emission array cathodes manufactured by plasma processing

The first operation of a gyrotron oscillator employing an FEA cathode was demonstrated at the University of Strathclyde (Garven et al 1996) [14, 22]. The design parameters of the FEA cathode, were similar to those of a magnetron injection gun with an achievable electron beam current of 50 - 100 mA and measured beam power of 720 W CW. Coherent microwave radiation was detected in both the TE_{02} mode at 30.1 GHz and the TE_{03} mode at 43.6 GHz with a starting current of 1 mA.

One of the main advantages of the FEA cathode over its traditional counterparts was in the ability to control the spatial distribution of individual components of the beam. This was achieved by individually addressing each of the ten FEAs by supplying a separate control voltage to the Nb grid (or gate) connections on each chip, with a common Si tip cathode potential.

The FEA chips, which were manufactured by GEC using a plasma processing technique, were operated CW for lifetimes of tens of hours with minimal degradation in performance. There are two points to be noted from these results which must be emphasized with respect to the future of FEAs in high power mm-wave devices; (1) optimization of chip lifetime and (2) increase of beam power. This

work suggests that chips of the design employed at Strathclyde would operate successfully with emission currents up to 6 mA. Ten such chips would therefore supply 60 mA, at 40 kV to produce a 2.4 kW electron beam. This is a modest extrapolation of these results since both multiple chip operation and CW 10 mA operation from a single chip were demonstrated.

In the Strathclyde experiment, the maximum generated power was power supply limited since operating the FEAs outside the safe operation line resulted in increased grid currents. At any one time only 3 chips were operated which for the maximum power of 720 W represents an average of 6 mA per chip at 40 kV. The maximum measured beam power from a single FEA chip was 375 W, emitting 9.37 mA with an accelerating potential of 40 kV, corresponding to a current density of 0.5 A cm^{-2} . Measurement of the radiation power density in the far-field gave an estimated 1 W of absolute power from this gyrotron oscillator, during operation with a 100 W electron beam. This represents a significant conversion efficiency for a low current gyrotron of approximately 1%.

The results from the University of Strathclyde demonstrate that FEA cathodes can be used not only in high power electron gun designs, but also in high power mm-wave devices. Relativistic electron beams with powers of up to 720 W from FEAs were propagated through a gyrotron cavity and radiated coherently via the CRM mechanism. It was shown that FEA lifetimes were not unduly affected by high voltage operation, given adequate shielding. Lifetimes on the order of several hours of operation were achievable with currents of $>5 \text{ mA}$ per chip under non-ideal conditions, namely, a vacuum of $1 \times 10^{-8} \text{ mbar}$ and 50 kV accelerating potential with multiple chip operation.

5. Applications of electron beams to new microwave sources.

One important family of microwave sources is the electron cyclotron resonance maser family which includes the gyrotron, gyro-TWT, cyclotron autoresonance maser (CARM) and gyro-BWO. The gyrotron has become an established and very successful microwave oscillator but hitherto, gyro-TWT's have presented difficulties as broad band high power amplifiers. This is due to a twofold problem related to the phase velocity of the interaction. Close to cut-off the wave group velocity of a smooth waveguide is small and therefore the amplifier is susceptible to oscillation, and far from cut-off, at high Doppler upshifts, the system's efficiency suffers due to particle velocity spread, whilst remaining vulnerable to oscillation at lower frequency (near cut-off) resonances. An ideal eigenwave dispersion for a gyro-TWT would be one which has small ("zero") axial wavenumbers (k_z), while at the same time possessing a large wave group velocity $\partial\omega/\partial k_z$ which is finite and approximately constant. As shown such an eigenwave dispersion may be realised in a radical new oversized circular cylindrical waveguide with a helical corrugation of the inner surface. This helical corrugation couples two partial waves of a regular waveguide with cut-off frequencies near and far below the operating frequency. This first partial wave resonantly interacts with the electrons and the admixture of the second wave makes the group velocity of the eigenwave non-zero. Changing the geometrical parameters of the corrugation one can control the eigenwave group velocity and adjust it to the longitudinal

velocity of an electron beam for a rather broad frequency band around the point where the longitudinal wavenumber is equal to zero. These features allow a very attractive regime of gyro-TWT operation to be realised where the interaction is less prone to oscillations and simultaneously possesses a weak sensitivity to the spread in electron velocity.

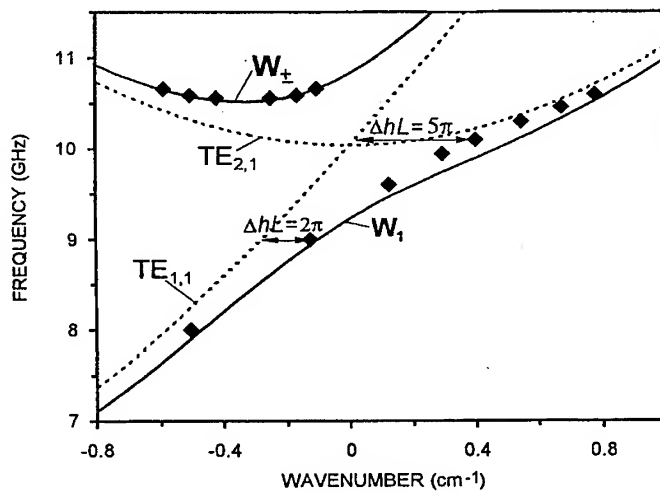


FIG. 3. Dispersion diagram for the operating helical waveguide: dotted and solid lines correspond to partial and eigen modes, respectively, "diamond" points are the results of "cold" measurements. The parameter, h , in this figure is equivalent to the axial wavenumber k_z .

Improvements in the quality of high-current electron beams have recently provided a significant advance in another member of the electron cyclotron maser family, namely the CARM. The Cyclotron Autoresonance Maser (CARM) is a Doppler upshifted cyclotron maser that benefits from an autoresonant interaction. Use of the CARM instability means the electron beam and the RF field stay in resonance as the electron beam loses energy to the field which indicates a high potential efficiency for the device. The emission frequency of the device is Doppler upshifted from the normal gyrotron frequency and hence the magnetic field required to achieve a particular output frequency is significantly reduced.

$$(5.1) \quad \omega = s\omega_c + k_z v_z$$

where ω is the angular frequency of the radiation, s is the harmonic number, k_z the axial component of the radiation field wave vector and v_z is the electron axial velocity. The relativistic cyclotron frequency, $\omega_c = 2\pi f_c = eB/\gamma m_0$, describes the angular frequency of rotation of the electrons in the axial magnetic field, where e/m_0 is the electron charge/mass ratio, γ is the Lorentz factor and B is the magnetic induction of the guiding magnetic field. The CARM is a fast-wave interaction, having a phase velocity greater than the speed of light and a large Doppler shift is observed for $v_z \approx \omega/k_z \approx c$.

For interaction with a mode of a waveguide, the wave dispersion relation

$$(5.2) \quad \omega^2 = c^2 k_\perp^2 + c^2 k_z^2$$

must also be satisfied, in which the cut-off frequency $\omega_{c0} = ck_{\perp}$ is dependent on the cavity cross section and eigenmode.

The efficiency of the CARM, like other microwave devices that have a large Doppler frequency upshift is dependent upon the quality of the electron beam. Bratman et al. at IAP, Nizhny Novgorod, Russia, have demonstrated experimentally that a fundamental CARM can achieve 26% electronic efficiency. CARM experiments at Strathclyde have been reported and Cooke et al. [23] have achieved operation of a CARM at the second harmonic. Up until now the usual way of achieving good beam quality in CARMs has involved only selecting the central part of a high current electron beam. This process known as beam "scraping" results in the real overall efficiency being much lower than the electronic efficiency based on just the selected beam. Recent cold cathode CARM experiments have used a velvet cathode. By modelling and careful electron gun design the need for beam scraping has been eliminated and almost 100% of the electron beam has been used. A thermionic cathode CARM experiment with the same electron gun geometry has been carried out to confirm this.

In the University of Strathclyde cold cathode CARM experiments a cold explosive field emission cathode, operating in the space-charge-limited regime, was used to produce a high current (~ 50 A), high quality, but short (~ 100 ns) beam. Due to gap closure, it was difficult to increase the duration of the electron beam from such a source. The pulsed power system used delivered a 300 kV pulse, which was approximately 100 ns in duration.

The CARM was operated using the second harmonic of the cyclotron frequency. An interaction efficiency of 3.9% was measured at a frequency of 14.27 GHz, using an 80 ns pulsed, 14 A electron beam of energy 300 keV, to produce a coherent microwave power of 170 kW. Emission occurred at 3.7 times the relativistic cyclotron frequency, due to the large Doppler frequency increase and second harmonic interaction.

An alternative power supply has been developed which is capable of producing a 800 kV pulse with a longer duration, which will be operated at a potential of 500 kV. This allows operation of the CARM at the fundamental frequency, but requires a redesign of the existing cold cathode diode system to operate at this voltage (Fig. 4).

Computer modelling of the electron beams is an essential part of designing new microwave sources. The computer models developed at Strathclyde are fully relativistic electron trajectory codes that can calculate (1) the space-charge limited emission current, (2) the current density profile of the e-beam, (3) the diode and beam currents, and (4) the velocity profile of the e-beam.

The new voltage pulse system with its greater potential, has required some modifications to be made to the existing diode to still produce a high quality beam with little scraping of the beam. The main modifications in the design of the higher voltage cold cathode are the necessary increase in the anode cathode spacing and the addition of a semicircular rim to the Pierce like electrodes to reduce field enhancement at the edge of the electrodes. The results of the computer model are shown in table 1, alongside the results of the original Pierce diode.

Table 1. Results of computer modelling of CARM cathodes.

Cathode	Original Pierce Cold	Modified Pierce Cold	Thermionic
Operating Voltage	300 kV	450 kV	500 kV
Diode Current	60 A	40 A	30 A
Beam Current	60 A	40 A	30 A
Emission Current Density	44 \rightarrow 82 Acm ⁻²	23 \rightarrow 30 Acm ⁻²	2.3 \rightarrow 2.7 Acm ⁻²
Parallel Velocity /c	0.683 \pm 0.026	0.8452 \pm 0.0005	0.8618 \pm 0.0003
Perpendicular Velocity /c	0.042 \pm 0.019	0.0389 \pm 0.0117	0.0302 \pm 0.0086
Pulse Duration	100 ns	100 ns	> 1 μ s

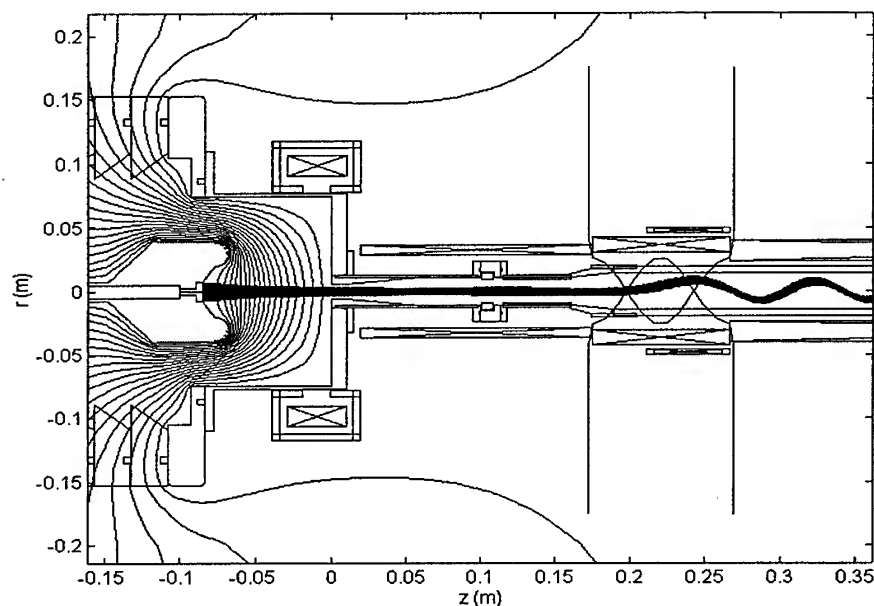


FIG. 4. CARM electron optical system with a cold cathode.

As the new power supply is capable of producing a longer pulse, to take advantage of this a thermionic cathode has been developed. The most significant modification to the diode geometry in the design of the thermionic cathode is the convergence of the beam. This was made necessary by the fact that a high current density is required at the anode aperture and the achievement of such a current emission density from a thermionic cathode would be almost impossible,

and would most certainly give a very short lifetime cathode. The CARM electron optical system with a thermionic cathode is shown in Fig. 5.

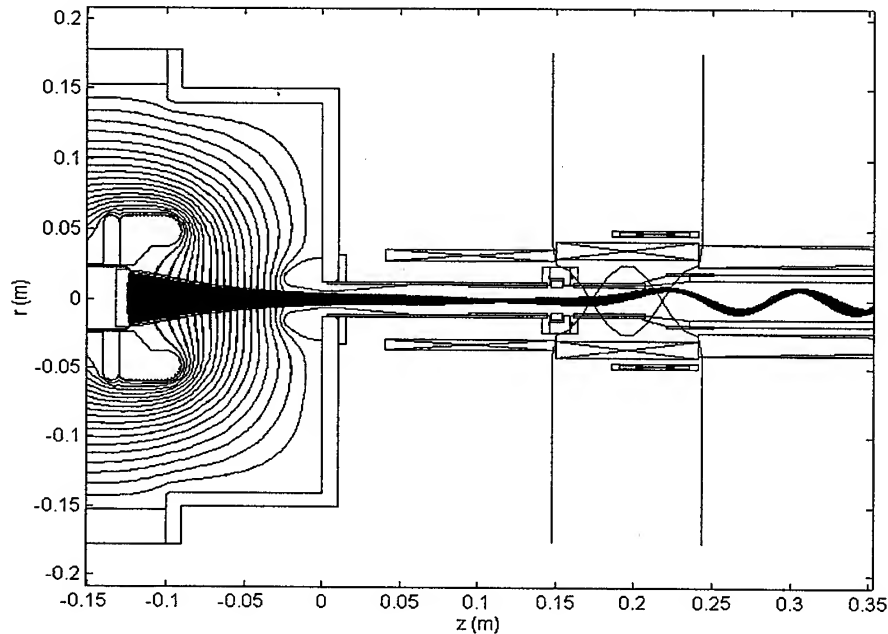


FIG. 5. CARM electron optical system with a thermionic cathode.

The computer modelling has enabled Pierce electrodes to be designed for the CARM electron gun virtually removing the need for scraping the electron beam and producing a higher quality beam which has resulted in a more efficient operation of the CARM. The experimental measurements of the electron beam transport and the CARM microwave output confirm the predictions of the computer modelling.

This ability to use all of the electron beam means that CARMs can now have a high enough real efficiency to be considered seriously for applications.

6. Superradiance phenomena

Superradiance (SR) and associated subjects such as the self-amplification of spontaneous emission (SASE) and the self-amplification of coherent spontaneous emission (SACSE) in free electron systems have become of considerable interest in recent years. Following considerable theoretical research of several pioneers in the field including N.S. Ginzburg, R.H. Bonifacio and B.W.J. McNeil, whose earlier papers are referenced in the more recent literature [19, 21, 24, 27], it has now become possible to demonstrate experimentally such phenomena for microwave wavelengths in free electron systems, [24, 27]. Superradiant emissions of millimetre-wave radiation have been studied by passing single short bunches of electrons through several types of free electron radiating systems. The experiments reported include cyclotron, Cherenkov (including BWO) and FEL super-

radiance. Robb et al. [19] in their theoretical treatment of superradiation pulses in an FEL system gave several references to the earlier works on superradiation. Recently cyclotron superradiance has been observed [24]. New experimental results from wiggler (FEL), rippled wall BWO and dielectric-lined waveguide forward wave Cherenkov superradiance experiments have recently become available. Some of the applications of these novel superradiant sources are also of interest as they provide MW pulses at subnanosecond pulse durations. This superradiance phenomenon includes features present in both stimulated (selfbunching and coherence) as well as spontaneous processes (absence of threshold). It is reasonable to consider SR in a specific situation when the electron pulse duration significantly exceeds the wavelength (otherwise it is effectively traditional spontaneous emission without selfbunching) while at the same time the electron pulse length is less than the interaction length. This is in contrast to the mechanism of stimulated emission of quasi-continuous electron beams which are used extensively in microwave electronics - TWT, BWO, CRM, FEL, etc. We have carried out a series of experiments to observe free electron superradiance and we have explored a range of different interaction mechanisms ie cyclotron, Cherenkov, BWO (effectively another variant of the Cherenkov mechanism) and FEL. A RADAN 303 modulator with a subnanosecond pulse sharpener was used as the driver to provide the intense subnanosecond electron bunches.

For the Cherenkov maser experiment a short electron bunch was passed through a dielectric-lined waveguide. Cherenkov maser emission was observed associated with the forward propagating wave under the Cherenkov synchronism condition. The dielectric material used was Mylar and Teflon in tubular form of wall thickness 2 mm inserted inside a metallic circular waveguide of inner diameter 10 mm and total length 25cm. A guiding magnetic field of up to 2T was applied. The best results were obtained from the Mylar insert which was constructed from multilayers of 0.05 mm thickness film. The electron bunch of 0.3 - 0.5 ns and 0.2-1 kA was obtained by applying a subnanosecond RADAN 303 accelerator pulse of 250 kV to a cold explosive emission cathode. The electron pulse was long compared to the radiation wavelength but short compared with the length of the interaction region. Cherenkov maser emission pulses of subnanosecond duration were observed at a power level of ~ 1 MW and frequency range 38 - 48 GHz.

Similarly when such bunches were passed through the periodic slow-wave structure, shown in Fig. 6, and interacted with backward propagating radiation, generation of ultrashort subnanosecond megawatt level K_a band microwave pulses based on BWO superradiance have been observed. However, in these first experiments rather low guide magnetic fields up to 2T were used. This value of magnetic field was less than the cyclotron resonance value. At the same time it is known from theoretical considerations and previous experimental studies of long (5 - 30 ns) pulse relativistic BWOs that as the magnetic field is varied BWOs have two operating ranges separated by the cyclotron absorption region. Cyclotron absorption arises when cyclotron resonance conditions are fulfilled for the fundamental harmonic of the wave propagating in the periodic structure. Based on this experience it is reasonable to assume that for the short pulse injection regime for high guide magnetic fields the peak power of SR spikes should

be several times higher as compared with those attained in the previous experiments. The increased power should be related first of all with the improved quality of the electron bunch injected by the explosive-emission cathode. Note also that the containment of the electron bunch in the strong magnetic field gives the possibility of decreasing the gap between the electrons and the slow-wave structure and as a consequence there results a substantial increase of the electron -electromagnetic wave coupling and the related gain. A superconducting magnet was used in a new series of experiments to generate a longitudinal magnetic field with strengths of up to 10 T. Using a permanent solenoid instead of the pulsed one used in the previous experiments permits us to operate in the burst-repetitive mode (25 pps) to actually create a novel source of powerful subnanosecond K_α band radiation.

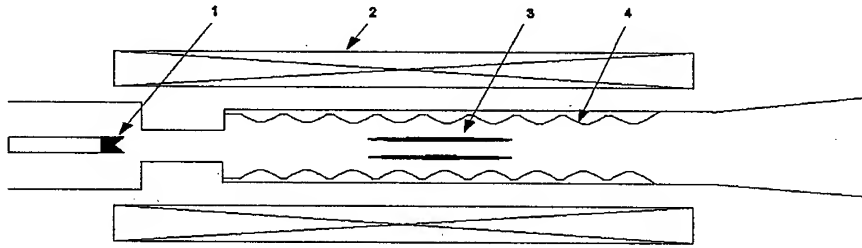


FIG. 6. Experimental configuration of the BWO (1) the cathode (2) the superconducting solenoid (3) electron bunch (4) slow-wave structure.

A RADAN 303 accelerator with a subnanosecond slicer was used to inject 0.3 - 0.5 ns, 0.1 - 1 kA, 220 keV electron pulses into a wiggler structure (Fig. 7). A short duration electron pulse was generated when this sub-nanosecond voltage pulse was applied across a magnetically-insulated coaxial diode which utilised a cold, explosive-emission cathode. The fast electron bunch current and accelerating voltage pulse were measured using a strip line current probe and an in-line capacitive probe respectively. For measurement of the radiation a hot-carrier germanium detector which had a transient characteristic of 200 ps was used. High-current electron pulses were transported through the interaction space of total length up to 30 cm in a longitudinal guide magnetic field of up to 1.4 T. The electron beam diameter was 4 mm. Transverse momentum, was imparted to the electrons by the helical wiggler. Adiabatic tapering of the wiggler entrance was used to provide smooth excitation of bounce-oscillations. In the regular section of the wiggler with total length 20 cm and period of 1.6 cm electrons moved along helical trajectories with constant longitudinal velocity. It was possible to switch the direction of the guide magnetic field. To facilitate the transportation of the high-current electron bunch through the interaction space the magnitude of the uniform magnetic field needs to be rather high and to exceed 1 T. In this case the strength of the magnetic field slightly exceeded the cyclotron resonance value. The superradiant pulses with typical duration 300 - 500 ps have been observed for both (conventional and reverse) directions of the guide magnetic. The max-

imum radiation power was obtained for a conventionally directed magnetic field of 1.3 T. This result can be explained by the fact that under the experimental parameters the transverse electron velocity for the conventional magnetic field direction exceeds the similar value under reverse field. The optimal amplitude of the wiggler field was about 0.2 T. According to measurements of the mode pattern the radiation was associated with excitation of the operating mode TE_{11} . The spectrum measurements using cut-off waveguides and metallic grids show good agreement with the frequency which is predicted from the FEL dispersion relation. The radiation frequency was approximately 28 GHz. Note that the waveguide diameter 9.8 mm and wiggler period were chosen to match the grazing condition for the operating TE_{11} mode. As follows from the theoretical considerations for waveguide propagation of radiation there are some advantages (like increasing gain) in generation of SR pulses under grazing conditions when the electron bunch velocity coincides with the electromagnetic wave group velocity. It should be noted that even under exact grazing conditions, the effects of electronic detuning caused by finite electron beam density results in the velocity of the electromagnetic wave differing from the electron bunch drift velocity and hence enabling the escape of electromagnetic energy from the electron bunch. For cyclotron SR this was proven experimentally because in this case it was possible by variation of the magnetic field and hence the gyrofrequency to approach and to shift the dispersion characteristic from the grazing condition. In the case of emission in a wiggler the bounce-frequency was in fact determined by the wiggler period and it was practically impossible to mismatch the system from the grazing condition. Therefore we have not been able to confirm experimentally that this grazing condition is the preferred one for the production of wiggler SR. The radiation power is quite small for short interaction lengths and increases drastically as this length increases. This can be interpreted as the natural level of spontaneous emission caused by the electron density fluctuations as well as the radiation from the front edges of the pulse being relatively small, while the observed electromagnetic pulse behaviour is related with the development of longitudinal selfbunching and coherent emission from the bunched electron pulse.

The observation of some radiation even when the length of the homogeneous section of the wiggler tends to zero is considered to be due to two factors. Firstly there is some magnetic bremsstrahlung produced from within the tapered sections of the wiggler and secondly even in the absence of a wiggler field there is some background cyclotron radiation from the electron motion in the uniform guide field. The maximum length of the homogeneous part of the wiggler was not sufficient to observe the nonlinear saturation regime. For the present experimental configuration the maximum power of the SR pulses was estimated as being in the range 100 - 200 kW.

In the cases of the cyclotron, BWO, Cherenkov, and FEL microwave interactions ultra-short (sub-nanosecond) and high-power (multi-megawatt) emissions identified as belonging to the family of interesting SASE, SACSE and superradiative phenomena have been identified in our experiments. In the FEL experiments carried out, single electron bunches with length 5 - 7 cm passing through a wiggler with total length 30cm radiated coherent, short 300 - 500 ps pulses at a wavelength of about 1.1 cm. Based on the experimental results and the

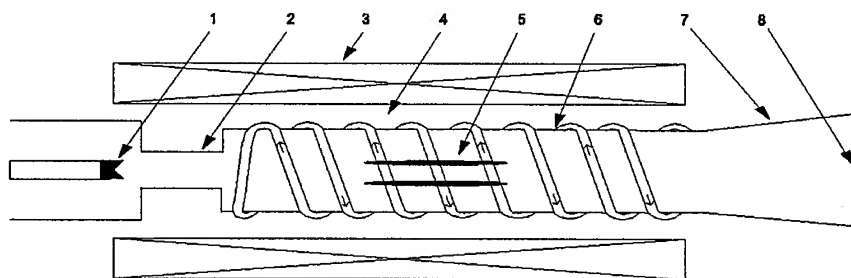


FIG. 7. Experimental configuration of the FEL interaction region (1) cathode (2) anode (3) guiding field solenoid (4) wiggler coil (5) electron pulse (6) drift chamber (7) horn (8) microwave window.

results of simulations we conclude that this high-power radiation is related with the development of selfbunching, on a radiation scale length, within the longer electron bunch during just a *single* passage of the *single* electron bunch through the interaction structure.

7. Conclusions

Several examples have been presented of novel electron beam sources including ones using low temperature plasmas and FEAs. The pseudospark discharge has been seen to produce a high brightness beam that can be used for exciting free electron devices and in particular a pseudospark-driven Cherenkov maser has been demonstrated.

The gyro-TWT has been shown to have a much more promising performance as a high-power amplifier as a result of introducing a new optimally structured interaction region.

By suitably designing the electron gun a thermionic cathode has been used to excite a CARM experiment with practically a 100% use of the electron beam.

Very short pulses of electrons have been produced with a novel short pulse electron accelerator. The interactions of these propagating short electron bunches with the appropriate structures have been shown to lead to a range of interesting new microwave devices including superradiative variants.

Acknowledgments

The author is grateful to his many present and former colleagues at Strathclyde University who have contributed to the work presented here including Drs. P. Aitken, S.J. Cooke, A.W. Cross, M. Garven, W. He, D.A. Jaroszynski, B.W.J. McNeil, G.R.M. Robb, K. Ronald, S.N. Spark, C.G. Whyte, P.R. Winning, A. Young and H. Yin. The very valuable discussions the author has enjoyed with M. Petelin and the research collaborations with V.L. Bratman, N.S. Ginzburg, G.G. Denisov, S.V. Samsonov, N.Y. Peskov and A.V. Savilov of

IAP, Nizhny Novgorod and with V.G. Shpak and M.I. Yalandin of IEP, Ekaterinburg have enabled the author to write this review paper. Support has been provided by the EPSRC, DERA, EEV, AEA Technology, JET, GEC, The Royal Society (London) and the Royal Society of Edinburgh.

References

1. R.A. CAIRNS and A.D.R. PHELPS, eds., *Generation and Application of High Power Microwaves*, IoP Publishing, ISBN 0-7503-0-474-X (pbk), ISBN 0-7503-0-451-0 (hbk), 333 pages, 1997.
2. J. BENFORD and J. SWEGLE, *High-Power Microwaves*, Artech House, Boston and London, 1992.
3. C.J. EDGCOMBE, Ed., *Gyrotron Oscillators*, Taylor and Francis, London, 1993.
4. H.P. FREUND and T.M. ANTONSEN, *Principles of Free-electron Lasers*, Chapman and Hall, London, 1992.
5. A.V. GAPONOV-GREKHOV and V.L. GRANATSTEIN, Eds, *Applications of High-Power Microwaves*, Artech House, Boston and London, 1994.
6. A.S. GILMOUR, Jr., *Microwave Tubes*, Artech House, Boston and London, 1986.
7. A.S. GILMOUR, Jr., *Principles of Traveling Wave Tubes*, Artech House, Boston and London, 1994.
8. V.L. GRANATSTEIN and I. ALEXEFF, *High-Power Microwave Sources*, Artech House, Boston and London, 1987.
9. S. HUMPHRIES, Jr., *Charged Particle Beams*, Wiley, New York, 1990.
10. J.D. LAWSON, *The Physics of Charged-particle Beams*, Oxford University Press, Oxford, 1988.
11. P. LUCHINI and H. MOTZ, *Undulators and Free-Electron Lasers*, Oxford University Press, Oxford, 1990.
12. T.C. MARSHALL, *Free-Electron Lasers*, Macmillan, New York, 1985.
13. R.B. MILLER, *Intense Charged Particle Beams*, Plenum Press, New York and London, 1982.

Research references

14. M. GARVEN, A.D.R. PHELPS, S.N. SPARK, D.F. HOWELL and N. CADE, *Field emission array experiments relevant to cold cathode gyrotrons*, *Vacuum*, **45**, 513-517, 1994.
15. B.W.J. MCNEIL, G.R.M. ROBB and A.D.R. PHELPS, *Universally scaled cyclotron resonance maser equations*, *J. Phys D: Appl. Phys.*, **27**, 1092-1096, 1994.
16. S.N. SPARK, A.W. CROSS, A.D.R. PHELPS and K. RONALD, *Megawatt, 330 Hz PRF tunable gyrotron experiments*, *Int. J. Infrared and MM waves*, **15**, 2003-2019, 1994.
17. A.W. CROSS, S.N. SPARK and A.D.R. PHELPS, *Gyrotron experiments using cavities of different ohmic Q*, *Int J. Electron.*, **79**, 481-493, 1995.
18. N.S. GINZBURG, A.S. SERGEEV, N.YU. PESKOV, I.V. KONOPLEV, G.R. M. ROBB and A.D.R. PHELPS, *Mode competition and control in free electron lasers with one and two dimensional Bragg resonators*, *Nucl. Inst. and Meth.*, **A 375**, 202-206, 1996.
19. G.R.M. ROBB, N.S. GINZBURG, A.D.R. PHELPS and A.S. SERGEEV, *Coherent spontaneous emission from short electron bunches in free space*, *Nucl. Inst. and Meth.*, **A 375**, 535-538, 1996.
20. N.S. GINZBURG, A.S. SERGEEV, N.YU. PESKOV, G.R.M. ROBB and A.D.R. PHELPS, *Mode competition and control in free electron lasers with one-and two-dimensional Bragg resonators*, *IEEE Trans on Plasma Science*, **24**, 770-780, 1996.
21. G.R.M. ROBB, N.S. GINZBURG, A.D.R. PHELPS and A.S. SERGEEV, *Stimulated coherent emission from short electron bunches in free space*, *Phys. Rev. Lett.*, **77**, 1492-1495, 1996.

22. M. GARVEN, S.N. SPARK, A.W. CROSS, S.J. COOKE and A.D.R. PHELPS, *Gyrotron experiments employing a field emission array cathode*, Phys. Rev. Lett., **77**, 2320-2323, 1996.
23. S.J. COOKE, A.W. CROSS, W. HE and A.D.R. PHELPS, *Experimental operation of a cyclotron autoresonance maser oscillator at the second harmonic*, Phys. Rev. Lett., **77**, 4836-4839, 1996.
24. N.S. GINZBURG et al., A.D.R. PHELPS et al., V.G. SHPAK et al., *Experimental observation of cyclotron superradiance under group synchronism conditions*, Phys. Rev. Lett., **78**, 2365-2368, 1997.
25. V.L. BRATMAN, A.D.R. PHELPS and A.V. SAVILOV, *Recovery of electron energy in cyclotron autoresonance masers*, Physics of Plasmas, **4**, 2285-2291, 1997.
26. B.W.J. MCNEIL, G.R.M. ROBB and A.D.R. PHELPS, *A self-consistent single-particle theory of the cyclotron resonance maser*, Journal of Physics D - Applied Physics, **30**, 1688-1696, 1997.
27. N.S. GINZBURG et al., A.D. RPHELPS et al., and V.G. SHPAK et al., *Experimental observation of superradiance in millimeter-wave band*, Nuclear Instruments and Methods in Physics Research A, **393**, 352-355, 1997.
28. P. AITKEN, B.W.J. MCNEIL, G.R.M. ROBB and A.D.R. PHELPS, *Scaled cyclotron resonance maser equations for a two resonant frequency interaction*, Journal of Physics D - Applied Physics, **30**, 2482-2489, 1997.
29. K. RONALD, A.W. CROSS, A.D.R. PHELPS, W. HE, H. YIN and S.N. SPARK, *Explosive cathode gyrotron experiments*, IEEE Trans. on Plasma Science, **26**, 375-382, 1998.
30. G.G. DENISOV, V.L. BRATMAN, A.D.R. PHELPS and S.V. SAMSONOV, *Gyro-TWT with a helical operating waveguide: new possibilities to enhance efficiency and frequency bandwidth*, IEEE Trans. on Plasma Science, **26**, 508-518, 1998.
31. P. AITKEN, B.W.J. MCNEIL, G.R.M. ROBB and A.D.R. PHELPS, *A comparison of the FEL and CRM operating simultaneously at two resonant frequencies*, Nuclear Instruments and Methods in Physics Research A **407**, 136-140, 1998.
32. A.W. CROSS, N.S. GINZBURG, W. HE, D.A. JAROSZYNSKI, N.Yu. PESKOV, A.D.R. PHELPS and C.G. WHYTE, *A 32 GHz Bragg free-electron maser (FEM) oscillator with axial guide magnetic field*, Nuclear Instruments and Methods in Physics Research A, **407**, 181-186, 1998.
33. A.V. SAVILOV, V.L. BRATMAN, A.D.R. PHELPS and S.V. SAMSONOV, *New opportunity of efficiency enhancement for FEL-oscillators*, Nuclear Instruments and Methods in Physics Research A, **407**, 480-484, 1998.
34. G.G. DENISOV, V.L. BRATMAN, A.W. CROSS, W. HE, A.D.R. PHELPS, K. RONALD, S.V. SAMSONOV and C.G. WHYTE, *Gyro-TWT with a Helical Interaction Waveguide*, Phys. Rev. Lett., **81**, 5680-5683, 1998.
35. H. YIN, W. HE, G.R.M. ROBB, A.D.R. PHELPS, K. RONALD and A.W. CROSS, *Coherent microwave generation from a pseudospark cathode Cherenkov maser*, Phys. Rev. ST Accel. Beams, **2**, 020701/1-5, 1999.

THEORY OF THE PLASMA-SHEATH TRANSITION

K. U. RIEMANN

INSTITUT FÜR THEORETISCHE PHYSIK, RUHR-UNIVERSITÄT BOCHUM

D-44780 Bochum, Germany

In typical cases, a quasi-neutral plasma body is shielded from a negative absorbing wall by a positive space charge sheath with a characteristic extension of some electron Debye lengths λ_D . Due to high ion losses to the wall, the formation of this positive sheath, however, may depend on special conditions. In the usual case of a small Debye length ($\lambda_D \rightarrow 0$), Bohm's criterion must be fulfilled. This condition requires that the sheath region is preceded by a quasi-neutral presheath. The aim of this paper is to elucidate the principal mechanism of the plasma-sheath transition and to discuss various problems related to the Bohm criterion. These discussions include the influence of collisions, magnetic field effects, and transient sheath phenomena.

1. Introduction

Like any conducting material, a plasma is essentially neutral, and excess charges can exist only in a thin surface layer with a characteristic extension of some (electron) Debye lengths λ_D . In contrast to other conducting materials, however, the plasma is usually bounded by absorbing walls. Due to the high mobility of the electrons, the walls are in typical cases negative, and the quasi-neutral plasma is shielded from the negative walls by a positive space charge *sheath*. The shielding mechanism, however, is impeded by ion losses to the wall. In the usual case $\lambda_D \ll L$ - where L is the smallest competing characteristic length of the plasma boundary region (e.g., ion mean free path) — a sheath can only be formed, if the *Bohm criterion* [1, 2] is fulfilled. In its simplest form it requires that the ions enter the sheath region at least with ion sound velocity c_s , i.e.,

$$(1.1) \quad v_z \geq c_s = (\kappa T_e / m_i)^{1/2}$$

with v_z = ion velocity component perpendicular to the wall, κ = Boltzmann's constant, T_e = electron temperature, and m_i = ion mass. To fulfill this condition, the ions must be accelerated in a quasi-neutral *presheath* region (possibly the total plasma) with an extension $L \gg \lambda_D$. The asymptotic transition $\lambda_D/L \rightarrow 0$ results in a singular two-scale problem (Fig. 1): For small but finite λ_D/L

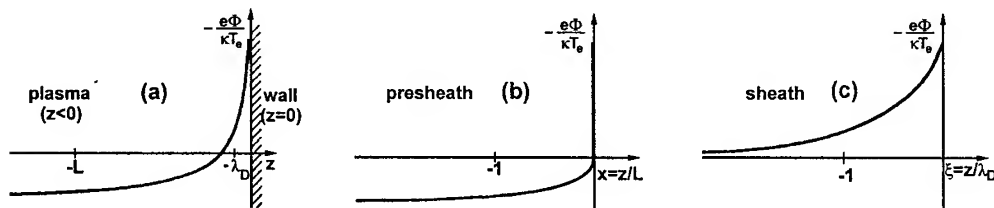


FIG. 1. Schematic potential variation in the plasma ($z < 0$) in front of a negative absorbing wall ($z = 0$). (a): λ_D/L small but finite. (b): $\lambda_D/L \rightarrow 0$, presheath scale. (c): $\lambda_D/L \rightarrow 0$, sheath scale.

(Fig. 1a) the electric potential Φ shows a steep gradient ($d/dz \sim 1/\lambda_D$) in the sheath, and a weak gradient ($d/dz \sim 1/L$) in the presheath. In the limiting case $\lambda_D/L \rightarrow 0$ we must distinguish the separate scales $x = z/L$ of the presheath (Fig. 1b) and $\xi = z/\lambda_D$ of the sheath (Fig. 1c). On the sheath scale [$z = O(\lambda_D)$] the presheath [$z = O(L)$] is infinitely remote and the “sheath edge” is characterized by a vanishing field ($d\Phi/d\xi \rightarrow 0$ for $\xi \rightarrow -\infty$). On the presheath scale [$z = O(L)$], in contrast, the sheath [$z = O(\lambda_D)$] is infinitely thin and the sheath edge is (usually) defined by a field singularity ($d\Phi/dx \rightarrow -\infty$) indicating the transition to a smaller scale. This singularity is related to the marginal (equality) form of the Bohm criterion [2, 3, 4, 5, 6].

Starting from the principles, we want to discuss in this paper general and special problems related to the plasma-sheath transition. In Sec. 2 we present the basic ideas of the two-scale analysis and introduce the separate sheath and presheath model zones. The connecting Bohm criterion is discussed in more detail in Sec. 3. The general two-scale considerations are concluded in Sec. 4 by a more sophisticated investigation of the sheath edge. In Secs. 5 and 6 we discuss special presheath and sheath problems, and Sec. 7 is concerned with time dependent sheaths. In Sec. 8, finally, the most important aspects are summarized.

Due to its strong inhomogeneity, the plasma boundary layer must, in principle, be investigated kinetically. The kinetic analysis, however, is involved and for many problems of practical importance not available. For this reason (and for the reason of transparency) we restrict our presentation basically to a simple fluid model. We shall, however, in addition discuss all important consequences of the more appropriate kinetic analysis.

2. Two-scale analysis

2.1. Basic equations

To elucidate the principal problem, we consider a stationary plasma composed of electrons (e), singly charged positive ions (i), and neutrals. The neutral component constitutes a background responsible for ionization and collisional friction. Apart from that the neutrals are not of interest for us. The potential is governed by Poisson's equation

$$(2.1) \quad \Delta\Phi = -\frac{e}{\epsilon_0}(n_i - n_e).$$

The electron density n_e is assumed to be a known function

$$(2.2) \quad n_e = n_e(\Phi)$$

of the electric potential Φ . [In explicit examples, we shall use the Boltzmann factor but, in principle, $n_e(\Phi)$ may be an arbitrary monotonic function]. For the time being we exclude magnetic fields (see Sec. 5.5) and start from the ion fluid equations

$$(2.3) \quad \nabla \cdot (n_i \mathbf{v}_i) = S_i \quad \text{and}$$

$$(2.4) \quad m_i \mathbf{v}_i \cdot \nabla \mathbf{v}_i = -e_i \nabla \Phi - \frac{1}{n_i} \nabla p_i - \left(\nu_{ci} + \frac{S_i}{n_i} \right) m_i \mathbf{v}_i$$

to calculate the ion density n_i . Here, \mathbf{v}_i designates the ion flow velocity, S_i the ionization rate, and ν_{ci} an effective ion collision frequency. The ion pressure $p_i = n_i \kappa T_i$ and the ion temperature T_i are assumed to follow an adiabatic law

$$(2.5) \quad \nabla p_i = \gamma_i \kappa T_i \nabla n_i, \quad T_i n_i^{1-\gamma_i} = \text{const},$$

where the coefficient $\gamma_i \in [1, 3]$ depends on the flow conditions [2, 7]. Finally, we restrict ourselves to (quasi) one-dimensional geometries with

$$(2.6) \quad \mathbf{v}_i = v_i \mathbf{e}_z, \quad \nabla = \mathbf{e}_z \frac{d}{dz}, \quad \text{div} = \frac{1}{A} \frac{d}{dz} A = \frac{A'}{A},$$

where we use the variation $A(z)$ of an area element to specify the geometry [e.g., $A = 4\pi(R \pm z)^2$ for spherical geometry]. In accordance with Fig. 1, the plasma is described by $z < 0$, and $z = 0$ designates the wall position. With these specifications we obtain the basic equation system

$$(2.7) \quad \frac{d^2 \Phi}{dz^2} + \frac{A'}{A} \frac{d\Phi}{dz} = -\frac{e}{\epsilon_0} [n_i - n_e(\Phi)]$$

$$(2.8) \quad \frac{d}{dz} (n_i v_i) = S_i - \frac{A'}{A} n_i v_i$$

$$(2.9) \quad m_i v_i \frac{dv_i}{dz} + e \frac{d\Phi}{dz} + \frac{\gamma_i \kappa T_i}{n_i} \frac{dn_i}{dz} = - \left(\nu_{ci} + \frac{S_i}{n_i} \right) m_i v_i$$

to determine $\Phi(z)$, $v_i(z)$, and $n_i(z)$.

2.2. Length scales

The system of Eqs. (2.7)–(2.9) involves four different length scales, namely

- 1) the Debye length $\lambda_D = \left(\frac{\epsilon_0 \kappa T_e}{n_s e^2} \right)^{1/2}$,
- 2) the ion mean free path $\lambda_c = c_s / \nu_{ci}$,
- 3) the ionization length $\lambda_{io} = c_s n_s / S_i$, and
- 4) the curvature radius $R_c = |A/A'|$.

Here, we refer to characteristic charged particle densities n_s and to characteristic ion velocities c_s . (To be definite, let us choose the sheath edge density and the ion sound velocity). The Debye length is related to Poisson's equation, the other three length originate from the ion fluid equations. (In Sec. 5.5 we shall supplement the list by the ion gyro radius ρ_i). Our boundary analysis is concerned with the smallest of these ion lengths, i.e., with $L \sim \min(\lambda_c, \lambda_{io}, R_c)$.

The asymptotic case $\lambda_D/L \rightarrow 0$ results in a separate two-scale problem [8]: The *sheath* (scale λ_D related to space charges) is so small that the ion processes with the characteristic lengths λ_c , λ_{io} , and R can be neglected. Consequently the sheath is planar and collisionless. On the other hand, the *presheath* (scale L related to the ion processes) is so large that it must be quasi-neutral. (For a formal derivation of the sheath and presheath approximations see Appendix A). Since the quasi-neutrality approximation reduces the order of the differential equation set, the presheath (plasma) solution cannot be adapted to the appropriate boundary conditions at the wall. Consequently, the sheath is necessary to connect the presheath solution with the wall.

2.3. Sheath and sheath condition

The sheath potential Φ is determined by Poisson's equation

$$(2.10) \quad -\epsilon_0 \frac{d^2 \Phi}{dz^2} = \rho = e(n_i - n_e).$$

The "sheath edge" ($\Phi = 0$) is represented by the boundary condition

$$(2.11) \quad d\Phi/dz \rightarrow 0 \quad \text{for} \quad z/\lambda_D \rightarrow -\infty$$

of a decaying wall distortion (transition to the "larger" plasma scale $L \gg \lambda_D$, see Fig. 1c). Observing the quasi-neutrality $n_i = n_e$ of the sheath edge $\Phi = 0$, linearizing, multiplying with the field strength $E = -d\Phi/dz$, and integrating yields

$$(2.12) \quad \epsilon_0 E^2 + \frac{d\rho}{d\Phi} \Big|_{\Phi=0} \Phi^2 = 0.$$

Consequently, the sheath edge boundary condition requires the general **sheath condition**

$$(2.13) \quad \frac{d\rho}{d\Phi} \Big|_{\Phi=0} = e \frac{d(n_i - n_e)}{d\Phi} \Big|_{\Phi=0} \leq 0.$$

To evaluate Eq. (2.13) we refer to Eqs. (2.8) and (2.9). As discussed above, within the asymptotic analysis $\lambda_D/L \rightarrow 0$, the *sheath scale* is distinguished by collisionless ion motion and planar geometry. Consequently, we have $S_i = 0$, $\nu_{ci} = 0$, and $A = 1$. (For the formal justification see Appendix A). Eliminating dv_i/dz we thus obtain

$$(2.14) \quad \frac{dn_i}{d\Phi} = \frac{en_i}{m_i v_i^2 - \gamma_i \kappa T_i}.$$

Defining an electron "screening temperature" T_e^* (see Sec. 3.3) by

$$(2.15) \quad \frac{dn_e}{d\Phi} = \frac{en_e}{\kappa T_e^*},$$

we obtain from Eqs. (2.13) – (2.15) the general **hydrodynamic Bohm criterion**

$$(2.16) \quad m_i v_{is}^2 \geq m_i c_s^2 = \kappa (T_{es}^* + \gamma_i T_{is}),$$

where the index s refers to the sheath edge. Bohm's original criterion [1] refers to $T_i = 0$.

2.4. Presheath and sheath edge

In the presheath (typical scale length $L \gg \lambda_D$), S_i , ν_{ci} , and A' must *not* be neglected. On the other hand, we have quasi-neutrality $n_i = n_e$ (see Appendix A). Utilizing the definition of Eq. (2.15), we obtain from Eqs. (2.8) and (2.9)

$$(2.17) \quad [m_i v_i^2 - \kappa (T_e^* + \gamma_i T_i)] \frac{dn_e}{dz} = m_i v_i (n_e \nu_{ci} + 2S_i - n_e A'/A).$$

Obviously we have a singularity $dn_e/dz = \pm\infty$ (and hence $d\Phi/dz = \pm\infty$) if the bracket [...] on the left hand side (l.h.s.) vanishes, i.e., if the Bohm criterion (2.16) is fulfilled with the equality sign. (For the exceptional case that the right hand side (r.h.s.) vanishes at the same location see Sec. 4.1). From hydrodynamics we know the corresponding sound barrier singularity. In a plasma, this singularity occurs at the speed c_s of ion acoustic waves. It indicates the breakdown of the quasi-neutral approximation and represents the sheath edge (see Fig. 1b, cf. [3, 5, 9]). Thus we have the important result that the Bohm criterion (2.16) is fulfilled usually in the marginal (equality) form (see Sec. 4.1).

3. The Bohm criterion

The Bohm criterion (2.16) introduced in the previous section is a *necessary* condition for the decay of a stationary sheath in the *asymptotic* case $\lambda_D/L \rightarrow 0$ (see Sec. 4.2). It was derived from a *local* expansion at the *sheath edge* and allows *no* statements on the *global* sheath structure (see Sec. 6). In particular we

emphasize that the Bohm criterion is *no* sufficient condition for a *stable sheath* and *no* sufficient condition for a *monotonic* sheath.

Usually (see Section 3.6, 3.7, and 4.1), the Bohm criterion holds with the equality sign and constitutes an important boundary condition for the separate plasma (presheath) and sheath analysis. In this section we shall discuss various generalizations and interpretations of the Bohm criterion.

3.1. More than one positive ion component

To generalize the Bohm criterion for different *positive* ion components, the ion density n_i must be replaced by the total positive space charge. This yields

$$(3.1) \quad \sum_i e_i \frac{dn_i}{d\Phi} = \sum_i \frac{n_i e_i^2}{m_i v_i^2 - \gamma_i \kappa T_i}$$

in place of Eq. (2.14), where i now is an index denoting the various ion components. Engaging again the definition (2.15) we thus obtain from the *general* sheath condition (2.13) the (hydrodynamic) multicomponent Bohm criterion [10]

$$(3.2) \quad \sum_i \frac{e_i^2 n_{is}}{m_i v_{is}^2 - \gamma_i \kappa T_{is}} \leq \frac{e^2 n_{es}}{\kappa T_{es}^*},$$

where the index s again refers to the sheath edge. The sheath edge charge densities n_{is} and n_{es} in this relation are related by the quasi-neutrality condition

$$(3.3) \quad \sum_i e_i n_{is} = e n_{es},$$

but they are not apriori known and must be calculated self-consistently. This is a difficulty impeding the separate presheath and sheath analysis in multicomponent plasmas.

A second difficulty arises from the fact that there is only *one* Bohm criterion, whereas we need boundary conditions for $N > 1$ ion components. This second difficulty can be resolved by an inspection of the corresponding presheath problem. Replacing again $e n_i$ by $\sum_i e_i n_i$, we obtain in place of Eq. (2.17)

$$(3.4) \quad \left[1 - \frac{\kappa T_e^*}{e^2 n_e} \sum_i \frac{e_i^2 n_i}{m_i v_i^2 - \gamma_i \kappa T_i} \right] \frac{dn_e}{dz} = \sum_i \frac{e_i}{e} m_i v_i \frac{n_i \nu_{ci} + 2S_i - n_i A'/A}{m_i v_i^2 - \gamma_i \kappa T_i}.$$

Obviously we have again a singularity when the bracket [...] on the l.h.s. vanishes, i.e., when the Bohm criterion (3.2) is fulfilled in the equality form. For a system with N ion species, however, there is not only one singularity, but the bracket vanishes in N different points [10, 11]. Only *one* of these singularities (namely that located immediately in front of the wall) is related to the sheath edge and to Bohm's criterion. The remaining $N-1$ singularities are located in the presheath region and must be removed. The removal of these singularities yields the missing $N-1$ boundary conditions mentioned above. Since the locations of

these singularities are not apriori known, this again is an involved self-consistency problem. (A similar difficulty arises in the analysis of non-neutral systems [12]).

3.2. Kinetic Bohm criterion

So far we have considered only the hydrodynamic approach. The (more rigorous) *kinetic* form of the Bohm criterion is easily obtained by a re-interpretation of the multicomponent Bohm criterion: Considering different *groups* of ions with equal velocity \mathbf{v} (and hence zero temperature) in place of different components, we can substitute

$$(3.5) \quad \sum_i e_i n_i \dots \rightarrow e \int d^3\mathbf{v} f_i(z, \mathbf{v}) \dots,$$

where f_i denotes the ion distribution function. With the definition of average values

$$(3.6) \quad \langle a \rangle_i = \frac{1}{n_i} \int a(\mathbf{v}) f_i(z, \mathbf{v}) d^3\mathbf{v},$$

we thus arrive at the **kinetic Bohm criterion**

$$(3.7) \quad \frac{1}{m_i} \langle v_z^{-2} \rangle_{is} \leq \frac{1}{\kappa T_{es}^*}$$

in the form first given by Harrison and Thompson [13]. Again, the index s refers to the sheath edge, and the index z is to remind that we are concerned in the Bohm criterion with the velocity component perpendicular to the wall only. From the same argument it is only a little step to account both for different ion groups and ion species and to write down the **multicomponent kinetic Bohm criterion** [10]

$$(3.8) \quad \sum_i \frac{e_i^2 n_{is}}{m_i} \langle v_z^{-2} \rangle_{is} \leq \frac{e^2 n_{es}}{\kappa T_{es}^*}.$$

It should be observed that the velocity average $\langle v_z^{-2} \rangle_{is}$ in the Bohm criterion reflects the critical density contribution of *slow* ions. It diverges if f_i does not tend to zero for $v_z \rightarrow 0$ (e.g., for a shifted Maxwellian ion distribution).

Simultaneously this critical contribution is related to an incorrect point in the short "derivation" of the kinetic Bohm criterion given above. By the way, the same mistake was made in numerous papers beginning with the original derivation of Harrison and Thompson (see [14]): The linearization utilized in Sec. 2.3 is valid only for $\Phi \ll m_i v_i^2 / e_i$, and this condition is violated for sufficiently low ion velocities. Actually, the derivation of the kinetic sheath condition must *not* start from Rel. (2.13), because it turns out that the space charge density ρ can *not* be expanded in powers of the potential Φ . Starting from the correct expansion (in $\Phi^{1/2}$) and using the boundary condition Eq. (2.11), however, the results of Eqs. (3.7) and (3.8) can be rigorously confirmed [2, 10].

Like in the hydrodynamic case, the kinetic Bohm criterion is usually fulfilled *marginally* (i.e., with the equality sign), and this equality form is closely related to the sheath edge singularity [6, 2]. Exceptions from this general rule will be discussed in Sec. 4.1.

3.3. Non-Maxwellian electrons

For Maxwellian electrons, the temperature T_e^* defined by Eq. (2.15) agrees with the thermodynamic temperature T_e (Boltzmann factor). In non-equilibrium situations, however, there is no unique way to define a temperature, and we must distinguish various possible definitions. The temperature T_e^* of the Bohm criterion is identical with that electron temperature determining the ion sound velocity and the Debye length. To distinguish it from the familiar energetic definition, Godyak et al. [15] have proposed the name “screening temperature” for T_e^* . In various special cases (e.g., accounting for electron emission from the wall [2, 16, 17]), T_e^* may be explicitly calculated from Eq. (2.15). Generally, it can be shown (see e.g., [10]) that the screening temperature corresponding to an arbitrary electron distribution $f_e(\mathbf{v})$ may be obtained from the relation

$$(3.9) \quad \frac{m_e}{\kappa T_e^*} = -\frac{1}{n_e} \int \frac{1}{v_z} \frac{\partial f_e}{\partial v_z} d^3\mathbf{v}.$$

To give an explicitly example: The frequently used ansatz of a “hyper-Gaussian” electron distribution $f_e = C \exp(-mv^2/2w_0)^\gamma$ results in the screening temperature

$$(3.10) \quad \kappa T_e^* = 2w_0 \Gamma(\frac{3}{2\gamma}) / \Gamma(\frac{1}{2\gamma}).$$

3.4. Negative ions

Negative ions ($e_i < 0$) are included in the above presentation, if they fulfill the *same conditions* as the positive ions. Indeed, the multicomponent Bohm criteria (3.2) and (3.8) depend only on the *squares* of the ion charges e_i . This form of a negative ion Bohm criterion was given in [18].

The assumption of the *same conditions* requires in particular that the negative ions traverse the sheath and are absorbed at the wall. This, however, is true only for high ion energies (low sheath voltage or low $|e_i|/m_i$, e.g., for negative dust particles). Usually, negative ions are reflected and cannot penetrate the sheath. Consequently, they should be accounted for in exactly the same way as the electrons are [2, 19, 20]. Therefore we have to replace en_e by $en_e - \sum_j^{(-)} e_j n_j$, where the sum is extended over all negative ion components j . Defining in analogy to Eq. (2.15) effective screening temperatures T_j^* by

$$(3.11) \quad \frac{1}{n_j} \frac{dn_j}{d\Phi} = \frac{-e_j}{\kappa T_j^*},$$

we obtain Eqs. (3.2) and (3.8) in the modified form [10]

$$(3.12) \quad \sum_i^{(+)} \dots \leq \frac{e^2 n_{es}}{\kappa T_{es}^*} + \sum_j^{(-)} \frac{e_j^2 n_{js}}{\kappa T_{js}^*},$$

where the sum on the l.h.s. is extended over the positive ion components.

3.5. Relation to ion acoustic waves

Starting from the general electrostatic dispersion relation for a stationary and homogeneous system and neglecting the phase velocity ω/k in comparison to all relevant *electron* velocities (instantaneous electron reaction, $\omega \ll \omega_{pe}$; cf. Sec. 7), we obtain the ion acoustic **dispersion relation** [10]

$$(3.13) \quad \sum_i \frac{e_i^2 n_i}{m_i} \left\langle \left(v_z - \frac{\omega}{k} \right)^{-2} \right\rangle_i = \frac{e^2 n_e}{\kappa T_e^*} (1 + k^2 \lambda_D^2).$$

The brackets $\langle \rangle$ denote average values of the ion terms. Comparing with Eq. (3.8), we see that the ion acoustic dispersion relation is fulfilled at the sheath edge in the long wavelength (quasi-neutral) limit $k\lambda_D \ll 1$ for zero phase velocity $\omega/k = 0$, if the kinetic Bohm criterion is fulfilled marginally. This generalizes a result of Allen [4]. The same conclusion results if the corresponding hydrodynamic dispersion relation [10]

$$(3.14) \quad \sum_i \frac{e_i^2 n_i}{m_i (v_i - \omega/k)^2 - \gamma_i \kappa T_i} = \frac{e^2 n_e}{\kappa T_e^*} (1 + k^2 \lambda_D^2)$$

is compared with Eq. (3.2).

This relation enables an interpretation of the Bohm criterion in terms of an information loss at the sheath edge [21]: Low frequency ($\omega \rightarrow 0$) long wavelength ($k\lambda_D \rightarrow 0$) ion acoustic waves generated by the wall distortion cannot penetrate into the quasi-neutral plasma. This interpretation is closely related to the boundary condition (2.11) and to the fact that we have *one* universal presheath solution for various wall conditions (see Sec. 2.2).

3.6. Relation to the ion acoustic sound barrier

In Sec. 2.4 we have argued that the quasi-neutral solution breaks down with a field singularity $d\Phi/dz \rightarrow -\infty$ if the ions attain ion sound speed (ion acoustic sound barrier). Within the presheath we have therefore $v_i < c_s$. On the other hand, the sheath requires $v_i \geq c_s$. From these statements it appears self-evident [3, 5, 9] that the sheath edge is distinguished as well (i) by a *field singularity* $d\Phi/dz \rightarrow -\infty$ as (ii) by the *marginal* validity ($v_{is} = c_s$) of the Bohm criterion.

It should be noted, however, that the formation of a shielding *sheath* is actually possible for *all* ion velocities $v_{is} \geq c_s$. Consequently, if the quasi-neutral approximation does *not* break down with a singularity, the Bohm criterion may be *over-satisfied*, and the plasma solution may merge *smoothly* into the sheath (cf. Secs. 4.1 and 7.1).

3.7. Smooth plasma-sheath transition

Recalling that the Bohm criterion is equivalent to Eq. (2.13), it appears evident that its *marginal* validity guarantees a smooth transition at the sheath edge: The sheath solution merges with continuous slope $d\rho/d\Phi = 0$ into the quasi-neutral presheath solution $\rho \equiv 0$.

Even though this interpretation is very suggestive, it should be used with some care. First, there are exceptions from the rule that the Bohm criterion is fulfilled in the marginal form. Secondly, in Sec. 3.2 we have pointed to the fact that there are mathematical problems in deriving the *kinetic* Bohm criterion from Eq. (2.13). Finally, it should be observed that the "smooth transition" refers only to the *potential* representation. As a function of the *space coordinate* z , in contrast, the transition shows a singularity if the Bohm criterion holds marginally, and becomes smooth if the Bohm criterion is oversatisfied. These problems lead us to a refined discussion of the plasma-sheath transition.

4. Sheath edge and plasma-sheath transition

The *quasi-neutral* presheath (plasma) and the *plane collisionless* sheath are described by completely different approaches. As a consequence, the *sheath edge* - the model zone interface - represents a critical "point" that should be considered more carefully. The refined analysis proves, indeed, so delicate that there are principal differences in the fluid and in the kinetic analysis.

4.1. Sheath edge and field singularity

a) Fluid analysis

Usually, the sheath edge is defined by a singularity related to the ion sound speed (see Sec. 3.6). There are, however, exceptions from this rule. From Eq. (2.17) we conclude that this can happen only if the bracket (...) on the r.h.s. vanishes in the sonic point $v_i = c_s$. Usually, the collision term $n_e \nu_{ci}$ and the ionization rate S_i make the bracket positive. In *widening* geometries, however, the term $n_e A'/A$ may produce a change of sign and hence enable a *smooth* transition of the quasi-neutral solution through the sonic point (cf. the supersonic flow in a Laval nozzle). For illustration we consider a collisionless ($\nu_{ci} = 0$) cylindrical plasma column (radius R) with a *given* ionization profile [22]

$$(4.1) \quad S_i \sim \exp(-r^2/L^2).$$

Potential profiles resulting from a quasi-neutral cold ($T_i = 0$) fluid analysis are shown in Fig. 2a.

For ratios $R/L < x_c = 1.5286 \dots$ the ionization term dominates the geometry effect, and we find physically valid solutions (fat lines) starting in the origin and ending at $r = R$ in a turning point representing the sheath edge singularity. For $R/L > x_c$, however, the effect of the widening geometry prevails in the outer region of the column, and the sonic point is passed smoothly within the plasma body at $r = x_c L$. At this point all information on the boundary condition at the

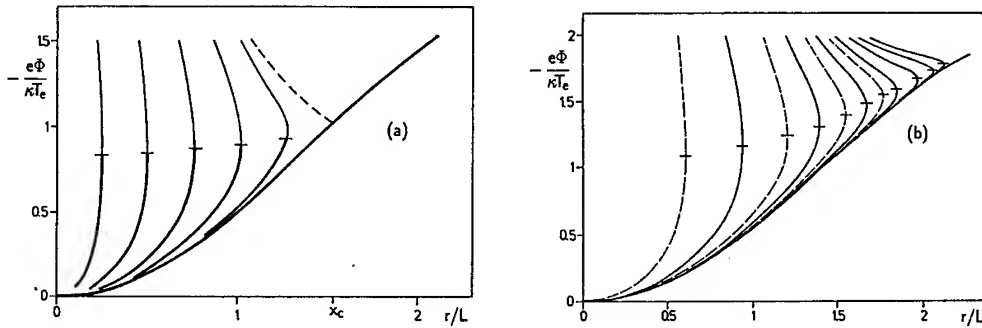


FIG. 2. Radial potential profiles in a collisionless cylindrical plasma column with an ionization rate described by Eq. (4.1), quasi-neutral analysis [22]. The turning points (marked by small horizontal lines) represent the sheath edge and terminate the physical validity of the curves. (a): Cold fluid approach, $x_c = 1.5286 \dots$ (b): Kinetic analysis.

wall is lost (cf. Sec. 3.5). Consequently, the quasi-neutral potential profiles for *all* ratios $R/L > x_c$ are represented by *one universal* curve describing simultaneously the expansion into vacuum ($R = \infty$).

b) Kinetic analysis

Due to the delicate influence of slow ions, the conclusions presented above cannot be simply transferred to the kinetic analysis of the sheath edge. Starting from the stationary ion Boltzmann equation

$$(4.2) \quad v_z \frac{\partial f_i}{\partial z} - \frac{e}{m_i} \frac{d\Phi}{dz} \frac{\partial f_i}{\partial v_z} = C(z, v, f_i)$$

the following results can be derived [2, 6, 10]:

- (a) The sheath edge shows the usual field singularity if the "source function" C does not exactly vanish for $v_z = 0$.
- (b) If the sheath edge field is singular **or** if the source function C is symmetric in v_z , the Bohm criterion is fulfilled marginally.
- (c) If the sheath edge field is finite **and** the source function is *not* symmetric, the Bohm criterion is over-satisfied.

Except for artificial models (e.g., [23, 24]) with academic source terms C , in a kinetic analysis the sheath edge is therefore *always* distinguished by a field singularity and by the marginal form of the Bohm criterion. This is in apparent contradiction to the fluid analysis. Considering again the collisionless plasma column with an ionization rate given by Eq. (4.1), we can perform the corresponding kinetic analysis [22]. The resulting potential profiles are shown in Fig. 2b. In accordance with the statements given above, *all* potential curves now end in a field singularity representing the sheath edge. Comparing, however, Figs. 2a and 2b in detail, shows that the apparent contradiction is actually of minor importance. (For a more detailed discussion see [22]).

4.2. Plasma-sheath transition for finite λ_D

Returning to the usual case, the sheath edge is distinguished by a field singularity $d\Phi/dz \rightarrow -\infty$ in the quasi-neutral presheath analysis. On the sheath scale, in contrast, the sheath edge is *defined* by the boundary condition $d\Phi/dz \rightarrow 0$ of vanishing field [see Eq. (2.11)]. This singular behaviour was occasionally regarded as a lack [25] or even contradiction [26] of the asymptotic two-scale analysis. Various attempts have therefore been made to eliminate this “drawback” by a criticism [25, 27] or modification [26, 28, 29, 30] of the Bohm criterion. These attempts, however, miss the kernel of the problem and are suitable to blur the correct interpretation of the two-scale analysis [31, 32].

Actually, there is a principal problem for *all* — even arbitrarily small — values of $\varepsilon = \lambda_D/L$: Due to the sheath edge singularity the presheath and sheath solutions cannot be matched smoothly. This problem is closely related to the problem of a consistent definition of the sheath edge for finite $\varepsilon = \lambda_D/L$. To solve these problems, the *transition region* near the sheath edge must be analysed accounting both for space charge *and* for the dominant presheath processes. For small scale ratios $\lambda_D/L \ll 1$ this leads us to an “intermediate scale” [33] with a characteristic scale length ℓ_m with $\lambda_D \ll \ell_m \ll L$. Intermediate scale investigations were performed for various special problems [34, 35, 36, 37, 38]. We shall sketch here the basic ideas and discuss the solution.

a) Fluid analysis

To analyse the transition region near the sheath edge we start from Poisson’s equation (2.10). The electron density $n_e(\Phi)$ is a given function of the potential Φ . To account for the different mechanisms of the presheath and of the sheath, we write the ion density formally in the *two* argument form $n_i(\Phi, z)$. The first argument Φ represents the dynamic density decrease caused by a collisionless field acceleration in plane geometry, and the second argument z is used to account for the influence of the presheath processes [geometry (A), collisional friction (ν_{ci}), and ionization(S_i) see Eqs. (2.8) and (2.9)].

We characterize the sheath edge by $z = 0$ and $\Phi = 0$ and expand n_i and n_e . Since the sheath edge is quasi-neutral and the Bohm criterion holds in the equality form, we have $n_{is} = n_{es}$ and $\partial n_i / \partial \Phi|_0 = dn_e / d\Phi|_0$ (see Sec. 3.7). Neglecting higher order terms, Poisson’s equation therefore reads

$$(4.3) \quad -\frac{\varepsilon_0}{e} \frac{d^2 \Phi}{dz^2} = \frac{1}{2} \frac{\partial^2 (n_i - n_e)}{\partial \Phi^2} \bigg|_0 \Phi^2 + \frac{\partial n_i}{\partial z} \bigg|_0 z.$$

To compare the relative significance, we denote the terms in Eq. (4.3) by (I), (II), and (III): The space charge density (I) related to the curvature of the potential is balanced with the sheath dynamics (II) and with the presheath processes (III). In the sheath analysis the term (III), and in the presheath analysis the term (I), is neglected.

Within the transition region all three terms have the same order of magnitude. If we denote the typical length scale of the transition region by ℓ_m and the typical magnitude of the potential by Φ_m , we can estimate the orders of magnitude of the three terms by simple scale arguments. Denoting the typical charged

particle density by n_s and utilizing the temperature definition of Eq.(2.15) we find

$$(4.4) \quad (\text{I}) \sim \frac{\varepsilon_0 \Phi_m}{e \ell_m^2}, \quad (\text{II}) \sim \frac{n_s e^2}{\kappa^2 T_e^*} \Phi_m^2, \quad \text{and} \quad (\text{III}) \sim \frac{n_s}{L} \ell_m.$$

Equating the orders of magnitude, we find the appropriate scaling [34, 35, 38]

$$(4.5) \quad \ell_m \sim \lambda_D^{4/5} L^{1/5} \quad \text{and} \quad \Phi_m \sim \left(\frac{\lambda_D}{L} \right)^{2/5} \frac{\kappa T_e^*}{e}$$

of the transition region. The significance of this transition region can be demonstrated with accordingly normalized variables

$$(4.6) \quad \zeta = \frac{z}{\ell_m} \sim \frac{z}{\lambda_D^{4/5} L^{1/5}} \quad \text{and} \quad w = -\frac{\Phi}{\Phi_m} \sim -\left(\frac{L}{\lambda_D} \right)^{2/5} \frac{e\Phi}{\kappa T_e^*}.$$

As an example, we show in Fig. 3 numerical calculations for a collision dominated plasma ($L = \lambda_c$) in front of an absorbing wall [38].

For $\varepsilon = \lambda_D/\lambda_c = 10^{-3}$ the presheath (Fig. 3a) and sheath (Fig. 3b) solutions resemble the asymptotic structure sketched in Fig. 1. With growing ε , however, it appears arbitrary to distinguish a presheath and a sheath region. Replotting the same results with the intermediate scale variables (Fig. 3c), a *common* transition region for all values of ε becomes apparent.

By an appropriate definition of ζ and w (see Appendix B), Poisson's equation (4.3) for the asymptotic intermediate scale potential variation can be brought into the *universal* form

$$(4.7) \quad \frac{d^2 w}{d\zeta^2} = w^2 + \zeta.$$

Here, the term $d^2 w/d\zeta^2$ represents the space charge, and the term ζ on the r.h.s. all presheath processes. Neglecting these terms, respectively, we find the "left" and "right" asymptotic limits

$$(4.8) \quad w_l^2 + \zeta = 0 \quad \text{and} \quad \frac{d^2 w_r}{d\zeta^2} = w_r^2$$

representing the presheath (w_l) and sheath (w_r) approximations on the intermediate scale. With the boundary condition $w \rightarrow w_l$, Eq. (4.7) can be solved numerically. The result shown in Fig. 4 demonstrates that there is indeed a universal continuous solution $w(\zeta)$ merging smoothly into the presheath and sheath limits w_l and w_r .

For $\varepsilon = \lambda_D/L \rightarrow 0$ the whole transition region $\zeta = O(1)$, $w = O(1)$ is mapped into *one* presheath point $z/L \sim \varepsilon^{4/5} \zeta \rightarrow 0$, $e\Phi/\kappa T_e^* \sim \varepsilon^{2/5} w \rightarrow 0$: The *sheath edge*. The corresponding sheath limit $z/\lambda_D \sim \varepsilon^{-1/5} \zeta \rightarrow -\infty$, $e\Phi/\kappa T_e^* \rightarrow 0$ confirms the sheath boundary condition (2.11). The electric field

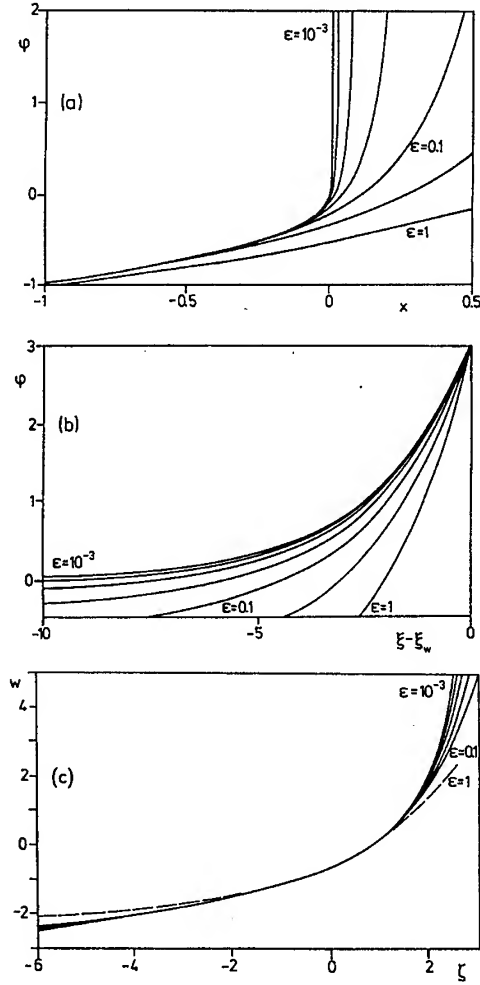


FIG. 3. Potential profiles of a collision dominated plasma (constant collision frequency ν_{ei} , $\lambda_c = c_s/\nu_{ei}$) in front of a wall, $\epsilon = \lambda_D/\lambda_c = 10^{-3} \dots 1$. (a): Presheath scale, $x = z/\lambda_c$, $\varphi = -e\Phi/\kappa T_e$. (b): Sheath scale, $\xi = z/\lambda_D$, $\varphi = -e\Phi/\kappa T_e$. (c): Intermediate scale, $\zeta = \epsilon^{-4/5}z/\lambda_c$, $w = -\epsilon^{-2/5}e\Phi/\kappa T_e$.

$$(4.9) \quad E_m \sim \frac{\Phi_m}{\ell_m} \sim \frac{\kappa T_e^*}{e \lambda_D^{2/5} L^{3/5}}$$

in the transition region justifies and elucidates the limits

$$(4.10) \quad \frac{e \lambda_D E_m}{\kappa T_e^*} \sim \epsilon^{3/5} \rightarrow 0 \quad \text{and} \quad \frac{e L E_m}{\kappa T_e^*} \sim \epsilon^{-2/5} \rightarrow \infty$$

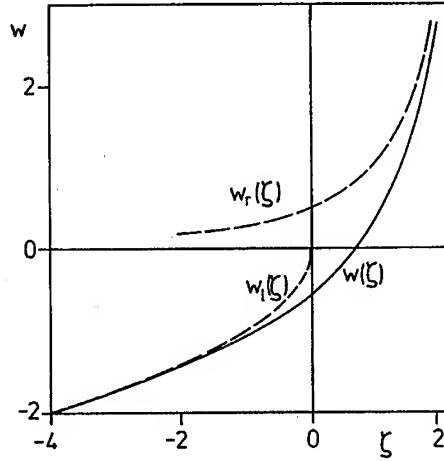


FIG. 4. Asymptotic potential variation $w(\zeta)$ on the intermediate scale [see Eqs. (4.6) and (4.7)]. The limiting curves $w_l(\zeta)$ and $w_r(\zeta)$ represent the presheath and sheath approximations [(see Eq. (4.8)].

of a vanishing sheath edge field on the sheath scale and an infinite field on the presheath scale without any contradiction.

With growing ε the extension of the sheath transition region grows, and the definition of a sheath edge becomes fuzzy. Correspondingly, the ion velocity range [cf. Eq. (B2)]

$$(4.11) \quad v_i/c_s = 1 + O(\varepsilon^{2/5})$$

of the transition region confirms the marginal validity $v_i = c_s$ of the Bohm criterion for $\varepsilon = 0$ and makes the definition of a limiting velocity gradually unsharp for $0 < \varepsilon \ll 1$ [38]. For $\varepsilon \geq O(1)$, finally, there is *no* basis for a scale separation and *no* Bohm criterion.

(b) Kinetic analysis

Due to the critical density contribution of slow ions, in a kinetic analysis n_i cannot be expanded in powers of Φ (cf. Sec. 3.2), and the term (II) in Eq. (4.3) must be replaced by a term of the form $B\Phi^{3/2}$, where the order of magnitude of the coefficient B is given by $n_s(e/\kappa T_e^*)^{3/2}$. Correspondingly, the term (II) in Eq. (4.4) must be replaced by

$$(4.12) \quad (\text{II}') \sim n_s \left(\frac{e\Phi_m}{\kappa T_e^*} \right)^{3/2}.$$

Following the same steps as above, we obtain

$$(4.13) \quad \ell'_m \sim \lambda_D^{6/7} L^{1/7}, \quad \Phi'_m \sim \left(\frac{\lambda_D}{L}\right)^{4/7} \frac{\kappa T_e^*}{e}, \quad \text{and} \quad E'_m \sim \frac{\kappa T_e^*}{e \lambda_D^{2/7} L^{5/7}}.$$

This "regular" kinetic scaling was rigorously derived in [2], but until now never confirmed in explicit models. Existing models [36, 37] result in the "singular" scaling

$$(4.14) \quad \ell''_m \sim \lambda_D^{8/9} L^{1/9}, \quad \Phi''_m \sim \left(\frac{\lambda_D}{L}\right)^{4/9} \frac{\kappa T_e^*}{e} \quad \text{and} \quad E''_m \sim \frac{\kappa T_e^*}{e \lambda_D^{4/9} L^{5/9}}$$

of the transition region. This different scaling is caused by an *enhanced* influence of slow ($m_i v_i^2 \sim e \Phi_m$) ions [2], if a singular source term $C \sim \delta(\mathbf{v})$ is used in Eq. (4.2). In a rough estimate we can account for this by a modified contribution

$$(4.15) \quad (\text{III}') \sim (\kappa T_e^* / e \Phi_m)^{1/2} (\text{III})$$

in Eq. (4.4). The comparison of (I), (II'), and (III') confirms Eq. (4.14).

5. The presheath

The integration of the sheath equations is, in principle, straight forward (see Sec. 6). The presheath analysis, in contrast, involves the full difficulty of an inhomogeneous plasma in a self-consistent field. The presheath region may include the entire plasma body in some cases (e.g., the collisionless plasma column). In other cases it may be advantageous to consider a separate presheath model with an extension L small compared with the plasma extension Λ (e.g., the Knudsen layer of a collision dominated plasma [39]). We don't want to present here involved specific plasma models but we are interested in general features.

5.1. The mechanisms of the presheath

The sheath condition (2.13) requires that the dynamic ion density decrease at the sheath edge must not exceed the electron density decrease. Of course this condition must be also fulfilled in the quasi-neutral presheath. Since the Bohm criterion is *not* fulfilled in the presheath, there must be a mechanism lessening the ion density decrease by field acceleration. Let us demonstrate this for the case of cold ions ($T_i = 0$) [2].

We start from the logarithmic derivative of the ion current density $j_i = n_i v_i$. Utilizing the quasi-neutrality $n_i = n_e$ and engaging the temperature definition (2.15) we obtain

$$(5.1) \quad \frac{\kappa T_e^*}{m_i v_i^2} \frac{d}{dz} \left(\frac{m_i}{2} v_i^2 \right) + e \frac{d\Phi}{dz} = \frac{\kappa T_e^*}{j_i} \frac{dj_i}{dz}.$$

Since the Bohm criterion is *not* fulfilled in the presheath, we have $\kappa T_e^* / m_i v_i^2 > 1$ and hence

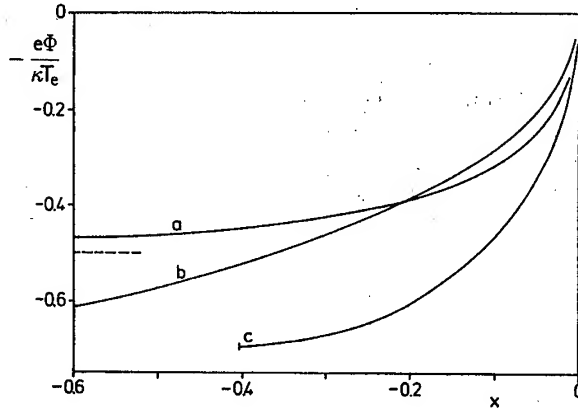


FIG. 5. Potential profiles of elementary presheath models [2] ($T_i = 0$, $T_e = \text{const}$, $n_e = n_s \exp(-e\Phi/\kappa T_e)$). a: Geometric presheath (Plasma in front of a spherical probe [40], $x = (r - R)/R$). b: Collisional presheath (Charge exchange model with constant mean free path λ_c , $x = z/\lambda_c$). c: Ionization presheath (Plane symmetric plasma [50], $S_i \propto n_e/L$, $x = z/L$).

$$(5.2) \quad \frac{d}{dz} \left(\frac{m_i}{2} v_i^2 + e\Phi \right) < \frac{\kappa T_e^*}{j_i} \frac{dj_i}{dz}.$$

Consequently, in the presheath (i) the ion current density j_i increases approaching the wall and/or (ii) the total ion energy $m_i v_i^2/2 + e\Phi$ decreases due to a retarding force. The presheath mechanism is therefore based on at least one of the following effects:

- a) Concentrating geometry (\Rightarrow ion current density increase)
- b) Collisions (\Rightarrow ion retardation by friction)
- c) Ionization (\Rightarrow current increase *and* effective retardation).

Remembering that we have, so far, considered only one space direction (z), we must take into account the additional possibility that energy is transferred into ion velocity components parallel to the wall. This enables a fourth mechanism:

- d) Magnetic field (\Rightarrow ion orbit deflection).

In our basic equations (2.7)-(2.9) we have accounted for the effects a)-c). In the following we shall briefly discuss typical features of presheath solutions dominated respectively by *one* of these effects (see Fig. 5). The magnetic presheath d) will be discussed in Sec. 5.5.

5.2. Geometric presheath

The mechanism of the geometric presheath is based on the *increasing* ion current density in a *concentrating* geometry. In plane or in a widening geometry no presheath is possible without elementary processes (cf. Sec. 4.1). A typical example for the geometric presheath is the collisionless plasma ($\lambda_c \gg R$) in

front of a spherical or cylindrical probe of radius R . Curve a of Fig. 5 shows the potential profile for a simple cold ion model in spherical geometry [40], the limit $r = \infty$ of the undisturbed plasma is indicated by a dashed line. The quasi-neutral potential profile ends at the sheath edge with a field singularity. The total potential drop $\kappa T_e/2e$ across the presheath corresponds to the minimum value required by the Bohm criterion. Due to the angular momentum related to the thermal ion motion, a kinetic analysis of the geometric presheath is involved [41, 42]. For a more comprehensive discussion we refer to discourses on probe theory (e.g., [43]).

5.3. Collisional presheath

Describing the transport in a collision dominated plasma in the approach of diffusion and mobility, the quasi-neutral approach breaks down in front of the wall with a potential divergence [44]. This divergence is frequently avoided by an artificial cutoff at the Bohm velocity [45]. A consistent analysis of the boundary layer, however, must account for ion inertia [46]. Curve b of Fig. 5 shows the result of a simple fluid analysis [2]. Corresponding kinetic results [47] are in qualitative agreement. Again, the quasi-neutral solution runs into the typical sheath edge *field* singularity. Far away from the wall ($x = z/\lambda_c \rightarrow -\infty$) the potential profile has a logarithmic shape indicating that there is no undisturbed plasma: A small residual field is required to drive the ion current. This shows that the pure collisional presheath represents only a boundary region (Knudsen layer, extension few λ_c) of the collision dominated plasma. Within the plasma body ionization and geometry must be accounted for [39].

With respect to the assumption $\lambda_D/\lambda_c \rightarrow 0$ of the asymptotic analysis it should be observed that this condition refers to the *local* Debye length at the sheath edge. Due to the strong density decrease in front of the Knudsen layer, this basic requirement is frequently not or only poorly fulfilled in collision dominated plasmas. Consequently, it must not surprise if the Bohm criterion is violated [48] in strongly collisional situations (see Sec. 4.2).

5.4. Ionization presheath

A presheath mechanism governed exclusively by ionization is realized in the Tonks–Langmuir model [49] of a collisionless plane symmetric plasma between two parallel walls. In this case the presheath comprises the half plasma body extending from the midplane to the wall (sheath edge). The ionization rate S_i and the plasma extension L are coupled by the plasma balance (ion production = loss to the wall). In its original form, the system refers to ions generated from cold neutrals.

The famous *kinetic* analysis [49] of this problem in 1929 represents the birth of all plasma–sheath transition analysis. Beginning with the work of Harrison and Thompson [13], the analysis was repeated and extended in numerous papers. Curve c of Fig. 5 shows the potential profile from the midplane ($x = -0.404$ in Fig. 5) to the sheath edge ($x = 0$) in a cold fluid approach [50] with $S_i \propto n_e$. The plasma potential drop $e\Delta\Phi/\kappa T_e = \ln 2$ (resp. = 0.854 in kinetic analysis)

is higher than the minimum value required by the Bohm criterion (cf. Sec. 5.2). This shows that the generation of ions at rest can be interpreted as an effective retardation force.

A surprising result was obtained, when Emmert et al. [23] investigated a Tonks–Langmuir model accounting for the production of *hot* ions: The sheath edge was *not* distinguished by a field singularity. In accordance with our statement in Sec. 4.1, this strange result is produced by an artificial source term in the Emmert model. Corresponding calculation with a Maxwellian source [51] exhibited the usual sheath edge singularity. (For a more detailed discussion of this aspect we refer to [2, 24, 52]).

The plane Tonks–Langmuir model is particularly suitable to exhibit the basic properties of the ionization presheath. For practical applications, however, the corresponding cylindrical model appears more relevant. Of course, the ionization mechanism of the presheath is then superimposed by the effect of the *widening* geometry. This can cause difficulties if the ionization mechanism is essentially restricted to the plasma kernel [53] (see also Sec. 4.1).

5.5. Magnetic presheath

The mechanism of the magnetic presheath is based on the ion orbit deflection in a strong (more or less wall parallel) magnetic field \mathbf{B} . To provide an ion transport to the wall, we must account for field lines intersecting the wall at a finite angle $\alpha = \arctan B_z/B_\perp$ [54, 55] and/or for collisions [56]. Since the basic differences in these transport mechanisms result in different presheath properties, we refer to a fluid analysis [57] accounting both for an oblique magnetic field and for ion collisions (charge exchange with constant collision frequency ν_{ci}). The analysis assumes a Boltzmann electron distribution and starts from the ion momentum equation [cf. Eq. (2.9)]

$$(5.3) \quad m_i v_{iz} \frac{dv_i}{dz} + \left(e \frac{d\Phi}{dz} + \frac{\gamma_i \kappa T_i}{n_i} \frac{dn_i}{dz} \right) \mathbf{e}_z = e \mathbf{v}_i \times \mathbf{B} - \nu_{ci} m_i \mathbf{v}_i.$$

The results may be summarized as follows. The typical extension of the magnetic presheath is determined by the ion gyro-radius $\rho_i = c_s/\omega_c$, where $\omega_c = eB_\perp/m_i$ is the ion cyclotron frequency. All potential profiles (see Fig. 6) exhibit the expected sheath edge field singularity in front of the wall.

In the plasma region ($z \rightarrow -\infty$) the profiles show the logarithmic shape discussed in Sec. 5.3. (An undisturbed plasma region is obtained if ionization is accounted for [58]). At the sheath edge the Bohm criterion

$$(5.4) \quad v_{iz} = c_s \quad (z/\rho_i \rightarrow 0)$$

is fulfilled in the equality form.

For high collision frequencies ($\nu_{ci} \gg \omega_c \tan \alpha$) the potential profile of Behnel's model [56] ($\alpha = 0$) is approached. With *decreasing* collision frequency the potential drop begins to *increase* because the transport *across* the magnetic field lines is impeded. With further decreasing collision frequency ($\nu_{ci} < \omega_c \tan \alpha$) the competing transport *along* the field lines gains growing influence, and the

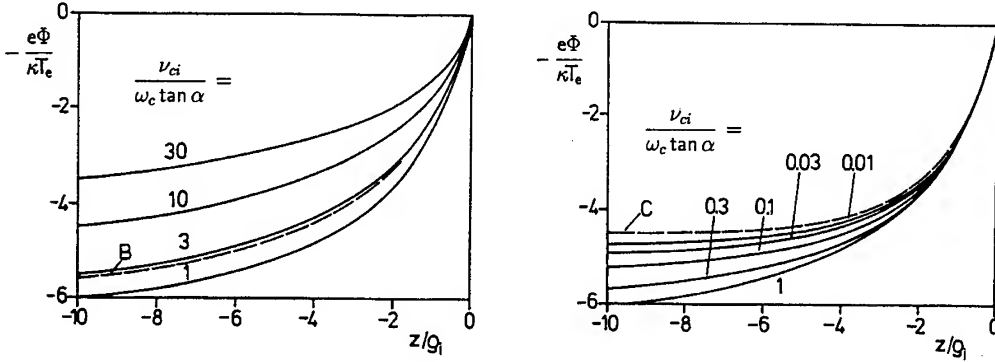


FIG. 6. Potential profiles in the magnetic presheath for $\tan \alpha = B_z/B_\perp = 0.01$ and various values of ν_{ci} ; $\rho_i = c_s/\omega_c$. B: Behnel's model ($\alpha = 0$, $\nu_{ci} = 0.03 \omega_c$). C: Chodura's model ($\nu_{ci} = 0$).

potential drop *decreases* again. In the limiting case $\nu_{ci} \rightarrow 0$ (Chodura's model [54, 55]) finally, the logarithmic divergence of the potential for $z \rightarrow -\infty$ disappears and the potential tends to a constant value: Seemingly there is now an undisturbed plasma region.

Investigating the dominating presheath mechanism, we find a competing effect of ion friction ($v_{i\parallel} < c_s$) and ion acceleration in $\mathbf{E} \times \mathbf{B}$ -direction ($v_{i\parallel} > c_s$) depending on the ion flow velocity $v_{i\parallel}$ along the magnetic field lines. For $\nu_{ci} \approx 0.3 \omega_c \tan \alpha$, $v_{i\parallel}$ becomes sonic at the sheath edge. With decreasing collision frequency the sonic point is shifted into the plasma region, and in the limiting case $\nu_{ci}/(\omega_c \tan \alpha) \rightarrow 0$ it moves to $z = -\infty$. Consequently, Chodura's model [54, 55] is subject to an *additional* Bohm criterion

$$(5.5) \quad v_{i\parallel} = c_s \quad (z/\rho_i \rightarrow -\infty)$$

for the flow *along* the magnetic field lines. This shows that there is actually *no* undisturbed plasma region: In the collisionless limit $\nu_{ci} = 0$ the magnetic presheath is preceded by a *plasma presheath* accelerating the ions to ion sound velocity: The *total* presheath mechanism depends therefore always on collisions (or other "velocity drivers" [59]), a "pure" magnetic presheath is not possible. Eq. (5.5) has important consequences for the theory of probes in magnetized plasmas [60, 61]. For the effect of drifts we refer to [62, 63].

In principle, the above fluid analysis must be considered somewhat questionable: In a distance of some ρ_i in front of the wall the ion orbits are "bent open", and the transition from closed to open orbits cannot be adequately described in fluid theory. Kinetic analyses [64, 65, 66], however, have essentially confirmed the hydrodynamic results.

6. The sheath

In Secs. 2 and 4 we have studied the *local* space charge formation near the sheath edge. Here, we are interested in some aspects referring to the *global*

sheath structure.

6.1. Formal integration of the sheath equations

Starting from the boundary conditions at the sheath edge, the sheath analysis is straight forward. In the hydrodynamic analysis (cf. Sec. 2.1) the r.h.s. of Eqs. (2.8) and (2.9) becomes zero. Together with the adiabatic law (2.5), the equations can be integrated and yield n_i as a function of the potential Φ . The same is true in the kinetic analysis, because the ion distribution $f_i(v_i, \Phi) = f_{is}([v^2 - 2e\Phi/m_i]^{1/2})$ is explicitly determined by the ion distribution function f_{is} at the sheath edge. Observing Eq. (2.2), the r.h.s. of Poisson's equation (2.10) is therefore a known function of Φ . Multiplying with $d\Phi/dz$ and engaging the boundary condition (2.11) we can integrate analytically and obtain in the case of a *monotonic* sheath

$$(6.1) \quad \left(\frac{d\Phi}{dz}\right)^2 = \frac{2e}{\epsilon_0} \int_0^\Phi [n_e(\phi) - n_i(\phi)] d\phi.$$

A second integration yields the space coordinate z as a function of Φ . Consequently, the whole sheath analysis is reduced to simple quadratures, and the intrinsic difficulties of the boundary layer problem are caused by the presheath analysis.

6.2. Non-monotonic sheaths

The validity of the Bohm criterion excludes oscillatory solutions *near the sheath edge*. This correct statement is the root of a frequent misunderstanding: The Bohm criterion does *not* guarantee an over all monotonic sheath potential.

The fact that electron emission from the wall can cause a non-monotonic double layer is known since Langmuir [67] and was described in detail by Prewett and Allen [17]. Negative space charges in the sheath can, however, also be produced by hot electrons originating from the plasma [2]: In the case of different negative particle components (negative ions and/or different electron groups), the Bohm criterion and the sheath edge region are essentially dominated by the *coldest* component [see Eq. (3.12)]. The final density decrease within the sheath, in contrast, is determined by the *hottest* component.

6.3. Child-Langmuir law and electron step models

Assuming cold ions ($T_i = 0$) and Boltzmann distributed electrons we have

$$(6.2) \quad n_i = \frac{n_s c_s}{v_i} = \frac{n_s}{(1 - 2e\Phi/\kappa T_e)^{1/2}} \quad \text{and} \quad n_e = n_s \exp \frac{e\Phi}{\kappa T_e},$$

and obtain from Eq. (6.1)

$$(6.3) \quad \left(\frac{d\Phi}{dz}\right)^2 = \frac{2n_s \kappa T_e}{\epsilon_0} \left[\left(1 - \frac{2e\Phi}{\kappa T_e}\right)^{1/2} + \exp \frac{e\Phi}{\kappa T_e} - 2 \right].$$

For *high negative sheath voltages* we may neglect terms of order 1 and smaller in comparison to $e\Phi/\kappa T_e$. Utilizing this approximation and integrating once more we obtain the **Child–Langmuir law** [68]

$$(6.4) \quad \Phi(z) = - \left(\frac{9j_{is}}{4\epsilon_0} \right)^{2/3} \left(\frac{m_i}{2e} \right)^{1/3} (z - z_0)^{4/3},$$

where $j_{is} = en_s c_s$ designates the ion current entering the sheath. The integration constant z_0 can be considered as an approximate representation of the sheath edge position. For high sheath voltages $e|\Phi_0| \gg \kappa T_e$ the sheath thickness

$$(6.5) \quad d \approx \frac{2^{5/4}}{3} \left(\frac{e|\Phi_0|}{\kappa T_e} \right)^{3/4} \lambda_D$$

is therefore large compared with the Debye length λ_D .

This is the basis for *electron step models*: The extension ($< \sim 10\lambda_D$) of the “Langmuir sheath”, i.e., that part of the sheath where electrons are still important, is small in comparison to the thickness d of the “unipolar ion sheath”. Neglecting the Langmuir sheath width, the electron density profile is therefore modelled by a step at $z = s$ with $n_e = n_i$ for $z < s$, and $n_e = 0$ for $z > s$.

In principle, this approximation is convenient and justified for sufficiently high sheath voltages. It should be observed, however, that the sheath edge conditions $\Phi = 0$, $d\Phi/dz = 0$, $n_i = n_s$, and $v_i = c_s$ refer to the *plasma side* of the electron step and must *not* be used as boundary conditions for the ion sheath [69]. To give an explicit rule, let us assume that the edge of the unipolar ion sheath is defined by $n_e = 0.1 n_s$. Neglecting the electron correction, we then read from Eqs. (6.2) and (6.3) an appropriate set of boundary conditions

$$(6.6) \quad \Phi \approx -2.3 \frac{\kappa T_e}{e}, \quad \frac{d\Phi}{dz} \approx -0.9 \frac{\kappa T_e}{e\lambda_D}, \quad n_i \approx 0.5 n_s, \quad v_i \approx 2c_s$$

for the “edge” of the unipolar ion sheath.

6.4. Collisions in the sheath

For high sheath voltages the sheath thickness d is large compared with the Debye length λ_D [see Eq. (6.5)]. In contrast to the Langmuir sheath, the unipolar ion sheath may therefore be influenced or even dominated by collisions, even if $\lambda_D \ll \lambda_c$ is fulfilled. Utilizing a “viscous drag model” [70], Eq. (6.4) can be generalized to the relation [71]

$$(6.7) \quad \Phi(z) = - \left(\frac{9j_i}{4\epsilon_0} \right)^{2/3} \left(\frac{m_i}{2e} \right)^{1/3} \left(1 + \frac{12\pi}{125} \frac{z - z_0}{\lambda_c} \right)^{1/3} (z - z_0)^{4/3},$$

accounting in a convenient way for charge exchange collisions with constant mean free path λ_c . Depending on the ratio $(z - z_0)/\lambda_c$, Eq. (6.7) interpolates between the collisionless limit $d \sim |\Phi|^{3/4}$ of Eq. (6.5) and the collisional limit $d \sim |\Phi|^{3/5}$ [72]. For the effect of collisions in the sheath on the ion distribution in front of the wall we refer to [71].

7. Time dependent sheath problems

So far we have dealt exclusively with stationary systems. Due to the growing technological importance of radio frequency- (RF-) and pulsed discharges, however, there is an increasing interest in time dependent sheaths. We shall sketch here only few basic problems of this wide field.

7.1. The problem of a dynamic Bohm criterion

Recalling the derivation of the Bohm criterion in Sec. 2.2, we note that the sheath condition depends basically on the dynamic ion density decrease resulting from the ion current continuity and from the energy conservation law. Both conservation laws are *not* valid in non-stationary systems and, consequently, we expect *no* significance of the Bohm criterion for time dependent sheaths.

In contrast to this general statement, Prewett and Allen [73] investigated quasi-neutral ion rarefaction waves and found special similarity solutions running into a uniformly moving sheath edge distinguished by the "*dynamic Bohm criterion*"

$$(7.1) \quad v_{is} - u = c_s.$$

Here, v_i designates the ion flow velocity, and u is the velocity of the moving sheath edge. Subsequently, a general significance of the dynamic Bohm criterion was claimed by some authors [74] and questioned by others [75].

From theoretical considerations as well as from various numerical calculations we conclude that there is no general and unambiguous solution of this problem. Referring again to scale arguments, we have to distinguish three characteristic times. On the very fastest time scale $\tau_e = \omega_{pe}^{-1}$, the electrons neutralize the presheath and form a sheath adapted to the transient boundary conditions. During this phase the ions do not at all react and, consequently, there is no influence on the Bohm criterion. Let us consider this electron reaction as an *instantaneous* process. The "fast" time scale is then determined by the reaction time $\tau_s = \lambda_D/c_s = \omega_{pi}^{-1}$ of the ions in the *sheath*. On this time scale the sheath is intrinsically non-stationary, and the Bohm criterion has no significance. On the "slow" time scale $\tau_p = L/c_s$ we have a quasi-stationary sheath and a non-stationary presheath. Consequently, during this phase the Bohm criterion will usually be fulfilled in the *in*-equality form (cf. Sec. 3.6).

The special solutions addressed by the dynamic Bohm criterion (7.1) can actually be interpreted as a stationary sheath in a moving coordinate system. Special sheath problems related to RF- and pulsed discharges will be discussed in the next subsections.

7.2. RF-sheath problems

The question on the validity of the Bohm criterion in front of the electrode sheath in RF-discharges is a problem of great practical importance. A systematic investigation has to start from the boundary condition (2.11) of a decaying sheath potential. According to the non-linear reaction of the sheath, this condition must

be fulfilled for the DC self-bias ($\omega = 0$) as well as for all harmonics ($\omega = m\omega_0$) of the applied RF-current. Recalling the interpretation of Sec. 3.5, we can relate this condition to the ion acoustic dispersion relation. In the approach of an instantaneous electron reaction ($\omega \ll \omega_{pe}$) and cold ions ($T_i = 0$) we obtain from Eq. (3.14)

$$(7.2) \quad [\omega_{pi}\lambda_D/(v_i - \omega/k)]^2 = 1 + k^2\lambda_D^2,$$

and find four (real or complex) wave numbers k_1, \dots, k_4 for any *real* value of ω [76]. These solutions are shown in Fig. 7 for three representative ion velocities (a) $v_i < c_s$, (b) $v_i = c_s$, and (c) $v_i > c_s$. k_1 and k_2 correspond to ion-acoustic waves with *positive* group velocities propagating (if present) from the plasma into the sheath: These modes do not violate the sheath condition. k_3 and k_4 are

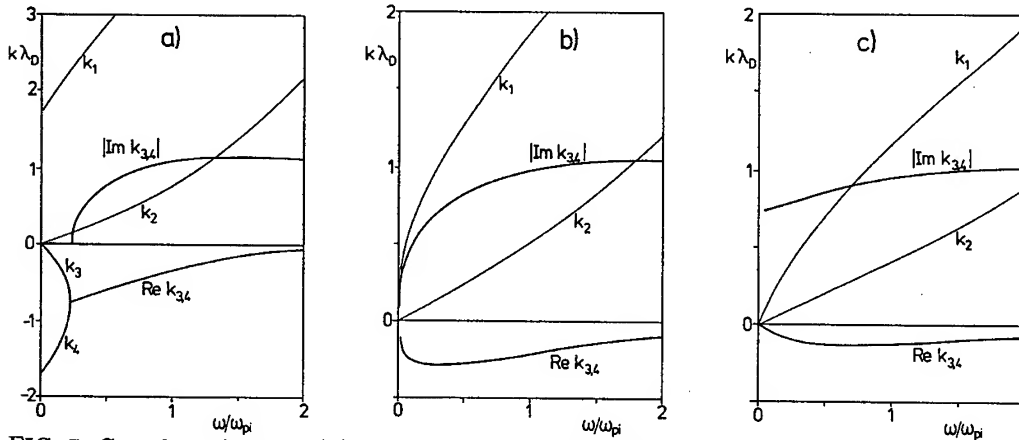


FIG. 7. Complex solutions $k(\omega)$ of the ion acoustic dispersion relation [cf. Eq. (7.2)] for real ω , a): $v_i = 0.5 c_s$; b): $v_i = c_s$; c): $v_i = 1.5 c_s$.

in general complex. For high v_i and ω they describe the *electron* screening effect shielding the sheath potential from the plasma. With decreasing ion velocity and frequency the screening is impeded by the *ion* reaction. For $v_i < c_s$ and $\omega \rightarrow 0$, finally, we obtain an *undamped* mode k_3 with *negative* group velocity propagating the sheath disturbance into the plasma.

Excluding this "forbidden" mode we see that the DC Bohm criterion $v_{is} \geq c_s$ holds equally in the RF-case for *all* frequencies $\omega_0 \ll \omega_{pe}$ [76, 77]. It should be observed, however, that the sheath edge position is determined by the slowly decaying DC self-bias and not by the strongly damped RF modes.

Analysing the RF-sheath, it is advised to distinguish the low-frequency range $\omega_0 < \omega_{pi}$ and the high-frequency range $\omega_0 > \omega_{pi}$. In a first approach, the low-frequency sheath can be considered quasi-stationary [78]. In the high-frequency regime, in contrast, the ions can hardly follow the alternating field, and the sheath is distinguished by an oscillating electron front.

This supplies the basis for *electron step models* (cf. Sec. 6.3) of the collisionless high-amplitude high-frequency sheath [79, 80, 81]: The ion density $n_i(z)$ is stationary, because the ions are only influenced by the time averaged potential

$\bar{\Phi}(z)$. The electron density is modelled by an oscillating step with $n_e = n_i$ for $z < s(t)$ and $n_e = 0$ for $z > s(t)$. In principle, the basic assumptions of this model are justified. It must be observed, however, that the step position is *not* identical with the sheath edge (see above). Therefore it is difficult to formulate appropriate boundary conditions at the step position. In [82] it is shown that usual step models start from inconsistent boundary conditions and, as a consequence, fail in certain parameter regimes (see Fig. 8).

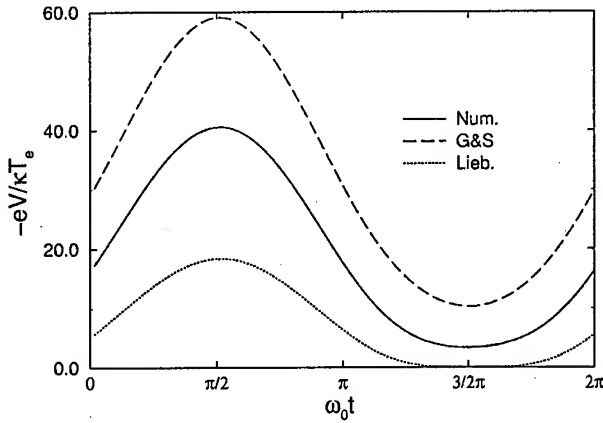


FIG. 8. The total sheath voltage $V(t)$ for a moderately high RF current amplitude $j_{RF} = 2en_s c_s \omega_0 / \omega_{pi}$ calculated from the step models [79] (Lieb.) and [80] (G&S) in comparison with the numerical solution (solid curve).

7.3. The formation of a high-voltage sheath

The dynamic sheath evolution is of great importance in “plasma immersion ion implantation”, where negative high-voltage pulses are used to bombard the surface of a workpiece with energetic ions. To illustrate the basic process, we consider the reaction of a collisionless plasma on a pulse $\Phi_0 = -U_0$, $eU_0 \gg \kappa T_e$ with zero rise time. At the moment ($t = 0$) when the pulse is switched on, the electrons are repelled quasi-instantaneously (timescale ω_{pe}^{-1}), and a nearly homogeneous *ion matrix sheath* of thickness $s_0 \approx (2eU_0/\kappa T_e)^{1/2} \lambda_D$ is formed. The subsequent sheath evolution shows two different phases, as can distinctly be seen from the ion current j_i to the target surface. Fig. 9 shows the results of a numerical calculation in comparison with two different analytical approaches [83, 84] based on electron step models (see Sec. 6.3).

During the initial “matrix extraction phase” ($\omega_{pi} t < 3$), the ions extracted from the matrix sheath form a high current peak $j_i \sim (eU_0/\kappa T_e)^{1/2} n_s c_s$. In the later “sheath expansion phase” ($\omega_{pi} t > 3$) the sheath width $s(t)$ grows and the ion current relaxes *slowly* to the Bohm current $j_i = n_s v_s$. Finally, a stationary Child-Langmuir sheath with $s_\infty = d \gg s_0$ [see Sec. 6.3, Eq. (6.5)] is formed.

Investigating the validity of the Bohm criterion, we note that — on the time

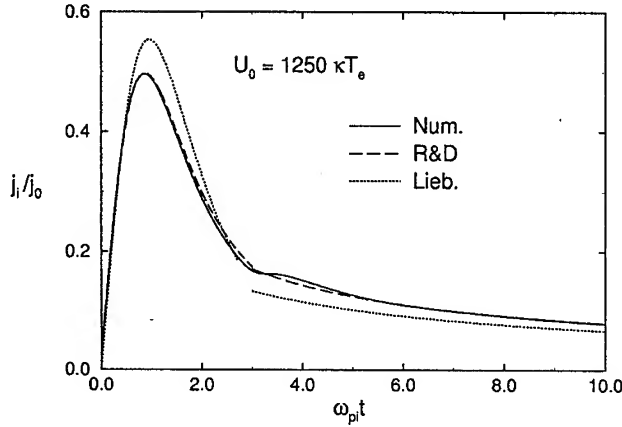


FIG. 9. Normalized ion current density j_i/j_0 at the target surface for a high-voltage pulse $U_0 = 1250\kappa T_e$; $j_0 = (2U_0/\kappa T_e)^{1/2} n_s c_s$. The numerical solution of the cold fluid equations (solid curve) is compared with the analytical models [83] (Lieb.) and [84] (R&D).

scales considered - the ions flow continuously with ion sound velocity c_s from the presheath into the sheath. Consequently, the *stationary* Bohm criterion is marginally fulfilled. Since the sheath edge moves initially with high velocity $u \sim (eU_0/\kappa T_e)^{1/2} c_s$ into the plasma, the *dynamic* Bohm criterion is by far *over*-satisfied.

8. Summary and closing remarks

The positive space charge sheath shielding a quasi-neutral plasma from the potential distortion caused by an absorbing negative wall has an extension of some (local) electron Debye length λ_D . Usually λ_D is small compared with competing lengths L of the boundary layer (Sec. 2.2). This is the basis of an asymptotic *two-scale analysis* ($\lambda_D/L \rightarrow 0$) of a collisionless planar sheath and a quasi-neutral presheath (Sec. 2, Appendix A).

In the simplest case, the sheath formation depends on a high directed ion velocity $v_{is} \geq c_s$ (ion acoustic speed) at the *sheath edge* (Sec. 2.3). This condition — the *Bohm criterion* — requires that the ions are pre-accelerated in the presheath. The quasi-neutral presheath solution breaks down at the sound barrier with a singularity representing the sheath edge (Sec. 2.4). Consequently, the Bohm criterion is usually fulfilled in the *marginal* form $v_{is} = c_s$.

Bohm's original criterion refers to the simplified model of monoenergetic cold ions and Boltzmann distributed electrons. It can be generalized to account for different positive (Sec. 3.1) and negative (Sec. 3.4) ion components and for arbitrary ion (Sec. 3.2) and electron (Sec. 3.3) distribution functions. In its kinetic form [Eqs. (3.7) and (3.8)], the Bohm criterion depends decisively on the contribution of *slow* ions and requires that the sheath edge ion distribution

function vanishes for zero ion velocity. In any case the (generalized) Bohm criterion guarantees that all information on the boundary conditions at the wall is lost at the sheath edge (Sec. 3.5).

A more refined analysis of the plasma sheath transition (Sec. 4) shows that there are exceptions from the rule that the sheath edge is distinguished by a field singularity and by the marginal validity of the Bohm criterion. Different conditions for such exceptions in the kinetic and in the hydrodynamic analysis (Sec. 4.1) are due to the critical role of slow ions. In the usual case, the sheath edge singularity impedes a consistent matching of the plasma- and sheath solutions. A smooth transition is obtained from a *universal* intermediate scale analysis accounting for space charge *and* for presheath processes (Sec. 4.2, Appendix B). This analysis determines the actual sheath edge field strength $E_m \sim \kappa T_e / (e \lambda_D^{2/5} L^{3/5})$ [hydrodynamic analysis, see Eqs. (4.9), (4.13), and (4.14)] and confirms the marginal validity of the Bohm criterion for small but finite λ_D/L .

The quasi-neutral presheath (Sec. 5) providing the necessary ion acceleration may be a special boundary layer region (e.g., the Knudsen layer) or may extend over the whole plasma. Its mechanism (Sec. 5.1) is based on at least one of the following processes: (a) geometric current concentration (Sec. 5.2), (b) collisional ion friction (Sec. 5.3), (c) ionization (Sec. 5.4), or (d) magnetic ion orbit deflection (Sec. 5.5). The magnetic presheath needs the support of a second mechanism. As a consequence, there is an additional Bohm criterion [Eq. (5.5)] for the "pure" magnetic presheath.

In contrast to the presheath analysis, the integration of the sheath equations is straightforward (Sec. 6.1). It should be observed, however, that the complication of a non-monotonic sheath structure is *not* generally excluded by the Bohm criterion (Sec. 6.2). For high negative sheath voltages the electrons play a minor role, and a *unipolar* ion sheath with a thickness $d \gg \lambda_D$ is formed (Sec. 6.3). The unipolar sheath can conveniently be described by electron step models. The electron step, however, must not be confused with the sheath edge [see Eq. (6.6)]. Despite the scaling $\lambda_D \ll \lambda_c$, in a "thick" unipolar sheath ion collisions may become important (Sec. 6.4).

All statements given so far hold for *stationary* systems. For intrinsically time dependent sheaths (Sec. 7) the Bohm criterion is in general *not* valid. In some special cases a *dynamic* Bohm criterion may be applied (Sec. 7.1). For RF-discharges (Sec. 7.2) and pulsed discharges (Sec. 7.3) the Bohm criterion holds in the *stationary* form. Basic sheath properties of these discharges may be derived from suitable electron step models.

We have presented a broad review of problems related to the plasma-sheath transition. We did, however, *not* intend to give a complete survey. In particular the special problems discussed represent a subjective selection. From a general point of view we must draw attention to the basic assumption of *absorbing* walls. (The principal influence of ion reflection and emission from the wall is discussed in [2]). Finally, we remark that we have considered only *wall* sheaths. For an introduction into the extensive problem area of *double layers* separating different plasma regions we refer to the review papers [85] and [86].

Appendix A: Asymptotic two-scale analysis

To introduce the different sheath and presheath scales, it is convenient to use dimensionless quantities

$$\begin{aligned}
 (A1) \quad \varphi &= -\frac{e\Phi}{kT_{es}^*}, \quad \hat{n}_{i,e} = \frac{n_{i,e}}{n_s}, \quad u = \frac{v_i}{c_s}, \\
 \nu(u) &= \frac{L}{c_s} \nu_{ci}, \quad \sigma = \frac{L}{c_s} \frac{S}{n_s}, \quad a = \frac{L}{A} \frac{dA}{dz}, \\
 \tau &= \frac{\gamma T_i}{T_{es}^* + \gamma T_i}, \quad \text{and} \quad s = \frac{z}{\ell}
 \end{aligned}$$

with $c_s^2 = \kappa(T_{es}^* + \gamma T_{is})/m_i$. With these variables and parameters the basic equation system (2.7)–(2.9) reads

$$(A2) \quad \hat{n}_i - \hat{n}_e(\varphi) = \frac{\lambda_D^2}{\ell^2} \left[\frac{d^2 \varphi}{ds^2} - \frac{\ell}{L} a \frac{d\varphi}{ds} \right]$$

$$(A3) \quad \frac{d}{ds}(\hat{n}_i u) = \frac{\ell}{L} [\sigma - a \hat{n}_i u]$$

$$(A4) \quad u \frac{du}{ds} - \frac{d\varphi}{ds} = -\frac{\ell}{L} \left(\nu + \frac{\sigma}{\hat{n}_i} \right) u + \tau \left(\frac{1}{\hat{n}_i} \frac{d\hat{n}_i}{ds} - \frac{1}{\hat{n}_e} \frac{d\hat{n}_e}{ds} \right).$$

So far we did *not* specify the characteristic length ℓ , but of course it is self-suggesting to choose (i) the “inner” or “sheath” scale $\ell_i = \lambda_D$ or (o) the “outer” or “presheath” scale $\ell_o = L$. Correspondingly, we distinguish the inner and outer space variables

$$(A5) \quad \xi = s_i = z/\lambda_D \quad \text{and} \quad x = s_o = z/L.$$

For a fixed *finite* ratio $\varepsilon = \lambda_D/L$, these two scales are naturally equivalent. For $\varepsilon \rightarrow 0$, however, we must distinguish the *different* sheath and presheath limits: On the inner scale ($\ell_i/L = \varepsilon$) we obtain the system

$$(A6) \quad \hat{n}_i - \hat{n}_e(\varphi) = \frac{d^2 \varphi}{d\xi^2}$$

$$(A7) \quad \frac{d}{d\xi}(\hat{n}_i u) = O(\varepsilon)$$

$$(A8) \quad u \frac{du}{d\xi} - \frac{d\varphi}{d\xi} - \tau \left(\frac{1}{\hat{n}_i} \frac{d\hat{n}_i}{d\xi} - \frac{1}{\hat{n}_e} \frac{d\hat{n}_e}{d\xi} \right) = O(\varepsilon)$$

resulting in the asymptotic ($\varepsilon \rightarrow 0$) model of a collisionless planar sheath. The corresponding outer scale ($\lambda_D/\ell_o = \varepsilon$) equations

$$(A9) \quad \hat{n}_i - \hat{n}_e(\varphi) = O(\varepsilon^2 \frac{d^2 \varphi}{dx^2})$$

$$(A10) \quad \frac{d}{dx}(\hat{n}_i u) = \sigma - a \hat{n}_i u$$

$$(A11) \quad u \frac{du}{dx} - \frac{d\varphi}{dx} = -\left(\nu + \frac{\sigma}{\hat{n}_i}\right) u + O(\varepsilon^2 \frac{d^2 \varphi}{dx^2})$$

show, that the asymptotic ($\varepsilon \rightarrow 0$) presheath model is quasi-neutral.

Appendix B: Intermediate scale analysis

We refer to the dimensionless equations of Appendix A. To avoid an involved expansion accounting a priori for *all* terms we start from the separate sheath and presheath representations and characterize the sheath edge by [cf. Sec. 3.7, Eqs.(A1), and (2.15)]

$$(B1) \quad \varphi = 0, \quad u = 1, \quad \hat{n}_i = \hat{n}_e = 1, \quad \frac{d\hat{n}_i}{d\varphi} = \frac{d\hat{n}_e}{d\varphi} = -1.$$

Expanding equations (A10) and (A11) near the sheath edge ($x \rightarrow 0$, "inner" expansion on the outer scale) we obtain after some calculation in lowest order in φ and $u - 1$

$$(B2) \quad \left(u - \frac{1}{u}\right) \frac{du}{dx} = a_s - \nu_s - 2\sigma_s \quad \text{and} \quad \varphi = u - 1,$$

where the index s refers again to the sheath edge. The zero of the bracket on the l.h.s. corresponds to the sound barrier singularity ($u = 1$). We are here not interested in the exceptional case of a non-singular transition at the ion sound speed (see Sec. 4.1). Consequently, the r.h.s. of Eq. (B2) is always negative. By an appropriate choice of the length L [cf. Eq. (A1)] we can therefore dispose without lack of generality

$$(B3) \quad a_s - \nu_s - 2\sigma_s = -1.$$

Recalling the order of magnitude of the terms neglected in Eqs. (A9)–(A11) we thus obtain the representation

$$(B4) \quad \varphi^2 + x = O(\varepsilon^2 \frac{d^2 \varphi}{dx^2})$$

of the sheath edge vicinity.

The corresponding expansion of the sheath equations (A6)–(A8) near the sheath edge ($\xi \rightarrow -\infty$, "outer expansion" on the inner scale) is somewhat lengthy because it must be performed to quadratic order in φ and $u - 1$. Expanding the electron density in the form

$$(B5) \quad \hat{n}_e(\varphi) = 1 - \varphi + c\varphi^2 + \dots$$

(with $c = \frac{1}{2}$ for the usual ansatz of a Boltzmann factor) we arrive finally at

$$(B6) \quad \frac{d^2\varphi}{d\xi^2} = \frac{\frac{3}{2} - c}{1 + \tau_s} \varphi^2 + O(\varepsilon\xi).$$

With the correction $O(\varepsilon\xi)$ we account for the terms neglected in the sheath equations (A6)–(A8). Recalling $\varepsilon = \lambda_D/L$ and rewriting Eqs. (B4) and (B6) on an “intermediate scale” with

$$(B7) \quad \zeta = \frac{z}{\ell_m} = \frac{L}{\ell_m} x = \frac{\lambda_D}{\ell_m} \xi,$$

we have the alternative representations

$$(B8) \quad \varphi^2 + \frac{\ell_m}{L} \zeta = O\left(\frac{\lambda_D^2}{\ell_m^2} \frac{d^2\varphi}{d\xi^2}\right) \quad \text{and} \quad \frac{\lambda_D^2}{\ell_m^2} \frac{d^2\varphi}{d\xi^2} = \frac{\frac{3}{2} - c}{1 + \tau_s} \varphi^2 + O\left(\frac{\ell_m}{L} \zeta\right)$$

of the sheath edge vicinity. Since both representations must be consistent, we conclude that a *uniformly* valid representation must read

$$(B9) \quad \frac{\lambda_D^2}{\ell_m^2} \frac{d^2\varphi}{d\xi^2} = \frac{\frac{3}{2} - c}{1 + \tau_s} \left(\varphi^2 + \frac{\ell_m}{L} \zeta\right).$$

Introducing the re-normalized potential

$$(B10) \quad w = \left(\frac{L}{\ell_m}\right)^{1/2} \varphi = - \left(\frac{L}{\ell_m}\right)^{1/2} \frac{e\Phi}{\kappa T_{es}^*}$$

and choosing

$$(B11) \quad \ell_m = \left(\frac{1 + \tau_s}{\frac{3}{2} - c}\right)^{2/5} \lambda_D^{4/5} L^{1/5},$$

results in Eq. (4.7).

Acknowledgement

This work was done within the activities of the SFB 191 of the Deutsche Forschungsgemeinschaft.

References

1. D. BOHM, in *The Characteristics of Electrical Discharges in Magnetic Fields*, edited by A. Guthry and R.K. Wakerling, Mc Graw-Hill, New York, Chap. 3, p. 77, 1949,
2. K.U. RIEMANN, J. Phys. D: Appl. Phys., **24**, 493, 1991.
3. P.C. STANGEBY and J.E. ALLEN, J. Phys. A: Math. Gen., **3**, 303, 1970.
4. J.E. ALLEN, J. Phys. D: Appl. Phys., **9**, 2331, 1976.

5. P. STANGEBY, in *Physics of Plasma-Wall Interaction in Controlled Fusion*, eds. D.E. Post and R. Behrisch Plenum, New York 1986.
6. K.U. RIEMANN, *Phys. Fluids* **B**, **1**, 961, 1989.
7. F.F. CHEN, *Introduction to Plasma Physics*, Plenum New York, 2nd edition p. 84, 1974.
8. M. VAN DYKE, *Perturbation Methods in Fluid Mechanics*, Academic Press, New York 1964.
9. J.G. ANDREWS and P.C. STANGEBY, *J. Phys. A: Math. Gen.*, **3**, L39, 1970.
10. K.U. RIEMANN, *IEEE Trans. Plasma Sci.*, **23**, 709, 1995.
11. M.S. BENILOV, *J. Phys. D: Appl. Phys.*, **29**, 364, 1996.
12. R.N. FRANKLIN, *Plasma Phenomena in Gas Discharges*, Clarendon, Oxford, Sec. 4, 6, 1976.
13. E.R. HARRISON and W.B. THOMPSON, *Proc. Phys. Soc.*, **74**, 145, 1959.
14. L.S. HALL, *Proc. Phys. Soc.*, **80**, 309, 1962.
15. V.A. GODYAK, R.B. PIEJAK and B.M. ALEXANDROVICH, *J. Appl. Phys.*, **73**, 3657, 1993.
16. G.D. HOBBS and J.A. WESSON, *Heat flow through a Langmuir sheath in the presence of electron emission* *Heat flow through a Langmuir sheath in the presence of electron emission* *Heat flow through a Langmuir sheath in the presence of electron emission*, *J. Plasma Phys.*, **9**, 85, 1967.
17. P.D. PREWETT and J.E. ALLEN, *Proc. R. Soc. A*, **348**, 435, 1976.
18. DEUTSCH and E. RAUCHLE, *Phys. Rev. A*, **46**, 3442, 1992.
19. R.L.F. BOYD and J.B. THOMPSON, *Proc. Roy. Soc. A*, **252**, 102, 1959.
20. N.St.J. BRAITHWAITE and J.E. ALLEN, *J. Phys. D: Appl. Phys.*, **21**, 1733, 1988.
21. A. CAVALIERE, F. ENGELMANN and A. SESTERO, *Phys. Fluids*, **11**, 158, 1968.
22. K.U. RIEMANN, *Phys. Fluids* **B**, **3**, 3331, 1991.
23. G.A. EMMERT, R.M. WIELAND, A.T. MENSE and J.N. DAVIDSON, *Phys. Fluids* **23**, 803, 1980.
24. H. VAN DEN BERG, K.U. RIEMANN and G. ECKER, *Phys. Fluids* **B**, **3**, 838, 1991.
25. L.S. HALL, *Phys. Fluids*, **4**, 388, 1961.
26. V.A. GODYAK and N. STERNBERG, *IEEE Trans. Plasma Sci.*, **18**, 159, 1990.
27. E. ZAWAIDEH, N.S. KIM and F. NAJMABADI, *Phys. Fluids*, **B**, **2**, 647, 1990.
28. V.A. GODYAK, *Phys. Letters*, **89A**, 80, 1982.
29. H.B. VALENTINI, *Phys. Plasmas*, **3**, 1459, 1996.
30. H.B. VALENTINI and F. HERRMANN, *J. Phys. D: Appl. Phys.*, **29**, 1175, 1996.
31. K.U. RIEMANN and H.P. VAN DEN BERG, *Phys. Fluids* **B**, **3**, 1300, 1991.
32. K.U. RIEMANN and P. MEYER, *Phys. Plasmas*, **3**, 4751, 1996.
33. S. KAPLUN, *Fluid Mechanics and Singular Perturbations*, Academic Press, New York, 1967.
34. S.H. LAM, *Proc VIIIth Int. Conf. on Phenomena in Ionized Gases*, vol. I, p. 545 (Vienna: IAEA 1967)
35. C.H. SU, *Proc VIIIth Int. Conf. on Phenomena in Ionized Gases*, vol. I, p.569 (Vienna: IAEA 1967)
36. R.N. FRANKLIN and J.R. OCKENDON, *J. Plasma Phys.*, **4**, 371, 1970.
37. K.U. RIEMANN, *J. Physique Coll.*, **40**, C7, 831, 1979.
38. K.U. RIEMANN, *Phys. Plasmas*, **4**, 4158, 1997.
39. K.U. RIEMANN, *J. Phys. D: Appl. Phys.*, **25**, 1432, 1992.
40. J.E. ALLEN, R.L.F. BOYD and P. REYNOLDS, *Proc. Phys. Soc.* **70**, 297, 1957.
41. S.H. LAM, *Phys. Fluids*, **8**, 73, 1965.

42. M.J.M. PARROT, L.R.O. STOREY, L.W. PARKER and J.G. LAFRAMBOISE, *Phys. Fluids*, **25**, 2388, 1982.
43. P.M. CHUNG, L. TALBOT, K.J. TOURYAN, *Electric Probes in Stationary and Flowing Plasmas*, Springer, Berlin 1975.
44. W. SCHOTTKY, *Phys. Z.*, **25**, 342, 1924.
45. R.L.F. BOYD, *Proc. Phys. Soc.*, **B**, **64**, 795, 1951.
46. K.B. PERSSON, *Phys. Fluids*, **5**, 1625, 1962.
47. K.U. RIEMANN, *Phys. Fluids*, **24**, 2163, 1981.
48. H.B. VALENTINI, D. WOLFF and E. GLAUCHE, *J. Phys. D: Appl. Phys.*, **28**, 716, 1995.
49. L. TONKS and I. LANGMUIR, *Phys. Rev.*, **34**, 876, 1929.
50. G. KINO and E.W. SHAW, *Phys. Fluids*, **9**, 587, 1966.
51. R.C. BISSEL and P.C. JOHNSON, *Phys. Fluids*, **30**, 779, 1987.
52. R.C. BISSEL, P.C. JOHNSON. and P.C. STANGEBY, *Phys. Fluids B*, **1**, 1133, 1989.
53. L.D. TSENDIN, *Sov. Phys. Tech. Phys.*, **23**, 890, 1978.
54. R. CHODURA, *Phys. Fluids*, **25**, 1628, 1982.
55. R. CHODURA, *Contr. Plasma Phys.*, **28**, 303, 1988.
56. J. BEHNEL, Report 85-O2-118 SFB 162 Bochum/Jülich 1985
57. K.U. RIEMANN, *Phys. Plasmas*, **1**, 552, 1994.
58. K.U. RIEMANN, *Contr. Plasma Phys.*, **34**, 127, 1994.
59. P.C. STANGEBY, *Phys. Plasmas*, **2**, 702, 1995.
60. Th. DAUBE, K.U. RIEMANN and H. SCHMITZ, *Contrib. Plasma Phys.* **38**, 145, 1998.
61. W. WOLTERS, Th. DAUBE, K.U. RIEMANN and K. WIESEMANN, *Plasma Phys. Controlled Fusion*, **41**, 721, 1999.
62. P.C. STANGEBY and A.V. CHANKIN, *Phys. Plasmas*, **2**, 707, 1995.
63. I.H. HUTCHINSON, *Phys. Plasmas*, **3**, 6, 1996.
64. H. SCHMITZ, K.U. RIEMANN, and Th. DAUBE, *Phys. Plasmas* **3**, 2486, 1996.
65. Th. DAUBE, K.U. RIEMANN and H. SCHMITZ, *Phys. Plasmas*, **3**, 117, 1998.
66. Th. DAUBE and K.U. RIEMANN, *Phys. Plasmas*, **6**, 2409, 1999.
67. I. LANGMUIR, *Phys. Rev.*, **33**, 954, 1929.
68. C.D. CHILD, *Phys. Rev.*, **32**, 492, 1911.
69. N. STERNBERG and V.A. GODYAK, *Physica D*, **97**, 498, 1996.
70. C.W. JURGENSEN and E.S. SHAQFEH, *J. Appl. Phys.*, **64**, 590, 1988.
71. K.U. RIEMANN, U. EHLEMANN and K. WIESEMANN, *J. Phys. D: Appl. Phys.*, **25**, 620, 1992.
72. R. WARREN, *Phys. Rev.*, **98**, 1658, 1955.
73. P.D. PREWETT and J.E. ALLEN, *J. Plasma Phys.*, **10**, 451, 1973.
74. N.St.J. BRAITHWAITE, L.M. WICKENS, *J. Plasma Phys.*, **30**, 133, 1983.
75. J.W. CIPOLLA and M.B. SILEVITCH, *J. Plasma Phys.*, **25**, 373, 1981.
76. K.U. RIEMANN, *Phys. Fluids B*, **4**, 2693, 1992.
77. J.E. ALLEN and M.A. SKORRIK, *J. Plasma Phys.*, **50**, 2434, 1993.
78. A.M. POINTU, *J. Appl. Phys.*, **60**, 4113, 1986.
79. M.A. LIEBERMAN, *IEEE Trans. Plasma Sci.*, **16**, 638, 1988.

80. V.A. GODYAK and N. STERNBERG, *Phys. Rev. A*, **42**, 2299, 1990.
81. V.A. GODYAK, R.B. PIEJAK and N. STERNBERG, *IEEE Trans. Plasma Sci.*, **21**, 378, 1993.
82. J. GIERLING and K.U. RIEMANN, *J. Appl. Phys.*, **83**, 3521, 1998.
83. M.A. LIEBERMAN, *J. Appl. Phys.*, **66**, 2926, 1989.
84. K.U. RIEMANN and Th. DAUBE, *J. Appl. Phys.*, **86**, 1202, 1999.
85. J.E. ALLEN, *Plasma Phys. Controlled Fusion*, **27**, 1343, 1985.
86. M.A. RAADU and J.J. RASMUSSEN, *Astrophys. Space Sci.*, **144**, 43, 1988.

STUDIES AND APPLICATIONS OF DENSE MAGNETIZED PLASMAS

M. SADOWSKI

THE ANDRZEJ SOLTAN INSTITUTE FOR NUCLEAR STUDIES (IPJ)

05-400 Otwock-Świerk by Warsaw, Poland e-mail: msadowski@ipj.gov.pl

This invited lecture concerns pulsed experiments with dense plasmas ($n_e > 10^{16} \text{ cm}^{-3}$), carrying high-intensity currents ($I > 10^5 \text{ A}$), which produce strong magnetic fields influencing motion of charged particles. Various Z-Pinch (linear and cylindrical) experiments are reviewed, and the most important results are described. Also presented are different Plasma-Focus (non-cylindrical) pinch experiments as well as important characteristics of X-ray pulses, relativistic electron beams (REB), energetic ion streams, and nuclear fusion products (mainly fast protons and neutrons). Particular attention is paid to possible applications of the X-ray pulses, e.g. for X-ray microscopy and lithography, as well as to applications of pulsed particle beams, e.g. for material tests and engineering. The international collaboration in dense magnetized plasma research is described, and prospects of the International Center for Dense Magnetized Plasmas (ICDMP) are presented.

1. Introduction

In nature and in laboratories one can observe plasmas of very different density and various velocity distributions (characterized often by different electron and ion temperatures). In dense plasmas the electron concentration (n_e) is higher than 10^{16} cm^{-3} . When this parameter is larger than 10^{20} cm^{-3} the plasma is called a super-dense one. The definition of high-temperature plasmas is a question of convention [1]. Energy distributions of electrons and ions are often different from Maxwellian ones. In spite of these deviations plasmas are characterized by electron temperature (T_e) and ion temperature (T_i). These temperatures are usually expressed in energy units (1 eV corresponds to 11600 K). When T_e and T_i are below 0.1 eV the plasma is called a cold one. If T_e and T_i are within the range from 0.1 eV to 5 eV one speaks about low-temperature plasmas. When T_e or T_i is higher than 5 eV one can speak about the high-temperature plasma.

Plasmas are also characterized by other parameters, and particularly by an electron cyclotron frequency (ω_{ce}) and ion cyclotron frequency (ω_{ci}), which are described by

$$(1.1) \quad \omega_{ce} = \frac{eH}{m_e c} \quad \text{and} \quad \omega_{ci} = \frac{Z_i e H}{m_i c}$$

where H is the magnetic field strength, m_e and m_i are electron mass and ion mass, respectively. A frequency of electron-ion collisions (ν_{ei}) depends strongly on plasma parameters [1]. Under an assumption of the Maxwellian electron-energy distribution one can show the proportionality

$$(1.2) \quad \nu_{ei} \sim \frac{n_i Z_i^2}{T_e^{3/2}}.$$

If the ion cyclotron frequency is higher than the frequency of electron-ion collisions ($\omega_{ci} > \nu_{ei}$), motion of ions is strongly influenced by a magnetic field and the plasma is magnetized.

The oldest methods used to produce high-temperature dense magnetized plasma (DMP) were based on high-voltage high-current discharges between metal electrodes. The simplest configuration involves two hemispherical, conical or plane electrodes placed at a chosen distance within a vacuum chamber. After filling up this chamber with a working gas or gaseous mixture (under an appropriate low pressure) the main discharge is initiated by the application of a high-voltage pulse between the electrodes. If these electrodes are adjusted along a common z -axis the discharge forms a cylindrical column (Z-Pinch) that undergoes the self-compression by its own azimuthal magnetic field, as shown in Fig. 1.

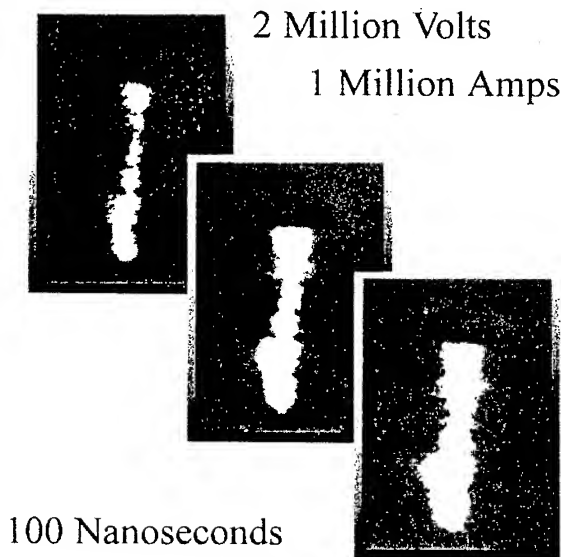


FIG. 1. Subsequent phases of a high-current Z-Pinch discharge showing development of plasma instabilities, as observed within the Nevada Terawatt Facility in USA.

Another important electrode configuration, studied very extensively, was a system composed of coaxial tubular electrodes of different diameters. The metal electrodes were separated by a tubular glass (or ceramic) insulator embracing the inner electrode at one end. Such electrodes were used in coaxial plasma guns of the Marshall type [2] as well as in Plasma-Focus (PF) devices of the Filippov- or Mather-type [3, 4]. In the Marshall guns a working gas was injected into the tubular inter-electrode region by a fast-acting valve, placed within the center of the inner electrode. When a ring-shaped gas cloud was formed a high-voltage pulse was applied and a plasma discharge was initiated. Such coaxial plasma guns were capable to produce pulsed plasma streams (jets) and they were used as plasma injectors in many laboratory- and space-experiments [5]. On the contrary to the Marshall-type plasma guns operated with the gas puffing, the PF devices were usually run under a static initial pressure, which was considerably higher than that in the conventional coaxial injectors. An example of a PF-type discharge is presented in Fig. 2.

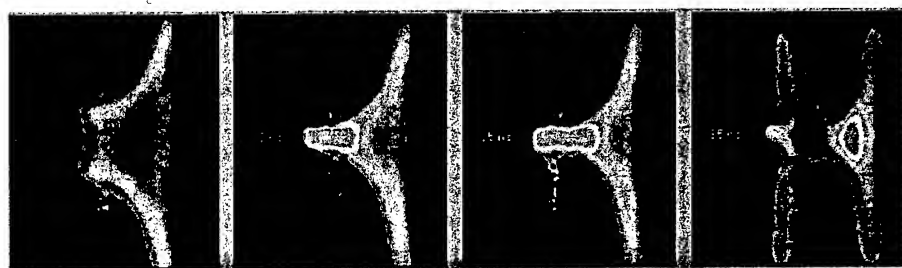


FIG. 2. Color-enhanced pictures of different phases of the PF discharge, as obtained at IFPiLM in Poland, using a high-speed quadro-camera with the exposition time of about 1 ns and a frame distance of 10 ns.

The main aim of this invited lecture was to present various Z-Pinch and PF experiments and to describe the most important characteristics of X-ray pulses, charged particle streams, and nuclear fusion products emitted from DMP discharges performed with deuterium filling. Particular attention should be paid to different applications of DMP facilities.

2. Studies of Z-Pinch discharges

The cylindrical Z-Pinches were investigated from the very beginning of research on controlled nuclear fusion (CNF) started in the 50 s. Those studies were aimed on the generation and heating a pure deuterium plasma up to temperatures enabling close collisions of deuterons and their fusion producing a lot of nuclear energy [1]. High-temperature dense deuterium plasmas were produced successfully and fusion-produced fast neutrons were obtained in numerous Z-Pinch machines. It has, however, been impossible to protect the pinching plasma column from a fast development of magneto-hydrodynamic (mhd) instabilities and to increase its lifetime in order to obtain a high neutron (and energy) yield from fusion reactions.

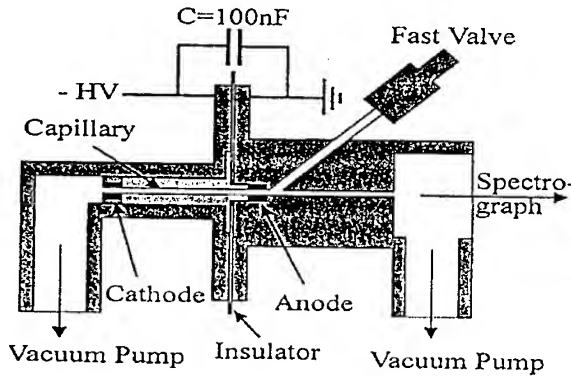


FIG. 3. Schematic of the capillary Z-Pinch device used at the Ruhr University in Germany [8] for spectroscopic studies of DMP.

Numerous Z-Pinch experiments have been performed in various plasma laboratories all over the world [6, 7]. Many investigators have studied low-energy Z-Pinch discharges within different gases in order to study parameters of DMP. In some experiments the use has been made of capillary discharges useful for spectroscopic studies, as shown in Fig. 3. In other experiments there were applied gas-puffed cylindrical layers, which were first ionized by high-voltage pulse and after that compressed by high currents. Numerous investigators tried also to use solid fibers (wires) to produce DMP [6, 7]. The main problem was to achieve a relatively stable pinch.

The pressure balance of the pinch column is given by the so-called Bennett relation [1]

$$(2.1) \quad \mu_0 I^2 = 16\pi NT$$

where N is the total number of plasma particles per unit of length. In an isolated Z-Pinch column the energy losses, resulting from the Bremsstrahlung radiation, should be equal to the joule heating. The energy and pressure balance equations give then the result that the steady state can be established at a constant current $I_{PB} = 1.4 \cdot 10^6$ A (the so-called Pease-Braginski current). The corresponding internal energy per unit length is then given by

$$(2.2) \quad NT = \frac{\mu_0 I_{PB}^2}{16\pi} = 5 \cdot 10^4 \text{ [J/m]}.$$

It can be easily seen that at the high-temperature $T = 50000$ K and $n_{solid} = 10^{22} \text{ cm}^{-3}$, for the pinch column (with the radius r_p) one needs

$$(2.3) \quad N = \pi r_p^2 n = 7 \cdot 10^{18} \text{ [m}^{-1}] \quad \text{and} \quad r_p = 15 \cdot 10^{-6} \text{ [m]}.$$

It means that very thin solid fibers should be applied for Z-Pinch experiments. Basing on this principle numerous experiments were performed with solid deuterium fibers, but they were not very successful in reaching high neutron yields [6, 7, 9].

Taking into consideration that DMP discharges can emit very intense X-ray pulses, particular efforts have been devoted to experiments with thin metal wires or multi-wire cylindrical arrays. Small-scale Z-Pinch experiments with thin wires were performed in many countries, in Russia, UK, USA, Germany, Czech Republic and Poland. In some cases interesting non-linear phenomena in DMP were observed, e.g. the formation of quasi-spherical regions [10], shown in Fig. 4.

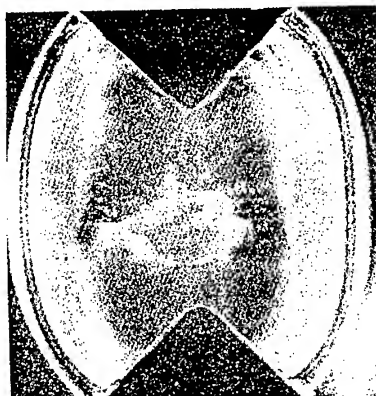


FIG. 4. Quasi-spherical stable DMP structure observed in a gas-embedded Z-Pinch between conical electrodes, within a low-energy (0.5 kJ) experiment under higher pressure (50 kPa) of argon.

The most famous and most powerful Z-Pinch experiments with multi-wire arrays have been carried out at the Sandia Laboratory in USA. The use was made of the SATURN facility [11, 12] operating with HV lines shorted by means of spring mechanisms. A scheme of this facility is shown in Fig. 5.

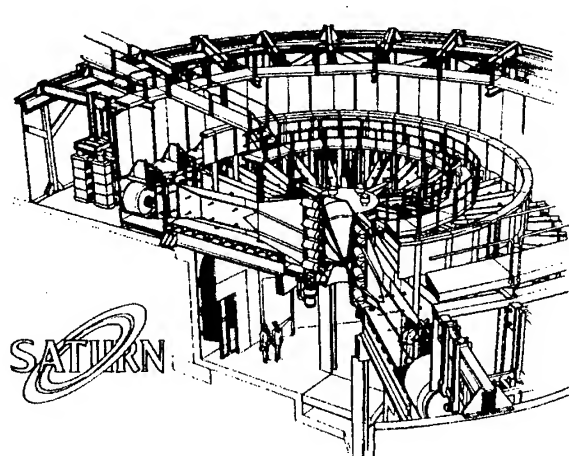


FIG. 5. Schematic of the SATURN facility operated at the Sandia Laboratory in USA.

Experiments carried out with the SATURN machine equipped with different wire arrays (a 12.5 mm-diameter array of 70 tungsten wires of 7.5 mm in diameter, and 25 mm-diameter array of 300 tungsten wires of 5.1 mm in diameter) showed that Z-Pinches can be scaled to greater than 150 ns implosion times without degradation in implosion uniformity and efficiency [13]. Examples of discharge currents traces and X-ray pulses are presented in Fig. 6.

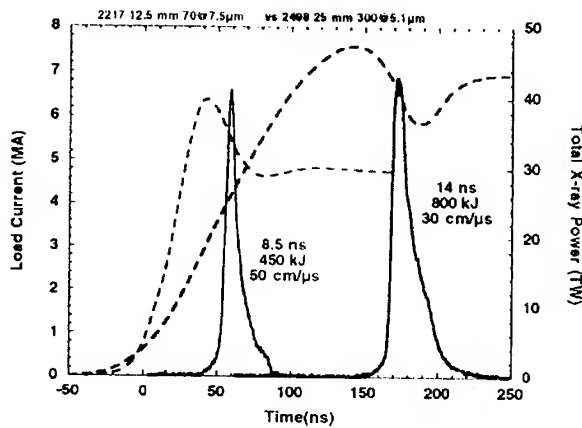


FIG. 6. Comparison of current waveforms and total X-ray pulses from different Z-Pinch experiments performed with tungsten-wire arrays within the SATURN facility.

The SATURN facility has been converted in the Z machine, which can deliver 27 MA currents to a relevant short circuit load. Recent experiments have been carried out with 480-wire arrays, which have produced record X-ray pulses reaching 290 TW. Such powerful X-ray pulses can be used to trigger nuclear fusion reactions. It has been estimated that, to reach a high fusion yield, one needs above 1000 TW, 16 MJ X-ray pulses. To achieve this goal the Sandia Laboratory has started to build the X-1 machine [12, 13].

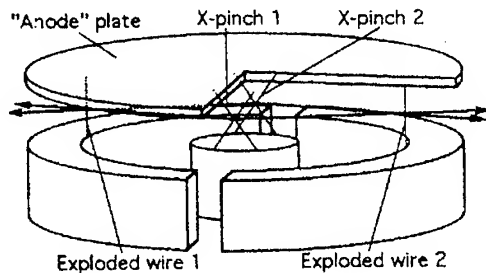


FIG. 7. One of the X-ray back-lighting arrangements developed at the Cornell University [14]. Two wire loads, which are placed between the anode and separate half-cylinder electrodes, are back-lighted by the radiation from two X-Pinches located on the central electrode.

Simultaneously with the design and construction of large Z-Pinch facilities there are carried out studies to improve methods of DMP diagnostics. A valuable

technique is based on the use of X-ray pulses for the back-lighting of DMP objects. Such diagnostic X-ray pulses can be supplied from point-like X-Pinches produced by special crossed-wire arrangements. A point source of X-rays is used to cast a shadow image of DMP directly on film, as shown in Fig. 7.

The X-ray back-lighting technique makes possible to study fine structures of DMP produced from X-Pinches and multi-wire arrays. Some examples are presented in Fig. 8 and 9.

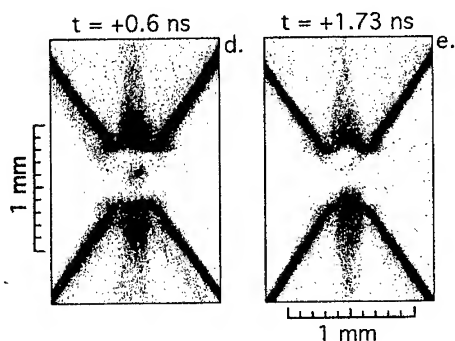


FIG. 8. Back-lighted images of X-Pinch discharge formed by two crossed $17\mu\text{m}$ molybdenum wires.

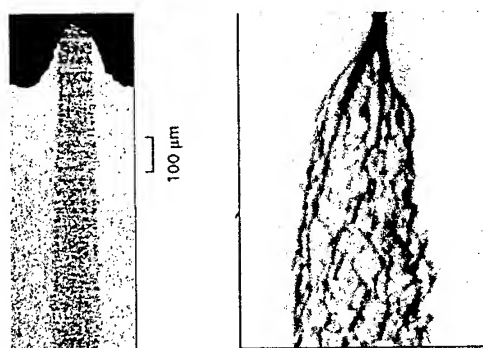


FIG. 9. Back-lighted images of a $12.7\mu\text{m}$ aluminum wire and $13\mu\text{m}$ tungsten wire. The first picture was taken for a 1.25 kA/wire shot at $t = 0.17\mu\text{s}$, and the second - for 2.5 kA/wire shot at $t = 2.2\mu\text{s}$ [14].

Such diagnostic techniques are applied to study dense core and coronal plasmas in order to select appropriate materials and to optimize wire-arrays for powerful Z-Pinch experiments.

3. Studies of Plasma-Focus discharges

The most popular PF configurations were developed independently by N.V. Filippov and by J.W. Mather at the late 50 s. N.V. Filippov investigated PF

discharges in large diameter systems with relatively short electrodes (diameter/length $\gg 3$), equipped with solid front plates [2]. In such systems the axial acceleration of a current sheath (CS) layer is short in comparison with the radial compression (collapse) phase of the CS between the end plates of the two electrodes. J.W. Mather studied PF discharges between two relatively long coaxial electrodes (diameter/length < 3) with free outlets [3]. In that case the axial acceleration phase lasts longer, the radial compression phase is shorter, and the dense PF region is formed on the symmetry axis in front of the electrode outlets, i.e. in free space, at some distance from the electrode edges. Under such conditions, a plasma discharge starts at the surface of the main insulator by high-voltage breakdown and the build-up of a distinct CS. After that it is accelerated in the axial direction by electromagnetic forces rising from interactions of an azimuthal magnetic field with quasi-radial currents. When the CS layer is blown out the inter-electrode gap, a part of it is subject to the radial compression forming a dense quasi-axial pinch column (the PF region), as shown in Fig. 10.

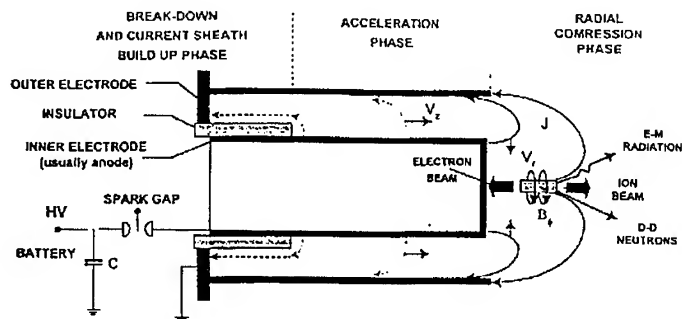


FIG. 10. Schematic view of a Mather-type PF machine. There are marked different positions of the current-sheath (CS) layer during successive phases of the discharge development.

Numerous PF experiments were performed in many laboratories dispersed all over the world [15, 16]. The most of them was carried out with the Mather-type electrodes. In Poland PF studies were started in the late 60 s. The first Mather-type devices (PF-20 and PF-150, of energy equal to 20 kJ and 150 kJ, respectively) were built at IBJ in Świerk, and after tests they were transferred to the Military Academy of Technology (WAT) in Warsaw, where a new plasma research center was organized (IFPiLM). During the 70 s, in Świerk there was built the PF-360 machine, which constituted a module of a megajoule PF facility. The PF-360 device was used for various optimization tests, and in particular for studies of the DMP dynamics and the emission of X-rays, electron- and ion-beams, as well as fusion products (fast neutrons and protons). Some studies were performed within the international collaboration [17]. After numerous modifications of the PF-360 device, it is still under exploitation at IPJ. A general view of PF-360 device is shown in Fig. 11.

Investigation of the X-ray emission, as performed with the X-ray pinhole

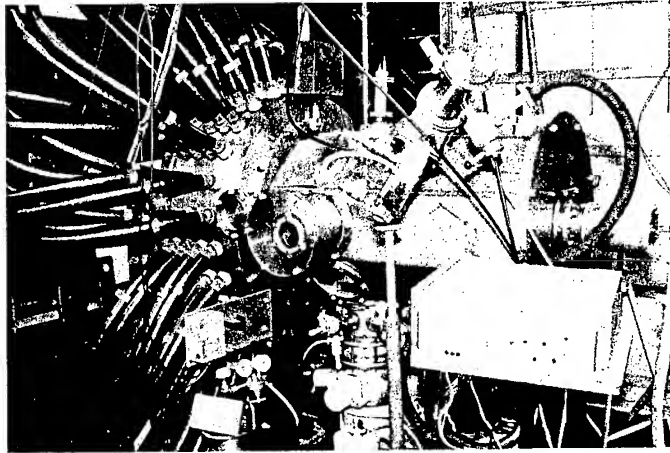


FIG. 11. General view of the PF-360 experimental chamber with some diagnostic equipment for X-ray, ion, and neutron measurements.

camera, revealed that at higher discharge currents there appear plasma filaments. Although some investigators claimed that the quasi-radial filaments in the CS layer collide and annihilate completely during its radial compression [18], it was proved experimentally that during that current filaments can remain or even be formed within the pinch column [19], as presented in Fig. 12.

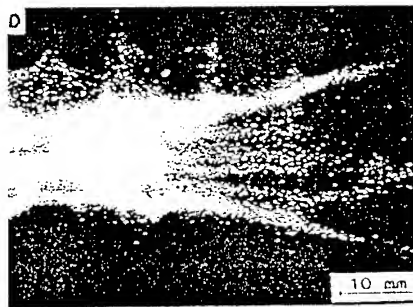


FIG. 12. Soft X-ray pinhole picture of a PF discharge, which shows the appearance of quasi-axial filaments inside the DMP column.

Numerous PF experiments at lower discharge currents and with heavy gas admixtures revealed that inside the DMP column there are formed small regions of the increased X-ray emission, so-called hot-spots [20, 21], as shown in Fig. 13.

Studies of the X-ray emission from PF discharges were performed in many laboratories by different pinhole cameras, special diodes, and crystal spectrometers. At IPJ the use was made of the MAJA-PF device, which is shown in Fig. 14.

Simultaneously with X-rays there were studied relativistic electron beams (REBs), emitted through the central electrode in the up-stream direction, and

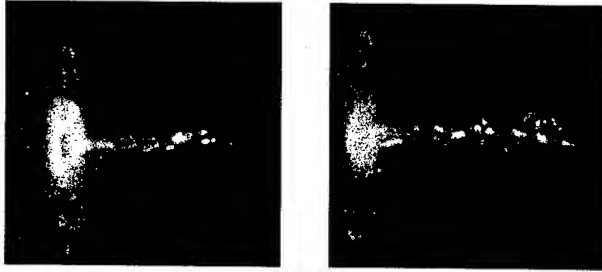


FIG. 13. Soft X-ray pinhole pictures of two PF discharges, which show the formation of distinct brilliant regions (hot-spots) inside the DMP column.

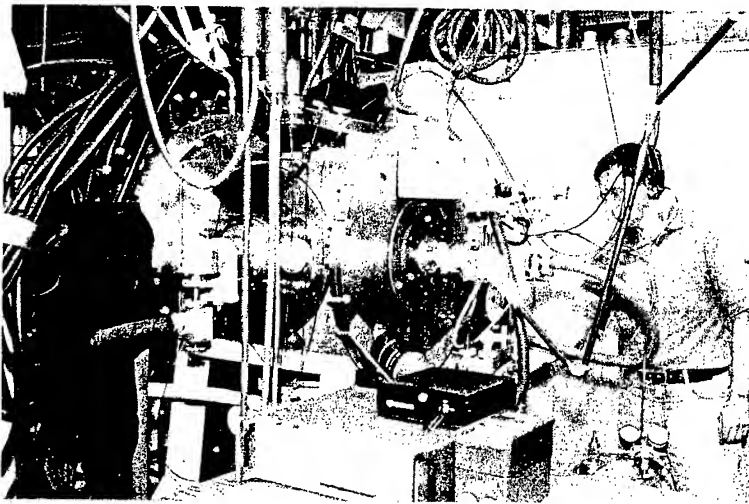


FIG. 14. General view of the MAJA-PF experimental chamber with an ion pinhole camera (on the axis), the X-ray pinhole camera (above) and two crystal spectrometers placed side-on (in the front and behind the chamber).

energetic ion beams - emitted mostly along the z -axis. Using X-ray pinhole cameras and Cerenkov-type detectors of REBs, it was found that the hot-spots are formed along the z -axis in a determined sequence, starting from the electrode outlet, and the corresponding REB signals are well correlated with the emission from hot-spots [21], as shown in Fig. 15.

On the basis of X-ray spectral measurements, from an analysis of the intercombination and resonance lines of the He-like argon lines, it was estimated that within the hot-spots the electron concentration is higher than 10^{20} cm^{-3} , and the electron temperature is above 1 keV. Detailed spectral measurements, as performed with two crystal spectrometers with mutually perpendicular dispersion planes [22], revealed considerable differences in relative intensities of the spectral lines of argon ions, as presented in Fig. 16.

The different relative intensities of the considered spectral lines have been

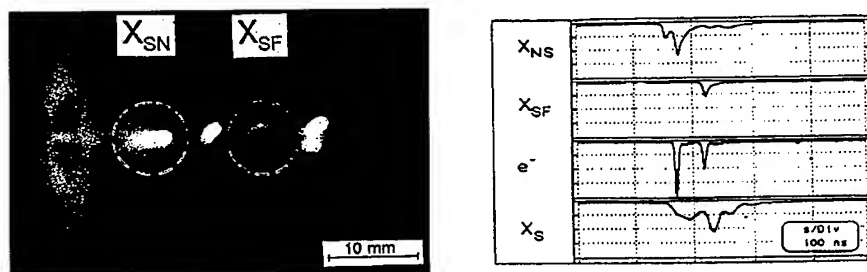


FIG. 15. X-ray pinhole picture from a single PF discharge performed with the $(D_2 + Ar)$ filling and an oscillogram, which shows X-ray signals from different regions, corresponding REBs, and the total soft X-ray emission.

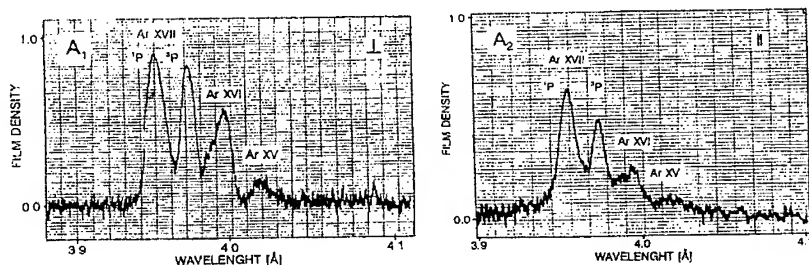


FIG. 16. X-ray spectra of a DMP column produced within the MAJA-PF device, which were registered by means of two identical spectral spectrometers placed side-on, but with mutually perpendicular dispersion planes.

explained by different polarization of these lines, which was probably induced by directed motion of some electron streams. In fact, the appearance of supra-thermal electrons has been confirmed also by the emission of the Ka lines. Simultaneously with electron streams moving radial, there were generated also REBs propagating along the z-axis, which could escape through a hollow inner electrode. Such REBs were measured with the Cerenkov-type detectors and magnetic analyzers placed at relatively large distances (from 40 cm to 100 cm) from the DMP region [23]. Energy spectra of these REBs extended from about 60 keV to above 600 keV, as shown in Fig. 17.

Simultaneously with electrons, strong local electric fields generated within a DMP column can also accelerate primary ions, which propagate mostly along the z-axis. The fast ion beams were registered in various PF experiments [24, 25, 26, 27], e.g. in a moderate-size PF machine powered by a 70 kJ, 50 kV condenser bank, there was obtained about 1015 deuterons of energy above 300 keV, and about 1012 deuterons of energy ranging several MeV [28].

Ion measurements along the z-axis, which were carried out by means of ion pinhole cameras equipped with nuclear track detectors (NTDs) and various absorption filters, proved that the ions form numerous micro-beams of different energy, as shown in Fig. 18

Mass- and energy-analysis of the axial ion beams, which was performed by

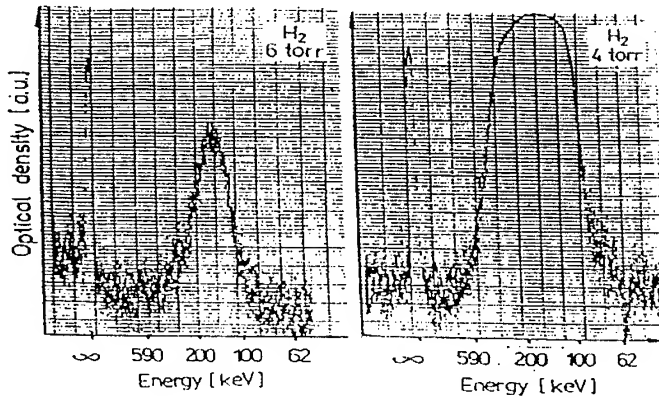


FIG. 17. Energy spectra of REBs, as measured on the z-axis behind the collector of the PF-360 device, for two PF discharges performed under different initial pressures.



FIG. 18. Ion pictures taken behind different absorption filters: (A) $1.5 \mu\text{m}$ Al-filter, $E_D > 220$ keV; (B) $6.0 \mu\text{m}$ Al-filter, $E_D > 700$ keV; (C) $10 \mu\text{m}$ Al-filter, $E_D > 1.5$ MeV; and (D) $30 \mu\text{m}$ Al-filter, $E_D > 2.1$ MeV.

means of Thomson-type spectrometers at different PF devices, showed that ion energy spectra extend from several dozen keV to several hundreds keV, and in some cases up to several MeV [27]. Examples of the ion energy distributions, which were obtained from DMP experiments performed with the MAJA-PF device, are presented in Fig. 19.

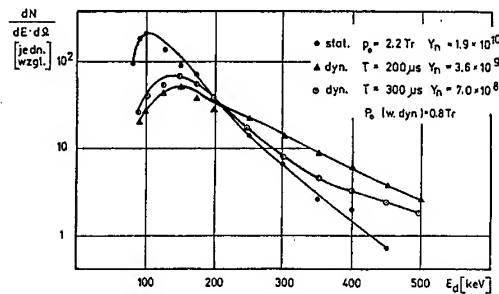


FIG. 19. Energy spectra of fast deuterons emitted from the MAJA-PF device, which was operated under static and dynamic gas conditions.

Measurements of ion angular distributions, carried out in different PF devices, revealed that close to the z-axis there appears a characteristic local minimum, as shown in Fig. 20.

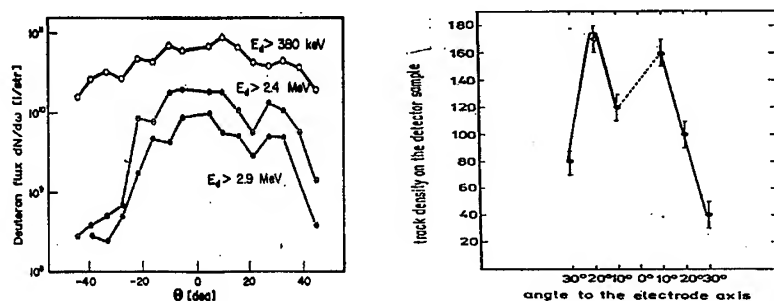


FIG. 20. Angular distributions of fast deuterons emitted from the PF-360 device (on the left) and the PF-1000 facility (on the right) [29].

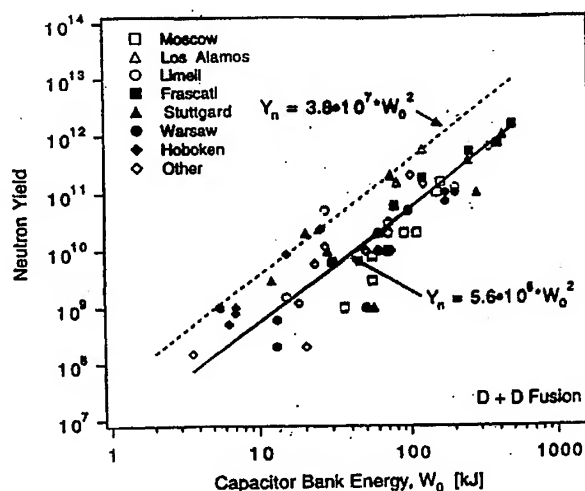


FIG. 21. Neutron yields from PF devices operated with the D_2 filling at different input energies.

Particular attention in PF experiments was paid to the optimization of a fusion yield from D-D reactions. Numerous measurements were carried out in many plasma laboratories, and a promising scaling of the neutron yield (Y_n) versus the input energy value (W_0) was observed up to energies ranging about 500 kJ, as presented in Fig. 21.

It was, however, found that the neutron emission saturates or even decreases when the charging voltage and the initial energy input as well as the discharge current values are increased above certain limits, as shown in Fig. 22.

PF experiments, which were performed with the use of insulators made of different materials [17] or with an additional gas-puffed targets [30], demonstrated

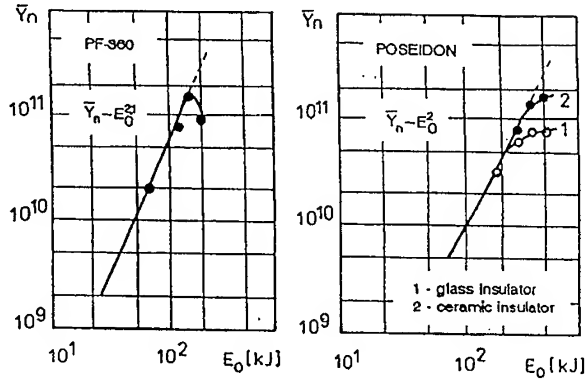


FIG. 22. Neutron yield scaling versus the initial energy value, as observed for PF-360 device in Świerk and for POSEIDON facility in Stuttgart [17].

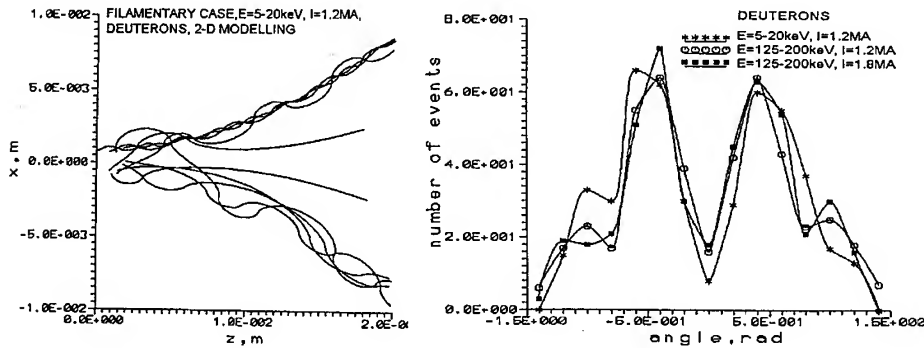


FIG. 23. Projections of trajectories for 10 deuterons (5-10 keV), as computed for 1.2 MA discharge through six flower-like filaments (on the left), and an angular distribution of deuterons of different energies for the same filamentary configuration (on the right).

that the saturation of neutron yields can be shifted towards higher input energies. The optimization of neutron yields from PF discharges remains the main task for many investigators and it is of particular importance for future large-scale DMP experiments.

In theoretical studies particular attention has recently been paid to influence of current filaments on motion of accelerated deuterons undergoing the fusion reactions. Numerical computations of ion trajectories have been performed for different numbers and various configurations of the filaments [31], according to observations from the performed PF experiments. The modeling for the "flower-like" configuration has given a qualitative agreement with the measured angular distribution of fast deuterons, as shown in Fig. 23.

A new trend in DMP research in Poland is to use a collapsing CS layer as a driver for very thin (foam) liners [32]. Using this method, well-shaped plasma columns of about 2 mm in diameter and 10 mm in length, showing hot cores of

about 1 mm in diameter, have been obtained in the PF-1000 machine [32, 33]. It has also been observed that such foam liner plasma is relatively stable during the compression phase, as shown in Fig. 24.

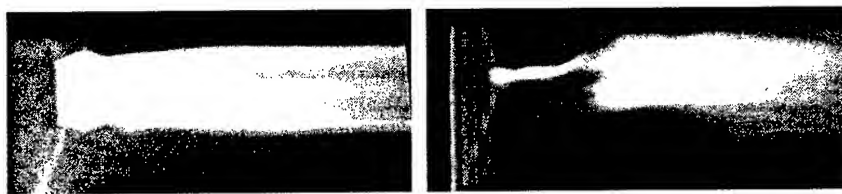


FIG. 24. Streak pictures of the PF current sheath interaction with a foam liner, which was placed on the axis of the PF-1000 facility [33].

Such experiments with the compression of thin liners open new prospects for future large-scale PF facilities and for fusion-oriented research.

4. Applications of Z-Pinch and PF facilities

The Z-Pinch and PF devices can be used for basic studies in the field of plasma physics. In particular such experimental facilities can be applied in research on the development and dynamics of DMP discharges. This is of particular importance for investigation of high-energy density states and for studies of strongly non-linear phenomena, e.g. of the hot spots and plasma filaments described in previous sections.

The Z-Pinch and PF facilities can also be applied for research on X-ray lasers. In fact, many plasma experiments oriented on the X-ray lasers have used Z-Pinch plasmas as targets.

for pumping laser beams [34]. Some investigators have also observed the optical inversion and X-ray lasing without additional laser pumping, i.e. using only a plasma column formed within a Z-Pinch discharge [35, 36].

Intense X-ray pulses emitted from DMP discharges can be used for X-ray microscopy (XMI). The application of a short wavelength radiation makes possible observations of objects smaller than in a conventional optical microscope. First X-ray microscope systems, based on small-angle reflections from crystal surfaces, were developed for studies of micro-targets bombarded with high-intensity laser pulses. In those cases the use was made of the X-ray emission from the target plasma. For an active X-ray microscope analysis of non-radiating objects one needs an external X-ray source, e.g. an X-ray laser.

A scheme of such an X-ray microscope was developed at the Princeton University, USA [37]. The system is called COXRALM (Composite Optical X-Ray Laser Microscope) and it uses an SXL laser emitting CVI-18.2 nm line radiation. This radiation is transmitted through a vacuum-tight SiN window of $\sim 0.1 \mu\text{m}$ in thickness. The radiation pulse penetrates an investigated object, e.g. living cell placed under normal pressure, and it is used for the production of a replica. Pictures of living cells, taken from replicas produced by means of this X-ray microscope, ensure the spatial resolution of about 100 nm.

An X-ray pulse for the X-ray microscopy can also be taken from a small Z-pinch or PF device. A scheme of the X-ray microscope using PF discharges was designed and constructed in Aachen, Germany [38]. In the center of the system there is placed a small PF device oriented upward and powered by a condenser bank, placed in the basis shielded with a Faraday screen. The PF chamber is usually filled with nitrogen, and during PF discharges the X-ray pulses penetrate an appropriate window, upon which are located investigated objects. The scheme of this system and an example of its application are shown in Fig. 25.

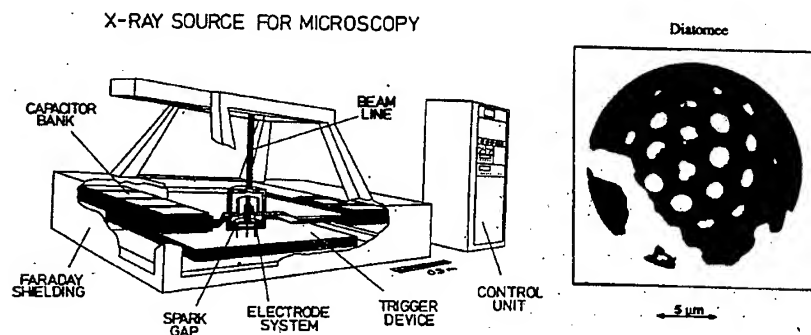


FIG. 25. Schematic of the PF-type system used for the X-ray microscopy [38]. Taking X-ray microscopic pictures, e.g. of the living Diatomee bacteria (shown on the right), one can discern details with the resolution of about 200 nm.

X-ray pulses emitted from DMP discharges can also be used for technological purposes, e.g. for X-ray lithography (XLI). Due to the use of the short-wave radiation it is possible then to map smaller objects and to pack more circuits upon a wafer, e.g. with distances below 100 nm. As an X-ray source one can use a PF-type device which scheme was presented above. The problem is that the X-ray emission from a typical PF machine contains a continuous spectrum and spectral lines of excited ions. Therefore, it is necessary to optimize X-ray pulses by using appropriate working gas, e.g. neon, which emits intense lines within the wavelength region from about 0.9 to 1.4 nm [39]. Comparison of the typical and optimized spectra is presented in Fig. 26.

The X-ray pulses for the lithography can also be obtained from a gas-puffed Z-Pinch device. A scheme of the gas-puffed Z-Pinch machine equipped with a special cylindrical pulsed valve, which injects a gas stream into the inter-electrode region, was developed e.g. at the Imperial College in London, UK [40]. When a HV pulse is applied between the electrodes, the quasi-cylindrical gas shell is ionized and it undergoes the radial compression by electromagnetic forces. The total X-ray yield depends on a time delay between the opening of the gas valve (injecting argon) and the application of high voltage between the electrodes. The system generates about 450 J of X-rays, what corresponds to about 5-10% of the initial energy delivered from a capacitor bank.

The PF-type sources of X-ray pulses for industrial lithography have been developed in Japan [41] and Singapore [42]. A scheme of the PF device adopted for industrial applications is shown in Fig. 27.

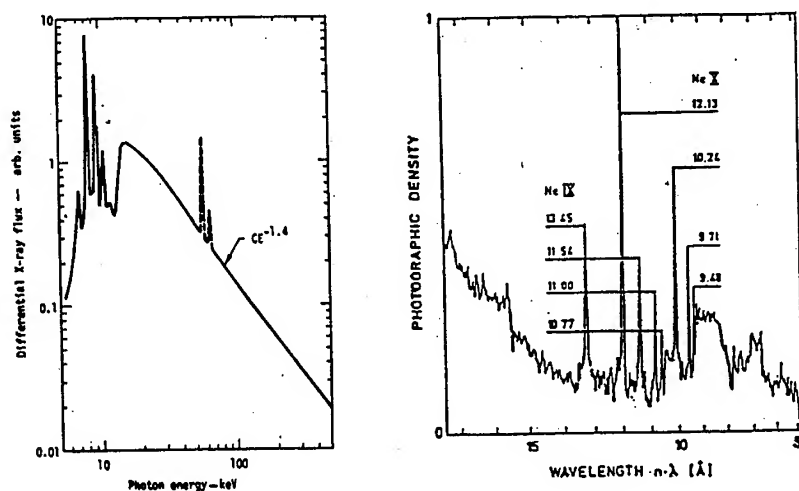


FIG. 26. Typical X-ray spectrum from a PF machine (on the left), as measured by R.L. Gullikson and R.H. Barlett in 1975. On the continuous spectrum there are visible distinct spectral lines of some excited ions. On the right - the optimized X-ray emission from a PF machine operated with neon, and designed for the X-ray lithography:

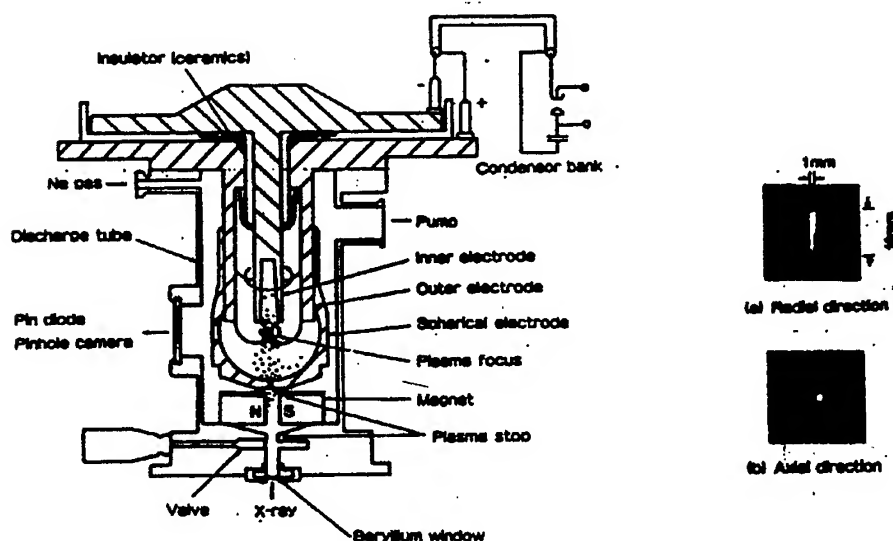


FIG. 27. Cross-sectional view of the PF-type X-ray source (on the left) designed for micro-lithography [41, 42] and X-ray images of the neon plasma (on the right), as taken with pinhole cameras.

Powerful X-ray pulses, as emitted from large Z-Pinch and PF facilities, are also used for research on influence of intense radiation on different materials and electronic equipment, including the modeling of nuclear explosions. The fast

development of X-radiating plasma sources is illustrated by a diagram presented in Fig. 28.

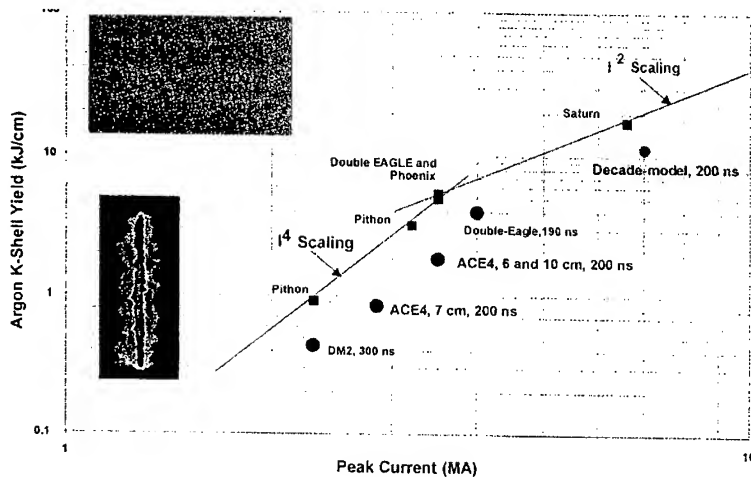


FIG. 28. X-ray yields (from the argon k-shell) versus the peak current value, as obtained in a series of Z-Pinch experiments performed in USA [43].

Since in the experiments with the Z machine at the Sandia Laboratories there were achieved 290 TW X-ray pulses, US experts have already designed the next-generation facility (so-called X-1 machine), which could deliver 1000 TW, 16 MJ in X-ray pulses needed for inertial confinement fusion. It is an attractive alternative to laser-based fusion experiments, because of its higher efficiency and lower costs. It has been proposed to enclose the Z-Pinch within a radiation chamber (Hohlraum) that traps the radiation and heats up a fusion fuel pellet located on the z-axis. The key is that the X-rays (generated as the pinch collapses) can be contained to bathe and to heat the fuel pellet uniformly. One of the proposed configurations is presented in Fig. 29.

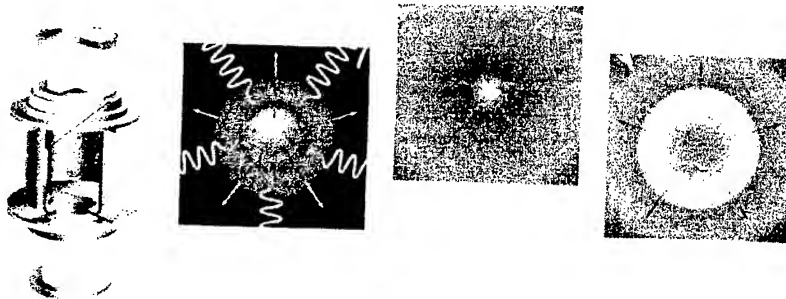


FIG. 29. Schematic of a triple Hohlraum with the fusion pellet placed in the center. According to this scheme the powerful X-radiation from two side Z-Pinches vaporize outer layer of the pellet, which bursts outward and implodes inward, inducing the ignition of the nuclear fusion reactions [12].

Also corpuscular emission from Z-Pinch and PF facilities can be used for different applications. Energetic ion and electron beams can be used for material testing and engineering. Fast neutrons (2.4 MeV neutrons from D-D reactions or 14.1 MeV neutrons from D-T reactions) can be used for radiography or activation analysis, e.g. by (np) or (n γ) reactions.

Particular attention is paid to possible uses of high neutron yields ($> 10^{12}$ neutrons/shot) from large PF facilities for the construction of a hybrid (fusion-fission) reactor [44]. Some investigators are even more optimistic [44, 45], proposing to achieve the breakeven in new large PF facilities of a 10-30 MJ scale, as shown in Fig. 30.

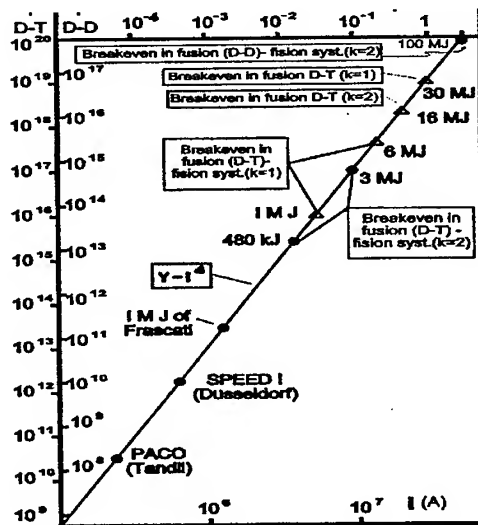


FIG. 30. Optimistic scaling of the PF experiments [45] The neutron yield versus the discharge current, as measured or estimated for D-D and D-T reactions, respectively. The symbol k describes the ratio of fusion energy to input energy.

Prospects of the 10-30 MJ PF facilities, proposed as the next-generation DMP systems, will of course depend on the mastering of the neutron saturation effects described above. On the other hand, to design and construct new large DMP facilities it is necessary to develop the international scientific cooperation.

5. International collaboration in DMP research

In history of DMP research one can find numerous examples of the international scientific cooperation. Plasma investigators from different countries participated in Z-Pinch and PF experiments performed in England, France, Germany etc. [6, 7]. The recent Z-Pinch and PF studies have also performed by international teams [16, 46]. In Poland the PF studies have been carried out within a frame of the scientific cooperation with foreign plasma research centers for many years. In particular there was active collaboration with plasma groups operated at the IPF in Stuttgart, Germany, the Kurchatov Institute in Moscow, Russia, and the

Kharkov Institute of Physics and Technology, in Kharkov, Ukraine. For example - extensive studies of the ion emission were performed in the collaboration with the IPF team [17, 26], and research on polarization of X-ray lines was carried out together with visitors from the Kurchatov Institute [22]. Small-scale Z-Pinch experiments were performed by the joint Czech-Polish team [10], and some low-energy PF experiments were carried out by Argentine-Polish teams [47, 48]. Recent experiments with PF-360 and PF-1000 facilities have also been performed with the participation of investigators from the countries mentioned above.

To promote the international collaboration in DMP research, several years ago a group of plasma experts from 16 countries, which was organized under auspices of UNESCO, elaborated a proposal of the International Center for Dense Magnetized Plasma (ICDMP) [49]. That proposal summarized knowledge about PF research [49, 50] and it showed that a collaborative effort is needed to investigate strong non-linear and turbulent phenomena in DMP. The PF configuration was proposed as the initial load for a 1-MJ facility, because PF technology (based on 10-100 kV capacitor banks) is less complicated and less costly than MV pulsed power technology. The PF device enables also larger numbers of shots to be performed.

Different countries (in a chronological order: Italy, Poland, China, Romania, and Argentina) offered sites and some equipment for setting the ICDMP, and the ICDMP Steering Committee was established at UNESCO in 1994. During the meeting held in Prague, Czech Republic, in 1995, representatives of 8 countries endorsed the project. The ICDMP proposal was also recommended by the IAEA Advisory Group Meeting, held in Vienna, Austria, in 1996. Finally, the ICDMP Steering Committee meeting, as held in Palaiseau, France, in 1997, decided that the ICDMP should be located at the IFPiLM in Warsaw, Poland. It was taken into account that there is available an appropriate laboratory building as well as the PF-1000 machine with some sophisticated diagnostics, as shown in Fig. 31.

The Steering Committee meeting, as held in Kudowa, Poland, in July 1998, decided to submit a new application for the UNESCO assistance. Mr. Federico Mayor - Director General of UNESCO - visited Warsaw in September 1998, and he promised a financial assistance in the organization of ICDMP. He proposed also to prepare an official agreement between UNESCO and the National Atomic Energy Agency (NAEA) of Poland. Such a document has already been signed by NAEA and it should be co-signed by UNESCO in August 1999. According to the UNESCO Draft Program and Budget for 2000-2001 the establishment of ICDMP is to be supported from a regular budget of UNESCO. The recent ICDMP Steering Committee meeting, as held in Warsaw on July 7-9, 1999, decided to undertake new measures to accelerate the official establishment of ICDMP. It has just been proposed to call the ICDMP Organization Meeting in Warsaw in November 1999.

According to the ICDMP Proposal and the Agreement mentioned above, the main objectives of the Center shall be as follows:

- Contribution to the progress of knowledge in the field of DMP physics and technology; through research, training and education;

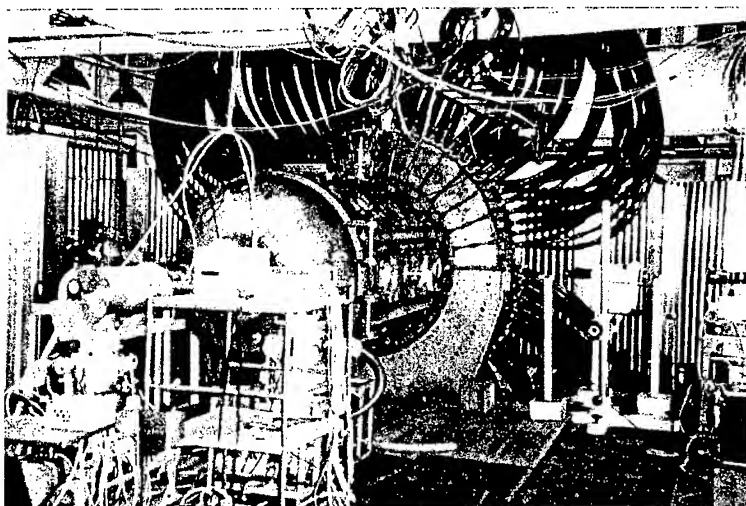


FIG. 31. General view of the PF-1000 experimental chamber and of some diagnostic equipment. Dynamics of PF discharges is studied with high-speed cameras placed side-on, and ion beams are measured with a Thomson analyzer adjusted along the z-axis. X-ray and neutron equipment is placed side-on and above the chamber.

- Promotion of implementation of research findings into practical applications;
- Support and maintenance of international scientific cooperation, exchange and communication;
- Dissemination of information on scientific achievements.

The resources necessary for the ICDMP activities shall consist of the contribution allocated by IFPiLM, contributions of UNESCO and contributions of states and institutions declaring their participation in the Center activities.

6. Summary and conclusions

The most important conclusions from the review presented above can be summarized as follows:

- Z-Pinch & PF discharges are sources of intense electromagnetic and corpuscular radiation pulses. Electromagnetic radiation extends from radio waves to hard X-rays. Corpuscular radiation contains fast electrons, protons, deuterons, heavy ions (depending on working gas and impurities), as well as fusion neutrons (from D-D or D-T reactions).
- The optimization of such discharges leads to the emission of very intense X-ray pulses, e.g. the Z machine in Sandia Laboratory (using multi-wire liners) can emit > 2 MJ of X-rays in a few nanosecond pulse, with the maximum power > 290 TW, at 45% efficiency.

- The fast deuterons or protons (depending on gas) are emitted in the form of pulsed micro-beams forming ion bunches. A moderate 60 kJ, 50 kV, PF machine can produce $> 10^{15}$ deuterons/pulse of energy > 300 keV. Energy spectra indicate that the ions are accelerated in strong (> 50 MV/cm) local electrical fields, which appear within a DMP column.
- Similar processes are responsible for the acceleration of pulsed electron-beams in the direction opposite to ions. Measurements show e-beams of energy ranging from several tens to several hundreds keV, emitted in pulses of the nanosecond scale.
- Applications of Z-Pinch & PF machines extend from basic plasma research to material studies, and from modeling of nuclear explosions to design of fusion reactors. The post cold-war era makes possible an effective international collaboration in research on DMP. This opportunity is enhanced also by the organization of ICDMP under auspices of UNESCO and IAEA.

References

1. N. A. KRALL, A. W. TRAVELPIECE, *Principles of Plasma Physics*, McGraw Hill Co., New York, 1973.
2. J. MARSHALL, *Phys. Fluids*, **3**, 135, 1960.
3. N. V. FILIPPOV et al., *Nuclear Fusion Suppl.*, **2**, 577, 1962.
4. J. W. MATHER, *Phys. Fluids*, **8**, 336, 1965.
5. L. A. ARTSIMOVICH, Ed., *Plasma Accelerators - in Russian*, Mashinostroyeniye, Moscow, 1973.
6. M. G. HAINES, A. KNIGHT, Eds., *Dense Z-Pinches*, Third Int. Conf., London, AIP Conf. Proc. 229, 1993.
7. N. PEREIRA, J. DAVIS, Eds., *Dense Z-Pinches*, Fourth Int. Conf., Vancouver, AIP Conf. Proc. 409, 1997.
8. H. J. KUNZE et al., [in:] *Proc. Intern. Symp. PLASMA'97, Jarnoltowek/Opole*, **2**, 132, 1997.
9. M. G. HAINES, [in:] *Dense Z-Pinches*, AIP Conf. Proc. 409, 1997.
10. P. KUBES et al., [in:] *PLASMA'95, Proc. 2nd Nat. Symposium, Warsaw*, **1** 63, 1995.
11. M. K. MATZEN, *Physics of Plasmas*, **4**, 1519, 1997.
12. G. YONAS, *Sci. American*, August, 45, 1998.
13. C. DEENEY, [in:] *Proc. ICOPS'99, Monterey*, 1999.
14. T. A. SHELKOVENKO, S. A. PIKUZ, A. R. MINGALEEV, D. A. HAMMER, *Rev. Sci. Instrum.* **70**, 667, 1999.
15. F. FOLKERSKI, Ed., *Proc. Int. Workshop on PF and Z-Pinch Research*, Toledo, Imperial College Rep., 1995.
16. E. INFELD, M. SADOWSKI, H. BRUZZONE, Eds., *Proc. Int Workshop on PF Research*, Kudowa, 1997.
17. H. HEROLD, A. JERZYKIEWICZ, M. SADOWSKI, H. SCHMIDT, *Nuclear Fusion* **29**, 1255, 1989.
18. W. H. BOŚTICK, [in:] *Proc. 3rd Europ. Conf. CF&PP, Utrecht*, **1**, 120, 1969.
19. M. SADOWSKI, H. HEROLD, H. SCHMIDT, M. SHAKHATRE, *Phys. Lett* **105A**, 117, 1984.
20. H. KROMPHOLZ, L. MICHEL, K. H. SCHONBACH, N. FISHER, *Appl. Phys.* **13**, 29, 1977.

21. L. JAKUBOWSKI, M. SADOWSKI, [in:] Proc. 22nd EPS Conf. CF&PP, Bournemouth, **2**, 181, 1995.
22. L. JAKUBOWSKI, et al., [in:] Dense Z-Pinches, Fourth Int. Conf., Vancouver, AIP Conf. Proc. **409**, 443, 1997.
23. J. ŻEBROWSKI et al., [in:] PLASMA'97, Proc. Int. Symposium, Jarnoltowek/Opole, **1**, 129, 1997.
24. R.L. GULLICKSON, H.L. SAHLIN, J. Appl. Phys. **49**, 1099, 1978.
25. G. GERDIN, W. STYGAR, F. VENNERI, J. Appl. Phys. **52**, 3269, 1981.
26. A. MOZER, M. SADOWSKI, H. HEROLD, H. SCHMIDT, J. Appl. Phys. **53**, 2959, 1982.
27. M. SADOWSKI, [in:] BEAMS'96, Proc. 11th Int. Conf. High-Power Particle Beams, Prague, **1**, 170, 1996.
28. H. HROLD et al., [in:] Proc. 14th EPS Conf. CF&PP, Aachen, **1**, 477, 1983.
29. M. SHOLZ et al., [in:] PLASMA'95, Proc. 2nd Nat. Symposium, Warsaw, **2**, 15, 1995.
30. H. SCHMIDT et al., J. Tech. Phys. **38**, 121, 1997.
31. A. PASTERNAK, M. SADOWSKI, J. Tech. Phys. Spec. Suppl. **39**, 45, 1998.
32. L. KARPINSKI et al., [in:] PLASMA'97, Proc. Int. Symposium, Jarnoltowek//Opole, **1**, 117, 1997.
33. E.V. GRABOVSKII et al., [in:] BEAMS'98, Proc. 12th Int. Conf. High-Power Particle Beams, Heifa, 1998.
34. G. J. TALLENTS, Editor, X-Ray Lasers 1990, Institute of Physics Conference Series No. 116, 1990.
35. J. R. PORTER et al., Phys. Rev. Lett., **68**, 796, 1992.
36. P. KUBES et al., [in:] PLASMA'99, Proc. Int. Symposium, Warsaw, J. Tech. Phys., **40**, 173, 1999.
37. A. MOROZOV, et al., [in:] PLASMA'95, Proc. 2nd Nat. Symposium, Warsaw, Vol.2, 247, 1995.
38. M. DEHL et al., *Status of the laboratory X-ray microscope*, WE-Heraeus-Seminar, Bad Honnef, 1991.
39. J. EBERLE et al., [in:] Microelectronics Engineering, Amsterdam, 1985.
40. P. CHOI et al., *A small gas-puff Z-pinch X-ray source*, Imperial College Report, London, 1988.
41. M. TANIGUCHI et al., SPIE **1089**, 240, 1989.
42. S. LEE et al., IEEE Trans. Plasma Sci., **26**, 1119, 1998.
43. K. WARE, [in:] Pulsed Power 1999, Proc. 12th IEEE Int. Conf., Monterey, CA, 1999.
44. J. BRZOSKO et al., [in:] Current Trends in Int. Fusion Research, Proc. 2nd Symp., New York, 1997.
45. J. POUZO et al., [in:] Current Trends in Int. Fusion Research, Proc. of 3rd Symp., New York, 1999.
46. ICOPS'99, Proc. Int. Conf on Plasma Science, Monterey, CA, 1999.
47. M. M. MILANESE et al., [in:] PLASMA'97, Proc. Int. Symposium, Jarnoltowek/Opole, Vol.1, 137, 1997.
48. H. KELLY, et al., IEEE Trans. Plasma Sci., **26**, 113, 1998.
49. International Centre for Dense Magnetised Plasmas; A Proposal, UNESCO, Paris, 1995.
50. A. BERNARD, H. BRUZZONE, P. CHOI, H. CHUAQUI, V. GRIBKOV et al., J., Moscow Phys. Soc., **8**, 93, 1998.

COMPLEXITY IN LASER PLASMA INSTABILITIES

M. ŠKORIĆ¹, T. SATO², A. MALUCKOV³, M. JOVANOVIĆ⁴

¹VINČA INSTITUTE OF NUCLEAR SCIENCES

POB 522, 11001 Belgrade, Yugoslavia

²THEORY AND SIMULATION CENTER, NATIONAL INSTITUTE FOR FUSION SCIENCE

Toki-shi, 509-5292, Japan

³THE GRADUATE INSTITUTE FOR ADVANCED STUDIES

Hayama, Kanagawa 240-01, Japan

⁴DEPARTMENT OF PHYSICS, UNIVERSITY OF NIŠ

P.O.B. 91, 18001 Niš, Yugoslavia

High intensity laser interaction with a plasma exhibits a rich variety of strongly nonlinear plasma phenomena. In an underdense plasma, stimulated Raman scattering (*SRS*) and stimulated Brillouin scattering (*SBS*) are two laser parametric instabilities of a greatest relevance. We show examples of isolated nonlinear *SRS* and *SBS* and discuss some of the experimental *SRS* anomalies that largely depart from the standard theory. As an example of a complex interplay between nonlinear *SRS* and *SBS* we show results of their anti-correlated behavior. Based on a concept of self-organization we put forward a simple model of *SRS* capable of reproducing basic experimentally observed anomalous features. Finally, we close with an example of fascinating new physics observed in *SRS* induced by an ultra-short pulse relativistic-intensity laser.

1. Introduction

Laser plasma interactions are a useful model for exploring strongly nonlinear plasma phenomena. In particular, high intensity laser coupling with a hot plasma exhibits various nonlinear plasma processes including laser parametric instabilities. In laser driven inertial confinement fusion (*ICF*) research, great concern is related to nonlinear laser parametric instabilities operating in an underdense plasma; such as, stimulated Brillouin scattering (*SBS*) and stimulated Raman scattering (*SRS*) [1, 2, 3]. Stimulated scattering of laser light apart from an undesirable energy loss frequently produces hot electrons that can pre-heat the *ICF* target. It is a purpose of this lecture to review some of complex and highly nonlinear laser plasma phenomena related to scattering of laser light in a plasma.

It is this physical situation where observed anomalous features point out to an inadequacy of standard linear alike theories [1, 2, 4].

Firstly, we shall focus on examples of isolated nonlinear *SBS* and *SRS* plasma processes. Further, we point out that certain experimentally observed anomalies could possibly result from a complex interplay of two and more coexisting nonlinear plasma instabilities. In particular, we discuss the question of self-consistency in plasma modeling and coexistence and interplay between nonlinear stimulated Brillouin and Raman scattering. The term Complexity in a more rigorous sense denotes evolution of highly nonlinear far from equilibrium systems exhibiting instabilities, structural bifurcation and self-organization to complex ordered states [5]. Following the concept of self-organization, we put forward a simple self-consistent model of stimulated Raman scattering, capable of producing basic anomalous features similar to those observed in high intensity laser plasma experiments [6, 7].

2. Stimulated Raman and Stimulated Brillouin Scattering

Parametric instabilities are of a great concern in the high-intensity laser-plasma interaction experiments ($I > 10^{15}$ W/cm²) since they can produce reflection and scattering of incoming laser light and generate hot electrons [1, 2, 3].

Laser driven parametric instabilities were first considered for gases. However, it appears that the self-consistent electric fields created by charged particles in a plasma lead to more complex behavior than in gases and solids. More precisely, parametric instabilities are due to laser light wave coupling with normal modes of the medium. The normal modes in a plasma are either low frequency electrostatic waves, the ion sound waves, or high frequency electrostatic waves, the electron plasma (Langmuir) waves. A parametric coupling between three or more waves can occur when momentum and energy matching conditions are satisfied (vide infra).

Further, we concentrate on stimulated Brillouin scattering instability and stimulated Raman instability because these are the two most important instabilities in the underdense- coronal plasma and of basic relevance to the coupling of laser energy to a target. *SBS* is the parametric decay of the incoming laser light into another laser light wave and an ion sound wave. This process can occur at any plasma density below critical density (the density where the laser frequency equals local electron plasma frequency) and is weakly sensitive to the density non-uniformity. *SRS*, on the other hand, is the decay of the incoming laser light into second light wave and a Langmuir (electron plasma) wave. It takes place below the quarter of the critical density, first as an absolute instability while at lower densities *SRS* turns into a convective instability [8]. Below critical density several other parametric instabilities can also exist, such as, e.g., electromagnetic decay instability, two-plasmon decay instability and filamentation instability (see Fig. 1). Each instability is limited by the dispersion relation and the frequency and wavenumber matching conditions. Initially, most of the theory has been addressing the linear behavior of laser parametric instabilities. Typically, instability threshold and exponential growth rate in weak and strong coupling limits were analytically calculated for various parametric processes [1, 2, 9]. However,

it appeared that in most experiments, these instabilities are almost always in a nonlinear state [10]. Moreover, it often happens that laser parametric instabilities saturate through strongly nonlinear regimes that correspond to large amplitude waves leading to plasma heating through wavebreaking and electron trapping [2, 11].

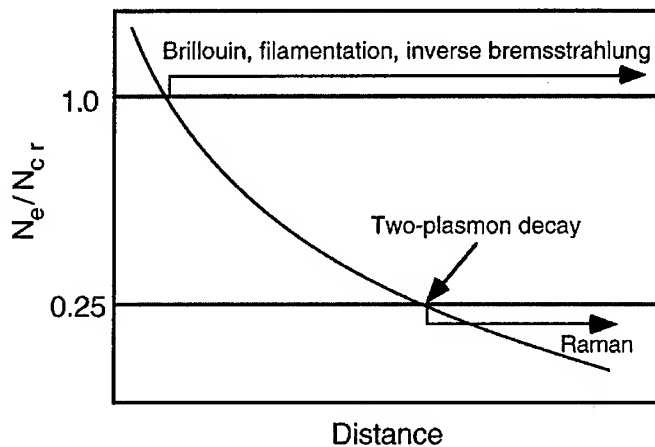


FIG. 1. Regions of underdense (corona) plasma where various laser instabilities can exist.

3. Anomalous regimes of SRS

Extensive experimental studies of nonlinear stimulated Raman backscattering [3, 8, 10] have been followed by analytics, fluid and particle simulations [1, 2, 7, 12]. In a strongly driven case, Raman instability exponentiates until arrested by nonlinear and dissipative effects. The saturation comes, basically, through pump depletion and/or higher order nonlinearities as well as kinetic dissipation related to electron trapping and Langmuir wave breaking [1, 2]. While pump depletion is readily included in fluid modeling, the latter effects are inherently kinetic. However, after more than two decades of intensive particle simulation studies, nonlinear Raman scattering is understood to possess relatively clear, albeit anomalous overall features [2]. Suppression of *SRS* is highly desirable in connection with a need to reduce hot electron generation. Indeed, correlation between hot electron generation and *SRS* was found in many experiments. A primary source for hot electron generation is understood to be due to large amplitude Langmuir waves excited in a plasma. In Fig. 2 the fraction of the laser energy in hot (supra-thermal) electrons was plotted versus the measured fraction of the energy of Raman scattered laser light [10]. Excellent correlation has also been found in temporally resolved data.

As a result of electron trapping and breaking of large Langmuir waves a hot tail-suprathermal electron population is generated [2, 11]. The corresponding velocity of hot (fast) electrons roughly equals the phase velocity of the electron plasma wave. As a general feature, two temperature (Maxwellian-like) electron

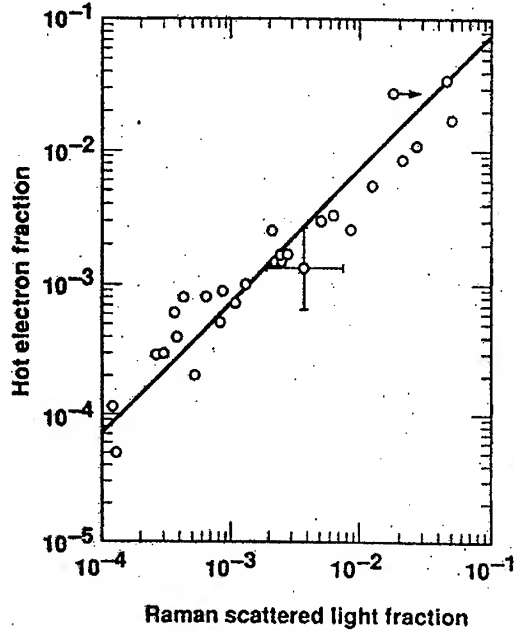


FIG. 2. The fraction of laser energy in hot (supra-thermal) electrons as inferred from hard x-rays versus the measured fraction of energy in Raman backscattered light; after [10].

distribution is recorded, for the thermal (bulk) and suprathermal (hot tail) electrons. Energy exchange leads to an increase of the bulk temperature at the expense of plasma wave dissipation. However, actual details of this complex scenario are determined by wave turbulence and the electron transport, both influenced strongly by boundary and other plasma conditions. Thus, qualitative understanding of anomalous Raman features has enabled useful scaling relations and semi-empirical formulae, typically extracted from the averaged (time and shot) short-run data [2]. Generally taken, a realistic long time saturation (e.g. $>10,000$ plasma wave periods) does not appear to be assessable to even high performance particle simulation due to required computer time and limitations of the numerical scheme involving large number of particles [2, 13]. It is this situation that has motivated us to address a problem of anomalous Raman in a long time evolution. In the last section, we study a *SRS* saturation to self-organizing plasma states using a general concept of complexity in plasmas in a system open to an environment [6]. We develop a phenomenological hybrid kinetic-fluid model to try to emulate basic physics of anomalous Raman as a precursor to state-of-the-art particle simulation with open boundaries, planned for the future.

Moreover, in many experiments scattered light associated with SRS has been measured with features that are difficult to explain using linear theory [4]. Also, there have been several hypotheses concerning the origin of observed spectra including those that questioned the dominant role of SRS. Recently, Thomson scattering was used to image the Langmuir wave spectrum in frequency and

wavenumber, related to SRS in exploding foil and solid targets [14]. While the observed Langmuir waves were consistent with SRS, substantial spectral broadening in both frequency and wavenumber, in particular, has puzzled these authors [14]. We believe that above spectral anomalies can be explained by a theoretical model of SRS due to Škorić [7, 13]. This simple 3-wave model predicts an intermittent transition to chaos in space and time with growing laser intensity, resulting in anomalous SRS features; such as, incoherent broadening of frequency and wavenumber spectra (vide infra).

4. Interplay between laser plasma instabilities

The interaction of laser light and different plasma modes that takes place in the coronal plasma often do not appear in isolation, and consequently a rich interplay between laser plasma instabilities is observed [4]. Of particular importance is the interaction between two scattering instabilities: stimulated Raman and stimulated Brillouin instability. For those plasma parameters of interest to *ICF*, it was found that *SRS* and *SBS* can coexist over large underdense plasma regions, while their growth and saturation may be affected by each other. On the other hand, a simultaneous presence of *SRS* and *SBS* suggests the possibility for various couplings between Langmuir and ion sound waves. We discuss simple examples of direct and indirect interplay between *SRS* and *SBS* and consider their effect which can invalidate scaling to experiments using linear instability growth rate.

The first experimental observation of competition between stimulated Brillouin and stimulated Raman scattering was reported in early eighties [15]. When the temporal evolution of *SRS* and *SBS* light was compared, a strong correlation was observed between saturation level of *SRS*, and the level of *SBS* light. In a preformed plasma, driven with 1 nsec CO_2 laser pulse, direct observation of Langmuir waves associated with *SRS* and ion waves related to *SBS* was made possible. An early quenching of *SRS* by *SBS* produced ion sound waves was found (see Fig. 3). The Langmuir waves were observed only during the early part of the laser pulse, and disappeared coincidental with the onset of ion sound wave driven by *SBS* [15].

An attempt was made to examine a possibility to suppress stimulated Raman and Brillouin scattering by increasing a collisionality of a plasma. Indeed for *SRS*, collisional suppression has been demonstrated, as it appears that high enough electron-ion collision rate can strongly damp *SRS* driven Langmuir waves to effectively halt the instability growth. We show the fraction of the laser energy that was Raman scattered in disk experiments, plotted in Fig. 4 versus estimated value of the collision frequency to the instability growth rate [16]. The Raman reflectivity drops strongly around theoretically predicted value of the collision over growth rate close to 0.3. It also appears plausible to expect regimes with suppressed stimulated Brillouin scattering by increasing the ion sound damping. A direct way to enhance ion damping is to increase Landau damping by changing plasma composition to include protons. As expected, a reduction of *SBS* was observed in early CO_2 laser experiments, as well as in recent gas bag and

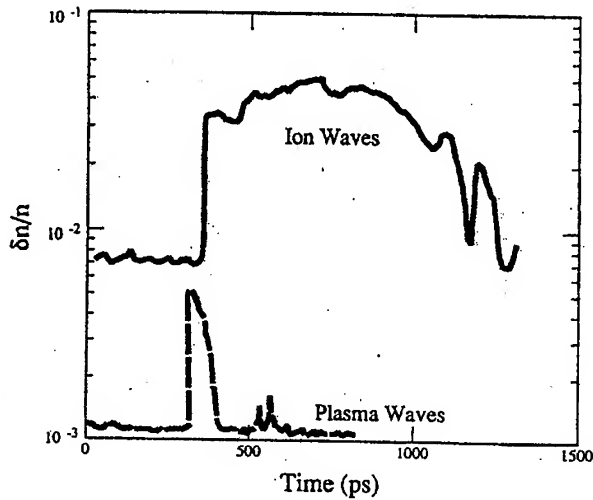


FIG. 3. Levels of ion sound waves from *SBS* and Langmuir waves from *SRS* obtained by Thomson scattering in a preformed plasma with a CO_2 laser. The Langmuir waves due to *SRS* were observed only during an early time and disappeared coincidental with the ion sound waves driven by *SBS*; after [15].

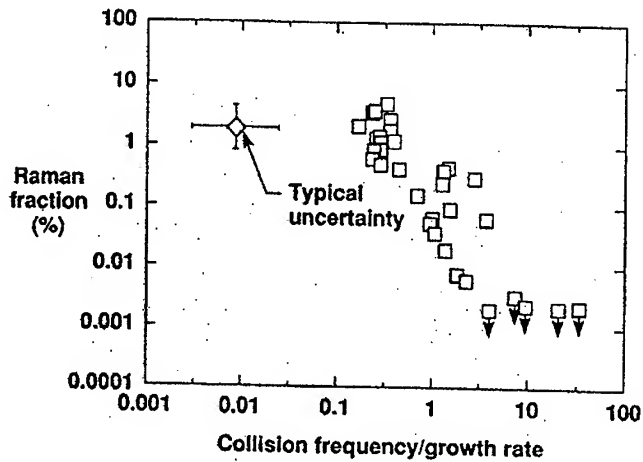


FIG. 4. The measured fraction of the light Raman scattered from Au disks versus estimated ratio of the electron-ion collision frequency to the *SRS* growth rate. The disks were irradiated with 0.3 microns laser light at various intensities; after [16].

toroidal hohlraum targets using Nova laser [4]. However, rather unexpectedly, novel regimes are also found where larger ion wave damping enhances the stimulated Raman scattering [4]. It turned out, that even if the linear growth rate of *SRS* is independent of ion sound damping the saturation level of *SRS* driven Langmuir wave can depend on the secondary parametric process. Namely, the

so called Langmuir decay instability which is the Langmuir decay into another Langmuir plus ion sound wave has a threshold proportional to both electron and ion damping rates [17, 18]. For larger ion damping the threshold is higher, leading to higher electron density fluctuation and higher reflectivity of saturated *SRS*. Indeed, an increase of *SRS* with ion sound damping observed in recent gas bag experiments is shown in Fig. 5. The ion damping was varied by changing the proton impurity fraction. A regime is clearly seen where *SRS* reflectivity increases with damping [19]. The early time results correspond to higher temperatures. Indeed, in this novel nonlinear regime one finds that *SRS* and *SBS* appear to be anti-correlated.

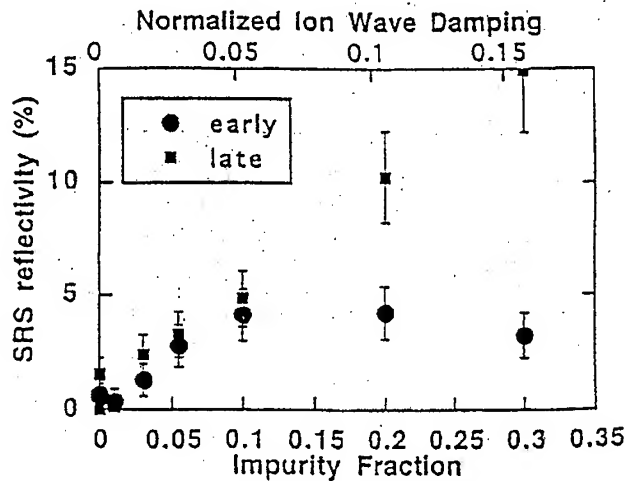


FIG. 5. *SRS* reflectivity measured with gas bag targets versus the proton impurity fraction and normalized ion sound damping; after [4, 19]. A novel regime in which *SRS* reflectivity increases with ion sound damping is evident.

Understanding of nonlinear saturation of *SRS* and *SBS* is critical for the success of laser fusion with targets designed to achieve ignition; such as those recently proposed for the National Ignition Facility (NIF) [20, 21]. The NIF, currently under construction at Livermore, USA with nominal laser energy of 1.8 MJ in 192 laser beams, is expected to achieve ignition in both direct and indirect (X-ray) driven ICF [22, 23, 24]. To validate performance of high-gain, direct-drive target design planned for the NIF, intensive studies of laser-plasma interactions in the coronal plasma were recently undertaken [25]. On the basis of these experiments, it was concluded that *SRS* and *SBS* were not likely to present a serious problem for direct drive. However, above statement applies for the nominal spatially averaged NIF laser intensity. The multi-beam phase plate smoothing tends to produce many speckles with intensities several times higher than the average, to be a potential source of strong *SRS*.

In the indirect drive approach to ICF with large multi-beam laser systems, several laser beams will be focused and overlap near the laser entrance hole of the hohlraum [22]. Corresponding important effects of multiple laser beams on *SRS*

and SBS and their competition and interplay were only recently investigated [26]. The competition between SBS and SRS was found to be modified compared to a single beam case. The observed inhibition of SBS and enhancement of SRS was explained to be due to already mentioned secondary process of Raman driven Langmuir decay instability [4, 26].

Finally, we stress the importance of self-consistent calculations based on the correct zero-order plasma state [4]. Recently, it was pointed out that in laser produced plasmas, the electron velocity distribution can be rather different from Maxwellian, even if effect of induced plasma waves is neglected. The usual Maxwellian velocity distribution is the special case with $n = 2$ power in the exponent, while higher n 's correspond to the so-called, super Gaussian distributions which are depleted in high energy electrons. A number of effects can modify the electron distribution. For example, collisional absorption (inverse Bremsstrahlung) preferentially heats slower, more collisional electrons. Therefore, when the rate of electron heating is greater than the rate at which they are equilibrated, the heated distribution function becomes super Gaussian. More generally, nonlocal transport results in distribution functions with n larger than 2; while at high intensities one finds super Gaussian distributions with n as large as 5. Modified electron distributions can result in many important effects, ranging from changes in instability thresholds and growth rates to variations in the atomic physics [4].

5. Self-organization of saturated SRS

5.1. Background

Self-organization (*SO*) is a generic process which describes a spontaneous formation of an ordered structure in a nonlinear far-from equilibrium system. Energy pumping, nonlinear instability, entropy production and expulsion are key governing processes. An open system was found to exhibit different features in *SO*, depending on whether the energy pumping is instantaneous—final state of minimum energy, or continuous—the dynamical state of intermittence [5, 6].

In this section, an attempt is made to study kinetic self-organization through a process of stimulated Raman backscattering (*SRBS*) in an underdense plasma [7]. As described, stimulated Raman scattering is a resonant three-wave (3WI) parametric instability which corresponds to the decay of an incident electromagnetic pump wave into a scattered wave plus an electron plasma wave (EPW). Important effects, especially in the context of laser-fusion [2], are input energy loss, plasma heating and generation of suprathermal (hot) electrons. However, to account for these effects, kinetic treatment of highly nonlinear electron interaction with EPW is required. To emulate these effects we apply a hybrid three-wave phenomenological kinetic model of *SRBS*, recently proposed by Škorić et al. [12]. We focus at dissipative structures that evolve at plasma micro- and macro-scales and attempt to relate entropy rate extrema to structural transitions between different states of *SO*. The basic theoretical facts about hybrid model are shown in the second part. Characteristic numerical results in the context of *SO* are exposed in the third and fourth part of this section.

5.2. Hybrid model

The basic equations are coupled three-wave equations [1, 7, 27] for slowly varying complex amplitudes of a pump (a_0), backscattered wave (a_1) and *EPW* (a_2), respectively:

$$(5.1) \quad \begin{aligned} \frac{\partial a_0}{\partial t} + V_0 \frac{\partial a_0}{\partial x} &= -a_1 a_2, \\ \frac{\partial a_1}{\partial t} - V_1 \frac{\partial a_1}{\partial x} &= a_0 a_2^*, \\ \frac{\partial a_2}{\partial t} + V_2 \frac{\partial a_2}{\partial x} + \Gamma a_2 + i\sigma |a_2|^2 a_2 &= \beta_0^2 a_0 a_1^*. \end{aligned}$$

The wave-particle interaction [2] is modeled by a damping term in the *EPW* equation of (5.1), Γa_2 which includes a phenomenological anomalous kinetic dissipation and entropy balance related to a kinetic self-organization. Parameter Γ consists of: collisional damping (Γ_{coll}), 'linear' (Landau) damping by hot resonant electrons ($\gamma_l \sim n_h$), where $n_h(t)$ stands for spatially averaged hot electron density:

$$(5.2) \quad \frac{dn_h(t)}{dt} = \frac{n_b(L, t)}{L} \int_{v_h - v_{tr}(L, t)}^{v_h + v_{tr}(L, t)} v f_b dv - a \frac{v_h(t) n_h(t)}{L},$$

(n_b is bulk electron density, f_b is bulk distribution function, v_h is velocity of hot electrons which equals the *EPW* phase velocity, v_{tr} is trapping velocity and a is particle transport parameter), and nonlinear damping due to trapped resonant bulk electrons (in the thermal Maxwellian) [2, 11]:

$$(5.3) \quad 2\gamma_{nl} W(t) = \frac{mn_b(L, t)}{2L} \int_{v_h - v_{tr}(L, t)}^{v_h + v_{tr}(L, t)} v^3 f_b(v) dv,$$

where $W(t)$ is spatially averaged *EPW* energy.

Open boundaries and reemittance of fresh ambient electrons [28] is assumed. The particles (bulk and hot electrons) and energy (wave and particle) are being exchanged between a plasma and an environment through open boundaries with a conservation of particle number and total energy in the system. Accordingly, heat balance equation (effect of plasma heating; E_b , E_h and $S_{tot} \rightarrow S_b + S_h + S_q$ are the average bulk and hot electron energy or corresponding energy flux of the bulk, hot and return ambient electrons, respectively) takes a form:

$$(5.4) \quad \frac{dW(t)}{dt} = \frac{d(E_b(t) + E_h(t))}{dt} + k \cdot S_{tot} \Big|_0^L.$$

5.3. Simulation

The simulation is made via central-difference numerical code [7], which is complemented by equations for generation of resonant electrons (5.2) and heat balance equation (5.4) in the wave-particle system.

Parameters are: $n_0 = 0.1n_{cr}$, $T_{b0} = 0.5$ keV, plasma length is equal to 16 microns with the pump intensity, $\beta_0 = 0.0253$, capable of driving absolutely unstable SRS [9, 27]. Openness of a system, k (0-1) was chosen as a bifurcation parameter. The effect of self-organization at large (wave-fluid) macro-scales is illustrated in Fig. 6. Depending on k the system shows characteristic features of different dynamical regimes: steady-state ($k = 0.007$), quasi-periodic ($k = 0.05$), periodic ($k = 0.5$) and intermittent regime ($k > 0.9$).

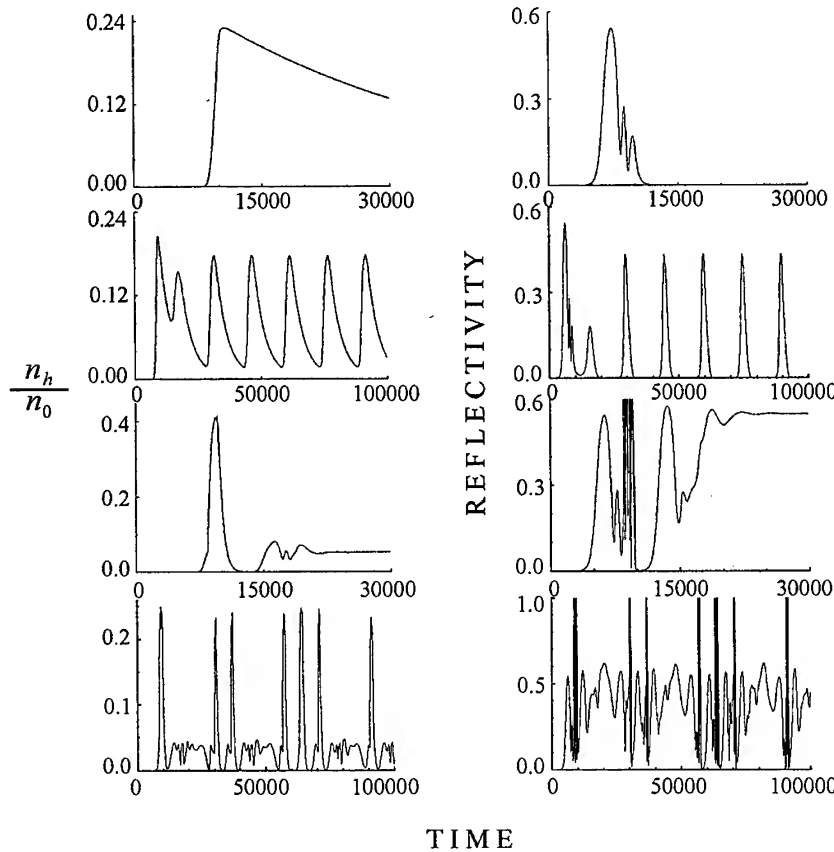


FIG. 6. Density of hot electrons and reflectivity versus time $[\omega_0^{-1}]$ for $k = 0.007, 0.05, 0.5, 0.9$ (top to bottom), respectively.

We find an increasing complexity with a control parameter, along the generic route, from the steady-state, quasi-periodic to intermittently chaotic [6, 12]. In an intermittent regime all dynamical variables show quasi-periodic oscillations which are interrupted by chaotic bursts in space and time. The corresponding SRS backscatter spectrum readily recovers anomalies similar to those observed in experiments [7, 13]. In particular, increased incoherent spectral broadening both in frequency and wavenumber, at least qualitatively, agree with those recently reported [7, 13, 14]. In Fig. 7 we illustrate the micro-scale (kinetic) self-organization via temporal evolution of the electron distribution function. In

the treatment bi-Maxwellian (bulk-hot) electron distribution, as suggested by kinetic and particle-in-cell (*PIC*) simulations [2, 13], was assumed. One can readily observe an essential connection and interplay between two levels of *SO* in a dissipative plasma.

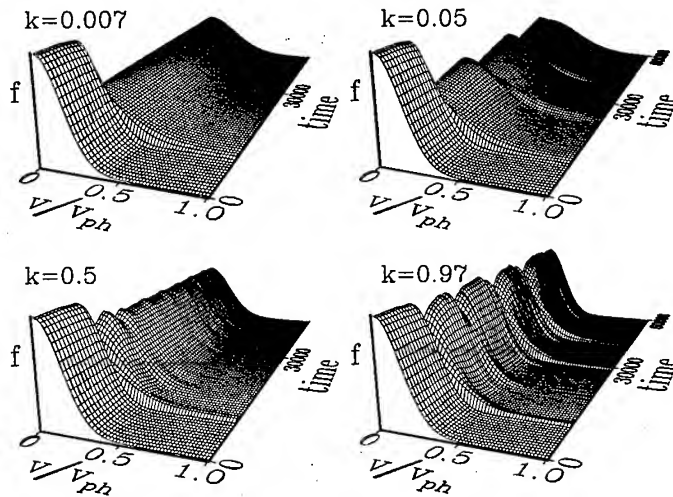


FIG. 7. Three-dimensional view of the electron velocity distribution in time for different saturated Raman regimes, as indicated by values of parameter k . Micro-kinetic scale self-organization of varying complexity is revealed in both thermal and suprathermal (hot) regions of the electron distribution.

5.4. Dissipative structures and entropy rate

Self-organization in a strongly nonlinear far-from-equilibrium system leads to a creation of ordered states that reflect an interaction of this system with its environment. These novel dynamical structures or patterns, named dissipative structures to stress the crucial role of dissipation in their creation, have become a central theme of the science of complexity [6, 7, 12]. On the other hand, there is a fundamental role of the entropy, in particular, the rate of entropy change in an open system [5]. The rate of entropy production and its removal basically governs self-organization features of a system. A large amount of effort has been spent in attempts to relate the entropy rate extrema to structural bifurcations and transitions between different ordered states [6, 7].

First, we focus at self-organized dissipative structures developed at the macro-scale. Indeed, in this model, basic wave and fluid density variables were assumed to vary slowly in space-time. Therefore, we expect that original spatial-temporal profiles, found in simulations, should correspond to large dissipative structures, self-organized at macro-scale levels. As an illustration, we plot the plasma wave profiles (Fig. 8), in particular, to reveal a genuine spatial-temporal nature of an intermittent regime as compared to regular dynamical regimes of

the steady-state and quasi-periodic type [2, 12]. Spatial-temporal complexity of quasi-steady and traveling wave patterns with regular and chaotic features is found in different states of self-organization.

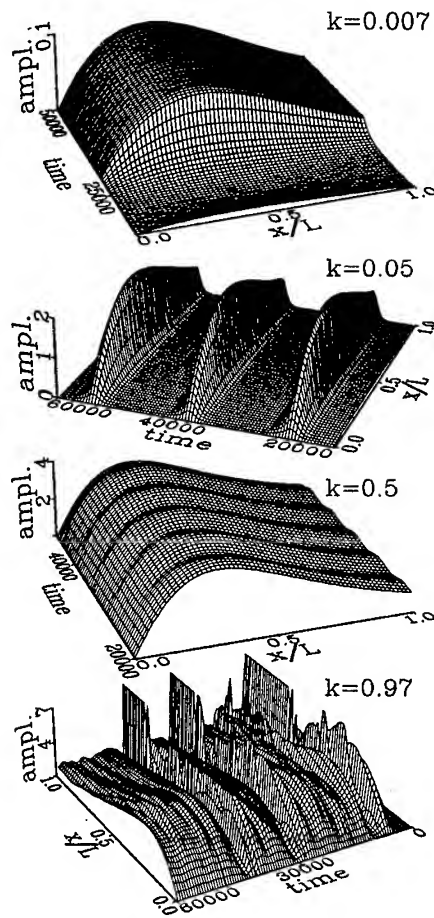


FIG. 8. Spatial-temporal profile of the electron plasma wave for varying k values. Different dissipative structures are seen on the route to complexity, from the steady-state via quasi-periodic to intermittent regimes.

Further, in Fig. 9 we plot the entropy rate $dS(t)/dt$ in time together with a spatial-temporal profile of the scattered wave energy. We calculate the entropy S related to distributions $F_i = n_i f_i$, as: $S(t) = S_b(t) + S_h(t)$, where

$$S_i(t) = - \int_0^L dx \int_{-\infty}^{\infty} dv F_i(x, v, t) \ln F_i(x, v, t)$$

where $i = b, h$.

For an intermittent regime, featuring an interchange between chaotic and laminar phases, we find a clear evidence of structural transitions corresponding to the maximum (positive) and minimum (negative) entropy rate. As a striking example of self-organization in an open system we find a rapid entropy jump which coincides with an onset of a chaotic phase. Subsequent anomalous dissipation and entropy growth is halted by a sudden entropy expulsion into the environment. Negative burst in entropy rate indicates a bifurcation from a chaotic, back to a laminar quasi-periodic phase. An intermittent nature of this regime is shown through a repetitive pattern of behavior. We note that complex dissipative wave structures are mapped onto a more simple entropy rate time series. Intervals of near zero entropy rate during a laminar phase, mean a net balance between the entropy production and its expulsion. This serves as a possible example of a stationary nonequilibrium state realized in a strongly nonlinear open system [6].

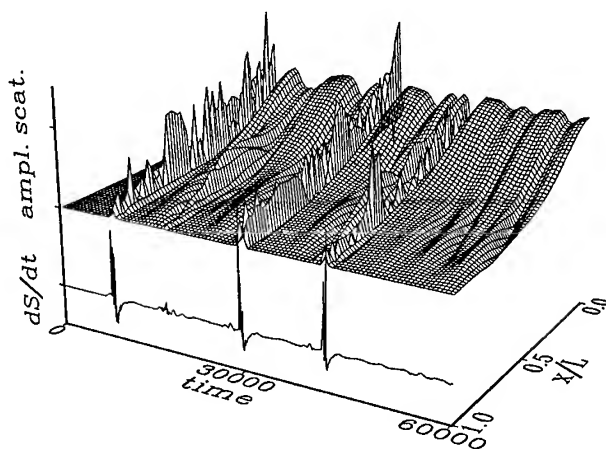


FIG. 9. Intermittent dissipative backscatter-wave structures versus the corresponding entropy rate in time. Positive entropy jump coincides with an onset of chaos, while a negative burst indicates a transition from a chaotic to a laminar phase of *SO* at macro-scales.

A hybrid nature of this model also allows us to recover kinetic properties of self-organization. To show the self-organization featuring micro-levels, we plot the electron velocity distribution function. In Fig. 7 we see a three-dimensional view of the electron velocity distribution in time for different saturated Raman regimes, as indicated by values of parameter k . Kinetic self-organization of varying complexity is revealed in thermal and suprathreshold (hot) regions of the electron distribution. In Fig. 10, we further plot the electron distribution in time versus the entropy rate related to an intermittent regime. Once again, an evidence of micro-scale structural transitions that correspond to entropy rate extrema, is found. Indeed, one is able to observe a complex connection and interplay between macro and micro levels of self-organization in an open dissipative

plasma.

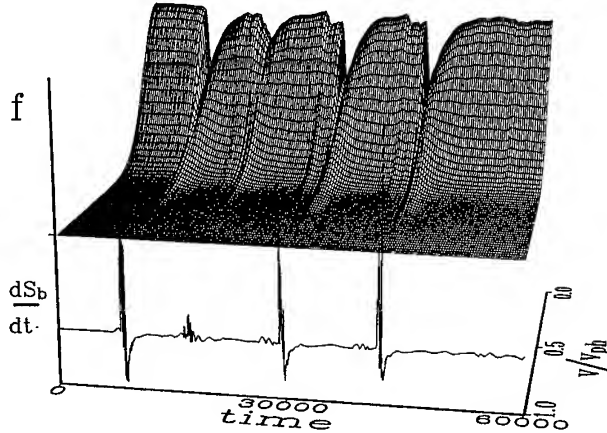


FIG. 10. Intermittent electron distribution versus the entropy rate in time. Similar to Fig. 9, structural bifurcations at micro-scales, correspond to entropy rate extrema.

5.5. Discussions

We believe that above findings appear to be a first indication of a generic intermittent scenario in a kinetic self-organization of anomalous Raman instability. At this point we may note that one is able to claim a consistency with the working hypothesis and general scenario of self-organization in plasmas [6, 12]. As a further step, we expect an important justification of our hybrid -modeling of saturated Raman complexity by the novel open boundary particle simulation code, currently under development [28]. As an early illustration, we show in Fig. 11, recent particle-in-cell simulation data for a model of an isolated plasma slab in a vacuum [13]. For same plasma parameters, particle simulations (Fig. 11) show an evident support of above Raman reflectivity pattern (Fig. 6, right top), obtained for a closed ($k = 0.007$) system.

6. Summary

In this review we have addressed some important examples of a complex plasma behavior related to nonlinear *SRS* and *SBS* instabilities. As an introduction we have discussed nonlinear saturation of the isolated Raman and Brillouin scattering in laser plasmas. We have pointed out the failure of standard nonlinear parametric theory to reproduce experimentally observed *SRS* anomalies. As an example of a complex interplay we show data on coexisting and anti-correlated *SRS* and *SBS*. Applying the general concept of self-organization, for the first time to *SRS*, we have constructed a simple but powerful 3WI model for anomalous *SRS* evolution that shows consistency with particle simulations.

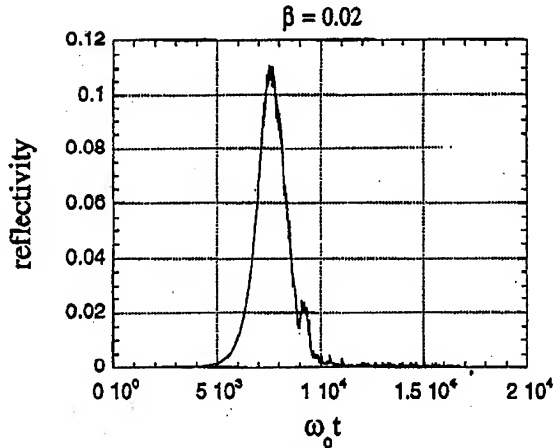


FIG. 11. Simulation data for Raman reflectivity in time, obtained by an one-and-two-halves electromagnetic, relativistic, particle-in-cell code. (after [13]). Initial plasma parameters were the same as above, with a pump equal to 0.02.

Finally, we turn to an example of fascinating new physics that was recently observed as one moved into a regime of collective effects in plasmas induced by ultra-short pulse ultra-high intensity ($I > 10^{18}$ W/cm²) laser. A Livermore-UCLA collaboration has observed a subpicosecond version of classic laser plasma stimulated Raman backscatter [29]. The backscattered light displays anomalous spectral signatures that strongly depend on laser intensity. Broad and modulated frequency spectrum that spreads to the blue side of the standard Raman shifted line, that is obviously different from classic *SRS*, was typically observed (see Fig. 12). The use of prepulse did not significantly affect the modulation, hence

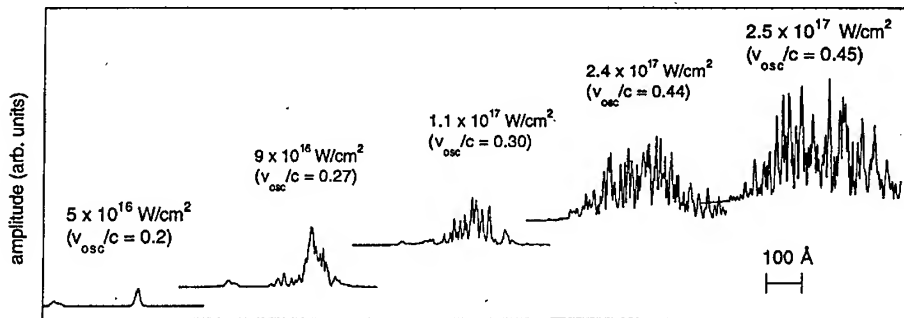


FIG. 12. Spectra of backscattered light as a function of laser pulse intensity demonstrating a transition from classic *SRS* to anomalous backscattering; after [30]; and private communication.

ruling out the ionization as a probable cause. More recently similar results were reported by Rutherford, Limeil and Livermore groups. Above spectral anomalies were recovered and explained in the framework of a simple theoretical three-wave fluid model of *SRS*, by some of these authors [7]. Moreover, it was shown [7, 12] that backscatter complexities; i.e., modulated and incoherently broadened spectra follow a quasi-periodic and intermittent route to chaos (vide supra), while a spectral blue shift was attributed to a relativistic decrease of plasma frequency. These findings were reinforced by results obtained by $1\frac{1}{2}$ -dimensional, fully relativistic particle in cell simulations [13].

Acknowledgements

We acknowledge the partial support and the visiting professorship, granted to one of us (M.M.Š) by the Ministry of Education, Science, Culture and Sport (Monbusho) of Japan. This work was supported in parts by the Ministry of Science and Technology of the Republic of Serbia, Project-01E11.

References

1. D.W. FORSLUND, J.M. KINDEL, E.L. LINDMAN, *Phys. Fluids*, **18**, 1002, 1975.
2. W.L. KRUER, *The Physics of Laser Plasma Interactions*, Addison, N. Y. (1988); *ibid.*, *Phys. Fluids*, **B3**, 2356, 1991
3. H.A. BALDIS, E.M. CAMPBELL and W.L. KRUER, *Physics of Laser Plasmas*, North-Holland, Amsterdam, 1991.
4. W.L. KRUER, B.B. AFEYAN, A.E. CHOU, R.K. KIRKWOOD, D.S. MONTGOMERY, P.W. RAMBO, S.C. WILKS, *Phys. Scripta*, **T75**, 7, 1998; and references therein.
5. G. NICOLIS and I. PRIGOGINE, *Exploring Complexity*, Freeman, N.Y., 1989.
6. T. SATO and the Complexity Simulation Group, *Phys. Plasmas*, **3**, 261, 1996.
7. M.M. ŠKORIĆ, M.S. JOVANOVIĆ, M. RAJKOVIC, *Phys. Rev.*, **E53**, 4056, 1996 *Europhys. Lett.*, **34**, 19, 1996.
8. W. SEKA, B.B. AFEYAN, R. BONI, L.M. GOLDMAN, R.W. SHORT, K. TANAKA and T.W. JOHNSTON, *Phys. Fluids*, **28**, 2570, 1985.
9. M.N. ROSENBLUTH, *Phys. Rev. Lett.*, **29**, 565, 1972.
10. R.P. DRAKE, R.E. TURNER, B.F. LASINSKI, K.G. ESTABROOK, E.M. CAMPBELL, C.L. WANG, D.W. PHILLION, E.A. WILLIAMS, W.L. KRUER, *Phys. Rev. Lett.*, **53**, 1739, 1984.
11. T.M. O' NEIL, *Phys. Fluids*, **8**, 2255, 1965.
12. M.M. ŠKORIĆ, T. SATO, A. MALUCKOV, M.S. JOVANOVIĆ, *Phys. Review*, **E60**, 7426, 1999.
13. S. MIYAMOTO, K. MIMA, M. ŠKORIĆ, M. S. JOVANOVIĆ, *J. Phys. Soc. Japan*, **67**, 1281, 1998.
14. K.L. BAKER, R.P. DRAKE, K.G. ESTABROOK, B. SLEAFORD, M.K. PRASAD, B.L. FONTAINE and D.M. VILLENEUVE, *Phys. Plasmas*, **6**, 4284, 1999.
15. H.A. BALDIS, D.M. VILLENEUVE, C. LABAUNE, D. PESME, W. ROZMUS, W.L. KRUER, P.E. YOUNG, *Phys. Fluids*, **B3**, 2341, 1991.
16. R.P. DRAKE, *Comments Plasma Phys. Controlled Fusion*, **12**, 181, 1989.
17. S.J. KARTUNNEN, *Phys. Rev.*, **A23**, 2006, 1981.
18. R.P. DRAKE and S.H. BATHA, *Phys. Fluids*, **B3**, 293, 1991.

19. R.E. KIRKWOOD, B.J. MACGOWAN, D.S. MONTGOMERY, B.B. AFEYAN, W.L. KRUEER, J.D. MODDY, K.G. ESTABROOK, C.A. BACK, S.H. GLENZER, M.A. BLAIN, E.A. WILLIAMS, R.L. BERGER, B.F. LASINSKI, *Phys. Rev. Lett.*, **77**, 2706, 1996.
20. J.A. PAISNER, J.D. BOYES, S.A. KUMPAN, W.H. LOWDERMILK and M.S. SOREM, *Laser Focus World*, **30**, 75, 1994.
21. D.S. MONTGOMERY, B.B. AFEYAN, J.A. COBBLE, J.C. FERNANDEZ, M.D. WILKE, S.H. GLENZER, R.K. KIRKWOOD, B.J. MACGOWAN, J.D. MOODY, E.L. LINDMAN, D.H. MUNRO, B.H. WILDE, H.A. ROSE, D.F. DUBOIS, B. BEZZERIDES, H.X. VU, *Phys. Plasmas*, **5**, 1973, 1998.
22. J. LINDL, *Phys. Plasmas*, **2**, 3933, 1995.
23. T.R. DITTRICH, S.W. HAAN, M.M. MARINAK, S.M. POLLAIN, D.E. HINKEL, D.H. MUNRO, C.P. VERDON, G.L. STROBEL, R. MCEACHERN, R.C. COOK, C.C. ROBERTS, D.C. WILSON, P.A. BRADLEY, L.R. FOREMAN and W.S. VARNUM, *Phys. Plasmas*, **6**, 2164, 1999.
24. M.D. ROSEN, *Phys. Plasmas*, **6**, 1690, 1999.
25. S.P. REGAN, D.K. BRADLEY, A.V. CHIROKIKH, R.S. CRAXTON, D.D. MEYERHOFER, W. SEKA, R.W. SHORT, A. SIMON, R.P.J. TOWN, B. YAAKOBI, J.J. CARROLL III and R.P. DRAKE, *Phys. Plasmas*, **6**, 2072, 1999.
26. C. LABAUNE, H.A. BALDIS, B. COHEN, W. ROZMUS, S. DEPIERREUX, E. SCHIFANO, B.S. BAUER and A. MICHARD, *Phys. Plasmas*, **6**, 2048, 1999.
27. D.J. KAUP, A. RIEMAN and A. BERS, *Rev. Mod. Phys.*, **51**, 275, 1979.
28. H. TAKAMARU, T. SATO, R. HORIUCHI, K. WATANABE and Complexity Simulation Group, *J. Phys. Soc. Jap.*, **66**, 3826, 1997.
29. C.J. JOSHI, P.B. CORKUM, *Phys. Today*, **48**, 36, 1995.
30. C.A. COVERDALE, C.B. DARROW, C.D. DECKER, N.M. NAUMOVA, T.ZH ESIRKEPOV, A.S. SAKHAROV, S.V. BULANOV, W.B. MORI, K.C. TZENG, *Plasma Phys. Reports*, **22**, 685, 1996.

ELECTRON BEAM-PLASMA INTERACTION IN LABORATORY AND SPACE

S. TORVÉN

ALFÉN LABORATORY, ROYAL INSTITUTE OF TECHNOLOGY
Stockholm, Sweden

Electron beam-plasma interaction in inhomogeneous plasmas is considered. Generation of spatially localised Langmuir waves by fast electron clouds in the solar wind, which give rise to type III Solar Radio Bursts, is one example of the complex wave growth generated by inhomogeneous beams, involving processes as reabsorption and localisation of the wave energy density. Acceleration of electrons and generation of localised Langmuir waves in the auroral zone are also discussed. Such waves have been observed in the upper ionosphere, but they have also been invoked to explain the sharply localised density spikes observed at low altitudes. Then recent laboratory experiments on localisation of wave energy density due to density gradients in beam-plasma discharges are discussed. High frequency (hf) probes for electric field measurements are described. Concentration of wave energy density in sharply localised hf spikes with high amplitudes has been observed, and density spikes may also form at the positions of the hf spikes due to enhanced ionisation. In some cases the hf spikes have been identified as standing waves, surrounded by regions with propagating waves.

1. Introduction

The interaction between electron beams and plasmas is one of the earliest investigated collective phenomenon in plasma physics. The first experimental observations were made by Langmuir. The beam represents a source of free energy, and its energy can be trapped by the waves so the wave amplitudes increase, simultaneously as the beam velocity distribution is modified by the waves and finally may become stable. The excitation of high frequency (hf) waves ($\omega \approx \omega_{pe}$) and their growth, dispersion and saturation have been studied intensely for plasmas that are homogeneous in the beam direction, and different types of velocity distributions have been considered. The evolution of the growing waves and the beam velocity distribution are treated by the quasilinear equations which can handle the entire spectrum of growing modes. Strong simplification occurs if the fastest growing mode dominates or if the boundary conditions single out a dominating mode. Then single wave models can be used. Much of the theoretical work has been confirmed by well controlled experiments in beam-plasma discharges and

in double and triple plasma devices. For sufficiently weak bump-on-tail distributions the dispersion relation is not much influenced by the beam, and in a weakly magnetized plasma it is essentially the same as for Langmuir waves. In such a case the beam merely acts as a "pump wave" for wave-electron interaction, wave-wave interaction, and strong Langmuir turbulence. In this paper electron beam-plasma interaction will be considered when the beam is strongly inhomogeneous and varying in time or when the background plasma is strongly inhomogeneous. Only weakly magnetized ($\omega_{ce} < \omega_{wp}$) and non-relativistic plasmas will be discussed. Inhomogeneities in the beam or the background plasma give rise to new phenomena that differ from the classical treatment of beam-plasma interaction. This situation often prevails in space plasmas, and effects of inhomogeneities have also been studied in laboratory plasmas. In Section 2 the excitation of localised Langmuir waves by a weak bump-on-tail instability in the solar wind plasma will be described. These waves give rise to Type III Solar Radio Bursts. Quasilinear theory, wave-wave interaction, and strong turbulence have been applied to interpret the observed data. Localised Langmuir waves are also excited in the ionosphere due to the energetic, precipitating electrons in the auroral zone, discussed in Section 3. The waves have been observed at altitudes between 500 and 1000 km, but electron beam-plasma interaction has also been proposed to occur at low altitudes (110-150 km) to explain observations of sharply localised regions with enhanced density. In Section 4 some properties of beam-plasma discharges are discussed and probes are described which are suitable for measurements of the intensity of the hf-field in laboratory discharges. In Section 5 experimental investigations of electron beam-plasma interaction are described when there are strong density gradients in the direction of the beam. This is the case, for instance, in front of the cathode or the electron gun which inject the beam. In such gradients the electric hf field may concentrate in narrow "hf spikes" with very high amplitudes. Particle simulations confirming the experimental results are also presented. They show that the hf spikes can form without trapping of waves in density cavities. Conclusions are presented in Section 6.

2. Generation of Langmuir waves in the solar wind by fast electron clouds

Type III solar radio bursts are electromagnetic waves which are generated in the solar wind all the way between the Sun and the Earth's orbit. The radiation is caused by fast electron clouds which are emitted from the sun in connection with solar flares. The electron clouds have much higher velocities than the solar wind plasma, and they excite Langmuir waves via a weak bump-on-tail instability as shown by in situ measurements [1]. The bump in the velocity distribution, and also the magnetic field, are so weak that the dispersion relation may be approximated by the dispersion relation for Langmuir waves. The wave frequency is close to the local plasma frequency. The generally accepted model for the electromagnetic wave generation is scattering of Langmuir waves into transverse waves by thermal ions, leading to fundamental radio emission at the plasma frequency and harmonic emission [2]. In observations by the Ulysses spacecraft it was possible to trace the emission from an individual electron cloud up to the

Earth's orbit (Reiner et al. 1995 [3]). Since the cloud follows the magnetic field lines, an instantaneous view of the interplanetary extension of the solar magnetic field was obtained. Recent in situ measurements (Ergun et al. 1998 [1]) have confirmed earlier data, but indications were obtained that oblique waves also may be important.

There is a basic difficulty, usually called "Sturrock's dilemma", with the excitation of the Langmuir waves by the beam. Sturrock 1964 [3] argued that linear theory predicts so strong wave growth that the beam can travel only a few thousand kilometres before its velocity is dispersed by the waves and its free energy is lost. However, since type III solar radio bursts can be observed up to the Earth's orbit, the beam must survive over long distances and still be able to excite waves. Consider a cloud in the x - v plane (x distance, v velocity) which initially has a certain spatial extension in an interval around $x = 0$ and a monotonically decreasing velocity distribution there. When the velocity distribution of the cloud is observed at a fixed position at some distance x , which is large compared with the initial extension, only some of the faster electrons have arrived, and slower electrons are absent. The fast electrons may accordingly form an energetic bump on the tail of the electron velocity distribution, and the velocity distribution will get a positive slope in some velocity interval. Waves will be excited with phase velocities in that interval. The wave energy generated should move with the slow group velocity and therefore stay at approximately the position, where it is excited, while the electrons pass. Some time later the faster electrons have left the position considered and slower electrons arrive so the bump is continuously shifted to lower velocities. Therefore the waves, that were excited, may now have phase velocities in an interval where the slope of the distribution function is negative and may accordingly be reabsorbed by the electron stream. In this way the wave energy is carried back to the particles, and little energy may be trapped from the electron stream.

This qualitative picture has been investigated by several authors [3]. Ryutov and Sagdeev 1970 [3] found an approximate, self-similar solution of the quasilinear equations. This type of solution has recently been further elaborated by Mel'nik and Kontar 1998 [3]. Quasi-linear theory predicts a growth of wave amplitudes until the bump on the tail tends to be smeared out and a plateau is formed in the distribution. Ryutov and Sagdeev assumed that the quasilinear relaxation is so fast that the distribution function of the beam can be described by a plateau distribution during the passage of the stream. When observed at a given position, the wave energy is seen to increase and then decrease to a low value when the electron cloud has passed. This model has been partially confirmed by numerical solutions of the quasilinear equations. Takakura and Shibabashi 1976 [3] used the one dimensional quasilinear equations, including spontaneous emission. A plateau is rapidly formed, and re-absorption of wave energy is observed. Magelssen and Smith, 1977 [3] used the same equations with realistic solar wind parameters. They traced the cloud to distances beyond the Earth's orbit and found approximate self-similar behaviour, that is, when the passage of the cloud is observed at any fixed position a similar behaviour is observed. The velocity distribution in the front of the cloud is unstable and waves are excited. Then a plateau is observed and waves are reabsorbed.

Wave-wave interaction has also been combined with the quasilinear equations [4]. Langmuir waves in resonance with the beam may be scattered by ion waves and obtain longer wave lengths and higher phase velocities. If this process sufficiently rapidly removes the wave energy in resonance with the beam, the resonant wave level may be so low that the beam is not much modified. This may also be considered as a stabilization mechanism for the beam and was proposed by Kaplan and Tsytovitch 1967 [4] as the clue to Sturrock's dilemma. Using the one-dimensional kinetic equations, including wave-wave interaction, the time evolution of the velocity distribution and the wave energy density was evaluated by Grogard 1982 [4]. The measured velocity distribution from the ISEE-3 spacecraft (Lin et al. 1981 [1]) was used in the boundary data. The characteristic feature of the resulting weak Langmuir turbulence, that is, the concentration of the energy density in a "condensate" built up around wave numbers $k \approx 0$, was observed, and good agreement with the measured distribution was obtained. Here plateau formation is partially inhibited by the wave scattering.

The work described above resolves Sturrock's dilemma but does not explain the spiky and intermittent nature of the waves which may appear as sharply localised structures. Rapid amplitude variations in time have been observed, and measured amplitudes may change by many orders of magnitudes over a few seconds. Langmuir wave collapse in density cavities has been introduced to explain this [5]. In this unstable process the density cavity traps waves and contracts, and the wave energy is finally released as particle energy (wave collapse). The state obtained, when many such cavities form, interact, and collapse, has been called strong Langmuir turbulence. This may be excited by modulation instability. However, in simulations this route to strong Langmuir turbulence is often superseded by "nucleation instability", that is, a collapsed and relaxing cavity forms the seed for new wave trapping (Doolen et al. 1985 [5]). Experimental evidence of wave trapping in density cavities and wave collapse has also been obtained in a number of weak beam experiments (e.g. Cheung and Wong 1985 [5] and McFarland and Wong 1997 [5]). A review on nonlinear wave collapse and strong turbulence has been given by Robinson 1997 [5].

It has not been possible to show convincingly that strong turbulence is of importance to explain the clumpy Langmuir waves. Also waves with intensities well below estimated thresholds for wave collapse are spiky, indicating a linear process. A model has been proposed (Robinson 1992 [6]) where a marginally stable state is assumed to exist with a small net dissipation, consistent with the propagation of the beam up to 1 AU. Then low frequency density fluctuations, which are observed in the ambient solar wind plasma, are introduced. They may randomly modulate the spatial growth rate about the marginally stable state leading to spatially inhomogeneous growth and damping. Besides, the low density fluctuations may have a level that is sufficient to scatter Langmuir waves out of resonance with the beam at a fast rate. This model has been elaborated by several authors [6], and it is able to account for several of the observed features of the Langmuir waves in the solar wind plasma.

3. Generation of electron beams in the ionosphere

In the ionosphere and the magnetosphere energetic electrons move along the magnetic field lines and give rise to auroral arcs when they meet the Earth's atmosphere. They also interact with the background electrons and excite Langmuir waves as shown by rocket measurements at altitudes between 500 and 1000 km. It is generally believed that the electron acceleration takes place in potential drops along the magnetic field lines. Fig. 1 shows proposed equipotential contours which are consistent with recent observations. The direction of the magnetic field is downwards in the plane of the paper, the transverse distance is in the north-south direction, and the east-west direction is out from the paper. The two U-shaped equipotential contours shown (Mozer et al. 1980 [7]) have the lowest potential in the middle and have an electric field, parallel with the magnetic field which accelerates electrons downwards and give rise to auroral arcs. The typical extension of a U-shaped structure in north-south direction is only of the order of 10 km whereas the extension in the east-west direction is large. Between the bright auroras there is a dark region (black aurora) where electrons are accelerated upwards.

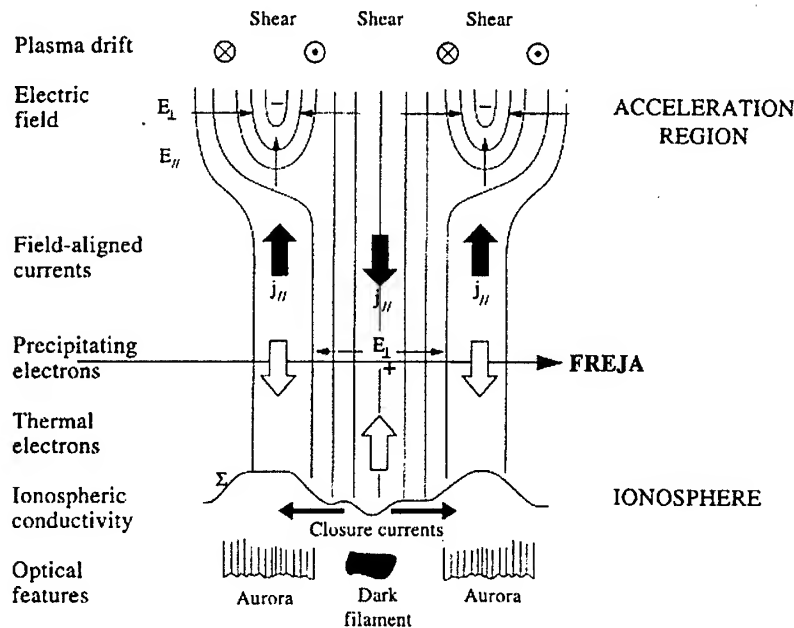


FIG. 1. Proposed U-shaped equipotential contours above the auroral zone of the Earth, consistent with recent measurements by spacecrafts. The U-shaped structures accelerate electrons downwards and give rise to auroral arcs. Between the bright arcs there is a dark region (black aurora) where electrons are accelerated upwards. The direction of the magnetic field is downward in the plane of the paper, the transverse direction is north-south, and the east-west direction is out from the paper. The typical extension of the U-shaped potential in the north-south direction is 10 km (from Marklund and Karlsson 1997 [7]).

The equipotential contours are parallel with the magnetic field lines at sufficiently high altitudes. Strong evidence of the corresponding electric field along the magnetic field has been obtained from recent measurements by the spacecraft FAST (Ergun et al. 1998 [7]). The measurements show a very strong correlation between the transverse potential drop at high altitudes and the energy of upgoing positive ions. Measurements by Freja (Marklund and Karlsson 1997 [7]), above the black aurora, show that electrons are accelerated upwards there, and the transverse potential drops measured are closely correlated with the energy of the upgoing electrons. Again U-shaped potential structures, but now with reversed electric fields, may be used as a model.

Langmuir waves excited by the precipitating electrons have been observed by rockets, between 500 and 1000 km [7]. They propagate nearly parallel to the geomagnetic field, and the waves have been correlated to electron fluxes with energies of the order of keV. Strong modulations of the fluxes have been observed so the velocities are dispersed when the beam propagates towards lower altitudes - similar to the scenario discussed for excitation of waves in the solar wind plasma. The waves appear in bursts, and duration of 0.1 s and peak amplitudes up to 500 mV/m have been measured. Evidence of positive slopes in the velocity distribution, parallel to the geomagnetic field, has also been obtained. To explain the spiky nature of the waves, numerical simulations of strong Langmuir turbulence have been made. However, the formation of coherent, collapsing wave packets was not observed for the ionospheric parameters (Newman et 1994 [8]), and another mechanism for localising wave energy has been proposed (Muschietti et al. 1995 [8]). This is based on the kinetic interaction between streaming electrons and a localised Langmuir wave packet. This may tap energy from an electron beam and in this way further localise the wave energy (Fraiman and Kostyukov 1993 [8]).

It has also been suggested that beam-plasma interaction at much lower altitudes may explain the narrow density spikes observed there. In the night-side auroral zone the plasma density has a maximum at about 100 km (the E-layer) caused by ionisation due to precipitating electrons. Measurements in radar scattering experiments have shown a fine structure in the form of narrow density spikes, with extents of less than 5 km, which are observed in the height range 110 - 150 km on the top side of the E-layer (Wahlund and Opgenoorth 1989 [9]). It is not possible to explain such structures without introducing localised electric fields, and these authors suggested that waves, produced by electron beam-plasma instability, may reach such a high amplitude, that the electron energy in the oscillatory motion exceeds the ionisation energy of the neutral gas. More recently Schlesier et al. 1997 [9] used the same technique to study the auroral density spikes, and strong Langmuir turbulence was proposed to generate them (Mishin and Telegin 1989 [9]). Similar density spikes have been observed in recent experiments in beam-plasma discharges, described in Section 5, but any possible connection has not yet been explored. Any measurement of hf fields at these altitudes does not seem to have been performed so localised dc fields may also generate the density spikes. Striations in gas discharge plasmas is a similar phenomenon in this case.

Altitude distributions of luminosities for homogeneous auroral arcs agree

fairly well with the luminosities that are calculated by assuming only collisional interaction between precipitating electrons and the neutral gas (Rees 1989 [9]). However, narrow layers having strongly enhanced luminosities and altitude extensions of only a few kilometres also exist at the same altitudes as the density spikes (Oguti 1975 [9], Stenbaek-Nielsen and Hallinan 1979 [9], Mishin et al. 1981 [9]). They have been called enhanced aurora (Hallinan et al. 1985 [9]). The characteristics of the density spikes agree with the characteristics of the luminous layers in several respects, and it has been proposed that the two types of layers are identical.

4. Electron beam-plasma discharges and high frequency probes

Many experimental investigations of nonrelativistic beam-plasma interaction have been done in beam-plasma discharges where an energetic electron beam is shot into neutral gas. For sufficiently low neutral gas density, the beam-plasma discharge is not ignited because only primary electrons ionise the gas, and the population of secondary electrons is negligible. The beam electrons are neutralised by the positive ions. This type of discharge is usually called "quasineutral electron beam". When the neutral density is increased so the background pressure becomes typically 10^{-3} mm Hg, the beam-plasma discharge is suddenly ignited at a certain threshold pressure. The electron number density may increase by several orders of magnitudes, and it becomes much higher than the beam density (Nezlin 1993 [10]). The important feature at the transition is that the dc plasma potential now is such that a significant fraction of the beam electrons can be trapped in the discharge volume, after the velocity dispersion by beam-plasma interaction. The beam energy can then be used efficiently for excitation and ionisation of the background gas. Assuming a given energetic tail in the electron velocity distribution, the plasma in a beam-plasma discharge is maintained in the same way as the positive column of a low pressure arc, operating in the "ion free fall regime" (Tonks and Langmuir 1929 [10]). The well-known pressure threshold for this type of plasma (e. g. Poletaev 1951 [10]) is similar as the threshold observed for beam-plasma discharges. The conditions discussed above also holds when a weak axial magnetic field, which does not perturb the ion motion significantly, is present. There is also a critical limit for the power of the beam which must be sufficient to maintain the discharge.

As proposed by many authors, also the high frequency field may be of importance for the heating of the electron gas, that is, some of the wave energy, originating from the beam, is transferred back to the electrons (e. g. Getty and Smullin 1963). This statement is of course trivial if the electric hf field is so strong that the energy in the oscillatory electron motion exceeds the ionisation energy during a significant fraction of the period, as discussed in the Sections 3 and 5 in connection with localised hf spikes.

A device for beam-plasma discharges, used in recent experiments at the Alfvén Laboratory, is shown in Fig. 2. There is a plane Lanthanum Hexaboride cathode in the right part of the tank. The end plate to the left is at floating potential, and all the current flows across the weak magnetic field until the electrons hit the anode ring which is concentric with the cathode. In this

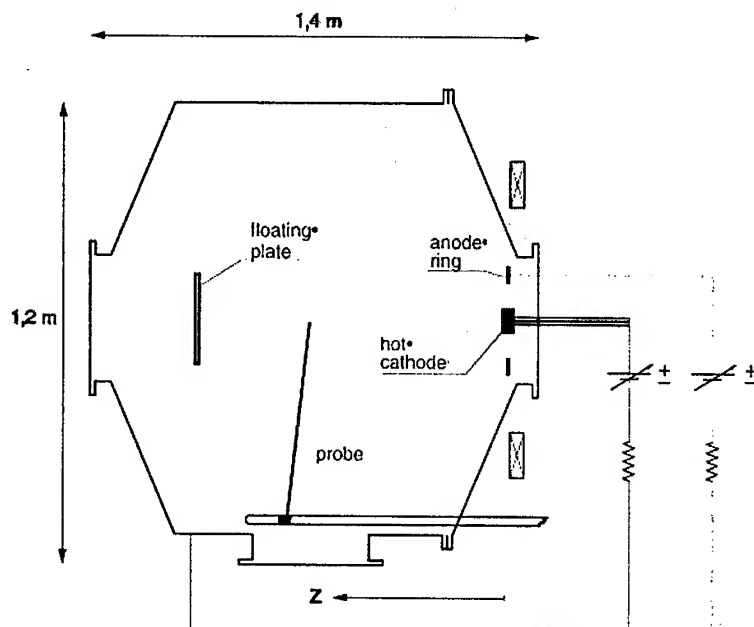


FIG. 2. Electron beam-plasma discharge used at the Alfvén Laboratory. Electrons are emitted from a plane, hot Lanthanum Hexaboride cathode, placed opposite to a plate kept at floating potential. The electric current flows across the weak magnetic field to the anode ring which is concentric with the cathode. In this way a beam-plasma discharge can be maintained at lower neutral gas densities than in a straight discharge (from Gunell et al. 1996b [11]).

configuration a beam-plasma discharge can be maintained at lower background pressure than in a straight discharge. Typical parameters are $n_e \approx 2 \cdot 10^{18} \text{ m}^{-3}$, $T_e \approx 6 - 8 \text{ eV}$. The background pressure for argon is typically 10^{-4} mm Hg .

Probes represent a simple diagnostic tool in beam-plasma discharges, and good estimates of the absolute electric field level can be obtained for frequencies up to 1 GHz (Torvén et al. 1995 [11]). A single probe with a coaxial outer conductor is not suitable for such measurements since the potential of the outer conductor is badly defined, and double probes must be used. In the simplest construction the probe tips are just the continuation of the inner conductors of two miniature coaxial cables. The outer conductors are carefully joined at the probe tips to have a common potential there. This unknown potential is eliminated by taking the difference signal. Since it is not possible to maintain a high and frequency independent impedance in the circuit, matched ($R = 50 \Omega$) cables are preferable. The probe tips can then be considered as short circuited. The generator EMF is approximately given by $E_0 b$ where E_0 is the field to be measured and b is the distance between the probe tips which is of the order of the Debye length. This holds for wave lengths much longer than b and wire radii much less than b . The short circuiting condition requires that surface charges $\pm q$ generate an EMF equal to q/C which counteracts the EMF due to E_0 . Here C is the capacitance between the probe tips. The net potential drop

accordingly vanishes for $q/C = E_0 b$, and the displacement current due to surface charges becomes $i\omega C E_0 b$ for a harmonically varying E_0 . This relation between the current measured and E_0 holds for not too short probe tips which can be checked in calibration experiments without plasma.

To obtain the relative magnitudes of the displacement current and the plasma conduction current in a particular plasma experiment, one can measure how the signal level varies with the dc bias of the probe when a constant field level is measured in the plasma. In tests (Torvén et al. 1995 [11]), where the frequency of the wave field is of the order of the plasma frequency (400 MHz), the signal level is constant for dc biases above the plasma potential. Then it decreases in an interval below plasma potential by typically some ten percent before it finally reaches a new constant level at potentials well below plasma potential. The lower level may be identified with the displacement current. However, the small difference in the signals shows that the conduction current is of little significance at the frequencies considered and when b is of the order of the Debye length.

The main disturbance of the plasma comes from the probe shafts. To avoid the presence of the shafts within the beam-plasma discharge, the probe tips can be connected with the coaxial cables by two thin wires which are wound in a spiral structure (Gunell et al., 1996a [11]). This structure does not pick up any hf current which is checked in calibration experiments. The qualitative picture is that the effect of the electric charge, that accumulates in one half-turn of the spiral as a response to hf field, is cancelled by the charge on the neighbouring half-turn. In this way several probes can be kept as close as 5 - 10 mm from each other in simultaneous measurements without introducing a severe perturbation of the plasma.

5. Experimental investigations of electron beam-plasma interaction in strong density gradients

A zero-order density gradient, which is maintained by processes approximately independent of the beam-plasma interaction, may lead to a sharp spatial concentration of the hf field in spikes which disperse the beam velocities in the gradient region. In laboratory plasmas this means that all the interaction may occur already in the gradient in front of the hot cathode or the electron gun which injects the beam. This effect has recently been studied experimentally in weakly magnetized plasmas [11], but it has also been observed in a strongly magnetised plasma (Bollinger et al. 1974 [11]). Observations of strong scattering of the beam in a thin layer (the "meniscus") in the presheath of a cathode were published a long time ago [12]. Strong scattering of beam electrons by a localised structure was also observed by Nezlin 1964 [12]. In this Section recent experiments will be reviewed and compared with particle simulations in the case when the beam moves towards increasing density. In a recent experiment (McFarland and Wong 1998 [11]) it was shown that localisation of wave energy occurs also for decreasing density in the beam direction.

5.1. Beam-plasma interaction at an electric double layer

An electric double layer is characterised by a density minimum at the double layer position, and the electron beam formed will move in a region with increasing density. Investigations of such a beam-plasma system (Gunell et al.1996a [11]) are reviewed here. A modified version of the device shown in Fig. 2 was used to generate the double layer. A background plasma was generated by discharges from filaments at the wall. The double layer was formed by applying a voltage to an anode plate, and a beam-plasma discharge was obtained between the double layer and the anode plate. By varying the discharge current, the double layer can be moved to different axial positions. A weak magnetic mirror field (typically 15 Gauss at the double layer) was used to stabilise the position of the double layer. Typical parameters were $\omega_p \approx 2.1$ GHz, $v_b/v_t \approx 3.5$, $n_b/n \approx 0.03$, and $\Delta v_b \approx 0.1v_b$. Here v_b is the beam velocity, v_t the thermal velocity, n_b the beam density, and Δv_b the full half-width of the estimated beam distribution.

Fig. 3 shows time averaged profiles of the hf field, the plasma density, and the plasma potential, including the double layer potential profile.

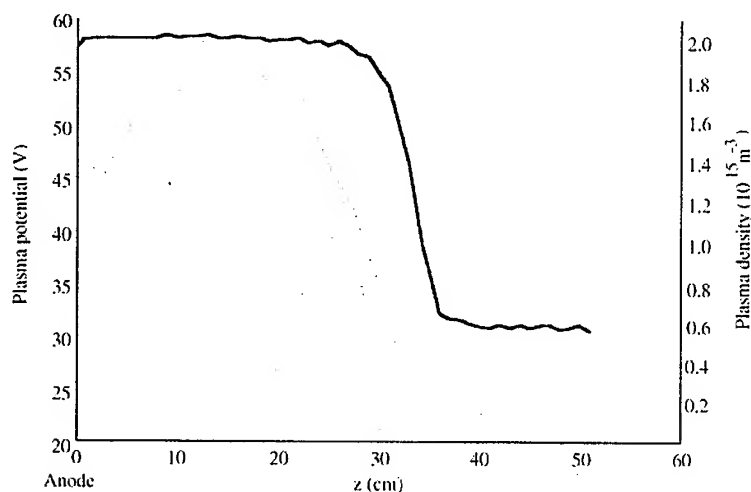


FIG. 3. Profiles of the plasma potential with the double layer drop (full thick line), the plasma density (full thin line), and the time averaged hf field level (broken-dotted line) (from Gunell et al. 1996 [11]).

The potential drop over the double layer was close to 30 V. The high frequency field is concentrated to the region where the density has a gradient. As will be shown below by time resolved measurements, there is a narrow hf spike moving irregularly back and forth which gives rise to the time averaged hf signal. Fig. 4 (a) shows the time resolved field. It has a dominating harmonic at about 350 MHz, which is close to the plasma frequency, and a maximum level of about 4 kV/m. The field appears as short wave packets which give rise to the fast amplitude modulations shown in Fig. 4 (b). There are also strong modulations on the ion acoustic time scale, as shown in Fig. 4 (c), and these have a simple

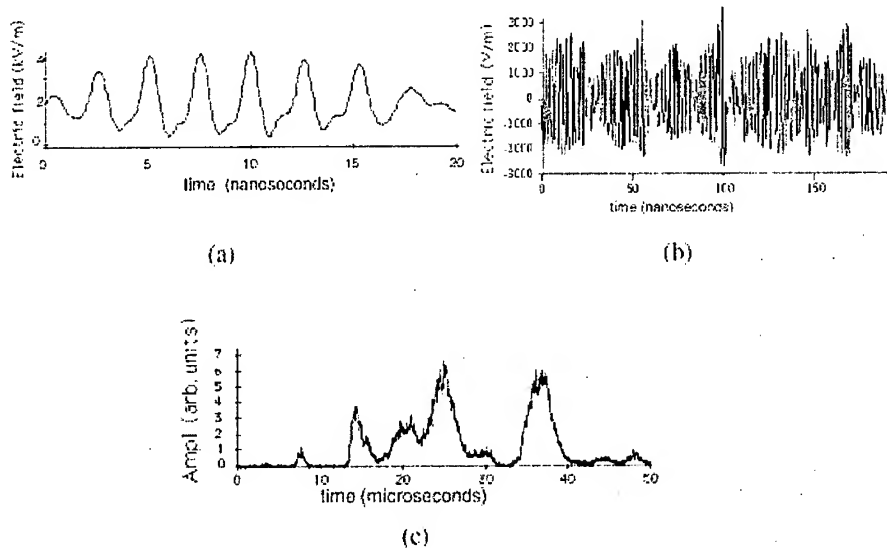


FIG. 4. Examples of hf field oscillations. (a). The field oscillates close to the plasma frequency and appears as wave packets which give rise to the fast amplitude modulations shown in diagram (b). Characteristic amplitude modulations on the ion time scale are shown in the lower diagram (from Gunell et al. 1996 [11]).

explanation as is shown below.

Probe measurements show that ion acoustic density fluctuations with rms values up to 20 low frequency fluctuations in the wave frequency, wave length, and growth of the high frequency waves. Time resolved measurements are therefore necessary to obtain the true hf field profiles. Simultaneous measurements were done with three probes which were aligned in the beam direction. The signal was triggered on the maximum level of the middle probe, and the two other probes were moved to different positions, starting from a minimum separation of less than 1 cm between the probes, and their maximum signals were measured within ± 10 ns from the triggering point to allow for propagation of the waves. The result is shown in Fig. 5 where the crosses denote the time resolved hf spike. This is much more narrow than the time averaged spike, which is also shown for comparison. Its full width at half maximum is only about 1.8 cm or less than two wave lengths of the wave mode in the ambient plasma. Similar results were obtained when the triggering probe was moved to different positions within the time averaged hf region, showing that the spike has an irregular motion back and forth. Additional tests confirmed this. The apparent motion is partly caused by the fluctuations in the double layer position, but it was concluded that fluctuations of the growth and damping rates, due to low frequency density fluctuations, also contribute. The apparent ion acoustic modulations of the hf-field (Fig. 4 (c)), measured by a stationary probe, are accordingly simply caused by the spike passing the probe.

Time averaged correlation measurements indicated that the slow beam mode,

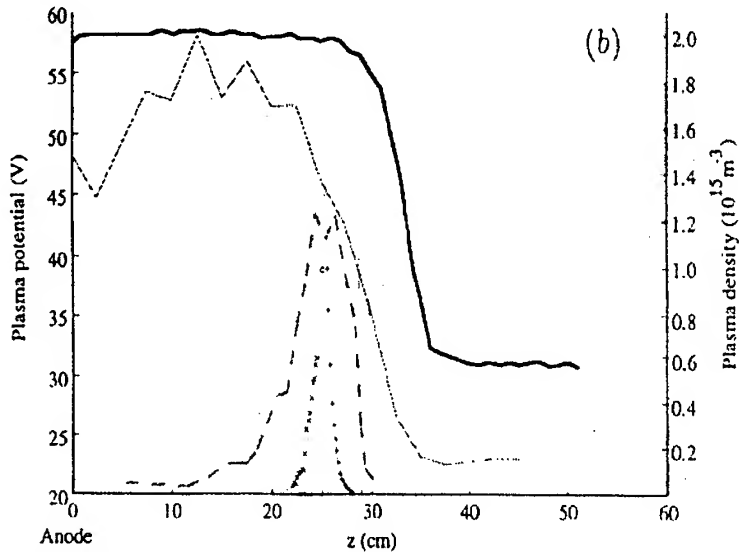


FIG. 5. The time resolved hf spike (crosses). This is much more narrow than the time averaged spike which is shown for comparison (from Gunell et al. 1996 [11]).

as evaluated theoretically for an infinitely long and axially homogeneous plasma ([14], Löfgren and Gunell 1998 [13]), dominated. The amplitude variation in the hf spike may formally be interpreted in terms of growth and damping, and exponential fits were good over nearly two orders of magnitudes. Approximate agreement with the spatial growth for a thin beam in homogeneous plasma (O'Neil and Malmberg 1968 [14]) was obtained, and the maximum field observed agreed approximately with saturation by wave trapping (Kainer et al. 1972 [14]). The damping showed agreement with linear Landau damping by the ambient plasma. However, new experiments described below and a closer examination of the results (Löfgren and Gunell 1997 [14], Löfgren and Gunell 1998 [13]) showed that the hf spike hardly can be explained by growth rates evaluated for homogeneous plasmas and that the hf spike may be connected with plasma diode resonances and wave reflection.

5.2. Beam-plasma interaction in the gradient in front of a plane cathode

Measurements have also been performed in the density gradient in front of a plane Lanthanum Hexaboride cathode to increase the parameter range (Gunell et al. 1996b [11], Gunell and Löfgren 1997 [11]). Here the device shown in Fig. 2 was used. Beam energies of 35, 95, and 210 eV, determined by the cathode sheath voltage drops, were applied. The cathode had no control grids, and a density gradient existed in the sheath and the pre-sheath region. The existence of a hf spike in this region was confirmed by simultaneous measurements with three probes as described above. Here the measurements were also combined with conditional sampling to get space-time diagrams of the electric field amplitude in the plasma. Time records of the field were measured by the three probes. The

following two conditions were applied to select subsets of the data in the 35 eV case considered here. The wave amplitude at the position of the triggering probe should be constant, within 1%, over at least two wave periods, and the amplitude should be between 1 and 1.5 kV/m. The maximum amplitude observed was about 3 kV/m. The result is shown in the grey scale plot in Fig. 6 (a) with

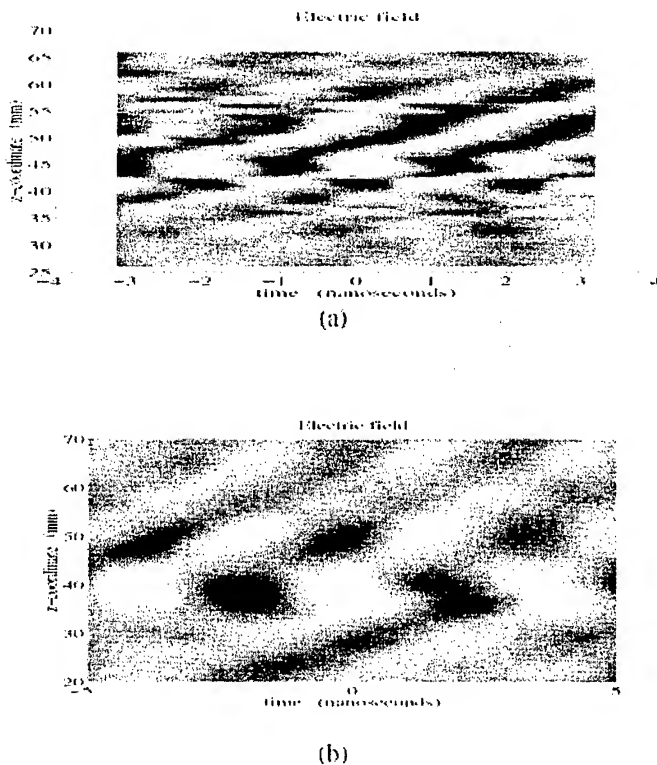


FIG. 6. The upper diagram shows a measured space-time diagram for the electric field amplitude, given in grey scale with white as maximum. The hf spike appears as a standing wave at $z \approx 45$ mm, and it is surrounded by regions where propagating waves dominate. The lower diagram shows a simulated space-time diagram using the same parameters as in the experiment. The hf spike appears between 35 and 40 mm (from Gunell et al. 1996 [11]).

white is maximum amplitude. $z=0$ represents the cathode surface. At $z = 45$ mm a structure is seen which was interpreted as a standing wave. This is surrounded by regions where forward propagating waves are dominating.

The PIC code PDP1 was used to compare the experimental results with simulations. The diode was initially filled with plasma. The initial ion density varied linearly between $z = 0$ and $z = 100$ mm which was similar to the ion density variation in the experiment. The density was then constant up to $z = 300$ mm. Electrons with a temperature of 0.15 eV were injected and self-consistently accelerated up to an energy of 35 eV in the cathode sheath and the pre-sheath that formed. The beam density was 5% of the electron density in the homo-

geneous plasma region. Fig. 6 (b) shows a space-time plot of the electric field in the simulations, recorded between 3 and 3.01 μs . Here a high level of ion sound fluctuations have not had time to develop so conditional sampling was not necessary. The similarity between experiments and simulation is obvious. As in the experiments, there is a central region at about $z = 40$ mm with a standing wave. This is surrounded by regions with an interference pattern where the forward travelling wave dominates. Thus a similar spike is obtained as in the experiments.

Fig. 7 shows eleven plots of the instantaneous electric field profiles, covering a half-period of the oscillation period and taken between simulation times of 2.006 and 2.008 μs . The hf spike appears as a standing wave. The corresponding

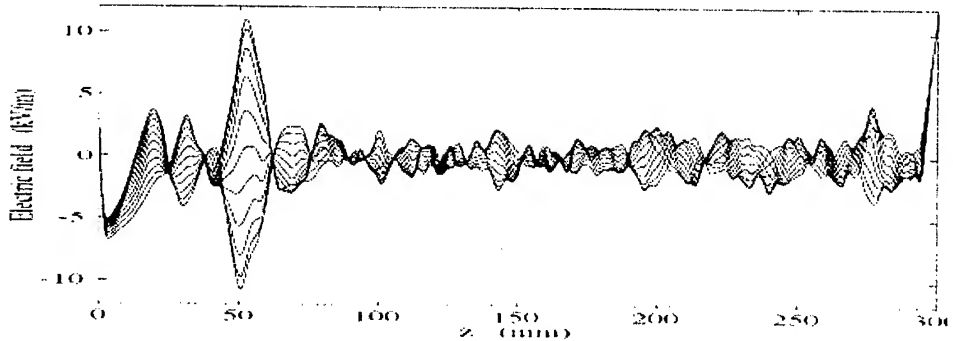


FIG. 7. Simulated electric field profiles shown during a half-period. The hf spike appears as a standing wave at $z \approx 50$ mm, and it is surrounded by regions where waves propagating forwards are dominating. The initial plasma density varied linearly between $z = 0$ and $z = 100$ mm and was constant between 100 and 300 mm (from Gunell et al. 1996 [11]).

density profile showed a deep density cavity at the position of the hf spike after 3 μs . However, the hf spike forms long before any evidence of the density cavity, showing that cavity formation is a secondary effect. Phase space diagrams from the simulations show that the beam velocity is entirely dispersed at the position of the hf spike.

More recent experiments in a beam-plasma discharge by Gunell et al. 1998 [11] showed that the hf field in the spike can be as strong as about 40 kV/m. The kinetic energy in the oscillatory electron motion then exceeded the ionisation potential of the background gas during a significant fraction of the wave period. A density spike was then formed at the position of the hf spike due to enhanced ionisation when the background density of neutral atoms was sufficiently high. Enhanced luminosity in a thin layer was also observed. Such spikes may be connected with the density spikes observed on the top side of the E-layer in the auroral zone (see Section 3).

Plasma diodes with strong zero order gradients in density and potential have been used to obtain theoretical models of beam-plasma interaction in inhomogeneous plasmas. The resonances and eigenfrequencies of a plasma diode with

a realistic zero-order gradient were studied theoretically by Leavens and Love 1970 [13], using the linearised Vlasov-Poisson equations for the time dependent variables. It was concluded that a weak beam gives only a slight perturbation of the eigenfrequencies and that instability is confined to only a few modes. Theoretical models and particle simulations have also been used to show that the spatial growth rate is reduced and the Landau damping rate is increased due to the inhomogeneity (Lin and Rowe 1972 [13]). Resonances in inhomogeneous plasma diodes, without beams, have been studied for a long time (e. g. Herlofson 1951 [13], Crawford and Harker 1972 [13], Ku et al. 1998 [13]). A linearized fluid model was used by Löfgren and Gunell 1998 [13] to evaluate the eigenmodes in a diode with a density gradient that started from vanishing density at the low potential boundary and varied linearly up to the homogeneous region of the diode. No beam was applied. Waves were found in the region where $\omega > \omega_p$, that is, between the low potential boundary and the density gradient, and the waves were reflected at points determined by the local plasma frequency. The wave pattern had a shape similar to the one given by Airy functions, as expected. Since the amplitude was strongly enhanced at the cut-off point, wave reflection was proposed as one candidate for the hf spike. In the PIC-simulations reported by the same authors, a beam was present, and two eigenmodes were clearly observed. In this case waves were also observed beyond the cut-off point, where $\omega < \omega_p$. In this region wave modes similar to the slow space charge wave mode may grow and propagate, being excited by the wave field at cut-off. Evidence of this has recently been obtained in a theoretical diode model (Löfgren, to be published).

6. Conclusions

Much of the research of low power beams in plasmas is now concentrated on space plasmas where electron beams are generated due to acceleration processes. Space experiments have to some extent replaced laboratory experiments and posed problems connected with inhomogeneous beams and background plasmas, as the complex wave growth process in the solar wind shows. The spatial localisation of the wave energy is another problem. Localised wave generation may be caused by density fluctuations in the ambient plasma which give rise to fluctuating growth and damping rates in a marginally stable state. Strong turbulence is also a possibility. An electron beam may also transfer energy to a packet of Langmuir waves and thereby localise the wave energy. This has been proposed to explain the wave localisation in the auroral zone. The hf spikes formed in density gradients represent another localisation mechanism which also should work for gradients caused by low frequency density fluctuations with appropriate wave lengths in the ambient plasma. The electrostatic energy density in the hf spikes can exceed the thermal energy density in beam-plasma discharges where the hf spikes also may generate density spikes by enhanced ionisation. Small scale laboratory experiments with well controlled parameters, combined with particle simulations and theoretical models to interpret the experimental data, represent a powerful method to attack problems connected with inhomogeneous beams and plasmas. It is expected that investigations of beam-plasma interaction should

be strongly concentrated on inhomogeneous systems in the future. Small scale laboratory experiments will hopefully be an important part of this work, because such experiments are needed, not only for checking theoretical models, but also for disclosing new phenomena in plasmas.

Acknowledgement

The author thanks dr M. Raadu for valuable discussions.

References

1. D.A. GURNETT and R.R. ANDERSON, *Science*, **194**, 1159, 1976; D.A. GURNETT and R.R. ANDERSON, *J. Geophys. Res.*, **82**, 632, 1977; R.P. LIN, D.W. POTTER, D.A. GURNETT and F.L. SCARF, *Astrophys. J.*, **251**, 364, 1981; R.P. LIN, W.K. LEVEDAHL, W. LOTKO and D.A. GURNETT, *Astrophys. J.*, **308**, 954, 1986; G.B. HOSPODARSKY and D.A. GURNETT, *Geophys. Res. Lett.*, **22**, 1161, 1995; G.A. DULK, Y. LEBLANC, P.A. ROBINSON, J.L. BOUGERET and R.P. LIN, *J. Geophys. Res.*, **103**, 17223, 1998; R.E. ERGUN, D. LARSON, R.P. LIN, J.P. MCFADDEN, C.W. CARLSON, K.A. ANDERSSON, L. MUSCHIETTI, M. MCCARTHY, G.K. PARKS, H. REME, J.M. BOSQUED, C. D'USTON, T.R. SANDERSON, K.P. WENZEL, M. KAISER, R.P. LEPPING, S.D. BALE, P. KELLOG and J.-L. BOUGERET, *Astrophys. J.*, **503**, 435, 1998.
2. V.L. GINZBURG and V.V. ZHELEZNYAKOV, *Soviet Astron. A. J.*, **2**, 653, 1958; D.B. MELROSE, *Space Sci. Reviews*, **26**, 3, 1980; M.V. GOLDMAN, G.F. REITER and D.R. NICHOLSON, *Phys. Fluids*, **23**, 388, 1980.
3. P.A. STURROCK 1964, "AAS-NASA Symp. on the Physics of Solar Flares", p. 357 (Editor W. N. Hess, NASA SP-50, Washington, D. C. 1964); D.D. RYUTOV and R.Z. SAGDEEV, *Sovj. Phys. JETP*, **31**, 396, 1970; V.V. ZAITSEV, N.A. MITYAKOV and V.O. RAPOPORT, *Solar Phys.*, **24**, 444, 1972; B.N. LEVIN, *Solar Phys.*, **92**, 317, 1984; T. TAKAKURA and H. SHIBAHASHI, *Solar Physics*, **46**, 323, 1976; Magelssen and Smith 1977; R.J.M. GROGNARD, *Solar Phys.*, **81**, 173, 1980; L. MUSCHIETTI, *Solar Physics*, **130**, 201, 1990; M.J. REINER, J. FAINBERG and R.G. STONE, *Science*, **270**, 461, 1995; V.N. MELNIK and E.P. KONTAR, *Physica Scripta*, **58**, 510, 1998.
4. S.A. KAPLAN and V.N. TSYTOVITCH, *Astron. Zh.*, **44**, 1036, 1967 (*Soviet Astron. AJ*, **11**, 956, 1968); S. BARDWELL and M.V. GOLDMAN, *Astrophys. J.*, **209**, 912, 1976; D.F. SMITH, *Astrophys. J.*, **216**, L 53, 1977; R.J.M. GROGNARD, *Solar Physics*, **81**, 173, 1980.
5. V.E. ZHAKAROV, Z.H. EKSPERIM, *Teor. Fiz.*, **62**, 1745, 1972 (*Soviet Phys. JETP* **35**, 908, 1972); K. PAPADOPOULOS, M.L. GOLDSTEIN and R. A. SMITH, *Astrophys. J.*, **190**, 175, 1974; S. BARDWELL and M.V. GOLDMAN, *Astrophys. J.*, **209**, 912, 1976; D.R. NICHOLSON, M.V. GOLDMAN, P. HOYNG and J.C. WEATHERALL, *Astrophys. J.*, **223**, 605, 1978; B. HAFIZI, J.C. WEATHERALL, M.V. GOLDMAN and D.R. NICHOLSON, *Phys. Fluids*, **25**, 392, 1982; G.D. DOOLEN, D.F. DUBOIS and H.A. ROSE, *Phys. Rev. Lett.*, **54**, 804, 1985; P.Y. CHEUNG and A.Y. WONG, *Phys. Fluids*, **28**, 1538, 1985; D.L. NEWMAN, P.A. ROBINSON and M.V. GOLDMAN, *Phys. Rev. Lett.*, **62**, 2132, 1989; C.T. DUM, *J. Geophys. Res.*, **95**, 8095, 1990; M.D. MCFARLAND and A.Y. WONG, *Phys. Plasmas*, **4**, 945, 1997; P.A. ROBINSON, *Reviews of Modern Physics*, **69**, 507, 1997.
6. D.F. SMITH and D. SIME, *Astrophys. J.*, **233**, 998, 1979; L.M. CELNIKIER, L. MUSCHIETTI and M.V. GOLDMAN, *Astron. Astrophysics*, **181**, 138, 1987; P.A. ROBINSON, *Solar Phys.*, **139**, 147, 1992; P.A. ROBINSON, *Phys. Plasmas*, **3**, 192, 1996; P.A. ROBINSON, *Sol. Phys.*, **168**, 357, 1996; I.H. CAIRNS and P.A. ROBINSON, *Physics of Space Plasmas*, 13 (Ed. T. Chang and J. E. Jasperse, MIT, Cambridge, MA) p.223, 1995; I.H. CAIRNS and P.A. ROBINSON, *Physics of Space Plasmas*, 14 (Ed. T. Chang and J.E. Jasperse, MIT, Cambridge, MA, 105, 1995).
7. F.S. MOZER, C.A. CATELL, M. K. HUDSON, R.L. LYSAK, M. TEMERIN and R.B. TORBERT, *Space Sci. Rev.*, **27**, 155, 1980; J.P. MCFADDEN, C.W. CARLSON and M.H. BOEHM, *J. Geophys. Res.*, **91**, 12079, 1986; M. TEMERIN, J. MCFADDEN, M. BOEHM, C.W. CARLSON and W. LOTKO, *J. Geophys. Res.*, **91**, 5769, 1986; J. MCFADDEN, C.W. CARLSON and M.H. BOEHM, *J. Geophys.*

- Res., **92**, 11133, 1987; R.E. ERGUN, C.W. CARLSON, J.P. MCFADDEN, J. H. CLEMMONS and M.H. BOEHM, J. Geophys. Res., **96**, 225, 1991; G. MARKLUND and T. KARLSSON, J. Geophys. Res., **102**, 17509, 1997; R.E. ERGUN et al., Geophys. Res. Lett., **25**, 2025, 1998.
8. D.L. NEWMAN, M.V. GOLDMAN, R.E. ERGUN and M.H. BOEHM, J. Geophys. Res., **99**, 6367, 1994; D.L. NEWMAN, M.V. GOLDMAN and R.E. ERGUN, J. Geophys. Res., **99**, 6377, 1994; G.M. FRAIMAN and I.Yu. KOSTYUKOV, Physica Scripta, **47**, 221, 1993; L. MUSCHIETTI, I. ROTH and R. ERGUN, Phys. Plasmas, **1**, 1008, 1994; L. MUSCHIETTI, I. ROTH and R. ERGUN, J. Geophys. Res., **100**, 17481, 1995.
9. T. OGUTI, J. Atm. Terr. Phys., **37**, 1501, 1975; H.C. STENBAEK-NIELSEN and T.J. HALLINAN, J. Geophys. Res., **84**, 3257, 1979; E. MISHIN, V. IVCHENKO and G. MILINEVSKI, Adv. Space Res., **1**, 163, 1981; T.J. HALLINAN, H.C. STENBAEK-NIELSEN and C.S. DEEHR, J. Geophys. Res., **90**, 8461, 1985; M. REES, Physics and Chemistry of the Upper Atmosphere, Cambridge University Press, New York, 1989; J.-E. WAHLUND and H.J. OPGENOORTH, J. Geophys. Res., **94**, 17223, 1989; E. MISHIN and V. TELEGIN, Geomagnetism and Aeronomy (English Ed.), **29**, 1, 1989; A. SCHLESIER, E. MISHIN and K. SCHLEGEL, Geophys. Res. Lett., **24**, 1407, 1997.
10. L. TONKS and I. LANGMUIR, Phys. Rev., **34**, 876, 1929; I.A. POLETAEV, Zh. Tekh. Fiz., **21**, 1021, 1951; W.D. GETTY and L.D. SMULLIN, J. Appl. Phys., **34**, 3241, 1963; M.V. NEZLIN, *Physics of Intense Beams in Plasmas*, Institute of Physics Publishing, Bristol, 1993;
11. L.D. BOLLINGER, W. CARR, H. LIU and M. SEIDL, Phys. Fluids, **17**, 2142, 1974; Yu.Ya. BRODSKII, S.I. NECHUEV, YA.Z. SLUTSKER, A.M. FEIGIN and G.M. FRAIMAN, Sov. J. Plasma Phys., **15**, 688, 1989; S. TORVÉN, H. GUNELL and N. BRENNING, J. Phys. D: Appl. Phys., **28**, 595, 1995; H. GUNELL, N. BRENNING and S. TORVÉN, J. Phys. D: Appl. Phys., **29**, 643, 1996; H. GUNELL, J.P. VERBONCEUR, N. BRENNING and S. TORVÉN, Phys. Rev. Lett., **77**, 5059, 1996; H. GUNELL and T. LÖFGREN, Phys. Plasmas, **4**, 2805, 1997; H. GUNELL, R.H. SCHRITTWIESER and S. TORVÉN, Phys. Lett. A, **241**, 281, 1998; M.D. MCFARLAND and A.Y. WONG, Phys. Rev. Lett., **80**, 5540, 1998; M. WENDT and T. KLINGER, to be published.
12. H.J. MERRIL and H.W. WEBB, Phys. Rev., **55**, 1191, 1939; T.K. ALLEN, R.A. BAILY and K.G. EMELEUS, British J. Appl. Phys., **6**, 320, 1955; D.W. MAHAFFEY, G.C. MCCULLAGH, A. GARSADDEN and K.G. EMELEUS, Proc. Roy. Irish Acad., **61A**, 77, 1961; M.V. NEZLIN, Sov. Phys. JETP, **19**, 26, 1964.
13. N. HERLOFSON, Arkiv f. Fysik, **3**, 247, 1951; W.M. LEAVENS and C.H. LOVE, Phys. Fluids, **12**, 330, 1969; W.M. LEAVENS and C.H. LOVE, Phys. Fluids, **13**, 732, 1970; A.T. LIN and J.E. ROWE, Phys. Fluids, **15**, 171, 1972; F.W. CRAWFORD and K.J. HARKER, J. Plasma Phys., **8**, 261, 1972; C. WAHLBERG, J. Plasma Physics, **18**, 415, 1977; Yu.Ya. BRODSKII, S.I. NECHUEV, YA.Z. SLUTSKER, A.M. FEIGIN and G.M. FRAIMAN, Sov. J. Plasma Phys., **15**, 688, 1989; G.M. FRAIMAN and I.Yu. KOSTYUKOV, Physica Scripta, **47**, 221, 1993; S. KUHN, Contrib. Plasma Phys., **34**, 495, 1994; T. LÖFGREN and H. GUNELL, Phys. Plasmas, **5**, 590, 1998; V.P.T. KU, B.M. ANNARATONE and J.E. ALLEN, J. Appl. Phys., **84**, 6536, 1998; V.P.T. KU, B.M. ANNARATONE and J.E. ALLEN, J. Appl. Phys., **84**, 6546, 1998;
14. T.M. O'NEIL and J.H. MALMBERG, Phys. Fluids, **11**, 1754, 1968; J.R. APEL, Phys. Fluids, **12**, 291, 1969; S. KAINER, J. DAWSON, R. SHANNY and T. COFFEY, Phys. Fluids, **15**, 493, 1972; L. MUSCHIETTI and C.T. DUM, Phys. Fluids B, **3**, 1968, 1991; T. LÖFGREN and H. GUNELL, Phys. Plasmas, **4**, 3469, 1997.

Topical invited lectures

MODELING OF RADIO-FREQUENCY AND DIRECT CURRENT GLOW DISCHARGES IN ARGON

A. BOGAERTS and R. GIJBELS

DEPARTMENT OF CHEMISTRY, UNIVERSITY OF ANTWERP

Universiteitsplein 1, B-2610 Wilrijk-Antwerp, Belgium

A hybrid modeling network, consisting of Monte Carlo, fluid and collisional-radiative models for the various plasma species (electrons, argon ions, fast argon atoms, argon atoms in various excited levels, copper atoms and ions, also in various energy levels) has been developed for glow discharges, both in the direct current (dc) and the capacitively coupled radio-frequency (rf) mode at 13.56 MHz. The typical results, like electrical characteristics, densities of the various plasma species, collisions in the plasma, cathode-sputtering and optical emission intensities, are presented and compared between the two operation modes. It is found that for the same input power and pressure, the rf-mode requires lower voltages than the dc-mode, in good correlation with experiment. The cathode-sputtering (erosion) rate and the optical emission intensities are, however, calculated to be more or less similar for both discharge modes, which is also in agreement with experiment.

1. Introduction

Glow discharges are used in a large number of application fields, e.g., the semiconductor industry (for etching and deposition of layers), the materials technology (for deposition of protecting films), the laser-, lamp- and plasma display panel industry, and also in analytical chemistry, for the spectroscopic analysis of solid materials (e.g., [1, 2]). In the latter application field, direct current (dc) discharges are very often applied, due to their simplicity and ease of operation. The material to be analyzed is then used as the cathode of the glow discharge, which is being sputtered by the plasma species. The sputtered atoms can become ionized or excited in the plasma. The so-formed ions can be measured in a mass spectrometer whereas the excited sputtered atoms create characteristic photons, which can be detected with an optical emission spectrometer. However, the straightforward application of a dc glow discharge is limited to the analysis of conducting materials, because non-conducting cathode materials would be charged up due to positive ion bombardment, preventing the cathode from being sputtered any further. To widen the application field to the analysis of

non-conducting materials as well, interest is nowadays being shifted to radio-frequency discharges, mainly at 13.56 MHz (e.g., [3, 4]). Indeed, the material to be analyzed serves now as the rf-electrode of the discharge, and charge accumulation due to positive ion bombardment can be neutralized due to negative charge accumulation by electron bombardment during part of the rf-cycle.

For good analytical practice, a thorough understanding of the glow discharge processes is desirable. We try to obtain this by modeling. Of course these models are not only valid for analytical glow discharges, but they can also be applied to glow discharges used in other application fields. In previous years we have developed a comprehensive modeling network (consisting of Monte Carlo, fluid and collisional-radiative models) for the various species present in a dc glow discharge, i.e., electrons, argon ions, fast argon ground state atoms, argon atoms in various excited levels, sputtered copper atoms and the corresponding ions, also in the ground state and in various excited levels (e.g., [5, 6, 7, 8, 9, 10, 11]). More recently, we have developed a similar model, consisting of the same sub-models, for a 13.56 MHz rf discharge (see e.g., [12, 13, 14, 15]). In the present paper, a brief overview of the modeling network is given, and some typical results are presented and compared for the two operation modes. The typical conditions for spectrochemical glow discharges are: argon discharge gas at several Torr pressure, 500-1200 V discharge voltage, 1 - 100 mA current and 1 - 100 W electrical power. The discharge cells are typically a few cm³ in volume.

2. Description of the models

In the literature, different modeling approaches are presented to describe glow discharges: analytical or global models (e.g., [16]), fluid approaches (e.g., [17]), collisional-radiative models (e.g., [18]), full solutions of the Boltzmann equation (e.g., [19]), Monte Carlo methods (e.g., [20]), particle-in-cell models (e.g., [21]) and hybrid combinations of the above mentioned models (e.g., [22]). All the above models have their particular advantages and disadvantages, i.e., some of the models give a quick prediction but are only crude approximations, whereas other models are more accurate but require a long calculation time. Therefore, we use a specific model depending on the type of plasma species to be described. Indeed, the "fast" plasma species, like fast electrons, which are not in equilibrium with the electric field (which means that the electrons gain more energy from the electric field than they lose locally by collisions), are treated with a Monte Carlo model, which is most accurate for such species. The "slow" plasma species, on the other hand, like slow electrons, atoms, ions in the bulk plasma, for which a Monte Carlo model would take a very long calculation time, are handled with a fluid model, because the "equilibrium-approach" is justified here. Furthermore, the atoms and ions in excited levels are described with a collisional-radiative model, which can be considered as a kind of fluid model. All the different models are then combined into a hybrid modeling network, to present an overall picture of the glow discharge. The different species assumed to be present in the plasma, and the models used to describe these species, are presented in Table 1. The Monte Carlo models are developed in three dimensions; the fluid and collisional-

radiative models are only in two dimensions, because the cell geometry to be simulated has a cylindrical symmetry, and hence the three dimensions could be reduced to two dimensions (axial and radial direction). In the following, each of these models will be briefly explained.

Table 1. Overview of the species assumed to be present in the plasma, and the models used to describe these species

Plasma species	Model
thermal Ar atoms	no model, assumed uniformly distributed
electrons	Monte Carlo model for fast electrons fluid model for slow electrons
Ar ions	fluid model (together with the slow electrons + coupled to Poisson equation) Monte Carlo model in sheath
fast Ar atoms (created from Ar ions by collisions)	Monte Carlo model in sheath
excited Ar atoms (65 levels)	collisional-radiative model
Cu atoms: thermalization process	Monte Carlo model
Cu atoms + ions: ground + excited levels	collisional-radiative model
Cu ions	Monte Carlo model in sheath

2.1. Monte Carlo model for the fast electrons

Electrons are emitted from the cathode or rf-electrode due to positive argon ion bombardment, and they are accelerated in the sheath due to the strong electric field. These electrons are followed with a Monte Carlo model, as well as the electrons created in the sheath by ionization collisions.

A large number of "super-electrons", corresponding to several "real" electrons, is followed, one after the other, as a function of time. During successive time-steps, their trajectory is calculated with Newton's laws, and their collisions are treated with random numbers. Indeed, the probability of collision during that time-step is calculated (yielding a value between 0 and 1) and compared to a randomly created number between 0 and 1. If the calculated probability is lower than the random number, no collision takes place. If the collision probability is higher than the random number, a collision event occurs. Collision processes taken into account in this model are elastic collisions with Ar atoms, electron impact ionization, excitation and de-excitation between the different Ar and Cu (excited) levels, and electron-electron Coulomb scattering. To determine which collision takes place, the partial collision probabilities of the various collision types are calculated, and the total collision probability (= the sum of the partial probabilities) is subdivided in intervals with lengths corresponding to these partial probabilities. Then, a second random number is generated and

the interval into which this random number falls, determines the type of collision that takes place. Further, the new energy and direction after collision are also determined by random numbers, based on energy conservation laws and on differential scattering cross sections. Then, the same procedure is repeated for the next electron during the same time-step, until all electrons are followed. Then, we proceed to the next time-step. This procedure is repeated during a large number of time-steps until (periodic) steady-state is reached. This happens already, in the rf-case at 13.56 MHz, after two rf-cycles (i.e., about $1.5 \cdot 10^7$ seconds). It should be mentioned that in the dc-case, the calculations can also be carried out independently of time.

In order to reduce the calculation time, only "fast" electrons are followed with this Monte Carlo model. When the electrons arrive in the bulk plasma and have energies lower than the threshold for inelastic collisions, they are "transferred to the slow electron group", to be followed with the fluid model (see below). More details of this Monte Carlo model can be found in Refs. [5, 6, 8, 12].

2.2. Fluid model for slow electrons, Ar ions and potential distribution

The slow electrons are followed with a fluid model, together with the Ar ions. The equations to be solved in this model are the first two (or three) moments of the Boltzmann transport equation, i.e., the mass continuity equations for slow electrons and Ar ions (Eqs. 2.1 and 2.2), and the momentum continuity equations for electrons and ions, which could be reduced to the transport equations, based on diffusion and drift in the electric field (Eqs. 2.3 and 2.4). Moreover, for the electrons also the electron energy balance equation is solved (Eq. 2.5). Finally, these equations are coupled to Poisson's equation, to obtain self-consistently the potential distribution from the electron and ion densities (Eq. 2.6):

$$(2.1) \quad \frac{\partial n_{Ar+}(z, r, t)}{\partial t} + \nabla \cdot \overline{j_{Ar+}}(z, r, t) = R_{Ar+}(z, r, t),$$

$$(2.2) \quad \frac{\partial n_e(z, r, t)}{\partial t} + \nabla \cdot \overline{j_e}(z, r, t) = R_e(z, r, t),$$

$$(2.3) \quad \overline{j_{Ar+}}(z, r, t) = \mu_{Ar+} n_{Ar+}(z, r, t) \overline{E}^{eff}(z, r, t) - D_{Ar+} \nabla n_{Ar+}(z, r, t),$$

$$(2.4) \quad \overline{j_e}(z, r, t) = \mu_e n_e(z, r, t) \overline{E}(z, r, t) - D_e \nabla n_e(z, r, t),$$

$$(2.5) \quad \frac{\partial w_e(z, r, t)}{\partial t} + \nabla \cdot \left(-\frac{5}{3} \mu_e w_e(z, r, t) \overline{E}(z, r, t) - \frac{5}{3} D_e \nabla w_e(z, r, t) \right) = -e \overline{j_e}(z, r, t) \cdot \overline{E}(z, r, t) - R_{w,e}(z, r, t),$$

$$(2.6) \quad \nabla^2 V(z, r, t) + \frac{e}{\epsilon_0} (n_{Ar+}(z, r, t) - n_e(z, r, t)) = 0, \overline{E} = -\nabla V,$$

where n and j are the argon ion and electron densities and fluxes, R_{Ar+} and R_e are the argon ion and electron creation rates, μ and D are the ion and electron mobility and diffusion coefficient, E and E^{eff} are the electric field and the effective electric field (as felt by the ions, see [12]), w_e is the electron energy density (i.e., ε_e times n_e), $R_{w,e}$ presents the energy loss by collisions, V is the electric potential, and e and ε_0 are the electron charge and vacuum permittivity, respectively.

These equations are strongly coupled and solving them is no straightforward mathematical problem. The method we used was developed by Goedheer and coworkers [23, 24] and is based on the Scharfetter-Gummel exponential scheme [25, 26].

Finally, it should be mentioned that the electrons in this fluid model, especially in the rf-case, can gain again some energy from the electric field, and they give rise to some more inelastic collision processes which should be taken into account in the model. In the rf-case, it was demonstrated that the ionization produced by these slow fluid-electrons which gain again sufficient energy from the oscillating electric field (i.e., so-called a-ionization) is clearly dominant compared to the ionization calculated in the Monte Carlo model [12]. Further details about this fluid model are found in Refs. [6, 8, 12].

2.3. Monte Carlo model for the Ar ions and fast Ar atoms

Because a fluid model is less suitable for species not in equilibrium with the electric field (which means that they gain more energy from the electric field than they lose by collisions), and since the Ar ions are not in equilibrium with the rather high electric field in the sheath region adjacent to the rf-electrode (cathode), these species are also described with a Monte Carlo model in this region. Furthermore, this model also treats the fast Ar atoms, which are created from the Ar ions in the sheath by charge transfer and momentum transfer scattering collisions. The principle is the same as for the electron Monte Carlo model. Collision processes incorporated in this Monte Carlo model are charge transfer collisions for the Ar ions, and momentum transfer collisions, ionization, excitation and de-excitation collisions for the different Ar and Cu excited levels, for both the Ar ions and fast Ar atoms. In this Monte Carlo model, the Ar ions and fast Ar atoms are also followed as a function of time, until periodic steady state is reached, which is the case after about 25 - 30 rf-cycles for these species. For more details, we refer to Refs. [7, 13].

2.4. Collisional-radiative model for the Ar excited levels

64 excited Ar levels are incorporated in this model. Some of them are individual levels (e.g., the 4s levels), but most of them are effective levels (i.e., a group of individual levels with similar excitation energy and quantum numbers). For each of these levels, a balance equation is solved, with different populating and depopulating processes. The processes taken into account include electron, Ar ion and atom impact ionization, excitation, de-excitation and three-body recombination for all levels, radiative recombination and radiative decay between all

levels, and Hornbeck-Molnar associative ionization for the levels with excitation energy above 14.71 eV. Moreover, for the Ar 4s levels some additional processes are incorporated, like Ar^*-Ar^* (associative) ionization, Penning ionization of sputtered Cu atoms, three-body collisions with Ar atoms, and radiation trapping for the resonant levels, which radiate to the Ar ground state. The radiation trapping is described by means of an escape factor, which represents the fraction of photons that can really escape from the plasma without being reabsorbed by the argon ground state atoms. Transport of the excited species (by diffusion) can be neglected with respect to the collision and radiation processes. The fact that all these processes are of collisional or radiative nature explains the name of this model. More information about this model can be found in Refs. [9, 14].

2.5. Monte Carlo model for the thermalization of the sputtered Cu atoms

When the Cu atoms are sputtered from the cathode (due to Ar ion, fast Ar atom and Cu ion bombardment), they have energies of 5 - 10 eV, which they lose almost immediately by collisions with the Ar gas atoms, until they are thermalized. Because this thermalization process occurs almost "immediately", it is finished before the Cu atoms start to move by diffusion. Because both processes are, hence, separated in time, their description can be subdivided in two separate models. The thermalization process is treated in a Monte Carlo model, similar to the electron Monte Carlo model (for more details of this thermalization model: see Ref. [10]). It results in a so-called thermalization profile (i.e., distribution of thermalized Cu atoms as a function of distance from the electrode), which serves as initial distribution for the diffusion of the thermalized Cu atoms, which is described in the next model.

2.6. Collisional-radiative model for the Cu atoms, Cu^+ and Cu^{++} ions in the ground state and in various excited levels

As mentioned above, the further transport of the sputtered Cu atoms after thermalization occurs by diffusion. Moreover, these Cu atoms can be ionized and/or excited. The behavior of the Cu atomic and ionic ground state and excited levels is described again in a collisional-radiative model. 8 Cu atomic levels, 7 Cu^+ ionic levels, as well as the Cu^{++} ions (no subdivision in different levels) are considered in this model; again most of the levels are effective levels, consisting of various individual levels. For each level, a balance equation is constructed with different populating and depopulating processes. The processes taken into account for each level are electron and atom impact ionization, excitation, de-excitation and radiative decay, as well as three-body recombination to the highest excited levels, Penning ionization by Ar metastable atoms and asymmetric charge transfer with Ar ions for some specific levels. Furthermore, transport occurs by diffusion for the Cu atoms and by diffusion and drift in the electric field for the Cu ions, but this is again negligible for the excited levels compared to the collision and radiation processes. More detailed information about this model can be found in Refs. [11, 15].

2.7. Monte Carlo model for the Cu ions in the sheath

Similar to the Ar ions, the Cu ions are not in equilibrium either with the high electric field in the sheath adjacent to the rf-electrode (cathode), and are therefore also described with a Monte Carlo model in this region. This model is very similar to the Ar ion and fast Ar atom Monte Carlo model. It should be mentioned that these two Monte Carlo models in the sheath region are especially important for calculating the Ar ion, fast Ar atom and Cu ion flux energy distributions bombarding the rf-electrode (cathode), which are needed to calculate the amount of sputtering.

2.8. Coupling of the models

All these models are coupled to each other due to the interaction processes between the different plasma species, and the output of one model serves as the input for the next model (e.g. creation rate of certain species due to collisions of other kinds of species). Therefore, all the models are solved iteratively until final convergence is reached. More information about this coupling, which is identical for the dc and rf mode, can be found, e.g., in Ref. [27]. The whole calculation procedure for one set of discharge parameters takes several days on a Digital personal workstation.

3. Results of the models

3.1. Electrical characteristics

There is essentially a difference between the type of input and output parameters in the dc and rf model. In the dc model, the voltage, gas pressure and temperature are used as input parameters, and the electrical current (and hence also the power) follow from the calculations. In the rf model, on the other hand, the electrical power is used as input parameter, beside the gas pressure and temperature, and the voltage (both rf amplitude and dc bias voltages) result as output values. However, the dc case can also be simulated with the rf model (when keeping the voltage at the cathode constant), and the results were totally identical to the dc model results.

In order to check the modeling calculations against experimental values, we have performed the calculations for typical cell dimensions used experimentally, although we have approximated the rather complicated experimental cell geometry by a simple cylinder, with length equal to 2 cm and diameter equal to 2.5 mm. The cathode or rf-electrode is placed at one end of the cylinder (hence also with diameter of 2.5 mm) and the other cell walls are grounded. Because of the large difference in size of rf-electrode and grounded electrode, it is expected that, in the rf-case, the dc-bias voltage is fairly negative. Indeed, typical experimental discharge conditions reveal, at a frequency of 13.56 MHz, a dc bias voltage of -627 V and an rf amplitude voltage of 764 V, for a gas pressure of about 6 Torr and electrical power of 10 W [28]. It is also observed experimentally that the dc operation mode yields similar analytical characteristics (sputter-erosion rates,

optical emission intensities) at the same power and pressure values, but that this occurs at the higher voltage of 1100 V [28].

Fig. 1 presents the calculated (solid line) and experimental (dashed line) potentials at the rf-electrode as a function of time in the rf-cycle. Both have a

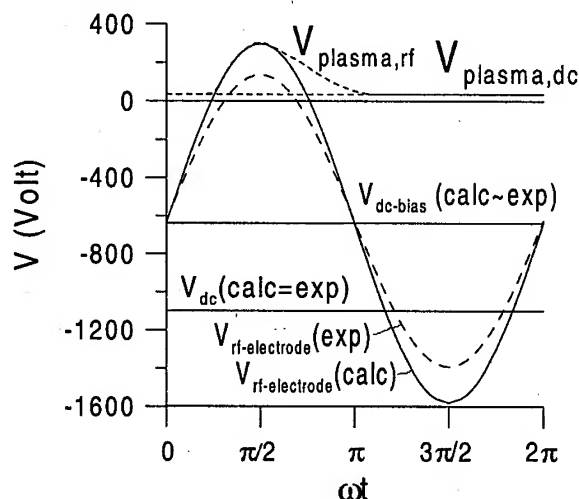


FIG. 1. Electrical potential at the rf-electrode ($V_{rf-electrode}$: calculated (solid line) and experimental (dashed line)), dc-bias voltage ($V_{dc-bias}$) and plasma potential ($V_{plasma,rf}$ in the rf-discharge. Also shown are the voltage (V_{dc}) and plasma potential ($V_{plasma,dc}$) in the dc discharge. Operating conditions: $p = 6$ Torr, $P = 10$ W.

sinusoidal profile. Indeed, this is used as input in the model. Experimentally, however, the real profile differs slightly (less than 10% for the present case) from a perfect sinusoidal profile. The potential at the rf-electrode is negative during most of the rf-cycle, in both the real and the calculated conditions, and becomes only positive around $\pi/2$. The calculated rf-amplitude voltage is about 937 V, which is about 170 V higher than the experimental value (i.e., 764 V). The calculated dc-bias voltage of - 640 V is however in very good agreement with experiment (i.e., - 627 V). Also the calculated voltage in the dc case, for exactly the same conditions of power and pressure, is presented, and is equal to -1100 V. This value is also in very good agreement with the measured value. Although the absolute values of these calculation results, in particular the rf-amplitude, are not in exact agreement with the experimental values, the correct trend is certainly predicted. Indeed, the rf voltages (both rf-amplitude and dc-bias) are clearly lower than the dc voltage for the same conditions of pressure and power, which indicates that the rf mode yields more efficient ionization, due to the movement of electrons in the oscillating electric field (see further). The plasma potentials in the rf mode and dc mode are, however, very similar to each other, as is also illustrated in Fig. 1. The rf plasma potential is rather high (almost 300 V, i.e., equal to the potential at the rf-electrode) around $\pi/2$, but decreases to values of about 35 V during most of the rf-cycle, which is equal to the dc plasma potential.

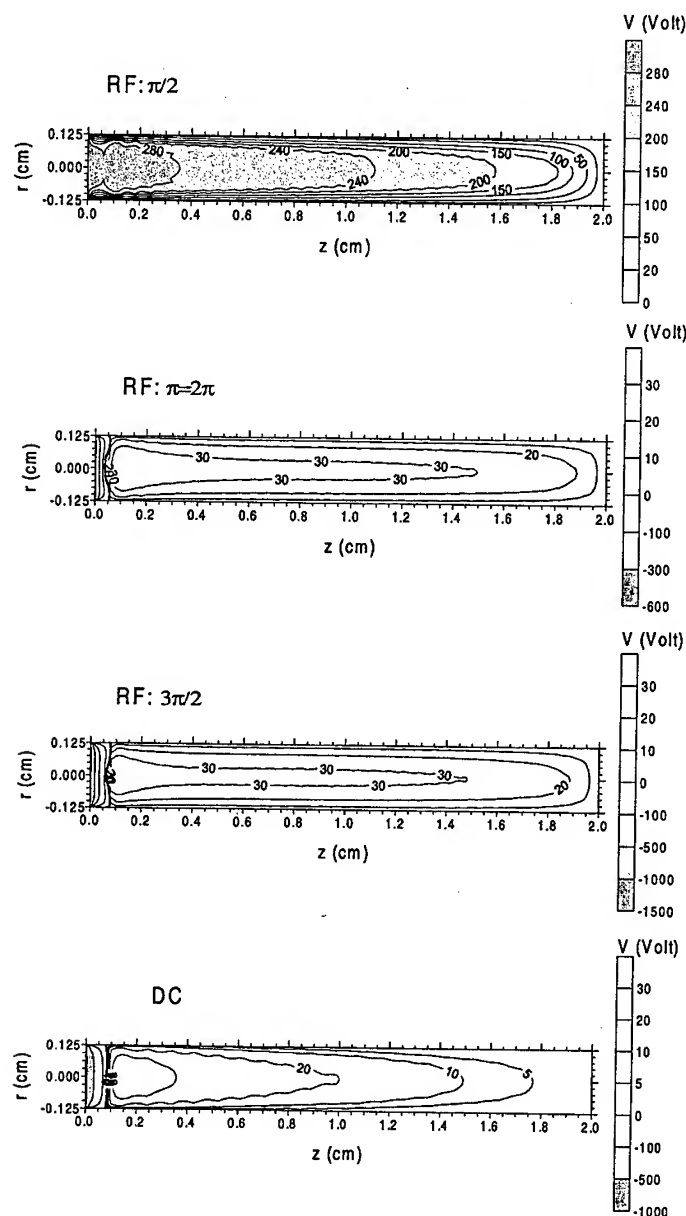


FIG. 2. Two-dimensional potential distributions in the rf-discharge, at 4 times in the rf-cycle, and in the dc-discharge. Same operating conditions as in Fig. 1.

The two-dimensional potential distributions, at four times in the rf-cycle in the rf-case, and the dc potential distribution, are presented in Fig. 2. At $\omega t = \pi/2$, the potential is rather high throughout the main discharge volume, but it decreases gradually, and close to the grounded walls more rapidly, to zero

at the grounded cell walls. Hence, at this time in the rf-cycle, there is no rf-sheath adjacent to the rf-electrode, but rather adjacent to the grounded cell walls. At $\omega t = 0, \pi$ and 2π , the potential is very negative (i.e., -640 V, the dc-bias) at the rf-electrode and it increases rapidly to zero at 0.4 mm from the rf-electrode. It reaches a positive value of about 35 V in the bulk plasma. A similar potential distribution is also observed around $\omega t = 3\pi/2$, but the potential at the rf-electrode is even more negative (i.e., about -1580 V, equal to the sum of the rf-amplitude and dc-bias). This large potential has dropped to zero at about 0.6 mm from the rf-electrode, and the value in the bulk plasma is also about 35 V. The potential distributions at $\omega t = 0, \pi$ or 2π and $\omega t = 3\pi/2$ strongly resemble the dc potential distribution, which is also shown in Fig. 2. It is -1100 V at the cathode, goes through zero at about 0.8 mm from the cathode, and reaches also a value of 35 V in the bulk plasma (negative glow). Hence, for the discharge conditions and cell geometry under study, it can be concluded that, except around $\omega t = \pi/2$, the rf potential distribution looks very much like a dc potential distribution due to the large dc-bias, so that the present rf discharge can be considered as a dc discharge with an rf sine-wave superimposed to it.

Not only the electrical potential follows from the calculations; also the electrical current. Fig. 3 depicts the total rf-current, as a function of time in the rf-cycle, as well as the individual contributions of electron current, ion current

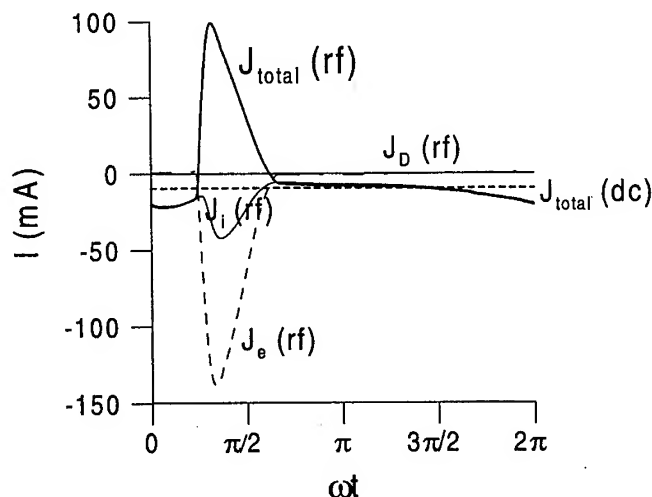


FIG. 3. Total electrical current at the rf-electrode ($J_{total}(rf)$) in the rf-discharge, and contributions of the ion current ($J_i(rf)$), electron current ($J_e(rf)$) and displacement current ($J_D(rf)$), also at the rf-electrode, as a function of time in the rf-cycle. Also shown is the total electrical current at the cathode in the dc-discharge ($J_{total}(dc)$). Same conditions as in Fig. 1.

and displacement current (i.e., due to the movement of the rf-sheath). As follows from Fig. 3, the latter contribution is negligible at our discharge conditions. Indeed, the rf-sheath varies only in thickness between 0 mm (around $\omega t = \pi/2$), 0.4 mm (around $\omega t = 0, \pi$ and 2π) and 0.6 mm (around $\omega t = 3\pi/2$), as could be observed in Fig. 2. This is not a large variation, and the positive charge in the

rf-sheath does not change enough to yield a large displacement current. During most of the rf-cycle, the current at the rf-electrode is attributed to ions bombarding the rf-electrode. However, around $\omega t = \pi/2$, a large electron current is drawn towards the rf-electrode. This is necessary to compensate for the positive charge accumulation at the rf-electrode due to the capacitive coupling of the rf-power, and it results in a net zero current at the rf-electrode, when integrated over the entire rf-cycle. Also plotted in Fig. 3 is the calculated current in the dc case, for the same conditions of power and pressure. It is equal to (-) 9 mA, which is most of the time lower than the instantaneous values in the rf-case (which is of course logical, because the dc voltage is higher for the same power value as in the rf-case).

3.2. Densities of the plasma species

In Fig. 4 the calculated argon ion densities in the rf and dc discharge are illustrated. The argon ion density was found to be constant throughout the entire

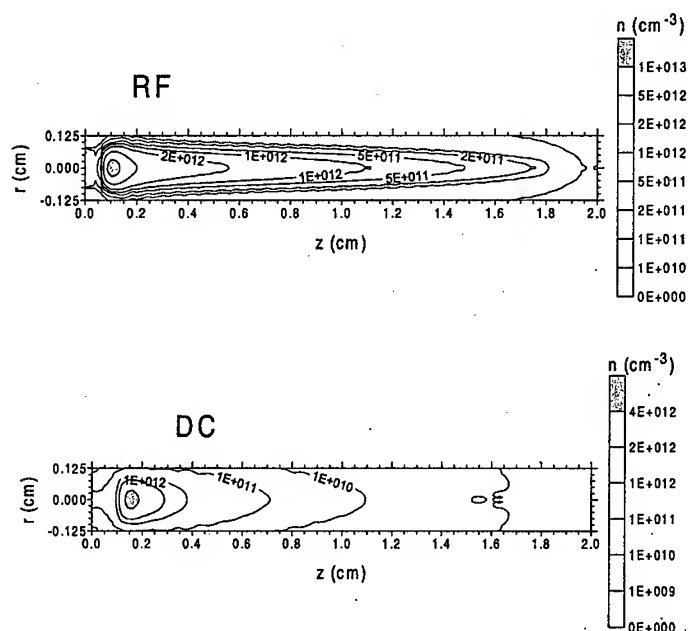


FIG. 4. Two-dimensional Ar ion density profile in the rf- and the dc-discharge. Same operating conditions as in Fig. 1.

rf-cycle. Qualitatively, the profiles look rather similar to each other, i.e. a low and nearly constant value in the sheath, a maximum between 0.1 and 0.2 mm from the electrode, and then decreasing to low values at the grounded cell walls. The rf density appears, however, to be a factor of 2.5 higher than the dc argon ion density, which is not unexpected, taking into account the somewhat higher rf-current and the more efficient rf ionization. Moreover, the rf argon ion density drops much slower to low values as a function of distance from the electrode than

the dc argon ion density. From this (and also from the electron and metastable argon atom density profiles; see below) it can be concluded that in the rf case, the discharge vessel is much more filled with plasma than in the dc case.

The electron density (not shown) is characterized by the same profile (also in absolute numbers) as the argon ion density, but it is zero in the sheath yielding a net positive space charge (and hence a strong potential drop; see above). Only around $\omega t = \pi/2$ in the rf-case, the electron and argon ion densities are equal to each other, yielding charge neutrality not only in the bulk plasma, but also in the sheath adjacent to the rf-electrode.

The calculated argon metastable densities ($4s[3/2]_2$ level) in both the rf and the dc case, are presented in Fig. 5.

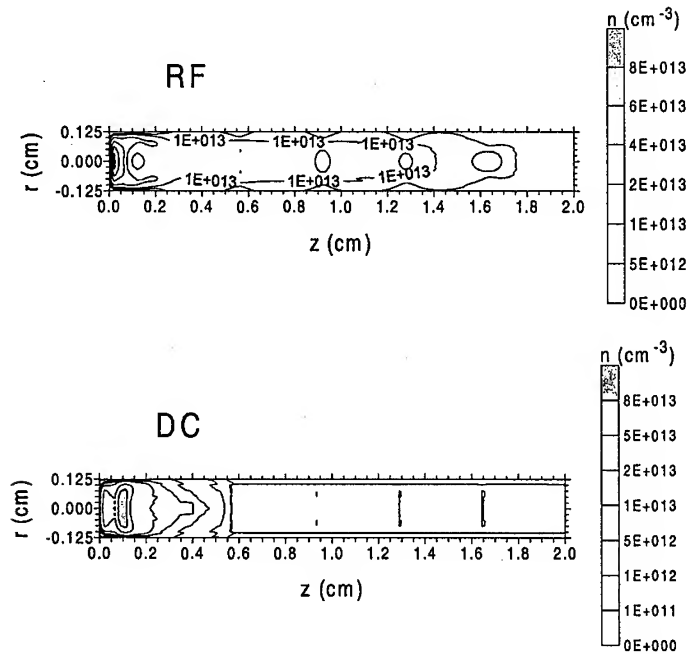


FIG. 5. Two-dimensional Ar metastable atom density profile ($4s[3/2]_2$ level) in the rf- and the dc-discharge. Same operating conditions as in Fig. 1.

Again, the metastable densities appear to be constant throughout the entire rf-cycle. Looking at the absolute values, the metastable densities are characterized by the same peak values in both the dc and rf discharge. The location of the peaks is, however, different. Indeed, the rf metastable density shows a pronounced peak adjacent to the rf-electrode and it has also rather high values throughout the entire bulk plasma. The latter is due to excitation by α -electrons around $\omega t = \pi/2$. Indeed, as has been demonstrated in ref. [12], electrons in the bulk plasma can become slightly heated by the moderate electric field in this region around $\omega t = \pi/2$ (see also Fig. 2), and they have just high enough energy to cause excitation and ionization (see also below). This excitation, which occurs primarily around $\omega t = \pi/2$, is responsible for the rather high values in

the bulk plasma. In the dc case, the metastable density shows a distinct peak at the interface between sheath and negative glow and is also quite high adjacent to the cathode. However, it is very low in the bulk plasma, due to the absence of α -electrons which can cause excitation here.

Fig. 6 presents the calculated sputtered copper atoms densities (in the ground state) in the rf (again constant in time) and dc discharge. The relative profiles

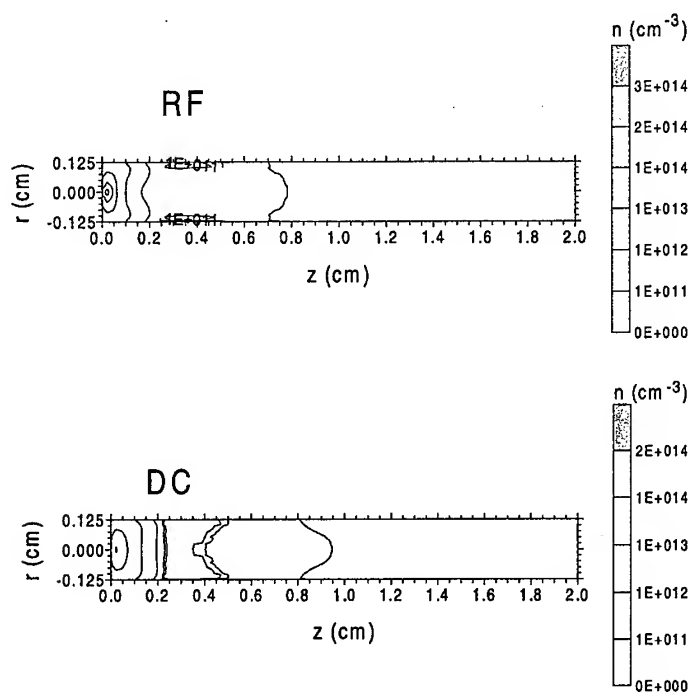


FIG. 6. Two-dimensional sputtered Cu atom density profile in the rf- and the dc-discharge. Same operating conditions as in Fig. 1.

are almost identical, i.e., low values at the electrodes and a maximum at less than 0.5 mm from the cathode (or rf-electrode). Also the absolute values are very similar. The value in the rf discharge is slightly higher (i.e., a factor of 1.5, only at the maximum of the profile), which is attributed to the somewhat more efficient sputtering (see below). The calculated copper ion densities (in the ground state) are also very similar to each other, both in relative profiles (i.e., maximum around 1 mm) and even in absolute values, as is demonstrated in Fig. 7. This finding is not straightforward, taking into account the clear differences in electric potentials, currents and argon ion and electron densities in both discharge modes (see above). It turns out that, although the model predicts slightly less efficient sputtering in the dc discharge, this appears to be compensated by slightly more efficient ionization. Finally, this good correlation between copper atom and ion densities in both discharge modes is in excellent agreement with experimental observations, where it is found that the rf and dc modes, at the same values of power and pressure but different values of voltage

(see above) yield very similar analytical characteristics (which are of course in close relation to the sputtered species) [28].

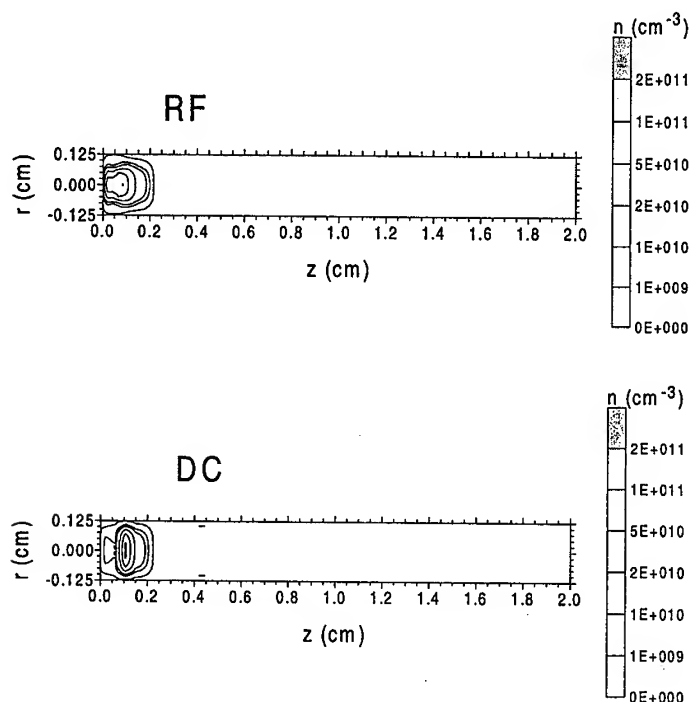


FIG. 7. Two-dimensional Cu in density profile in the rf- and the dc-discharge. Same operating conditions as in Fig. 1.

3.3. Ionization in the plasma

In Fig. 8 the electron impact ionization rate of argon in one dimension is plotted as a function of distance from the rf-electrode. In the rf model, the ionization due to electrons is described both in the Monte Carlo and the fluid model. Indeed, as mentioned before, the Monte Carlo model treats only the fast electrons, and once they are slowed down below the threshold for inelastic collisions in the bulk plasma, these electrons are transferred to the fluid model. However, these slow electrons can again be heated by the oscillating electric field (due to the movement of the rf-sheath) and by the moderate electric field in the bulk plasma around $\omega t = \pi/2$ (see above, Fig. 2). Hence, these electrons can produce some more ionization, which is typical for an rf-discharge and is called " α -ionization". The ionization rates due to Monte Carlo electrons (i.e., the electrons emitted by the rf-electrode and the fast electrons created in collisions from the first group; they produce so-called " γ -ionization") and due to fluid electrons, at four times in the rf-cycle, are presented in the top and middle parts of Fig. 8, respectively. The Monte Carlo (γ) ionization reaches a maximum at the sheath-bulk plasma interface. The fluid (α) ionization at times $\omega t = \pi, 3\pi/2$ and 2π also reaches

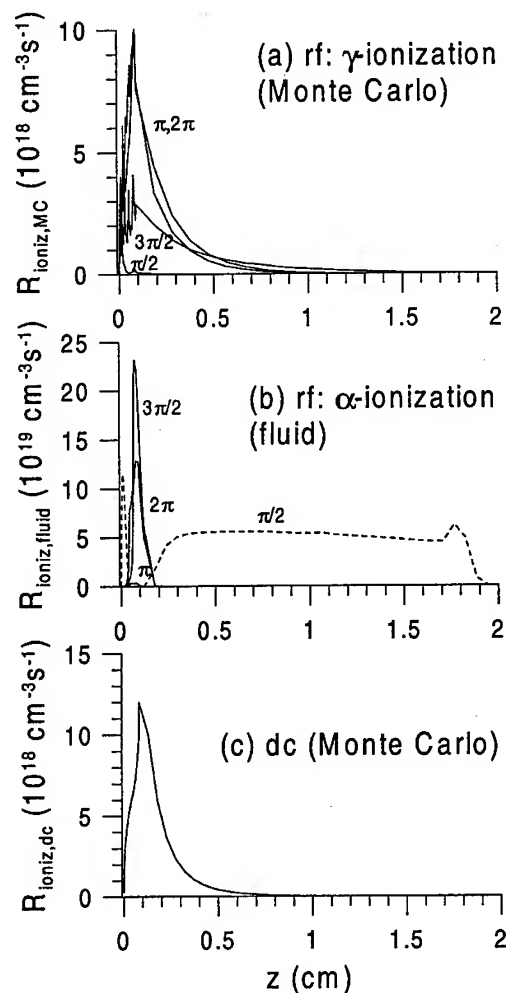


FIG. 8. Electron impact ionization rates as a function of distance from the rf-electrode/cathode, (a) in the rf-discharge at four times, calculated by the Monte Carlo model (γ -ionization), (b) in the rf-discharge at four times, calculated by the fluid model (α -ionization), (c) in the dc-discharge. Same operating conditions as in Fig. 1.

a maximum here, caused by electrons which are drawn towards the rf-electrode around $\omega t = \pi/2$ and then accelerated back towards the bulk plasma at later times, when the rf-sheath develops again and has a strongly negative electric field. The fluid ionization at $\omega t = \pi/2$ (presented by the dashed line in the middle part of the figure) is characterized by a peak adjacent to the rf-electrode (caused by the electrons drawn towards the rf-electrode) and a broad maximum in the entire bulk plasma (caused by electrons accelerated here by the moderate electric field). The latter broad maximum is also in correspondence with the

rather high values of the argon metastable density in the bulk plasma, as has been explained before. The lower part of Fig. 8 presents the electron impact ionization rate in the dc case. It reaches also a maximum at the sheath-negative glow interface, similar to the γ -ionization in the rf case, and is somewhat higher in magnitude than the time-averaged γ -ionization. However, in the dc case no α -ionization takes place, so that the overall dc ionization is lower than the overall rf ionization, yielding a higher dc voltage for the same conditions of power and pressure, in agreement with experiment.

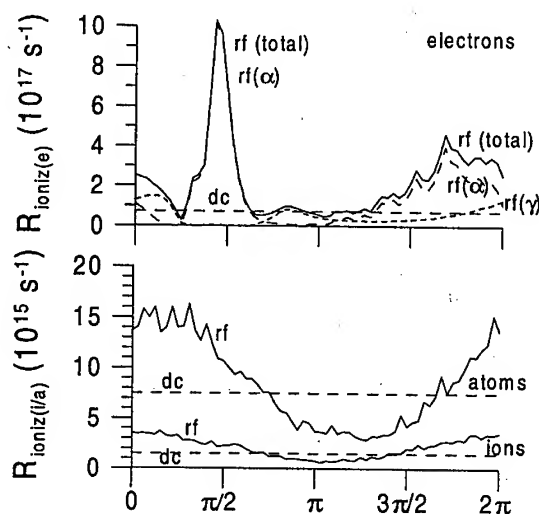


FIG. 9. Ionization of argon integrated over the entire discharge volume, in the rf-discharge (as a function of time in the rf-cycle) and the dc-discharge. Upper part: electron impact ionization (and individual contributions α and γ ionization), lower part: fast Ar ion and atom impact ionization. Same operating conditions as in Fig. 1.

This is also illustrated in Fig. 9, which presents the ionization rate, integrated over the entire discharge volume, as a function of time in the rf-cycle. It is clear (upper part of the figure) that most of the rf ionization is due to fluid electrons (a-ionization). The latter is especially important around $\omega t = \pi/2$, as was expected already from the broad maximum in Fig. 8. Also shown for comparison is the dc ionization rate, integrated over the entire discharge volume. It is somewhat higher than the g-ionization, but clearly lower than the a-ionization, as was illustrated already in Fig. 8. The lower part of Fig. 9 shows the ionization rate due to fast Ar ions and atoms, both in the rf mode and the dc mode. It appears that these processes occur at a similar rate in both operation modes, when averaged over time. The cross sections of Ar ion and atom impact ionization start to rise only for energies above several 100 eV. Since the Ar ions and atoms can only reach high energies adjacent to the rf-electrode/cathode (where they have gained energy from the high electric field in the sheath), these processes only occur in this region. Integrated over the entire discharge region they are, therefore, of minor importance compared to electron impact ionization (see the left axis of upper and lower part of Fig. 9). We calculated relative contributions

for electron, Ar ion and Ar atom impact ionization of about 95%, 1% and 4%, respectively, in the rf-case, and about 89%, 2% and 9%, respectively, in the dc-case [29]. The reason that electron impact ionization is even more important in the rf-case is of course due to the dominant role of α -ionization.

3.4. Optical emission intensities

As mentioned in the introduction, dc and rf glow discharges are used in analytical chemistry, often in combination with optical emission spectrometers, to measure emission intensities. The collisional-radiative models for Ar and Cu, which we have briefly described above, allow to calculate the populations of various excited levels. When multiplying the latter with the Einstein transition probabilities for radiative decay, the optical emission intensities can be obtained, which are of interest for glow discharge optical emission spectrometry. Fig. 10 presents, as an example, the calculated Ar atomic spectra, both in the rf and dc mode. The

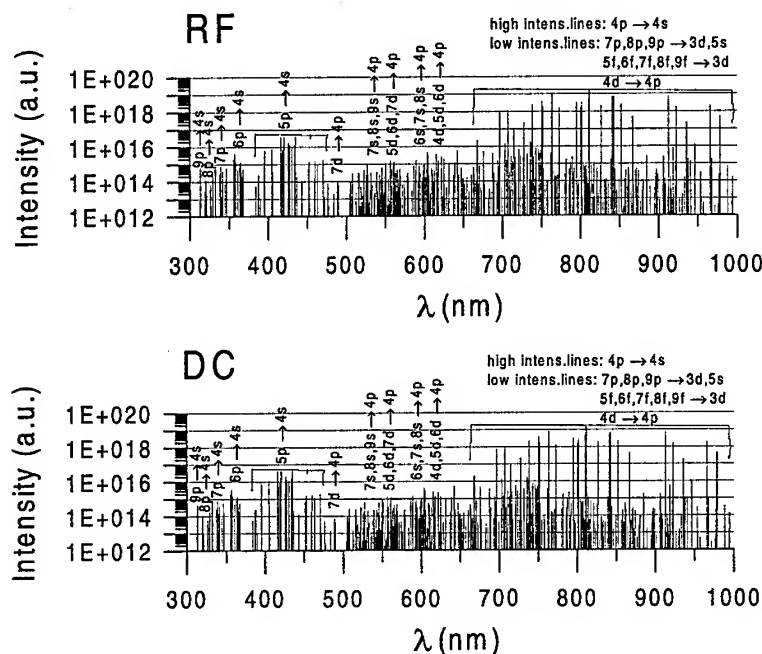


FIG. 10. Ar atomic optical emission spectra in the rf and dc-discharge. Same operating conditions as in Fig. 1.

rf-spectrum is presented at $\omega t = 3\pi/2$; it varies only slightly as a function of time. It is clear that both spectra are almost identical, in spite of the different conditions of voltage and current (and electron and argon ion density). This is in excellent agreement with experiment, where it is also found that the rf and dc discharge, at the same conditions of power and pressure, but different values of voltage, yield very similar optical emission intensities. From both spectra it is obvious that the lines in the region 700-1000 nm, i.e., the so-called red

lines, corresponding to 4p-4s transitions, are the most intense ones. However, beside that, also the lines in the region 400-450, i.e., the so-called blue lines, corresponding to 5p-4s transitions, have rather high intensities, and there are many more lines, of lower intensity, throughout the whole spectrum studied. It was demonstrated before that the calculated spectrum, at least for the dc case where we have checked it, agreed very well with experimental spectra from the literature [30].

3.5. Sputtering at the cathode

Finally, the model is also able to calculate the amount of sputtering at the rf-electrode/cathode, based on the flux energy distributions of the Ar ions, fast Ar atoms and Cu ions calculated with the Monte Carlo models, and on an empirical formula for the sputtering yield as a function of the bombarding energy. Fig. 11 illustrates the net sputtering flux in the rf mode (as a function of time in the rf-cycle) and in the dc mode. The net sputtering flux is the result of the

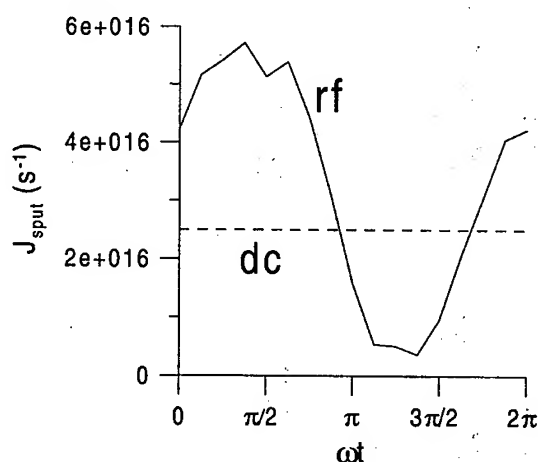


FIG. 11. Sputtering rate at the rf-electrode/cathode in the rf- and dc-discharge. Same conditions as in Fig. 1.

total sputtering flux, calculated in the way mentioned above, minus the flux of redeposited Cu atoms onto the electrode. The latter can be quite high, so that the net sputtering flux is only about 30-40% of the total sputtering flux. It can be deduced from Fig. 11 that, averaged over time, the rf sputtering flux is only slightly higher than the dc sputtering flux. This is not too much in discrepancy with experiment, where similar sputtering (erosion) rates are obtained in both the dc and rf mode, at the same values of power and pressure. Indeed, on one hand, the dc discharge is characterized by a higher voltage, yielding somewhat higher ion and atom energies at the cathode, which give rise to more efficient sputtering, but on the other hand, the rf discharge yields higher ion currents bombarding the rf-electrode, which leads of course also to more sputtering. It appears therefore that the combination of both effects yields more or less similar

sputtering in both operation modes.

Finally, it should be mentioned that the fast Ar atoms play a dominant role in sputtering, with a calculated contribution of about 70% in the rf-case and 60% in the dc-case. The Ar ions and Cu ions seem to contribute for about the same extent to the sputtering at the discharge conditions under study, i.e., Ar ions: about 17% (rf) and 21% (dc) and Cu ions (called "self-sputtering"): about 13% and 19% in the rf and dc case, respectively. The fact that the sputtering is predominantly caused by fast Ar atoms explains also why the rf case predicts more efficient sputtering around $\omega t = \pi/2$ and lowest sputtering around $\omega t = 3\pi/2$. Indeed, it was found in Ref. [13] that the fast Ar atoms have their maximum energy and maximum flux at the rf-electrode around $\omega t = \pi/2$, and that their energy and flux reach a minimum value around $\omega t = 3\pi/2$ [13].

4. Conclusion

A hybrid set of models (Monte Carlo, fluid and collisional-radiative models) has been developed for an argon glow discharge, both in the dc and the capacitively coupled rf mode. The species described with these models are the electrons, Ar ions, fast Ar atoms, Ar atoms in various excited levels, sputtered Cu atoms and the corresponding Cu ions, also in the ground state and in various excited levels. Some typical results, like electrical characteristics (voltages and currents), densities, ionization rates, optical emission spectra and information about sputtering, are presented here, as an example of what can be predicted with the models. It is found that the rf discharge requires lower voltages (both rf-amplitude and dc-bias) than the dc discharge, due to the more efficient ionization (i.e., so-called a-ionization). The calculated voltages are in reasonable agreement with experimental values, for the same conditions of power and pressure. On the other hand, the rf discharge is characterized by somewhat higher electrical currents (which is of course logical, in order to yield the same power values) and higher Ar ion and electron densities. Moreover, the argon ion, electron and argon metastable atoms have higher densities throughout the whole discharge in the rf case, whereas their densities drop rather quickly in the dc case. Hence, it can be concluded that the discharge vessel is much more filled with plasma in the rf case than in the dc case. The Cu atom and ion densities are, however, calculated to be more or less similar in both operation modes. This is also true for the optical emission spectra and the sputtering rates at the rf-electrode/cathode. The latter is also in good agreement with experiments. Beside the absolute values, the relative shapes of the profiles are also quite similar for both modes, except from a faster drop in the dc case. It can thus be concluded that, for the discharge conditions under investigation (i.e., rather high pressure, power and dc-bias, and small cell geometry), the rf discharge looks very much like a dc discharge.

Acknowledgments

A. Bogaerts is indebted to the Fund for Scientific Research (FWO-Flanders) for financial support. The authors also acknowledge financial support from the

Federal Services for Scientific, Technical and Cultural Affairs (DWTC/SSTC) of the Prime Minister's Office through IUAP-IV (Conv. P4/10). Finally, we wish to thank W. Goedheer, J. Vlcek and R. Carman for their valuable contributions to our models.

References

1. R.K. MARCUS, *Glow Discharge Spectroscopies*, Plenum Press, New York, 1993.
2. R. PAYLING, D.G. JONES, A. BENGTON, *Glow Discharge Optical Emission Spectrometry*, Wiley, Chichester, 1997.
3. D.C. DUCKWORTH and R.K. MARCUS, *Anal. Chem.*, **61**, 1879, 1989.
4. V. HOFFMANN, H.-J. UHLEMANN, F. PRASSLER, K. WETZIG, D. BIRUS, *Fresenius' J. Anal. Chem.*, **355**, 826, 1996.
5. A. BOGAERTS, M. van STRAATEN, R. GIJBELS, *Spectrochim. Acta Part B*, **50B**, 179, 1995.
6. A. BOGAERTS, R. GIJBELS, W.J. GOEDHEER, *J. Appl. Phys.*, **78**, 2233, 1995.
7. A. BOGAERTS, R. GIJBELS, *J. Appl. Phys.*, **78**, 6427, 1995.
8. A. BOGAERTS, R. GIJBELS, W.J. GOEDHEER, *Anal. Chem.*, **68**, 2296, 1996.
9. A. BOGAERTS, R. GIJBELS, J. VLCEK, *J. Appl. Phys.*, **84**, 121, 1998.
10. A. BOGAERTS, M. van STRAATEN, R. GIJBELS, *J. Appl. Phys.*, **77**, 1868, 1995.
11. A. BOGAERTS, R. GIJBELS, R.J. CARMAN, *Spectrochim. Acta Part B*, **53B**, 1679, 1998.
12. A. BOGAERTS, M. YAN, R. GIJBELS, W.J. GOEDHEER, *J. Appl. Phys.*, **86**, 2990, 1999.
13. A. BOGAERTS, R. GIJBELS, *IEEE Trans. Plasma Sci.*, in press.
14. A. BOGAERTS and R. GIJBELS, *Spectrochim. Acta B*, in press.
15. A. BOGAERTS and R. GIJBELS, *Spectrochim. Acta B*, in press.
16. S.V. BEREZHNOI, I.D. KAGANOVICH, L.D. TSENDIN, V.A. SCHWEIGERT, *Appl. Phys. Lett.*, **69**, 2341, 1996.
17. J.-P. BOEUF, *Phys. Rev. A*, **36**, 2782, 1987.
18. J. VLCEK, *J. Phys. D: Appl. Phys.*, **22**, 623, 1989.
19. J. BRETAGNE, G. DELOUYA, J. GODART, V. PUECH, *J. Phys. D: Appl. Phys.*, **14**, 1225, 1981.
20. Z. DONKO, K. ROZSA, R.C. TOBIN, *J. Phys. D: Appl. Phys.*, **29**, 105, 1996.
21. M. SURENDRA and D.B. GRAVES, *IEEE Trans. Plasma Sci.*, **19**, 144, 1991.
22. Z. DONKO, *Phys. Rev. E*, **57**, 7126, 1998.
23. J.D.P. PASSCHIER, W.J. GOEDHEER, *J. Appl. Phys.*, **73**, 1073, 1993.
24. J.D.P. PASSCHIER, W.J. GOEDHEER, *J. Appl. Phys.*, **74**, 3744, 1993.
25. H.K. GUMMEL, *IEEE Trans. Electron. Devices*, **11**, 455, 1964.
26. D.L. SCHARFETTER, H.K. GUMMEL, *IEEE Trans. Electron. Devices*, **16**, 64, 1969.
27. A. BOGAERTS, R. GIJBELS, *Plasma Phys. Reports*, **24**, 573, 1998.
28. V. HOFFMANN, private communication.
29. A. BOGAERTS, R. GIJBELS, *Spectrochim. Acta Part B*, in press.
30. A. BOGAERTS, R. GIJBELS, J. VLCEK, *Spectrochim. Acta Part B*, **53**, 1517, (1998).

NON EQUILIBRIUM EFFECTS IN PLASMA EXPANSION FLOWS

G. COLONNA, I. ARMENISE, M. CATELLA, M. CAPITELLI

CENTRO DI STUDIO PER LA CHIMICA DEI PLASMI, CNR AND DIPARTIMENTO DI CHIMICA,
 UNIV. BARI

via Orabona 4, 70126 Bari Italy. E-mail: cscpgc08@area.ba.cnr.it.

A selfconsistent model which couples fluid dynamics, state to state vibrational kinetics and Boltzmann equation for the electron energy distribution function has been developed for studying high enthalpy expanding flows. The results show strong non-equilibrium vibrational distributions along the nozzle axis generated by the recombination process. Moreover non Maxwell electron energy distribution functions are also present as a result of second kind collisions of electrons with vibrationally and electronically excited states.

Symbols

A : nozzle cross section
 c_p : constant pressure specific heat
 c_{ps} : constant pressure specific heat of s-th species
 c_{sv} : mass fraction of the s-th species in the v-th level
 c_v : constant volume specific heat
 c_{vs} : constant volume specific heat of s-th species
 f_{sv} : fraction of the molecule (atom) s-th in the v-th level
 h : enthalpy per unit mass
 h_i : internal enthalpy per unit mass
 h_T : translational enthalpy per unit mass
 H_{fs} : molar formation enthalpy of s-th species
 J_{el} : electron energy flux due to elastic collision
 J_{e-e} : electron energy flux due to electron-electron collisions
 J_E : energy flux due to electric field
 m : mean molar mass
 m_s : molar mass of s-th species
 \dot{n}_{sv} : molar source term of s-th species in the v-th level
 n_e : electron density
 $n(\varepsilon)$: electron energy distribution function in eV^{-1}

P	: pressure
Q_e	: heat production per mole due to electron collisions
R	: ideal gas constant
R_p	: rate coefficient for a generic inelastic or superelastic process p
S_{in}	: electron source term due to inelastic collision
S_{sup}	: electron source term due to superelastic collision
T	: gas temperature
T_v	: vibrational temperature
u	: longitudinal axial speed
x	: nozzle position along the axis
α	: c_v/R
α_e	: ionization degree
α_s	: c_{vs}/R
χ_s	: molar fraction of s-th species
ε	: electron energy
ε_p^*	: threshold energy of the electron molecule collision process p
ε_p	: energy exchanged in the electron-molecule collision process p
ε_{sv}	: v-th level energy of the s-th species
ρ	: mass density
ρ_{sv}	: mass density of the s-th species in the v-th level
σ_p	: cross section for an inelastic or superelastic process p .

The effects of chemical and thermal non equilibrium in modifying the characteristics of flow fields have been widely studied in the past [1]. The approach commonly used to take into account thermal non equilibrium consists in assigning different temperatures to the relevant degrees of freedom of the system [1] i.e. translational " T ", vibrational " T_v " and an electron temperature " T_e ". This point of view implies Boltzmann distributions for translational and internal degrees of freedom [2].

However under several experimental conditions (gas expansion, discharge and post discharge) vibrational distributions and electron energy distribution function do not follow Boltzmann and Maxwell distributions [3, 4, 5]. Therefore the concept of temperature becomes meaningless. In these conditions a self-consistent treatment of the kinetics of heavy particles and electrons [6] is necessary to take into account the coupling existing between all the degree of freedom of the system.

All these problems are present in supersonic expansion of high temperature gases: the "hot" gas rapidly cools down while expanding through a nozzle, contemporarily decreasing its pressure and increasing the speed. As a consequence, the flow characteristic time becomes comparable (if not shorter) with the relaxation time of the vibrational distribution and therefore nonequilibrium vibrational distributions arise. The coupling between vibrational and chemical kinetics and fluid dynamics has been studied in one dimensional nozzle model for air mixtures [7, 8] and for pure nitrogen [9] flows, showing dramatic effects. In particular strong departures of the global chemical rates (integrated over the vibrational distribution) from the Arrhenius trend have been calculated thus emphasizing the inapplicability of the multitemperature approach. In this work the

model has been completed adding the electron kinetics and the electron-molecule collisions.

The kinetic scheme considers the selfconsistent coupling between vibrational kinetics, Boltzmann equation for the electron energy distribution function (eedf) and fluidynamics i.e. the same level of sophistication used for modeling the boundary layer of a blunt body re-entering in the atmosphere with hypersonic speed [10]. On the other hand the presence of electronically excited states and their consequences on eedf has been considered in a parametric form. In all the reported cases the ionization degree has been considered frozen along the nozzle axis.

1. Theoretical model

To model the expansion flow we use stationary Euler equations adapted for the quasi one-dimensional nozzle, i.e. the mass continuity

$$(1.1) \quad \frac{\partial \rho(x)u(x)A(x)}{\partial x} = 0$$

momentum continuity

$$(1.2) \quad \rho(x)u(x) \frac{\partial u(x)}{\partial x} + \frac{\partial P(x)}{\partial x} = 0$$

energy continuity

$$(1.3) \quad \frac{\partial}{\partial x} \left[h(x) + \frac{u^2(x)}{2} \right] = 0$$

completed with the perfect gas state equation

$$(1.4) \quad P = \frac{\rho RT}{m}.$$

This system is not closed because the enthalpy is not defined and depends on the considered model. In general it can be expressed as the sum of different contributions

$$(1.5) \quad h(x) = h_T(x) + h_i(x)$$

where $h_T(x)$ is the translational enthalpy

$$(1.6) \quad h_T(x) = \frac{RT}{m} \sum_s \alpha_s \chi_s = \frac{\alpha RT}{m}$$

and $h_i(x)$ is the internal enthalpy which, in the state-to-state approach, can be expressed as

$$(1.7) \quad h_i(x) = \frac{1}{m} \sum_s \chi_s \left[H_{fs} + \sum_v f_{sv} \epsilon_{sv} \right]$$

In this model, the concentration of each quantum level is considered as an independent species, therefore a separate continuity equation for each level should be written as

$$(1.8) \quad \frac{\partial \rho_{sv}(x) u(x) A(x)}{\partial x} = A(x) m_s \dot{n}_{sv}$$

or in terms of mass fraction

$$(1.9) \quad \frac{\partial c_{sv}(x) u(x) A(x)}{\partial x} = \rho_{sv} = \frac{m_s}{\rho(x) u(x)} \dot{n}_{sv}$$

where \dot{n}_{sv} is the time derivative of the number density of species s in the level v .

The solution of such a system for the nitrogen, oxygen and air kinetics has been discussed elsewhere [7, 8, 9] in the absence of electron-molecule collisions.

Due to the high temperature in the reservoir, the electron density is high enough to make the following processes to be important in state-to-state vibrational kinetics of nitrogen molecules:



The rate coefficients of such processes are calculated integrating the cross section over the energy range according the relation

$$(1.16) \quad R_p = \int_0^{\infty} v(\varepsilon) \sigma_p(\varepsilon) n(\varepsilon) d\varepsilon$$

considering the cross section null below the threshold energy ε_p^* . The electron energy distribution $n(\varepsilon)$ is calculated solving the Boltzmann equation for electron kinetics in the homogenous, quasi-isotropic approximation [4, 5]

$$(1.17) \quad \frac{\partial n(\varepsilon, t)}{\partial t} = -\frac{\partial}{\partial \varepsilon} (J_E + J_{el} + J_{e-e}) + S_{in} + S_{sup}.$$

The source terms S in eq.(1.17) depend on the level concentration and gas composition, therefore there is non-linear coupling between fluid, master and Boltzmann equations (see Fig. 1). In principle, electrons should be taken in the energy continuity equation, but it is not trivial to evaluate the electric field contribution. It is also possible to consider the electron contribution as a source term, modifying equation (1.3) as

$$(1.18) \quad \frac{\partial}{\partial x} \left(h + \frac{u^2}{2} \right) = \frac{Q_e}{mu}$$

where Q_e (heat production due to electron collisions) is given by

$$(1.19) \quad Q_e = n_e \sum_p \Delta \varepsilon_p R_p \chi_p$$

where χ_p is the molar fraction of the molecule in the particular state involved in the collision p .

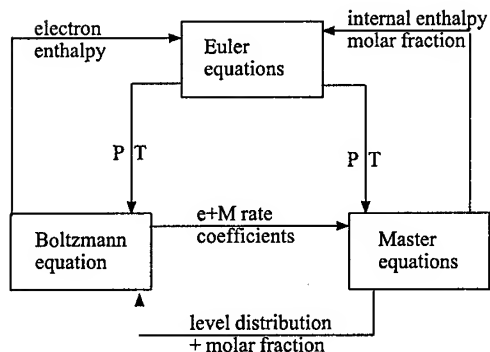


FIG. 1. Scheme of the coupling between Euler, Boltzmann and master equations.

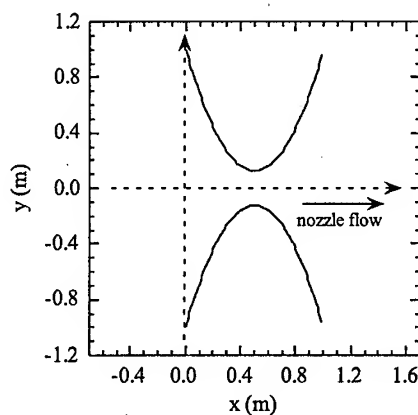


FIG. 2. Longitudinal section of the parabolic nozzle, with a simplified version of the scheme used in works for gas discharges [11] and post discharge conditions [12].

To complete the kinetic scheme the electron loss/production processes and the quenching of electronic excited states of molecule [11, 12] should be considered. The physical characteristics of the nozzle expansion make inefficient the electron-ion recombination therefore such a process can be neglected. The same thing cannot be said for the electronically excited states, even if for sake of simplicity also the electronically excited state kinetics have been neglected, analyzing the effect of electronic superelastic collision parametrically. In particular processes (1.12-1.15) are considered only for the electron kinetics keeping constant the excited states fraction and the ionization degree while the other processes (e-V) are considered for the coupling between the two kinetics.

2. Results and discussion

The model described above has been applied to expanding flows through a parabolic nozzle (see Fig. 2). Different reservoir conditions have been considered, accounting also for the presence of the electric field, the reduced field (E/N) of which considered as a parameter.

The reservoir pressure is about 1 atm. The reservoir temperature ranges in the interval 5000 - 8000 K: in such conditions the nitrogen passes from the predominance of molecules ($T = 5000$ K) to that one of atoms ($T = 8000$ K). Ionization degree ranges from 10^{-7} to 10^{-2} and $N_2(A^3)$ level concentration from 10^{-9} to 10^{-3} . The bulk of results have been obtained without including an electrical field ($E/N = 0$). Some cases with $E/N = 40$ Td have been also considered.

The contribution of electron-molecule collisions in equation (1.8) is proportional to the ionization degree and it has the same form of vT processes considering a rate coefficient given by $\alpha_e R_p$.

We have studied 5 cases, all of them characterized by an ionization degree $\alpha_e = 10^{-2}$.

- a) no coupling with electron kinetics (b)
- b) with e-V, $N_2(A^3)/N_2 = 10^{-9}$, $E/N = 0$, no e-e collisions (c)
- c) with e-V, $N_2(A^3)/N_2 = 10^{-9}$, $E/N = 0$, e-e collisions (d)
- d) with e-V, $N_2(A^3)/N_2 = 10^{-3}$, $E/N = 0$, no e-e collisions (g)
- e) with e-V, $N_2(A^3)/N_2 = 10^{-3}$, $E/N = 0$, e-e collisions (g)
- f) with e-V, $N_2(A^3)/N_2 = 10^{-3}$, $E/N = 40$ Td, e-e collisions (h)

e-V processes refer to forward and reverse processes described by eq.(1.10).

To explain the main characteristics of the flux through the nozzle we have reported in Fig. 3 the temperature and pressure profiles: moving toward the

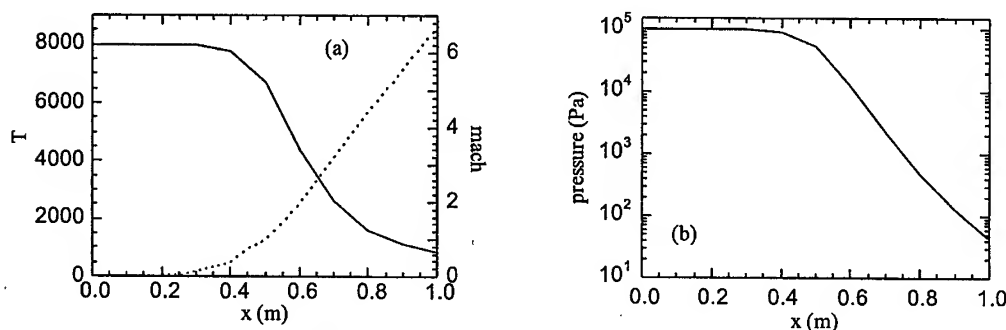


FIG. 3. Temperature and Mach number profiles (a) and pressure profile (b) for $T_0 = 8000$ K, with a simplified version of the scheme used in works for gas discharges [11] and post discharge conditions [12].

exit, the expanding gas cools down while its speed increases and the pressure decreases. The characteristic time of the flow after the throat becomes comparable with the vibrational relaxation time and therefore the energy stored in the internal degrees of freedom is trapped. Under these conditions vibrational

temperature is much higher than translational one thus promoting the so called v-v up pumping ending in the formation of highly non equilibrium vibrational distributions. On the other hand recombination of atomic nitrogen is favored by cooling resulting in the formation of extended tails in the vibrational distribution.

In Fig. 4 we have reported the vibrational distributions calculated without the electron kinetics (case a). Different behaviours can be observed for low and high vibrational quantum number distribution: for $v < 10$ the distribution shows a Boltzmann trend, cooling as the gas expands after the throat, for $v > 20$ the distribution is dominated by the recombination and as the gas expand, lower the temperature, stronger the recombination and higher the distribution tail.

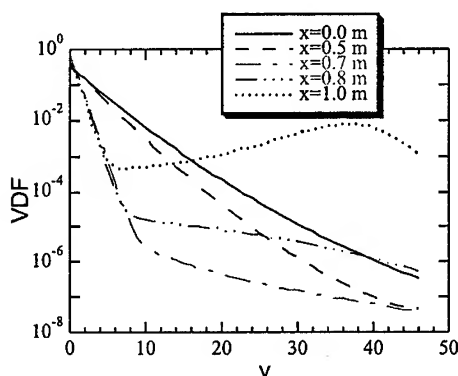


FIG. 4. Vibrational distributions at different nozzle position for $T_0 = 8000$ K in case a, with a simplified version of the scheme used in works for gas discharges [11] and post discharge conditions [12].

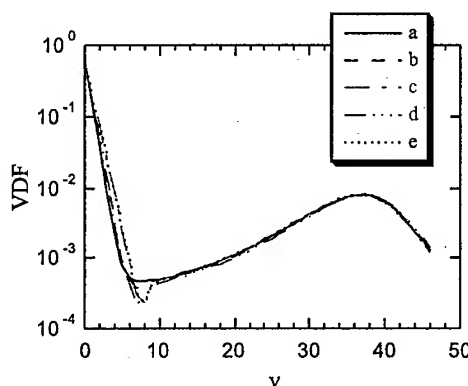


FIG. 5. Vibrational distributions at nozzle outlet for $T_0 = 8000$ K in different cases (the curve label refers to the case described in the text), with a simplified version of the scheme used in works for gas discharges [11] and post discharge conditions [12].

When the electron-molecule processes are considered the vibrational distributions are weakly modified (see Fig. 5), due to the dominance of vT processes by atom collisions and the electron energy distribution functions (eedf) follow the vibrational ones and depend on the considered inelastic and superelastic processes. If only e-V processes are considered the eedf's shows strong non equilibrium properties in all the nozzle positions (Fig. 6). The small peaks between 5 and 7 eV are due to second kind collisions with electronically excited state and modulated by e-V collisions. Including e-e collisions (Fig. 7), all these structures disappear and the distributions become maxwellian. When the fraction of electronically excited states is equal to 10^{-3} the eedf's show stronger non equilibrium effects due to the superelastic electronic collisions (Fig. 8a). In this case the e-e collisions (see Fig. 8b) push the distribution towards a maxwellian, but the non equilibrium structures are still present.

When the electric field is turned on (case f) the eedf's are mainly determined by the electric field (see Fig. 9b) and, as a consequence, the part of the vibrational distribution interesting the low lying vibrational levels is determined

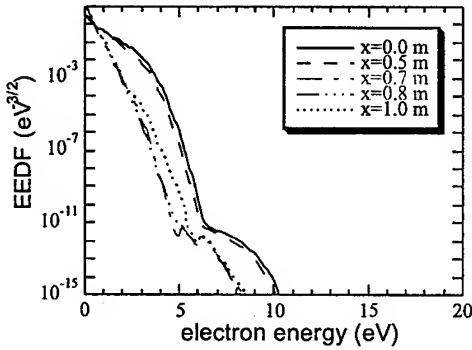


FIG. 6. Electron energy distribution functions (EEDF) at different nozzle positions for $T_0 = 8000$ K in case b, with a simplified version of the scheme used in works for gas discharges [11] and post discharge conditions [12].

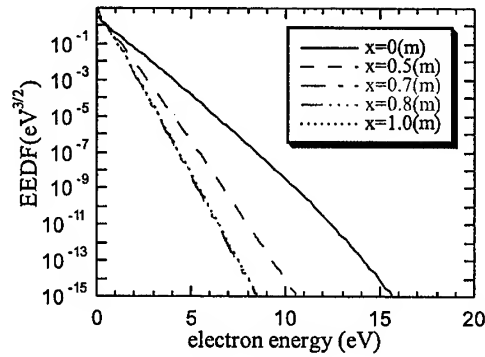


FIG. 7. Electron energy distribution functions (EEDF) at different nozzle positions for $T_0 = 8000$ K in case c, with a simplified version of the scheme used in works for gas discharges [11] and post discharge conditions [12].

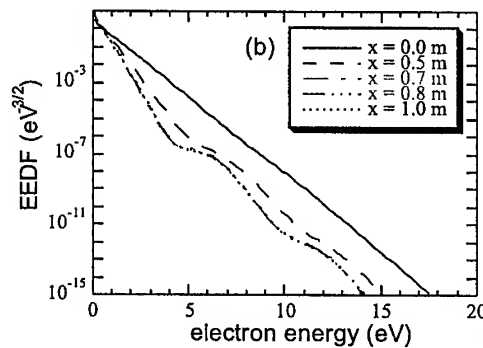
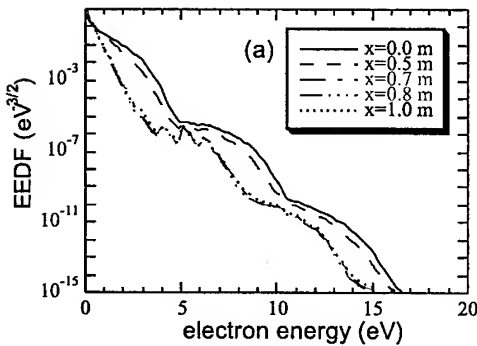


FIG. 8. Electron energy distribution functions (EEDF) at different nozzle positions for $T_0 = 8000$ K in case d (a) and in case e (b), with a simplified version of the scheme used in works for gas discharges [11] and post discharge conditions [12].

by e-V collisions while the tail is still controlled by atom recombination (Fig. 9a). Let us now consider the results for a low enthalpy case i.e. for a lower temperature of the reservoir. In this case we should expect a minor role of vibrational degree of freedom in affecting both the vibrational distribution and the first part of eedf. On the contrary the presence of metastable states should be emphasized because the second kind collisions involving metastable molecules find an higher concentration of low energy electrons compared to previous case.

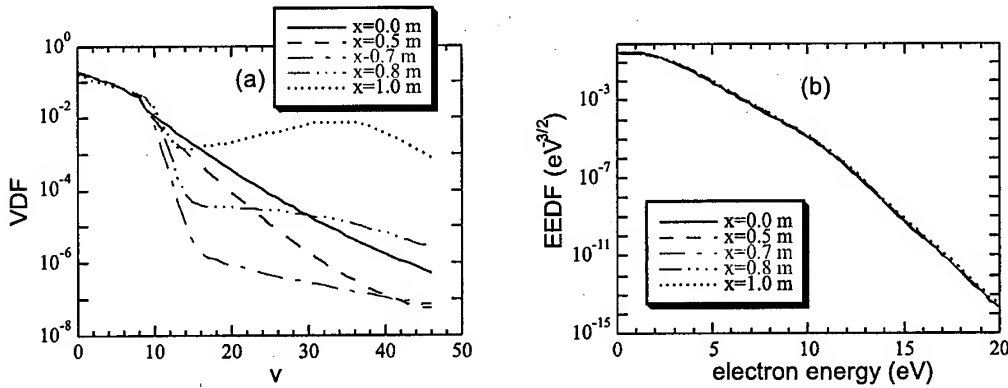


FIG. 9. Vibrational (a) and electron energy (b) distribution functions at different nozzle positions for $T_0 = 8000$ K with $E/N = 40$ Td (case f), with a simplified version of the scheme used in works for gas discharges [11] and post discharge conditions [12].

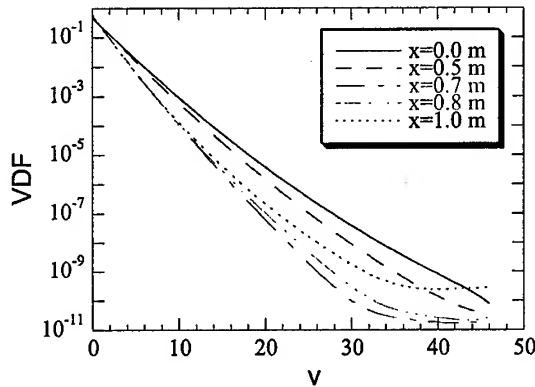


FIG. 10. Vibrational distributions at different nozzle positions for $T_0 = 5000$ K in case a, with a simplified version of the scheme used in works for gas discharges [11] and post discharge conditions [12].

This is indeed the case as reported in Figs 10, 11 - 13ab. In particular Fig. 10 reports the vibrational distribution for the different positions in the nozzle without considering the presence of free electrons. The lower temperature of reservoir is such to decrease the dissociation degree so that the tail of the distribution which is populated by the recombination process is much lower than the previous case (compare Fig. 10 with Fig. 4). At the same time the Boltzmann character of the distribution extends in any case up to level $v = 30$ while for $T_0 = 8000$ K already at $v = 5$ we can see non equilibrium effects (still compare Fig. 10 with Fig. 4).

Figure 11a-b reports both the vibrational distributions and eedf for the different conditions at the exit of the nozzle in the presence of free electrons. We can

observe that the presence of e-V processes spread the different vibrational distributions even though the effects are observable for concentrations of vibrational states less or equal to 10^{-3} . The presence of metastable states considerably affects eedf creating self-repeating structures due to second kind collisions. These structures disappear in the presence of electron-electron collisions which tend to maxwellize eedf.

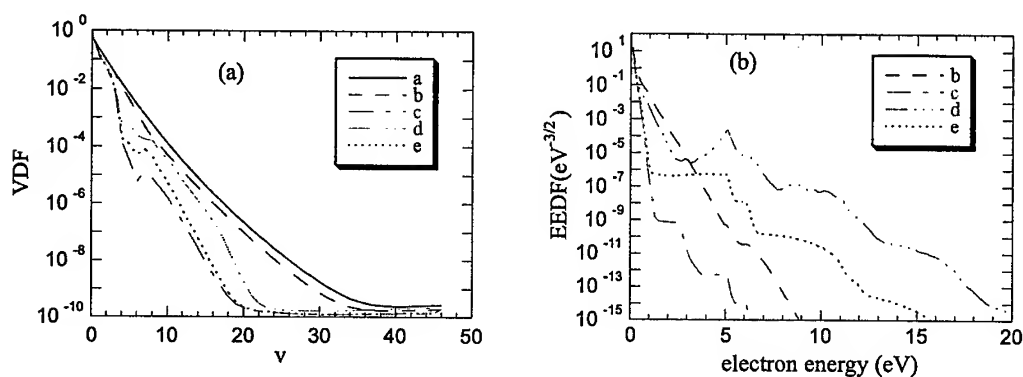


FIG. 11. Vibrational (a) and electron energy (b) distributions at nozzle outlet for $T_0 = 5000$ K in different cases (the curve label refer to the case described in the text), with a simplified version of the scheme used in works for gas discharges [11] and post discharge conditions [12].

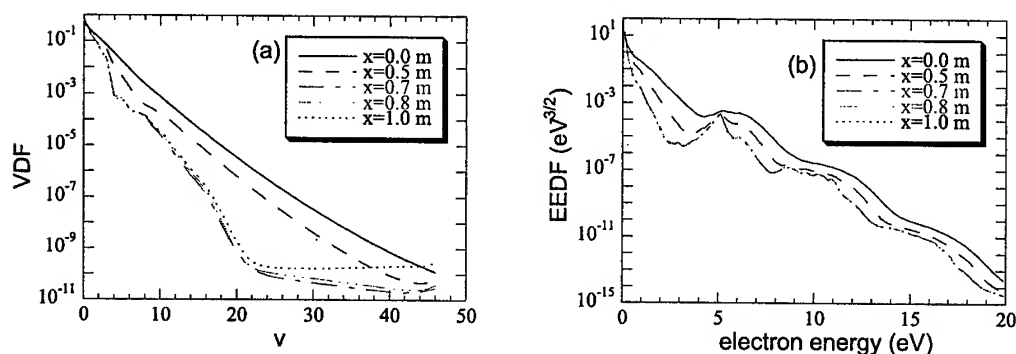


FIG. 12. Vibrational (a) and electron energy (b) distributions at different nozzle positions for $T_0 = 5000$ K in case d, with a simplified version of the scheme used in works for gas discharges [11] and post discharge conditions [12].

Details for the cases d and e are respectively reported in figures 12a-b and 13a-b. In these cases the structures are well evident and the presence of an electric field reduces their magnitude being however unable to completely destroy them.

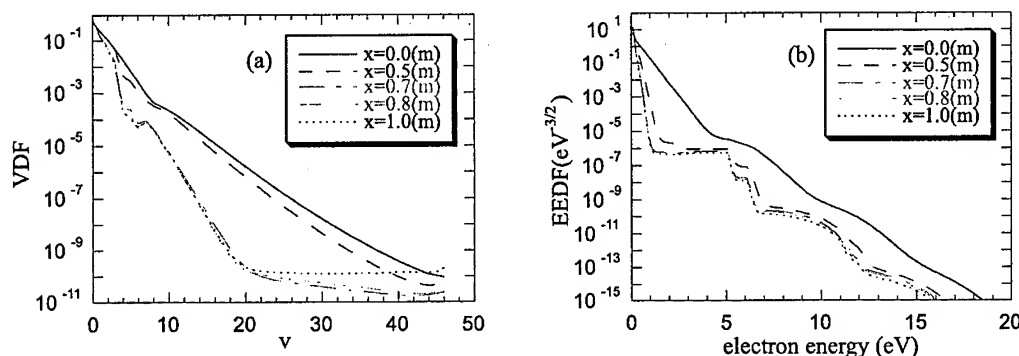


FIG. 13. Vibrational (a) and electron energy (b) distributions at different nozzle position for $T_0 = 5000$ K in case e, with a simplified version of the scheme used in works for gas discharges [11] and post discharge conditions [12].

3. Conclusions

In this paper we have reported for the first time to our knowledge a complete kinetic scheme which couples fluid dynamics, state to state vibrational kinetics and Boltzmann equation for the electron energy distribution function. This model is used for characterizing high enthalpy flows through nozzle expansion.

The model is selfconsistent for the vibrational degree of freedom taking into account the presence of metastable states and of electrons in parametric form.

The results show highly structured vibrational and electron energy distribution functions along the x-axis of the nozzle.

Improvement of the present results can be achieved in the future by eliminating the numerous assumptions made in the present work on metastable and ionization kinetics as well as on the parametric assumption of the electric field.

Dedicated experiments for the different distributions should be developed to experimentally characterize this reaction room in view of the possible application in material and space technologies.

Acknowledgements

This work has been partially supported by ASI (Agenzia Spaziale Italiana) and by MURST (project n 9802276194004).

References

1. W.G. VINCENTI, C.H. KRUGER, *Introduction to Physical Gas Dynamics*, Wiley and Sons, New York 1965.
2. C. PARK, *Non Equilibrium Hypersonic Aerothermodynamics*, Wiley and Sons, New York 1990.
3. C.E. TREANOR, J.W. RICH, R.G. RHEM, *Vibrational Relaxation of Anharmonic Oscillators with Exchange-Dominated Collisions*, J. Chem. Phys., **48**, 4, 1798-1807, 1968.

4. G. CAPRIATI, G. COLONNA, C. GORSE, M. CAPITELLI, *A Parametric Study of Electron Energy Distribution Functions and Rate and Transport Coefficients in Nonequilibrium Helium Plasmas*, Plasma Chem. Plasma Proc., **12**, 3, 237-260, 1992.
5. G. COLONNA, C. GORSE, M. CAPITELLI, R. WINNKLER, J. WILHELM, *The Influence of Electron-Electron Collisions on Electron Energy Distribution Functions in N₂ Post Discharge*, Chem. Phys. Lett., **213**, 1, 5-9, 1993.
6. M. CAPITELLI, C. GORSE, *Non Equilibrium Plasma Kinetics*, Nonequilibrium Processes in Partially Ionized Gases 45-63, Ed. M.Capitelli, N.Bardsley, Plenum Press, New York, 1990.
7. G. COLONNA, M. TUTTAFESTA, M. CAPITELLI, D. GIORDANO, *NO Formation in One-Dimensional Nozzle Air Flow with State-to-State Nonequilibrium Vibrational Kinetics*, AIAA paper 98-2951, 1998.
8. G. COLONNA, M. TUTTAFESTA, M. CAPITELLI, D. GIORDANO, *NO Formation in One-Dimensional Nozzle Air Flow with State-to-State Nonequilibrium Vibrational Kinetics: the Influence of O₂+N=NO+O reaction*, AIAA paper 99-3685, 1999.
9. G. COLONNA, M. TUTTAFESTA, M. CAPITELLI, D. GIORDANO, *Influence on Dissociation Rates of the State-to-state Vibrational Kinetics of Nitrogen in Nozzle Expansion*, 21st International Symposium on Rarefied Gas Dynamics, July 26-31 1998, Marseille (France), in press.
10. G. COLONNA, M. CAPITELLI, *Electron and Vibrational Kinetics in the Boundary Layer of Hypersonic Flow*, J. Thermophys. Heat Transf., **10**, 12, 406-412, 1996.
11. A. GARSCADDEN, N. RAJESH, *Non-Equilibrium Electronic and Vibrational Kinetics in H₂ - N₂ and H₂ Discharges*, Plasma Sources Sci. Technol., **4**, 2, 269-280, 1995.
12. C. GORSE, M. CAPITELLI, *Coupled electron and Excited-State Kinetics in a Nitrogen Afterglow*, J. Appl. Phys., **62**, 10, 4072-4076, 1987.

THE INVERSE FARADAY EFFECT IN PLASMAS AND ITS POSSIBLE APPLICATIONS

S. ELIEZER ¹

PLASMA PHYSICS DEPARTMENT SOREQ NRC
 Yavne 81800, Israel

Circular polarized laser light can produce very high and controllable magnetic fields in plasmas due to the inverse Faraday effect. This magnetic field combined with the naturally occurring toroidal fields gives a spheromak like magnetic bottle. The inertial confinement in this scheme is supported by the magnetic forces. The Lawson criterion for a DT plasma might be achieved for a plasma density of $5 \cdot 10^{21} \text{ cm}^{-3}$ and confinement during 20 ns. In order to increase the plasma density and temperature a Z pinch cumulation process is suggested.

1. Introduction

The generation of very large magnetic fields in laser produced plasmas is well known for the last thirty years [1]. Magnetic fields of the order of megagauss have been routinely observed. The mechanism proposed to explain the generation of these magnetic fields usually are based on the crossed electron temperature and density gradients which produce a field in the $\nabla n_e \times \nabla T_e$ direction. For other possible models see Haines [2]. In an axially symmetric plasma system, the magnetic field is in the toroidal direction, that is perpendicular to the laser irradiation. To a good approximation the toroidal field is given by

$$(1.1) \quad B_\theta \simeq 3 \cdot 10^7 \text{ (Gauss)} \left(\frac{T_e}{1 \text{ keV}} \right)^{1/2} \left(\frac{1 \mu\text{m}}{L_T} \right) \left(\frac{A}{Z} \right)^{1/2},$$

where T_e is the electron temperature, L_T is the transverse density scale length, i.e. of the order of the laser irradiation radius, A is the mass number and Z is the degree of ionization of the plasma material. For a fully ionized aluminum target, a laser spot of about $100 \mu\text{m}$ (radius) and an electron temperature of 1 keV, the toroidal magnetic field is about 0.4 MGs. Higher magnetic fields were attained with a smaller radial laser spot.

¹The work presented in this paper was done in collaboration with: Y. Paiss, Z. Henis, I. Vorobeichik, Y. Horovitz, E. Kolka, M. Piera and J.M. Martinez-Val

In this paper the production of magnetic fields in laser produced plasmas by a different and more fundamental technique is presented. This phenomena, which is based on the Inverse Faraday effect (IFE), is induced by circularly polarized laser light (CPLL). The magnetic field arises in the plasma because electrons quiver with the oscillating electric field of the incoming laser light and if the laser is circularly polarized, then the electrons will describe a circular motion. The "net" effect of this is a circular current on the edge of the plasma, which generates the magnetic field [3].

The inverse Faraday effect was treated theoretically by different models, involving the solution of the Maxwell equation for light propagating in plasma, at various levels of approximation.

The dispersion relation of a circularly polarized wave was obtained from the magnetic dipoles related to the circular motion of single electrons [4]. The axial magnetic field induced by CPLL was estimated using a classical single plasma model [3]. Recently the magnetic field generation was calculated in a self-consistent way, considering two sources. One source is related to the circular motion of single electrons in the wave, which is equivalent to a magnetic dipole. The second source is related with the inhomogeneity of both the electron density and the intensity of the laser beam. The calculations show that the magnetic field is proportional to the laser irradiance [3, 4, 5]:

$$(1.2) \quad \frac{B}{B_c} = \frac{1}{2} \left(\frac{eE_0}{m\omega c} \right)^2 \left(\frac{\omega_p^2}{\omega^2} \right) \left(1 + \frac{L_a^2}{L_a^2 + L_n^2} \right) \exp \left(- \left(\frac{r^2}{L_a^2} + \frac{r^2}{L_n^2} \right) \right)$$

$$(1.3) \quad B_c [\text{Gauss}] = \frac{mc\omega}{e} = \frac{1.07 \cdot 10^8}{\lambda_L (\mu\text{m})}.$$

$E_0^2 = 4\pi I_L/c$ is the electric field of the laser, I_L is the laser peak intensity, ω is the laser frequency, m and e are the electron mass and charge, c is the light velocity, L_a and L_n describe the laser and the plasma profiles: $E(r) = E_0 \exp(-r^2/L_a^2)$, $n(r) = n_0 \exp(-r^2/L_n^2)$, $\omega_p = (4\pi n_0 e^2/m)^{1/2}$ is the classical plasma frequency at the center of the plasma distribution.

The effect describe above is called the linear inverse Faraday effect. The order of magnitude of this magnetic field in the Z direction, i.e. in the direction of the CPLL irradiance, is given by

$$(1.4) \quad B_Z^L \simeq 3.0 \cdot 10^4 (\text{Gauss}) \left(\frac{n_e}{n_c} \right) \left(\frac{\lambda_L}{1 \mu\text{m}} \right) \left(\frac{I_L}{10^{14} \text{ W/cm}^2} \right),$$

where n_c is the electron plasma critical density, and B_Z^L is the axial magnetic field due to the linear (L) IFE.

An additional mechanism for the axial magnetic field generation is by the ponderomotive force [6] coupled with the irradiance of CPLL. This effect is called the nonlinear inverse Faraday effect. The ponderomotive force resulting from the inhomogeneity of the laser is the low frequency part of the Lorentz force and is proportional to $\text{grad}(E^2)$ in the classical regime and to $\text{grad}(\gamma)$ in the relativistic regime. E is the electric field of the laser and $\gamma = \left(1 + (eE_0/m\omega c)^2 \right)^{1/2}$. The

axial magnetic field induced by the ponderomotive force is obtained by calculating the low frequency component of the magnetic field, using the continuity equation of a cold plasma, the relativistic equation of motion and the Maxwell equations. In the case of a circularly polarized laser this magnetic field is given by:

$$(1.5) \quad \frac{B}{B_c} = (\gamma(0) - \gamma(r))^{1/2} \frac{\omega_p(0)}{\omega}$$

$\gamma(0)$ and $\omega_p(0)$ are the value of γ and the plasma frequency at the center of the beam. In the non-relativistic limit this model gives for $L_n \gg L_a$:

$$(1.6) \quad \frac{B}{B_c} = \left(\frac{\omega_p}{\omega} \right) \left(\frac{eE_0}{m\omega c} \right) \left(1 - \exp \left(-\frac{r^2}{L_a^2} \right) \right)^{1/2}.$$

The magnitude of the nonlinear (NL) axial magnetic field is thus given for a non-relativistic plasma by

$$(1.7) \quad B_Z^{NL} \simeq 6.5 \cdot 10^5 \text{ (Gauss)} \left(\frac{n}{n_c} \right)^{1/2} \left(\frac{I_L}{10^{14} \text{ W/cm}^2} \right)^{1/2}.$$

The inverse Faraday effect was also studied experimentally. Axial magnetic fields of the order of 10^{-5} Gauss were detected in non absorbing materials (glasses) at low laser irradiance of 10^7 W/cm^2 [7]. An inverse Faraday effect of $(2 \cdot 10^{-2} \text{ Gs})$ was also measured in a low-density plasma ($\sim 3 \cdot 10^9 \text{ cm}^{-3}$) subjected to MW pulses of circularly polarized microwaves [8].

In section 2 the measurements of the optical IFE produced by CPLL are described in the range of $10^9 - 10^{14} \text{ W/cm}^2$ of laser irradiances.

The IFE generated magnetic field is much more readily controllable than the "hydrodynamic" and "thermo" magnetic fields. The IFE fields are switched on and off over the laser pulse duration by simply irradiating or not with a CPLL, therefore this magnetic field may be induced even with femtosecond laser pulses.

In sections 3 and 4 possible applications of the induced IFE magnetic field are suggested. In section 3 the possibility of creating a mini spheromak-like magnetic field configuration in a laser produced plasma is described, while in section 4 a cumulation phenomena related to a Z pinch device is proposed. The paper is concluded with a short conclusion in section 5.

2. Experimental evidence of the IFE in laser-plasma interaction

Two diagnostic methods were used to measure the axial magnetic field generated by the interaction of a circularly polarized laser light with a solid target. At low irradiances ($10^9 - 10^{11} \text{ W/cm}^2$) the axial magnetic field induced by the CPLL was measured from the voltage signal induced by the magnetic field in an output coil, and at high irradiances (up to $2 \cdot 10^{14} \text{ W/cm}^2$) was measured by the Faraday effect.

The main laser system is based on a Continuum NY-60 Nd: YAG oscillator followed by one triple passed and one double passed amplifiers. The laser pulse

duration was 7 ns and the spot diameter was in the range 100-200 μm . The laser energy was up to 100 J. For the low laser irradiance the target was a ring made of ferrite, with a 350 μm air gap and a 500 μm diameter hole drilled through the ferrite into the gap. The laser was irradiated through the hole and created a plasma by ablating the ferrite on the other side of the air gap. A CPLL induced toroidal current was created in the plasma which generated an axial magnetic field associated with an appropriate magnetic flux. Due to the high permeability of the ferrite, this flux penetrated into the ferrite and the magnetic field lines closed through the ring. The time derivative of this magnetic flux induced a voltage signal in the output coil, which was measured by a GHz oscilloscope.

The calibration was done with a fast pulse generator, delivering rectangular pulses, 10 ns duration with a rise time of 1 ns. In the calibration experiment the pulse generator was connected to the ferrite ring through an input coil similar to the output used in the laser experiments. The magnetic field generated in the input coil is given by $B = -\frac{1}{NS} \int_0^{\tau_r} \mathcal{E}_c dt$, B is the magnetic field, \mathcal{E}_c is the voltage on the coil, N is the number of the coil loops, S is the cross area of the ferrite ring and τ_r is the rise time of the pulse generator. A calibration curve is obtained by measuring the voltage of the output signal as a function of the magnetic field.

At low intensity the ferrite target was irradiated only by the oscillator (without the amplifiers), operating at 10 Hz and the output signal is an average of 10^4 shots. The focal spot diameter was 200 μm . The magnetic field measured in this experiment was (455 ± 220) Gs.

A characteristic feature of the inverse Faraday effect is the change in voltage when a right handed CPLL is changed to a left handed CPLL. This feature is seen in the experiments where the voltage signal changes sign when the polarity of the CPLL changes from right to left. Similar results were observed at higher intensities, up to 10^{11} W/cm². At higher peak intensities, for the geometry of the experiment and assuming a spatial Gaussian profile of the beam, a plasma is created through ablation of the walls of the hole in the ferrite, causing a drastic reduction of the magnetic flux that penetrates in to the ferrite.

At higher irradiances the axial magnetic field was measured using the Faraday rotation diagnostic. This method is based on the rotation of the plane of polarization of a double frequency (2ω) linear polarized probe laser beam in the presence of a magnetic field. The angle of rotation is given by:

$$(2.1) \quad \phi \text{ (deg)} = 3.02 \cdot [\lambda_p(\mu\text{m})]^2 \cdot \int_0^L \frac{n_e(\text{cm}^{-3})B(\text{MG})dz(\mu\text{m})}{10^{21} \sqrt{1 - \frac{n_e}{n_{cp}}}}.$$

z is the distance along the ray path, L is the plasma length, B is the magnetic field component along the path, λ_p is the wavelength of the probe beam, n_e is the density of the plasma, and n_{cp} is the critical density for the probe beam.

The main laser beam, 7 ns, 1.06 μm and intensities in the range 10^{12} - 10^{14} W/cm² irradiates an aluminum target. In the irradiance range of $5 \cdot 10^{13}$ - $3.5 \cdot 10^{14}$ W/cm² the laser focal spot (diameter) was 100 μm and the laser energy was changed between 30 J to about 80 J. For lower irradiances ($2 \cdot 10^{12}$

- $5 \cdot 10^{13}$ W/cm²) the focal spot diameter was 200 μ m. These spot dimensions were consistent with plasma scale lengths as measured with an x-ray pinhole camera. The 2ω probe beam, 5 ns, 5 mJ, propagates into the plasma collinearly with the main beam, reflects from the critical surfaces and then is directed into an analyzer system, including two photodiodes, a $\lambda/2$ plate, a beam splitter and a high contrast polarizer. The angle of rotation of the polarization of the probe beam, after propagating through the plasma, is determined by the ratio of the signals of the two photodiodes and a calibration curve of the analyzer.

The calibration of the analyzer was done by reflecting the probe beam from a perfect mirror, located at the place of the target. A calibration curve was obtained by rotating the polarizer and measuring the ratio of the signal of the two photodiodes as a function of the rotation angle of the polarizer. The calibration curve had a shape of parabola with a very distinct minimum. The minimum angle that can be measured with this analyzer systems is 1° with an error of 10%. In the experiments the polarizer was aligned at an angle corresponding to the minimum of the calibration curve. The plasma length was measured by a pinhole camera. The magnetic field was obtained by unfolding the integral (2.1) assuming a linear density profile.

The experiments were performed for both circularly and linearly polarized light. In the range of intensities $10^{12} - 5 \cdot 10^{13}$ W/cm² the plane of polarization of the probe beam did not rotate in the experiments performed with linearly polarized laser light (LPLL). The scaling law of the measured axial magnetic field B from the experiments performed with circularly polarized laser, the inverse Faraday effect, in the above range of intensities, is $B \sim I^{1/2}$, as shown below in Fig. 1. At higher intensities of the order of $3 \cdot 10^{14}$ W/cm² a sudden increase of the axial magnetic field beyond the above scaling law is observed in the experiments performed with CPLL. At these high irradiance an axial magnetic field was observed also in experiments performed with linearly polarized light. This axial magnetic field in the experiments with LPLL was lower by 30% than the axial magnetic field in the experiments performed with CPLL. Axial magnetic fields created in targets irradiated by LPLL may be excited by other mechanisms, such as the dynamo effect [9, 10] or due to rippled surface irregularities [11]. These mechanisms are excited at large magnetic Reynolds numbers, $R_m = 20 (I_L \lambda_L^2)^{5/3} \left(\frac{2z}{A}\right)^{1/6} \frac{\tau_L}{z}$, I_L is the laser intensity in units of 10^{14} W/cm², λ_L is the wavelength in μ m, τ_L is the pulse duration in picoseconds, Z is the charge and A is the atomic number. For example, for an aluminum plasma with $Z = 10$ and a laser pulse with $I_L = 10^{14}$ W/cm², $\lambda_L = 1 \mu$ m, one gets R_m of about 14000.

The measured axial magnetic field [12, 13] as a function of the laser irradiance varying in a range of five orders of magnitude, measured with the two diagnostic methods describe here, is plotted in Fig. 1. The lines plotted in this figure correspond to theoretical models explained in section 1. One can see the increase of the magnetic field with the laser irradiance. The lower line in Fig. 1 displays the axial magnetic field as function of the laser intensity calculated by the linear inverse Faraday effect, assuming an electron density $n_0 = 10^{21}$ cm⁻³. The three upper lines are calculations of the magnetic field using the nonlinear inverse

Faraday effect, at electron densities of 10^{19} , 10^{20} , and 10^{21} cm^{-3} . The experimental results for laser intensities in the range $10^9 - 3 \cdot 10^{13}$ W/cm^2 fit well with the ponderomotive model calculated with an electron density of 10^{20} cm^{-3} . At 10^{14} W/cm^2 an increase in the magnetic field above 2 MGs seems to be present and it seems that neither the ponderomotive model nor the linear inverse Faraday effect can explain our experimental data.

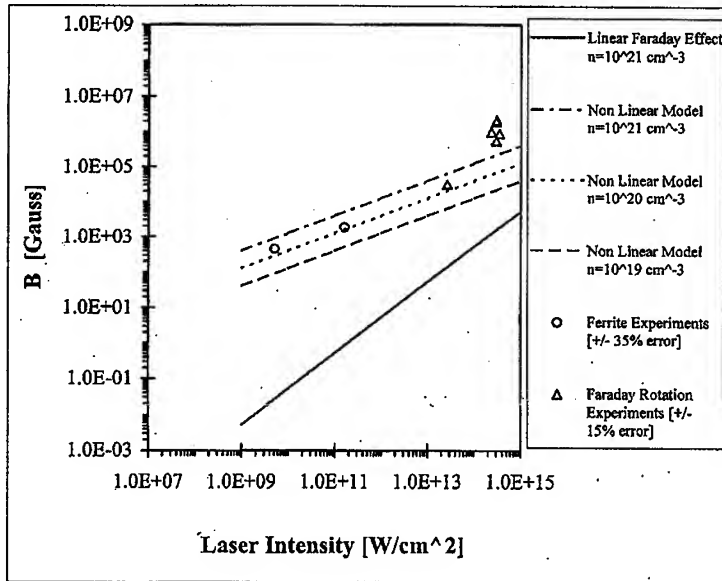


FIG. 1. The measured axial magnetic field as a function of the laser irradiance, the axial magnetic field calculated by the linear model with an electron density, $n_0 = 10^{21}$ cm^{-3} , the axial magnetic field calculated by the non linear model with an electron density, $n_0 = 10^{21}$ cm^{-3} , $n_0 = 10^{20}$ cm^{-3} and $n_0 = 10^{19}$ cm^{-3} .

3. A miniature magnetic bottle

In this section a new hybrid concept which involves both magnetic and inertial confinement is presented. A miniature "magnetic bottle" (see Fig. 2), induced by high power circularly polarized light is suggested [3, 14, 15].

The possibility of creating a tokamak-like magnetic field configuration in a laser-produced plasma is also relevant for confining [3, 16] intermediate densities (about 10^{21} cm^{-3}) for times about 100 ns in order to satisfy the Lawson criterion. Such an approach circumvents many of the complexities of inertial confinement fusion where very symmetric implosions using many laser beams are required. This intermediate fusion regime may also overcome the extremely large requirements on a tokamak device.

The concept of hot plasma confinement in a miniature magnetic bottle considered here relies on the hybrid use of inertial and magnetic confinements and

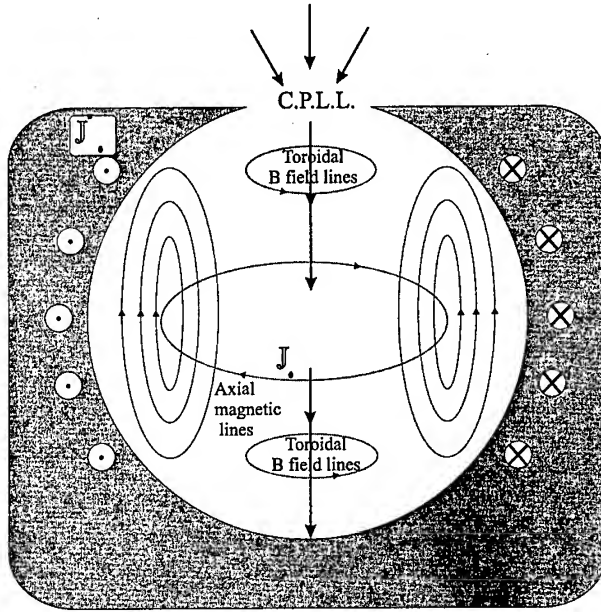


FIG. 2. A schematic miniature magnetic bottle.

megagauss field generation by CPLL. The schematic structure of the suggested configuration is as follows: a DT plasma is created inside a cylindrical or a spherical heavy conductor (or superconductor) shell with a hole. The plasma is irradiated by an intense circularly polarized laser beam. The CPLL creates a toroidal current in the plasma due to the finite size of the laser spot and density gradient in the plasma. The toroidal current in the plasma induces an axial magnetic field inside and outside the plasma and also induces a toroidal current in the walls in the opposite direction in order to reduce magnetic field penetration into the wall. This combination creates a magnetic field in the laser propagation direction near the center of the plasma and a magnetic field in the opposite direction near the wall. These magnetic fields are created in addition to the toroidal magnetic field formed by the $\nabla n_e \times \nabla T_e$ mechanism. Both the axial and the toroidal magnetic fields can be of the order of megagauss for typical parameters of laser fusion. The plasma is heated resonantly by the CPLL from a temperature of ~ 1 keV to ~ 5 keV during a time of a few nanoseconds. The process of magnetic field formation and plasma heating by CPLL lasts for a few nanoseconds, until the laser is turned off. After the laser is turned off, the plasma and the magnetic field are not in a steady state, and they go through a dynamic process of evolution. The plasma expands and exerts pressure on the walls. The magnetic field lines expand and diffuse both into the walls and inside the plasma. Also, heat diffuses from the plasma to the walls.

There are three time scales describing the plasma confinement in this scheme: the magnetic diffusion time, τ_B ; the heat diffusion time τ_H [15]; and the inertial confinement time, τ_h . τ_h is the hydrodynamic confinement time and therefore

determines the time scale in the change of the plasma density. The hot plasma applies a mechanical force on the wall of the vessel. This mechanism is equivalent to a (plasma) piston impinging on the wall and creating a shock wave through the wall. Therefore, assuming that the wall is thick, the inertial confinement time is determined by the piston velocity and the dense plasma radius (and not the thickness of the wall). During the expansion of the "piston", the plasma density decreases. It turns out that the value of τ_h is the most limiting time scale. For the parameters under consideration we get [15]

$$\tau_B > \tau_H > \tau_h \sim 30 \text{ ns.}$$

The Lawson criterion may be fulfilled for 3ω CPLL created plasma with a density of $5 \cdot 10^{21} \text{ cm}^{-3}$ and a confinement time of $\sim 20 \text{ ns}$.

4. An axial energy cumulation phenomenon

An alternative approach to thermonuclear fusion, that uses the elements of both the magnetic confinement fusion (MCF) and the inertial confinement fusion (ICF), was sought for many years and was already proposed by Sakharov in the former Soviet Union in the 40's. He considered creating a high temperature DT plasma in a strong magnetic field so that the charged ions and electrons were "stuck" to magnetic field lines, as in a tokamak. The hot magnetized plasma would then be imploded by an external force as in the (ICF) scheme. The implosion would heat and compress the relatively dense plasma and the strong magnetic field would help capture the energetic α particles produced during the fusion events. Since Sakharov's idea many examples can be found in the magnetic fusion literature showing that fusion reactions can be created in smaller-sized systems if one admits larger magnetic field, higher plasma density, and pulsed operation as with imploding liners [17, 18, 19, 20, 21]. The most interesting regime of density is $n \sim 10^{20} \text{ cm}^{-3}$, which is high compared with MCF, but low compared to ICF. This density regime at 10 keV temperature corresponds to megabars of pressure, which is intrinsically pulsed in nature. This intermediate density regime is called Magnetized Target Fusion (MTF). The name is chosen based on two general characteristics: 1) as with ICF, PdV work heats the fuel by compressing it inside an imploding wall, or pusher, and 2) magnetic field is embedded in the fuel to insulate it from the pusher.

An example of the above approach is the magnetically-driven imploding liner method for MTF. In the liner approach the fuel with an embedded magnetic field would be preheated and positioned inside a volume of centimeter dimensions, which is surrounded by a thin metal shell (or liner) that will act as the pusher. A current introduced on the outer surface of the liner would cause it to implode by self-pinching magnetic forces at a velocity of $\sim 10^6 \text{ cm/s}$. At peak compression a significant fraction of the liner kinetic energy would be converted to thermal energy of the fuel and the final fuel density and temperature would be designed to give significant fusion energy generation.

Let us consider a thin cylindrical shell coaxially positioned with a filament of radius a (see Fig. 3). The configuration is assumed to have a cylindrical

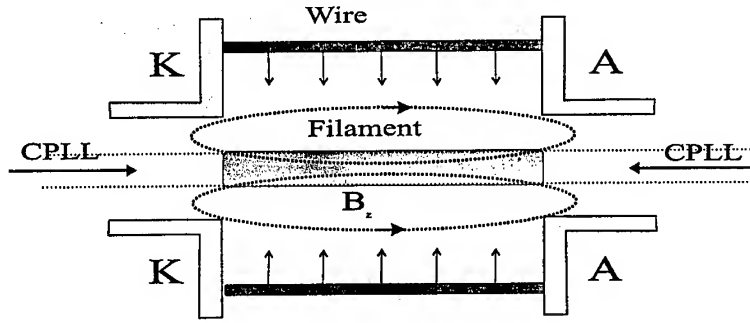


FIG. 3. A schematic Z-pinch energy cumulation device.

symmetry. A high current through the shell is accelerating the shell inward towards the filament. The filament is a porous material with a density of the order of the plasma critical density (i.e. the number of electrons per cm^3 is $10^{21}/\lambda_{\mu\text{m}}$, where $\lambda_{\mu\text{m}}$ is the laser wavelength in microns). The CPLL is absorbed along the filament and by the inverse Faraday effect a magnetic field between the filament and the shell is produced. The current generated by the CPLL will also produce a magnetic field (with an opposite sign to that between the shell and the filament) inside the filament, so that the net flux is zero. For a filament of radius a and a shell of radius r , the flux conservation requires $B_z(\text{in})a^2 = B_z(\text{out})(r^2 - a^2)$, where "in" and "out" refer to inside and outside the filament accordingly. In this case, only the "collision" between the shell and the filament is considered. Due to the short pulse duration of the lasers under consideration (nanoseconds or much shorter), the CPLL is applied during the period that $r - a \ll a$, so that $B_z(\text{in}) \ll B_z(\text{out})$. Using the "CPLL scenario", the laser duration time scale is much less than the timescale of the magnetic diffusion (into the filament). The diffusion time τ_B of the magnetic field to a distance l_B is given by

$$(4.1) \quad \tau_B \approx \frac{4\pi\sigma l_B^2}{c^2},$$

where σ is the electrical conductivity and c is the speed of light. Using Spitzer's conductivity

$$(4.2) \quad \sigma (s^{-1}) = \frac{8.70 \cdot 10^{13}}{Z \ln \Lambda} \left(\frac{T_e}{eV} \right)^{3/2}$$

Z is the plasma degree of ionization and $\ln \Lambda = 10$ for our parameters of interest. Eqs. (4.1) and (4.2) yield

$$(4.3) \quad \tau_B(s) \approx 3.84 \cdot 10^{-5} \frac{1}{Z} \left(\frac{T_e}{\text{keV}} \right)^{3/2} \left(\frac{l_B}{\text{mm}} \right)^2$$

i.e. for a 1 keV hydrogen plasma the magnetic field diffuses into 10 μm of filament during about 4 ns. In this case the above approximation is appropriate for laser pulse duration of about 4 ns or less.

Assuming a magnetic conservation between the shell and the filament the equation of motion for the shell and the filament are [22]

$$(4.4) \quad M_s \frac{d^2 r}{dt^2} = \frac{I_s^2}{100r} + \frac{B_{z0}^2 r}{4} \left[\frac{(r_0^2 - a_0^2)}{(r^2 - a^2)} \right]^2$$

$$(4.5) \quad M_f \frac{d^2 a}{dt^2} = \left[2(1 + Z) K_B T_0 a_0^{4/3} \left(\frac{M_f}{A_f m_p} \right) \right] \frac{1}{a^{7/3}} - \frac{B_{z0}^2 a}{4} \left[\frac{(r_0^2 - a_0^2)}{(r^2 - a^2)} \right]^2$$

r and a are the shell and the filament radius accordingly, r_0 and a_0 are their initial values when the CPLL is switched on and M_s and M_f are their appropriate mass per unit length. I_s is the value of the maximum current, assumed to be constant during the last stages of the shell collision with the filament, i.e. during the time that the laser is applied. B_{z0} is the initial magnetic field applied between the shell and the filament due to the inverse Faraday effect. T_0 is the initial temperature of the filament and Z is the ionization and A_f is the atomic mass number. m_p is the proton mass and K_B is Boltzmann's constant. Eqs. (4.4) and (4.5) are given in cgs units except I_s which is in Amperes.

The equations of motion to be solved, Eqs. (4.4) and (4.5), can be derived from a potential $U(r, a)$ given by

$$(4.6) \quad U(r, a) = A \ln \frac{r}{r_0} + \frac{B}{2} \left[\frac{(a^2 - a_0^2) - (r^2 - r_0^2)}{(r^2 - a^2)} \right] + C \left[\left(\frac{a_0}{a} \right)^{4/3} - 1 \right]$$

$$(4.7) \quad A = \frac{I_s^2}{100} \quad B = \frac{1}{4} B_{z0}^2 (r_0^2 - a_0^2) \quad C = 2(1 + Z) K_B T_0 \left(\frac{M_f}{A_f m_p} \right)$$

with the usual equations of motion:

$$(4.8) \quad M_s \frac{d^2 r}{dt^2} = - \frac{\partial U}{\partial r} \quad M_f \frac{d^2 a}{dt^2} = - \frac{\partial U}{\partial a}$$

An analysis of the potential U as a function of a for r as a parameter shows a minimum in the potential for small enough r . The problem under consideration is equivalent to an elastic collision of two point like particles where there is a reflecting wall at $a = 0$.

Preliminary simulations of this cumulation process [23] suggest that fusion conditions might be achieved by assuming a stable Z pinch process.

5. Conclusions

The two main approaches that are currently being pursued in controlled thermonuclear fusion, Inertial Confinement Fusion (ICF) and Magnetic Confinement Fusion (MCF) differ by twelve orders of magnitude in plasma density and confinement time. Two new schemes, the mini magnetic bottle and the cumulation Z pinch device, are presented here. In these devices the plasma density is in an

intermediate range $10^{21} - 10^{24} \text{ cm}^{-3}$. The concept suggested here relies on the hybrid use of inertial and magnetic confinements and megagauss field generation by circularly polarized laser light.

Experiments and calculations were performed to study the feasibility of the above scheme. Measurements of the inverse Faraday effect over 5 orders of magnitude of the laser irradiance are reported. The scaling law of the axial magnetic field with the laser irradiance is determined in the range of $10^9 - 10^{14} \text{ W/cm}^2$. Axial fields from 500 Gs up to 2.17 MGs were measured.

Zero dimension (i.e. time dependent) calculations show very optimistic results for fusion. Future studies will be aimed to perform simulations of the plasma evolution and of the energy gain in the above configurations.

References

1. For a review of magnetic fields in laser produced plasmas see, J.A. Stamper, *Laser Part. Beams*, **9**, 841, 1991 and references therein.
2. M.G. HAINES. *Magnetic field saturation mechanisms in laser-plasma interactions*. *Laser Interaction with Matter and Inertial Fusion* (Eds. G. Velarde, J.M. Martinez-Val, E. Minguez, J.M. Perlado, World Scientific Pub., Singapore, 1997) p. 219.
3. S. ELIEZER, Y. PAISS, H. STRAUSS, *Phys. Lett. A*, **164**, 416, 1992.
4. D. STEIGER, C.H. WOODS, *Phys. Rev. A*, **5**, 1467, 1972.
5. Z.M. SHENG, J. MEYER-TER-VEHN, *Phys. Rev. E*, **54**, 1833, 1996.
6. T. LEHNER, *Physica Scripta*, **49**, 704, 1994.
7. J.P. VAN DER ZIEL, P.S. PERSHAN, L.D. MALMSTROM, *Phys. Rev. Lett.*, **15**, 190, 1965; *Phys. Rev.*, **143**, 574, 1966.
8. J. DESCHAMPS, M. FITAIRE, M. LAGOUTTE, *Phys. Rev. Lett.*, **25**, 1330, 1970.
9. J. BRIAND, V. ADRIAN, M.E. TAMER, A. GOMEZ, Y. QUEMENER, J.P. DINGUIRARD, J.C. KIEFFER, *Phys. Rev. Lett.*, **54**, 38, 1985.
10. R. DRAGILA, *Phys. Fluids*, **30**, 925, 1987.
11. T. YABE, Y. KITAGAWA, A. ISHIZAJI, M. NAITO, A. NISHIGUCHI, M. YOKOYAMA, C. YAMANAKA, *Phys. Rev. Lett.*, **51**, 1869, 1983.
12. Y. HOROVITZ, S. ELIEZER, A. LUDMIRSKY, Z. HENIS, E. MOSHE, R. SHPITALNIK, B. ARAD, *Phys. Rev. Lett.*, **78**, 1707, 1997.
13. Y. HOROVITZ, S. ELIEZER, Z. HENIS, Y. PAISS, E. MOSHE, A. LUDMIRSKY, M. WERDIGER, B. ARAD, A. ZIGLER, *Phys. Lett. A*, **245**, 329, 1998.
14. E. KOLKA, S. ELIEZER, Y. PAISS, *Phys. Lett. A*, **180**, 132, 1993.
15. E. KOLKA, S. ELIEZER, Y. PAISS, *Laser Part. Beams*, **13**, 83, 1995.
16. A. HASEGAWA, H. DAIDO, M. FUJITA, K. MIMA, M. MURAKAMI, S. NAKAI, K. NISHIHARA, K. TERA, C. YAMANAKA, *Phys. Rev. Lett.*, **56**, 139, 1986.
17. A.R. SHERWOOD, F.L. RIBE, *Fast Liner Compression Fusion Systems*, Fusion 1, part B., p. 59, 1991.
18. L. LINDEMUTH, C. EKDAHL, R. KIRKPATRICK, R. REINOVSKY, R. SIEMON, P. SHEEHEY, F. WYSOCKI, V. CHERNYSHEV, V. MOKHOV, A. DEMIN, S. GARANIN, V. KORCHAGIN, I. MOROZOV, V. YAKUBOV, J. EDELMAN, J. HAMMER, D. RYUTOV, A. TOOR, D. MCDANIEL, J. DEGNAN, G. KIUTTU, R. PETERKIN, Jr., *Magnetic Compression/Magnetized Target Fusion (MACO/MTF): A Marriage of Inertial and Magnetic Confinement*, 16th IAEA Fusion Energy Conference, Montreal, Canada, October 7-11, 1996.

19. A.E. ROBSON, P.J. TURCHI, NRL Linus Program, *Pulsed high beta plasmas*, 3rd topical conference on pulsed high beta plasmas, Pergamon Press, Oxford, p. 477, 1976. Also: P.J. Technology (Plenum Press, New York, 1980), p. 375.
20. G.E. VEKSHTEIN, *Magnetothermal Processes in Dense Plasma*, Rev. Plas. Physics, **15**, 1, 1990.
21. R.P. DRAKE, J.H. HAMMER, C.W. HARTMAN, L.J. PERKINS, D.D. RYUTOV, *Submegajoule Liner Implosion of a Closed Field Line Configuration*, Fusion Tech., **30**, 310, 1996.
22. S. ELIEZER, J.M. MARTINEZ-VAL, *A potential formalism for an axial energy cumulation process*, (to be published).
23. J.M. MARTINEZ-VAL, M. PIERA, S. ELIEZER, Z. HENIS, I. VOROBICHNIK, *Laser induced magnetic cushion and inertial fusion energy* (to be published).

RECENT PROGRESS IN OUR UNDERSTANDING OF THE PHYSICAL PROCESSES IN ARCS IN GAS FLOW

M. T. C. FANG, J. D. YAN, and R. E. BLUNDELL

DEPARTMENT OF ELECTRICAL ENGINEERING AND ELECTRONICS,
UNIVERSITY OF LIVERPOOL
Liverpool L69 3GJ, UK

The conditions under which similarity and scaling laws exist are investigated. A quantitative analysis of the on-set of arc instability is given and the destabilizing mechanisms are identified. The existence of shock in some arc devices seriously disturbs the flow although the electric characteristics of the arc are little affected. Finally, computer simulation results of the operation of a complex industrial device, a high voltage auto-expansion circuit breaker, are given.

1. Introduction

Electrical arcs burning in an axially accelerating gas flow are used in many engineering applications, such as gas-blast circuit breakers, arc heaters, welding and material cutting, material processing, and arc plasma spraying systems [1]. These arcs are collision dominated, and, under most operational conditions, local thermal equilibrium (LTE) can be assumed. Thus, the behaviour of the arc column can be described by Navier-Stokes equations and the appropriate Maxwell's equations. The momentum equation is modified to take account of the Lorentz force and the energy equation of Ohmic heating and radiation transport. Arcs in gas flow can attain very high velocity and are often in turbulent state. Turbulence enhanced momentum and energy transport are often important in the determination of arc behaviour. These need to be taken into account in momentum and energy conservation by introducing appropriate arc turbulence models.

The applications of high pressure arcs are diverse, but the underlying basic physical processes are the same, with differing dominant energy transport processes for different applications. Of all fundamental processes, radiation transport, especially radiation absorption, is of extreme importance. Since the late sixties, much effort has been devoted to the understanding of internal radiation transport within the arc for complex molecular gases such as SF_6 and nitrogen inside an axisymmetric wall stabilised arrangement. Approximate radiation

transport based on net emission coefficient (devised by J. J. Lowke), which is a function of pressure, temperature, and arc radius, has been shown to be a good approximation for the radiation transport for arcs in gas flow [2]. There has been very little work on the nature of arc turbulence, especially regarding the mechanisms which drive arc instability and the on-set conditions for instability except that of Blundell et.al [6]. Turbulent arcs have been modelled along the same lines as fluid jets. For a number of arc devices, shock cannot be avoided. The interaction between an arc and shock is of fundamental interest.

The maturity of numerical techniques, the understanding of basic physical processes and the rapid advancement in computing power at an affordable price in the past decade have made computer modelling and simulation an inseparable tool for the understanding of arc discharge systems. However, computational effort is still substantial. It is therefore useful to explore the conditions under which arcs can be scaled. Establishment of scaling laws is important to extend the range of applicability of computational and experimental results.

The paper will discuss similar solutions and scaling laws, followed by a discussion on arc stability and arc-shock interaction, and finally a full computer simulation of a practical arc device, which encompasses all fundamental physical processes in high pressure arc, will be given and results compared with tests.

2. The governing equations

For an arc at LTE, the conservation equations can be written as

$$(2.1) \quad \frac{\partial}{\partial t}(\rho\Phi) + \nabla \cdot (\rho \vec{V} \Phi) - \nabla \cdot (\Gamma_{\Phi} \nabla \Phi) = S_{\Phi}$$

where Φ is the dependent variable, ρ the gas density, and \vec{V} the velocity. S_{Φ} the source term and Γ_{Φ} , the diffusion coefficient, are given in Table 1, where all unspecified symbols have their conventional meaning.

Table 1.

Equation	Φ	Γ	S_{Φ}
continuity	1	0	0
z-momentum	w	$\eta + \eta_t$	$-\partial P/\partial z + J_r B_{\theta} + \text{viscous terms}$
r-momentum	v	$\eta + \eta_t$	$-\partial P/\partial r - J_z B_{\theta} + \text{viscous terms}$
enthalpy	h	$(k + k_t)/c_p$	$\sigma E^2 - q + dP/dt + \text{viscous dissipation}$

The subscript l denotes laminar part of the transport coefficient and t the turbulent part (see Section 3). The equation of state for temperature below 1000 K is assumed to be ideal and the transport coefficients are usually non-linear functions of pressure and enthalpy. For axisymmetrical case, the net radiation loss per unit volume and time, q , is calculated using the method of [2]. To calculate the Ohmic heating, electric field strength is required for a given arcing current. For a number of arc devices, where boundary layer assumption is valid, Ohm's law can be simplified as

$$(2.2) \quad i = E \int_0^{\infty} \sigma 2\pi r dr$$

where i is the current and the electric field, E , is independent of r . For the general case, where boundary assumption cannot be made, E is computed from the electrostatic potential, ψ , determined from current continuity:

$$(2.3) \quad \nabla \cdot (\sigma \nabla \psi) = 0.$$

Robust algorithms for the solution of the arc governing equations are now available [3]. Some commercial CFD (computational fluid dynamics) packages can also be adapted to solve arc problems although they are less robust computationally and the outcome, to a large extent, depends on the skill of the user e.g. [4]. Computer simulated results give good agreement with test results, even for complex industrial devices [3, 4]. Thus, computer simulation has become an effective design aid.

3. Similar solutions and scaling laws

For a number of arc devices, the arc is burning in a supersonic nozzle (a convergent, divergent nozzle) with a cross section which is much smaller than the nozzle cross section. Boundary layer assumption can therefore be introduced. In addition to the highly non-linear transport properties which depend on the absolute value of temperature for a given pressure, radiation absorption and turbulent momentum and energy transport make the solutions of equation (2.1) explicitly dependent on the length. However, by choosing Prandtl mixing length model as the arc turbulence model, turbulent viscosity can be expressed as

$$(3.1) \quad \eta_t = \rho l_M^2 \left| \frac{dW}{dr} \right| = \rho C^2 \delta^2 \left| \frac{dW}{dr} \right|$$

where C is the turbulence parameter, l_M is the length scale for turbulent momentum transfer, which is related to the arc thermal radius, δ , defined by

$$\delta = \frac{1}{\sqrt{\pi}} \sqrt{\int_0^{\infty} (1 - \frac{\rho}{\rho_{\infty}}) 2\pi r dr}, \text{ where } \infty \text{ denotes the external flow.}$$

Turbulent Prandtl number is assumed to be unity. It should be noted that similarity analysis of arcs in gas flow without radiation loss and absorption was investigated by Ragaller and Tuma [8]. However, verification of the scaling laws was not given.

If we further neglect the pressure dependence of transport properties and we use the radiation transport model of [2] with the additional assumption that the net emission coefficient is proportional to pressure and inversely proportional to the arc radius defined as the position of the 4000 K isotherm, similarity parameters and scaling laws which fully determine the non-dimensional solutions of equation (2.1) can be derived [5] using characteristic values:

$$\begin{aligned}
\eta_T &= \frac{C^2}{(R^*T^*)^{3/8}(\sigma^*h_0^*)^{1/4}}(P_s^3I_c^2z_t)^{1/4} & I^* &= I_c & p^* &= P_s & z^* &= z_t \\
q^* &= \frac{gP_s}{r^*} = \frac{(\sigma^*h_0^*)^{1/4}}{(R^*T^*)^{1/8}} \left(\frac{P_s^5}{I_c^2} \right)^{1/4} & r^* &= \frac{(R^*T^*)^{1/8}}{(\sigma^*h_0^*)^{1/4}} \left(\frac{I_c^2z_t}{P_s} \right) \\
E^* &= \frac{(h_0^*/\sigma^*)^{1/2}}{(R^*T^*)^{1/4}} \left(\frac{P_s}{z_t} \right)^{1/2} & w^* &= (R^*T^*)^{1/2} & t^* &= \frac{z^*}{w^*} = \frac{z_t}{(R^*T^*)^{1/2}} \\
\rho^* &= \frac{P_s}{R^*T^*} & P_t^* &= \frac{\eta^*c_p}{k^*} = 1 & u^* &= \frac{(R^*T^*)^{5/8}}{(\sigma^*h_0^*)^{1/4}} \left(\frac{I_c^2}{P_s z_t^3} \right)^{1/4}
\end{aligned}$$

where the superscript * denotes the characteristic value, R the gas constant, I_c the discharge current, P_s the stagnation pressure, u and w are respectively the radial and axial velocity and q the net radiation loss. g is a factor equal to 1 but has a unit appropriate to give the right unit for q^* , and z_t is the distance between the nozzle entrance and the throat. The characteristic values for all the other quantities appearing in the above expressions are defined at 10000 K and 8 bar for SF_6 . Thus there are all together 14 dimensionless variables and 4 similarity parameters in the normalised governing equations. The 4 similarity parameters are:

$$\begin{aligned}
B_R &= \frac{C^2(\sigma^*h_0^*)^{1/4}}{(R^*T^*)^{1/8}} \left(\frac{P_s z_t^3}{I_c^2} \right)^{1/4}, \\
B_P &= \eta^*(\sigma^*h_0^*)^{0.5}(R^*T^*)^{0.25} \left(\frac{z_t}{P_s I_c^2} \right)^{0.5}, \\
B_Q &= \frac{(R^*T^*)^{3/8}\sigma^{*2}}{h_0^{*3/4}} \left(\frac{P_s z_t^3}{I_c^2} \right)^{1/4}, B_T = \frac{z_t}{t_I(R^*T^*)^{0.5}}.
\end{aligned}$$

Table 2.

Arc	I_c (amps)	di/dt (Amps/ μ s)	P_s (bar)	z_t (cm)
1	500	20	30	1.0
2	600	20	25	1.2
3	750	20	20	1.5
4	1000	20	15	2.0
5	1500	20	10	3.0

Similar solutions in different nozzles require that they have the same functional relationship, $A/A_t = f(z/z_t)$, the so-called affinely related nozzles, where A is the nozzle area and subscript t denotes that of nozzle throat. Of the 4 similarity parameters, B_Q and B_R are related, B_P represents the effect of laminar diffusion relative to convection, and B_T represents the ratio of the flow time

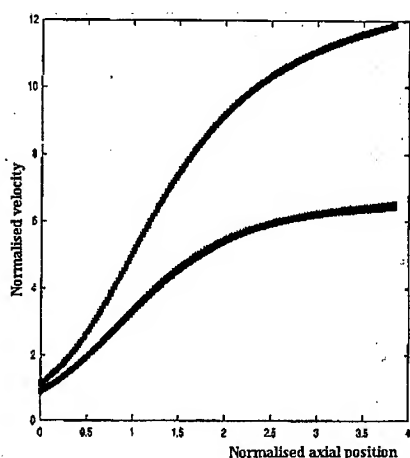


FIG. 1. Axis velocity plotted in normalised coordinates for the arcs listed in Table 2. The upper curve is for the dc plateau and the lower half way to current-zero.

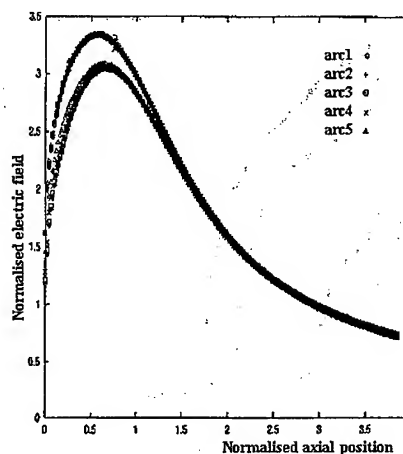


FIG. 2. Axial variation of the axial electric field plotted in normalised coordinates for the arcs in Table 2. The upper curve is for the d.c. plateau and the lower half way to current-zero.

scale to that of the current. B_Q and B_R represent respectively the effects of turbulence and radiation. Arc temperature measurements are extremely scarce and velocity measurements are even more scarce. Thus, computer simulated results obtained without introducing the assumptions necessary for the deduction of similarity parameters and scaling laws are used to check the similarity. This test is believed to be adequate since computer simulated results using equation (2.1) have been shown in agreement with test results. These simulated results are then normalised according to the scaling laws. Results are given for a linear current ramp with a plateau of I_c and a rate of decay of di/dt and for several stagnation pressures as given in Table 2. Figs 1, 2 and 3 show the results of axis velocity, electric field, and radial temperature profiles at one axial position for the 5 arcs shown in Table 2.

4. Arc stability

Arcs in axial gas flow are often turbulent. However, the stabilising and destabilising mechanisms are not known. Analogy between arc instability and shear layer instability is usually made. However, shear layer instability in fluid mechanics usually refers to incompressible fluid. For arc discharges, there is a strong density gradient associated with steep radial temperature gradient and radiation loss and Ohmic input are important. Thus, there is a strong coupling between momentum and energy balance. Axial and radial gradients and the highly non-linear nature make stability analysis extremely difficult. Further simplifications are necessary in order to render the problem to a mathematically tractable form to determine the physical processes leading to instability. The arc which is chosen for stability analysis is the so-called self-similar arc. For such an arc, the flow acceleration

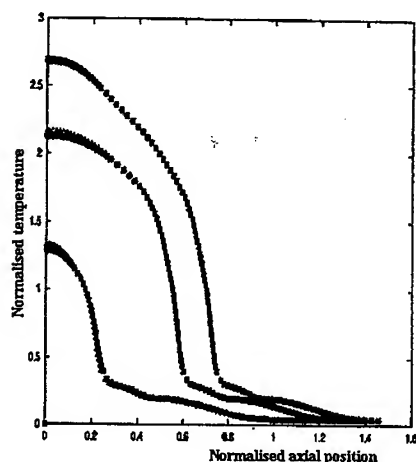


FIG. 3. Radial temperature distribution at axial position $z/z_t = 3$ plotted in normalised coordinates for the arcs listed in Table 2. The correspondence of the symbols to the data is the same as that given in Fig. 2. The upper curve is for the d.c. plateau, the middle half way to current-zero and the lower for current-zero.

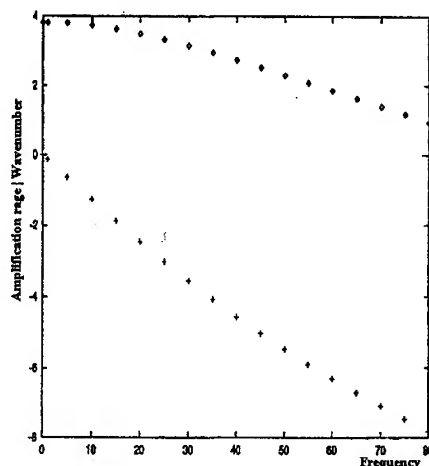


FIG. 4. Dependence of the amplification rate $-\alpha_I$ (diamonds) and the wave number α_R (pluses) on the non-dimensional frequency w for an arc in SF_6 with discharge conditions $I=500$ A, $P=8$ bar and $f_\infty = 5000/s$.

per unit length, f , is constant and thermodynamic state (e.g. temperature) does not vary with axial distance. This arc retains all features of arcs in accelerating flow but is sufficiently simple to carry out a quantitative stability analysis. The imposed pressure gradient is assumed to be much greater than the Lorentz force generated by the arcing current. Thus magnetic instability is excluded. For a self-similar arc, equations (2.1) can be written as:

$$(4.1) \quad \frac{\partial \rho}{\partial t} + \frac{1}{r} \frac{\partial}{\partial r}(\rho u r) + \frac{\partial}{\partial z}(\rho w) = 0$$

$$(4.2) \quad \rho \frac{\partial w}{\partial t} + \rho u \frac{\partial w}{\partial r} + \rho w \frac{\partial w}{\partial z} + \frac{\partial p}{\partial z} = \frac{1}{r} \frac{\partial}{\partial r}(r \eta \frac{\partial w}{\partial r})$$

$$(4.3) \quad \rho \frac{\partial h_0}{\partial t} + \rho u \frac{\partial h_0}{\partial r} + \rho w \frac{\partial h_0}{\partial z} = \frac{1}{r} \frac{\partial}{\partial r}(r \frac{\kappa}{c_p} \frac{\partial h_0}{\partial r}) + \sigma E^2 - q$$

where w and u are respectively axial and radial velocity, and $h_0 = h + 0.5w^2$. Ohm's Law assumes the same form as equation (2.2). For self-similar arc, $\frac{\partial w}{\partial z} = f = \text{constant}$, which is the flow acceleration per unit length. The pressure gradient can be expressed in terms of f and in the region remote from arc, f_∞ , is specified. The governing equations of a self-similar arc are still complex due to their highly non-linear nature. Equilibrium solutions are therefore obtained numerically in non-dimensional form with similarity parameters similar to Section 3.

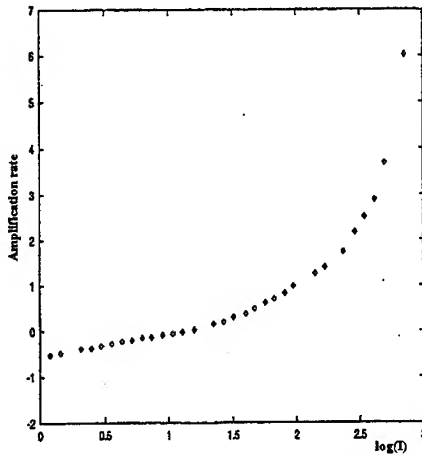


FIG. 5. Dependence of the amplification rate $-\alpha_I$ at $\omega = 0$ on the current for an arc in SF_6 at $P=8$ bar and $f_\infty = 5000/s$.

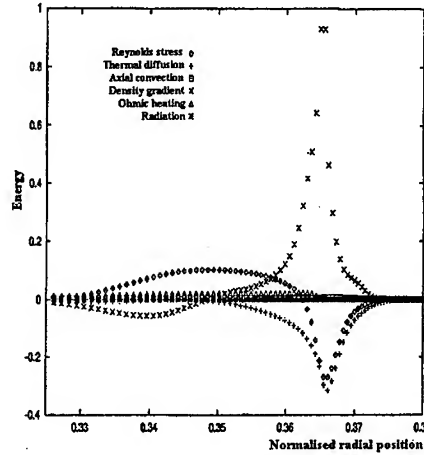


FIG. 6. Radial form of the integrands in equation (4.5) in the shear layer of an arc with discharge conditions $I=500$ A, $P=8$ bar, and $f_\infty = 5000/s$ and at a frequency $\omega = 0$. The absolute scale of the energy is arbitrary.

Small perturbations of the form

$$(4.4) \quad h'(r, z, t) \longrightarrow h'(r) \exp(i\omega t + i\alpha x), \quad \text{where} \quad x = \ln z$$

are imposed on the governing equations.

Flow conditions remote to the arc (i.e. the external flow) are fixed. Thus, instabilities associated with the fluctuations of the imposed flow are not considered. We investigate the convection instability by assuming the perturbation frequency, ω being real. The arc will be unstable if the imaginary part of α is negative. The normal modes analysis of the perturbed governing equations results in an eigenvalue problem which once again needs numerical solution [6]. The results of stability analysis (Fig. 4) show that the arc is more unstable at low frequencies and that the arc tends to be more unstable (Fig. 5) when current increases.

It is interesting to investigate the mechanism which drives the instability. For this purpose, we can derive equations for the mean square fluctuations of the perturbed quantities averaged in time and use the numerical results to determine the relative effects of different physical processes on stability. The mean square fluctuation for $\psi = Kh'$, where ' denotes perturbation and $dK = kdh$ with k the thermal conductivity, is given by

$$(4.5) \quad \frac{\partial}{\partial x} \int_0^\infty dr r \frac{\rho f}{K} (\psi'^2) = \int_0^\infty dr r \rho \left| \frac{dh}{dr} \right| (u' \psi') - \int_0^\infty dr r \left\langle \left(\frac{d\psi'}{dr} \right)^2 \right\rangle$$

$$+ \int_0^\infty dr \frac{r}{K} \left(\frac{\rho f}{2} + \rho u \frac{dh}{dr} \hat{\beta} + \hat{\sigma} E^2 - q_{em} \right) \langle \psi^2 \rangle - \int_0^\infty dr r \langle q'_{ab} \psi \rangle$$

where $\hat{\beta} = \frac{d\beta}{dh} = \frac{d}{dh} \left[\ln \left(\frac{\kappa^{3/2}}{\rho} \right) \right]$ is a material property of the gas, q_{em} is the perturbed net radiation emission in the core of the arc, and q_{ab} is the perturbed radiation absorption in the absorption region.

The results in Fig. 6 show that the energy exchange to the instability from the mean flow occurs almost entirely in the steep density gradient (high temperature gradient) region [6]. These results are in marked contrast to jet-like flows for which compressible effects are frequently neglected. At low currents, the damping effects are small. In practice, it is often observed that arcs at low currents are unstable. This may be due to fluctuations in external flow and finite amplitude perturbations effects, which have not been included in the stability analysis.

5. Arc-shock interaction

Shocks are generated when supersonic flow encounters a sudden compression, and in the case of a supersonic nozzle the pressure at the flow exit is the source of compression. The presence of an arc in the nozzle reduces the effective flow cross section for cold gas because of the low gas density in the arc region. As a result the shock in the cold flow around the arc moves upstream in comparison with the case without the arc.

Shocks developed in the surrounding cold flow cannot penetrate into the arc column because the flow in the arc is subsonic due to strong Ohmic heating. An arc interacts with shock in its surrounding cold flow through flow coupling. The steep pressure rise associated with the shock in the cold flow (Fig. 7) penetrates into the arc region and imposes an adverse axial pressure gradient.

The flow field in the box is visualised in Figure 8

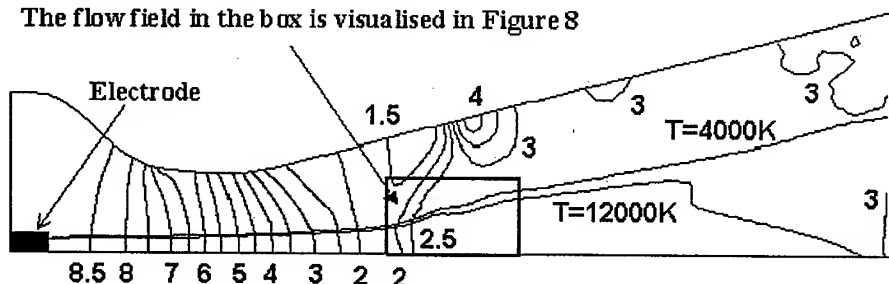


FIG. 7. Pressure and temperature contours for a 500 A SF_6 arc. The exit pressure is $3 \cdot 10^5$ Pa and upstream stagnation pressure is $9 \cdot 10^5$ Pa.

As a result, the flow inside the arc region is decelerated (Fig. 8) and the arc column has to be broadened to maintain the mass flow rate carried by the arc. The distorted shape of the arc column further modifies the effective flow area for the surrounding cold flow and the shock. The centre of the shock in the

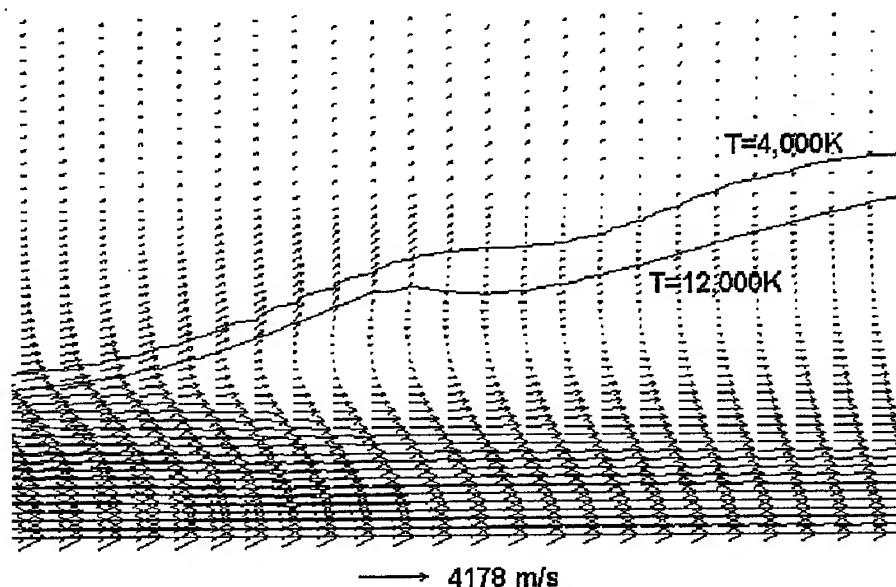


FIG. 8. Broadening of the arc column by flow separation in the arc-shock interaction region for a 500 A arc. Conditions are the same as in Fig. 7. The position of this figure is shown in Fig. 7.

cold flow moves upstream as current increases. The expansion of the arc and the broadening of the arc due to interaction with the shock act as a compression wedge for the shock impinging on the arc thermal boundary. The broadening of arc column due to arc-shock interaction reduces the arc voltage by 12-15% in the current range from 200 to 1500 A under the conditions given in Fig. 7. More significantly, flow deceleration in the arc column due to arc-shock interaction can create a very hot (12000 K) patch in the nozzle when the arcing current reduces to zero in a transient case. This will leave a weak dielectric insulation spot in a circuit breaker and has adverse effect on its performance.

6. Computer simulation of an industrial device

The understanding of the physical processes occurring in arcs in gas flow and the robust algorithms successfully developed for the solution of equation (2.1) and the relevant Maxwell's equations have made possible to simulate the operation of a whole arc device on a PC. As an example, computer simulation results of the operation of a high voltage auto-expansion circuit breaker (Fig. 9) are given, which include the moving contact and the radiation induced inner wall ablation of the PTFE nozzle. The effects of Lorenz force, radiation transport, Ohmic heating and turbulence are included. Temperature, pressure, velocity, and electric fields are computed as a function of time while the current varies sinusoidally. Pressure measurements are in good agreement with the simulated

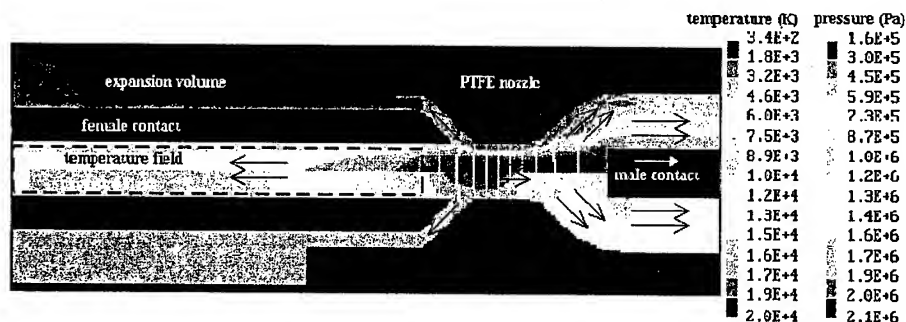


FIG. 9. Temperature, pressure and electrostatic potential distributions in a model auto-expansion circuit breaker with an instantaneous current of 18.5 kA at 6.2 ms. Upper half: temperature field, lower half: pressure field. The white arrow indicates the moving contact and the black arrows show the direction of gas flow. The arcing current is sinusoidal with a frequency of 50 Hz. The peak current is 20 kA and the arcing duration is 10 ms. The broken box indicates a transparent (to flow) electric current collector to support the axisymmetric arc. The filling pressure of SF_6 is 6.9 bar absolute.

results as shown in Fig. 10 for a 245 kV auto-expansion circuit breaker which has a similar structure as that in Fig. 9. Thus, arc modelling based on correct

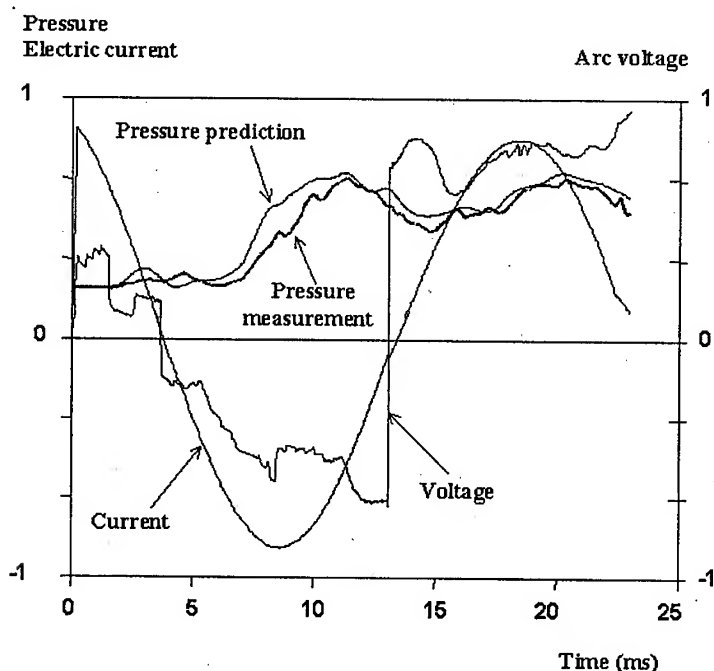


FIG. 10. Predicted and measured pressure variation in the expansion volume of a 245 kV auto-expansion circuit breaker. The peak arcing current in this case is 27 kA.

understanding of the physical mechanisms is a powerful tool to aid optimum design of industrial arcing devices. It should be noted that Claessens et al [9] reported computer simulated results with a simplified treatment for the arc region at high current.

7. Conclusions

For arcs under LTE, sufficiently accurate model is now available for a quantitative description of the operation of complex devices with axisymmetry. For non-axisymmetric arcs, radiation transport calculation needs to be based on partial characteristics rather than the method adopted here. Similarity and scaling laws are shown to exist for arcs in supersonic nozzle. Stability analysis indicates that arc instability is strongly associated with the density gradient which is caused by strong radiation absorption. Arc turbulence model should therefore take density effects into account. This remains to be done. For practical arc devices, in some regions of the device and/or under certain operational conditions, departure from LTE is expected. These are important for material processing and are active research areas.

Acknowledgement

The authors thank the Engineering and Physical Sciences Research Council of the UK and VA Tech Reyrolle Ltd for support.

References

1. M.T.C. FANG and E. PFENDER (Editors), IEEE Trans. on Plasma Science, Special Issue on High-Pressure Arcs and High-Frequency Thermal Plasmas, **25**, 807-808, 1997.
2. J.F. ZHANG, M.T.C. FANG and D.B. NEWLAND, J.Phys.D: Appl Phys, **20**, 368-379, 1987.
3. R.E. BLUNDELL, K. CHEN and M.T.C. FANG, Proc. of XIIIth Symposium on Physics of Switching Arcs, Vol. II (Invited papers), 210-216, 1998.
4. J.D. YAN, M.T.C. FANG and W. HALL, IEEE Trans. on Power Delivery, **14**, 1, 176-181, 1999.
5. R.E. BLUNDELL and M.T.C. FANG, J.Phys D: Appl. Phys., **30**, 628-635, 1997.
6. R.E. BLUNDELL, M.T.C. FANG and A. VOUDAS, IEEE Trans. on Plasma Science, **25**, 5, 852-859, 1997.
7. J.D. YAN and M.T.C. FANG, IEEE Trans. on Plasma Science, **25**, 5, 840-845, 1997.
8. K. RAGALLER and D.T. TUMA, IEEE Trans. On Plasma Science, **9**, 75, 1981
9. M. CLAESSENS, K. MOLLER and H.G. THIEL, J. Phys. D: Appl. Phys., **30**, 1899-1907, 1997.

COMPLETE TEMPERATURE MONITORING IN A PILOT TRANSFERRED-ARC PLASMA FURNACE

J. M. BADIE, PH. BERTRAND and G. FLAMANT

INSTITUT DE SCIENCE ET DE GÉNIE DES MATÉRIAUX ET PROCÉDÉS
IMP-CNRS, B.P.5, 66125 Font-Romeu Cedex, France

Temperature distribution in a transferred-arc plasma furnace for steel remelting is presented. Arc, bath and insulating wall temperatures are measured on the basis of Atomic Emission Spectroscopy (AES) and Multi-Wavelength Pyrometry (MWP). Both molten bath used as anode and cathode situations are examined and compared. In the former case, temperatures in the range 10000 - 25000 K are determined for a 250 mm length arc (86 V, 1760 A), and the corresponding molten steel temperature is about 2000 K. In the latter case, electron density is higher near the anode than it is near the cathode (reverse to anode case) and the temperature gradient is smooth between the electrodes is smooth ($9000\text{ K} < T < 11500\text{ K}$). Bath temperature is 150 K lower than in the anode configuration.

1. Introduction

Arc heating of molten steel is an increasing market for plasma torch suppliers: about 30 new plants have been commissioned during the last 10 years. Generally, this secondary heating stage is performed to compensate heat losses or to raise steel temperature to optimum levels before casting. Three technologies are now available: graphite electrodes and plasma torches which are transferred arc requiring a bottom electrode and 3-phase AC arcs which do not require a bottom electrode (Ladle furnaces use graphite electrodes and tundish heaters are equipped with plasma torches constructed with tungsten or copper electrodes [1]). Even if only a 4.5 MW maximum power may be obtained with tungsten electrode plasma torches operating in 3-phase AC with argon, this technology is under development for low carbon steel grade. In addition, a power increase larger than 50% may be reached with mixtures of molecular gas.

In the view of quality concerns, process reliability and process design, the temperature control inside the plasma furnace is of great importance:

- *Arc temperature*: effect of electric power and arc length on the temperature distribution, relation between arc temperature and radiative transfer in the furnace cavity (refractories working temperature limit).

- *Metallic bath temperature*: the impurities rate transfer to the melt depends on the temperature as well as the material quality after casting.
- *Furnace refractories temperature*: the refractories operating temperature is very near the limit. Their erosion and failure (process reliability) are highly dependent on the temperature level and gradient.
- Finally, the comparison between the measured temperature distribution and simulated temperature profile gives reference points for *process design* and scaling-up.

Accounting for these remarks, measurements were performed in a 200 kW pilot plasma tundish operated by EDF-DER (Les Renardières, France). Arc temperature was obtained by Atomic Emission Spectroscopy (AES), molten bath and refractory wall temperatures were determined by Multi Wavelength Pyrometry (MWP). Measurement methods are first presented in this paper, then experimental data are discussed for two electric polarities of the steel molten bath: positive and negative.

2. Measurement system and methods

2.1. Atomic Emission Spectroscopy

The experimental setup is schemed in Fig. 1. The electric arc image is made by a lens (focal distance 30 mm) at one end of a fiber optic mounted on a $z-r$

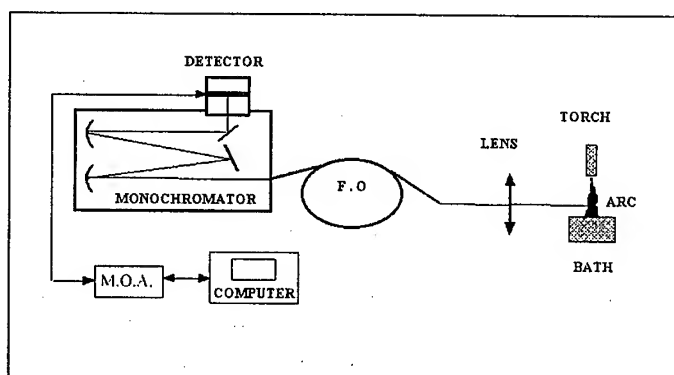


FIG. 1. Experimental setup for AES measurements.

displacement system. The other end is connected with the monochromator. The size reduction ratio of the arc column is 5, accounting for the fiber core diameter, the resulting spatial resolution is about 2 mm.

The monochromator is equipped with three diffraction gratings: 300, 1200 and 1800 lines/mm, the medium grating is used with 20 μm inlet slot. The detector is the CCD matrix of a multichannel optical analyzer (MOA). The spectral width of each photodiode is about 0.038 nm at $\lambda = 425$ nm, consequently the spectral domain extent is 23 nm, centered to the selected wavelength.

After a first analysis of the spectra (Fig. 2 and Fig. 3) two measurement methods are used for arc temperature determination.

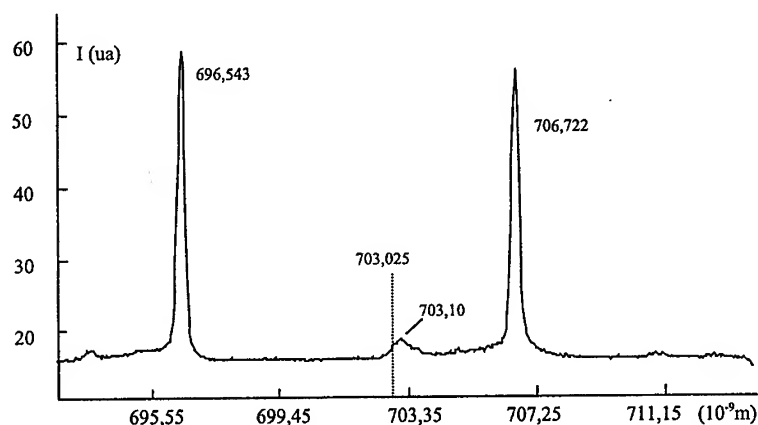


FIG. 2. Ar I lines far from the cathode.

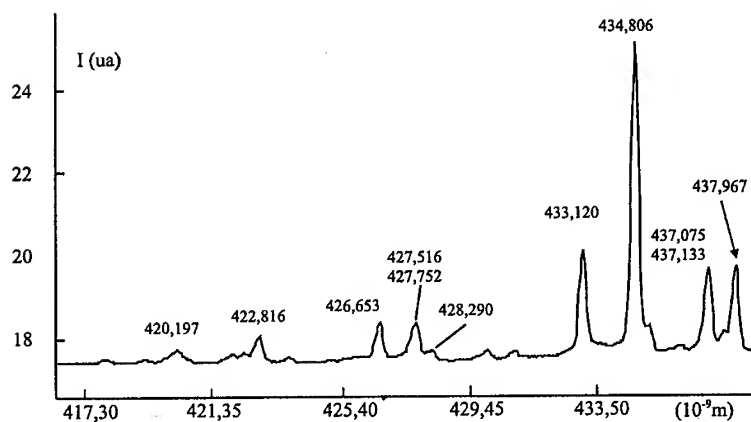


FIG. 3. Ar II lines the attachment zone.

For temperature lower than 15 000 K, the plasma electron density is obtained from the shift of the 703 nm line of neutral argon (Ar I) as shown in Fig. 2. This shift was extensively study by [2] who have proposed a calibration of $\delta\lambda$ versus N_e with respect to a well known reference, the H_β line (N_e determination). This measurement is not based on LTE hypothesis, but this latter assumption is made to calculate the related temperature from equilibrium composition calculation.

The Stark shift of an atomic line $\delta\lambda$ depends mainly on the electron density (N_e), it may be written [2] as :

$$(2.1) \quad \delta\lambda = \left(\frac{d}{W} + 2B \right) 10^{-22} W N_e,$$

where d and W are respectively the shift and the half-width of the line due to electrons. B characterizes the effect of ions on the line shift. For the 703 nm line and $T = 10\,000$ K, it comes: $d = 0.0608$ nm, $W = 0.06$ nm and $B = 0.0703$ [3]. For $N_e < 2 \cdot 10^{22} \text{ m}^{-3}$, the shift $\delta\lambda$ is not linear and the calibration of [2] is used.

For temperature higher than 15000 K (Fig. 3), the intensity ratio method is used for lines of Ar^+ (Ar II): 434.806 nm, 427.752 nm and 427.516 nm lines are selected, and the corresponding transition characteristics are listed in Table 1.

Table 1. Characteristics of selected Ar II lines

$\lambda(\text{nm})$	$E_k(\text{cm}^{-1})$	g_k	$A_{ki}(10^8 \text{s}^{-1})$
427.516	183091	4	0.26
427.752	172214	4	1.00
434.806	157234	8	1.24

To determine the temperature we do not use the Abel inversion, as a result, a mean value is obtained from the measurement. However, the error related to the maximum temperature along the axis may be estimated assuming a radial parabolic temperature profile with a maximum at T_M and a minimum at T_m , $T_m = 7000$ K (negligible emission). On this basis the integrated radial N_e distribution or line intensity may be calculated and the corresponding integrated temperature may be determined. This latter is equivalent to the measured temperature (T_{int}). For $T_M = 10000$ K and $T_M = 15000$ K the integrated temperature T_{int} is equal to 9714 K and 14090 K respectively, i.e. differences in the range 300 K - 1000 K. The same calculation for Ar II gives a 1500 K difference at $T_M = 29890$ K. To conclude, the maximum temperature in the discharge is underestimated with an error ranging from 2% to 6%.

The combination of both methods permits to determine temperature in the range 9000-30000 K, with possible comparison around 15000 K. Accounting for working conditions, the measured data are significant of the maximum electron density or temperature in the discharge, but gives underestimated values with differences ranging from 300 K to 1500 K.

2.2. Multiwavelength Pyrometry

A multiwavelength high speed pyrometer has been specially developed for on-line monitoring and control of temperature conditions in various industrial processes: CO_2 laser welding, plasma cladding, plasma-arc steel refining, plasma spraying, etc. [4]. The combination of high operation speed (sampling time 50 μs by photodiode), wide temperature range (1300-3500 K) and varying size of target area (a circle from 400 μm up to 1 cm in diameter) provides the means for real-time temperature monitoring.

The pyrometer is composed of two components: the optical head and the opto-electronic unit. Selection of wavelength in the range 1-1.6 μm is performed

by a diffraction grating, a linear array of 12 InGaAs photodiodes is used as detector. The other characteristics of the pyrometer are listed in Table 2.

Table 2. Characteristics of the multiwavelength pyrometer

Parameters	1-spot MWP
Temperature range, K	1300-3500
Wavelength range, μm	1.0-1.573
Measuring distance, mm	700
Number of photodiodes	12
Special resolution, mm	1600
Sampling time, μs	50 for each photodiode
Length of the optical, m	10

The idea of getting the temperature from spectral intensities measurements without knowing the emissivity is not new: it has been pioneered by [5], [6] and many others for the past 30 years. Authors [7] as early as 1972 stated the argument of "redundant information" in thermal radiation spectra that should allow this: also the stress was put on the advantages coming from modern computer capabilities and least squares method and consequently from allowed increasing the number of spectral channels; multiwavelength pyrometry and spectroradiometry are still expected to give the "true" temperature.

Since beginning of 90's, IMP-CNRS [8] has been involved in multi wavelength pyrometry. [8] have analysed all existing methods and developed their own. Here is presented one which is commonly called "inverse radiant temperature transformation" method, called by [8] "Wien/log transformation". This is the simple extension to a multiple channel instrument of what is done currently for classical monochromatic optical pyrometry; using Wien's approximation, and replacing the term logarithm of emissivity by a wavelength polynomial fit permits to solve the so linearised system, provide the number of channels is in excess of the unknown, model parameters plus 1 (the temperature).

The Wien:Log transformation, or so called "inverse radiant temperature transformation" uses the following equations :

$$(2.2) \quad 1/T_i = 1/T_0 - \lambda_i/c_2 \ln \varepsilon_i$$

$$(2.3) \quad \text{with} \quad \ln(\varepsilon_i) = \sum_{n=0}^{N-2} a_n \lambda_i^n \quad i = 1, N,$$

where i corresponds to the measured channels, N is the number of channels, T_i are the measured brightness temperature, T_0 is the true temperature, ε is the emissivity and λ is the wavelength.

The N data $1/T_i$ are fitted versus λ and compared with $\lambda_i/c_2 \log \varepsilon_i - 1/T_0$. The Y -intercept of the fit allows to determine T_0 .

Concerning the measurement uncertainty, two parts must be discussed:

- (i) The calibration error is ± 5 K at 2000 K (i.e. 0.25%). This permits to appreciate a temperature difference of 10 K versus time or position.
- (ii) The uncertainty due to the method for true temperature calculation (equation (2.2) and (2.3)) may be estimated at ± 20 K $-\Delta\varepsilon/\varepsilon = 5\%$.

When a temperature variation along the surface of one material is checked, only the calibration uncertainty is to be considered if the temperature change is limited to some tens degrees without phase transformation (the emissivity variation is generally negligible in this situation).

3. The pilot plasma tundish

The plasma furnace is schemed in Fig. 4, it operates in the transferred arc mode combining a refractory insulated cavity and a plasma torch (Tektronics

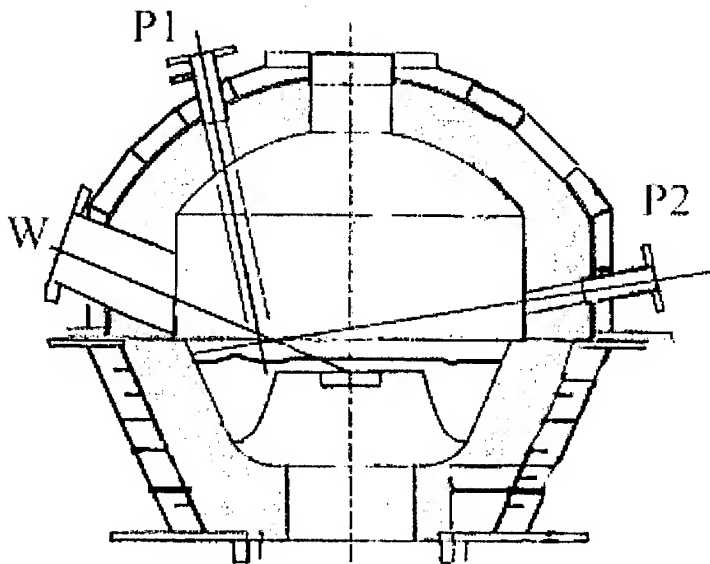


FIG. 4. Schematic representation of the plasma furnace (without the plasma torch).

technology). The furnace bottom is equipped with a metallic electrode to permit the arc attachment. The cavity diameter is about 0.65 m at the level of the liquid metal surface. The plasma torch is inserted at the top and it operates either as cathode or anode with argon. In the former configuration, tungsten tip is used for cathode and copper plate for anode, thus nominal power is about 200 kW ($U = 90$ V, $I = 2300$ A). For the plasma torch operating as anode, the maximum power is 170 kW (1765 A). Operating parameters used during measurement are listed in Table 3. Three optical accesses may be used for measurements:

- Two small diameter ports (P_1 and P_2 in Fig. 4) located on top of the furnace and on the side wall. They permit bath temperature and refractory wall temperature measurement respectively.
- A large side window (W in Fig. 4) which gives access to the arc zone for measurements in the plasma. In addition, the bath surface may be also seen through this window, in particular the arc root.

Table 3. Plasma arc operating parameters during measurements (L = arc length)

Parameters	Bath as anode		Bath as cathode	
	$L = 200$ mm	$L = 250$ mm	$L = 150$ mm	$L = 200$ mm
I (A)	2070	1760	1000	1765
U (V)	88	86	88	93
Argon flow rate (Nm ³ /h)	6	6	15	15

4. Experimental results

Experimental data are presented for two configurations: the metallic bath as anode and the metallic bath as cathode.

4.1. Metal bath as anode

Arc Temperature: Electron density (N_e) variation along the axis (z direction) of the arc column and starting from the bath surface is plotted in Fig. 5 for two arc lengths, 200 mm and 250 mm, and argon flow rate 6 Nm³/h.

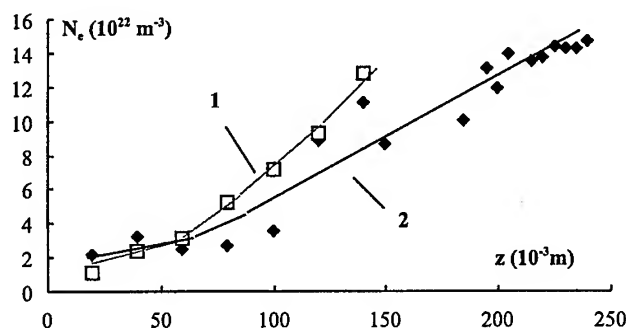


FIG. 5. Electron density along the plasma arc axis: 1: $L = 0.2$ m, $I = 2200$ A, 2: $L = 0.25$ m, $I = 1760$ A.

N_e seems to be higher in the short arc than in the long arc. Fig. 6 plots N_e versus dimensionless arc length representation, it shows no significant difference between both previous situations. This means that electron densities are the same at a given z/L value even with a 25% current intensity difference.

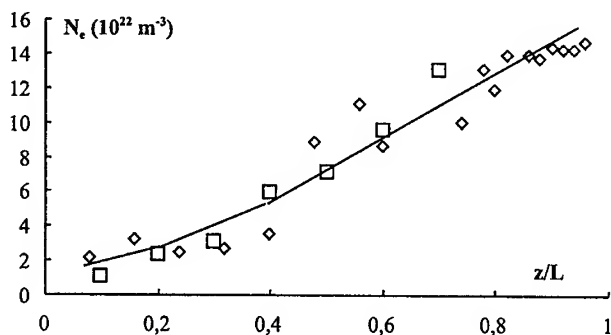


FIG. 6. Electron density along the plasma arc as a function of dimensionless distance from the metal bath \square : $L = 0.2$ m, $I = 2200$ A, \diamond : $L = 0.25$ m, $I = 1760$ A.

Nevertheless, this remark must be lessened considering the measurement accuracy (about 15%) which is probably insufficient to detect such a small difference.

The corresponding temperature distributions are shown in Fig. 7. Temperature is obtained on the basis of an equilibrium calculation neglecting iron vapor

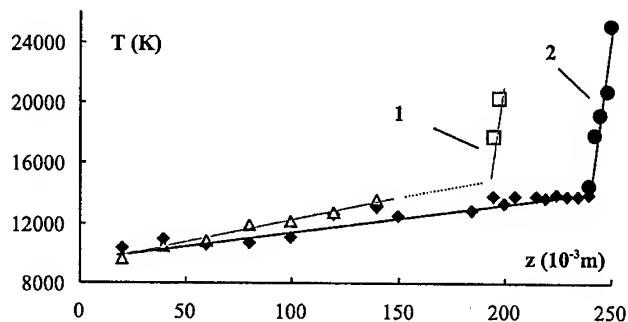


FIG. 7. Temperature distribution along the arc axis 1: $L = 0.2$ m, $I = 2200$ A, 2: $L = 0.25$ m, $I = 1760$ A.

whose concentration should be of the order of of maximum 1.6% as computed by [9]. For such an iron vapor content in the arc, an equilibrium calculation of the Ar-Fe system, for the same electron density (measured), gives an estimation of the related uncertainty. It is less than 3% at $T = 10000$ K and less than 0.2% at $T = 13000$ K. Both distributions exhibit a characteristic shape: a slight temperature rise from the bath surface to the cathode along the main arc, length, and a very sharp rise at 10 mm from the cathode (plasma torch). In the first part of the arc the temperature gradient is linear and $\Delta T/\Delta z \approx 20$ K/mm and for both arc lengths the temperature is about 9000 K at 20 mm from the molten steel. At the slope break, the temperature is about 14000 K for both cases and it rises up to nearly 25000 K at the cathode surface. In this thin cathode zone the thermal gradient is about 1000 K/mm. In the arc attachment region maximum

temperatures in the range 23500-25000 K have been previously determined by [10] and [11].

For the 250 mm long arc, at $z = 240$ mm distance from the bath, lines of both Ar I and Ar II may be observed and we may compare both temperature measurement methods. On the basis of the line shift method (Ar I) the temperature is 13900 K, and at the same position a temperature of 14430 K is obtained from the intensity ratio method (Ar II). This result proves the coherence between the chosen spectroscopic measurement methods.

The radial temperature distribution is illustrated in Fig. 8 at $z = 248$ mm, $z = 200$ mm and $z = 20$ mm. A strong temperature decrease from the axis to the

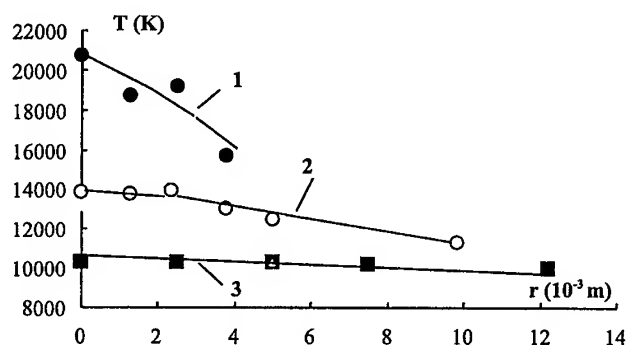


FIG. 8. Radial temperature distribution as a function of z position ($L = 0.25$ m, $I = 1757$ A)
1: $Z = 0.248$ m, 2: $Z = 0.2$ m, 3: $Z = 0.02$ m.

arc border is shown at the cathode vicinity: the gradient reaches 1300 K/mm at $z = 248$ mm. In this region, the diameter of isotherm 15000 K may be estimated to be 85 mm, the corresponding current density is 3100 A/cm². The temperature profiles flatten very rapidly from the cathode to the anode (decreasing z values), the temperature gradient is about 240 K/mm at the middle of the arc and 100 K/mm at 20 mm from the metal surface. The consequence of the integral method (no Abel inversion) on the results is a profile flattening with 1500 K uncertainty along the axis.

Surface Temperature: Temperature obtained with the 250 mm long arc will be commented. The measurements are performed with the MWP sighted either through ports P_1 , P_2 or through window W .

The insulator wall temperature near the bath surface is measured using port P_2 . First of all, the influence of the plasma arc emission on the pyrometer signal is illustrated in Fig. 9. The variations of brightness temperature for nine wavelengths are plotted versus time as well as the true temperature calculated from equations (2.2) and (2.3) with $N = 9$. At time $t = 54.9$ s the electric power is switched off; the resulting temperature decrease during one second is shown in Fig. 8 and an estimation of the arc perturbation on the temperature signal may be based on the temperature variation during the first 50 ms just after the arc vanishing. The temperature drop during this time is 30 K and the corrected wall temperature is 1950 K. The power is then switched on and the transient

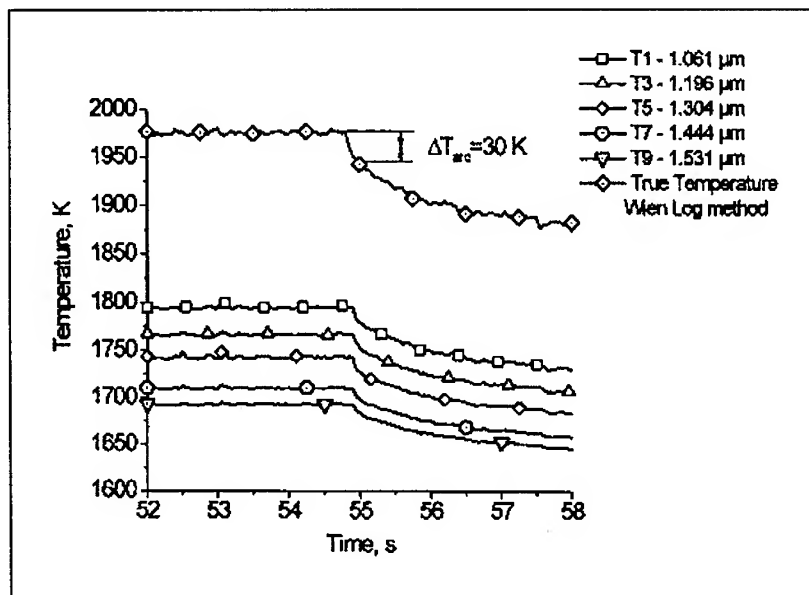


FIG. 9. Wall temperature as a function of time during arc switch off (port P_1)
 $L = 0.25$ m, $I = 1760$ A.

heating period is shown in Fig. 10, a temperature gradient of about 1 K/s is measured. The temperature spikes in Fig. 10 are probably due to arc movements in the sighting zone which perturbate the pyrometer signal.

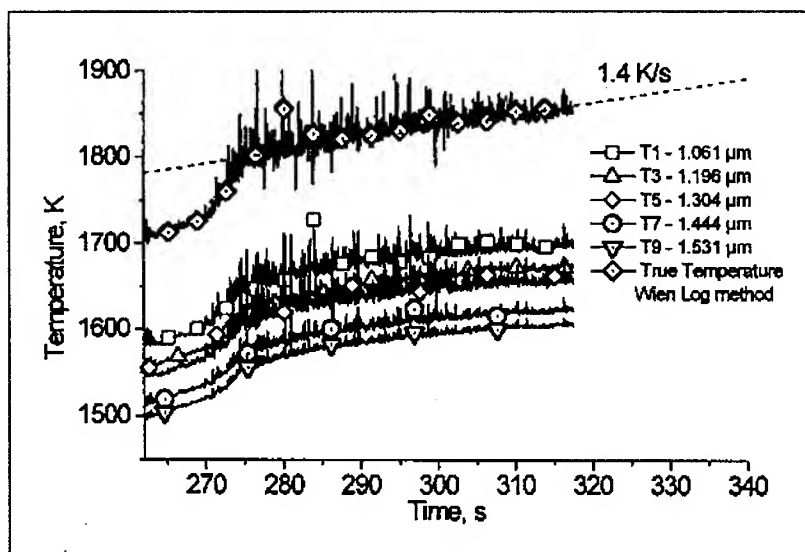


FIG. 10. Wall temperature as a function of time after arc switch on (port P_1 , $L = 0.25$ m).

Fig. 11 illustrates the pyrometer sensitivity and its potential interest for process control. At time $t = 100$ s, window W is opened for cleaning, air enter in the furnace results in arc voltage rise, and therefore the arc power and the insulating wall temperature increase. This phenomenon is clearly recorded by the MWP, thus which may be used for process defects detection.

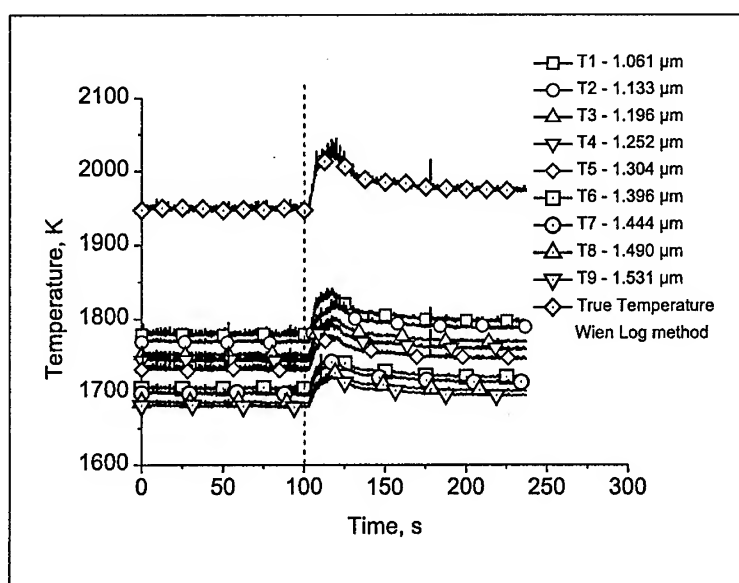


FIG. 11. Wall temperature variation during window- W -opening (port P_1 , $L = 0.25$ m).

The steel bath surface temperature at steady state is plotted in Fig. 12, port P_1 is used for this measurement. The temperature spikes in the plot are due to the molten steel surface deformation: waves are created on the liquid surface by the plasma jet then they propagate radially; their passing in the pyrometer sighting results in large reflexion contributions (mirror effect) which affect strongly the pyrometer signal. Temperature spikes (200 K - 300 K) are observed but the base line permits to estimate the mean temperature. Let us notice that without parasitic contribution, the metal surface temperature is the same that the insulating wall temperature: 1950 K. At the same position, the metal temperature is higher for a 200 mm long arc: 1990 K. In order to estimate the temperature variation on the molten bath, measurements were performed through the large window W used for AES examination. First the influence of arc emission on MWP signal is evaluated by switching off the arc. A 20 K perturbation is estimated at the arc border. In the pyrometer wavelength range (1.06 - 1.531 μm), emission due to iron vapor is null because no Fe emission line exists at wavelengths larger than 0.8 μm . If the pyrometer sights through the arc itself (Port W), the perturbation is higher and measurements are difficult to interpret. As a consequence, the MWP is sighted just before the arc root and moved from the center (arc zone) to the right (insulating wall). The resulting temperature variation is plotted in Fig. 13. The temperature is about 50 K

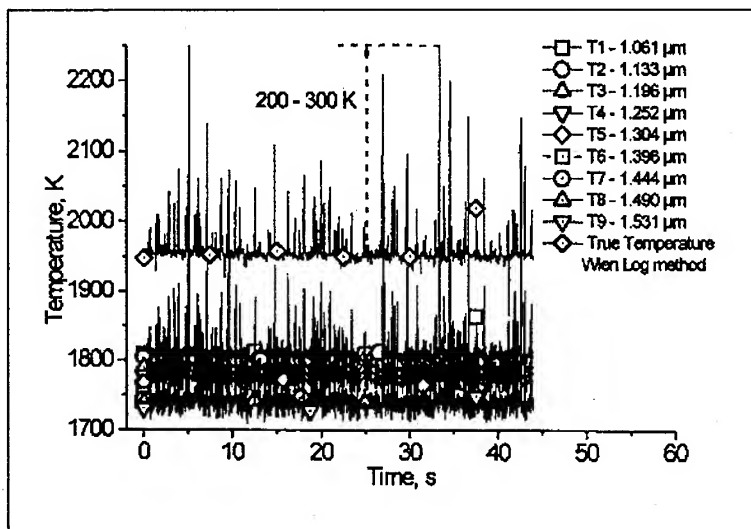


FIG. 12. Metal bath temperature versus time (port P_1) $L = 0.25$ m, $I = 1760$ A.

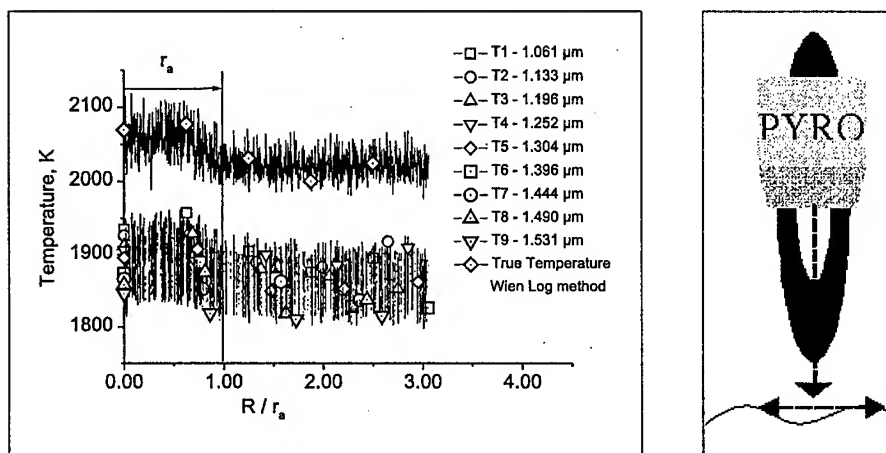


FIG. 13. Bath temperature distribution as a function of the distance from the jet impact zone (port W).

higher in the plasma jet impact zone than in the middle of the bath, at the wall an additional 50 K more temperature decrease is determined. Finally a maximum temperature difference of 100 K is measured at the metal bath surface.

4.2. Metal bath as cathode

The plasma electrode (anode) is a water cooled copper plate 26 mm in diameter. Measurements are performed for two arc lengths 150 mm and 100 mm, respectively 998 A (88 V) and 1765 A (93 V), and a constant gas flow-rate: $15 \text{ Nm}^3/\text{h}$. This argon flow rate is 2.5 times higher than for the previous situation. With

the arc working in reverse polarity, its attachment area is more important than when the base is anode thus resulting with the mean line of sight measurements performed in a lower density close to the bath and more iron vapor should be entrained in the arc.

Arc Temperature: Electron densities and temperature are illustrated in Fig. 14 and Fig. 15 respectively.

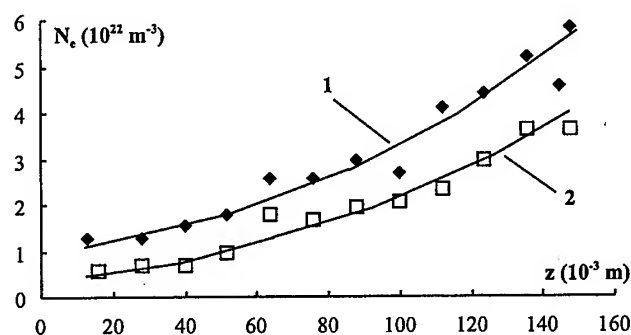


FIG. 14. Axial electron density versus arc length for bath as cathode
1: $L = 0.15$ m, $I = 1000$ A, 2: $L = 0.2$ m, $I = 1765$ A.

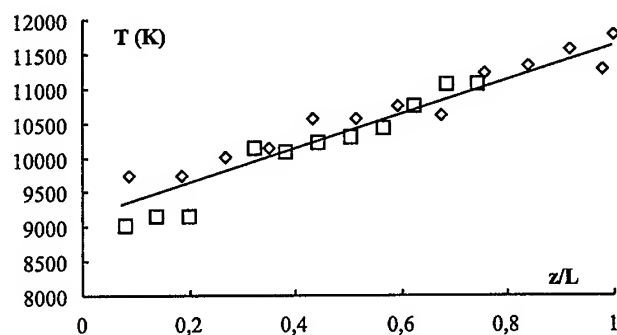


FIG. 15. Axial temperature distribution versus dimensionless distance from the bath surface
◇: $L = 0.15$ m, $I = 1000$ A, □: $L = 0.2$ m, $I = 1765$ A.

Distance $z = 0$ corresponds to the cathode, i.e. the molten steel surface. By comparing with previous situation, the lowest electron density is measured at the cathode and the highest at the anode. But, N_e is larger for the short arc than for the long arc as it was observed in Fig. 7. Electron density is about two fold less than when the bath was anode, with maximum value of about $6 \cdot 10^{22} \text{ m}^{-3}$ near the plasma torch surface. Corresponding temperature in a T versus z/L plot (Fig. 15) illustrates the linear increase of arc temperature from the cathode to the anode in the range 9000-11500 K, without any temperature break. Corre-

sponding slope is 12.5 K/mm. In the radial direction, the temperature variation is also very small even near the anode where 80 K/mm gradient is measured. Ar II lines have never been observed in this situation.

Bath Temperature: The surface temperature is measured during the metal heating duration (in particular during the transition from solid state to liquid state). Data are shown in Fig. 16. A characteristic temperature may be detected

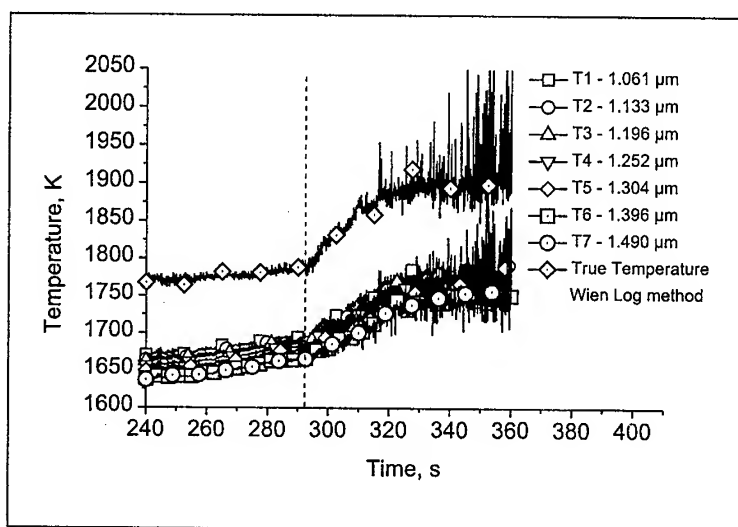


FIG. 16. Bath temperature during cathode bath heating $L = 0.2$ m, $I = 1765$ A.

during the transition (break on plot Fig. 16). This phenomenon occurs at time $t = 292$ s in the plot and the corresponding surface temperature is 1800 K. This measurement is in agreement with iron melting temperature: 1808 K and it may be considered as a validation of the true temperature calculation method. When the liquid surface area increases, the MWP signal perturbations are very important in the arc zone due to intense metal surface movement (high argon flow rate). Far from the arc region, the bath temperature is 1875 K at steady state, i.e. some tens degrees higher than the carbon steel melting temperature.

4.3. Comparison between experimental data

Changing the plasma torch polarity (from thermal emitting hot cathode to cold anode) and plasma gas flow rate results in arc radial extension and consequently temperature reduction. When the metal bath is the cathode, the energy transfer to the liquid is less efficient than when it is the anode and the resulting surface temperature is about 100 K less with comparable electric power: for a 200 mm long arc the power was respectively 164 kW and 182 kW.

Numerical simulation of transferred arc plasma tundish for operating conditions very close to ours ($P = 200$ kW, $I = 2000$ A, $L = 150$ mm, 300 kg of iron) was proposed first by [9] and [12] and then recently by [13]. Trenty's work [9], [12] overestimates both the arc temperature near the cathode and the molten

bath thermal equilibrium. A comparison between measured and calculated temperature profiles is illustrated in Fig. 17. The differences are much larger in the cathode region than in the rest of the arc, temperature as high as 36000 K is predicted at the electrode surface. We think that this difference is not due to metal vapor (accounted in the model) but is connected with the method used for the simulation of the cathode zone.

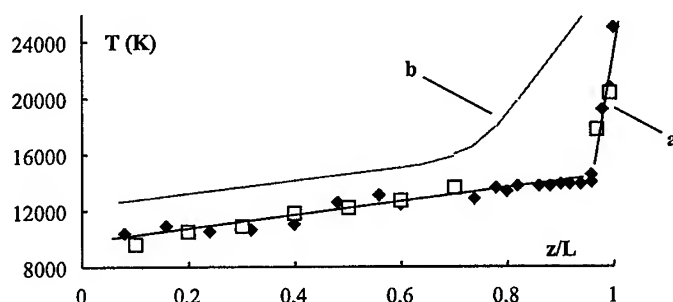


FIG. 17. Comparison of temperature distribution along the arc axis (bath as anode)
a: this work, b: prediction from [11].

According to the same simulation, the upper part of the bath is a convection-dominated zone with two recirculation domains and an equilibrium temperature of about 2380 K, i.e. about 400 K higher than the measured surface temperature. Recent simulation accounting for radiative transfer [13] gives more realistic results both in the arc: 27000 K at the cathode tip and on the refractory surface: about 2100 K near the bath.

5. Conclusion

Plasma arc and surface temperatures have been measured in a 200 kW plasma tundish. The comparison between data for two bath polarities (anode or cathode) shows a strong difference concerning both arc temperature distribution and metal surface mean temperature. In the former case (anode), the temperature distribution exhibits a sharp break about 1 cm from the plasma torch and the plasma temperature reaches about 25000 K near the cathode. The mean bath temperature is about 2000 K with 100 K overheating at the plasma jet impact. In the latter case (cathode), the heat transfer to the metal is insufficient: the liquid temperature is just above the melting point and the plasma arc electron density is two fold less than in the anode configuration. The effect of arc current (with a constant arc length) was not examined.

Surface temperature measurements during transients prove the instrument availability for being used as a sensor for process control (defect detection, temperature regulation ...).

The comparison between our measurements and simulation data performed by EDF-DER shows clearly the importance of the radiative transfer phenomena

in the furnace and the difference reduction tendency thanks to the last model improvements. This shows that combining fitted numerical simulation and accurate measurements give a decisive advantage for plasma process scaling-up.

Acknowledgement

This work was supported by EDF-DER under contract N° 751114/00.

Notation

- a_n : Constant in Eq. (2.3)
- A_{ki} : Transition probability (s^{-1})
- B : Ion interaction parameter (Eq.1)
- C_2 : Constant in Eq. (2.2) $C_2 = 1.4388 \cdot 10^{-2}$ mK
- d : Line shift due to electrons in Eq. (2.1) (nm)
- D : Distance from the furnace (or arc) axis
- E_k : Transition energy (cm^{-1})
- g_k : Statistical weight
- I : Current intensity (A)
- L : Arc length (m)
- N_e : Electron density (m^{-3})
- P : Electric power (kW)
- r : Radial position in the plasma arc (m)
- T : Temperature (K)
- U : Arc voltage (V)
- z : Vertical distance from the metal bath (m)
- W : Line halfwidth in Eq. (2.1) (nm)
- $\delta\lambda$: Stark line shift in Eq. (2.1) (nm)
- ε_i : Emissivity at wavelength λ_i
- λ : Wavelength (nm or μm)

References

1. D. NEUSCHUTZ, *Arc heating of clean steel melts: a comparison between graphite and tungsten electrode systems*, High Temperature Material Processes, **2**, 261-275, 1998.
2. J.M. BADIE, E. BILLOU, G. VALLBONA, *Measures du déplacement de la raie 703 nm de l'argon: application à la détermination de la densité électronique dans un plasma d'argon*, Revue de Physique Appliquée, **25**, 527-533, 1990.
3. H.R. GRIEM, *Spectral line broadening by plasma*, Academic Press, New-York, 1974.
4. P.H. BERTRAND, M. IGNATIEV, G. FLAMANT, I. SMUROV, *Pyrometry applications in thermal plasma processing*, to be published in Vacuum, 1999.
5. D.Ya. SVET, *Determination of the emissivity of a substance from the spectrum of its thermal radiation and optimal methods of optical pyrometry*, High Temperatures-High Pressures, **8**, 493-498, 1976.
6. P.B. COATES, *Multiwavelength pyrometry*, Metrologia, **17**, 103-109, 1981.
7. H.A. GERBIE, R.A. BOHLANDER, R.P. FUTRELLE, *Properties of photons determined by interferometric spectroscopy*, Nature, **240**, 391-394, 1972.

8. PH. BERTRAND, C. ROYERE, M. IGNATIEV, I. SMUROV, G. FLAMANT, *Multiwavelength pyrometry for temperature monitoring and measurement in industrial application*, 7th Int. Symp. on Temperature and Thermal Measurement in Industry and Science, 1-3 June, DELFT (The Netherlands), 1999.
9. L. TRENTY, *Modélisation du chauffage de bains métalliques par un plasma d'arc transféré*, PhD. Thesis, Ecole Centrale de Paris, 30 janvier 1997.
10. X. ZHOU, J. HEBERLIN, *Characterization of the arc cathode attachment by emission spectroscopy and comparison with theoretical predictions*, Plasma Chemistry and Plasma Processing, **16**, 1, 2295-2445, 1996.
11. J.F. COUDERT, A. GRIMAUD, *Etude expérimentale d'un générateur à arc transféré sous argon à pression atmosphérique*, Université de Limoges, rapport ARD: E4404E, 1989.
12. L. TRENTY, A. BOUVIER, C. DELALONDRE, O. SIMONIN, J.B. GUILLOT, *Numerical investigation of an anodic metal bath heated with a transferred arc*, Progress in Plasma Processing of Materials, Ed. Begell Hous inc., New York, 527-534, 1999.
13. A. DOUCE, A. BOUVIER, C. DELALONDRE, J.B. GUILLOT, *3-D numerical modeling of an anodic metal bath heated with a transferred arc*, Progress in Plasma Processing of Materials, Ed. Begell House inc., New York, pp 203-208, 1999.

METAL DROPLET FORMATION IN GAS METAL ARC WELDING

J. HAIDAR

CSIRO TELECOMMUNICATIONS AND INDUSTRIAL PHYSICS

PO Box 218, Lindfield, NSW 2070, Australia

A two-dimensional dynamic treatment has been developed for description of arc and electrode properties in gas metal arc welding (GMAW). The theory is a unified treatment of the arc, the welding wire anode and the cathode, and includes a detailed account of sheath effects near the anode. The wire anode is included as a dynamic entity and the volume of fluid method is used to handle the movement of the free surface of the molten metal at the tip of the wire, accounting for effects of surface tension, inertia, gravity, arc pressure, viscous drag force of the plasma, magnetic forces and Marangoni effect, and also for the effects of wire feed rate in GMAW. Results of calculations made for a mild steel wire of diameter 0.16 cm are in good agreement with experimental measurements of droplet diameter and droplet detachment frequency at currents between 150 and 330 A, which includes the transition between "globular" and "spray" transfer. Quantitative predictions are also made of the amount of metal vapour that is generated from the welding droplets at the tip of the welding wire.

1. Introduction

In gas metal arc welding (GMAW), an electric arc is struck between a workpiece, usually the cathode and a welding wire, usually the anode. Heat transfer from the arc and ohmic heating in the wire cause the tip of the wire to melt, creating droplets that are transferred through the arc to the workpiece. The characteristics of droplets formed at the tip of the welding wire are determined by the combined effect of forces acting on the molten metal at the tip of the wire, thermal phenomena within the wire and heat transfer from the arc.

Here we present a two-dimensional treatment, including the arc, the welding wire and the workpiece cathode. [1-6] The treatment is based on the dynamic conservation equations of mass, energy, momentum and current, and includes a free surface treatment for the surface of the metal drop. The forces considered are gravity, effective inertia, surface tension, arc pressure, viscous drag force and magnetic forces, and also the effects due to the variation of surface tension with temperature. An electrode sheath region is included for the anode. The dynamics of the weld pool in tungsten arc welding (GTAW) can also be modelled by changing the electrode properties, configuration and polarity. Predictions can

be made as a function of time, of droplet shape together with the distributions of current density, temperature, velocities and pressure, both within the arc and the wire anode. A full description of the model, together with calculation results for wires of mild steel for various arc conditions, can be found elsewhere [1]–[6]. The results of calculations show an important transition between globular transfer, where drop diameters are larger than the diameter of the wire, and spray transfer, where droplet diameters are less than the diameter of the wire. Calculations are also made of the amount of metal vapour generated from the surface of the droplet while it is attached to the wire.

2. Theoretical considerations

Fig. 1 is a schematic representation of the calculation domain for GMAW. We use a cylindrical coordinate system, r and z , assuming rotational symmetry around the z -axis. The calculation domain has an anode region, representing the weld-

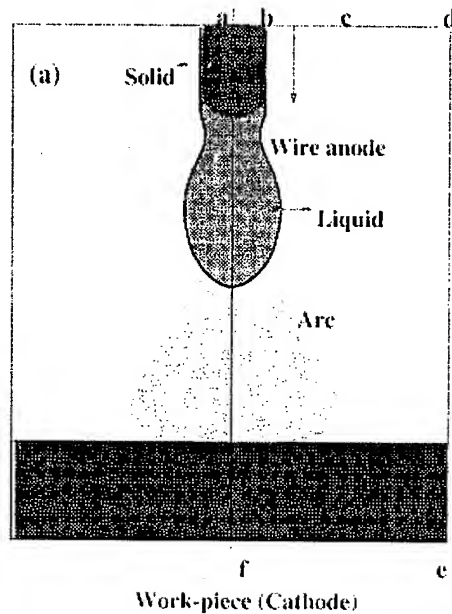


FIG. 1. A schematic diagram of the arc and the electrodes.

ing wire, an arc region and a cathode region, and also an anode sheath region. The anode region is treated as a dynamic medium, including solid and liquid phases, the boundaries of which change with time, depending upon the shape and volume of the molten metal. However, we consider the cathode shape to be fixed in space and time. In the arc region, we assume that the plasma is in local thermodynamic equilibrium (LTE) and the flow is laminar. The dynamic differential equations governing the arc and the electrodes are:

$$(2.1) \quad \frac{\partial \rho}{\partial t} + \vec{\nabla} \cdot (\rho \vec{v}) = 0$$

$$(2.2) \quad \frac{\partial \rho h}{\partial t} + \vec{\nabla} \cdot \rho \vec{v} h = \vec{\nabla} \cdot \left(\frac{\kappa}{c_p} \vec{\nabla} h \right) + \frac{5k_b}{2e} \vec{j} \cdot \vec{\nabla} T + \frac{j^2}{\sigma} - U$$

$$(2.3) \quad \frac{\partial \rho \vec{v}}{\partial t} + \vec{\nabla} \cdot (\rho \vec{v} \vec{v}) = -\vec{\nabla} P + \vec{j} \times \vec{B}_\theta + \vec{\nabla} \Pi + \rho \vec{g}$$

$$(2.4) \quad \vec{\nabla} \cdot (\sigma \vec{\nabla} V) = 0$$

$$(2.5) \quad \vec{j} = -\sigma \vec{\nabla} V$$

$$(2.6) \quad \frac{1}{r} \frac{\partial}{\partial r} (r B_\theta) = \mu_0 j_z$$

Π is the viscous stress tensor, g is gravity. P is pressure, T is temperature, v is velocity, j is current density, V is electric potential and B_θ is azimuthal magnetic field. Input material functions required for the arc plasma and the electrodes are density ρ , viscosity η , specific heat c_p , thermal conductivity κ , electrical conductivity σ , enthalpy h and the radiation loss from the plasma U per unit of volume. For calculations in this paper for pure argon with a wire of mild steel, details about data for the input material functions for the plasma and the electrodes can be found in references [1]–[6].

The effects of metal vapour issued from the electrodes on the plasma material functions are neglected. However, these effects may have an important influence on the calculated plasma temperature. For the droplet at the tip of the welding wire, the effects of metal vapour on the calculated droplet characteristics are only small. Further discussion about the effects of metal vapour is presented in section 3. Also, a detailed analysis of these effects on both the plasma and the welding droplets is given by Haidar [3].

For the cathode, we use a simple treatment based on conductivity considerations at the plasma-cathode interface [1]. For GMAW, where the cathode is usually a non-refractory metal, there may be important electrode sheath effects. However, here, the model is used primarily to predict properties of droplets at the anode, and there is a strong convective flow directed towards the plane cathode so that effects of boundary conditions at the cathode on droplet shape should be small.

For the thermal phenomena within the wire, we consider effects due to the wire feed rate, convection, latent heat at the solid-liquid interface, ohmic heating, conduction, radiation and evaporation from the droplet surface and heat transfer from the plasma. For the heat transferred from the plasma to the wire, we include a detailed treatment of the plasma-anode interactions, accounting for space charge effects in the sheath region immediately in front of the droplet surface. Accordingly, the energy balance of the wire is modified to account for

the special energy requirements at the wire surface and equation 2.2 is modified to include on the right hand side:

$$(2.7) \quad S_a = j_i \left(V_i - V_s + \frac{5k_b}{2e} T_a \right) + j_e \left(\phi + \frac{5k_b}{2e} T_p \right) - q_{ev} L - \epsilon \sigma_{SB} T_a^4$$

where the first two terms on the right hand side of this equation are due to current transfer and sheath effects. The third term, $q_{ev} L$ describes evaporation from the wire surface and the fourth term, $\epsilon \sigma_{SB} T_a^4$, describes radiation from the wire surface. j_e and j_i are the current densities in the sheath of the wire anode due to electrons and ions respectively. j_e and j_i together with the voltage drop across the sheath V_s ($V_s < 0$) are calculated from a one dimensional treatment of the anode sheath [1]. V_i is the first ionization potential of the plasma gas and ϕ is the nominal work function of the wire surface. T_a is the temperature of the wire surface and T_p is the temperature of the plasma immediately in front of the wire. σ_{SB} is the Stefan-Boltzmann constant, ϵ is the electrode surface emissivity. $q_{ev} = P_{ev} m_a / 4 (m_a k_b T_a / 3)^{0.5}$ is the evaporation rate in g s^{-1} , and L , P_{ev} and m_a are respectively the latent heat of evaporation, the vapour pressure and the atomic mass of the wire material. As heat transfer from the plasma to the wire through charged particles is included in the sheath treatment, conventional heat conduction between the plasma and the wire is limited to heat transfer through neutral particles from the plasma.

Also, the energy balance of the plasma in front of the wire anode is equally modified to include a source term S_{ap} on the right hand side of equation 2.2, expressing the corresponding cooling effects due to the sheath.

$$(2.8) \quad S_{ap} = -j_i \left(V_i + \frac{5k_b}{2e} T_a \right) - j_e \left(\frac{5k_b}{2e} T_{e,s} - V_s \right) + j_R \left(\frac{2k_b}{e} T_a - V_s \right).$$

Evaporation from the droplet surface is considered using a Langmuir type model, where it is assumed that evaporation occurs in vacuum. As a consequence, the calculated evaporation rates represent an upper limit for possible evaporation from the droplet surface for droplets at the tip of the welding wire. The calculations show that even with this maximum evaporation model, the temperature of the droplet surface in the arc attachment region can reach more than 3000 K which is above the boiling temperature of mild steel, suggesting that evaporation from the droplet surface is mostly determined by the droplet surface temperature.

For the dynamic effects in the welding wire, inertia, gravity and magnetic pressure and the viscous drag are explicitly included in equation 2.3. The arc pressure at the arc-anode interface is included together with the surface tension pressure through a boundary condition specifying a change in the pressure just inside the liquid compared with the external plasma pressure. The surface tension pressure is expressed as $P_S = \gamma \left(\frac{1}{R_1} + \frac{1}{R_2} \right)$; γ is the surface tension coefficient at the local surface temperature and R_1 and R_2 are principal radii of curvature of the surface.

The effects of thermocapillary forces due to the variation of the surface tension coefficient with temperature are included by adding a source term $\nabla \xi$ to

the right hand side of the momentum equation at the droplet surface; ξ is a Marangoni stress tensor parallel to the surface of the molten metal, where $\xi = \left(\frac{\partial \gamma}{\partial T} \frac{\partial T}{\partial s} \right)$ and s is an element of length parallel to the surface relative to the (r, z) coordinate system.

The changes of the molten metal surface as a function of time are determined using the "volume of fluid" (VOF) method [1]. In this method, we solve the conservation equation of the fractional volume of anode metal, F . The VOF method allows tracking of the free electrode surface by connecting those cells with fractional metal volume less than one.

Internal boundary conditions at the arc-anode interface are set as described by Haidar. [1] For the solid-liquid interface within the anode region, we use a free pressure boundary condition corresponding to a constant velocity for cells within the solid metal. For calculations using equations 2.1-2.6, we use a fixed wire shape over a period δt , assuming that cells in the calculation domain are full of metal if $F \geq 0.5$ and full of gas if $F < 0.5$. Boundary conditions for the gas velocities are specified by setting normal velocities to zero for cells with $0 \leq F < 0.5$. This assumption is based on the approximation that the velocities of the metal are negligible relative to the gas velocities; maximum velocity in the metal was found to be generally less than 1% of the gas velocity. At the arc-anode interface we use a free surface boundary condition, and the energy balance equation is modified so that metal in the surface cells moves in or out of these cells at the same temperature.

External boundary conditions used in this paper are: a temperature of 300 K is set at the boundary of the calculation domain, and the pressure P is set to 1 atm at one point corresponding to point d in Fig. 1. For GMAW, the wire feed rate is incorporated through a boundary condition for v_z along ab . The arc current is specified through a boundary condition for j_z along ab , where j_z is assumed to be constant. The imposed external gas flow is set through a boundary condition on v_z along bc in Fig. 1.

For GMAW, the time varying shape of molten droplets is followed only while they are attached to the anode. Droplets are eliminated from the calculation domain after detachment from the wire. Detachment occurs when the radius of the neck of a droplet is comparable to one or two mesh points. Towards the end of droplet detachment, calculations are performed over a few grid cells only. The resulting low spatial resolution in the radial direction results in a slow radial movement of the molten metal, which may deform the shape of the wire towards the end of droplet detachment.

For the calculations in the present paper, we set the mesh size at the plasma-electrode interfaces to 0.0075 cm for each electrode. For a region of up to 0.6 cm in the axial direction and up to 0.8 cm in the radial direction around the anode, we use a uniform mesh with a grid size of 0.0075 cm to account for the continuous movement of the free surface of the molten electrode.

The numerical procedure used for the present calculations follows the SIM-PL-EC representation of Patankar [8] as used by Haidar[1]; (a) equations 2.1 - 2.6 are solved at a time t for a given shape of the welding wire, (b) the distribution of F is determined using the velocity distribution obtained from (a), (c) the

surface of the droplet is reconstructed from the distribution of F , (d) the surface tension is updated using the new droplet surface configuration and (e) the time is increased by δt and a new round of calculation is started from (a).

3. Results and discussion

Results of calculations are presented in this section for arcs operating in pure argon at 1 atm, with an imposed external gas flow of 5 l/min. The wire anode is of mild steel and has a diameter 0.16 cm. The cathode is a water cooled disk, also of mild steel, with diameter 3 cm and thickness 0.5 cm. The calculation domain has a radius 5.5 cm and a length corresponding to the sum of the initial wire extension length, the arc length and the cathode plate thickness. The wire extension length, l , is calculated according to the arc current, wire feed rate, wire diameter, and wire material properties. At $t = 0$, the initial arc length is set to 0.8 cm, and the initial starting conditions correspond to an undeformed wire moving at a speed equal to the wire feed rate.

Table 1. Results of calculations for a mild steel wire of diameter 0.16 cm. I is arc current, v_{wire} is solid wire velocity, d is droplet diameter, dt is droplet formation time and ν_{drpl} is droplet detachment frequency. The length of the wire extension is 3.2 cm for currents below 250 A, 3 cm for 275 A, 2.4 cm for 300 A and 2.2 cm for 325 A.

I (A)	v_{wire} cm s^{-1}	d cm	dt ms	ν_{drpl} s^{-1}
150	3.55	0.43	570	1.8
200	6.4	0.31	120	8
225	8.1	0.21	30	30
250	10	0.17	13	75
275	10	<0.15	9	>110
300	10	<0.135	7	>145
325	10	<0.12	5	>200

The effects of surface tension have an important influence on the calculated droplet formation time. The surface tension coefficient depend on impurities in the metal wire. The concentration of impurities in the wire at the surface of the molten welding droplet may differ from their concentration in the bulk of the wire, depending upon several factors such as droplet surface temperature, vapor pressure of the impurities. As it is not possible to include these effects in the calculations, the calculated results may include some uncertainties due to surface tension coefficients. For calculations in this paper with a wire of mild steel, we use the values used by Lin and Eagar [9] and they range from 1.5 Nm^{-1} at 1800 K to 1.15 Nm^{-1} at 2700 K. According to Lin and Eagar, these values are for steel without surface active elements. For the calculations presented in this section, the effects due to the variation of the surface tension coefficient with surface temperature are limited to the effects of surface tension pressure $P_S = \gamma(T) \left(\frac{1}{R_1} + \frac{1}{R_2} \right)$, which is due to surface curvature; R_1 and R_2 are the radii

of curvature of the surface. The Marangoni effect expressed through the surface tension stress tensor $\nabla \xi$ is omitted.

Table 1 summarizes results for calculations made for a mild steel wire of diameter 0.16 cm with arc currents between 150 A and 325 A. Examples of the corresponding results of calculated droplet shape are shown in Fig. 2 for currents 200 A, 225 A, 250 A and 300 A. These results illustrate the transition from the

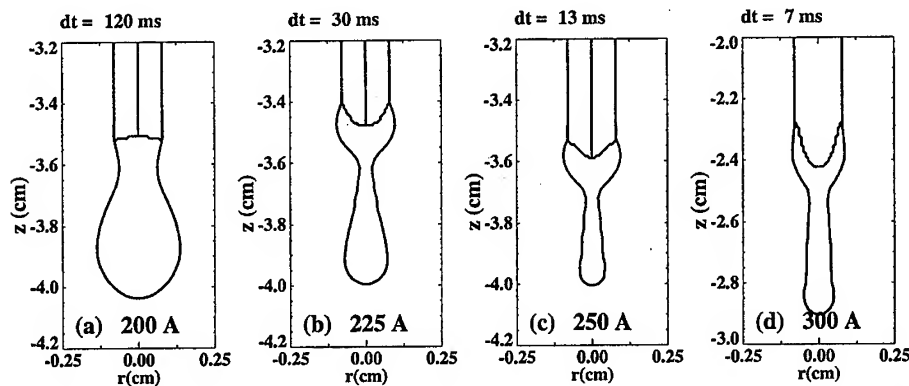


FIG. 2. Predicted droplet shapes at currents (a) 200 A, (b) 225 A, (c) 250 A and (d) 300 A. The wire is of mild steel and has a diameter 0.16 cm. dt is droplet formation time.

globular mode of metal transfer in Fig. 2(a) and (b) at currents below 250 A, to the spray transfer mode in Fig. 2(c) and 2(d) at currents above 250 A. At a current of 300 A, it is seen in Fig. 2(d) that the shape of droplets at the tip of the wire is somewhat cylindrical rather than elliptical as in Fig. 2(a) and 2(b). This cylindrical shape is consistent with the streaming mode of metal transfer observed in GMAW.

In Fig. 3 we compare the calculated droplet diameters in Table 1 with experimental measurements of Kim and Eagar [10]. The experimental measurements are for an argon shielding gas containing 2% oxygen, and the theoretical predictions are for pure argon. However, this is not expected to have a major effect on the validity of the comparison presented here [11].

Separate calculations made to simulate the effects of the various forces acting on the molten droplet at the tip of the welding wire show that the predominant effect for the transition from the globular mode of metal transfer to the spray mode of metal transfer is due to the radial component of the magnetic force $j_z \times B_\theta$. For calculations made without including the effects of $j_z \times B_\theta$, we find that large droplets are formed at the tip of the wire for all currents up to more than 300 A [5].

In Fig. 4 we present an example of the calculated instantaneous distributions of temperature and velocity. Fig. 4(a) shows temperature and Fig. 4(b) velocity for the globular mode of metal transfer at a current of 200 A, corresponding to the results in Fig. 2(b) at $t = 112$ ms. At this instant during droplet growth, the maximum temperature calculated in the droplet is around 3000 K near the droplet base in the arc-wire attachment region. The corresponding maximum velocity within the molten drop is 0.2 ms^{-1} , calculated on the wire axis near

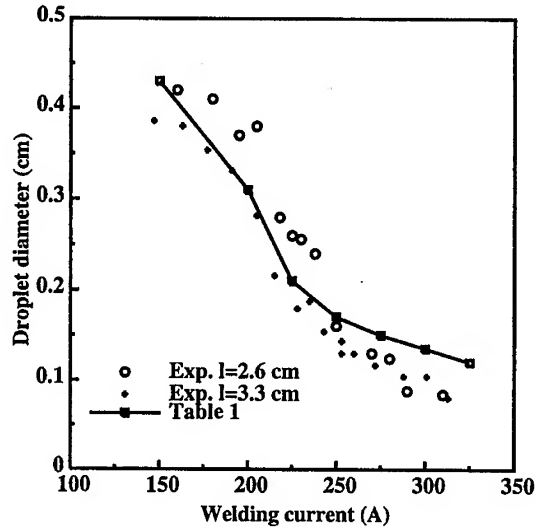


FIG. 3. A comparison between calculated droplet diameter (Table 1) and experimental measurements by Kim and Eagar [10]. l is the wire extension length.

the droplet neck. A maximum pressure of 3 kPa above atmospheric pressure is calculated in the neck region. The maximum current density at the surface of the droplet is $9 \cdot 10^3 \text{ Acm}^{-2}$. For the plasma, the maximum calculated values for temperature, pressure and velocity are respectively 21000 K, 1.2 kPa above atmospheric pressure and 305 ms^{-1} . The calculated voltage drop of the anode sheath is negative and is less than 2.4 V and the total arc voltage is 17 V.

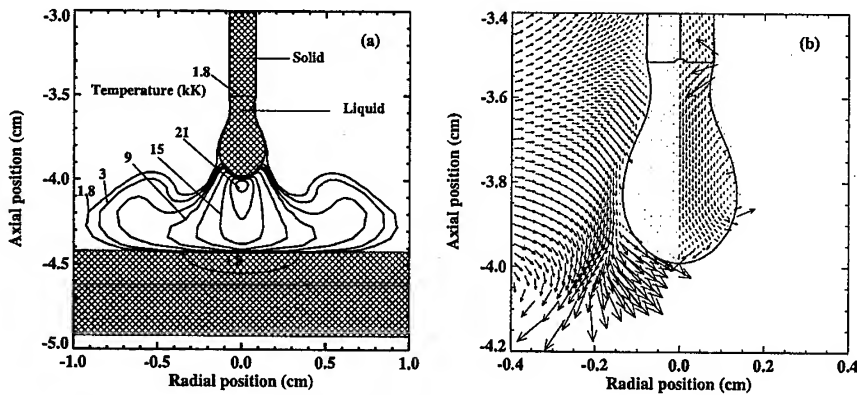


FIG. 4. Details of calculations at $t = 112 \text{ ms}$ for a mild steel wire of diameter 0.16 cm at a current of 200 A; (a) temperature contours within the arc and the electrode. The outermost contour is 800 K, the second is 3000 K and other contour intervals are 3000 K. (b) a vector plot of velocity within the molten metal droplet and the adjoining plasma; different scales are used for the plasma and the molten metal inside the droplet.

Metal vapour in the plasma may have a large influence on the calculated plasma temperatures. Here for calculations made without the effects of metal vapour, we calculate plasma temperatures of more than 20000 K in the central region of the arc around the arc axis, decreasing to less than 10000 K at radial positions about 5 mm from the axis. For GMAW, spectroscopic measurements of plasma temperatures in the literature [12] made using metal vapor lines suggest that the temperatures of the plasma in the central region of the arc are around 7000 K, for a wire of mild steel, increasing to more than 11000 K away from the arc axis. However, other measurements using an aluminium wire suggest a plasma temperature in excess of 17000 K [12] although steel and aluminium are expected to have similar influences on the plasma. These differences between the measured temperatures illustrate the difficulties of measuring the plasma temperature in GMAW and suggest large uncertainties in the measured temperature. Within the context of the model presented in this paper, heat transfer from the plasma to the wire depends more on the electron number density in the plasma than on the plasma temperature. As mentioned before, we expect that neglecting the effects of metal vapour will have only a minor influence on the calculated droplet characteristics, including evaporation from the droplet surface [3]. Numerical calculations made without including the direct effects of the plasma temperature show that the direct effects of plasma temperature contributes less than 10% to the evaporation from the wire surface. The main heating effects at the droplet surface are due to electron condensation and sheath effects. These heating effects are mostly determined by the electron number density in the plasma, n_e , and for the range of the calculated plasma temperatures for pure argon and the measured plasma temperature for metal-vapor argon plasma [12], we calculate similar values for n_e .

As mentioned before, the effects of Marangoni forces are not included in the calculations presented in Figs 2, 3 and 4. We find that for calculations with a mild steel wire of diameter 0.12 cm, the influence of the Marangoni forces increases droplet formation times by more than 50%, with increases in the current corresponding to the transition from the globular mode to the spray mode of metal transfer from around 200 A for calculations made without the Marangoni effect to more than 230 A when this effect is included. These results are consistent with experimental observations reported in the literature indicating changes in droplet size and droplet detachment frequency depending upon the purity of the gas and the composition of wire materials, which can have a large effect on γ .

In GMAW, formation of welding fume depends largely on heat transfer phenomena in the welding wire and in the arc. Heat transfer processes resulting in net contributions to the energy balance of the wire, including the welding droplet at the end of the wire, are ohmic heating in the wire by the arc current E_{oh} , heat transferred from the plasma to the droplet due to current transfer between the plasma and the wire E_e , conventional heat conduction from the plasma through neutral particles E_p , evaporation from the surface of the droplet at the tip of the wire E_v , heat losses due to metal transfer in the form of droplets detaching from the wire tip E_m , black body radiation from the wire surface E_r , and conduction through the end of the wire at a temperature of 300 K E_k . Here, we present results for the integrated values over the total volume of the wire of E_{oh} , E_e and

E_p , E_v , E_m , E_r and E_k .

In Fig. 5 we show details of calculated droplet shape as a function of time for a current of 200 A corresponding to the globular mode of metal transfer. The

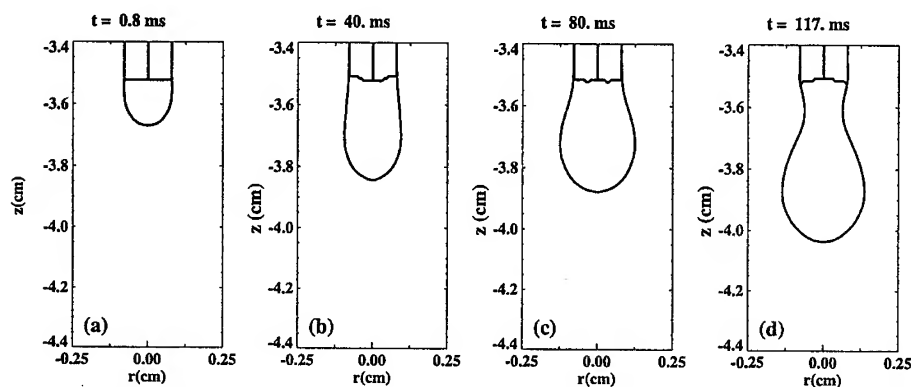


FIG. 5. Examples of drop development for a wire of mild steel. The wire diameter is 0.16 cm and the arc current is 200 A.

droplet shape in Fig. 5(a) is at a time $t = 0.8$ ms at the beginning of droplet growth and the droplet shape in Fig. 5(d) is at a time $t = 117$ ms just before droplet detachment. Fig. 6(a) shows details of heating effects in the wire; E_{oh} , E_e and E_p . Also, Fig. 6(a) shows the voltage drop in the wire V_{wire} taken as

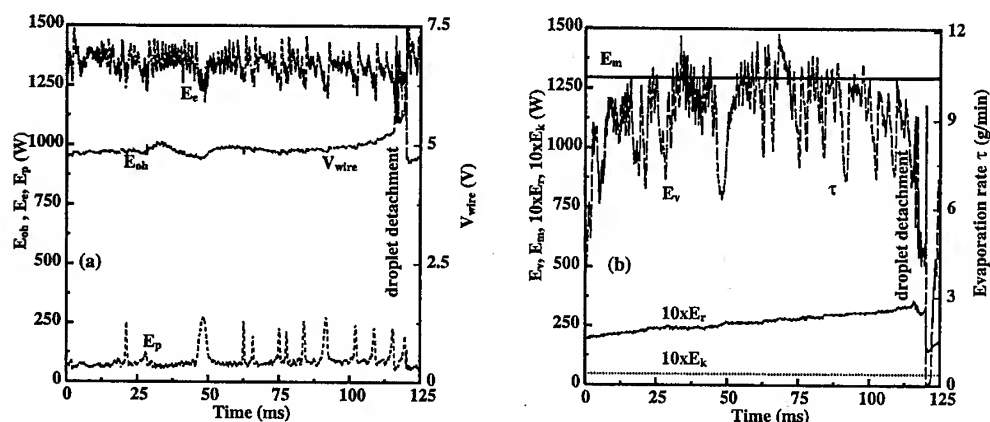


FIG. 6. 6(a): Variation in time of the heat components in the welding wire, E_{oh} , E_e and E_p . The voltage drop in the wire V_{wire} is also shown on the right hand side vertical axis. The arc current is 200 A. 6(b): A plot of total heat loss from the droplet due to evaporation E_v together with the instantaneous evaporation rate τ . E_m , E_r and E_k are also shown. The arc current is 200 A.

E_{oh}/I ; I is the arc current. Details of calculated heat losses from the wire are shown in Fig. 6(b); E_v , E_m , E_r and E_k . Heat losses from the wire due to droplet detachment occur only at the time of detachment. For the results in Fig. 6(b), E_m is shown as a time average quantity for comparison with other heat processes. Also, in Figure 6(b) we show the instantaneous evaporation rate

from the surface of the molten metal at the tip of the wire τ in gmin^{-1} , taken as $60 \times E_v/L$. As mentioned above, L is the latent heat of evaporation of the wire materials, and for mild steel we take L to be equal to 7415 Jg^{-1} .

It is seen in Fig. 6(a) that ohmic heating in the wire and the corresponding wire voltage drop remain almost unchanged during most of the formation time of the droplets. However, towards the end of droplet growth at the tip of the wire during necking of the droplet, there is an increase in E_{oh} and thus V_{wire} due to a decrease in the cross section area of the wire at the level of the droplet neck. For the energy due to current transfer E_e , we calculate large oscillations of up to 300 W, resulting from a combination of factors, including oscillations in the droplet base and changes to the volume of the molten metal droplet at the tip of the wire due to droplet growth. These surface oscillations are due to physical effects mostly associated with pressure variations inside the molten metal droplet. Most forces acting on the droplet can change direction depending upon the current density distribution and the droplet shape. We find that gravity is the only force that tend to stabilise the droplet. For calculations made without the effects of gravity, we calculate increases in the amplitude of the droplet surface oscillations [5].

For the evaporation from the droplet surface, it is seen in Fig. 6(b) that there are large variations in the calculated evaporation rate, synchronised with the oscillations in E_e and E_p observed in Fig. 6(a). For droplets at the tip of the welding wire, we find that the calculated droplet surface temperature near the droplet base in the region of the arc-wire attachment region is near the boiling temperature of the wire material, which is around 3000 K. Thus, most of the metal vapour from the droplet is emitted from the region of the droplet surface near the droplet base. As mentioned before, arc instabilities result in transitory increases in the size of the arc-wire attachment region. As a result, the average heat per unit of area incident on the droplet surface due to current transfer decreases, leading to transitory decreases in the evaporation from the droplet surface. We suggest that these calculated arc instabilities are equivalent to the erratic arc behavior usually observed in arc welding at currents corresponding to the globular mode of metal transfer.

On a time scale larger than that of the calculated arc instabilities, the average evaporation rate from the droplet surface remains almost unchanged during droplet growth, suggesting that τ is mostly limited by the droplet surface temperature and not by the surface area of the droplet. The average evaporation rate for the results in Fig. 6(b) is 8.9 gmin^{-1} . Heat losses due to conduction and black body radiation are very small compared to E_e and E_{oh} .

Fig. 7 and 8 show details for calculations at a current of 300 A corresponding to the spray mode of metal transfer. Fig. 7 shows examples of droplet development from a time $t = 22.4 \text{ ms}$ in Fig. 7(a) at the beginning of droplet growth just after detachment of the preceding droplet to a time $t = 29.2 \text{ ms}$ in Fig. 7(d) just before droplet detachment. Fig. 8(a) shows the calculated heat effects in the wire; E_{oh} , E_e , E_k and E_r , and also V_{wire} . Heat losses due to evaporation E_v , together with calculated evaporation rates in gmin^{-1} are shown in Fig. 8(b). The droplet shape in Fig. 7(a) at $t = 22.4 \text{ ms}$ corresponds to the minimum wire voltage in Fig. 8(a) and to the minimum evaporation rate in Fig. 8(b). The

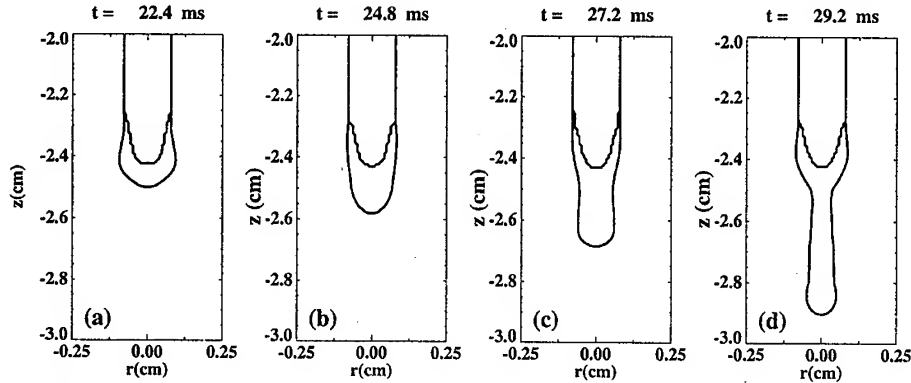


FIG. 7. Examples of drop development for a wire of mild steel. The wire diameter is 0.16 cm and the arc current is 300 A.

droplet shape in Fig. 7(d) at $t = 29.2$ ms just before droplet detachment corresponds to the maximum wire voltage in Fig. 8(a) and the maximum evaporation rate in Fig. 8(b). It is seen in Fig. 8(b) that the voltage drop in the wire V_{wire} is around 4 V near the beginning of droplet growth, increasing to more than 10 V at $t = 29.2$ ms just before droplet detachment due to changes in the droplet length and shape. The sharp increase in V_{wire} towards the end of the droplet growth, just before droplet detachment, is due to a decrease in the cross sectional area of the wire at the level of the droplet neck. It is also seen that detachment of the droplet results in a sharp decrease in V_{wire} associated with the loss of the droplet.

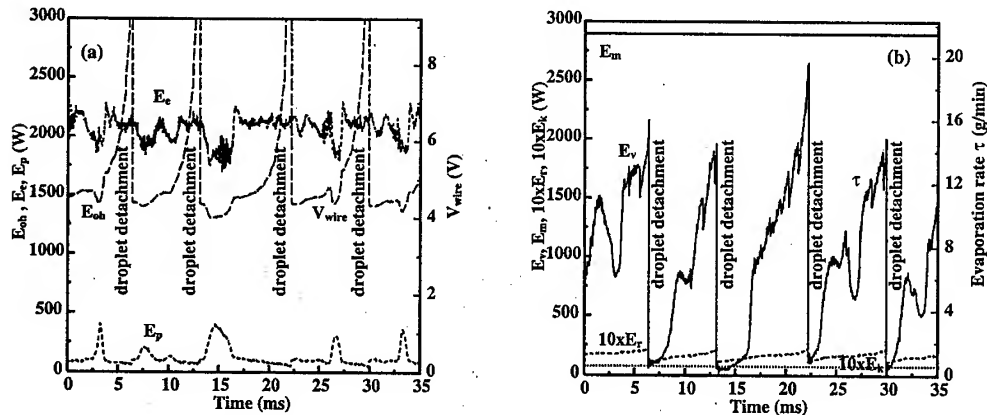


FIG. 8. 8(a): Variation in time of the heat components in the welding wire, E_{oh} , E_e and E_p . The voltage drop in the wire V_{wire} is also shown on the right hand side vertical axis. The arc current is 300 A. 8(b): A plot of total heat loss from the droplet due to evaporation E_v together with the instantaneous evaporation rate τ . E_m , E_r and E_k are also shown. The arc current is 300 A.

The heat transfer to the wire due to current transfer, E_e , remains largely unaffected by droplet detachment. However, it can be seen in Fig. 8(a) that

there are oscillations in all of E_e , E_{oh} and E_p due to changes in the droplet shape during droplet growth at the tip of the wire. These oscillations may reflect the unsteady nature of the welding arc. As mentioned before, heat conduction through the wire bulk and heat loss due to black body radiation are very small at 7 W and 16 W respectively.

Fig. 8(b) shows that the heat loss due to evaporation, E_v , increases from less than 200 W just after detachment of the preceding droplet to more than 2000 W just before droplet detachment. This heat of evaporation has some correlation with ohmic heating in the wire bulk by the arc current, both rising sharply in time as the droplet grows at the tip of the wire. Also, the calculated evaporation rate increases from less than 1 gmin⁻¹ just after detachment of the preceding droplet to more than 10 gmin⁻¹ just before droplet detachment, resulting in an average evaporation rate of around 8.9 gmin⁻¹.

In Fig. 9, we present the average evaporation rate τ together with the percentage θ of metal vapour produced relative to the consumed wire for arc currents between 150 A and 325 A. It is seen that τ has a minor local maximum of 8.9

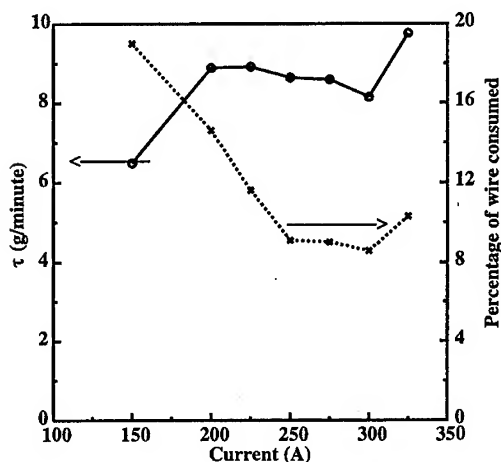


FIG. 9. Average evaporation rate in gmin⁻¹ as a function of arc current.

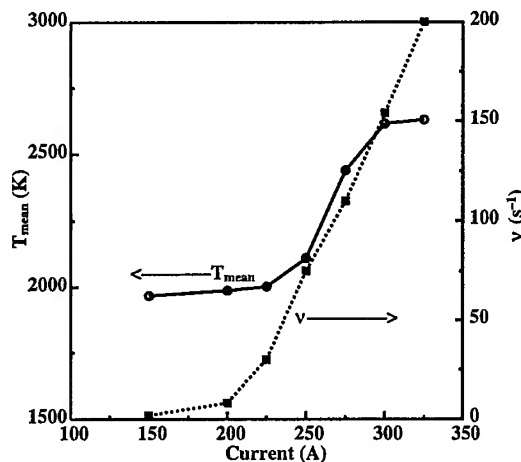


FIG. 10. Calculated mean droplet temperature and droplet detachment frequency for arc currents between 150 A and 325 A.

gmin⁻¹ at a current of 200 A in the globular mode of metal transfer, decreasing to 8.1 gmin⁻¹ at a current of 300 A in the spray mode of metal transfer. For a current of 325 A, τ is high again. The percentage of metal vapour produced relative to the consumed wire decreases from more than 19% at 150 A to around 8% at currents above 300 A.

Fig. 10 shows the calculated mean temperature of droplets T_{mean} at the time of detachment from the wire. Here, it is seen that there is an increase in T_{mean} at a current of around 250 A, corresponding to the transition from the globular mode to the spray mode of metal transfer. For currents in the globular mode of metal transfer, T_{mean} is around 2000 K, increasing to more than 2600 K at a current of 300 A in the spray mode of metal transfer. Also, Fig. 10 shows the

corresponding variation of the calculated droplet detachment frequency ν . The variation of T_{mean} is strongly correlated with that of ν , both increasing sharply at around 250 A, at the transition from the globular to the spray mode of metal transfer. The increase in T_{mean} with arc current at this transition is due to increases in the ratio of the droplet surface area that is covered by plasma to the droplet volume, leading to a more efficient heating of the molten metal droplet.

For the results in this paper, ohmic heating in the wire and the droplet contributes about 80% of the heat required to melt the wire metal fed into the arc. Heat losses from the wire are dominated by evaporation and cooling effects due to droplet detachment. For current transfer at the droplet surface, the resulting heating effects are localized on the surface and they are primarily responsible for increasing the surface temperature and causing evaporation.

In GMAW, measurements of fume formation rates (FFR) for mild steel wires indicate that the measured FFR are less than 0.5 gmin^{-1} , corresponding to less than 1% of the weight of the consumed wire. The calculations in this paper show that the calculated evaporation rate from the droplet, during droplet growth at the wire tip, are more than 6 gmin^{-1} for all currents above 150 A.

We suggest that the large differences between the calculated evaporation rates and the measured FFR are mainly due to recondensation of most of the metal vapour emitted from the droplet on the surface of the work piece. In GMAW, the arc magnetohydrodynamics result in a strong plasma flow in the arc directed downwards from the droplet towards the workpiece. This plasma flow drives most of the metal vapour away from the region near the droplet and towards the surface of the workpiece, which is at a low temperature, providing suitable conditions for the recondensation of the metal vapour. Preliminary calculations of the recondensation effects performed for an arc current of 300 A suggest that more than 85% of metal vapour emitted from the welding wire recondenses on the surface of the workpiece.

The presence of an important recondensation process at the surface of the weld pool in GMAW is supported by the experimental measurements of Acinger et al [13], who found that the vapour collected on the workpiece represented around 4 to 5% of the total weight of the wire consumed for arc currents between 280 and 300 A. However, because of the experimental arrangement, metal vapour from the droplets was only partly collected. For the calculations in this paper at a current of 250 A, we predict that the metal evaporated from the droplets formed at the tip of the wire is around 10% of the total consumed metal. For experimental conditions similar to those used by Acinger et al., measured FFR is less than 1% of the consumed wire [14]. The experimental measurements of Acinger et al. suggest that most of the metal vapour from the metal wire fed into the arc is condensed on the workpiece.

Another possible reason for the large difference between the calculated evaporation rates and the measured FFR is the assumption regarding evaporation from the droplet surface. As mentioned before, for the calculations in this paper, we use a Langmuir type model and the calculated evaporation rates represent an upper limit.

4. Summary

Predictions have been made of droplet formation in gas metal arc welding for mild steel wires of diameter 0.16 cm. The predicted droplet diameter and droplet detachment frequency agree with experimental measurements in the literature. Also, predictions have been made for the transition from the globular to the spray mode of metal transfer that agree with experiment. Predictions have also been made for metal vapour emission which indicate a large amount of metal vapour in the plasma and an important recondensation at the surface of the workpiece cathode.

Acknowledgement

This work is part of a research project sponsored by the Cooperative Research Centre on Welding and Joining of Materials, Australia.

References

1. J. HAIDAR, J. Appl. Phys., **84**, 3518-29, 1998.
2. J. HAIDAR, J. Appl. Phys., **84**, 3530-40, 1998.
3. J. HAIDAR, J. Appl. Phys., **85**, 3448-59, 1999.
4. J. HAIDAR and J. J. LOWKE, J. Phys. D: Appl. Phys., **29**, 2951-60, 1996.
5. J. HAIDAR, J. Phys. D: Appl. Phys., **31**, 1233-44, 1998.
6. J. HAIDAR and J. J. LOWKE, IEEE Transactions on Plasma Science, **25**, 931-36, 1997.
7. C. W. HIRT and B. D. NICHOLS, J. Comput. Phys., **39**, 201-25, 1981.
8. S. V. PATANKAR, *Numerical heat transfer and fluid flow*, McGraw-Hill, N Y, pp 56 and 126.
9. M. L. LIN and T. W. EAGAR, Weld. J., **64**, 163-69, 1985.
10. Y. S. KIM and T. W. EAGAR, Weld. J., **71**, 269-78, 1993.
11. P. G. JONSSON, A. B. MURPHY and J. SZEKELY, Weld. J., **74**, 48-58, 1995.
12. J. F. LANCASTER, *The Physics of Welding*, ed. J F Lancaster, Pergamon Press, Oxford, 1984.
13. K. ACINGER, L. SIPEK and E. SMARS, Proc. 11th Int. Conf. on Gas Discharges, (London, 1970). p. 519.
14. I. IOFFE, D. MACLEAN, N. PERELMAN, I. STARES and M. THONRTON, J. Phys. D: Appl. Phys., **28**, 2473-77, 1995.

PULSED CORONA FOR SUSTAINABLE TECHNOLOGY

E. J. M. VAN HEESCH, A. J. M. PEMEN, K. YAN, P. P. M. BLOM, P. A. H. J. HUIJBRECHTS,
P. C. T. VAN DER LAAN

HIGH-VOLTAGE AND EMC GROUP, EINDHOVEN UNIVERISTY OF TECHNOLOGY

P. O. Box 513, 5600MB Eindhoven, The Netherlands

Highly active coronas with a peak power of up to 25 MW p/m corona wire and kJ/liter energy densities in the streamer channels can be produced by pulsed power. Since the voltage pulses are short, full breakdown does not occur even though the discharge currents are hundreds of Amperes. A matched pulsed power source can deposit up to 80% of its electrical energy into such a controlled discharge. Reliable and efficient sources characterized by 100 kV, 150 ns wide pulses at 1000 Hz have passed 400 hours of operation. The area of applications is growing: VOC control, hot gas cleanup, water and air purification and sterilization.

1. Introduction

Pulsed power is used to generate high-voltage discharges for corona production in gases and in liquids [1, 2, 3], see Fig. 1. The energy is deposited at a high repetition rate in brief pulses and fairly homogeneously in the medium. Operating over a wide pressure and temperature range and in various media, corona generates ions, electrons, free radicals and excited molecules. Bond cleavage by electrons, interactions through radicals, charging of aerosols and damage by local UV, high fields and shock waves are some of the important mechanisms in applications. Pollutants as well as micro-organisms are attacked [2, 3, 4, 5, 6].

The specific parameters of the pulsed power source are determined by a match between the reactor processes, the transient corona load and the pulse source. With respect to EMC, methods have been developed to effectively suppress interference [7]. Sensitive apparatus for analysis can therefore operate correctly, close to the pulse source. With a technology that runs reliably for a variety of processes we have a promising alternative to existing techniques for purification and environmental protection.

Research is concentrating on the separate energy conversion steps and attainable efficiencies and effects of specific pulsed power corona processes. Key items are process technology, reactor design, pulsed power reliability, streamer corona and conversion efficiency. Key parameters are: electrode dimensions, gas

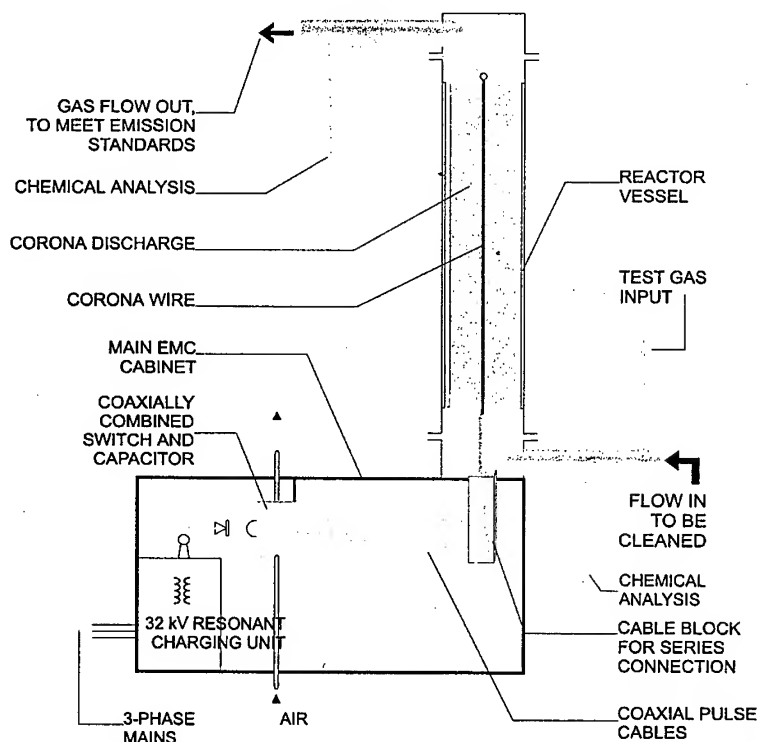


FIG. 1. Main components of a pulsed power corona unit for air treatment.

or liquid composition, process temperature, residence time, discharge duration, energy density of the discharge, voltage level, pulse rise time and pulse repetition rate.

Results are used for development of real applications over a wide range [2, 3, 4, 5, 6, 8, 9, 10, 11, 12]: from NO removal to water treatment, soil cleanup and odor reduction. Interesting examples can be given for cleaning of biogas from wood gasifiers, inactivation of micro-organisms, odor removal and decomposition of VOC's.

2. Micro-organisms

The use of pulsed electric fields (PEF) for pasteurization of milk and fruit juices has gained much popularity and is a promising non-thermal alternative to conventional pasteurization methods. Possible mechanisms of inactivation of bacteria cells with PEF are perforation of the cell membrane due to high voltages across the membrane or due to current concentration in the pores. In a cell membrane, protein channels and pores are present [13, 14]. The opening and closing of many channels constituted by proteins depends on the trans-membrane voltage difference [6, 15, 16]. When PEF is applied, many voltage-sensitive protein channels may open, and when the voltage difference reaches 150-500 mV, the

lipid bilayer breaks down.

It is observed that when a cell membrane is exposed to an electric field larger than about 25 kV/cm, irreversible electric breakdown of the cell membrane occurs [5, 17]. The extent of inactivation depends on the strength, duration and form of the electric pulses [18]. Pulses with a duration of 100 - 200 ns are reported to provide an efficient inactivation of micro-organisms [19]. Various types of treatment chambers are connected to pulse sources (Fig. 2), [20, 21, 22] and are tested for effectiveness. A number of patents exists in this field, such as the patent [23], obtained for the treatment chamber shown in Fig. 2a.

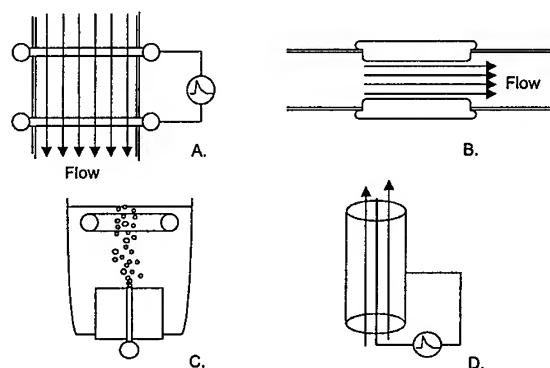


FIG. 2. Types of treatment chambers for inactivation of micro-organisms by pulsed power.

A - Perpendicular flow. B - Parallel flow. C - Bubbling needle. D - Wire cylinder.

If taste and food qualities are not the important issues a more effective pulsed power method for inactivation of micro organisms is direct application of pulsed corona in the liquid [20, 21, 22]. This pulsed corona method (PCOR) is based on the creation of inhomogeneous electric fields that are sufficiently high to generate corona discharges in the liquid. Discharge products such as radicals, ozone, aqueous electrons and UV are produced directly in the liquid to inactivate the bacteria.

An airflow can also be treated with pulsed corona to kill or to remove micro organisms. Here a similar interaction of discharge products and organisms is the supposed mechanism. A second possible mechanism in gases is electrostatic precipitation (ESP) of bacteria. In this case the collected dust of micro organisms would have to be collected in an extremely careful way to reach the required considerable reduction on a log scale.

Both PEF and PCOR require high voltages that are generated across a liquid load. To effectively apply high voltage to a conducting liquid, fast rise times and narrow pulses are needed to reduce the amount of dissipation.

The liquid, considered as a combination of resistance and capacitance, responds to the pulse by means of characteristic RC time constants and voltage division over impedance ratios. Various subsystems in the liquid have different constants. The time constant of the liquid itself may vary from less than a nanosecond to ten nanoseconds. Cell membranes have time constants in the same

range. The pulse source connected to this liquid system produces a waveform which also depends on the impedance (and inductance) of the source.

3. Biogas

Pulsed power for biogas conditioning but also for the synthesis of chemicals from biomass sources can be a welcome tool for sustainable technology.

We concentrate on the removal of tar in the high temperature gas in the exhaust of a thermal biomass gasifier. Pulsed corona seems to be the only efficient and simple technology that is perfectly matched for high temperature conditioning of gases [24, 25]. For conventional technology, cleaning of a high temperature gas flow is a serious problem in many cases of thermal gasification, waste incineration and similar.

We showed that pulsed corona runs excellently at temperatures of 800°C and higher, even under polluted conditions, see Fig. 3. Adapting pulsed high

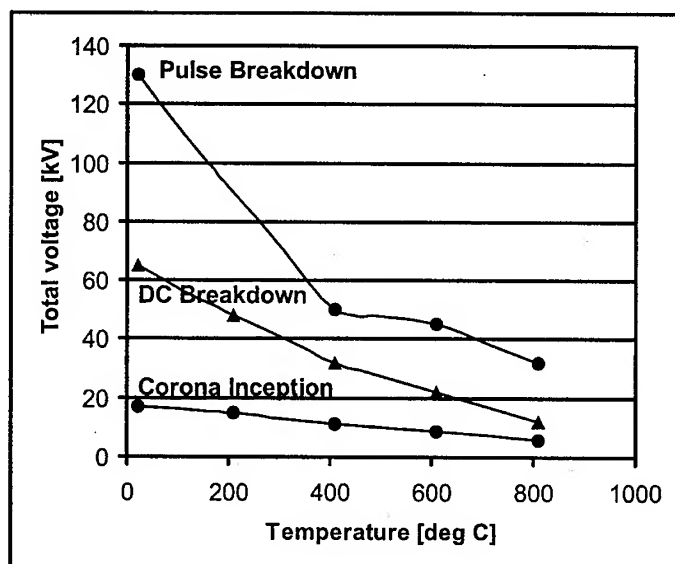


FIG. 3. Existence region for pulsed corona as a function of temperature (ms pulses, low repetition rate).

voltage to deposit intense electric energy into a hot gas we can promote cracking of various undesired tar components [24, 25, 26].

Our pulsed power research concentrates on efficient methods for pulsed high-voltage generation and on matching of pulse forming networks to high-temperature gaseous media.

An intense cleaning effect was found at low temperatures. For several hydrocarbons we measured a high removal efficiency at acceptable levels of input energy. Well controlled energy transfer from source to corona was found to be

possible for hot exhaust gas. These findings now are extrapolated to design our corona treatment of hot biogas.

4. Conversion of electric power into corona assisted chemical processes

To convert electrical power from the mains AC to the processes in a reactor one often has the following energy transfer steps, see Fig. 4. After a converter

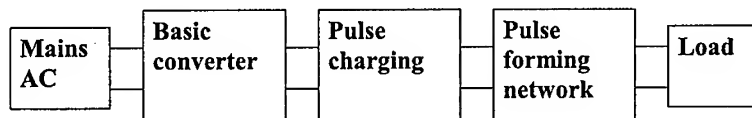


FIG. 4. Main components of a system for generation of repetitive high-voltage pulses.

for AC mains power, a pulse charging circuit uses this power to produce high-voltage pulses. The pulse charging unit contains resonant charging circuits, pulse compression techniques and pulse transformers. It also contains solid state switches and magnetic or gas discharge switches. The pulse forming network adapts the pulse to be fed to the load. The load is the pulsed corona reactor.

Energy is transferred in three steps:

1. Mains AC power is converted into high voltage pulses
2. High-voltage pulses are transferred to the corona discharges in the reactor
3. Discharge energy is finally converted into useful processes inside the reactor

We consider the efficiency of each conversion step. For step 1, efficiencies of up to 90% are achievable. The efficiency of step 2 depends on the electrical matching between load and source impedance. The source impedance can be adapted but the impedance of the load is not completely under control; since the load is a pulsed corona discharge, the impedance depends on voltage and corona development. The corona development itself is also strongly affected by the impedance of the pulse source. We aim at the development of discharge chambers and electrode structures that offer a more constant impedance at a value matching the output impedance of the pulse source. Adversely one can try to adapt the pulse source impedance so that it matches the less controllable load. However, one has to keep in mind the effect of source impedance on discharge impedance. Efficiencies of energy transfer from source to load will be as low as 30% if matching is not well achieved. More optimized configurations are being developed that achieve efficiencies of up to 80% [27].

In the final step discharge energy is converted into chemical processes. The efficiency of these processes cannot be expressed in terms of percentages. One has to use a unit such as the removed fraction X of a substance divided by energy density. This energy density E is the energy yield after step 2 divided by the gas volume to which it is applied. Here we also introduce the power P into the discharge and the gas flow F passing the reactor. The energy transferred to each

discharge is denoted by Q and the number of discharges per second is f . The following relations then apply:

$$(4.1) \quad P = Qf$$

$$(4.2) \quad E = Qft/(Ft) = P/F$$

First order chemical reactions are found to obey [2, 3, 28]:

$$(4.3) \quad X = 1 - \exp(-E/\Delta E),$$

where ΔE is an activation level specific for each type of chemical process. Specific values are given in Table 1.

5. Pulsed power generation

Mains AC power is converted to charge a primary storage capacitor. An inductor and a switch are needed to couple the energy to the next capacitor. The resonant charging technique allows an efficient transport of the energy. Note that the use of a resistor to charge a capacitor would lead to considerable losses since the energy dissipated by the resistor would in fact be equal to the energy transported to the capacitor.

The switch to start the charging process for each charging cycle (pulse) can be a thyristor. The thyristor must be closed on command and will open automatically at the first zero crossing of the current.

If two equal capacitors are used the result is near perfect transfer of all charge from the first capacitor to the next one. The voltage is transferred unchanged to the next capacitor.

This principle of charge transport is often applied in pulse compression circuits [29]. Intermediate pulse transformers can play the role of the charging inductance. The pulse transformer is used to also raise the voltage. Accordingly the component value of the next capacitor must be reduced by the square of the transformer ratio to maintain equal capacitor values in the equivalent transformer diagram.

Resonant circuits can be part of a multistage magnetic compression system. The inductors are then allowed to saturate. Usually all capacitors have equal values. Energy is transported from one capacitor to the next one by a current through the inductor during the time that it is saturated. The unsaturated inductor of the next stage acts as an isolation until it also saturates at the end of the half period of the previous section. If the saturated inductance of the next stage is smaller than the saturated inductance of the previous one, the pulse duration is compressed.

The last high voltage capacitor of the resonant charging section is available to be discharged across the load. To connect this capacitor to the load, we use a pulse forming network (PFN) that is constructed like a transmission line. A spark gap is inserted between the last capacitor and the PFN to start the final pulse. The purpose of the PFN is pulse shaping, impedance matching and sometimes also voltage multiplication.

We constructed a PFN as a transmission line transformer (TLT) [30, 31]. It is made of 4 coaxial cables, each 50Ω and 12 m long. The inputs of all four cables are connected in parallel between the switched electrode of the spark gap and the return conductor of the last resonant charging section. At the other end the cables are connected in series to the load Z_L . The braid of the first cable is connected to the return conductor of the load. The central conductors of the first, second and third cable are connected to the braid of the next cable. The central conductor of the fourth cable is connected to the load.

In an equivalent circuit diagram each cable can be represented as a voltage source of twice the input voltage V_0 in series with the cable impedance Z_0 . The load for each cable is the combination of the other cables, the actual load plus an impedance for each cable that represents the return path for the wave that will propagate in the air between the braid and any other available conductor. This latter wave, called the secondary wave, travels back to the switch. The impedance of this wave structure is represented in the equivalent circuit diagram by Z_S . The resulting circuit is given in Fig. 5.

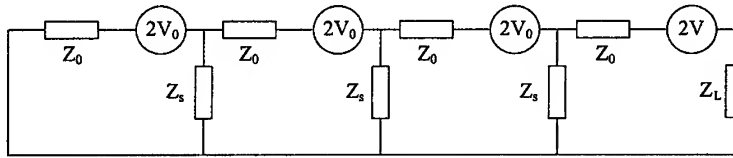


FIG. 5. Equivalent circuit diagram for the reflection at the end of the transmission line transformer.

For a simple calculations we use equal values for the secondary wave impedances. We also have to realize that after reflection of the secondary wave, it returns to the output load before reflections of the primary wave return. The above diagram therefore only allows an estimate of the initial voltage multiplication.

For an arbitrary number of cables n , Wilson [31] has given a general formula:

$$(5.1) \quad V_{out} = \frac{(2V_0 + V_T) \cdot Z_L}{Z_0 + Z_T + Z_L}$$

where:

$$(5.2) \quad V_T = \frac{4V_0 \cdot Z_S \cdot Q}{(B+1) \cdot Z_0} \quad Z_T = \frac{2Z_S \cdot Q}{B+1}$$

$$Q = \frac{1 - \left(\frac{B-1}{B+1}\right)^{2n-2}}{1 + \left(\frac{B-1}{B+1}\right)^{2n-1}} \quad B = \sqrt{1 + 4 \cdot \frac{Z_S}{Z_0}}$$

In our case of four cables, $Z_0 = 50 \Omega$, $Z_L = 200 \Omega$ and $Z_S = 1000 \Omega$, the formulas gives a voltage multiplication of 3.7 for the TLT system. In our design, ferromagnetic cores are used to increase Z_S . The cores form a magnetic circuit around each cable braid. The introduced inductance strongly reduces the

current on the braid. Note that the formula can only serve as an indication since a number of simplifying assumptions were made.

The impedance of the load affects the gain. To match the output impedance of the TLT, the load must have an impedance of n times the cable impedance; in the examples here the cable impedance is $50\ \Omega$ and a load matching the output impedance is $200\ \Omega$. A matched load will achieve the best energy transfer from cable to load.

To make accurate designs of TLT systems we must use a circuit analysis program (such as Microcap). The coaxial cables are represented by ideal lines and are interconnected as a TLT. The secondary waves can run on three additional ideal lines connected to the nodes where central conductors and braid meet. Inductors and resistors can be used to simulate the ferrites in this analysis. The resistors represent the losses in the core material. The load is a voltage dependent resistor to simulate the corona discharge. The voltage wave form at the entrance of the corona reactor is calculated for a charging voltage of 30 kV. The result is compared with measurements of the real voltage, see Fig. 6. It is clear from Fig.

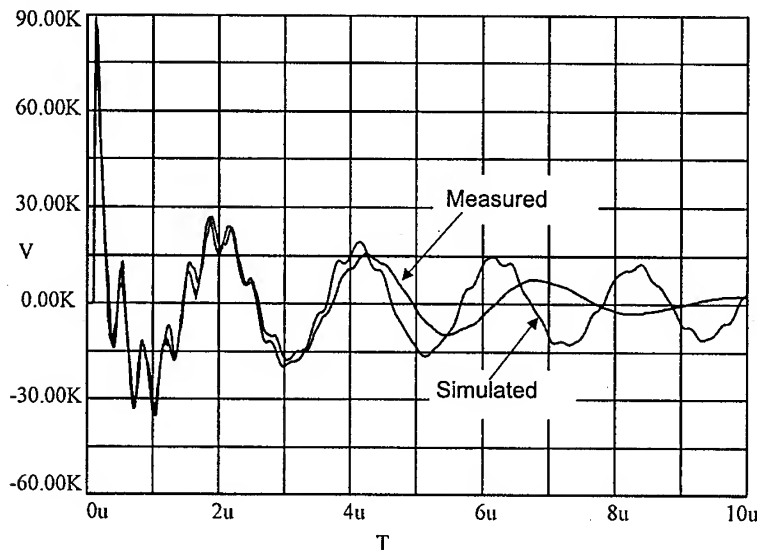


FIG. 6. Simulated and measured voltage wave forms at the entrance of the corona reactor.

6 that the circuit analysis can be a powerful tool to investigate the design of a pulse source connected to a corona discharge if we allow a suitable expression for the corona impedance.

6. Data of the Eindhoven pulsed power source

This heavy duty pulse source, developed during 1995, produces 100 kV pulses (10 ns rise time, 150 ns wide) at a maximum repetition rate of 1000 pulses per second (pps) [10]. This patented design [32] has an overall efficiency of up to 80% for the energy transfer from mains AC power to corona energy in gas flows

at pulse repetition rates below 600 pps. Failureless operation of this unit has passed the 400 hours mark. Fig. 7 gives a simplified diagram of the pulse source. The source is mounted in an EMC cabinet. The corona treatment chamber is placed on top of it as an extension of the EMC cabinet. For the production of

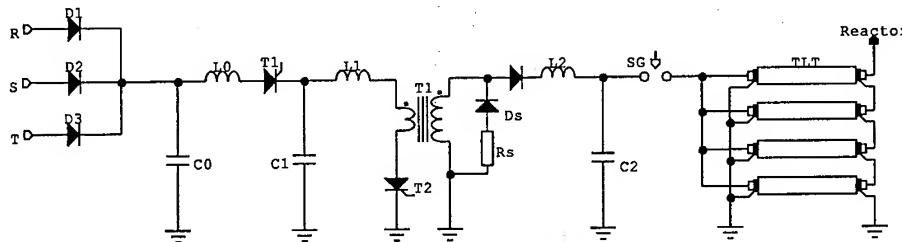


FIG. 7. Simplified circuit diagram of pulse source for 100 kV, 150 ns pulses and 1.5 kW average corona power.

the high-voltage pulse three subsequent modules are used: resonant charging of a 32 kV capacitor C_2 (a 1:60 pulse transformer is part of the charging inductor), a fast spark gap for 32 kV switching and finally a transmission line transformer (TLT) to produce the 100 kV pulses.

The transformer has an iron (N2-112) C-core (SU180C) with thin (0.05 mm) laminations. Its cross-sectional area is 46 cm² and its iron length is 68 cm. It is a core-type transformer with two coil sets. The primary of each set has 10 thick flat copper turns. The secondary high voltage coils have 600 turns each and are equipped with field-control rings. Each high-voltage coil is epoxy insulated during a vacuum potting process. The two coil sets are connected in parallel. A metallic screen connected to the core removes the inter-coil capacitance. A small core gap (0.3 mm) is maintained to keep the core far below saturation during repetitive single polarity pulses.

A low inductance spark gap (50 nH, coaxial with the high-voltage capacitor) discharges the capacitor into the TLT. An automatic triggering, derived via 2 M Ω from the voltage reversal at the transformer secondary is added to prevent misfiring of the spark gap. After each high-voltage pulse, part of the energy returns to the low voltage resonant circuits. This surplus of energy is partially reused in the next pulse.

The reliability of the spark gap is excellent, after 10⁹ pulses (total transferred charge 200 kC) only minor electrode wear is visible. The gap has to be flushed continuously with air (30 Nm³/h typically for high repetition rates of the source).

The actually produced and the simulated output voltages across the corona load are given in Fig. 6.

7. Electromagnetic compatibility and measuring systems

We use the principle of the EMC-cabinet to considerably reduce the transfer impedance between large interference currents and electronics [7, 33]. The cabinet acts as an EMC-wall with on one side the interference currents and on the

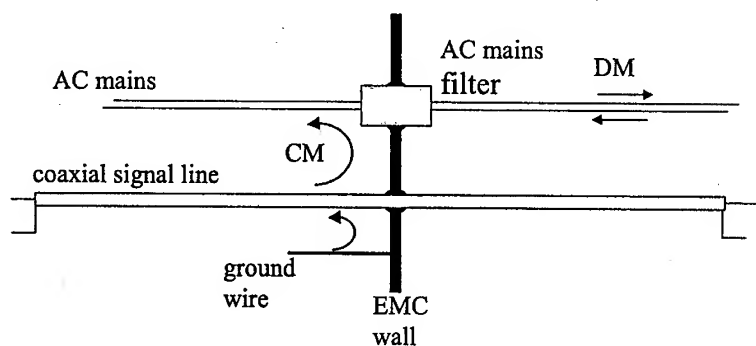


FIG. 8. An EMC wall to create regions with and without large CM currents and to reduce the transfer impedance between them.

other side the sensitive apparatus. As shown in Fig. 8, the wall connects the leads going to both sides of it. The large interference currents however, cannot cross the wall since they are common mode (CM) currents: the wall itself closes (short circuits) all CM paths. Differential mode currents such as signal and power can pass the wall since their current loop continues on both sides of the wall.

In our pulsed power source for corona processing we use these principles to construct an application that was included in the patent [32]. Two separate EMC walls are constructed: one to separate the pulse source from the rest of the world, the other one to surround the sensitive electronics of the pulse source. Both walls are equipped with adequate mains filters and coaxial cable feedthroughs. The corona reactor is connected to the pulse source and is an extension of the 'EMC region' of this source.

The base of the corona reactor is constructed as a one-turn Rogowski coil (a toroid of rectangular minor cross section) to measure the total corona current I_X (subscript X for external to the discharge) to the reactor [32, 10].

The high voltage is fed into the reactor via a HV feedthrough, which contains a capacitive sensor to form a Differentiating-Integrating (DI) measuring system for the external (corona) voltage V_X [34, 35, 36].

In our DI-system, the large differentiated signal is transported via a coaxial cable to the passive RC input section of an integrator just behind the wall of the EMC cabinet for sensitive electronics. The integrator restores the original waveform but it also acts as an effective EMC filter. Large common mode currents are allowed to flow on the signal cables from sensor to integrator and back via grounding systems. A sufficiently low transfer impedance of the entire set up, cables, passive integrator and EMC-cabinet, leaves the digital measuring electronics undisturbed.

Signal evaluation and corrections for the 50 W load of the integrators were made as follows:

$$(7.1) \quad V_X = k_1 V_{out1} + \alpha_1 \int k_1 V_{out1} dt$$

$$(7.2) \quad I_X = k_2 V_{out2} + \alpha_2 \int k_2 V_{out2} dt,$$

where V_{out1} and V_{out2} are the integrator outputs, k_1 and k_2 are the calibration factors and α_1 and α_2 are the known correction factors for the integrator droop. In case an extra active integrator section is used, the droop can be reduced in the hardware.

The E-field at the wall inside the reactor is measured by means of a grid-sensor, mounted flush with the surface of this electrode [37, 38, 39]. Fig. 9 shows the construction of this sensor.

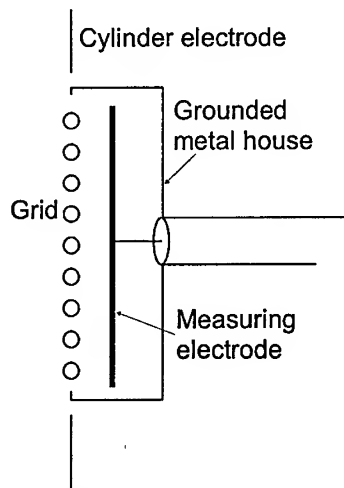


FIG. 9. A grid sensor in the wall of the reactor can detect either E-field or ions.

It consists of a measuring electrode (a brass plate with a diameter of 30 mm) behind a grounded stainless steel grid (mesh size 1.4 mm). The distance between the plate and the grid is 2 mm. Charge carriers, which produce a conduction current at the cylinder, cannot enter the grid sensor due to a repelling E-field between the grounded grid and the plate, which is at a DC bias voltage of 15 Volt.

This bias voltage and the voltage pulse at the central wire have the same polarity. Since the grid is not perfectly shielding, still some 2% of the corona E-field is seen by the plate. This transient field produces a displacement current to the plate which can easily be detected. To obtain the total displacement current I_D to the cylinder electrode, the current to the plate of the E-field sensor needs to be multiplied by a factor that accounts for the ratios of surface area and grid penetration. Finally the current must be integrated in the time domain to obtain the displacement charge Q_D , which is proportional to the E-field at the cylinder. The bandwidth of this system is 0.5 Hz - 50 MHz.

Operating as ion sensor, a forward DC-bias voltage (900 V) on the plate is applied to attract the ions into the grid sensor towards the plate. The resulting

conduction current to the plate is a measure for the number of ions arriving at the sensor. The mesh size of the grid should be small enough to strongly reduce the corona E-field, as is necessary for the ion measurements.

The total corona current, measured externally as I_X , can be represented [1] as a conductive component I_C (passing charge carriers) plus a displacement component (changing E -field) I_D . This component, measured separately with the E -field sensor, equals the current I_0 due to the changing external voltage V_X across the vacuum capacitance C_0 between the electrodes, plus the capacitive current I_S due to the movement of space charge in the gas:

$$(7.3) \quad I_X = I_C + I_D = I_C + I_0 + I_S$$

$$(7.4) \quad I_0 = C_0 dV_X/dt$$

8. Discharge development

Both positive and negative corona show similar behavior in a wire-cylinder geometry. The voltage pulses are applied between the corona wire and the cylinder. Intense pulsed corona discharges of up to 250 A/m (i.e. per meter of corona wire) peak current occur at high pulsed voltages. These intense discharges are well distributed over the volume and do not lead to full breakdown.

Actually, we can distinguish two pulsed corona modes: a moderate mode occurring above the usual corona inception voltage and a highly active mode starting at a second, higher inception voltage. Fig. 10 shows the measured re-

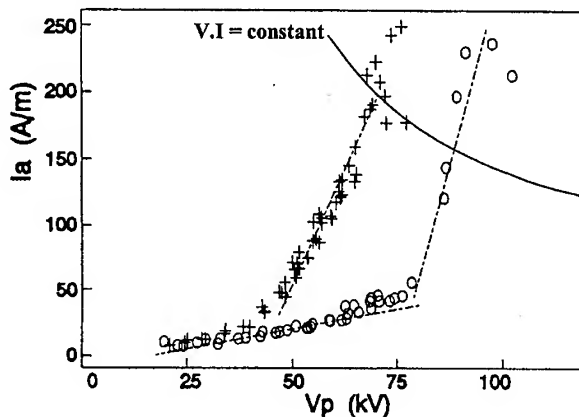


FIG. 10. Peak corona current as a function of peak pulse voltage. A 15 kV bias voltage that was also fed to the corona wire has to be added to obtain the total voltage. Pulses are 500 ns wide. The "+" markers indicate positive wire, the "o" indicates negative wire. The moderate and highly active mode are indicated by dashed lines. The line of constant $VI = \text{const}$ indicates a constant peak-power value.

lation between the peak current and the peak voltage for the case of corona in 360 Torr of air (simulating the density of air at 400°C). The pulses have a rise time of

20 ns, are 500 ns wide and are added to a constant bias voltage of 15 kV. In this experiment the corona vessel has a smooth wall and a diameter of 29 cm. The transition from moderate to active can be seen near a value of 55 kV total voltage with a positive wire and near 90 kV with a negative wire. Both voltages are the sum of bias and peak pulse. Both polarities can have equally high intensities and energy input if the negative wire has a higher voltage. This is indicated by the line $VI = \text{constant}$ in Fig. 10. Negative coronas can therefore be equally efficient for applications as positive coronas. The disadvantage of negative polarity is a higher voltage pulse source, the advantage is a higher E -field.

To describe the development of a single high-intensity corona pulse we use the CCD pictures and the electrical measurements collected in Fig. 11. After the start of each pulse, we see many narrow discharge channels, streamers, grow from the wire towards the cylinder, during the initial streamer phase [1]. The strongly inhomogeneous space charge at the streamer head creates a large E -field, which causes an enhanced ionization and further growth of the initial streamers towards the cylinder. Each streamer carries a current of 0.1 - 1 A. The capacitance between the streamer head and the cylinder acts as a limiting impedance for the current through the initial streamer. The conductive streamer phase starts after the arrival of the initial streamers at the cylinder. The development of the initial streamer into a complete channel between the wire and the cylinder results in a disappearance of the capacitance between the streamer head and the cylinder. This allows a much larger current (1-10 A) to flow through each streamer; many streamers in parallel carry the large current of the pulsed corona discharge.

The energy injected in each discharge is measured from the voltage and current wave forms. Both voltage and total current are detected at the entrance of the high voltage pulse in the corona reactor vessel. Multiplication of these signals and integration in time gives us the value of the total energy per pulse. In addition we can further distinguish the components of the energy input by the components of the total current: capacitive current to the wire-cylinder capacitance (I_0), capacitive current of the streamer development (I_S), the sum these which is the total capacitive current (I_D) and the conduction current (I_C) after the streamers reach the other electrode. The time integral of each current component is the associated charge Q (with respective subscript).

An example of measured wave forms is given in Fig. 12. Each of the current components is used to obtain the associated energy input. This result is plotted in the lower part of the figure. It can be seen that the total energy (subscript X) grows to a value of 1.7 J. The energy related to the initial streamer development (subscript S) reaches 0.6 J. The conductive streamer phase finally adds 1.1 J. The energy stored in the cylinder capacitance (subscript 0) disappears again, as expected. The energy input during equally high negative voltage pulses at the wire shows a similar pattern though the energy levels are lower than at the same positive voltage (0.8 J total, 0.3 J initial and 0.5 J conductive phase). The lower levels are a consequence of the already mentioned higher inception voltage of the high intensity negative coronas. The measurements show that about 2/3 of the energy is transferred during the conductive streamer phase. The efficiency of

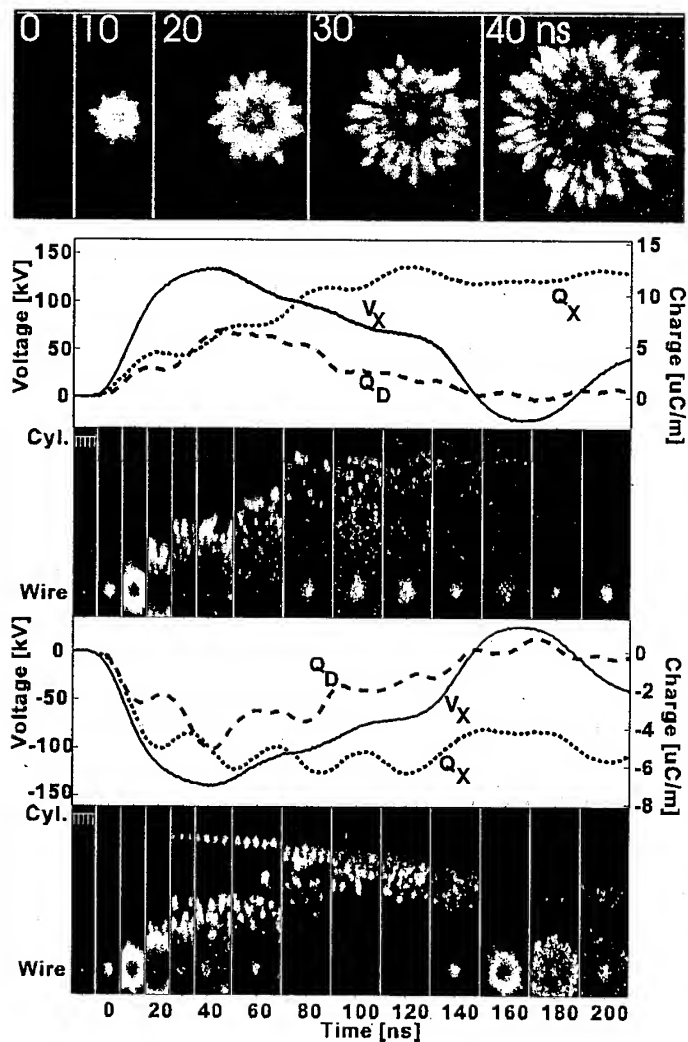


FIG. 11. Upper part: CCD images, axial view in the cylinder with the wire in the center, 5 ns gating and 10 ns steps from the start of the voltage pulse. Cylinder diameter 29 cm corresponding to the height of each picture. Lower part: CCD movie composed of slices of many axial images. Cylinder and wire position are indicated. Positive and negative corona development are compared. Measured voltage (V_X), total charge (Q_X) and capacitive charge (Q_D) are also indicated. The difference between Q_X and Q_D occurs shortly before visible discharge activity has reached the cylinder.

both energy contributions with respect to chemical processes has not been distinguished. The conversions obtained during various chemical processes will be given here as the result of the total deposited energy. The energy densities reported in the next sections therefore are derived from the total energy divided

by the treated gas volume.

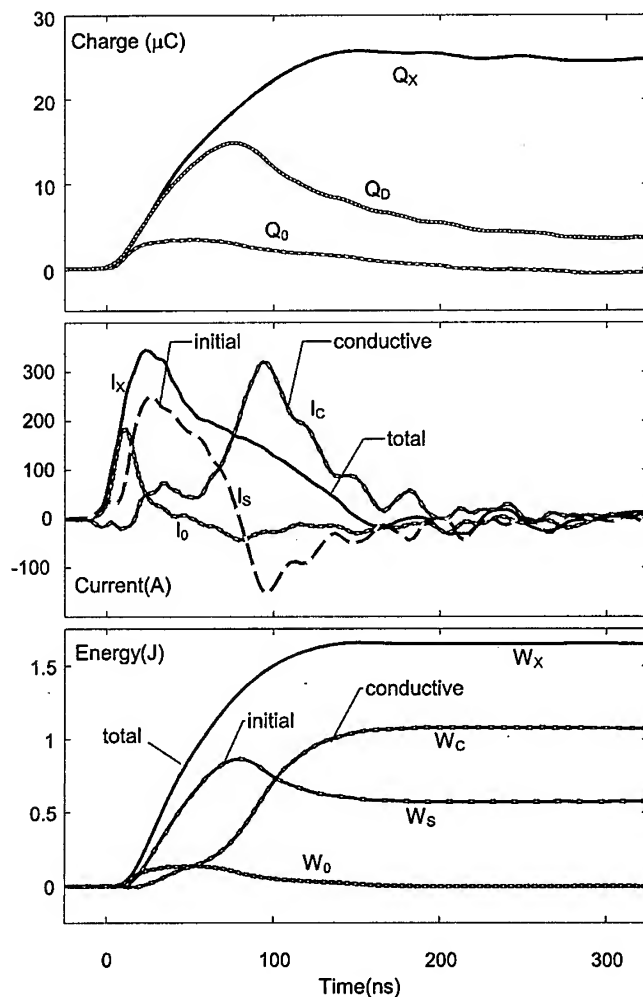


FIG. 12. Development of the components of charge, current and deposited energy during corona development. The pressure is atmospheric (air), the cylinder diameter is 25 cm and the pulse rise and width are 10 ns and 50 ns. The subscripts are as follows: X for total, externally seen, S for initial phase, C for conductive phase, O for vacuum capacitive contribution.

Finally we report the results of a comparison of efficiencies at equal voltage amplitudes as a function of polarity, type of wire and type of cylinder. We compared a smooth wire, a threaded wire (M8 thread), a smooth cylinder and a cylinder covered with needles. The three main energy conversion steps were considered. The results are summarized in Fig. 13. For a correct interpretation of the data we note that unavoidable slight variations occur in the efficiency between the separate experiments made to collect the data. Apart from this effect we may conclude from Fig. 13 that the considered electrode shapes only

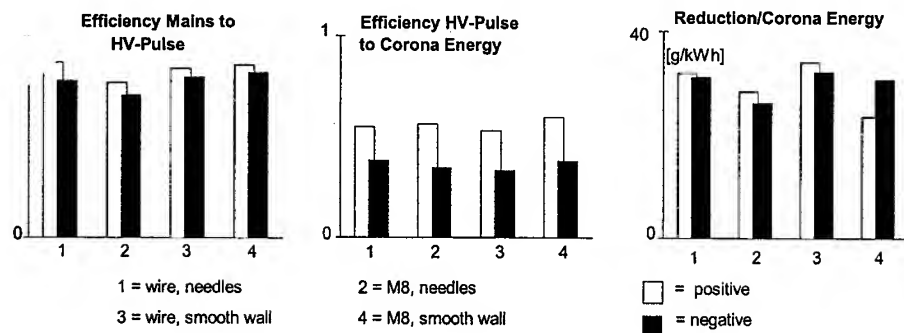


FIG. 13. Separate efficiencies of the three mains conversion steps as a function of electrode shape and polarity (equal pos. and neg. amplitudes). Atmospheric air with NO to be converted.

have minor effects. For the polarity however, we see an effect: the conversion of pulse energy into discharge energy is more effective in the case of a positive wire. This finding can be attributed to the higher inception voltage for highly active negative corona, shown in Fig. 10. By raising the pulse amplitude, the efficiency for a negative wire could be improved. Also important to note is that the NO conversion efficiency is not significantly affected by polarity.

9. Results of various applications

The pulsed corona process was applied in air flows to test the removal efficiency of various gaseous chemical pollutants. One or two pulse sources with maximum 1.5 kW corona power each were connected to one or two (in series) 3 m long corona reactors to process an air flow of 20 - 500 Nm³/h. The results are summarized in Table 1. Experimental procedures are described in [10].

Processes aimed at sterilization were performed in air and water flows. The experiments are described in [21]. The results can be summarized by giving the energy needed per liter of gas or water, to reduce the number of micro-organisms by one factor of ten (see table 2). It can be seen from this table that inactivation indeed occurs but that the energy cost almost scales as the mass density of the medium. The inactivation of spores still has to be improved considerably to make it a feasible technology.

The results also show that direct application of corona to liquids ('PCOR') is more effective than PEF treatment. However, PEF treatment is needed when one has to avoid the formation of radicals in the liquid. Many food products should not be injected with radicals. For ranges of applications the given efficiencies are still inadequate for commercialization. For the PEF method to become more practical the pulse form has to be adapted to the yet not well known requirements of cell inactivation. The high energy losses during PEF are only caused by considerable Ohmic dissipation in the liquid. Geometry and pulse shape need optimization. Similar optimizations are needed for the PCOR treatment but here we have more degrees of freedom: electron, radical and UV production may also

be optimized and higher local E-fields are possible since local discharge activity is a desired feature here.

Table 1. The measured efficiencies of corona processing

Substance	M [kg/kmol]	Concentration [ppm]	Mass flow [g/h]	Corona Power [kW]	Corona energy kWh/kg load to reach 63% removal	ΔE [J/liter]
NO	30	213	6.5 - 23	0.15 - 1.10	15	16.5
Toluene	92	125 - 450	18-40	0.13 - 1.16	24	98.8
Styrene	104	30 - 190	15-87	0.25 - 2.54	7	11.3
1,1,1 TCA	133	80 - 1000	4-25	0.13 - 1.13	180	135
Pentane	72	80 - 1000	6-73	0.14 - 1.04	88	185
Methane	16	450 - 500	35 - 37	2.1 - 2.7	-	5000
Ethylene	28	150 - 2500	17-114	0.18 - 1.23	12	41.2
Propane	44	10 - 500	1.7-36	0.16 - 1.15	180	
Butane	58	50 - 2000	9-111	0.14 - 1.19	75	

Table 2. Summary of efficiencies of various tested methods on inactivation of micro-organisms.

Medium	Treatment Type	Efficiency (kJ/L per log reduction)
Air	PCOR, wire-cylinder	0.002
Water	PCOR, needle - air bubbles	25
Water	PCOR, needle - N ₂ bubbles	32
Water	PEF, bacteria	85
Water	PEF, spores	500

Other applications that are becoming attractive are under investigation: odor removal, improved particle collection, fouling prevention/removal in flow systems, mussel control in cooling systems, and more. Our tests at a food processing plant show that odors can be removed at reasonable energy cost.

10. Conclusions

Highly active coronas with peak power densities of up to 25 MW per meter corona wire and energy densities of 2 kJ/l in the streamers can be produced by pulsed power. Since the voltage pulses are sufficiently short, breakdown does not occur even though the discharge currents are hundreds of Amperes. With a negative wire this high intensity occurs at a higher voltage than with a positive wire. A well matched pulsed power source can deposit up to 80% of its electrical energy into such a controlled discharge. Part of this energy is deposited during the

streamer growth but a considerable fraction can be released into the conductive streamer phase. Often, both energy contributions are useful in corona assisted processing. Reliable and efficient pulse sources are built using resonant charging, pulse transformers and pulse forming networks. Solid state switches are used in the low voltage sections and long-life spark gaps are needed for fast high-voltage switching. Alternative techniques for high voltage switching are fast solid state closing switches (combined with inductive storage [40, 41, 42, 43]), or the slower magnetic closing switches. The performance is characterized by: 100 kV, 150 ns wide, 1000 Hz and 400 hours of operation. The area of applications is growing: VOC and odor control, hot gas cleanup, water and air purification, sterilization, and fouling prevention. The efficiencies of the investigated processes (styrene and odor control and air sterilization) are promising.

Acknowledgements

This work is part of the European Joule program and the Dutch STW, Novem, EnergieNed and CPS research and funding programs. The partners Convex, ISET, Frigem, NIZO, Montair and WekTec are gratefully acknowledged for their valuable contributions.

References

1. P.P.M. BLOM, *High Power Pulsed Corona*, Ph.D. thesis, Eindhoven University of Technology, February 1997.
2. *Nonthermal Plasma Techniques for Pollution Control, Part B: Electron Beam and Electrical Discharge Processing*, Edited by Bernie M. Penetrante and Shirley E. Schultheis, NATO ASI Series, Springer-Verlag, Berlin Heidelberg, 1993.
3. L.A. ROSOCHA in *Plasma Science and the Environment*, Edited by Wallace Manheimer, Linda E. Sugiyama and Thomas H. Stix, AIP Press, Woodbury, NY, pp. 209-296, 1997.
4. *Managing Hazardous Waste with Electricity*, The American Chemical Society, Chemtech Magazine, Special Issue edited by Abraham P. Gelbein, Vol. 3, April 1996.
5. P. DE JONG and E.J.M. VAN HEESCH, Review: *Effects of Pulsed Electric Fields on the Quality of Food Products*, *Milchwissenschaft*, **53**, 1, 4-8, 1998.
6. K. SCHOENBACH, R.J. BARKER, *Nonthermal Medical/Biological Treatments with Pulsed Electric Fields*, 12th IEEE Int. Pulsed Power Conference, paper O17A, Monterey CA, 1999.
7. P.C.T. VAN DER LAAN, A.P.J. VAN DEURSEN, *Linear EMC-methods applied to power systems*, Proc. 10th Int. Symp. on High-Voltage Engineering, Montreal, Canada, Vol. I, pp. 59-66 Aug. 25-29, 1997.
8. B.M. PENETRANTE, et al., *Electron Beam and Pulsed Corona Processing of Volatile Organic Compounds in Gas Streams*, *Pure and Appl. Chem.*, **68**, 5, 1083-1087, 1996.
9. R.A. ROUSH, et al., *Effects of Pulse Risetime and Pulse Width on the Destruction of Toluene and NO_x in a coaxial Pulsed Corona Reactor*, Conference Record of the 22nd International Power Modulator Symposium, pp. 79-84, IEEE, 1996.
10. H.W.M. SMULDERS, S.V.B. VAN PAASEN, E.J.M. VAN HEESCH, *Pulsed Power Corona Discharges for Air Pollution Control*, IEEE Trans. on Plasma Science, Vol. 26, pp. 1476-1484, No. 5, October 1998.
11. K.P. FRANCKE, H. MIESSNER, D. RIEDEL, R. RUDOPH, *Plasma Assisted Catalytic Control of Stripper Gas Flow in Soil Groundwater Remediation* [in German], paper PQ13, BFPT-99, German Association for Plasma technology, Stuttgart, March 1999.

12. M. GROTHAUS, M.K.KHAIR, P. PAUL, E.R. FANICK, D.R. BANNON, *A Synergistic Approach for the Removal of NO_x and PM from Diesel Engine Exhaust*, 12th IEEE Int. Pulsed Power Conference, paper O17C, Monterey CA, 1999.
13. A.J.H. SALE, W.A. HAMILTON, *Biochim., Biophys. Acta*, **148**, 781-788, 1967.
14. P.M. VASSILEV and H.T. TIEN, in *Structure and properties of cell membranes*, Vol. III Methodology and properties of membranes (Ed. G. Benga), CRC press, Boca Raton, pp. 64-94, 1985.
15. T.Y. TSONG, *Biochem. Bio Eng.*, **24**, 271-295, 1990.
16. E. NEUMAN, in *Electroporation and electrofusion in cell biology*, (Eds. E. Neumann, A.E. Sower, C.A. Jordan), Plenum Press, New-York, pp. 61-73, 1989.
17. G.V. BARBOSA-CANOVAS, *Non-Thermal Preservation of Foods*, Marcel Dekker Publ., New York, 1998.
18. U. ZIMMERMAN, R. BENZ, *J. Membrane Biol.* **53**, 33-43, 1980.
19. K.H. SCHOENBACH, F.E. PETERKIN, R.W. ALDEN, S. BEEPE, *IEEE Trans. Plasma Science*, **25**, p 284, 1997.
20. E.J.M. VAN HEESCH, R.H.P. LEMMENS, B. FRANKEN, K.J. PTASINSKI, F.L.S. GEURTS, *Pulsed corona for breaking up air bubbles in water*, Proc. International Conf. on Dielectric Liquids, ICDL-93, Baden-Dätwill, 1993, and *IEEE Trans. On Dielectrics and Electrical Insulation*, Vol. 1, No. 3, June 1994, pp.426-431.
21. E.J.M. VAN HEESCH, A.J.M. PEMEN, A.H.J. HUIJBRECHTS, P.C.T. VAN DER LAAN, K.J. PTASINSKI, G.J. ZANSTRA and P. DE JONG, *A Fast Pulsed Power Source Applied to Treatment of Conducting Liquids*, Special Issue of IEEE Transactions on Plasma Science, 1999.
22. I. LISITSYN, I.V. LYSITSYN, H. NOMIYAMA, S. KASUKI, H. AKIYAMA, *Water Treatment By Pulsed Streamer Discharges*, 12th IEEE International Pulsed Power Conference, Paper O15E, Monterey CA, 1999.
23. P. DE JONG and E.J.M. VAN HEESCH, PEF Treatment System, Dutch patent, application No. 1009334, International patent pending, 1998.
24. E.J.M. VAN HEESCH, A.J.M. PEMEN, K. YAN, S.V.B. VAN PAASEN, K.J. PTASINSKI, Z. MATYAS, P.A.H.J. HUIJBRECHTS, B.J. HULTERMANS, P. ZACHARIAS, *Experimental Program of the Pulsed Corona Tar Cracker*, 12th IEEE International Pulsed Power Conference, Paper O17E, Monterey CA, 1999.
25. E.J.M. VAN HEESCH, A.J.M. PEMEN and P.C.T. VAN DER LAAN, *Pulsed Corona Existence up to 850° C*, Proceedings of 6th Int. Symp. On High-Voltage Eng., New Orleans, paper 42.23, 1989.
26. E.J.M. VAN HEESCH, A.J.M. PEMEN, S.V.B. VAN PAASEN, K.J. PTASINSKI, P. ZACHARIAS, *Hot Biogas Conditioning Using Pulsed Corona*, Hakone VI Int. Symposium on High Pressure Low temperature Plasma Chemistry, Cork, Ireland, pp. 21-25, 1998.
27. E.J.M. VAN HEESCH, K. YAN, A.J.M. PEMEN, P.A.H.J. HUIJBRECHTS, F.M. VAN GOMPEL, Z. MATYAS, K.P.M. GOMMERS, S.V.B. VAN PAASEN, H.E.M. VAN LEUKEN, P.C.T. VAN DER LAAN, *Matching between a Pulsed Power Source and Corona Reactor for Producing Non-Thermal Plasma*, 14th Int. Symp. on Plasma Chemistry, Praha, Czech Republic, 1999.
28. S.V.B. VAN PAASEN, et al., *Decomposition of VOCs in a Continuous High-Voltage Pulsed Corona Process*, Proceedings 10th Intern. Symp. on High-Voltage Eng., Montreal, Canada, Vol. 6, pp. 365-368, 1997.
29. A.J. KEET, P.C.T. VAN DER LAAN, *Analysis of the Inductance of Toroidal Magnetic Switches*, European Transactions on Electrical Power Engineering (ETEP), Vol. 5, No. 5, pp. 333-339, September/October 1995.
30. I.A.D. LEWIS and F.H. WELLS, *Millimicrosecond Pulse Techniques*, 2nd Ed., Pergamon Press, London, pp. 109-111 1959.
31. C.R. WILSON, G.A. ERICKSON, P.W. SMITH, *Compact, repetitive pulsed power generators based on transmission line transformers*, Proc. 7th IEEE Pulsed Power Conference, Monterey, 1989

32. E.J.M. VAN HEESCH, H.W.M. SMULDERS, R.H.P. LEMMENS, P.C.T. VAN DER LAAN, *System for treating gases or fluids with pulsed corona discharges*, Dutch patent, application No. 10001732, International patent pending, 1996.
33. M.A. VAN HOUTEN, *Electromagnetic Compatibility in High-Voltage Engineering*, Ph.D. thesis, Eindhoven University of Technology, October 1990.
34. S. SHIHAB, *A Fast Response Impulse Voltage Measuring System for Testing of Gas Insulated Substations Equipment*, IEEE Transactions on Power Delivery, Vol. PWRD-1, No. 3, pp. 42-47, 1986.
35. G.G. WOLZAK, *The Development of High-Voltage Measuring Techniques*, Ph.D. thesis, Eindhoven University of Technology, December, 1983.
36. E.J.M. VAN HEESCH, P.C.T. VAN DER LAAN, *State-of-the-Art Digital Oscilloscopes and High-Voltage Measurements*, 2nd European Conf. High-Voltage Measurements and Calibration, ERA Report 94-0776, Leatherhead UK, 1994.
37. R.T. WATERS, *Diagnostic Techniques for Discharges and Plasmas*, Electrical Breakdown and Discharges in Gases, NATO ASI Series, Plenum Press New York, 1983, Vol. B 89b, pp. 203-265.
38. O.J. TASSICKER, *Measurement of Corona Current Density at an Electrode Boundary*, Electronics Letters, 5, 13, 285-286, 1996.
39. E.J.M. VAN HEESCH, P.P.M. BLOM, P.C.T. VAN DER LAAN, *An E-Field and Ion Sensor for High Intensity Pulsed Coronas*, XXI International Conference on Phenomena in Ionized Gases, Bochum, Germany, September 19-24, pp. 329-330, 1993.
40. S.K. LYUBUTIN, G.A. MESYATS, S.N. RUKIN, B.G. SLOVICOVSKII, *Repetitive Nanosecond All-Solid-State Pulsers Based on SOS Diodes*, 11th IEEE Int. Pulsed Power Conference, Baltimore, 1997.
41. V.I. BRYLEVSKY, V.M. EFANOV, A.F. KARDO-SYSOEV, I.G. TCHASHNICOV, *Power Nanosecond Semiconductor Opening Plasma Switches*, 1996 International Power Modulator Symposium, IEEE, Boca Raton, 1996.
42. I.G. GREKHOV, *Physical Basis of High Power Semiconductor Nanosecond Opening Switches*, 12th IEEE Intl. Pulsed power Conference, paper PC010, Monterey, CA, 1999.
43. S. RUKIN et al, *SOS-Based Pulsed Power: Development and Applications*, 12th IEEE Int. Pulsed Power Conference, paper O2H, Monterey CA, 1999.

NONLINEAR PHENOMENA AND SELF-ORGANIZATION STRUCTURES IN PLASMAS

V. I. KARAS¹, V. A. BALAKIREV¹, YA. B. FAINBERG¹, I. V. KARAS¹, E. A. KORNILOV¹,
V. D. LEVCHENKO², YU. S. SIGOV², G. V. SOTNIKOV¹

¹NATIONAL SCIENCE CENTER "KHARKOV INSTITUTE OF PHYSICS AND TECHNOLOGY"

Kharkov, Ukraine

² KELDYSH INSTITUTE OF APPLIED MATHEMATICS, RAS

Moscow, Russia

In the examined system the plasma wave is synchronous with the beam. The plasma wave is parametrically coupled with the fast electromagnetic wave (EMW) propagating in the vacuum gap between the plasma boundary and the conductive jacket. The coupling is stimulated by the plasma density periodic inhomogeneity. The second part of this report presents the results of 2.5-dimensional numerical simulation of both the modulation of long relativistic electron bunch (REB) in a plasma and the excitation of wake fields by these bunches.

1. Parametric excitation of electromagnetic radiation by electron beam in layer plasma waveguide

1.1. Physical model and equations

Let's investigate the transformation of the plasma oscillations excited by an electron beam into EMR during the nonlinear interaction of HF plasma with LF ion-sound waves in the magnetized plasma waveguide. While exciting a regular ion-sound wave in the nonisothermal plasma ($T_e \gg T_i$, $T_{e,i}$ are the electron- and ion temperatures), one creates the plasma density periodic inhomogeneity (the diffraction grating) with the depth of modulation $\delta n_s/n_0 = e\varphi_s/T_e$ (δn_s is the plasma density distortion amplitude, n_0 is the plasma equilibrium density, φ_s is the electric potential amplitude of the ion-sound wave). Plasma density periodic modulation provides for parametric coupling between the plasma- and electromagnetic (EM) waves. In the plasma waveguide the necessary condition of the process realization is the coexistence of both the EMW and plasma wave at the same frequencies. In the waveguide filled with plasma this condition is partially realizable [1, 2]. In this waveguide the EMW can propagate at the frequencies $\omega \leq \omega_p$ between the plasma- and the outer conductive jacket boundary. The EMW propagates in the vacuum gap. In plasma this wave is skinning. On

the other hand, the plasma wave amplitude exponentially decreases when the wave is moving away from the plasma boundary in vacuum.

The parametric process in question is realizable if the conditions of time-spatial synchronism are fulfilled for the longitudinal wave numbers and for the frequencies of the interacting waves:

$$(1.1) \quad \omega_l = \omega_t + \omega_s, \quad k_l = k_t + k_s.$$

Here ω_s, k_s are the frequency and the longitudinal wave number of the ion-sound wave, and $\omega_{l,t}, k_{l,t}$ are the frequencies and the longitudinal wavenumbers of the plasma wave and EMW, correspondingly.

Acting on plasma, the HF feedback caused by the HF pressure amplifies the ion-sound wave (the plasma density modulation depth).

Let's consider a homogeneous plasma cylinder with the radius a . The plasma is placed into the co-axial jacket of ideal conductivity and the radius $d > a$. The system is situated in the intense magnetic field directed along the waveguide axis z . Along this axis a monoenergetic electron beam is propagating (its radius b ($b \ll a$)). There are three waves excited in the waveguide: the plasma wave amplified by the electron beam, the ion-sound wave, and the EMW propagating in the vacuum gap between plasma and the jacket conducting ideally. All these waves move in the same direction (along the axis z). Below we limit ourselves with examination of the stationary processes of the wave interaction.

As been already it has mentioned, the HF field feedback action on plasma amplifies the plasma density modulation depth. The following equation describes the process:

$$(1.2) \quad \frac{\partial^2 \delta n}{\partial t^2} - c_s^2 \Delta \delta n = \frac{1}{16\pi} \frac{\omega_{pe}^2}{\omega^2 m} \Delta |E_z|^2$$

where E_z is the HF field longitudinal component. The Eq.(2) yields the reduced equation of the ion-sound wave amplitude. The amplitudes of the interacting waves are described with the system of the reduced equations in the dimensionless variables:

$$(1.3) \quad \begin{aligned} \frac{dC_l}{d\xi} &= iWC_t C_s \exp(-i\Delta_v \xi) + \rho + i\Delta_b C_l, \\ \frac{dC_t}{d\xi} &= iWC_l C_s^* \exp(i\Delta_v \xi), \\ \frac{dC_s}{d\xi} &= iWC_l C_t^* \exp(i\Delta_v \xi). \end{aligned}$$

Here one designates: $C_{l,t} = a_{l,t}/A_{l,t}$ are the dimensionless amplitudes of the HF plasma- and EM waves, $C_s = s_s/A_s$ is the dimensionless amplitude of the LF ion-sound wave, $A_t = A_l \sqrt{R_l/R_t}$, $A_s = A_l \sqrt{\omega_s R_l / \omega R_s}$, $A_l = m\omega V_0 \theta^2 / e\gamma_0$, $\theta = \gamma_0 (I_b c^3 / 4I_A \omega^2 R_l)^{1/3}$, $I_A = mc^3 / e \approx 17$ kA,

$$R_{l,t} = \frac{\omega}{8} \frac{k_{l,t} a^2}{(K_{l,t})^2} J_0^2(\lambda_{l,t}) \left[\frac{\omega_p^2}{\omega^2} + \frac{4}{\pi^2 K_{l,t}^2 a^2 \Delta_0^2 (K_{l,t}, K_{l,t} \eta)} \right],$$

$\lambda_{l,y}/a$ are the transversal wave numbers of the plasma- and EM waves in plasma, $K_{l,t} = \lambda_{l,t}/\sqrt{-\varepsilon}$, $\eta = d/a$, $\Delta_\nu = (k_l - k_t - k_s)L$ is the difference between the wave numbers of the interacting waves, $\Delta_b = (k_l - k_b)L$ is the initial difference between the beam velocity and the wave phase velocity,

$$(1.4) \quad W = \frac{1}{8} \sqrt{\frac{\omega_s \omega}{R_s R_t}} \frac{\omega_p^2}{\omega^2} Q a^2 \frac{m V_0^2}{2 T_e} \theta,$$

$$(1.5) \quad Q = \int_0^1 J_0(\lambda_l x) J_0(\lambda_t x) x dx,$$

$$(1.6) \quad R_s = \frac{1}{8} \frac{\omega_{pi}^2}{c_s^2},$$

ω_{pi} is the ion plasma frequency and c_s is the sound velocity.

In the presented expressions it's supposed that $\omega_t = \omega_l = \omega$ and the difference between the frequencies of the HF EMW and plasma wave is not taken into account. Physical sense of the coefficients $R(\alpha)$ ($\alpha = t, l, s$) is clear. They represent the ratio of the energy flow of the corresponding wave to the amplitude squared:

$$(1.7) \quad S_\alpha = R_\alpha |a_\alpha|^2.$$

On the right-hand side of this expression of the plasma wave amplitude the second term describes the plasma wave amplification by the beam.

1.2. Approximation of the given modulation depth of plasma density

To start with, let's consider a simpler physical case in which the plasma density modulation depth is given $C_s = C_{s0}$. In particular, the plasma layering may be produced by modulation of the external magnetic field [3]. In this situation the system of two coupled equations of the plasma- and EM waves amplitudes describes the process of radiation excitation.

$$(1.8) \quad \begin{aligned} \frac{dC_l}{d\xi} &= i\Lambda C_t \exp(-i\Delta_v \xi) + \rho + i\Delta_b C_l, \\ \frac{dC_t}{d\xi} &= i\Lambda C_l \exp(i\Delta_v \xi) \end{aligned}$$

Here $\Lambda = W C_{s0}$.

In this system, as in the equations of the beam particle motion, the integral describing the law of conservation of the system energy is included:

$$(1.9) \quad S_t + S_l + P_b = \text{Const.}$$

The $S_{t,l}$ is the total energy flow of the plasma- and EM waves, P_b is the beam power.

Analyzing the system (8), one applies the method of the numerical simulation of the nonlinear equation system in order to investigate the nonlinear stage of excitation of the coupled plasma- and EM waves. Numerical analysis has been performed for different values of the wave coupling parameter Λ when the difference $\Delta_b = 0$ (i.e., the interacting waves are strictly synchronized ($\Delta_\nu = 0$)). The coupling parameter Λ is varying within the limits 0...1.05. If $\Lambda_{cr} = 1.05$, the instability derangement takes place. At the Fig. 1 the dependencies of the plasma- and EM wave dimensionless amplitudes on the longitudinal coordinate are plotted for $\Lambda_{cr} = 1.05$ (the Fig. 1a) and $\Lambda_{cr} = 1.00$ (the Fig. 1b). When $\Lambda_{cr} = 1.05$

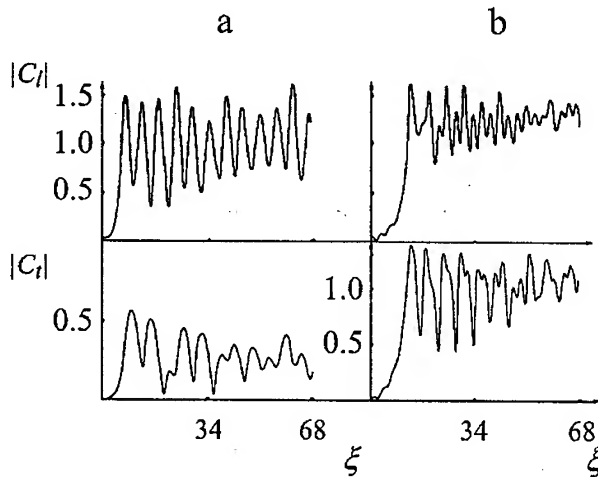


FIG. 1. Spatial amplitude dependence of the plasma $|C_i|$ and electromagnetic $|C_e|$ waves for different values of the Λ -parameter: a) $\Lambda = 1.05$, b) $\Lambda = 1.00$.

and the energy pumpover length essentially exceeds the amplification length, after exponential increase the amplitudes of the both waves amplitudes reach their maximums and then they start to oscillate. Oscillations of the plasma- and EM wave amplitudes are stipulated by the phase oscillations of the beam bunches trapped by this wave. The plasma- and the EM wave oscillations are opposite in phase. That is to say, the plasma wave amplitude maximum corresponds to the EMW amplitude minimum and v.v. Comparing the dimensionless amplitudes, one can see that the plasma wave amplitude is approximately in 3 times higher than that of the EMW. The EMW amplitude reaches its maximum at longer distances than the plasma wave. If $\Lambda_{cr} = 1.00$, the energy pumpover period is equal to the inverse increment. In this case the picture of the coupled wave excitation is different in its essence. At the initial stage the plasma- and EM waves amplitudes are increasing nonmonotonically. Then they get into their maximums located approximately at the same point. At the initial stage the amplitude oscillations are stimulated by energy pumpover from the plasma wave to the EMW and v.v. One should take into account that, in contrast to the wave amplitude, the electronic efficiency is increasing monotonely during this stage. The fact testifies to existence of the wave energy pumpover effect. At the first maximum the dimensionless wave amplitude values are the same approximately.

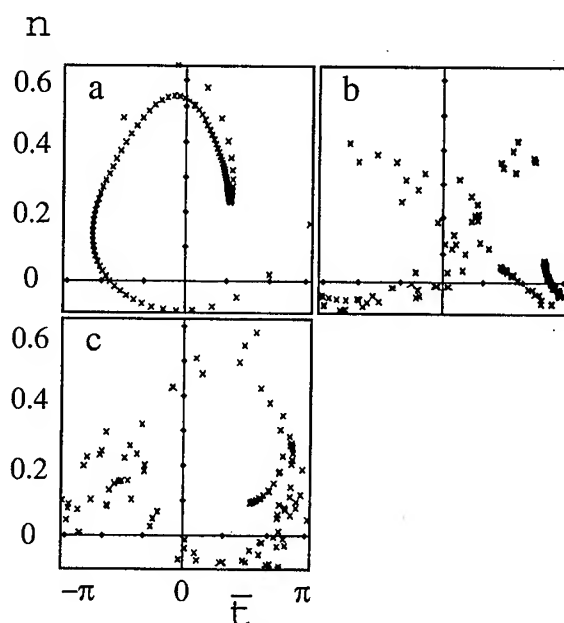


FIG. 2. The beam phase picture at the different points ξ : a)-120, b)-200, c)-280.

Behind the maximums the amplitudes oscillate irregularly. At the Fig. 2 the beam phase pictures are plotted for $\Lambda_{cr} = 1.00$. Here it is depicted that at large distances the bunch is being destroyed and the particles become greatly mixed on the phase plane. As a result, the amplitude oscillations are diminishing. At the Fig. 3 the dependences of the electronic efficiency and beam power relative

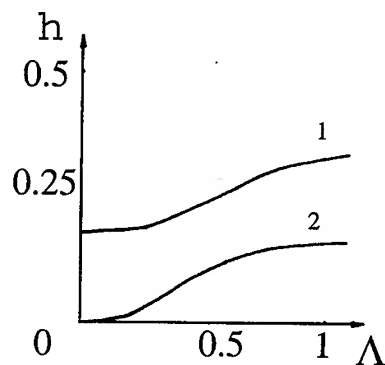


FIG. 3. Dependencies of the electronic efficiency (1) and relative losses of the beam power (2) on the parameter Λ .

losses by fast EMW excitation on the parameter Λ are given for $\theta = 0.2$. As it's evident, while the coupling parameter is increasing up to its critical value

Λ_{cr} , the maximum electronic efficiency is also increasing continuously. At the mentioned critical point the instability decays. In particular, when $\Lambda_{cr} = 1.00$, the efficiency is approximately equal to 32%. This is 1.8 times higher than in the absence of the wave coupling. A part of the beam power expended on EMR excitation increases with increase of the Λ . When $\Lambda_{cr} = 1.00$, approximately half of the total beam plasma losses is spent on radiation excitation and the plasma wave is excited by the other half of this power.

1.3. Analysis of the plasma wave decay to the EM- and ion-sound waves

Let's examine the system of the equations that take into account the influence of the HF plasma- and EM waves feedback on the LF ion-sound wave. In the absence of the electron beam the system (2) - (6) describes the decay instability of the plasma wave that produces the EM- and the ion-sound waves. This instability causes exponential increase both of the EM- and ion-sound waves. The corresponding dimensionless spatial increment is

$$(1.10) \quad \Gamma_d = W |C_{l0}|.$$

The decay instability increment is $\Gamma_d \approx W$ for the amplitude value $|C_{l0}| \approx 1$ determined by the beam particle trapped by the synchronous plasma wave field. If $W \geq 1$, the decay instability essentially influences the beam-plasma instability. Thus, the analysis demonstrates that HF plasma- and EM waves stimulate the ion-sound wave increase, i.e. they amplify the plasma density modulation depth.

The results of the numerical solutions of the systems (3) are presented in the [4], in which the plasma decay process is investigated. While the electron beam is being continuously injected into infinite homogeneous plasma, the decay of the plasma wave produces the plasma- and ion-sound waves. Numerical analysis demonstrates that the plasma wave transformation into EMW essentially influences the plasma-beam instability dynamics when $W^2 > 0.1$.

Energy interchange between the plasma- and EM waves modulates the wave amplitudes with the spatial period $\xi_{mod} (\xi_{mod} \sim W^{-2})$. The decay process stimulates the efficiency of the power pumpover from the beam. If $0.1 < W^2 < 2$, the beam power losses keep on increasing. At the maximum they are in 2 times higher than in the case of $W = 0$, in which the HF plasma wave is not transformed into EMR. When $W^2 > 2$, periodic modulation of the HF plasma wave parameters causes development of the stochastic instability [5]. This instability originates in phase mixing of resonance particles. The length of the effective energy interchange of the HF plasma wave with EMW decreases with the growth of the wave nonlinear interaction parameter W . For example, if $W = 1$, the EMW amplitude reaches its maximum when $\xi = 15$.

So, it is demonstrated that the nonlinear interaction between the plasma-, ion-sound- and EM waves essentially stimulates the increase in effectiveness of the beam energy transformation into the microwave radiation energy.

2. 2.5-Dimensional numerical simulation of relativistic electron bunch self-modulation in a plasma

2.1. Physical model and equations

The charged particle acceleration by charge density waves in a plasma and in uncompensated charged beams appears to be a most promising trend in the collective methods of acceleration [6, 7, 8]. The variable part of the charge density can be made to be very high (up to n_0 , where n_0 is the unperturbed plasma density); therefore, the accelerating fields can reach 10^7 to 10^9 V/cm. Chen et al. [9] have proposed a modification of the Fainberg acceleration method [6], consisting in using a train of bunches. In [10], Katsouleas has considered electron bunches with different profiles, namely, a bunch with a slow build-up in the density and its very quick fall-off, and also the bunch with of Gaussian-type distribution for different rise and fall-off times. It was established in [10] that the use of these nonsymmetric bunches instead of symmetric ones can provide the accelerating field E_{ac} value to be many times (10 to 20) higher than the retarding field E_{st} value. The so-called transformation coefficient $T = E_{ac}/E_{st} = \Delta\gamma_{ac}\gamma_b^{-1}$ is equal to $2\pi N$, where N corresponds to the number of wavelengths along the bunch length. The excitation of nonlinear stationary waves in the plasma by a periodic train of electron bunches has been studied in refs. [11, 12], where it is shown that the electric field of the wave in the plasma increases with γ (γ is the relativistic factor of the beam) at commensurable plasma and beam densities. The experiments undertaken in refs. [12, 13] on wake-field acceleration have demonstrated the importance of three-dimensional effects.

Here, we consider two different regimes with high amplitudes of plasma wake fields that are employed in the accelerator physics. The first regime makes use of an extended short beam, then the high-amplitude waves excited by this beam and having high-gradient longitudinal electric fields can be used to accelerate other bunches. In the second case, a strong focusing can be attained with a long narrow beam, making use of its intrinsic magnetic field which is unbalanced because of space charge compensation by the plasma.

Apart from the transverse forces, the bunch particles are also influenced by powerful longitudinal forces on the side of electric wake fields. The longitudinal fields will give rise to a longitudinal modulation of the electron bunch, i.e., to a splitting of an originally uniform bunch into microbunches with a modulation period $\lambda_p = 2\pi c/\omega_p = 3.36 \cdot 10^6 n_0^{-1/2}$ cm. In particular, in the plasma with a particle density of 10^{16} cm $^{-3}$ the modulation period is 0.3 mm. The effect of longitudinal REB modulation by wake fields can be used for developing plasma modulators of dense electron beams. It is pertinent to note one more feature of this phenomenon. Since the modulation frequency is coincident with the plasma frequency, the wake fields of microbunches are then combined coherently. Therefore, the electron bunch modulation will involve an increase in the amplitude of the wake field behind the bunch. This effect opens up a possibility of using long-pulse electron bunches to excite intense wake fields in a plasma. It is particularly remarkable that the effect of longitudinal modulation at a plasma frequency takes place for a long laser pulse, too [14].

Previously in [15], a theoretical study has been made into the process of modulation of long electron bunches in a plasma by longitudinal wake fields. Results were reported there for one-dimensional numerical simulation of nonlinear dynamics of bunch modulation. It was demonstrated in ref. [15] that the particle modulation of a long bunch moving in the plasma causes an increase in the wake wave amplitude. This effect is accounted for by coherent combining of fields excited by microbunches, into which the bunch is split in the course of modulation. The bunch is modulated at a plasma frequency. The investigation of the one-dimensional approximation is justified in the case of great transverse dimensions ($2\pi r_b/\lambda_p \gg 1$).

The present report deals with the 2.5-dimensional numerical simulation of wake fields by long REB.

The excitation of wake fields is investigated with an aid of the 2D3V axially symmetric version of the SUR code being, in turn, a further development of the COMPASS code [16]. Earlier, this code was used to simulate the induction accelerator [17], the modulated relativistic electron beam [18], and a single REB or a train of these bunches in a plasma [16, 18, 19, 20, 21].

The dynamic of REB is described by the relativistic Belyaev-Budker equations for the distribution functions $f_\alpha(\vec{r}, \vec{p})$ of the plasma particles of each species and by the Maxwell equations for the self-consistent electric E and magnetic B fields. We assume that, initially, a cold two-component back-ground plasma ($m_i/m_e = 1840$, where m_i and m_e are the ion and electron masses) fills the entire region $[0, L] \times [0, R]$, where $L = 100$ cm and $R = 10$ cm.

The scale on which the electric and magnetic fields vary is $m_e c \omega_p / e$. We assume that the plasma and bunch particles escape from the computation region through the $z = 0$ and $z = Z$ boundary surfaces and are elastically reflected from the $r = R$ surface. We also assume that cold background electrons and ions can return to the computation region from the buffer zones $z < 0$ and $z > Z$. The boundary conditions for the fields corresponds to the metal wall at the cylindrical surface $r = R$ and free emission of electromagnetic waves from the right and left plasma boundaries. The weight of the model particles was a function of the radial coordinate, and the total number of these particles was about 10^6 . All the calculations were carried out on a Pentium-133 personal computer with the use of the modified particle-in-cell simulation algorithm.

In order to analyze the dependence of the amplitude of the excited fields on the number of bunches injected into plasma we carried out a series of calculations.

2.2. Results and discussion

Figures 4 to 6 show spatial distributions of the longitudinal electric field E , electric charge density of electrons, longitudinal current density of electrons, respectively, for the instant of time $t = 60\omega_p^{-1}$ (a) and $t = 100\omega_p^{-1}$ (b).

It is seen from Fig. 4 that the longitudinal electric field rapidly grows reaching $0.8m_e c \omega_p / e$. Note that the original beam particle density was only 1.8% of the plasma electron density. The radial electric field E_r also grows, but it reaches a somewhat lower value $0.4m_e c \omega_p / e$. It is significant that: (i) the finite length of the initial bunch is responsible for the formation of the growing electric field;

(ii) the electric field has a rather high amplitude near the axis, this being due to microbunch pinching; (iii) the evolution of the instability, giving rise to microbunches, leads to some decrease in the phase velocity of the perturbed wake wave.

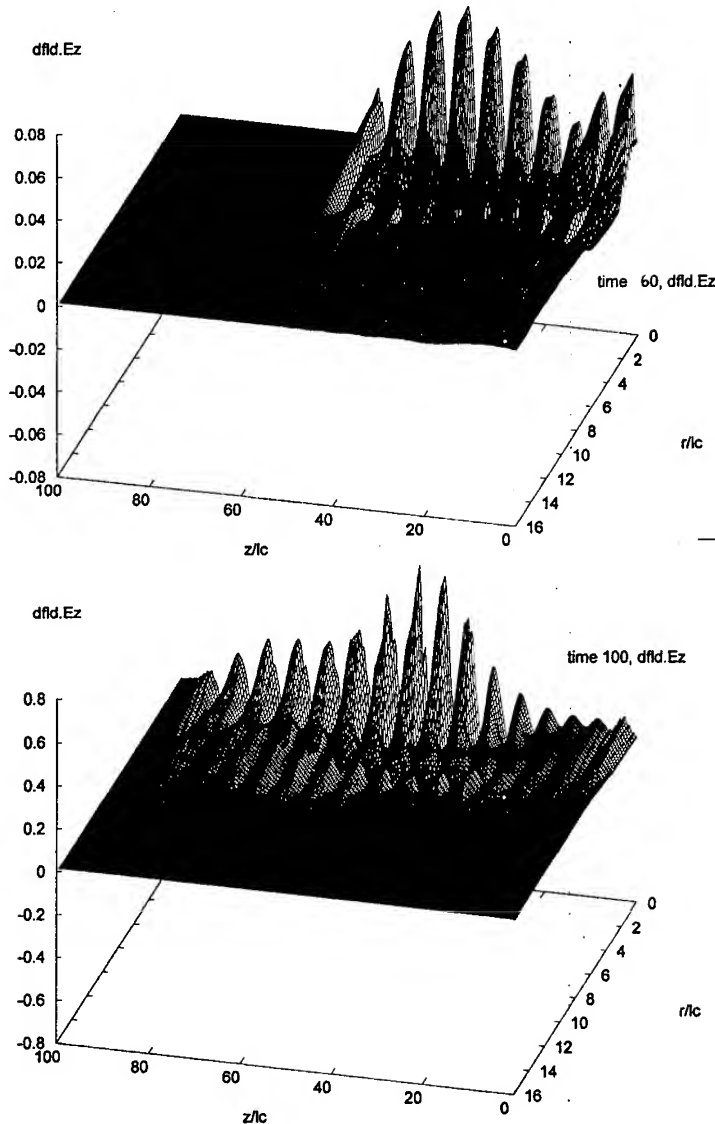


FIG. 4. Axial electric field E_z versus the axial z -coordinate and the radial r -coordinate.

From Fig. 5 it is seen that the electric charge density distributions of plasma electrons $el.Q$ are similar to the spatial distributions of the longitudinal electric field E_z . The highest density value is attained for the 8th microbunch and is $4.5n_0$. It is of importance to note that the maximum of the beam particle charge

density corresponds to the 5th microbunch rather than to the 8th microbunch and is equal to $1.6n_0$, this being two orders of magnitude higher than the initial beam particle density value in the long bunch.

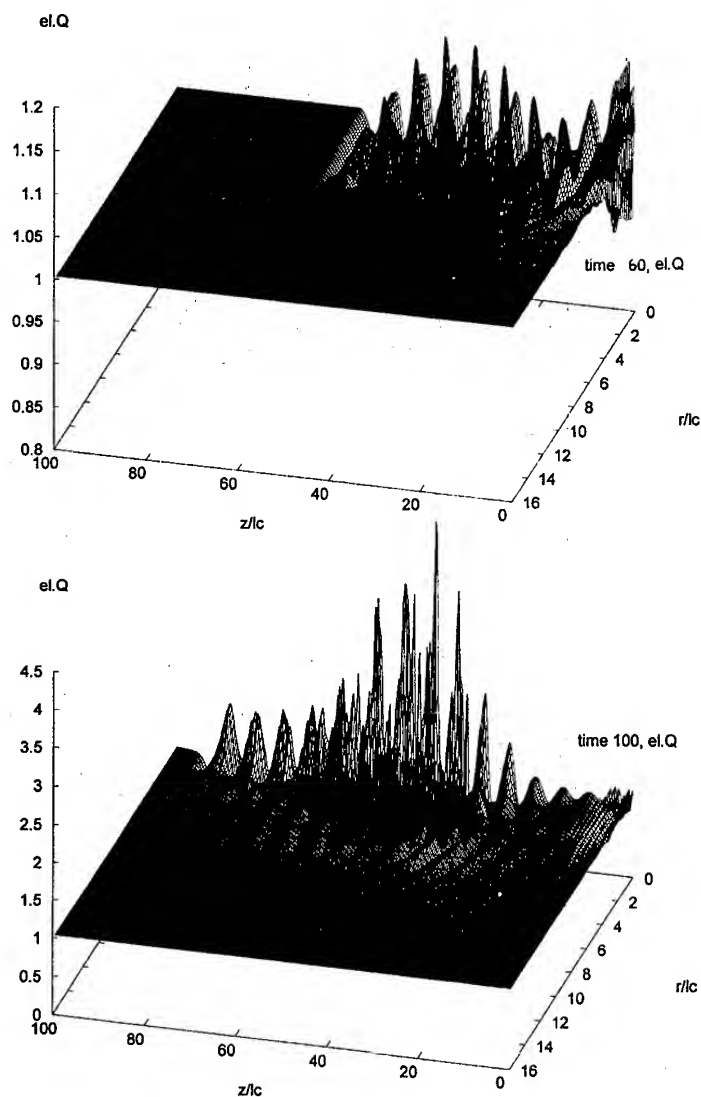


FIG. 5. Plasma electron density versus the radial r -coordinate and the axial z -coordinate.

The spatial distribution of the longitudinal current density of plasma electrons $el.J_{hz}$ (Fig. 6) also correlates rigidly with the longitudinal electric field E_z distribution. Here attention must be given to the peak current value for the 8th microbunch, which is two orders of magnitude higher than the initial longitudinal current value of REB particles.

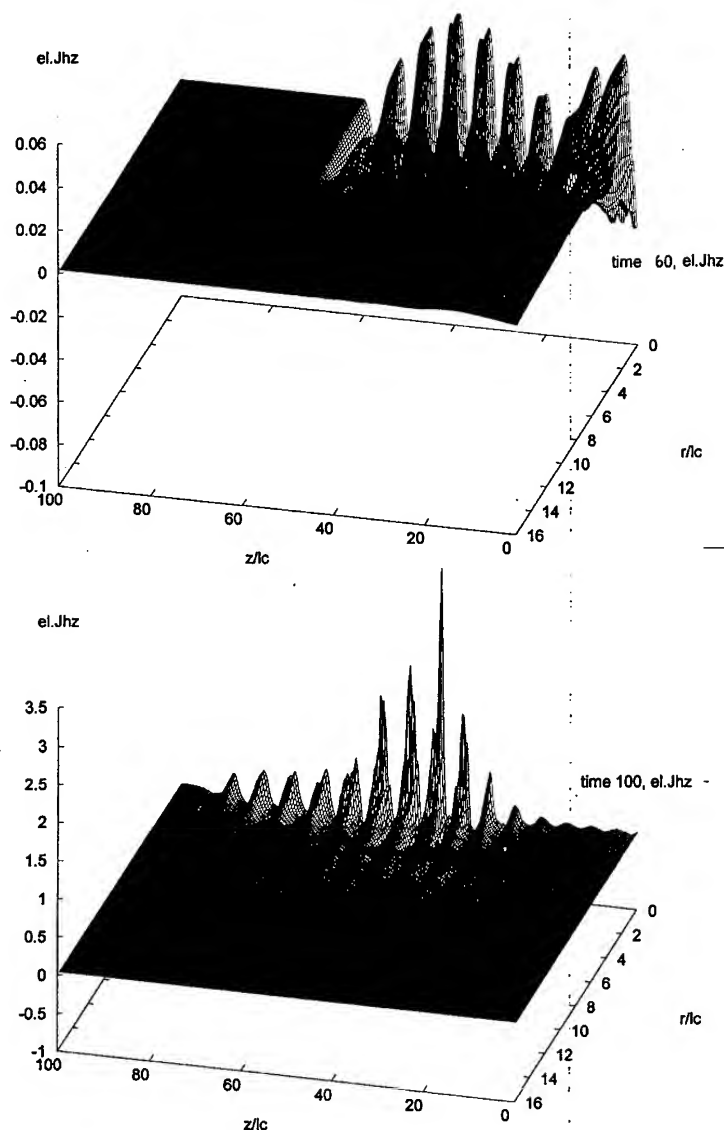


FIG. 6. Spatial distribution of the longitudinal current density of plasma electrons.

The present results show that the nonlinear picture in the plasma-REB system drastically differs from both the initial picture corresponding to the rigid REB and the one by the scenario following from the one-dimensional numerical modulation (cf. [15]). This supports in full measure the conclusion given in ref. [12] about the necessity of taking into complete account the three-dimensional effects and the nonlinear behavior of both the plasma and the bunch.

3. Conclusions

In this work the process of EMR excitation by an electron beam is also investigated in the case of the plasma waveguides where the plasma density varies along the system according to the periodic (harmonic) law. In the examined system the plasma wave is synchronous with the beam. The plasma wave is parametrically coupled with the fast EMW propagating in the vacuum gap between the plasma boundary and the conductive jacket. The coupling is stimulated by the plasma density periodic inhomogeneity.

It is demonstrated that in this system the process of the plasma wave parametric transformation into EMR stimulates the increase of efficiency of the power pumpover from the electron beam.

Plasma density periodic inhomogeneity may be realized by excitation of the short ion-sound wave in plasma. In this case the ponderomotive force of HF pressure creates the feedback of the plasma- and EM waves, which causes the increase of the ion-sound wave (the plasma density modulation depth amplification) and, correspondingly, diminution of the length of the plasma wave energy transformation into radiation.

The spatial density distributions of REB and plasma electrons obtained for the instances of time $t = 60\omega_p^{-1}$ and $t = 100\omega_p^{-1}$ show that the density ratio n_b/n_0 (the initial value being 0.018) reaches 0.04 as early as at $t = 60\omega_p^{-1}$. At $t = 100\omega_p^{-1}$, the highest beam particle density becomes commensurable with the plasma density, i.e., a very strong modulation of beam particle density is observed.

The spatial distributions of the longitudinal E_z and transverse E_r electric fields show that the E_z and E_r amplitudes grow owing to the enhancement in the density modulation. At $t = 100\omega_p^{-1}$ the highest longitudinal-field amplitude reaches $0.8m_e c\omega_p/e$, and the highest transverse-field amplitude is equal to $0.4m_e c\omega_p/e$. It is essential that the amplitude growth occurs only within a moderate REB length. Therefore, there is little point in using the REB of the length greater than that corresponding to the highest longitudinal-field amplitude, otherwise no increase in the excited wake field will be attained.

The undertaken numerical experiments have demonstrated that the nonlinear dynamics of the particles of plasma components and bunches results in the following effects: (i) the transverse dimension of bunches varies within a very wide range; (ii) close to the axis of the system an ion channel is formed, which is a contributory factor for the stabilization of bunch propagation and the growth of bunch-generated fields; (iii) an essential increase in the amplitudes of excited electric fields takes place in the case of a long bunch as a result of its self-modulation. However, bunches of optimum length should be used, since any excess of the optimum length of the bunch fails to provide, even at self-modulation, the growth in the amplitudes of excited electric fields.

References

1. A.K. BEREZIN et al., *Numerical Analysis of Dispersive Properties of Plasma Cylindrical Waveguides Placed into Magnetic Field*, Preprint KhPhTI 86-25, Moscow: CNI Atominform, 1986.

2. M.V. KUZELEV et al., *Spectra of Proper Oscillations of Co-Axial Plasma Waveguide in Finite Magnetic Field*, Preprint 23. Moscow: IOFAN, 1991.
3. P.I. MARKOV, I.N.ONISHCHENKO et al., *Electrodynamics of Corrugated Plasma Waveguide*, Plasma Phys., **19**, 1, 14-19, 1993.
4. N.G. MATSIBORKO, I.N.ONISHCHENKO et al., *Decay Instability of Plasma and Ion-Sound Oscillations during Stationary Injection of electron Beam into Plasma*, Plasma Phys., **1**, 5, 765-771, 1975.
5. G.M. ZASLAVSKY, *Stochasticity of Dynamic Systems*, Moscow: Nauka, 1984.
6. YA.B. FAINBERG, Proc. Symp. CERN, Geneva, **1**, 1, 84, 1956.
7. YA.B. FAINBERG, Sov. J. Plasma Physics, **13**, 350, 1987.
8. YA.B. FAINBERG, Plasma Physics Reports, **20**, 549, 1994.
9. P. CHEN, J.M. DAWSON, R.W. HUFF and T. KATSIOULEAS Phys. Rev. Lett., **54**, 693, 1985.
10. T. KATSIOULEAS, Phys. Rev. A, **33**, 2056, 1986.
11. A.TS. AMATUNI et al., Sov. J. Plasma Physics, **11**, 417, 1985.
12. J. ROSENZWEIG, FERMILAB Conf. 90/40, FNAL, Batavia, Illinois, 1990.
13. J. ROSENZWEIG et al., Phys. Rev. A, **44**, 6189, 1991.
14. C. JOSHI et al., IEEE J. Quant. Electr. 1987. QE-23, No 23, 1987, p. 1571.
15. V.A. BALAKIREV et al., Fizika Plazmy, **22**, 2, 165, 1996.
16. O. BATISHCHEV, V. KARAS', V. LEVCHENKO, and Yu. SIGOV, Plasma Physics Reports, **20**, 587, 1994.
17. V. KARAS', O. BATISHCHEV, Yu. SIGOV, and Ya. FAINBERG, Particle Accelerators, **281**, 37-38, 1992.
18. O. BATISHCHEV, Yu. SIGOV et al., Sov. J. Plasma Physics, **19**, 738, 1993.
19. O. BATISHCHEV, V. KARAS', Yu. SIGOV, and Ya. FAINBERG, Plasma Physics Reports, **20**, 583, 1994.
20. V. KARAS', Yu. SIGOV, Ya. FAINBERG, et al., Plasma Physics Reports, **23**, 285, 1997.
21. V. KARAS', V. BALAKIREV, G. SOTNIKOV, Yu. SIGOV, Ya. FAINBERG, V. LEVCHENKO, Proc. of 1997 Particle Accelerator Conference, Vancouver, Canada, May, 1997.

TAMING INSTABILITIES IN PLASMA DISCHARGES

T. KLINGER¹, N. O. KRAHNSTÖVER², T. MAUSBACH², A. PIEL²

¹INSTITUT FÜR PHYSIK DER ERNST-MORITZ-ARNDT UNIVERSITÄT ZU GREIFSWALD

Domstraße 10a, D-17489 Greifswald, Germany

²INSTITUT FÜR EXPERIMENTELLE UND ANGEWANDTE PHYSIK DER

CHRISTIAN-ALBRECHTS UNIVERSITÄT ZU KIEL

Olshausenstraße 40-60, D-24098 Kiel, Germany

Recent experimental work on taming instabilities in plasma discharges is discussed. Instead of suppressing instabilities, it is desired to achieve control over their dynamics, done by perturbing appropriately the current flow in the external circuit of the discharge. Different discrete and continuous feedback as well as open-loop control schemes are applied. Chaotic oscillations in plasma diodes are controlled using the OGY discrete feedback scheme [Ott *et al.*, Phys. Rev. Lett., **64**, 1196 (1990)]. This is demonstrated both in experiment and computer simulation. Weakly developed ionization wave turbulence is tamed by continuous feedback control. Open-loop control of stochastic fluctuations - stochastic resonance - is demonstrated in a thermionic plasma diode.

1. Introduction

Waves and instabilities in plasmas have been the subject of intense research for more than thirty years. The mathematical treatment of the problem is enormously simplified by making two assumptions: (i) the plasma is of infinite extent and (ii) perturbations due to instability are small, thus allowing for linearization. The reality of laboratory plasmas, however, demands for a better understanding of the *nonlinear* dynamics of instabilities in *bounded* plasmas. Nonlinearity combined with dissipation (as introduced by boundaries) can lead to chaotic behavior of oscillations and waves, the latter also known as weakly developed turbulence [1]. During the last two decades great progress was made in the understanding of the general principles of nonlinear dynamics. New applications of control theory were suggested by taking advantage of the stability analysis in the dynamical phase space [2]. It is the goal of the present paper to discuss our recent experiments and computer simulations, dealing with the active control of the nonlinear dynamics of instabilities in bounded plasma devices. We focus our attention on two distinct plasma problems, the stability of the current flow

in collisionless plasma diodes and ionization instabilities in collisional glow discharge plasmas. It is emphasized that the present approach differs conceptually from previous work on feedback control of plasmas [3].

The paper is structured as follows: In the next section we briefly outline the basic concepts of different control schemes. In Sec. 3 we discuss computer simulations and experiments on chaos control in collisionless plasma diodes. Sec. 4 is devoted to the control of weak ionization wave turbulence. The problem of taming stochastic behavior is addressed in Sec. 5, where the stochastic resonance phenomenon is demonstrated in a plasma diode. Conclusions are drawn in the final Sec. 6.

2. General overview of control of dynamical systems

2.1. Suppression and control of chaos

In many practical situations, it is of general interest to achieve control over the dynamics of a physical system. The most simple way to accomplish this task is to find a suitable control parameter and simply to select the desired state. However, this may be costly or even impossible if the access to the control parameter is limited by additional constraints. It is thus more promising to modify the dynamical system by introducing an additional degree of freedom that can be adjusted from exterior. This additional degree of freedom is typically a perturbation of either the control parameter or a suitable system input and it is the task of control theory to provide the optimal control signal.

Clearly a challenge is the control of the *chaotic* dynamics of a physical system. This problem is known as 'control of chaos' and a comprehensive overview over this rapidly growing field is given in the book edited by Schuster [2]. Subsequently we give a brief review of the most common chaos control strategies.

Schematic diagrams of four standard general control schemes are depicted in Fig. 1. It is distinguished between open-loop and closed-loop control [4]. We focus here on the control of chaos, i.e., the initial dynamics is irregular and it is desired to achieve a regular (more explicitly: a periodic) state. Open-loop control of chaos, Fig. 1(a), is usually done by weak, resonant harmonic perturbations [6, 7]. The control signal is pre-determined rather than obtained from the dynamics of the system. It is applied either to an accessible parameter or is simply superimposed on the input. Schematic diagrams of different closed-loop chaos control strategies are shown in Fig. 1(b-d). Classical feedback attempts to achieve a stationary state by perturbing the system by empirical feedback signals that are usually obtained by filtering, phase shift, and amplification [4]. The idea of chaos control, however, is more subtle. The goal of those strategies is to stabilize the unstable periodic orbits (UPOs) that are embedded within a chaotic attractor [8]. The main difference to classical feedback control is that the UPOs are not deformed, i.e., the controlled (regular) state is part of the uncontrolled dynamics. The most common feedback control schemes are the Ott-Grebogi-Yorke (OGY) method [9, 10] and the time-delayed autosynchronization (TDAS) method [11, 12]. The OGY scheme, Fig. 1(c), is in principle a standard linear parametric discrete feedback control method, but acting directly in the dynamical

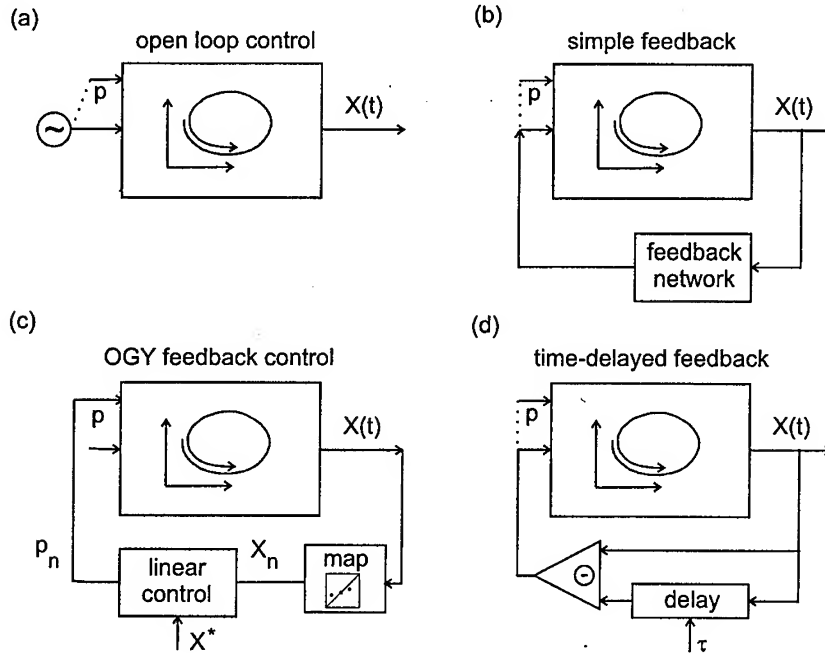


FIG. 1. Schematic diagrams of the four most important control schemes. (a) Resonant open loop control resp. taming, (b) classical closed-loop feedback control, (c) Ott-Grebogi-Yorke discrete feedback control, and (d) time-delayed autosynchronisation. From [5].

cal phase space. Though based on discrete time systems, it can be applied in the continuous-time case by considering the time-discrete system obtained from the induced dynamics in the Poincaré section. The OGY technique was seminal to the field and has an instructive geometrical interpretation, see Ref. [13]. In the TDAS scheme, the feedback signal is continuously generated by time delay of the signal to be controlled. This makes the analysis of the control process being a more difficult task and many results on TDAS control are hinged on numerical and semi-empirical methods [14]. Recently the stability analysis of TDAS, using Floquet theory, has shown that control is achieved only if the phase space orbits make an appropriate turn during their evolution [15].

2.2. Stochastic resonance

After briefly discussing how to control deterministic chaos, we may now turn our attention to the prospects of control of stochastic motion, where the reasoning in a low-dimensional phase space is generally inappropriate. At first glance it seems to be hopeless to tame a stochastic process. However, under certain conditions, external perturbations can influence stochastic behavior in a well-controlled way.

One such effect is known as 'stochastic resonance'. Stochastic resonance (SR) is a phenomenon in which the response of a nonlinear dynamical system to weak periodic input signals is optimized by the presence of a particular level of noise

[16, 17]. It is important to realize that SR does not achieve control in its very sense but introduces a certain coherence into a stochastic system. It is hence reasonable to consider it as a particular type of open-loop control scheme that does not rely on the presence of UPO, on low-dimensional dynamics, but on multistability and the presence of noise.

The basic SR mechanism can be explained in simple terms. Consider a symmetric bistable double-well system described by the potential

$$(2.1) \quad V(x) = \epsilon x - \alpha x^2 + \beta x^4 \quad (\alpha > 0, \beta > 0).$$

The graph of (2.1) is shown in Fig. 2 for (a) $\epsilon = 0$, (b) $\epsilon > 0$, and (c) $\epsilon < 0$. For $\epsilon = 0$ we obtain a symmetric double-well potential with two stable equilibrium points at $\pm c = \pm\sqrt{2\alpha/\beta}$. The black ball represents one of these

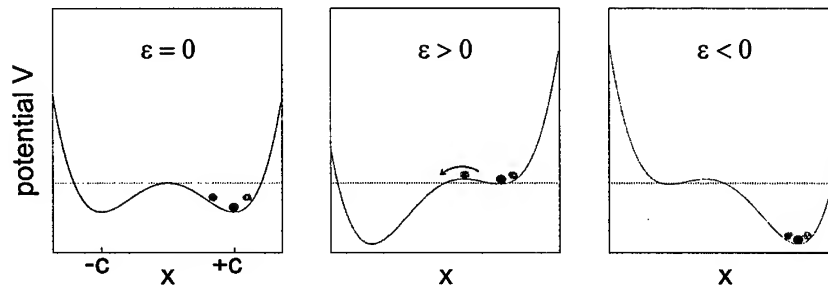


FIG. 2. Basic mechanism of stochastic resonance. The deformation of the double-well potential determines the stability of the equilibrium points.

equilibrium states and the two gray balls small deviations. If the double-well potential is perturbed by a negative force ($\epsilon > 0$) a deviation from the one equilibrium point $+c$ eventually leads to a spontaneous transition to the other at $-c$, i.e., the equilibrium point at $+c$ suffers a loss of stability. The perturbation by a positive force ($\epsilon < 0$) makes the equilibrium point at $+c$ being more stable. The parameter ϵ is now replaced by $A \cos \omega_i t + \sqrt{2\sigma} \xi(t)$, where $\xi(t)$ represents Gaussian distributed white noise of variance σ . The described changes of the stability become dynamic and the double-well is sinusoidally modulated while stochastically induced transitions between the equilibrium points occur. Due to the modulation, transitions become much more probable at fixed phase of the modulation signal. This makes the previously stochastic motion (in the unperturbed case) being more regular.

Generally speaking, SR is the cooperative effect between the noise and the weak signal that introduces to a certain degree 'coherence' in the system. As a consequence the dynamics becomes - on the average - periodic instead of fully stochastic. This is most clearly observed in the power spectrum by a sharp peak at ω_i appearing on the broad background noise.

3. Taming chaotically oscillating plasma diodes

Among the broad class of collisionless bounded plasmas, diode-like configurations play a highly important role [18]. A plasma diode is characterized by an emitter and a collector electrode, where charged particles are injected and absorbed, respectively. Many of the common plasma discharge configurations are in fact diodes, especially discharges operating with direct current (dc). In this section we show by experiment and computer simulation the control of chaos in plasma diodes.

3.1. The Pierce-diode

Of fundamental importance for basic studies of bounded plasmas is the Pierce-diode [19], an idealized one-dimensional model of a collisionless plasma diode. We note, however, that the Pierce-diode has no straightforward experimental correspondent though relationships between generalized Pierce-diodes and experimental thermionic diodes (see below) have been discovered [20, 21].

The Pierce-diode configuration consists of a beam of cold electrons that is injected at the emitter and, after transit, absorbed at the collector. The two electrodes are short-circuited and grounded. Ions are assumed to be immobile and form a homogeneous, neutralizing background charge. The classical result of linear theory is that the stability of the Pierce-diode is solely determined by the dimensionless Pierce-parameter [19]

$$(3.1) \quad \alpha = \frac{\omega_{pe} L}{v_0},$$

where $\omega_{pe} = \sqrt{n_0 e^2 / \epsilon_0 m_e}$ is the electron plasma frequency taken at the emitter. The Pierce-parameter represents the transit time L/v_0 in units of the phase of a plasma oscillation cycle (L is the distance between the electrodes). Above $\alpha = \pi$ the Pierce-instability (the bounded-plasma variant of the two-stream instability) leads to the transition from uniform to non-uniform equilibrium by a transcritical bifurcation.

With regard to chaotic dynamics, the most important phenomenon is the presence of a small stability window just below $\alpha = 3\pi$. At $\alpha \approx 2.9\pi$, a Hopf-bifurcation occurs and a stable limit cycle is born. It was discovered by Godfrey [22] that the establishment of periodic potential oscillations gives rise to low-dimensional chaos. The initial work on chaotic dynamics in the Pierce-diode [22, 23] was based on the numerical solution of integral equations derived from the set of fluid equations. The subsequently discussed results have been obtained by particle-in-cell (PIC) simulation using the Berkeley XPDP1-code [24].

In agreement with the previous fluid-simulations of Godfrey [22] and Lawson [23], the PIC-simulation of the Pierce-diode reveals in the parameter regime $\alpha \in [2.865\pi, 2.85\pi]$ a period doubling cascade to low-dimensional chaos [26, 25]. Prior to the cascade, single periodic oscillations of the plasma potential are established by a Hopf-bifurcation at $\alpha = 2.87\pi$. Fig. 3 shows the two-dimensional attractor reconstructions $\{\phi_{L/8}(t), \phi_{L/2}(t)\}$, where $\phi_{L/8}(t) = \phi_p(L/8, t)$ and

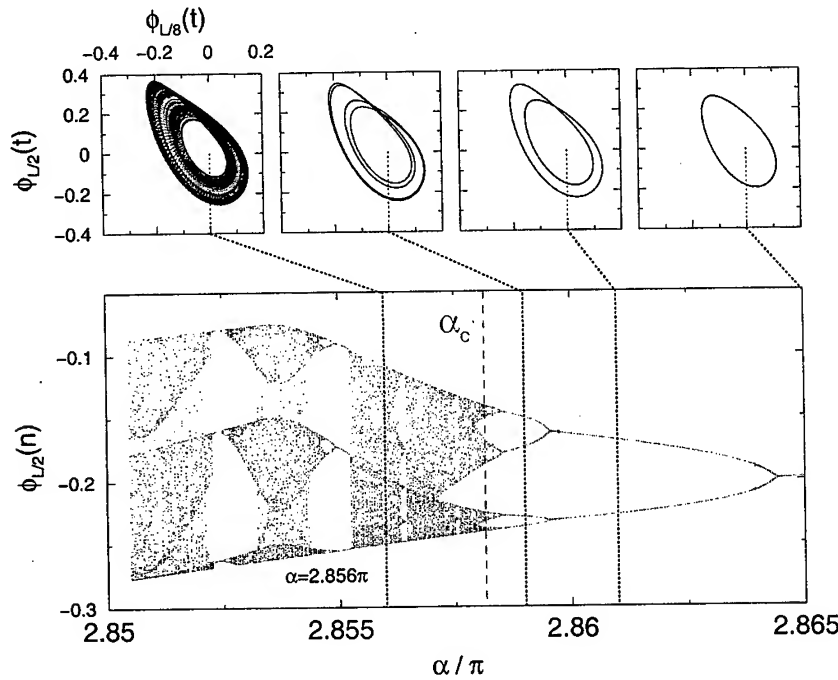


FIG. 3. Period doubling cascade to low-dimensional chaos in the Pierce-diode [25]. The results are obtained from a PIC-simulation. The top row shows selected attractor reconstructions $\{\phi_p(L/8, t), \phi_p(L/2, t)\}$.

$\phi_{L/2}(t) = \phi_p(L/2, t)$ are the electrostatic potential at $x = L/8$ and $x = L/2$, respectively. The bifurcation diagram is obtained from Poincaré sections of phase space attractors determined at the Pierce-parameter values in the above given range. The chaos transition shown in Fig. 3 follows perfectly the Feigenbaum-scenario and the bifurcation diagram has a striking similarity to those obtained from simple nonlinear mappings [27].

For the chaos control study, a fixed Pierce-parameter value of $\alpha^* = 2.856\pi$ is chosen where a chaotic state is well developed. Control of a periodic state means stabilization of the corresponding fixed point; the Poincaré section (see Fig. 3) yields the first return map $\phi(n+1) = F(\phi(n); \alpha^*)$ and the fixed point ϕ^* is given by the condition $\phi^*(n+1) = \phi^*(n)$. The feedback stabilization of the fixed point ϕ^* is achieved by systematic and straightforward application of the OGY-control algorithm [9]. The unstable fixed point is successfully stabilized using the control law

$$(3.2) \quad \phi(n) \in [\phi^* - \delta\phi_{\max}, \phi^* + \delta\phi_{\max}] \Rightarrow \Delta p_n = -K(\phi(n) - \phi^*)$$

with the feedback parameter value $K = -1.17 \pm 0.06$, which is explicitly calculated from the stability properties of the unstable fixed point ϕ^* [25]. In the present case, the control parameter adjustments p_n are taken to be small potential differences ΔU applied between the two electrodes. We note, however, that

similar results are obtained by perturbing with Δp_n the Pierce-parameter itself. The time evolution of the stabilization process is depicted in Fig. 4, where

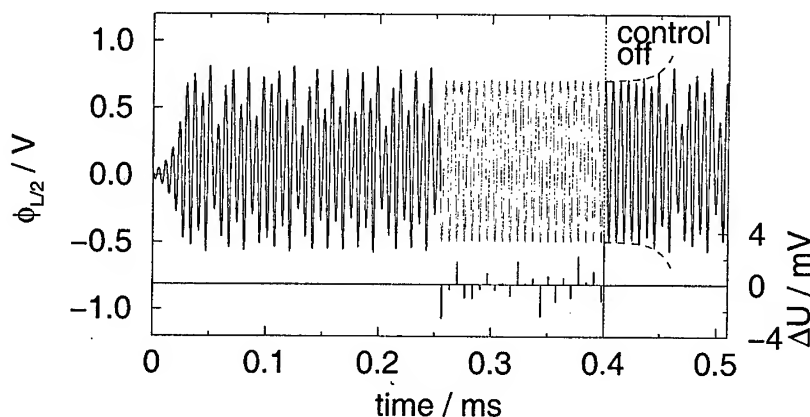


FIG. 4. Stabilization of the orbit of periodicity one by OGY-control [25]. The control is activated for $t = 0 - 0.4$ ms and then switched off. The phase space attractors for the un-controlled and the controlled state (gray lines) are shown in the right.

a time series of the mid-potential $\phi_{L/2}(t)$ is shown while the OGY-control is activated. After an initial transient the chaotic state is established. At $t \approx 0.26$ ms the potential enters for the first time the vicinity of the unstable fixed point and control is activated, cf. Eq. (3.2). As a result, the single periodic orbit is immediately stabilized. The root mean square (r.m.s.) values of parameter changes, shown in the lower trace of the diagram in Fig. 4, are small compared to the r.m.s. values of the mid-potential fluctuations, $\sigma_p/\sigma_\phi = 0.24\%$. At $t = 0.4$ ms the control is switched off and the unstable periodic orbit is left with exponential divergence $\propto \exp(\lambda_1 t)$.

With the same approach, higher periodic orbits are equally well controlled. For a period- N orbit, N fixed points and control laws have to be deduced from the 2^N -th return map. For a periodicity higher than four, control was found to be difficult to achieve due to numerical noise. We finally note that the above described chaos is by far too subtle to be observable in real experiments. Nonetheless, as we shall see in the following, revealing control experiments have been performed in thermionic plasma diodes.

3.2. The thermionic diode

Experiments were conducted in a cylindrical vacuum vessel (diameter 15 cm) with a filamentary tungsten cathode and an opposite anode plate made of stainless steel [28]. The electron density is typically in the order of 10^9 cm^{-3} and the electron temperature is $T_e \approx 2 \text{ eV}$. Ions are at gas temperature (Argon at $p \approx 0.1 \text{ Pa}$ is used as filling gas) due to charge exchange collisions.

Thermionic diodes establish different stable discharge states that are characterized by their axial potential profile [29, 30]. The anode glow mode (AGM)

is characterized by the formation of a virtual cathode [31]. It becomes unstable at a critical anode potential and potential relaxation oscillations occur [32, 33]. When the anode potential exceeds a certain threshold value, volume ionization takes place but the current is still limited by the virtual cathode. In this regime another type of relaxation oscillation is observed that can be explained by ion wave packets traveling from anode to cathode [34]. This mode is called Langmuir mode (LM) and is established if the plasma resistivity is large. At higher anode potential the virtual cathode region is fully neutralized and the electron current is limited only by the temperature of the filaments. This mode is called temperature limited mode (TLM) and is stable [35]. The three states are associated with a hysteresis in the current-voltage characteristic which, in the present case, is not very pronounced due to weak confinement [36]. To study the dynamical response of the discharge current (or plasma potential), a strong periodic force $U_{\sim} = 5 - 30 \text{ V}_{ss}$ is superimposed on the static anode potential, chosen between $U_d = 11 - 25 \text{ V}$.

The dynamical current-voltage characteristic, $I_d(t)$ versus $U_d(t) = U_a + U_{\sim}(t)$, can be interpreted as a phase space contour [38] since the discharge current response $I_d(t)$ and the (periodically driven) discharge voltage $U_d(t)$ can be seen as mutually independent dynamical variables. Such a set of variables spans at least a subspace of the dynamical phase space of the plasma system. Generally speaking, the discharge current response is determined by the ion dynamics resulting in the observed hysteresis [32]. Period doubling bifurcations are observed in the discharge current response at high modulation degrees of approximately 50% [37]. The global state of the system sensitively depends on the driver amplitude U_{\sim} which serves as appropriate control parameter. The bifurcation diagram in Fig. 5 (obtained from the stroboscopically mapped discharge current) clearly shows the period doubling cascade of the strongly driven thermionic diode with increasing driver amplitude. The period doubling sequence ends in a chaotic attractor at $U_{\sim} \approx 7.6 \text{ V}$. For $U_{\sim} > 7.6 \text{ V}$ a sequence of periodic and chaotic windows occur. In addition, Fig. 5 shows the reconstructed phase space attractors and power spectral densities of selected dynamical states. For increasing periodicity it is clearly seen the successively arising subharmonics. In the chaotic state the power spectrum is broad; only few peaks persist at integer multiples of the driver frequency. Although the driver amplitude was chosen as control parameter, in principle other parameters can be used. Similar results are obtained if the neutral gas pressure, the discharge length, the mean anode potential, or the heating current are changed. Note that a period-eight solution is difficult to observe due to intrinsic noise. To confirm that the complex dynamics of the periodically forced thermionic discharge is indeed chaotic, estimates of the correlation dimension D_2 and the Lyapunov spectrum [39] have been numerically calculated. The estimated Lyapunov exponents yield a Kaplan-Yorke dimension of $D_{KY} = 2.077 \pm 0.039$ in agreement with the attractor dimensionality $D_2 = 2.063 \pm 0.054$.

The chaotic current oscillations of the thermionic diode are controlled by using a simplified version of OGY-control (see Sec. 2), proposed by Bielawski *et al.* [40]. Here, the difference of successively samples is used instead of the deviation of the location of the unstable fixed point. This control method has

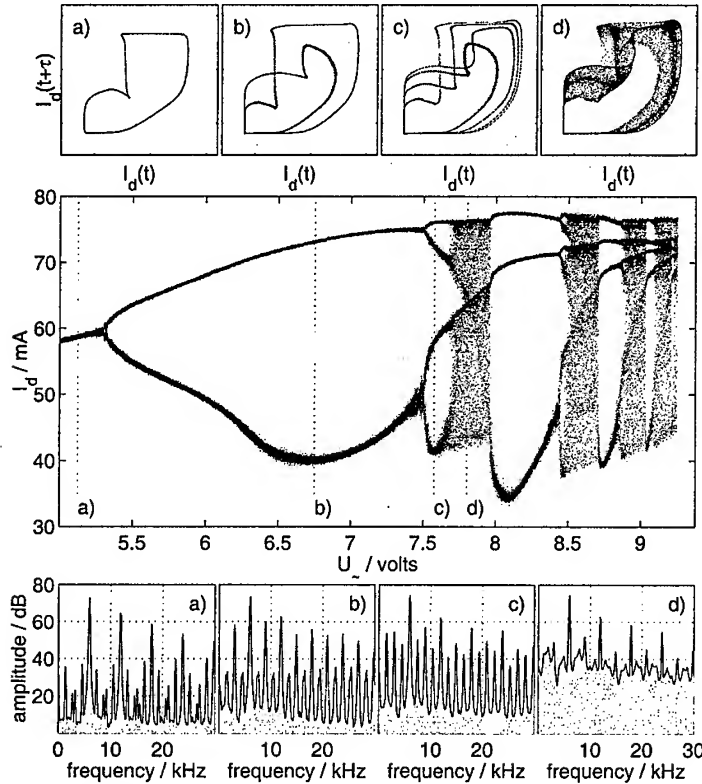


FIG. 5. The period doubling sequence of the strongly driven thermionic diode. The reconstructed phase space attractors (top row) and corresponding power spectral densities (bottom row) are shown for a period-one (a), a period-two (b), and a period-four orbit (c), and for a chaotic regime (d). From [37].

certain restraints that can be circumvented by the following modified control law (memory difference control, MDC [41]):

$$(3.3) \quad \Delta p_n = K \cdot (I_n - I_{n-1}) - N \cdot p_{n-1},$$

where again Δp_n denotes perturbations of the control parameter. K is the feedback gain factor, I_n is the stroboscopically sampled discharge current and $N \cdot p_{n-1}$ denotes an additional memory term, $N \in [-1, 1]$. As in the above case of the Pierce-diode, the feedback constants K and N are predetermined by a stability analysis of the return map. The control signal Δp_n changes at discrete time steps t_n (given by the stroboscopic sampling) the driver amplitude around the average value U_{\sim} . Fig. 6 shows the control of a period-one UPO, embedded within the chaotic attractor shown in Fig. 5(d). The figure shows the time series of the discharge current and the corresponding control signal. When control is activated, the UPO is stabilized after approximately 2 ms, as evident from the strict periodicity in the discharge current. The average degree of control

parameter (driver amplitude) perturbations does not exceed a value of 7%.

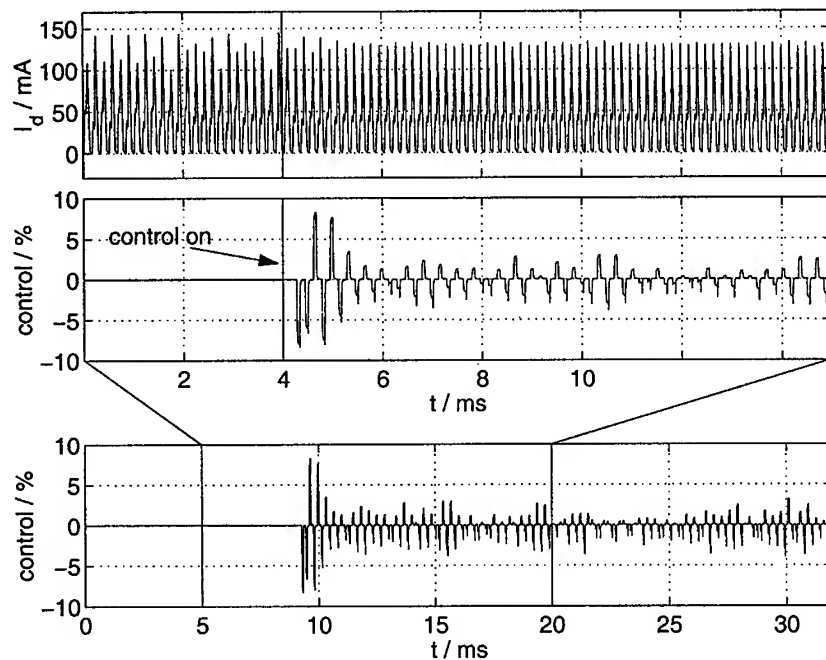


FIG. 6. Control of a period-one UPO embedded within the chaotic attractor shown in Fig. 5(d). In the top trace the time series of the discharge current is shown, the lower traces show the corresponding control signal. A rapid decay rate of the control signal amplitude is observed. The longer time series of the control signal (bottom trace) underlines that the magnitude does not exceed a value of 3%.

4. Taming weakly turbulent ionization waves

Ionization waves propagate in the positive column of simple cold-cathode collisional glow discharges. By use of noble gases, here neon, stepwise ionization processes become important owing to metastable states. The interplay of energy transfer between neutral gas atoms and electrons leads to low-frequency instabilities of the ionization degree of the plasma. This instability forms in the positive column a chain of striations that axially propagate, the ionization waves [42, 43, 44]. Ionization waves are essentially one-dimensional nonlinear waves that incorporate electron temperature fluctuations which lead to a local change of ionization and excitation of neutrals. In the following we describe experiments on the control of weakly developed ionization wave turbulence. Ionization wave turbulence was already the subject of intense research [45].

4.1. Experimental

Experiments are performed in simple glass discharge tubes of 400–800 mm length and 20–30 mm inner diameter. The neon gas pressure is between 100–200 Pa. The discharge current is limited by a series resistor in the external circuit and the discharge current may be varied between 5–20 mA. Fluctuations of the discharge current, the local electric field, and the integral light emission flux are recorded. Since the light emission is a local but non-intrusive diagnostic (in contrast to electrical probes) large arrays of photo-transistors or charge-coupled-devices (CCD) may be used without perturbing the plasma dynamics. This allows one to observe the spatio-temporal evolution of the essentially one-dimensional ionization wave dynamics.

4.2. Discrete feedback control

By modulating the discharge current with the sinusoidal output signal of a function generator, a quasiperiodic state is established and above a certain threshold value of the modulation degree $m = \tilde{I}_d/I_d$, a low-dimensional chaotic attractor establishes via break-up of the two-torus [46, 47]. The modulation degree (m is typically in the realm of only a few percent) is thus taken as the control parameter of the dynamics. Using stroboscopic sampling of the light fluctuations it is rather straightforward to apply simplified versions of the OGY control strategy. For further details we refer to the paper of Weltmann *et al.* [48].

4.3. Continuous feedback control

The above used OGY-type control techniques generally require a detailed knowledge of the return map of the dynamics. From the experimental point of view, this is no serious obstacle in periodically driven systems, where the driver period can be taken as clock to record stroboscopically the fluctuations. However, ionization waves chaos and turbulence frequently occurs without any external periodic driving force and the technical requirements on the on-line construction of the return map become demanding. In such cases, continuous feedback control is much more favorable since it does not rely on the knowledge of the Poincaré section. We describe subsequently experimental studies where autonomous ionization wave chaos is controlled by continuous feedback based on the TDAS scheme proposed by Pyragas (see Sec. 2).

The application of the TDAS-method is not as straightforward as in purely time-dependent systems, where the feedback signal is just the difference between the original and the time-delayed signal (see Sec. 2). The wave character of the ionization instabilities introduces an additional parameter in the control equations. Conditions for control do not only depend on the time delay τ but also on the axial position z of the detector (optical fiber). The preselection of the time delay τ corresponds to the preselection of a wavelength λ_τ . In addition, a phase matching condition (the Barkhausen condition) determines the possible detector positions.

In the following we discuss experiments, where the slowest p -wave mode in ionization wave turbulence is stabilized. Fig. 7 shows the stabilization process

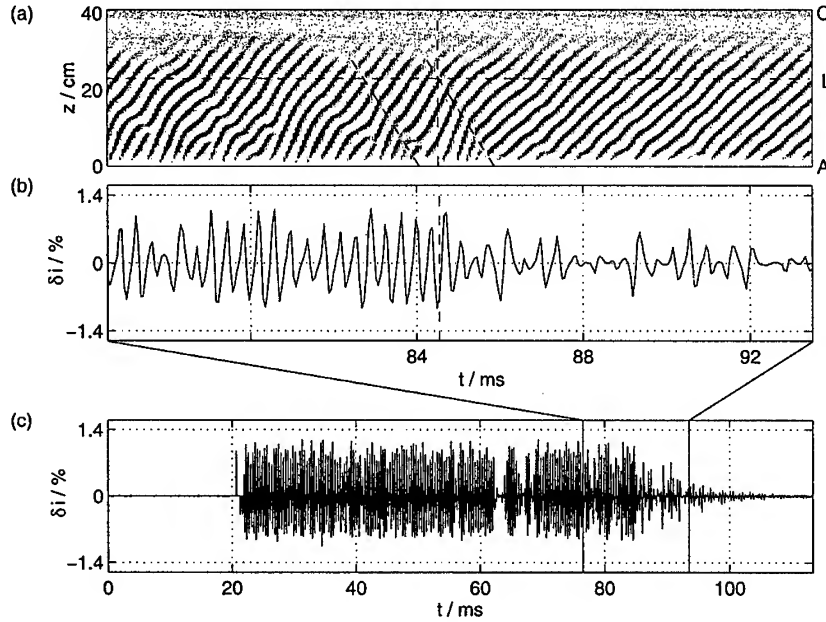


FIG. 7. Control of turbulent ionization waves by time delay auto-synchronization. In (a) the spatiotemporal representation of the ionization waves during the process of stabilization is shown. The horizontal dashed line marks the position of the optical fiber. Diagonal lines mark wave fronts of strong perturbations that propagate through the positive column from cathode to anode. (b) shows the control signal. Large amplitudes coincide with strong perturbations in the integral light emission. In (c) a longer time series of the control signal is depicted. The time lag between the onset of control and final synchronization is approximately $t = 100$ ms.

of turbulent ionization waves using the TDAS-method. In (a) the spatiotemporal diagram of the ionization waves shows that the stabilization process is dominated by synchronizing perturbation fronts that propagate from cathode to anode (diagonal dashed lines). The horizontal line marks the position of the optical detector at $L = 25$ cm, which exactly matches the phase matching condition if 10 wavelengths are assumed to exist in an effective discharge length $l = 45$ cm. The corresponding control signal in Fig. 7(b) shows that large amplitudes always coincide with large fluctuations in the integral light emission fluctuations, due to large perturbations that propagate from cathode to anode. The longer time series of the control signal (Fig. 7(c)) reveals a significant decay of the control amplitude ($\sim e^{-0.04}$ per period) until a minimum value of less than 0.1% is reached. The modulation degree (with respect to the dc discharge current) is very small when compared to open-loop or simple feedback control methods.

5. Taming of stochastic fluctuations

We now return to oscillating, thermionic plasma diodes, where we find exactly the necessary features for applying the concepts of stochastic resonance (SR) to

tame irregular behavior: bistability and intrinsic stochastic noise. As already mentioned in Sec. 2), SR is not chaos control in the sense of stabilizing unstable periodic orbits. SR is a *bona fide* resonance and may be used to reduce stochasticity in the dynamics of oscillating thermionic discharges. We note that SR was previously observed in a magnetoplasma [49].

In a recent SR-experiment conducted in a thermionic discharge we found that small periodic perturbations significantly reduce the low-frequency noise level, which is due to stochastically induced jumps between two oscillatory states [50]. The bistability of thermionic plasma diodes becomes evident by the well-known hysteresis in the $I_d(U_d)$ -characteristic [36, 51]. Knorr [52] suggested a phenomenological description based on bifurcation theory: It is introduced a classical potential $V(i)$ with an order parameter i , the appropriately normalized and rescaled discharge current. The expression for the classical potential reads

$$(5.1) \quad V(i) = i^4 + \alpha i^2 + ui,$$

where u is the (normalized) discharge voltage and α is a parameter. Eq. (5.1) is the canonical form of a cusp catastrophe [38]. The set of equilibrium points is given by $dV/di = 0$. Starting at low u -values the initially stable equilibrium state becomes unstable at the transition point with a vertical tangent in the equilibrium curve. It occurs a sudden jump and the other equilibrium state is established. The same happens in the reversed direction when u is decreased while sitting on the upper branch. This is considered as a heuristic model of the hysteresis in the establishment of the AGM and the LM/TLM in thermionic discharges. It is important to note, however, that the two equilibrium states are non-stationary, oscillating states. The classical potential (5.1) has the same form as the generic double-hump potential Eq. (2.1) in the general description of SR in Sec. 2. The stochastic behavior is understood as follows. The hysteresis curve of the magnetized thermionic discharge is very narrow, only a few Volts. Close to the transition points the above described strong nonlinear oscillations occur. Stochastic fluctuations in the oscillation amplitude (incoherence) occasionally induce transitions $\text{AGM} \leftrightarrow \text{LM}$ by increased and decreased ion production, respectively. The discharge voltage determines the closeness to either the AGM- or the LM-oscillation mode and thus controls the statistics of the sudden jumps.

To investigate the influence of a small perturbation signal, the dc discharge voltage $U_0 = 21.1 \text{ V}$ is modulated by a weak signal of a few tenths of millivolts. The modulation frequency is chosen to be of the order of the Kramers time which is estimated from the statistics of the unmodulated discharge. The result of the experiment is shown in Fig. 8. Without any modulation a stochastic sequence of AGM- and LM-oscillations is found [Fig. 8(a)]. To emphasize the stochastic nature of the behavior (and to facilitate the statistical analysis) a binarisation procedure was applied to the current signal: 1 is associated with the oscillating LM and 0 corresponds to the oscillating AGM. The lower trace in Fig. 8(a) shows the binary sequence. Modulation with a small signal of amplitude $U_i = 80 \text{ mV}_{\text{ss}}$ significantly changes the transition behavior [Fig. 8(b)]. At each minimum of the modulation signal there is increased probability for an $\text{LM} \rightarrow \text{AGM}$ -transition and at each maximum the same happens for the $\text{AGM} \rightarrow \text{LM}$ -transition. As

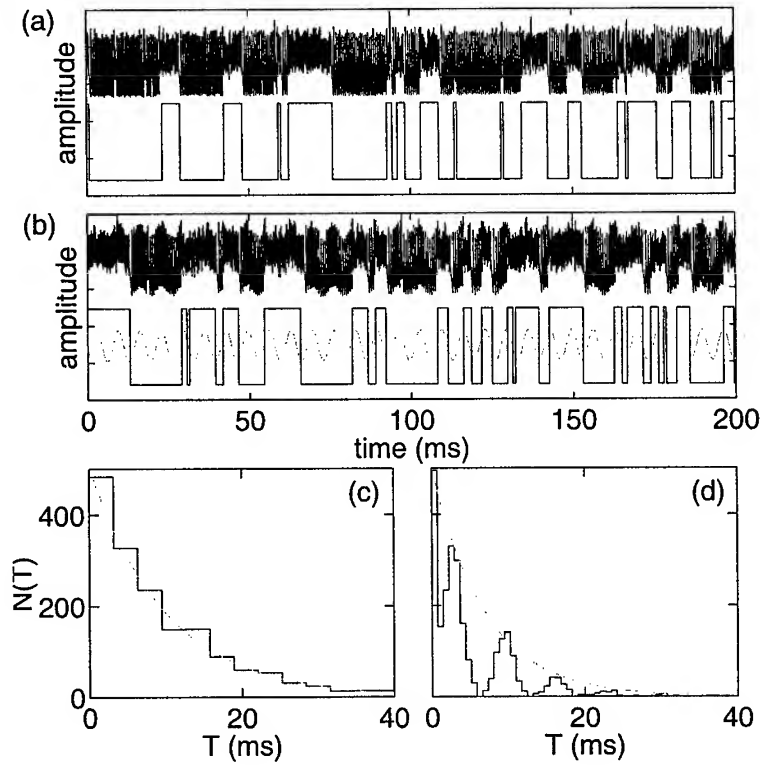


FIG. 8. Time series of the discharge current of a thermionic plasma diode. (a) Noise-induced between oscillating AGM and LM, the lower trace shows the binarisation. (b) Synchronisation of the jumps by a weak driver signal. (c) Histogram of the residence time of AGM/LM without perturbation and (d) with perturbation. The humps in (d) at integer multiples of the driver signal are taken as evidence for SR.

as a result a sharp peak arises at f_i in the power spectrum to the expense of the noise underground (not shown here). In addition, the binary sequence is much more periodic with a periodicity given by integer multiples of the driver signal. The difference between the two states becomes more clear by comparing the length histograms of the two binary sequences [Fig. 8(c) and (d)], also called 'residence time distribution' [53]. In the stochastic case, we find an exponential distribution whereas in the SR case the histogram shows pronounced humps at integer multiples of the driver signal period - a clear indication of predominantly periodic behavior. In conclusion, the stochastic behavior of the thermionic diode in its hysteresis regime is very efficiently suppressed (and thus controlled) by very weak modulation of the discharge voltage.

We finally note that the SR effect was recently demonstrated in an ionization wave experiment, where noise is externally superimposed on the discharge current of a neon glow discharge [54]. Due to space restrictions we cannot go into further detail and we refer the reader to the referenced paper.

6. Summary, conclusions and outlook

In the present paper it has been demonstrated the high performance of feedback control schemes that are based on the stability analysis in the dynamical phase space. In collisionless plasma diodes chaotic oscillations of current and plasma potential could be tamed by discrete feedback control, i.e., periodic states embedded in the chaotic attractor were successfully stabilized. This was demonstrated both for the classical Pierce diode (simulation) and for the strongly driven thermionic diode (experiment). Using this type of feedback schemes, it is possible to establish periodic operation of plasma diodes in regimes where usually chaotic oscillations occur. This general conclusion can well have engineering applications, in the field where plasma diode configurations are used as high-power microwave sources.

The recent success in chaos control was taken as encouragement to attack the problem of taming turbulence. This is a far more demanding task since the space extend enters in the control problem as an additional continuous parameter and is not anymore described in a low-dimensional phase space. We have shown that global, continuous feedback control can be used to stabilize periodic states of weakly developed ionization wave turbulence, which is by nature one-dimensional. Two- and three-dimensionally turbulent plasma waves as well as fully developed turbulence demand for more advanced control techniques, among which spatially distributed feedback is currently the most promising approach [2].

An example for the perspectives of open-loop control of stochastic behavior, the stochastic resonance phenomenon was experimentally demonstrated in a thermionic discharge diode. Stochastic resonance attracted much recent attention since only weak periodic signals can efficiently entrain noise-induced jumps in bistable systems.

Recent developments in the control theory of nonlinear dynamical systems have found new applications in the classical field of feedback control of laboratory plasmas. Future developments will focus on the control of extended systems, where many important developments are expected to happen in the field of the dynamics of plasma waves.

References

1. P. MANNEVILLE, *Dissipative Structures and Weak Turbulence*. San Diego: Academic Press, 1990.
2. H.G. SCHUSTER, ed., *Handbook of chaos control*. Weinheim: Wiley-VCH, 1999.
3. T.K. CHU and H.W. HENDEL, eds., *Feedback and dynamical control of plasmas*, AIP conference proceedings, New York: American Institute Physics, 1970.
4. K. OGATA, *Modern control engineering*. New Jersey: Englewood Cliffs, 2ed., 1990.
5. T. KLINGER, *Control of chaos in plasmas*, in *Handbook of Chaos Control* (H. G. Schuster, ed.), Wiley-VCH, 1999.
6. R. LIMA and M. PETTINI, *Suppression of chaos by resonant parametric perturbations*, Phys. Rev. A, **41**, 2, 726-733, 1990.
7. Y. BRAIMAN and I. GOLDBIRSCH, *Taming chaotic dynamics with weak periodic perturbations*, Phys. Rev. Lett., **66**, 20, 2545-2548, 1991.

8. C. GREBOGI, E. OTT, and J.A. YORKE, *Unstable periodic orbits and the dimension of multi-fractal chaotic attractors*, Phys. Rev. A, **37**, 1711-1724, 1988.
9. E. OTT, C. GREBOGI and J. A. YORKE, *Controlling chaos*, Phys. Rev. Lett., **64**, 11, 1196-1199, 1990.
10. F.J. ROMEIRAS, C. GREBOGI, E. OTT and W.P. DAYAWANSA, ' *Controlling chaotic dynamical systems*, Physica D, **58**, 165-192, 1992.
11. K. PYRAGAS, *ontinuous control of chaos by self-controlling feedback*, Phys. Lett. A, **170**, 421-428, 1992.
12. D.J. GAUTHIER, D.W. SUKOW, H.M. CONCANNON and J.E.S. SOCOLAR, *Stabilizing unstable periodic orbits in a fast diode resonator using continuous time-delay autosynchronization*, Phys. Rev. E, **50**, 3, 2343-2346, 1994.
13. T. SHINBROT, C. GREBOGI, E. OTT and J.A. YORKE, *Using small perturbations to control chaos*, Nature, **363**, 3, 411-417, 1993.
14. T. SHINBROT, *Progress in the control of chaos*, Adv. Physics, **44**, 2, 73-111, 1995.
15. W. JUST, T. BERNARD, M. OSTHEIMER, E. REIBOLD and H. BENNER, *Mechnism of time-delayed feedback control*, Phys. Rev. Lett., **2**, 203-206, 1997.
16. R. BENZI, A. SUTERA and A. VULPIANI, *The mechanism of stochastic resonance*, J. Phys. A: Math. Gen., **14**, L453-L457, 1981.
17. K. WIESENFELD and F. MOSS, *Stochastic resonance and the benifits of noise: From ice ages to crayfish and squids*, Nature, **373**, 5, 33-36, 1995.
18. S. KUHN, *The physics of bounded plasma systems (BPD's): Simulation and interpretation*, Contrib. Plasma Phys., **34**, 4, 495-538, 1994.
19. J.R. PIERCE, *Limiting stable current in electron beams in the presence of ions*, J. Appl. Phys., **15**, 721-726, 1944.
20. S. KUHN, *Linear longitudinal oscillations in collisionless plasma diodes with thin sheaths. Part II. Application to an extended Pierce-type problem*, Phys. Fluids, **27**, 7, 1834-1851, 1984.
21. H. KOLINSKY, F. GREINER and T. KLINGER, *The pierce diode as a model for the stability of thermionic gas discharges*, J. Phys. D: Appl. Phys., **30**, 21, 2979-2990, 1997.
22. B.B. GODFREY, *Oscillatory nonlinear electron flow in a Pierce diode*, Phys. Fluids, **30**, 5, 1553-1560, 1987.
23. W.S. LAWSON, *The Pierce diode with external circuit. II. Chaotic behavior*, Phys. Fluids, **B1**, 7, 1493-1501, 1989.
24. C.K. BIRDSALL and A.B. LANGDON, *Plasma Physics Via Computer Simulation*, New York: McGraw-Hill, 1st ed., 1985.
25. N. KRAHNSTOVER, T. KLINGER, F. GREINER and A. PIEL, *Controlling chaos in the Pierce diode*, Phys. Lett. A, **239**, 1,2, 103-109, 1998.
26. H. MATSUMOTO, H. YOKOYAMA and D. SUMMERS, *Computer simulation of the chaotic dynamics of the Pierce beam-plasma system*, Phys. Plasmas, vol. 3, no. 1, pp. 117-191, 1996.
27. P. COLLET and J.-P. ECKMANN, *Iterated Maps on the Interval as Dynamical System*, Basel: Birkhauser, 1980.
28. T. KLINGER, F. GREINER, A. ROHDE and A. PIEL, *Nonlinear dynamical behavior of thermionic filamentary low pressure discharges. Part II: Experimental*, Phys. Plasmas, **2**, 6, 1822-1836, 1995.
29. S.KUHN, *Axial equilibria, disruptive effects, and buneman instability in collisionless single-ended Q-machines*, Plasma Phys., **23**, 10, 881-902, 1981.
30. H. KLOSTERMANN, F. GREINER, T. KLINGER and A. PIEL, *Stable and unstable modes in a thermionic discharge at low pressure*, Plasma Sources Sci. Technol., **3**, 134-141, 1994.

31. F. GREINER, T. KLINGER, H. KLOSTERMANN and A. PIEL, *Experiments and particle-in-cell simulation on self-oscillations and period-doubling in thermionic discharges at low pressure*, Phys. Rev. Lett., **70**, 20, 3071-3074, 1993.
32. F. GREINER, T. KLINGER and A. PIEL, *Nonlinear dynamical behavior of thermionic filamentary low pressure discharges. Part I: Simulation*, Phys. Plasmas, **2**, 6, 1810-1821, 1995.
33. F. BAUER and H. SCHAMEL, *Spatio-temporal structures in collisionless electrostatic plasmas*, Physica D, **54**, 235-252, 1992.
34. W.X. DING, T. KLINGER and A. PIEL, *Low-frequency current oscillations in a linear hot-cathode discharge*, Phys. Lett. A, **222**, 409, 1996.
35. L. MALTER, E.O. JOHNSON and W.M. WEBSTER, *Studies of externally heated hot cathode arcs, part I. - modes of the discharge*, RCA Rev., **12**, 415-435, 1951.
36. R.A. BOSCH and R.L. MERLINO, *Sudden jumps, hysteresis, and negative resistance in an argon plasma discharge. I. Discharges with no magnetic field*, Contrib. Plasma Phys., **26**, 1, 1986.
37. T. MAUSBACH, T. KLINGER and A. PIEL, *Chaos and chaos control in a strongly driven thermionic discharge plasma*, Phys. Plasmas, 1999. At press.
38. E.A. JACKSON, *Perspectives of Nonlinear Dynamics*, vol. 1 & 2. Cambridge (UK): Cambridge University Press, 1991.
39. H.D.I. ABARBANEL, *Analysis of Observed Chaotic Data*, New York Berlin Heidelberg: Springer-Verlag, 1996.
40. S. BIELAWSKI, D. DEROZIER and P. GLORIEUX, *Experimental characterization of unstable periodic orbits by controlling chaos*, Phys. Rev. A, **47**, 4, 2492, 1993.
41. J.C. CLAUSSEN, T. MAUSBACH, A. PIEL and H.G. SCHUSTER, *Memory difference control of unknown unstable fixed points: Drifting parameter conditions and delayed measurement*, Phys. Rev. E, **58**, 6, 7256-7260, 1998.
42. N.L. OLESON and A.W. COOPER, *Moving striations*, Adv. Electron. Electron Phys., **24**, 155-278, 1968.
43. R.N. FRANKLIN, *Plasma Phenomena in Gas Discharges*, The Oxford Engineering Science Series, Oxford: Clarendon Press, 1976.
44. Y.P. RAIZER, *Gas Discharge Physics*. Berlin: Springer, 1991.
45. K. OHE, *Nonlinear phenomena of ionization waves*, in Proc. of XIXth ICPIG, Invited Papers (V.J. Zigman, ed.), (Belgrad, Jugoslavia), 150, 1989.
46. C. WILKE, H. DEUTSCH and R.W. LEVEN, *Experimental study of nonlinear behavior of a neon glow discharge*, Contrib. Plasma Phys., **30**, 659-669, 1990.
47. B. ALBRECHT, H. DEUTSCH, R. W. LEVEN and C. WILKE, *Three frequency quasiperiodicity and chaos in a neon glow discharge*, Physica Scripta, **47**, 196-203, 1993.
48. K.D. WELTMANN, T. KLINGER and C. WILKE, *Experimental control of chaos in a periodically driven glow discharge*, Phys. Rev. E, **52**, 2, 2106-2109, 1995.
49. L. I and J. LIU, *Experimental observation of stochastic resonancelike behavior of autonomous motion in weakly ionized rf magnetoplasmas*, Phys. Rev. Lett., **74**, 16, 3161-3164, 1995.
50. T. KLINGER and A. PIEL, *Stochastic resonance of plasma oscillations with intrinsic noise*, Phys. Rev. Lett., 1999. In preparation.
51. R.A. BOSCH and R.L. MERLINO, *Sudden jumps, hysteresis, and negative resistance in an argon plasma discharge. II. Discharges in magnetic fields*, Contrib. Plasma Phys., **26**, 13, 1986.
52. G. KNORR, *Hysteresis phenomena in plasmas and catastrophe theory*, Plasma Phys. Controlled Fusion, **26**, 949, 1984.
53. L. GAMMAITONI, P. HANGGI, P. JUNG and F. MARCHESONI, *Stochastic resonance*, Rev. Mod. Phys., **70**, 1, 223-287, 1998.
54. A. DINKLAGE, C. WILKE and T. KLINGER, *Spatiotemporal response to stochastic resonance in an excitable discharge plasma*, Phys. Plasmas Letters, 1999. At press.

KINETIC MODELING AND EXPERIMENTAL STUDIES OF LARGE-SCALE LOW-PRESSURE RF DISCHARGES

U. KORTSHAGEN and B. HEIL

UNIVERSITY OF MINNESOTA, DEPT. OF MECH. ENGINEERING
111 Church Street S.E., Minneapolis, MN 55455

A recent trend in plasma etching of semi-conductors has been the move towards discharge operation at low pressures of 2 - 20 mTorr. At these conditions the electron distribution functions shows modest but significant deviations from a fully nonlocal distribution. We have developed a model which addresses this regime of modest deviations from the nonlocal case with an efficient numerical scheme to solve the Boltzmann equation. Theoretical results are compared to results of two-dimensional Langmuir probe measurements. The measurements confirm the main assumptions used in our plasma model and show good agreement with the results of our model.

1. Introduction

Low-pressure gas discharges find wide-spread applications in plasma materials processing such as semi-conductor manufacturing and in discharge lighting. In particular, in semi-conductor processing the reduction of the feature size of electronic devices has made discharge operation at ever lower pressure necessary. While typical etch processes about a decade ago were run at pressures of several hundred mTorr to about one Torr, modern high-density low-pressure discharges operate at pressures of 2 - 20 mTorr. Over the same time also the discharge dimensions increased significantly due to the introduction of larger wafer sizes. Modern etch plasmas require plasma uniformities of better than a few percent over areas of eight to twelve inches.

The development of new plasma processes still proceeds mostly empirically since the predictive modeling of low-pressure plasmas still presents considerable difficulties. However, predictive plasma models could lead to a reduction of the development time and costs of new plasma processes so that a considerable demand for such "engineering-type" models exists.

Before the introduction of low-pressure high-density plasmas the use of fluid approximations for plasma modeling seemed physically appropriate. A number of plasma models were successfully developed to describe various gas discharges

using fluid approximations, e.g. [1 - 16]. With only a few exceptions these models consider low temperature plasmas as two-fluid systems made up of a "hot" electron fluid and a "cold" ion fluid which are collisionally coupled to the neutral gas background [8 - 10]. Fluid plasma models are particularly attractive due to their computational efficiency which makes them suitable for engineering-type plasma modeling.

However, the simple assumption of a two-temperature systems with a hot electron fluid and a cold ion fluid only incompletely captures the real properties of a gas discharge plasma. A general criticism of most fluid models is the inherent assumption of a Maxwellian distribution function of the electrons. In most gas discharges the degree of ionization is between 10^{-6} and 10^{-3} . As a consequence electron-electron and electron-ion collisions are not sufficiently effective compared to electron-atom collisions to thermalize the electron component. The non-Maxwellian character of the electron distribution function in gas discharge plasmas has been impressively demonstrated in numerous experimental [17, 18, 19, 20, 21, 22] and theoretical studies [23, 24, 25, 26, 27]. However, for low-pressure discharges operated at 2 - 20 mTorr a fluid approximation for the electrons seems even more questionable since the electron mean free path is of the same order as the typical discharge dimensions. In addition, a host of kinetic phenomena has been discovered in these discharges which cannot be described in a hydrodynamic framework: Due to the fact that the electron mean free path is of the order of the discharge dimensions the electron distribution function can no longer be determined under the assumption of a uniform plasma. New approaches were developed which took into account the significant spatial non-uniformity of the plasma condition and its influence on the electron distribution function [28, 29, 30]. Effects of "nonlocal" energy transport by the electrons were discovered [31, 32] which sometimes manifest in seemingly paradoxical behavior, for instance, that the mean kinetic energy of electrons decreases towards regions of high radiofrequency field strengths and increases towards regions of minimum RF field strength in capacitively coupled plasmas [33]. Most low-pressure high-density discharges operate with inductive coupling or wave coupling (helicon or surface wave) or RF power. The fact that the electron mean free path is often larger than the RF field skin depth leads to interesting phenomena of anomalous skin effect and "nonlocal" electrodynamics [34, 35]. The bounce frequency of electrons, i.e. the frequency with which electrons are reflected between adjacent sheaths in the discharge, is of the order of the RF field frequency which leads to stochastic, collisionless heating effects [36, 37, 38, 39, 40]. Finally, nonlinear effects due to wave magnetic fields are thought to influence the plasma density profiles [41].

In consequence, different techniques of kinetic treatment of the electrons were developed such as Monte-Carlo simulations [3, 42], Particle in Cell Monte Carlo collision methods [43], and the Convective scheme method [44, 45]. However, these methods are computationally very expensive and become impractical when two- or three-dimensional geometries have to be considered. Other studies focussed on the solution of kinetic equations derived from the Boltzmann equation [23, 24, 25, 26, 27]. These methods can be computationally much more efficient but they were initially limited to the study of spatially uniform plasmas. Only

recently these models were extended to address spatially non-uniform systems [28, 29, 30, 46] but at the expense of a significant loss of the computational efficiency.

For this reason, the "nonlocal approximation" (NLA) has recently attracted considerable attention. The NLA was invented in 1954 by Bernstein and Holstein [31] and renewed and extended by Tseng [32] in 1974. Its main advantage is that it reduces the kinetic description of the electrons in systems of arbitrary geometry to the solution of a spatially-averaged kinetic equation, which is a one-dimensional, ordinary differential equation in total energy. The method requires that the energy relaxation length considerably exceeds the discharge dimensions and that the electric field strength is moderate. Under these conditions the electrons perform a fast spatial motion with constant total energy while the "motion" in energy space is slow. The electron distribution function (EDF) is then a spatially uniform function of total energy. The EDF in terms of kinetic energy is found from a modified Boltzmann equation. More details on this method are given below and in review papers [47, 48].

While the NLA was successfully used to model a number of laboratory experiments [49, 50, 51, 52], it seems less suitable to the modeling of industrial size large-scale low-pressure plasmas. The reason for this is that large-scale plasma uniformity in industrial discharges is mainly achieved by suitable design of the reactor chamber and the RF electric field profiles. However, one peculiarity of the NLA is that the EDF is determined solely by spatial averages of the RF electric field distribution and that it tends to yield ionization profiles which are centered around the geometric center of the discharge. In industrial discharges very non-uniform fields are employed to produce ionization profiles which can peak in the plasma periphery in order to achieve more uniform plasma density profiles. The NLA is not capable of capturing these effects. For this reason we have developed a plasma model which uses an extended approach to solve the Boltzmann equation. This approach, which will be called the "hybrid approach" in the following, was first proposed by Kolobov and Hitchon [51]. He has implemented this approach and incorporated it into a fully self-consistent model of a low-pressure inductively coupled plasma. The results of this model have extensively been compared to an actual experiment. Results of this comparison are presented in this invited paper.

The paper is organized as follows: In Sec. 2 the plasma model is presented. The experiment is briefly described in Sec. 3 and model and experiment are compared in Sec. 4. Conclusions are given in Sec. 5.

2. Kinetic model of an inductively coupled plasma

Our model addresses an inductively coupled plasma at low pressures at which the EDF shows modest deviations from the fully nonlocal case. The model consists out of three main modules. We assume rotational symmetry around the z -axis so that the model can be formulated in two spatial dimensions: the radius r and the height z . The electron kinetics is treated in terms of the "hybrid approach". For the ions a simple fluid model is used. The model is complemented by an electromagnetic module for the determination of the RF induced electric field.

2.1. The hybrid kinetic model

The hybrid kinetic approach is based on the solution of the electron Boltzmann equation. We use the standard assumptions of the two-term approximation [53] and the effective field approximation [54, 25]. This means, that it is assumed that the distribution function F_0 is isotropic in velocity space and stationary. Temporal fluctuations are limited to higher order terms in the spherical harmonics expansion. Following the philosophy of the NLA, we chose a formulation in total electron energy in volts

$$(2.1) \quad \varepsilon = \frac{m_e v^2}{2e} - \Phi(r, z),$$

with m_e is the electron mass, e the elementary charge, v the electron velocity, and $\Phi(r, z)$ the stationary ambipolar potential. In the total energy representation the kinetic equation for the main part of the EDF F_0 is:

$$(2.2) \quad -\frac{1}{3v} \nabla_r \cdot \left(\frac{v^3}{\nu_m} \nabla_r F_0(\varepsilon, r, z) \right) - \frac{1}{3v} \frac{\partial}{\partial \varepsilon} \left(\frac{v^3}{\nu_m} E_{eff}^2(r, z) \frac{\partial F_0(\varepsilon, r, z)}{\partial \varepsilon} \right) = C_0(F_0(\varepsilon, r, z)).$$

The details of the derivation of this equation can be found in [47]. The electron velocity is a function of the total energy and position: $v = v(\varepsilon, r, z) = (2e/m_e \times [\varepsilon + \Phi(r, z)])^{1/2}$. The same applies to the momentum transfer collision frequency ν_m . The symbol $E_{eff}(r, z) = \tilde{E}(r, z)/\sqrt{2} \times \nu_m/(\nu_m^2 + \omega^2)^{1/2}$ is the effective field strength for Joule electron heating by the RF field with the amplitude $\tilde{E}(r, z)$ and the angular frequency ω . In this study we do not consider stochastic heating. $C_0(F_0(\varepsilon, r, z))$ is the collision operator. It involves terms for inelastic (excitation) collisions, ionization, elastic collisions, and Coulomb collisions. The inelastic collision term is given by

$$(2.3) \quad C_{0,exc.} = - \sum_k \left[\nu_{ex}^k(u) F_0(\varepsilon, r, z) - \frac{(u + u_{ex}^k)^{1/2}}{u^{1/2}} \nu_{ex}^k(u + u_{ex}^k) F_0(\varepsilon + u_{ex}^k, r, z) \right],$$

where the kinetic energy $u = u(\varepsilon, r, z) = \varepsilon + \Phi(r, z)$ has been used for clarity. The sum extends over all inelastic excitation processes k with collision frequencies ν_{ex}^k and threshold energies u_{ex}^k . For the ionization term we use the approximation that the energy in excess of the ionization energy is evenly distributed on the primary and the released electron [55]

$$(2.4) \quad C_{0,ion.} = - \sum_k \left[\nu_{ion}^k(u) F_0(\varepsilon, r, z) - \frac{4(2u + u_{ion}^k)^{1/2}}{u^{1/2}} \times \nu_{ion}^k(2u + u_{ion}^k) F_0(\varepsilon = 2u + u_{ion}^k - \Phi(r, z), r, z) \right].$$

The sum is extended over all ionization processes k with ionization frequencies ν_{ion}^k and ionization energies u_{ion}^k . For both ionization as well as excitation only processes involving gas atoms or molecules in the ground state are considered here. The inclusion of collisions with excited atoms or molecules would require a collisional-radiative model to determine the concentration of excited species which is beyond the scope of the current study.

The elastic collision term is given by

$$(2.5) \quad C_{0,elast.} = \frac{1}{u^{1/2}} \frac{\partial}{\partial \varepsilon} \left[u^{3/2} \kappa \nu_m \left(F_0 + \frac{k_B T_g}{e} \frac{\partial F_0}{\partial \varepsilon} \right) \right],$$

with $\kappa = 2me/M_a$, M_a the atom mass, T_g the gas temperature, and k_B the Boltzmann constant.

The well-known Fokker-Planck operator is used to include electron-electron collisions [56]:

$$(2.6) \quad \frac{\Gamma}{u^{1/2}} \frac{d}{d\varepsilon} \left[H(\varepsilon, r, z) F_0(\varepsilon, r, z) + \frac{2}{3} G(\varepsilon, r, z) \frac{dF_0(\varepsilon, r, z)}{d\varepsilon} \right],$$

with

$$(2.7) \quad H(\varepsilon, r, z) = \int_0^{u(r,z)} F_0(u', r, z) u'^{1/2} du',$$

$$G(\varepsilon, r, z) = \int_0^{u(r,z)} F_0(u', r, z) u'^{3/2} du'$$

$$(2.8) \quad + u^{3/2}(r, z) \int_{u(r,z)}^{\infty} F_0(u', r, z) du',$$

$$(2.9) \quad \Gamma = \left(\frac{2e}{m_e} \right)^{1/2} \frac{e^2}{8\pi\varepsilon_0^2} \ln \Lambda_C,$$

ε_0 is the dielectric constant and $\ln \Lambda_C$ is the Coulomb logarithm [56].

For our problem in a two-dimensional geometry, the kinetic equation (2.2) is a three-dimensional partial differential equation which can, in principle, be solved numerically. However, there are two problems which strongly complicate the efficient numerical solution of this equation: (a) The Fokker-Planck term (2.6) introduces a non-linearity into the problem and (b) the domain of integration is irregular with a curved boundary at the space-charge potential $\Phi(r, z)$ which constitutes the minimal total energy at each position (r, z) , i. e. $u(r, z) = 0$, see Fig. 1.

Instead of performing a complete solution of equation (2.2) it seems more beneficial for engineering-type calculations to look for more efficient, physically

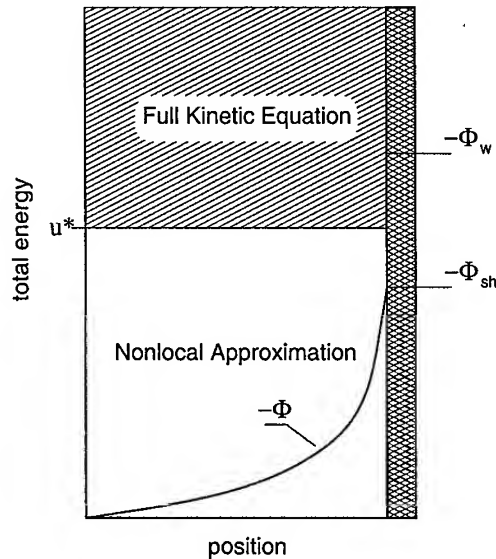


FIG. 1. Scheme of the partition of the domain of integration used in the hybrid kinetic scheme.

motivated approximations. The solution of Eq. (2.2) is highly simplified if the NLA is applicable by solving a spatially averaged kinetic equation which is only an ordinary differential equation. This approximation is justified if the energy relaxation length λ_ϵ is large compared to the discharge dimensions over the entire energy range of interest for the EDF. However, the energy relaxation length strongly depends on the type of collisions which can occur at a given energy:

$$(2.10) \quad \lambda_\epsilon = \begin{cases} \sqrt{\frac{M_a}{2m_e}} \lambda & , \text{ for elastic collisions,} \\ \sqrt{\lambda \lambda^*} & , \text{ for inelastic collisions.} \end{cases}$$

Thus, if we move to larger industrial discharges and/or higher pressures the energy relaxation length may not exceed the discharge dimensions for the entire energy range but at least for a part of it. In the energy range in which only elastic collisions are possible λ_ϵ exceeds the electron mean free path λ by the square root of the mass ratio M_a/m_e which is a number of the order of 100 since the energy loss of electrons in elastic collisions is very small. Even though this topic has not been studied in the literature one can suppose that vibrational and rotational excitation collisions behave similar to elastic collisions due to the relatively small energy loss for the electrons. In electron excitation "inelastic" collisions the energy loss is of the order of the entire kinetic energy and the energy relaxation is much faster. The energy relaxation length in this range is thus much shorter and it scales with the mean free path for inelastic collisions λ^* . The idea of the "hybrid approach" [51] is to take advantage of this effective division of the electron energy space into two parts and to treat these parts

with different approximations to solve the kinetic equation (2.2) (see Figure 1):

1. The low energy "elastic range" with ϵ less than the smallest excitation threshold energy u^* :

In this range λ_e at pressures of a few Pa is of the order of several meter and the traditional NLA is applicable. The EDF is a spatially uniform function of total energy. It can be determined by solving the spatially averaged kinetic equation of the NLA. Inclusion of Coulomb collisions is a standard technique [49].

2. The high energy "inelastic range" with ϵ greater than the smallest excitation threshold energy u^* :

In this energy range λ_e will be smaller than the typical discharge dimensions so that the full kinetic equation (2.2) has to be solved. This subdomain, however, is of regular shape with straight boundaries. For not too high degrees of ionization it can be justified to neglect Coulomb collisions as discussed below. This allows us to treat the full kinetic equation (2.2) as a linear equation which strongly simplifies its solution.

Coulomb collisions require some more discussion. The influence of Coulomb collisions on the EDF is different for the "elastic" and the "inelastic" energy range of the EDF for two reasons: Because the Coulomb cross sections scales with $1/u^2$ it is particularly effective at low kinetic energies. Furthermore, in the "elastic" range Coulomb collisions have to compete only with energy-conserving, elastic collisions. In contrast, in the "inelastic" range the EDF formation is dominated by inelastic collisions which strongly change the energy of the colliding electron. In numerical studies [57] of the efficiency of Coulomb collisions it was shown that modifications of the low energy part of the EDF can be observed for degrees of ionization as low as 10^{-6} or even smaller. In the "inelastic" range Coulomb collisions start to affect the EDF formation at degrees of ionization larger than 10^{-4} . Hence, we choose to include Coulomb collisions in the treatment of the "elastic" range using the traditional NLA, but to neglect them in the "inelastic" range. This approximation limits the applicability to degrees of ionization not much larger than 10^{-4} . While this condition is fulfilled in the comparison to our experiments presented below, we realize the need for a more consistent inclusion of Coulomb collisions in future work.

The efficiency of the "hybrid approach" is gained from solving the kinetic equation (2.2) only in a reduced energy space and by not including Coulomb collisions in the high energy range. This approach, though somewhat limited, seems reasonable for engineering-type calculations. The "hybrid approach" enables us to efficiently obtain more accurate ionization profiles, which allows the study of plasma uniformity, than would be possible with the traditional nonlocal approach. However, one has to realize that some physical information is lost by using the traditional NLA for the low energy part of the EDF. In particular, information about the electron fluxes is not directly accessible. If this information is required one either has to resort to solving the full equation (2.2) or to calculating the first order correction of the traditional NLA which would yield information about the electron flux [58].

Our practical implementation of the hybrid model uses the following scheme. The low energy part the EDF is determined using the traditional NLA. The spatially averaged form of Eq. (2.2) is solved for the spatially uniform part of the EDF $F_0^0(\varepsilon)$. For our particular case, this equation is

$$(2.11) \quad -\frac{\partial}{\partial \varepsilon} \left(\frac{v^3}{3\nu_m} E_{eff}^2 \frac{\partial F_0^0}{\partial \varepsilon} \right) = \overline{v C_0(F_0^0)},$$

where $C_0(F_0^0)$ is the collision operator *including the Fokker-Planck operator*. The overlined quantities represent averages performed over the part of the volume V_{ac} which can be accessed by electrons with a given total energy, i.e. for which $\varepsilon \geq -\Phi(r, z)$. This means the average of a quantity G is defined as

$$(2.12) \quad \overline{G}(\varepsilon) = \frac{2\pi}{V_0} \int_{V_{ac}} G(\varepsilon, r, z) r dr dz.$$

Here V_0 represents the total volume of the discharge. The accessible volume V_{ac} is defined by:

$$(2.13) \quad u(r, z) \geq 0 \quad \text{or} \quad \varepsilon \geq -\Phi(r, z), \quad \forall (r, z) \text{ in } V_{ac}.$$

The boundary of V_{ac} is thus given by $u(\text{boundary}) = 0$ (see Fig. 1). The specific form of the averaged coefficients can be found in [49]. The space charge potential $\Phi(r, z)$ and the RF electric field $E(r, z)$, both of which are initially unknown, are required to calculate the spatially averaged coefficients. Initially, best guess starting profiles for these quantities are used which are then successively improved in an iterative scheme. Equation (2.11) is solved for the entire energy range considered, i.e., the "elastic" and the "inelastic" range. This is necessary since the evaluation of the Coulomb collisions operator also requires knowledge of the high energy part of the EDF. The boundary conditions for equation (2.11) are: $dF_0^0/d\varepsilon|_{\varepsilon=0} = 0$, and $F_0^0(\varepsilon_\infty) = 0$, where ε_∞ is the maximum energy considered. We typically solve equation (2.11) on a grid with an energy spacing of 0.035 eV to 0.05 eV and 1000 nodes. After having found F_0^0 over the entire energy range only the part with $\varepsilon \leq u^*$ is used further.

For the high energy part of the EDF ($\varepsilon > u^*$) the complete kinetic equation (2.2) is solved using successive over-relaxation (SOR). The boundary conditions for this equation have essentially been described by Busch and Kortshagen [29]. Briefly:

1. boundary at $r = 0$: $\partial F_0 / \partial r = 0$.
2. the three "wall boundaries" at $z = 0$, $z = H$ (plasma height), $r = R$ (plasma radius):
for energies ε less than the potential energy at the wall, $-\Phi_w$,

$$\partial F_0 / \partial n = 0$$

where n is the direction normal to the wall. For energies above $-\Phi_w$:

$$(2.14) \quad vF_0(\varepsilon, r, z)u^{1/2} \frac{\delta\Omega}{4\pi} = -u^{1/2}D_r(\varepsilon, r, z) \frac{\partial F_0}{\partial n}$$

with $D_r = 2eu/(3m_e\nu_m)$, and the solid angle $\delta\Omega$ of the loss cone in velocity space given by [29, 59]

$$(2.15) \quad \delta\Omega = 2\pi \left(1 - \sqrt{\frac{-\Phi_w + \Phi_{sh}}{\varepsilon + \Phi_{sh}}} \right)$$

with Φ_{sh} the potential at the sheath boundary. Condition (2.14) states that the fraction of the thermal flux of electrons scattered into the loss cone, which leads to loss of electrons to the wall (left hand side), has to be balanced by spatial flux towards this position (right hand side). In our model we assume nonconducting walls. The wall potential is found from the requirement of locally balanced electron flux (left hand side of Eq. (2.14) integrated over energy) with ion flux which is found from the ion fluid model discussed below [60]. The potential at the sheath boundary is also found from this model. Even though Eq. (2.15) is an approximation which relies on the somewhat arbitrary definition of a sheath boundary, it was proven useful and accurate in comparison with Monte Carlo calculations of the EDF [59].

3. Boundary $\varepsilon = u^*$:

$\partial F_0/\partial\varepsilon = \partial F_0^0/\partial\varepsilon$ from nonlocal solution to ensure continuity of the electron flux in energy space. (We have also experimented with the alternative boundary condition $F_0^0 = F_0$ at $\varepsilon = u^*$ which typically also yields a smooth transition of the EDF slope since deviations from the nonlocal behavior of the EDF set in gradually for energies only slightly above u^* .)

4. Boundary at maximum ε_∞ : $F_0(\varepsilon_\infty) = 0$.

Since we do expect only slight deviations from the fully nonlocal EDF, we use the nonlocal EDF F_0^0 as a starting point for the iterative solution. Equation (2.2) is then solved in three dimensions — radial and axial direction as well as total energy on a mesh of $32 \times 32 \times 50$ points, respectively. Since the discretization in energy with $\Delta\varepsilon = 0.5$ eV appears relatively coarse, we have also tested more accurate discretizations with $\Delta\varepsilon = 0.2$ eV and 125 points in energy directions without having found significant changes in the results. In our practical implementation of the hybrid model we divide the energy range not exactly at u^* but at the slightly lower energy of 11.0 eV. We also simplify the numerical treatment by considering the coefficients v^3/ν_m and $v^3/\nu_mE_{eff}^2(r, z)$ as slowly varying in coordinate and energy space, respectively, so that their derivatives can be neglected compared to those of $\partial F_0/\partial r$ and $\partial F_0/\partial\varepsilon$. We will relax this approximation in the future. The EDF F_0 determined from this model is used to compute the spatial profile of the ionization frequency.

Since the vast majority of the electrons at any time is found in the elastic energy range which is described by the nonlocal EDF, we use the "generalized Boltzmann relation" between electron density and ambipolar potential known from the traditional NLA [47]:

$$\begin{aligned}
 n(\Phi(r, z)) &= \int_0^\infty u^{1/2} F_0(u, r, z) du \\
 (2.16) \qquad &= \int_{-\Phi(r, z)}^\infty (\varepsilon + \Phi(r, z))^{1/2} F_0^0(\varepsilon) d\varepsilon.
 \end{aligned}$$

2.2. Ambipolar potential and RF field

The electron kinetics model is coupled to an ion fluid model and the wave equation for the RF electric field. The space charge potential in the plasma is determined by a fluid model for the ions. For a high-density plasma the assumption of a quasineutral plasma bulk is well fulfilled. If one limits the consideration to the description of the quasineutral plasma bulk up to the sheath boundary, the solution of the Poisson equation may be avoided and be replaced by using the quasineutrality conditions $n_i = n_e = n$. For pressures of a few Pa and discharge dimensions of several tens of centimeters, the ion motion is usually collision-dominated. Thus, assuming mobility-limited ion motion the ion momentum and continuity equation can be combined to

$$(2.17) \qquad -\nabla \cdot [n(r, z) b_i (|\nabla \Phi(r, z)|) \nabla \Phi(r, z)] = n(r, z) \nu_i(r, z),$$

where b_i denotes the field-dependent ion mobility (cf. Ref. [49]) and $\nu_i(r, z)$ denotes the local ionization frequency. This equation is solved subject to the boundary condition that the Bohm criterion has to be fulfilled at the sheath boundary $e|\nabla \Phi(r, z)|_{sb} \cdot \lambda_i = \frac{1}{2} k_B T_{e,scr}$. Here λ_i is the ion mean free path, k_B denotes the Boltzmann constant and $T_{e,scr} = -ek_B^{-1} (\partial \ln F_0^0(\varepsilon) / \partial \varepsilon|_{\varepsilon=\Phi_{sb}})^{-1}$ is the so called screening temperature [61]. We use the screening temperature found from the nonlocal EDF F_0^0 for simplicity. The plasma density $n(r, z)$ for a given potential $\Phi(r, z)$ can be found from Eq. (2.16). Equation (2.17) is thus a two-dimensional nonlinear differential equation for the ambipolar potential $\Phi(r, z)$.

The RF electric field for a rotationally symmetric ICP has only an azimuthal component, $\mathbf{E} = \tilde{E} \mathbf{e}_\theta$, which can be determined from the complex wave equation. Assuming a harmonic time-dependence of the electric field we get:

$$(2.18) \qquad \left(\nabla^2 - \frac{\omega^2}{c^2} \right) \tilde{E}(r, z) = i\omega\mu_0 \left(\sigma(r, z) \tilde{E}(r, z) + j_{coil} \right).$$

Here c is the vacuum speed of light, μ_0 is the vacuum permeability. The symbol j_{coil} is the coil current density and $\sigma(r, z)$ is the kinetic conductivity of the plasma [49]. The solution of this equation is strongly simplified by the assumption of metallic walls at $r = 2R$, $z = 0$, and $z = 2H$, so that zero boundary conditions can be used at these boundaries. On axis ($r = 0$) the azimuthal field is also zero.

Both equations (2.17) and (2.18) are solved on a 64x64 mesh in radial and axial direction using a multigrid solver [62].

The iterative numerical scheme used to find a self-consistent solution of this set of equations has been described in great detail in Ref. [49] so that we provide only a brief sketch here: The computation starts with an initial guess for the plasma density profile and potential profile: a Bessel function variation in radial and a cosine profile in axial direction for the density and a flat potential profile $\Phi(r, z) = 0$ for the potential. (We use this starting potential, since we do not want to bias the algorithm to converge to a certain solution. Even though we have not observed multiple solutions also using other starting potentials, the existence of other solutions seems at least possible. Multiple solutions might manifest in actual experiments as mode transitions or jumps between different plasma density profiles). Using the initial plasma density profile we find the RF electric field profile by solving equation (2.18) assuming a cold-plasma Lorentz conductivity. A self-consistent set of EDF, potential, and RF field profile is found in an iterative scheme which uses three nested loops: In the innermost loop the EDF is determined by solving the "hybrid" model for a given coil current. Here, the SOR scheme to solve equation (2.2) is iterated until the relative change in the ionization frequency between two successive iterations at the middle of the r-z plane is less than 10^{-6} . Then the complete ionization profile is calculated. The potential profile resulting from this ionization profile is found from Eq. (2.17). The purpose of the innermost loop is to adjust the coil current such that the Bohm criterion is fulfilled at the sheath boundary. Once this is achieved, the resulting potential replaces the initial potential profile in the next-outer loop. The loop of updating the potential is repeated until the sum over the squared changes between two successive potentials taken at all 4096 potential nodes is less than 1.0. Finally, if a self-consistent potential profile has been found the RF field profile is iterated in the outermost loop using the same convergence criterion as for the potential profiles.

The use of the various approximations described above enables a very efficient modeling of the discharge. Typical computation times for a given set of parameters are of the order of a few minutes up to 20 minutes on a Pentium II class computer.

3. Experimental setup

A sketch of the experimental setup is shown in Fig. 2. The measurements have been performed in an inductively coupled plasma which is sustained in a Pyrex chamber with 14 cm inner radius. The top wall of the chamber is a flat 2.2 cm thick Pyrex plate. The bottom plate is a grounded, movable sheet metal which enable us to vary the discharge height between 5 - 11 cm. Here height was set to 7cm. A punched hole pattern in the metal plate allows pumping with a 1000 liter/s turbo pump as well as inlet of argon gas. Three induction coils with inner/outer radius of 3 cm/5 cm, 7 cm/9 cm, and 11 cm/13 cm allow variable coil combinations. Here we present only results for plasma excitation with the outermost coil. The coil is Faraday shielded to eliminate electrostatic coupling to the plasmas.

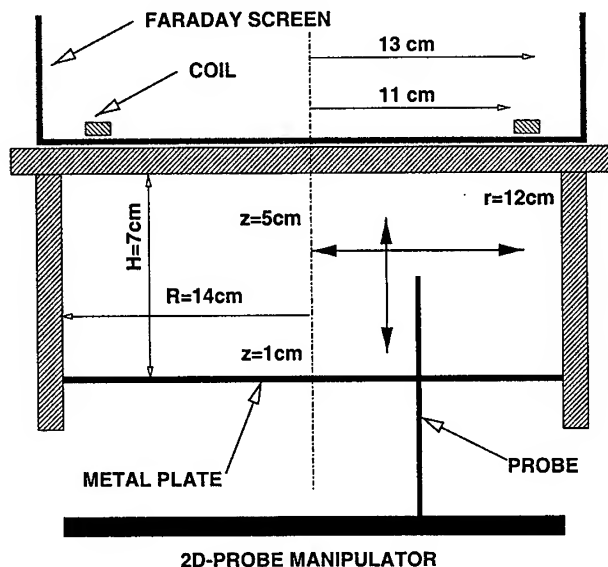


FIG. 2. Scheme of the experimental setup.

A Langmuir probe with 5 mm length and 0.125 mm diameter is introduced into the discharge through a radial slit in the bottom plate. A computer-controlled two-dimensional r - z probe manipulator enables fully automated two-dimensional probe scans of the EDF. In this study the probe was moved in an area of $r = 0 - 12$ cm (from axis) and $z = 1 - 5$ cm (from bottom plate) with a resolution of 1 cm in each direction. At each position typically 10000 probe characteristics were sampled and averaged with a fast 16 bit A/D card. The EDF is obtained using the Druyvesteyn formula [63] and absolute units. Integration of the EDF over energy yields the electron density [19].

4. Results

Fig. 3 and 4 show two-dimensional surface plots of measured EDF's in argon at 5 mTorr and 19.4 mTorr, respectively. The surface plots depict the EDF's at a given total energy, which is given by the negative of the probe voltage referenced to the absolute maximum of the plasma potential in the discharge. The EDF's are normalized to the volume averaged EDF: $\langle F_0 \rangle(\epsilon) = \int_{z_{min}}^{z_{max}} \int_0^{r_{max}} r F_0(\epsilon, r) dr dz / \int_{z_{min}}^{z_{max}} \int_0^{r_{max}} r dr dz$, which corresponds to the value of the nonlocal EDF [47]. Fig. 3 shows that the EDF at 5 mTorr is spatially almost constant at all energies which corresponds to the nonlocal limit for the EDF. At a total energy of 10 eV electrons only perform elastic collisions while at 17 eV inelastic collisions have a strong influence on the EDF. At 5 mTorr and 10 eV $\lambda_e \approx 12$ m and at 17 eV $\lambda_e \approx 26$ cm which exceeds the discharge radius in both cases. The maximum deviation from the nonlocal average is about or below 20% for all energies shown. At 19.4 mTorr (Fig. 4) significant deviations from the

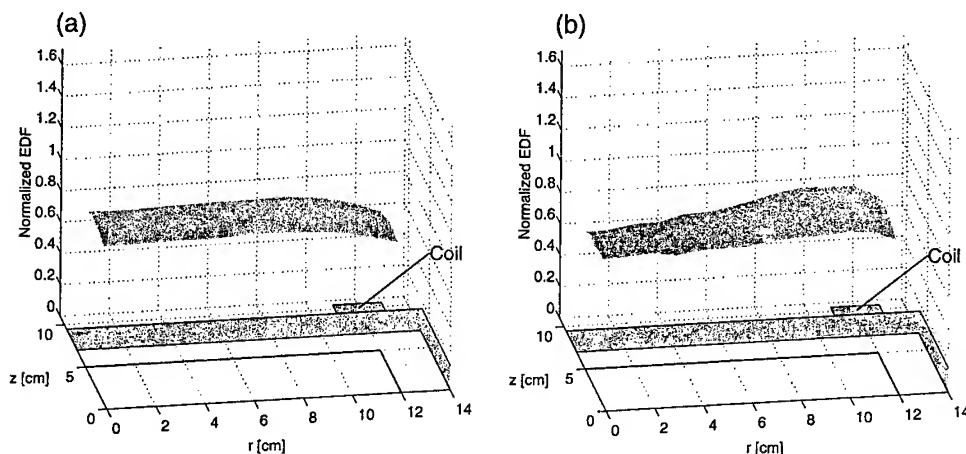


FIG. 3. Surface plots of EDF at 5 mTorr at two different total energies: (a) 10 eV, (b) 17 eV.

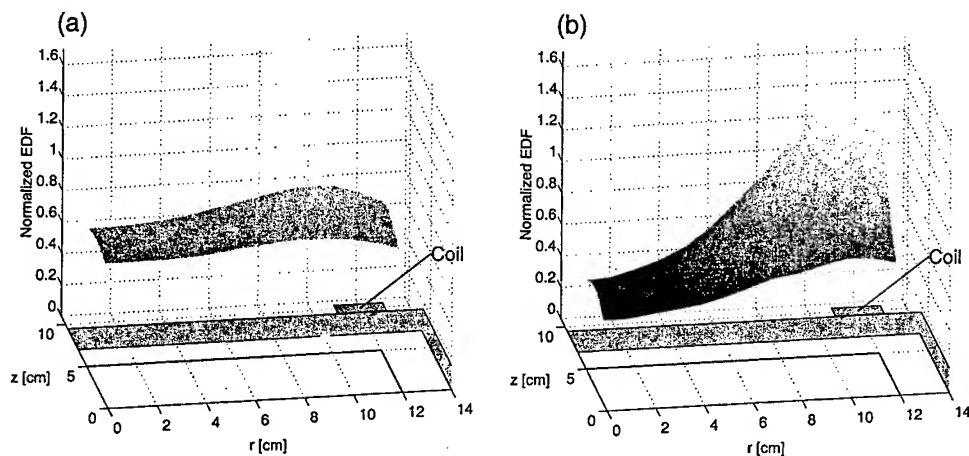


FIG. 4. Surface plots of EDF at 19.4 mTorr at two different total energies: (a) 10 eV, (b) 17 eV.

nonlocal average are visible at 17 eV. The EDF is elevated over the average value in regions of high RF electric fields. It decreases sharply towards regions of low electric field strength. For these energies $\lambda_E \approx 6$ cm which is smaller than the discharge radius. For 10 eV, however, the EDF is still almost constant across the discharge cross section. Since $\lambda_E \approx 3$ m for this energy, the elastic body of the EDF can still be considered nonlocal. The slight elevation of the EDF in regions of high electric field strength is favored by the strongly inhomogeneous RF field in the inductive discharge. Obviously, the EDF at 19.4 mTorr shows precisely the “hybrid” behavior which underlies our hybrid model: the elastic body of the EDF is (almost) nonlocal while significant deviations from the nonlocal average exist at energies in the inelastic part of the EDF.

In Fig. 5 we present a comparison of measured and calculated electron density profiles at pressures of 10 and 20 mTorr. The measurements show that with

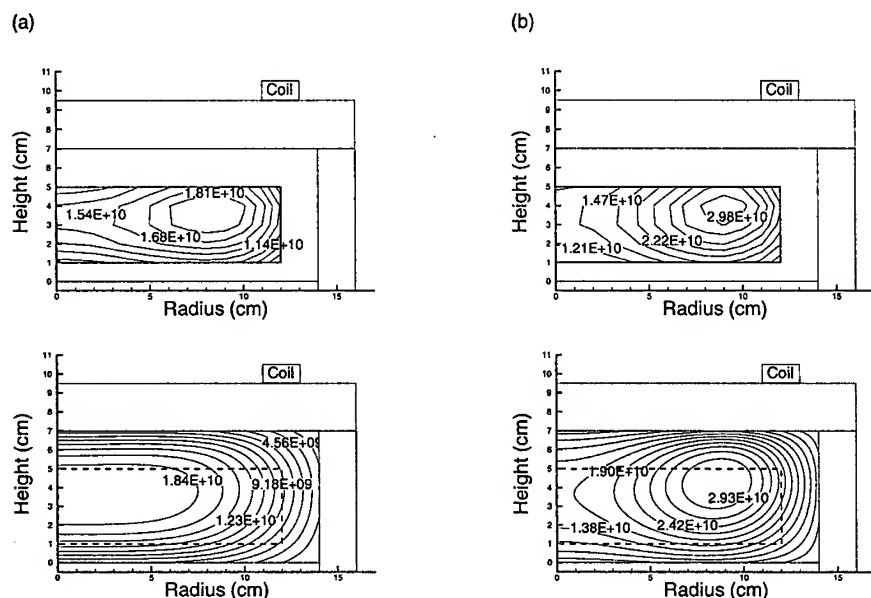


FIG. 5. Electron density profiles at (a) 10 mTorr, and (b) 20 mTorr. The upper graphs show experimental data, the lower graphs show results of the model. The dashed lines in the lower graphs mark the region accessible to the Langmuir probe. The electron densities are given in cm^{-3} .

increasing pressure the density profiles become more nonuniform and the position of the density maximum shifts to slightly larger radii. At 10 mTorr the variation between the maximum and the on-axis density is about 25%, at 20 mTorr it is already a factor of more than 2. The results of our model reflect the general trend reasonably well. The model produces slightly more uniform density profiles at 10 mTorr. A slight shift of the maximum from the axis is observed at 10 mTorr. The overall variation of the density over the range accessible to the Langmuir probe is about the same as observed in the measurements. The best agreement between model and measurements is found at 20 mTorr for which a purely nonlocal model would be least applicable. Both the position of the density maximum as well as the variation of the density between maximum and on-axis position is almost identical.

It should also be pointed out that the hybrid model presents a significant progress over models based on the traditional NLA since it is capable of describing the shift of the density maximum to an off-axis position with increasing pressure. A model based on the traditional NLA would typically always produce on-axis maxima of the density profile.

Fig. 6 shows a comparison of measured and calculated plasma potential profiles. First, the very good agreement between the calculated and measured absolute values of the plasma potential should be pointed out. The maximum

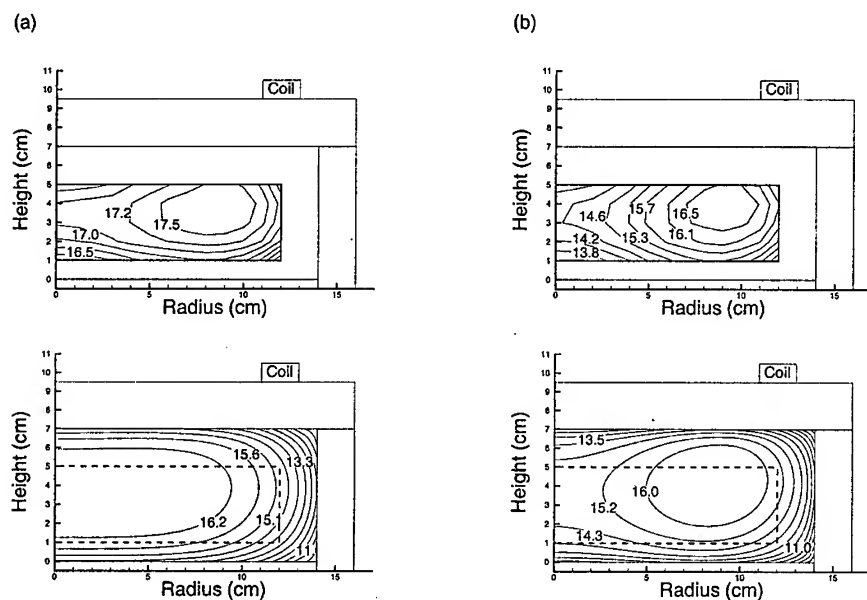


FIG. 6. Plasma potential profiles in volts at (a) 10 mTorr, (b) 20 mTorr. The upper graphs show experimental data, the lower graphs show results of the model.

values of the potentials related to the wall potential are: 17.75 V (exp.) and 16.8 V (model) at 10 mTorr, and 16.86 V (exp.) and 16.85 V (model) at 20 mTorr. Again, the best agreement between experiment and model is found at the highest pressure of 20 mTorr. Of course, the profiles of the potential mainly reflect the electron density profiles since electron density and potential are related to each other by the generalized Boltzmann relation (2.16).

The experimental and calculated profiles of the mean kinetic energy of the EDF's are plotted in Fig. 7. Experiment and model show the same trend of an increasing mean kinetic energy towards the region of high RF electric field. The general trend of a slight increase of the mean energy if moving away from the position of the maximum plasma potential can be explained with a "nonlocal" cutting of the low energy part of the EDF which has a slightly lower "temperature" than the part of the EDF between 5 - 10 eV. The best agreement is again found at 20 mTorr. It has to be noted that we estimate the error in the measured mean energies to be about 10% due to the limited number of current-voltage points recorded and the inaccuracy involved in the integration of the EDF.

Finally, we want to make some comments about electron fluxes. In a recent study, Kortshagen and Lawler [64] have shown that interesting flux pattern can arise in positive column plasmas, if the energy-resolved electron fluxes are considered. In a positive column plasmas, it can be shown that fluxes of electrons with a total energy of less than the first excitation threshold energy are outward directed. However, for electrons with a kinetic energy higher than the excita-

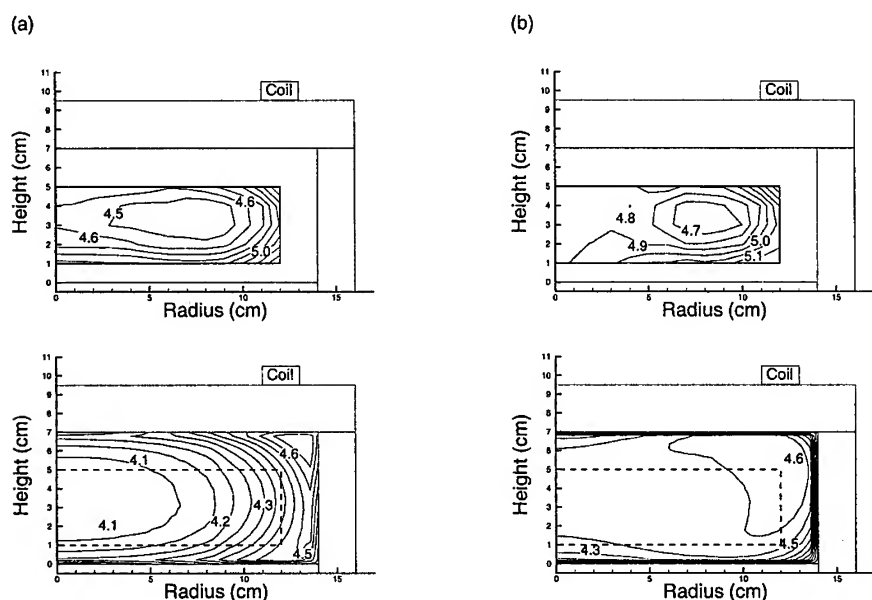


FIG. 7. Profiles of the mean kinetic energy in eV at (a) 10 mTorr, (b) 20 mTorr. The upper graphs show experimental data, the lower graphs show results of the model.

tion threshold line in Fig. 1 fluxes can be inward directed. The reason for this is that inelastic collisions act as a sink or absorption process for high energy electrons, since the electrons lose almost their entire kinetic energy and are "reemitted" as low energy electrons. Since in positive column plasmas the maximum of the plasma potential is found on axis, the maximum sink of high energetic electrons and the maximum source of low energy electrons is located around the axis, leading to the flux pattern discussed above. Some initial results of our studies of the ICP indicate that there are similarly interesting effects to be expected in this two-dimensional system. In particular, it is possible to find conditions under which the maximum of the plasma potential is still located on axis of the discharge, while the maximum heating of electrons occurs close the RF coil, as observed in Fig. 4(b). Under these conditions, it seems likely that at low total energies we will find electron fluxes which originate in the central region of the discharge around the axis, due to the maximum of low energy electron generation at the potential maximum. For total high energies, the origin of the fluxes is expected to shift towards the RF coil, since the strong RF field now provides the main source of high energy electrons while inelastic collisions around the axis provide a sink. This effect will be discussed in more detail in a forthcoming publication.

5. Conclusions

In this paper we have presented an efficient, two-dimensional kinetic model based on a hybrid kinetic approach to the solution of the Boltzmann equation. In this

approach the domain of integration of the Boltzmann equation is divided into two subdomains: The low energy "elastic" range is treated within the traditional nonlocal approximation. The high energy inelastic range is treated by solving the complete kinetic equation derived from the Boltzmann equation as a partial differential equation in two space dimensions and in total energy. Coulomb collisions are taken into account for the low energy, nonlocal part of the EDF in which these collisions are effective since they compete only with "weak" elastic collisions. In the high energy part Coulomb collisions are neglected since the Coulomb cross section is smaller and the Coulomb collisions compete with "strong" inelastic collisions [57]. This approach offers two main advantages: (a) The high energy domain, in which the complete kinetic equation is integrated, typically has a regular shape which simplifies the numerical formulation, and (b) the non-linearity introduced by Coulomb collisions can be avoided in the treatment of the full, multi-dimensional kinetic equation. It is only included in the much simpler problem of solving the nonlocal kinetic equation which is one-dimensional. The use of the hybrid model seems promising for fast engineering-type calculations in which basic information about plasma uniformity, mean kinetic energy and potential is required. Complete kinetic, self-consistent two-dimensional simulations can be performed in computation times of less than 20 minutes on Pentium II class computers.

Comparisons of our model with an actual experiment showed reasonable agreement. The best agreement was typically found at the highest pressure considered, a pressure at which a model based on the traditional NLA for the given discharge dimensions would certainly fail. Our model proved well capable of describing effects which are related to increasing deviations from a fully nonlocal EDF such as the shift of the maxima of plasma potential and plasma density to off-axis positions with increasing pressures.

However, to describe more detailed physical effects such as fluxes of electrons in energy space, a more sophisticated treatment of the Boltzmann equation is required. This would include Coulomb collisions over the entire energy range and a complete treatment of the low-energy part. Work on this topic for two-dimensional geometry is in progress and will be reported in future publications.

Acknowledgments

This work was supported by the National Science Foundation under grant ECS-9713137 and by the University of Minnesota Supercomputing Institute.

References

1. V. VAHEDI, C.K. BIRDSALL, M.A. LIEBERMANN, G. DIPESO and T.D. ROGNLIEN, *Verification of frequency scaling laws for capacitive radio-frequency discharges using two-dimensional simulations*, Phys. Fluids B, 5, 2719, 1993.
2. V. VAHEDI, G. DIPESO, C.K. BIRDSALL, M.A. LIEBERMANN and T.D. ROGNLIEN, *Capacitive rf discharges modelled by particle-in-cell Monte Carlo simulation. I: Analysis of numerical techniques*, Plasma Sources Sci. Technol., 2, 261, 1993.
3. M.J. KUSHNER, *Monte-Carlo simulation of electron properties in rf parallel plate capacitively coupled discharges*, J. Appl. Phys., 54, 4958, 1983.

4. M.J. KUSHNER, *Distribution of ion energies incident on electrodes in capacitively coupled rf discharges*, J. Appl. Phys., **58**, 4024, 1985.
5. M. SURENDRA, D.B. GRAVES and I.J. MOREY, *Electron heating in low-pressure rf glow discharge*, Appl. Phys. Lett., **56**, 1022, 1990.
6. M.SURENDRA and D.B. GRAVES, *Capacitively coupled glow discharge at frequencies above 13.56 MHz*, Appl. Phys. Lett., **59**, 2091, 1991.
7. R.W. BOSWELL and I.J. MOREY, *Self-consistent simulation of parallel-plate rf discharge*, Appl. Phys. Lett., **52**, 21, 1988.
8. J.D. BUKOWSKI, D.B. GRAVES and P. VITELLO, *Two-dimensional fluid model of an inductively coupled plasma with comparison to experimental spatial profiles*, J. Appl. Phys., **80**, 2614, 1996.
9. G. DIPESO, V.VAHEDI, D.W. HEWETT and T.D. ROGNLIEN, *Two-dimensional self-consistent fluid simulation of radio frequency inductive sources*, J. Vac. Sci. Technol., A, **12**, 1387, 1994.
10. P. VITELLO, J.N. BARDSLEY, G. DIPESO and G.J. PARKER, *Modeling an inductively coupled plasma reactor with chlorine chemistry*, IEEE Trans. Plasma Sci., **24**, 123, 1996.
11. D.J. ECONOMOU, T.J. BARTEL, R.S. WISE and D.P. LYMBERLOPOULOS, *Two-dimensional direct simulation Monte-Carlo (DSMC) of reactive neutral and ion flow in a high density plasma reactor*, IEEE Trans. Plasma Sci., **23**, 581, 1995.
12. D.P. LYMBERLOPOULOS and D.J. ECONOMOU, *Two-dimensional simulation of polysilicon etching with chlorine in a high density plasma reactor*, IEEE Trans. Plasma Sci., **23**, 573, 1995.
13. R.A. STEWART, P. VITELLO and D.B. GRAVES, *Two-dimensional fluid model of high density inductively coupled plasma sources*, J. Vac. Sci. Technol. B, **12**, 478, 1994.
14. V. VAHEDI, M.A. LIEBERMAN, G. DIPESO, T.D. ROGNLIEN and D. HEWETT, *Analytic model of power deposition in inductively coupled plasma sources*, J. Appl. Phys., **78**, 1446, 1995.
15. R.S. WISE, D.P. LYMBERLOPOULOS and D.J. ECONOMOU, *Rapid two-dimensional self-consistent simulation of inductively coupled plasma and comparison with experimental data*, Appl. Phys. Lett., **68**, 499, 1996.
16. M.J. KUSHNER, W.Z. COLLISON, M.J. GRAPPERHAUS, J.P. HOLLAND and M.S. BARNES, *A three-dimensional model for inductively coupled plasma etching reactors: Azimuthal symmetry, coil properties, and comparison to experiments*, J. Appl. Phys., **80**, 1337, 1996.
17. V.A. GODYAK and R.B. PIEJAK, *Abnormally low electron energy and heating-mode transition in low-pressure argon rf discharge at 13.56 MHz*, Phys. Rev. Lett., **65**, 96, 1990.
18. V.A. GODYAK, R.B. PIEJAK and B.M. ALEXANDROVICH, *Evolution of electron-energy-distribution function during rf discharge transition to the high-voltage mode*, Phys. Rev. Lett., **68**, 40, 1992.
19. V.A. GODYAK, R.B. PIEJAK and B.M. ALEXANDROVICH, *Measurements of electron energy distributions in low-pressure rf discharges*, Plasma Sources Sci. Technol., **1**, 36, 1992.
20. U. KORTSHAGEN and H. SCHLUTER, *Determination of the electron energy distribution function in surface wave produced plasma: II. measurements*, J. Phys. D: Appl. Phys., **24**, 1584, 1991.
21. U. KORTSHAGEN, *Experimental evidence on the nonlocality of the electron distribution function*, Phys. Rev. E, **49**, 4369, 1994.
22. J. BRETAGNE, W.G. GRAHAM and M.B. HOPKINS, *A comparison of experimental and theoretical electron energy distribution functions in a multicusp ion source*, J. Phys. D: Appl. Phys., **24**, 668, 1991.
23. C.M. FERREIRA and J. LOUREIRO, *Electron energy distribution and excitation rates in high-frequency argon discharges*, J. Phys. D: Appl. Phys., **16**, 2471, 1983.
24. A.B. SA, C.M. FERREIRA, S. PASQUIERS, C. BOISSE-LAPORTE, P. LEPRINCE and J. MAREC, *Self-consistent modeling of surface wave produced discharges at low pressures*, J. Appl. Phys., **70**, 4147, 1991.
25. R. WINKLER, H. DEUTSCH, J. WILHELM and Ch. WILKE, *Electron kinetics of weakly ionized hf plasmas. i. direct treatment and Fourier expansion*, Beitr. Plasmaphys., **24**, 285, 1984.

26. R. WINKLER, J. WILHELM and A. HESS, *Main features of electron kinetics in collision dominated steady-state rf plasmas*, Ann. Phys., **42**, 537, 1985.
27. R. WINKLER, M. CAPITELLI, M. DILONARDO, C. GORSE and J. WILHELM, *Electron kinetics of weakly ionized collision-dominated rf plasmas in CO*, Plasma Chem. Plasma Proc., **6**, 437, 1986.
28. M.J. HARTIG and M.J. KUSHNER, *Radially dependent solutions of Boltzmann's equation in low-temperature plasmas using a modified two-term expansion*, J. Appl. Phys., **73**, 1080, 1993.
29. C. BUSCH and U. KORTSHAGEN, *Numerical solution of the spatially inhomogeneous Boltzmann equation and verification of the nonlocal approach*, Phys. Rev. E, **51**, 280, 1995.
30. D. UHRLANDT and R. WINKLER, *Radially inhomogeneous electron kinetics in the dc column plasma*, J. Phys. D: Appl. Phys., **29**, 115, 1996.
31. I.B. BERNSTEIN and T. HOLSTEIN, *Electron energy distributions in stationary discharges*, Phys. Rev., **94**, 1475, 1954.
32. L.D. TSENDIN, *Energy distribution of electrons in a weakly ionized current-carrying plasma with a transverse inhomogeneity*, Sov. Phys. JETP, **39**, 805, 1974.
33. V.A. GODYAK and R. B. PIEJAK, *Paradoxical spatial distribution of the electron temperature in a low pressure rf discharge*, Appl. Phys. Lett., **63**, 3137, 1993.
34. V.A. GODYAK and V.I. KOLOBOV, *Negative power absorption in inductively coupled plasmas*, Phys. Rev. Lett., **79**, 4589, 1997.
35. V.A. GODYAK and R.B. PIEJAK, *Electromagnetic field structure in a weakly collisional inductively coupled plasmas*, J. Appl. Phys., **82**, 5944, 1997.
36. I.D. KAGANOVICH and L.D. TSENDIN, *Low-pressure rf discharge in the free-flight regime*, IEEE Trans. Plasma Sci., **20**, 86, 1992.
37. I.D. KAGANOVICH, I.V. KOLOBOV and L.D. TSENDIN, *Stochastic electron heating in bounded radio-frequency plasmas*, Appl. Phys. Lett., **69**, 3818, 1996.
38. V. KOLOBOV, L.D. LYMBERPOULOS and D.J. ECONOMOU, *Electron kinetics and non-Joule heating in near-collisionless inductively coupled plasmas*, Phys. Rev. E, **55**, 3408, 1997.
39. V.A. GODYAK and V.I. KOLOBOV, *Effect of collisionless heating on electron energy distribution in an inductively coupled plasma*, Phys. Rev. Lett., **81**, 369, 1998.
40. V.A. GODYAK, R.B. PIEJAK, B.M. ALEXANDROVICH and V.I. KOLOBOV, *Experimental evidence of collisionless power absorption in inductively coupled plasmas*, Phys. Rev. Lett., **80**, 3264, 1998.
41. R.H. COHEN and T.D. ROGNLIEN, *Electron kinetics in radio-frequency magnetic fields of inductive plasma sources*, Plasma Sources Sci. Technol., **5**, 442, 1996.
42. J.-P. BOEUF and E. MARODE, *A Monte-Carlo analysis of an electron swarm in a non-uniform field: the cathode region of a glow discharge in helium*, J. Phys. D: Appl. Phys., **15**, 2169, 1982.
43. C.K. BIRDSALL, *Particle-in-cell charged-particle simulations, plus Monte Carlo collisions with neutral atoms, PIC-MCC*, IEEE Trans. Plasma Sci., **19**, 65, 1991.
44. W.N.G. HITCHON, D.J. KOCH and J.B. ADAMS, *An efficient scheme for convection-dominated transport*, J. of Comput. Phys., **83**, 79, 1989.
45. W.N.G. HITCHON, G.J. PARKER and J.E. LAWLER, *Physical and numerical verification of discharge calculations*, IEEE Trans. Plasma Sci., **21**, 228, 1993.
46. L.L. ALVES, G. GOUSSET and C.M. FERREIRA, *Self-contained solution to the spatially inhomogeneous boltzmann equation in a cylindrical plasma positive column*, Phys. Rev. E, **55**, 890, 1997.
47. U. KORTSHAGEN, C. BUSCH and L.D. TSENDIN, *On simplifying approaches to the solution of the Boltzmann equation in spatially inhomogeneous plasmas*, Plasma Sources Sci. Technol., **5**, 1, 1996.
48. L.D. TSENDIN, *Electron kinetics in non-uniform glow discharge plasmas*, Plasma Sources Sci. Technol., **4**, 200, 1995.

49. U. KORTSHAGEN, I. PUKROPSKI and L.D. TSENDIN, *Experimental investigation and fast two-dimensional self-consistent modelling of a low pressure inductively coupled rf discharge*, Phys. Rev. E, **51**, 6063, 1995.
50. V.I. KOLOBOV, D.F. BEALE, L.J. MAHONEY and A.E. WENDT, *Nonlocal electron kinetics in a low-pressure inductively coupled radio-frequency discharge*, Appl. Phys. Lett., **65**, 537, 1994.
51. V. KOLOBOV and W.N.G. HITCHON, *Electron distribution function in a low-pressure inductively coupled plasma*, Phys. Rev. E, **52**, 972, 1995.
52. S.V. BEREZHNOI, I.D. KAGANOVICH and L.D. TSENDIN, *Fast modelling of the low-pressure radio-frequency collisional capacitively coupled discharge and investigation of the formation of a non-Maxwellian electron distribution function*, Plasma Sources Sci. Technol., **7**, 268, 1998.
53. I.P. SHKAROFSKY, T.W. JOHNSTON and M.P. BACHYNSKI, *The Particle Kinetics of Plasmas*, Addison-Wesley, Reading, MA, 1966.
54. L.D. TSENDIN, *Electron energy distribution in rf electric field*, Sov. Phys. Tech. Phys., **22**, 925, 1977.
55. S. YOSHIDA, A.V. PHELPS and L.C. PITCHFORD, *Effect of electrons produced by ionization on calculated electron-energy distributions*, Phys. Rev. A, **27**, 2858, 1983.
56. H. DREICER, *Electron velocity distributions in a partially ionized gas*, Phys. Rev., **117**, 343, 1960.
57. U. KORTSHAGEN and H. SCHLUTER, *On the influence of Coulomb collisions on the electron energy distribution function in surface wave produced plasmas argon plasmas*, J. Phys. D: Appl. Phys., **25**, 644, 1992.
58. G.J. PARKER and D. UHRLANDT, *Investigation of non-local approach in positive column discharges*, Bull. Americ. Phys. Society, **43**, 1479, 1998.
59. U. KORTSHAGEN, G.J. PARKER and J.E. LAWLER, *Comparison of nonlocal calculations and Monte-Carlo simulations of the electron distribution function in a positive column*, Phys. Rev., E, **54**, 6746, 1996.
60. U. KORTSHAGEN, *Kinetic modeling of the charging of nonconducting walls in a low pressure inductively coupled plasma*, J. Vac. Sci. Technol. A, **16**, 300, 1998.
61. K.U. RIEMANN, *The Bohm criterion and sheath formation*, J. Phys. D: Appl. Phys., **24**, 493, 1991.
62. W. HACKBUSCH, *Multi-Grid Methods and Applications*, Springer, Berlin, 1985.
63. M.J. DRUYVESTEYN, *Der niedervoltbogen*, Z. Phys., **64**, 781, 1930.
64. U. KORTSHAGEN and J.E. LAWLER, *Energy-resolved electron particle and energy fluxes in positive column plasmas*, J. Phys. D: Appl. Phys., 1999.

MODELING AND DIAGNOSTICS OF TWO-FREQUENCY PULSED CCP AND RELATED CHARGING IN THE MICROSTRUCTURE OF SiO₂ TRENCH

T. MAKABE

DEPARTMENT OF ELECTRONICS AND ELECTRICAL ENGINEERING KEIO UNIVERSITY
Yokohama 223-8522 JAPAN

More than a decade after low temperature plasma modeling was introduced in the field of semiconductor device fabrication for the design and development of a plasma reactor, modeling has passed into a new phase in a prediction for plasma processing. Fine pattern etching of SiO₂ is executed mainly by using two-frequency capacitively coupled plasma (2f-CCP) in perfluorocarbon. Herein, the plasma structure and the functions of 2f-CCP are reviewed and discussed based on the plasma modeling and the computerized tomography (CT) image.

1. Introduction

Great success in large scale integrated circuits (LSI) in the 1990s has depended primarily on plasma processing technology; i.e., fine pattern etching. High efficiency etching of nanometer pattern size by using a high density plasma is one of several recent trends [1]. A low temperature (nonequilibrium) plasma source for microelectronic device fabrications is produced by different excitation mechanisms by using reactors classified into three groups and power coupling these with plasmas. These groups are respectively termed capacitively coupled plasma (CCP), inductively coupled plasma (ICP), and antenna coupled plasma (ACP).

CCP is maintained by a voltage source driven by a radio frequency (rf). Plasma density proportional to the square of the frequency is obtained by changing from high frequency (HF) to very high frequency (VHF) at the constant amplitude of the applied voltage [2, 3, 4]. The upper frequency in CCP will be limited technically by a smooth coupling with the electrode. High density CCP driven by VHF, 100 MHz, will be within the possible range [5, 6]. Plasma production in CCP is realized by the wave-riding of the reflected electrons in the strong positive ion sheath at mid-pressure, and stochastic heating of electrons will be expected over the bulk plasma at low pressure.

High energy ions accelerated by a strong ion sheath are appropriate for the ion-assisted oxide etching. The modern reactive ion etcher (RIE) is composed of

a two frequency (2f)-CCP with two different functions; i.e., plasma production and ion acceleration [1, 6]. Each function should be controlled independently. A 2f-CCP consisting of a VHF (or HF) powered-electrode for plasma production and a low frequency (LF) bias-electrode for ion acceleration to the wafer is a promising process reactor practical for SiO_2 etching[7, 8] (See Fig. 1).

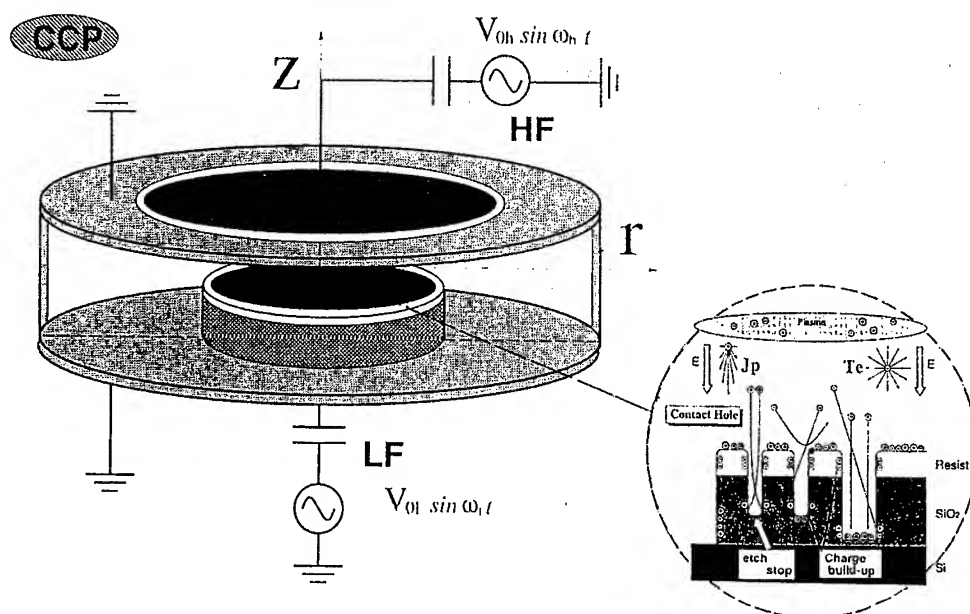


FIG. 1. Two frequency plasma reactor for oxide etching.

ICP is sustained by an external rf current source, and has the advantage of being high density with a low and thin sheath even at 13.56 MHz. It is appropriate for metal etching under conditions of low energy and a high flux of ions. The size-dependence of wafer processing uniformity on the equipment will be much more complicated in the mode of high bias voltage operation on the wafer, as compared with that of CCP, in which plasma is confined between parallel plates.

In this paper, the capability to predict a plasma structure and the function of 2f-CCP will be reviewed and discussed by means of a comparison between the numerical modeling and the experimental computerized tomography (CT) images in the oxide etching system at low pressure in CF_4/Ar .

2. Numerical modeling

2.1. System and governing equations

Low temperature plasma is produced mainly by the electron impact ionization of a feed gas molecule, and it is essential to describe the electron kinetics and the transport in the gas as precisely as possible. Under these circumstances,

low temperature plasma will be modeled by using the system of the Boltzmann equation (classical statistics) and Maxwell's equations under the database of the collision cross section and the reaction rate of the electron and positive and negative ions both in the gas phase and on the surface, subject to quantum physics under an appropriate boundary condition (See Fig. 2). The specific boundary conditions, caused by the kinetic and/or chemical energy of ions and neutral radicals, act on the surface etching or deposition of materials in a masked pattern.

Governing Equation System in Plasma Reactor

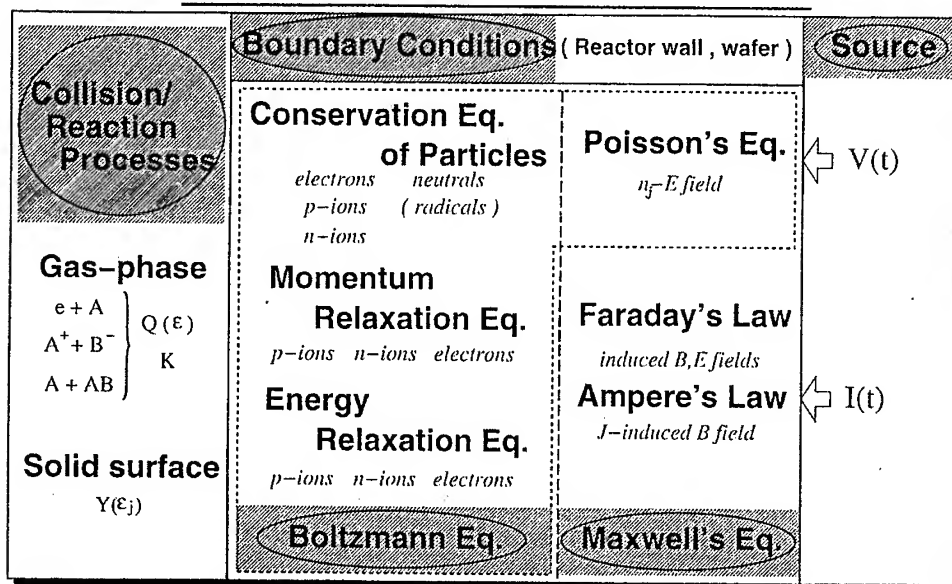


FIG. 2. Governing equation systems and related quantities.

In the pressure region where the mean free path L_e of the electron is much smaller than the reactor scale d , plasma is controlled mainly by the collision processes of the electron with the feed gas and its fragments. However, when the condition $L_e > d$ is realized under a condition of low pressure, the collision and reaction processes of charged particles and neutrals on the surface of the reactor and the electrodes, and on the wafer, will make a key contribution to the spatial plasma profile. In this context, the boundary condition is closely connected with the plasma structure. A large number of electrons are known to be effectively reflected or ejected on a metal or dielectric surface (see Fig. 3) [9]. The plasma structure is under the influence of the reflected or ejected electrons. More than several tens of percentages of electrons will be elastically reflected. This implies that a continuum model with swarm parameters will still be available even for a low pressure region with $L_e \sim d$.

Regarding a pressure range of application of the continuum model, it should be noted that the electron is spatially trapped with increasing frequency ω and

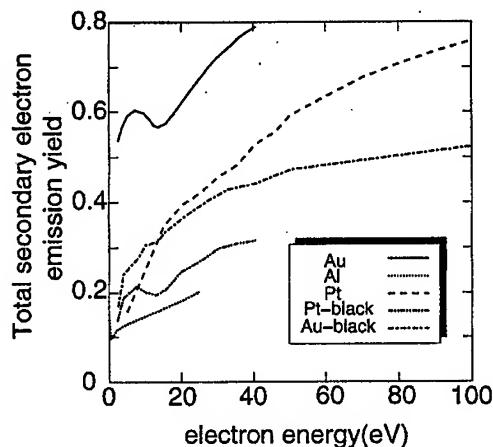


FIG. 3. Secondary electron emission yield on metals.

under a strong magnetic field B , which are applied externally in a plasma reactor. This condition will be qualitatively equivalent to a pressure increase from p to effective

$$p[1 + (\omega/R_m)^2]^{1/2}, \quad p[1 + (B/R_m)^2]^{1/2},$$

where R_m is the total collision rate of electrons.

Validity of a continuum model will be extended to lower pressure plasma sustained by a (V)HF source with/without a magnetic field surrounded by an elastic boundary layer. In our investigation, the relaxation continuum (RCT) model proposed in previous paper [10, 11] is employed to predict and to design the plasma structure and function.

2.2. Database needed for modeling

Plasma etching uses a chemically active electronegative feed gas. Perfluorocarbon (PFC) is usually used for oxide etching. CF_4 , the most simple PFC, is employed with a mixture of Ar; this selection was based on the presence of a database appropriate for the electron, ions and neutral fragments. Fig. 4(a) shows the set of cross sections of Ar and CF_4 used in this work, and the collision rates in $\text{CF}_4(5\%)/\text{Ar}$ mixture, derived from the direct numerical procedure of the Boltzmann equation [12], are described in Fig. 4(b) at 1 Torr as a function of dc- E/N over a wide range[13].

A long-lived excited molecule and dissociated neutrals may accumulate in a plasma reactor up to an amount comparable to that of the feed gas. It is important to consider the possibility of a heavy particle reaction of the ion, metastable molecule, and dissociative species produced by the collision between the electron and the feed gas. The collision/reaction processes and the rates considered here are listed in Table 1.

Table 1. Collision/reaction processes and the rates considered in CF₄/Ar.Charged Species: e, Ar⁺, CF₃⁺, F⁻Neutrals(sticking): CF₄(0), CF₃(0.001), CF₂(0.01), CF(0.1), F(0.005), F₂(0)

<i>Electron Collisions</i>				
Ar + e	→	Ar ⁺ + 2e	$k_i[E/N]$	Ionization
CF ₄ + e	→	CF ₃ ⁺ + F + 2e	$k_i[E/N]$	Ionization
CF ₄ + e	→	CF ₃ + F ⁻	$k_{a2}[E/N]$	Disso. Attachment
F ₂ + e	→	F + F ⁻	$k_{a2}[E/N]$	Disso. Attachment
Ar ⁺ + e	→	Ar	k_{re1}	$1.0 \cdot 10^{-12} \text{ cm}^3 \text{ s}^{-1}$
CF ₃ ⁺ + e	→	CF ₃	k_{re2}	$9.6 \cdot 10^{-7} \text{ cm}^3 \text{ s}^{-1}$
Ar ⁺ + F ⁻	→	Ar + F	k_{re3}	$1.0 \cdot 10^{-7} \text{ cm}^3 \text{ s}^{-1}$
CF ₃ ⁺ + F ⁻	→	CF ₃ + F	k_{re4}	$4.0 \cdot 10^{-7} \text{ cm}^3 \text{ s}^{-1}$
Ar ⁺ + CF ₄	→	Ar + F + CF ₃ ⁺	k_{ct}	$9.6 \cdot 10^{-10} \text{ cm}^3 \text{ s}^{-1}$
Ar + e	→	Ar* + e	$k_{ex}[E/N]$	Excitation
Ar* + e	→	Ar ⁺ + 2e	$k_{si}[E/N]$	Stepwise Ionization
Ar* + Ar*	→	Ar ⁺ + 2e	k_{mp}	$5.0 \cdot 10^{-10} \text{ cm}^3 \text{ s}^{-1}$
Ar* + e	→	Ar + e	k_{qe}	$4.0 \cdot 10^{-7} \text{ cm}^3 \text{ s}^{-1}$
Ar* + Ar	→	2Ar	k_{qn}	$1.2 \cdot 10^{-15} \text{ cm}^3 \text{ s}^{-1}$
Ar* + CF ₄	→	CF ₂ + F ₂ + Ar	k_{qC}	$6.0 \cdot 10^{-11} \text{ cm}^3 \text{ s}^{-1}$
F + F + M	→	F ₂ + M	k_{12}	$6.77 \cdot 10^{-28} \text{ cm}^6 \text{ s}^{-1}$
F ₂ + e	→	F + F	k_{a2}	Dissociation
CF _j + e	→	CF _{j-1} + F + e	k_{d1}	Dissociation
CF _j + e	→	CF _{j-2} + 2F + e	k_{d1}	Dissociation
CF ₄ + e	→	CF + 3F + e	k_{d1}	Dissociation
CF _j + F ⁻	→	CF _{j+1} + e	k_1	$5.0 \cdot 10^{-10} \text{ cm}^3 \text{ s}^{-1}$
CF ₂ + F ⁻	→	CF ₃ + e	k_1	$5.0 \cdot 10^{-14} \text{ cm}^3 \text{ s}^{-1}$
CF ₃ + F	→	CF ₄	k_6	$1.4 \cdot 10^{-11} \text{ cm}^3 \text{ s}^{-1}$
CF ₂ + F	→	CF ₃	k_7	$5.3 \cdot 10^{-13} \text{ cm}^3 \text{ s}^{-1}$
CF + F + M	→	CF ₂ + M	k_8	$7.0 \cdot 10^{-29} \text{ cm}^6 \text{ s}^{-1}$
CF ₃ + F ₂	→	CF ₄ + F	k_9	$3.3 \cdot 10^{-12} \text{ cm}^3 \text{ s}^{-1}$
CF ₂ + F ₂	→	CF ₃ + F	k_9	$4.6 \cdot 10^{-13} \text{ cm}^3 \text{ s}^{-1}$

3. Computerized tomography image

3.1. Experimental

The experimental system in 2f-CCP is described in detail in our previous study on two-dimensional optical emission spectroscopy[5, 6]. Parallel-plate aluminum electrodes 76 mm in diameter are positioned at 20 mm spacing on the central axis of a stainless chamber with an inner diameter of 200 mm. The side and back of each electrode, covered by a dielectric, is electrically shielded from the ground by an Al plate in order to prevent an additional discharge. (V)HF voltage at 13.56 MHz or 100 MHz is applied to the powered electrode, and the other

electrode is biased by a low frequency of 700 KHz. The rf discharge is sustained axially symmetric.

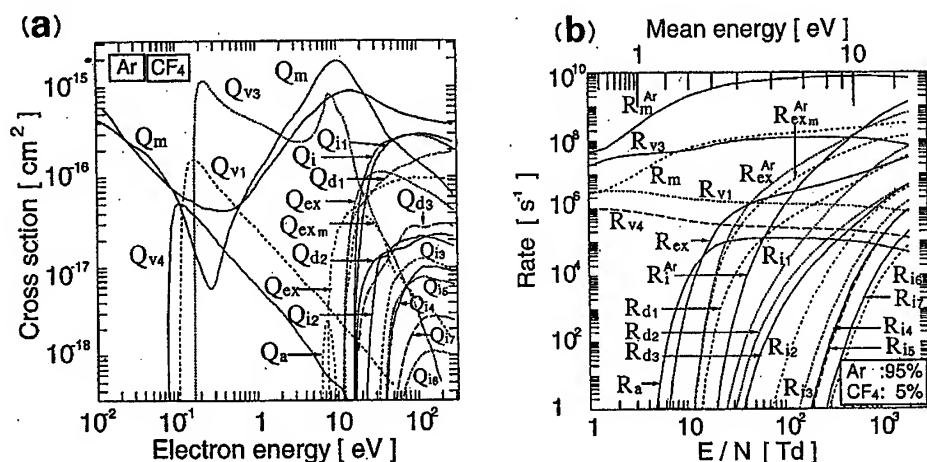


FIG. 4. Set of collision cross sections of electrons in Ar/CF₄ (a) and collision rates at 1 Torr (b) in CF₄(5%)/Ar.

The detection system consists of a monochromator with a photomultiplier in a single photon counting regime and appropriate discriminating and counting electronics. The input to the monochromator comes from one end of the optical fiber with the other end mounted to an optical system, consisting of a lens and a slit, which is fixed to a movable stage controlled by computer. Emission-selected computer tomography (CT) of an object in a $x-y$ plane at the axial position z requires a series of measurements of line integrals along the direction perpendicular to the z -axis.

3.2. Emission kinetics

Emission kinetics and physical quantities derived from CT are briefly described. The direct excitation rate to the j th level from the ground state with number density N is given by

$$(3.1) \quad \Lambda_j(z, r, t) = n_e(z, r, t) \left(\frac{2}{m} \right)^{1/2} \int_{\epsilon_j}^{\infty} N Q_j(\epsilon) f(\epsilon, z, r, t) \epsilon^{1/2} d\epsilon,$$

where n_e and m are the electron number density and the mass of the electron, respectively. $Q_j(\epsilon)$ is the excitation cross section to the j th level with a threshold energy of ϵ_j by the electron impact with energy ϵ . $f(\epsilon, z, r, t)$ is the electron energy distribution function at position (z, r) and time t . The number density of the excited molecule $N_j(z, r, t)$ satisfies the following continuity equation as

$$(3.2) \quad \frac{\partial}{\partial t} N_j(z, r, t) = \Lambda_j(z, r, t) + \zeta_j(z, r, t) + D_j \nabla^2 N_j(z, r, t) - \frac{N_j(z, r, t)}{\tau_{rad}} - k_q N N_j(z, r, t),$$

where $\zeta_j(z, r, t)$ is the sum of the rate due to the cascade transition and the stepwise excitation to the j th level. D_j is the diffusion coefficient, τ_{rad} the radiative lifetime, and k_q the self-quenching rate constant of the excited species. If the radiative lifetime is much shorter than the time constant for diffusion, $N_j(z, r, t)$ is expressed by the convolution integral

$$(3.3) \quad N_j(x, y, z, t) = \int_{-\infty}^t [\Lambda_j(x, y, z, t) + \zeta_j(x, y, z, t)] \exp\left[-\frac{t-t'}{\tau_{eff}}\right] dt'.$$

Here, τ_{eff} is the effective lifetime, written as

$$(3.4) \quad \tau_{eff}^{-1} = \tau_{rad}^{-1} + k_q N.$$

The spatiotemporal emission intensity $\Phi_{jk}(x, y, z, t)$ is expressed for the transition from the upper j to the lower k states of the excited molecule as

$$(3.5) \quad \Phi_{jk}(x, y, z, t) = k_o A_{jk} \int_{-\infty}^t [\Lambda_j(x, y, z, t) + \zeta_j(x, y, z, t)] \exp\left[-\frac{t-t'}{\tau_{eff}}\right] dt',$$

where k_o is the instrumental function, and A_{jk} is the transition probability from j to k . The time-dependent net excitation rate is given by the deconvolution procedure of eq.(5), as

$$(3.6) \quad [\Lambda_j(x, y, z, t) + \zeta_j(x, y, z, t)] = \mathbf{I}_n^{-1}[\Phi_{jk}(x, y, z, t)].$$

As in the case of a 2D image construction of axisymmetric $\Phi_{jk}(x, y, z, t)$ in a nonequilibrium plasma, 1D-line integrated emission data $\Phi_{jk}(x; z, t)$ at fixed z are transformed by Abel inversion; i.e.,

$$(3.7) \quad \Phi_{jk}(x; z, t) \xrightarrow{\text{Abel - Inversion}} \Phi_{jk}(r, z, t).$$

That is, the CT image is constructed by each of the formulae

(i) differential formula:

$$(3.8) \quad \Phi_{jk}(r, z) = -\frac{1}{\pi} \int_r^{r_o} \frac{\Phi'_{jk}(x, z)}{(x^2 - r^2)^{1/2}} dx,$$

(ii) integral formula:

$$(3.9) \quad \begin{aligned} \Phi_{jk}(r) = & -\frac{1}{\pi} \frac{[\Phi_{jk}(r_o, z) - \Phi_{jk}(r, z)]}{(r_o^2 - r^2)^{1/2}} \\ & + \int_r^{r_o} [\Phi_{jk}(x, z) - \Phi_{jk}(r, z)] \frac{x}{(x^2 - r^2)^{3/2}} dx. \end{aligned}$$

4. 1f-CCP at low pressure

4.1. Plasma maintenance at low pressure

Most of the investigations of the sustaining mechanism in rf CCP were performed at pressures of 50 mTorr - 10 Torr for low and moderate powers. Recent plasma etching is conducted at lower pressure, between 10 mTorr - 50 mTorr, and in a high power condition in order to achieve a fine pattern etching with high efficiency. Fig. 5 shows the spatiotemporally observed net production rate of

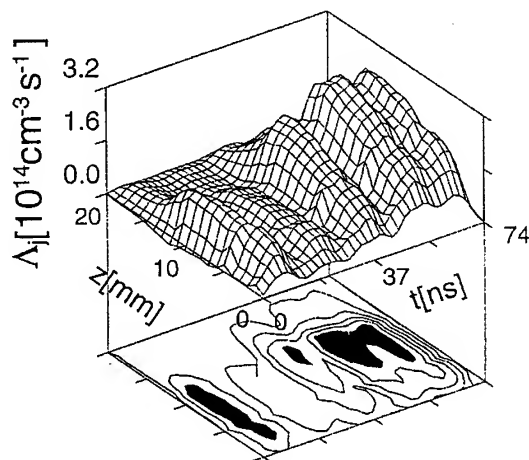


FIG. 5. Experimental net excitation rate of Ar(2p1) during one period in pure Ar at 50 mTorr for 13.56 MHz and 300 V. The powered electrode is located on the opposite side.

Ar(2p1) on the discharge axis (z) in Ar for frequency 13.56 MHz, amplitude 300 V, and pressure 50 mTorr. The net excitation rate is absolutely calibrated (see ref.[14]). The temporal characteristics are quite interesting as the proof of the sustaining mechanism. That is, even in a condition of low pressure, three temporal peaks, synchronized with the external voltage change, are exhibited as a function of one period of 13.56 MHz. First, there is the peak at 7 ns caused by the electrons that are reflected in front of the grounded electrode. The second appears at 41 ns by the influence of the reflected electrons in front of the powered electrode. Deep negative self bias voltage, -200 V at the powered electrode, produces a number of secondary electrons by ions incident on the metal surface in the phase of a negative voltage. The secondary electrons from the powered electrode over the range of times, 47 ns - 68 ns, significantly contribute to the maintenance of the rf discharge in high power conditions. As experimentally shown here, even in the condition that d is a few times of L_e at 50 mTorr, the 1f-CCP is still sustained by the temporal ionization multiplication of the heated secondary electrons in addition to that of the reflected ones in the high power condition. This indicates the absence of definite stochastic heating of electrons, independent of space and time. The situation will change in 2f-CCP driven at VHF.

4.2. Effect of feed gas on plasma structure

The difference in gas composition in the reactor will have an influence primarily due to the presence of massive negative ions on the plasma structure. Fig. 6 compares the 2D charged particle distributions in 1f-CCP in both Ar and

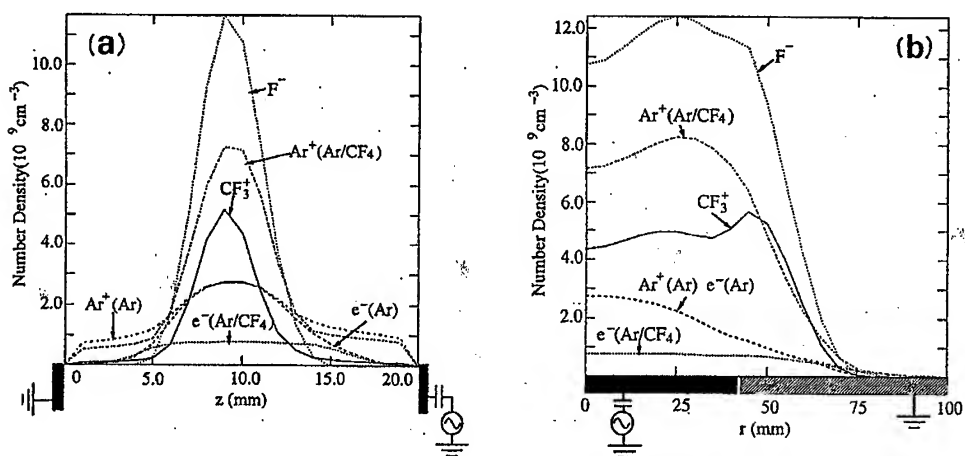


FIG. 6. Predicted density distribution in 1f-CCP in pure Ar and in $\text{CF}_4(5\%)/\text{Ar}$ at 50 mTorr for 13.56 MHz and 300 V. (a) axial distribution, (b) radial distribution at $z=10$ cm.

$\text{CF}_4(5\%)/\text{Ar}$. F^- is the main negative charge even at 5% of CF_4 due to accumulation resulting from entrapment between both sheaths in front of the electrodes, in spite of a very small production rate by the dissociative attachment of CF_4 . The validity of the numerical results is demonstrated by CT image of the net excitation rate of $\text{Ar}(3p5)$ at the same external condition. Appearance of CF_3^+ with a magnitude comparable with that of Ar^+ is caused by the high rate of charge transfer between Ar^+ and CF_4 [15]. This will be one of the specific characteristics of CCP in CF_4/Ar mixture.

4.3. Feed gas and etched nonvolatile particle transport

Etched particle transport from the reaction surface is an issue of concern with a CCP reactor. Fig. 7 shows one example of the flow of the feed gas and the

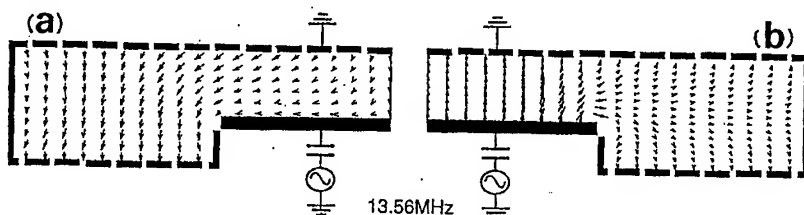


FIG. 7. Feed gas (a) and nonvolatile particle (b) flow in 1f-CCP for 13.56 MHz and 300 V at 50 mTorr in Ar.

physically sputtered nonvolatile particles for 13.56 MHz and 300 V at 50 mTorr in the reactor with a showerhead on the upper electrode [16]. The particle transport depends primarily on the dc-self bias voltage, and on the flow and pressure of the feed gas through the reactor geometry.

5. 2f-CCP and its CW operation

In a conventional RIE (1f-CCP), the wafer electrode has the responsibility for ion acceleration to the surface and for plasma production and maintenance in the presence of a large dc self bias voltage. In 2f-CCP, the application of a low frequency (LF) bias voltage to the wafer electrode will change the dominant plasma production /destruction processes on the (V)HF powered-electrode. The bias electrode will have additional effects on the plasma. That is, the presence of a dc self bias voltage on the wafer will produce secondary electrons by ions incident on the bias electrode, and confirm higher energy electrons inside the bulk plasma under a deep potential well in front of both electrodes. The high energy electrons will have a stochastic ionization between both sheaths, as was discovered in our previous study by the measurement of the ratio between the excited ion production and the neutral Ar(3p5)[6].

5.1. Functional separation

The basic idea of the different two frequency operation in each of the electrodes in CCP is one of *functional separation* between them. That is, the bias electrode with a wafer to be processed has the responsibility for the acceleration of positive ions to the surface for the purpose of reactive ion etching, while the powered electrode makes a contribution to the plasma production and the maintenance. In terms of the functional design, it will be essential to employ a VHF source at the powered plate and a LF voltage at the wafer electrode. The upper value of VHF will be limited by the capability of a uniform potential on the electrode. At several hundred MHz or UHF range, antenna coupling will be required with a plasma. At that point, the need for a local mode control of the electromagnetic field in front of the power supply will have to be addressed. Fig. 8 shows the spatial relation of the net production rate on the z axis in $\text{CF}_4(5\%)/\text{Ar}$ at 25 mTorr as a practical system for plasma etching, as a function of the bias voltage of LF (700 kHz), for the powered electrode driven at HF (13.56 MHz) with an amplitude of 300 V(a), and at VHF (100 MHz) with an amplitude of 50 V(b). The result is absolutely calibrated (see ref.[17]). The plasma density is kept at 10^{10} cm^{-3} in (a) and (b) without bias power. Obviously, the 2f-CCP at the VHF plasma source exhibits unaffected spatial characteristics such as changes in the bias amplitude, which is much more preferable for functional separation[6].

5.2. Additional function in 2f-CCP

In a conventional RIE (1f-CCP) system driven by HF power supply, it is essential to keep a lower sheath field in front of the grounded electrode and the reactor wall. The most significant difference between 1f-CCP and 2f-CCP systems at

HF(13.56 MHz) is the existence of a plasma structure surrounded by a strong positive ion sheath. That is, the efficiency to confine a higher energy electron between both electrodes is improved in the system of 2f-CCP at low pressure, when the high energy electron is supplied to the bulk plasma through the strong sheath acceleration of the secondary electrons produced by the ion impact on the wafer electrodes. This will lead to a higher plasma density at HF by a bias power application through the improvement in ionization efficiency in a bulk plasma that is caused by the presence of high energy electrons (See Fig. 8(a) and (b)). This indicates two important facts. One is the unsatisfactory charac-

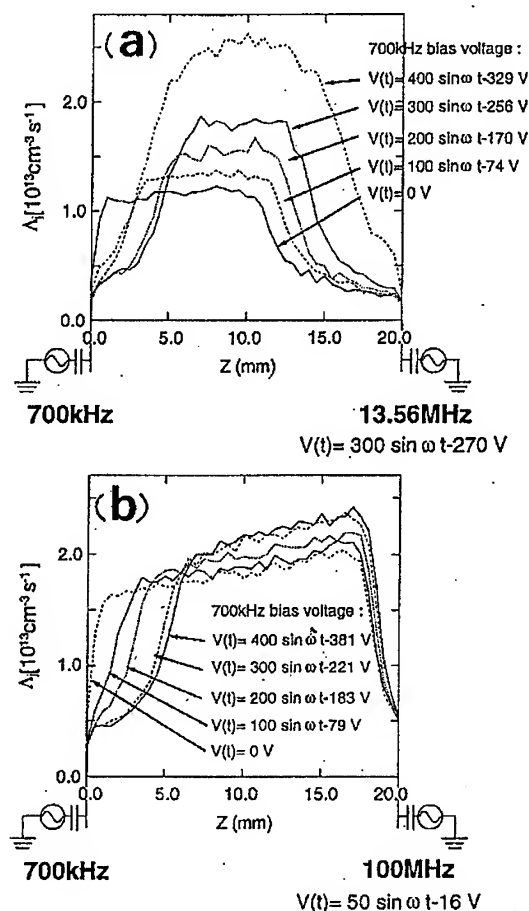


FIG. 8. Effect of LF(700 kHz) bias amplitude on the axial net production rate of Ar(3p5) in 2f-CCP at 25 mTorr in CF₄(5%)/Ar (experimental). Plasma is driven at 13.56 MHz (a) and at 100 MHz (b).

teristics for the purpose of functional separation. The other is the increase of the effective dissociation efficiency indicated by the electron excitation of the feed gas molecule by a high energy electron. Control of the high energy component of electrons in the bulk plasma will be achieved by changing the frequency for

plasma production from HF to VHF in order to reduce the amplitude of the sheath field in front of the powered electrodes.

Modern plasma etching is a system that maintains a high density plasma with a large area of uniformity in a radial direction at a low level of dissociation at low pressure. At HF operation with a strong sheath in front of the powered electrode, it will be difficult to separate the high density plasma production and the high efficiency of dissociation. On the other hand, when VHF is employed for the plasma production, the trapping of low energy electrons in bulk plasma is at first intrinsic. As shown in Fig. 8(a) and (b), the VHF plasma characteristics result in a low amplitude and low self bias voltage; i.e., there is a low sheath field in front of the powered electrode. This means that the extent of the low energy component of electrons in the VHF plasma reactor is much larger than that in the HF plasma reactor when the same plasma density is compared under these respective conditions. Given these physical mechanisms use of the VHF plasma source with LF bias electrode is preferable to achieve a high density plasma with a low degree of dissociation.

5.3. Effect of fixed parallel plates geometry

As discussed above, the uniform potential boundary in each of the fixed plates is realized in a simple reactor geometry in CCP driven at VHF. This system has structural advantages over the traditional HF system, and over other antenna-coupled plasma sources. The distance between the parallel plates will be designed finally by the gas flow inside the electrodes to keep the degree of stepwise collision processes at a low level as narrow as possible.

6. Pulsed operation of 2f-CCP

In a 2f-CCP, there are, in principle, three types of pulsed operation. One is the pulsed plasma production at the powered electrode under a LF-CW bias voltage application on the wafer. Another is the bias pulse operation during CW plasma production. The third is the bias voltage application synchronized with the rest period of the pulsed plasma source. In our previous paper, we investigated the mechanism of the bias pulse operation in the third technique [18, 19]. It will be essential to controlling the space potential close to the wafer as a function of duty ratio and the bias voltage amplitude. The impetus for the electron migration to the wafer as a drift wave lies in the sudden change of the applied power source. This causes plasma instability over the whole space between both electrodes, and the instability propagates through the bulk plasma to the wafer as the electron drift wave, in which the negative ion F^- is produced by the dissociative attachment of the front electrons with a higher energy component, as well as by the neutralization of the positive ion sheath in front of the wafer. These phenomena indicate that the mechanism has control over the showers of electrons and negative ions on the wafer. It is concluded that the electron is almost exhausted in the period of its acceleration towards the wafer. An insufficient supply of electrons with high energy, however, will introduce the limit of the practical application for charging free plasma processes.

We discuss herein the first practical technique to introduce a high energy negative charge on the wafer surface or inside the trench (hole) with high aspect ratio. Fig. 9 shows an example of the 2D electron density distribution during

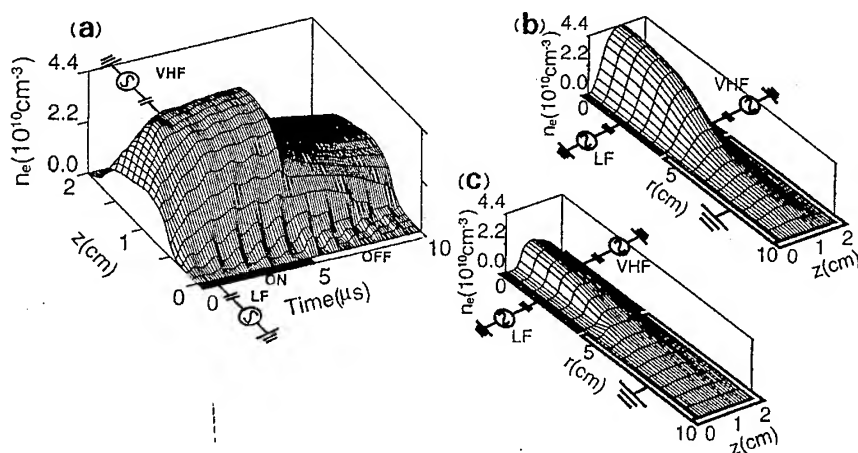


FIG. 9. Predicted electron density distribution in pulsed plasma driven at 100 MHz, 200 V, under LF bias voltage application of 1 MHz, 200 V at 30 mTorr in Ar. (a) $n_e(z, t)$, (b) $n_e(z, r)$ just before the switch-off phase, and (c) $n_e(z, r)$ just before the switch-on phase.

one period of the pulsed operation of the plasma production at 100 MHz and 200 V under LF-CW bias voltage of 1 MHz and 200 V at 30 mTorr in Ar[20]. The duty ratio is 0.5 with an on-time of $5\mu\text{s}$. The appearance of the synchronized electron flow with LF bias frequency to the wafer is shown in Fig. 9(a). When the feed gas is changed from pure Ar to $\text{CF}_4(5\%)/\text{Ar}$, the change of the plasma structure and its density occur as a result of the negative ion formation and the heavy particle collisions, as discussed in 4.2 in the case of 1f-CCP. Interest in the pulsed operation in the 2f-CCP reactor in $\text{CF}_4(5\%)/\text{Ar}$ will center on the mechanism of a negative ion supply to the wafer. Figure 10 shows a migration

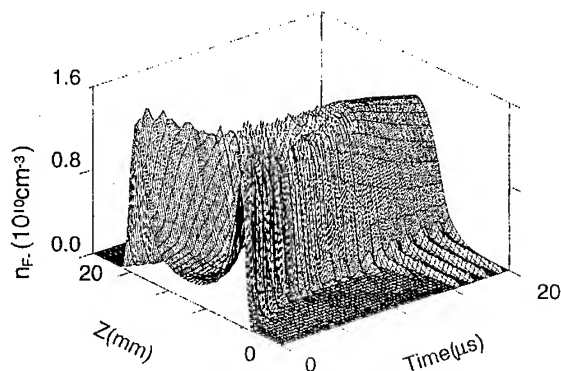


FIG. 10. Predicted negative ion (F^-) transport to the wafer in pulsed 2f-CCP driven at 27 MHz, 250 V, under LF-CW bias voltage at 800 kHz, 250 V at 100 mTorr in $\text{CF}_4(5\%)/\text{Ar}$.

of negative F^- ions toward the wafer during an off-period ($20 \mu s$) of the plasma source power due to the conversion process of the electron to F^- .

7. Charging on oxide etching

Charging is intrinsic to an insulator or metal on an insulator that is exposed to plasma. The SiO_2 trench is charged during plasma etching, since the time constant for charging is shorter than the time of layer by layer etching. Oxide etching is different from that of metals, in terms of the energy range of ions and in the etched surface potential. That is, ions with several hundred eV are used for oxide etching, while metal is etched by ~ 20 eV. In a metal etching, the wall will be kept at equipotential[21], though locally different surface potentials are realized during oxide etching due to high resistivity. Fig. 11 is an example of the

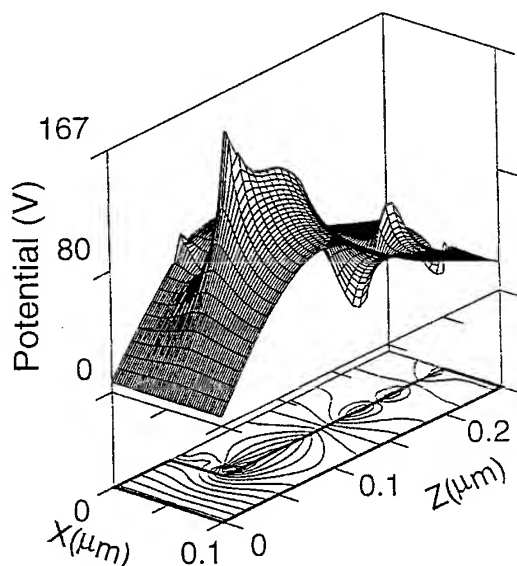


FIG. 11. Example of charging on the inside of SiO_2 trench etching.

charged potential in a trench of $0.1 \mu m$ width with an aspect ratio of 2 during SiO_2 etching at CW conditions of ion energy, 300 eV, and electron energy 3 eV [22]. A vibration of the local surface potential will take place.

Acknowledgments

The author wishes to express his thanks to Drs. N. Nakano, T. Kitajima, and Prof. Z. Lj. Petrović for their collaboration. The work is supported in part by Association of Super-Advanced Electronics Technologies (ASET) and Semiconductor Technology Academic Research Center (STARC).

References

1. S. NISHIKAWA, Edt. Digest of Papers Int. Forum on Semiconductor Technol., (Kyoto) (1998), M.Sasago Edt. *ibid.*(1999).
2. V. VAHEDI, C.K. BIRDSALL, M.A.LIEBERMAN, G. DiPESO, T.D. ROGNLIEN, *Phys.Fluids*, **B5**, 2719, 1993.
3. T. KITAMURA, N. NAKANO, T. MAKABE and Y. YAMAGUCHI, *Plasma Source Sci. Technol.*, **2**, 40, 1993.
4. P.M. MEIJER, J.D.P. PASSCHIER, W.J. GOEDHEER, J. BEZEMER, W.G.J.H.M. VAN SARK, *Appl. Phys. Lett.*, **64**, 1780, 1994.
5. T. KITAJIMA, Y. TAKEO, N. NAKANO and T. MAKABE, *J. Appl. Phys.*, **84**, 5928-5936, 1998.
6. T. KITAJIMA, T. TAKEO and T. MAKABE, *J. Vac. Sci. Technol. A*, **17**, 2510-2516, 1999.
7. T. TATSUMI, H. HAYASHI, S. MORISHITA, S. NODA, M. OKIGAWA, N. ITABASHI, Y. HIKOSAKA and M. INOUE, *Jpn. J. Appl. Phys.*, **37B**, 2394, 1998.
8. S. MORISHITA, H. HAYASHI, T. TATSUMI, Y. HIKOSAKA, S. NODA, M. OKIGAWA, M. MATSUI, M. INOUE and M. SEKINE, *Jpn. J. Appl. Phys.*, **37B**, 6899, 1998.
9. T. MAKABE, Technical report in IEEE of Jpn (in Japanese) ED-120, 1983.
10. K. OKAZAKI, T. MAKABE and Y. YAMAGUCHI, *Appl. Phys. Lett.*, **54**, 1742, 1989.
11. T. MAKABE, N. NAKANO and Y. YAMAGUCHI, *Phys. Rev.*, **A 45**, 2529, 1992.
12. K. MAEDA and T. MAKABE, *Jpn. J. Appl. Phys.*, **33**, 4173-4176, 1994.
13. M. KURIHARA, Z. LJ. PETROVIC and T. MAKABE, *J. Phys. D* (submitted).
14. F. TOCHIKUBO and T. MAKABE, *Meas. Sci. Technol.*, **2**, 1133, 1991.
15. E. FISHER, M.E. WEBER and P.B. ARMENTROUT, *J. Chem. Phys.*, **76**, 4932, 1982.
16. K. MAESHIGE, M. HASEBE, N. NAKANO, Y. YAMAGUCHI and T. MAKABE, submitted to *J. Appl. Phys.*
17. T. KITAJIMA, M. IZAWA, R. HASHIDO, N. MAKANO and T. MAKABE, *Appl. Phys. Lett.*, **69**, 758, 1996.
18. T. MAKABE, J. MATSUI and N. NAKANO, *Pure & Appl. Chem.*, **70**, 1187-1191, 1998.
19. M. SHIBATA, J. MATSUI, N. NAKANO, M. NAKAMURA and T. MAKABE, in preparation.
20. N. NAKANO and T. MAKABE, in preparation.
21. G.S. HWANG and K.P. GIAPIS, *J. Vac. Sci. Technol. B*, **15**, 70, 1997.
22. J. MATSUI, N. NAKANO, Z. LJ. PETROVIC and T. MAKABE, submitted to *Jpn. J. Appl. Phys.*

NONLOCAL TRANSPORT AND CORRELATIONS IN STRONGLY INTERACTING FERMION SYSTEMS

K. MORAWETZ^{1,2}, V. ŠPIČKA³, P. LIPAVSKÝ³

¹LPC-ISMRA, Bld MARECHAL JUIN, 14050 CAEN AND GANIL

Bld Becquerel, 14076 Caen Cedex 5, France

²FACHBEREICH PHYSIK, UNIVERSITY ROSTOCK

D-18055 Rostock, Germany

³INSTITUTE OF PHYSICS, ACADEMY OF SCIENCES

Cukrovarnická 10, 16200 Praha 6, Czech Republic

The formation of correlations due to collisions in an interacting Fermionic system is investigated. We present analytically the time dependent interaction energy with and without initial correlation. This short time behavior is characterized by the reduced density matrix possessing high energetic tails. After this short time regime the time evolution is controlled by small gradients. This leads to a nonlocal Boltzmann equation for the quasiparticle distribution and a functional relating the latter one to the reduced density matrix. The nonlocalities are presented as time and space shifts arising from gradient expansion and are leading to virial corrections in the thermodynamical limit.

1. Short time regime

The generalization of Boltzmann equation towards dense interacting systems is a still demanding and unsolved task. A huge variety of different attempts can be found in literature to incorporate modifications which leads to virial corrections in the equation of state, see citations in [1] - [7]. Starting from the theory of classical gases of hard spheres, Enskog introduced besides non-localities also static correlations [1, 2, 9, 10] and later on Weinstock [11] discussed dynamic correlations. An effort to describe the virial corrections for more realistic systems resulted in various generalizations of Enskog's equation [4, 8, 12, 13] and [13 - 14].

The pioneering contribution to quantum non-local corrections was made by Snider [13] who generalized Waldmann's equation [12] in such a way that it includes non-locality of collisions. Since then a number of similar theories have been developed. It was generally believed that this approach covered the virial

corrections until Laloë, Mullin, Nacher and Tastevin analyzed the so called Waldmann-Snider theory, coming to the conclusion that Snider's equation in its original form is not consistent with the second-order virial correction to the equation of state [21, 23]. In the series of papers [18, 23] Laloë, Tastevin and Nacher have introduced a concept of "free Wigner transform which wipes out the effect of the potential at short distances". The main idea of their approach is identical to the idea of quasiparticles in that the kinetic equation is not constructed for Wigner's distribution but for a subsidiary function, the free Wigner's transform, that is free of the correlated motion. Wigner's function is constructed from the free Wigner's transform in the final step. Since the free Wigner's transform includes only the on-shell contributions, as far as we can see, the free Wigner's transform is identical to the quasiparticle distribution. The intuitive theory of Laloë, Tastevin and Nacher has been confirmed by de Haan [20] who used Balescu's formal derivation of kinetic equations [5].

The on-shell approximations became so "well established" that the off-shell contributions are believed to be out of the scope of kinetic equations because of their genuine quantum character. This opinion has already been disproved by Prigogine. His approach, probably best represented by Balescu's formal expansion [5], shows that the off-shell contributions do not force any modification of the structure of the kinetic equation but they have to be included among its ingredients (in the renormalization of the single-particle energy and in the scattering integral). This is clearly the quasiparticle picture. Accordingly, the kinetic equation for quasiparticles does not imply that the off-shell processes be neglected but that they be recast into various renormalizations. Naturally, the off-shell contributions are essential in the $\rho[f]$ -functional as discussed by [25] and [26]. We will give an appropriate functional in the second part of the paper.

These kinetic equations describe different relaxation stages. During the very fast first stage, correlations imposed by the initial preparation of the system are decaying [27]. These are contained in off-shell or dephasing processes described by two-time propagators. During this stage of relaxation the quasiparticle picture is established [28, 29]. After this very fast process the second state develops during which the one-particle distribution relaxes towards the equilibrium value with a relaxation time. During this relaxation state the virial corrections are established and can be consistently described by a nonlocal Boltzmann kinetic equation [7]. We will present results for both stages here.

The formation of correlations is connected with an increase of the kinetic energy or equivalently the build up of correlation energy. This is due to rearrangement processes which let decay higher order correlation functions until only the one - particle distribution function relaxes. Because the correlation energy is a two - particle observable we expect that the relaxation of higher order correlations can be observed best within this quantity. Of course, the total energy of the system is conserved

$$(1.1) \quad \frac{\partial}{\partial t} \left(\langle \frac{p_1^2}{2m} \rangle(t) + E_{\text{corr}}(t) \right) = 0,$$

which means that the kinetic energy increases on cost of the correlation energy

$E_{\text{corr}}(t)$.

The kinetic equation in Born approximation for spatial homogeneous media including memory effects but no damping is called Levinson equation and reads [30, 31, 29]

$$(1.2) \quad \frac{\partial}{\partial t} \rho(t, k) = 2 \sum_b s_a s_b \int \frac{dp dq}{(2\pi)^6} V_{ab}(|q|)^2 \int_{t_0}^t d\tau \\ \times \cos \left[\left(\frac{k^2}{2m_a} + \frac{p^2}{2m_b} - \frac{(k-q)^2}{2m_a} - \frac{(p+q)^2}{2m_b} \right) (t-\tau) \right] \{ \rho(\tau, k-q) \rho(\tau, p+q) \\ \times (1 - \rho(\tau, k) - \rho(\tau, p)) - \rho(\tau, k) \rho(\tau, p) (1 - \rho(\tau, p+q) - \rho(\tau, k-q)) \}$$

with the spin (isospin,...) degeneracy s and the two particle potential V_{ab} . The Wigner distribution functions are normalized to the density as $s \int \frac{dp}{(2\pi)^3} \rho(p) = n$. The Boltzmann collision integral is obtained from equation (1.2) if: (i) One neglects the time retardation in the distribution functions, i.e. the memory effects and (ii) The finite initial time t_0 is set equal to $-\infty$ corresponding to what is usually referred to as the limit of complete collisions. The memory effect is condensed in the explicit retardation of the distribution function. This would lead to gradient contributions to the kinetic equation which can be shown to be responsible for the formation of high energetic tails in the distribution function [33, 34]. This effect will be established on the second stage of relaxation and will lead to virial corrections in chapter 2.

The second effect is contained in the energy broadening or off-shell behavior in (1.2). This is exclusively related to the spectral properties of the two-particle propagator and therefore determined by the relaxation of two-particle correlation. On this time scale the memory in the distribution functions can be neglected but we will keep the spectral relaxation in the off-shell cos-function of (1.2). The resulting expression for (1.2) describes then how two particles correlate their motion to avoid the strong interaction regions. This very fast formation of the off-shell contribution to Wigner's distribution has been found in numerical treatments of Green's functions [35, 36].

1.1. Sudden switching

Starting with a sudden switching approximation we consider Coulomb interaction and during the first transient time period the screening is formed. This can be described by the non-Markovian Lenard - Balescu equation [37] instead of the static screened equation (1.2) leading to the dynamical expression of the correlation energy. To demonstrate its results and limitations, we use Maxwellian initial distributions neglecting degeneracy.

From (1.2) we find with $\frac{\partial}{\partial t} E_{\text{corr}} = - \sum_a \int \frac{dk}{(2\pi)^3} \frac{k^2}{2m_a} \frac{\partial}{\partial t} \rho_a$ for the one-component plasma

$$\frac{\partial}{\partial t} \frac{E_{\text{corr}}^{\text{static}}(t)}{n} = - \frac{e^2 \kappa T}{2\hbar} \text{Im} \left[(1 + 2z^2) e^{z^2} (1 - \text{erf}(z)) - \frac{2z}{\sqrt{\pi}} \right]$$

$$(1.3) \quad \frac{\partial E_{\text{corr}}^{\text{dynam}}(t)}{\partial t} \frac{1}{n} = -\frac{e^2 \kappa T}{\hbar} \text{Im} [e^{z_1^2} (1 - \text{erf}(z_1))]]$$

where we used $z = \omega_p \sqrt{t^2 - it \frac{\hbar}{T}}$ and $z_1 = \omega_p \sqrt{2t^2 - it \frac{\hbar}{T}}$. This is the analytical quantum result of the formation of correlation for statically as well as dynamically screened potentials. For the classical limit we are able to integrate expression (1.3) with respect to times and arrive at

$$(1.4) \quad \begin{aligned} E_{\text{corr}}^{\text{static}}(t) &= -\frac{1}{4} e^2 n \kappa \left\{ 1 + \frac{2\omega_p t}{\sqrt{\pi}} - (1 + 2\omega_p^2 t^2) \exp(\omega_p^2 t^2) [1 - \text{erf}(\omega_p t)] \right\} \\ E_{\text{corr}}^{\text{dynam}}(t) &= -\frac{1}{2} e^2 n \kappa \left\{ 1 - \exp\left(\frac{\omega_p^2}{2} t^2\right) \left[1 - \text{erf}\left(\frac{\omega_p}{\sqrt{2}} t\right) \right] \right\}. \end{aligned}$$

In Fig. 1, this formulae are compared with molecular dynamic simulations [38] for two values of the plasma parameter $\Gamma = 0.1$ and 1. This parameter $\Gamma = \frac{e^2}{a_e T}$,

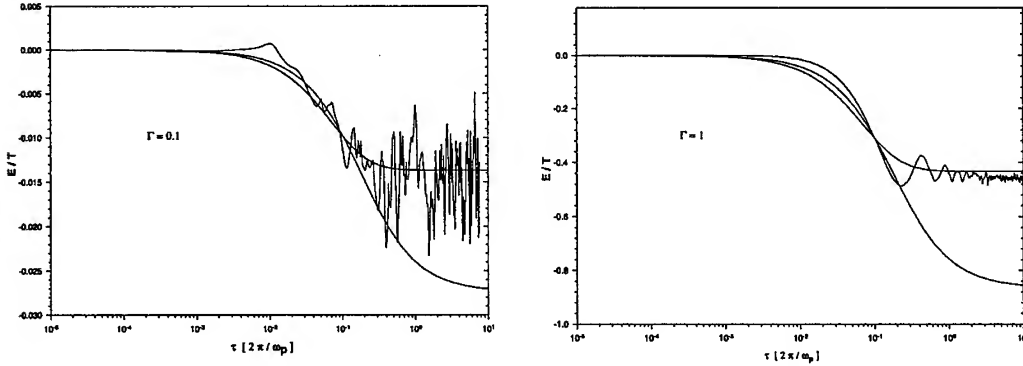


FIG. 1. The formation of correlation energy due to molecular dynamic simulations [38] together with the result of (1.4) for a plasma parameter $\Gamma = 0.1$ (left) and $\Gamma = 1$ (right). The upper curve is the static and the lower the dynamical calculation of (1.4). The latter one approaches the Debye-Hückel result.

where $a_e = (\frac{3}{4\pi n})^{1/3}$ is the Wigner-Seitz radius. The static result underestimates the dynamical long time result of Debye-Hückel $\sqrt{3}/2\Gamma^{3/2}$ by a factor of two, which can be seen from the long time and classical limit $b^2 = (\hbar\kappa)^2 \frac{m_a + m_b}{8m_a m_b T} \rightarrow 0$

$$(1.5) \quad \begin{aligned} E_{\text{corr}}^{\text{dynam}}(\infty) &= -\frac{e^2 \kappa \sqrt{\pi}}{2} \frac{1}{b} (1 - e^{b^2} \text{erfc}(b)) = -\frac{1}{2} e^2 n \kappa + o(b) \\ E_{\text{corr}}^{\text{static}}(\infty) &= -\frac{e^2 \kappa}{4} (1 - \sqrt{\pi} \text{erfc}(b)) = -\frac{1}{4} e^2 n \kappa + o(b). \end{aligned}$$

The first result represents the Montroll correlation energy [39]. For $\Gamma = 1$, see Fig. 1, non-ideal effects become important and the formation time is underestimated within (1.4). This is due to non-ideality which was found to be an expression of memory effects [32] and leads to a later relaxation.

1.2. Initial correlations

The situation of sudden switching of interaction may be considered as an artificial one. In the simulation experiment we have initial correlations which are due to the set up within quasiperiodic boundary condition and Ewald summations. This obviously results into an effective statically screened Debye potential, or at least the simulation results in Fig. 1 allow for this interpretation. Therefore we consider now initial correlations which lead besides the explicit collision integral in Born approximation (1.2) to a new collision term [57]

$$(1.6) \quad -2 \sum_{ab} s_a s_b \int_{t_0}^t dt_1 \int \frac{dq dp}{(2\pi)^6} V_{ab}(q) V_0^{ab}(q) \cdot \\ \cos \left[\left(\frac{k^2}{2m_a} + \frac{p^2}{2m_b} - \frac{(k-q)^2}{2m_a} - \frac{(p+q)^2}{2m_b} \right) (t - t_1) \right] \cdot \\ \left\{ \rho_0^a(k-q) \rho_0^b(p+q) (1 - \rho_0^b(p) - \rho_0^a(k)) - \rho_0^a(k) \rho_0^b(p) (1 - \rho_0^b(p+q) - \rho_0^a(k-q)) \right\}$$

with ρ_0 the initial Wigner distribution.

To show the interplay between collisions and correlations, we have calculated the initial two-particle correlation function in the ensemble, where the dynamical interaction $V(q)$ is replaced by some arbitrary function $V_0(q)$. Therefore the initial state deviates from thermal equilibrium except when $V(q) = V_0(q)$ and $\varrho(t_0) = \varrho_0$.

The additional collision term, \mathcal{I}_0 , cancels exactly the Levinson collision term (1.2) in the case that we have initially the same interaction as during the dynamical evolution ($V_0 = V$) and if the system starts from the equilibrium $\rho(t) \equiv \rho_0$.

On very short time scales we can again neglect the change in the distribution function and assume a Maxwellian initial distribution. The model interaction is now a Debye potential $V_i(q) = 4\pi e^2/[q^2 + \kappa_i^2]$ with fixed parameter $\kappa_i = \kappa_D$ and for the initial correlations $\kappa_i = \kappa_0$. We obtain for the change of kinetic energy from the kinetic equation

$$(1.7) \quad \frac{\partial}{\partial t} E_{\text{kin}}(t) = \mathcal{E}[V(q)^2](t) - \mathcal{E}[V_0(q)V(q)](t),$$

which can be integrated [29] to yield

$$(1.8) \quad E_{\text{kin}}(t) = E_{\text{total}} - E_{\text{init}}(t) - E_{\text{coll}}(t).$$

For the classical limit we obtain explicitly the time dependent kinetic energy

$$(1.9) \quad \frac{E_{\text{coll}}(t)}{nT} = -\frac{\sqrt{3}\Gamma^{3/2}}{4x} \partial_y (y\mathcal{F}(y))_{y=x\tau},$$

where $\mathcal{F}(y) = 1 - e^{y^2} \text{erfc}(y)$, $\tau = t\omega_p/\sqrt{2}$, $x = \kappa_D/\kappa$ and $\kappa^2 = 4\pi e^2 n/T = \omega_p^2 T/m$. The plasma parameter is given as usually by $\Gamma = \frac{e^2}{a_e T}$, where $a_e = (\frac{3}{4\pi n})^{1/3}$ is the Wigner-Seitz radius.

In Fig. 2, upper panel, we compare the analytical results of (1.9) with MD simulations [56] using the Debye potential V_i as bare interaction. The evolution of kinetic energy is shown for three different ratios x . The agreement between theory and simulations is quite satisfactory, in particular, the short time behavior for $x = 2$. The stronger initial increase of kinetic energy observed in the simulations at $x = 1$ may be due to the finite size of the simulation box which could more and more influence the results for increasing range of the interaction.

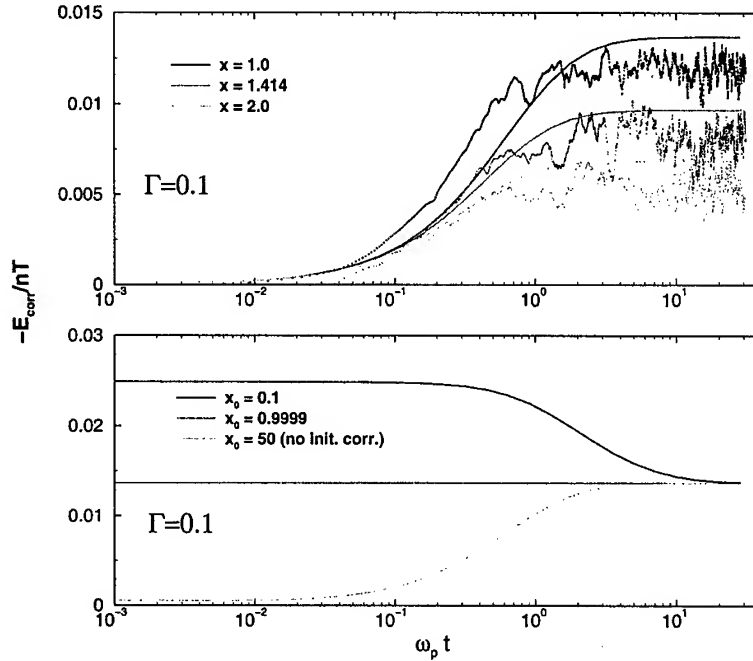


FIG. 2. The formation of correlation energy $-E_{\text{corr}} \equiv E_{\text{total}} - E_{\text{init}} - E_{\text{coll}} = E_{\text{kin}}$ in a plasma with Debye interaction V_i . The upper panel compares the analytical results (1.9) with MD simulations from [56] for three different ratios of κ_D to the inverse Debye length $x = \kappa_D/\kappa$.

In the lower panel we compare theoretical predictions for the inclusion of Debye initial correlations characterized by $x_0 = \kappa_0/\kappa$ where $x = \kappa_D/\kappa = 1$.

Now we include the initial correlations which leads to

$$(1.10) \quad \frac{E_{\text{init}}(t)}{nT} = -\frac{\sqrt{3}\Gamma^{3/2}}{2(x_0^2 - x^2)} [x\mathcal{F}(x\tau) - x_0\mathcal{F}(x_0\tau)],$$

where $x_0 = \kappa_0/\kappa$ characterizing the strength of the initial correlations with the Debye potential V_0 which contains κ_0 instead of κ_D . Besides the kinetic energy (1.10) from initial correlations, the total energy E_{total} (1.8) now includes the initial correlation energy which can be calculated from the long time limit of (1.9) leading to

$$(1.11) \quad \frac{E_{\text{total}}}{nT} = \frac{\sqrt{3}\Gamma^{3/2}}{2(x + x_0)}.$$

The result (1.8) is seen in Fig. 2, lower panel. We observe that if the initial correlation is characterized by a potential range larger than the Debye screening length, $x_0 < 1$, the initial state is over-correlated, and the correlation energy starts at a higher absolute value than without initial correlations relaxing towards the correct equilibrium value. If, instead, $x_0 = 1$ no change of correlation energy is observed, as expected. Similar trends have been observed in numerical solutions [40].

The characteristic time of formation of correlations at high temperature limit is given by the inverse plasma frequency $\tau_c \approx \frac{1}{\omega_p} = \frac{\sqrt{2}}{v_{th}\kappa}$. The inverse plasma frequency indicates that the long range fluctuations play the dominant role. This confirms the numerical finding of [27] that the correlation or memory time is proportional to the range of interaction. In the low temperature region, i.e., in a highly degenerated system $\mu \gg T$, one finds [29] that the build up time is the inverse Fermi energy, \hbar/ϵ_f in agreement with the quasiparticle formation time known as Landau's criterion. Indeed, the quasiparticle formation and the build up of correlations are two alternative views of the same phenomenon. The formation of binary correlations is very fast on the time scale of dissipative processes. Under extremely fast external perturbations, like the massive femto second laser pulses, the dynamics of binary correlations will hopefully become experimentally accessible.

2. Virial regime

Now we proceed and investigate how the relaxation into equilibrium is performed by the system. During this time scale the virial corrections should be established. We will convince ourselves firstly that the direct use of reduced density matrix as done so far for short time regimes is not possible.

2.1. Two shortcomings of kinetic equation for reduced density

On larger time scales we expect smoothed time-space gradients and will therefore develop a theory including first order gradients. We expand the Levinson equation up to first order memory and restrict first to homogeneous systems. The kinetic equation for the reduced density matrix [33] is then obtained, e.g. from (1.2)

$$(2.1) \quad \frac{\partial}{\partial t} \rho = \mathcal{I}_{\text{Boltz}} + \frac{\partial}{\partial t} \mathcal{I}_{\text{corr}}$$

where besides the usual Boltzmann term, $\mathcal{I}_{\text{Boltz}}$, there appears an additional off-shell term, $\mathcal{I}_{\text{corr}}$, which describes the correlation in the reduced density matrix.

The commonly used idea in the literature [3, 33] to obtain balance equations for the density, momentum or energy including virial correlations is to integrate (2.1) over 1, p or $p^2/2m$ respectively. In [33] the conclusion was drawn that the correlated part $\tilde{n}_c = -\int dp \mathcal{I}_{\text{corr}}$ combining with the left hand side of (2.1) should establish the density conservation

$$(2.2) \quad \frac{\partial}{\partial t} (n_f + \tilde{n}_c) = 0$$

where $n_f = \int dp \rho$ was interpreted as free (quasiparticle) density. This was in line with the treatment of [3] and others. Understanding this equation as the balance between free and correlated density one has to face a puzzle which was not noted in [33]. Carefully inspection reveals that the correlated part of the collision integral leads just to the opposite sign in the correlated density $\tilde{n}_c = -\int dp \mathcal{I}_{\text{corr}} = -n_c$ known from the Beth-Uhlenbeck equation of state [41, 42, 43]. Using the correct definition $\int dp \rho = n_f + n_c$ leads to an exact cancellation of n_c from the left hand side with the correlated part \tilde{n}_c from the right hand side. So one has either the choice to “reinterpret” the reduced density matrix as quasiparticle distribution leading to n_f , but which results into a wrong sign of the correlated density, or one has to face the exact cancellation of n_c in the balance equation and the incorrect conservation of n_f . We will show that the virial corrections will appear instead from internal gradients.

That these correlated parts do not provide the virial corrections but a relation between reduced density matrix and quasiparticle distribution have mostly not noted. We will present a solution of this puzzle by constructing an appropriate relation between reduced density matrix and quasiparticle distribution. The quasiparticle distribution will fulfill a kinetic equation consistent with the balance equations and the relation to the reduced density matrix is provided additionally by a fixed functional from the beginning.

The second puzzle is a more obvious hint that the Levinson equation fails to describe the long time evolution of a system. We can iterate the time derivative inside the collision integral on the right hand side of (2.1) to create an infinite series. Neglecting backscattering terms we estimate

$$(2.3) \quad \frac{\partial}{\partial T} \rho \geq \zeta[\rho] \mathcal{I}_{\text{Boltz}}[\rho]$$

with $\zeta = \sum_{n=0}^{\infty} \eta^{2^n-1}$ and η is similar to the back flow (second order response) [34]

$$(2.4) \quad \eta(p) = \int \frac{dk dq}{(2\pi\hbar)^6} V^2(q) \frac{\rho(k)\bar{\rho}(k+q)\bar{\rho}(p-q) + \bar{\rho}(k)\rho(k+q)\rho(p-q)}{(\epsilon_k - \epsilon_{k+q} + \epsilon_p - \epsilon_{p-q})^2}$$

with $\bar{\rho} = 1 - \rho$. As one can see η is positive but by no means every time smaller than one. Therefore ζ appears to be divergent at certain momentum situations. Therefore we conclude that the gradient expanded Levinson equation is not ergodic. This has been observed in numerical solutions of these non-Markovian kinetic equations [44]. Usually the energy rises continuously. We will show that a proper balance between off-shell terms in the reduced density and the kinetic equation for the pole part is necessary to ensure ergodicity.

2.2. Connection between reduced density matrix and quasiparticle distribution

The approach presented now is based on the real-time Greenfunction technique. We consider the two independent correlation functions for Fermionic creation operators $G^>(1,2) = \langle a(1)a^+(2) \rangle$ and $G^<(1,2) = \langle a^+(2)a(1) \rangle$, where cumulative variables means time, space, spin, etc $1 = t, x, s, \dots$. The time diagonal

part of $G^<$ yields the reduced density matrix or Wigner distribution function according to $\rho(x_1, x_2, t) = G^<(1, 2)_{t_1=t_2}$. For the latter one the time diagonal Kadanoff and Baym equation of motion reads [45]

$$(2.5) \quad i[G_0^{-1}, G^<](x_1, x_2, t, t) = i[G_0^{-1}, \rho](x_1, x_2, t) \\ + \int_{t_0}^t dt' \int dx' [G^<(x_1, x', t, t')\Sigma^>(x', x_2, t', t) + \Sigma^>(x_1, x', t, t')G^<(x', x_2, t', t) \\ - G^>(x_1, x', t, t')\Sigma^<(x', x_2, t', t) - \Sigma^<(x_1, x', t, t')G^>(x', x_2, t', t)]$$

where the Hartree-Fock drift term has the form $G_0^{-1}(1, 1') = (i\frac{\partial}{\partial t_1} + \frac{\nabla_1^2}{2m})\delta(1 - 1') - \Sigma_{HF}(1, 1')$ and $\Sigma^{<,>}$ are the analytic pieces ($t_1 <, > t_2$) of the selfenergy which is given by the two - particle Greenfunction $\Sigma(1, 2) = \int d^3V(1, 3)G_2(1, 3, 2, 3^+)$. The right hand side of (2.5) contains a non-Markovian collision integral and can be considered as a precursor of Levinson equation (1.2).

We want to construct a kinetic equation for a quasiparticle distribution f from this gradient expanded equation for the Wigner function ρ . The quasiparticle distribution should obey a kinetic equation which is rid of the off-shell terms causing high energy tails. Using gradient approximation we obtain a kinetic equation of the structure (2.1). We expect that the time derivative of the Wigner function on the left side of (2.5) should combine with the time derivative of the off-shell part of right hand side into a time derivative of a quasiparticle distribution f . We indeed obtain

$$(2.6) \quad \rho \approx zf - \int \frac{d\omega}{2\pi} \frac{\mathcal{P}'}{\omega - \epsilon} \sigma^<(\omega).$$

The wave function renormalization has been abbreviated as $z = (1 - \partial_\omega \sigma)^{-1} \approx 1 + \partial_\omega \sigma$. Using the spectral decomposition

$$(2.7) \quad \sigma(\omega) = \int \frac{d\omega'}{2\pi} \frac{P}{\omega - \omega'} \gamma(\omega')$$

with the imaginary part $\gamma = \sigma^> + \sigma^<$ one easily confirms this rearrangement. The \mathcal{P}' denotes the derivative of the principal value. We have fulfilled the task and give with (2.6) a connection between reduced density matrix ρ and the quasiparticle distribution f . We extrapolate the ansatz also for the correlation functions

$$(2.8) \quad g^<(\omega) = 2\pi z \delta(\omega - \epsilon) \left(\frac{1-f}{f} \right) - \frac{P'}{\omega - \epsilon} \sigma^<(\omega).$$

The spectral identity $a = g^> + g^<$ proofs that this ansatz is consistent with the extended quasiparticle picture which is obtained for small imaginary parts of the self-energy γ [42, 39, 34]

$$(2.9) \quad a(p\omega Rt) = \frac{2\pi\delta(\omega - \epsilon(pRt))}{1 + \frac{\partial\sigma(p, \omega, R, t)}{\partial\omega}|_{\omega=\epsilon}} - \gamma(p, \omega, R, t) \frac{\partial}{\partial\omega} \frac{\mathcal{P}}{\omega - \epsilon(pRt)}$$

where \mathcal{P} denotes the principal value. The quasiparticle energies $\epsilon(pRT)$ are a solution of the dispersion relation $\omega - \frac{p^2}{2m} - \sigma(p\omega RT) = 0$.

It is noteworthy to remark that (2.9) fulfills the spectral sum rules [46]

$$(2.10) \quad \int \frac{d\omega}{2\pi} a(p\omega RT) = 1$$

and the energy weighted sum rule [7]

$$(2.11) \quad \int \frac{d\omega}{2\pi} \omega a(p\omega RT) = \frac{p^2}{2m} + \Sigma_{HF}(p, R, T).$$

The limit of small scattering rates has been first introduced by [47] and for equilibrium nonideal plasmas [42, 46]. Later on the same approximation, but under the name of the generalized Beth-Uhlenbeck approach, has been used by [43] in the nuclear matter for studies of the correlated density. The authors in [48] have used this approximation for the study of the mean removal energy and high-momenta tails of Wigner's distribution. They use the name *extended quasiparticle approximation*. The non-equilibrium form has been introduced by [34] as a modified Kadanoff and Baym ansatz.

Using this ansatz in the Kadanoff-Baym equations (2.5) the known Landau-Silin equation for the quasiparticle distribution f follows

$$(2.12) \quad \frac{\partial}{\partial T} f + \nabla_k \epsilon \nabla_R f - \nabla_R \epsilon \nabla_k f = z((1-f)\sigma^< - f\sigma^>).$$

We repeat that the Landau-Silin equation (2.12) is coupled with a functional that specifies a relation between the quasiparticle distribution f and Wigner's function ρ via (2.6). Using different approximations for the self energy we obtain all known kinds of kinetic equations with the generalization that the internal gradients of collision integrals will yield the nonlocal or virial corrections. With the ladder summation results one obtains the nonlocal Boltzmann-Uehling-Uhlenbeck equation [7], using the random phase approximation leads to the nonlocal Lenard-Balescu equation, etc. As we see, this ansatz provides the correct connection between equations for the Wigner function and the quasiparticle Boltzmann equation (2.12). It has to be remarked that the theory presented here is valid up to first order gradient corrections. This implies that we will find from intrinsic gradients in the scattering integrals the virial corrections [7].

2.3. Nonlocal Boltzmann equation

The kinetic equation in its skeleton form (2.12) holds for rather general systems. To obtain its actual form, one has to evaluate its ingredients, the scattering integral and the quasiparticle energy. Within the same accuracy one has to evaluate the $\rho[f]$ -functional. In both cases it means to turn the self-energy $\Sigma^<$ into a functional of the quasiparticle distribution f . In this section we focus on the scattering integral. Our aim is to derive the scattering integral within the same approximations as the skeleton kinetic equation. This procedure leads to

the non-instant and non-local scattering integral. We choose as an approximation for the self energy the ladder or \mathcal{T} -matrix approximation appropriate for dense interacting systems of short range potentials

$$(2.13) \quad \Sigma^<(1, 2) = \mathcal{T}^R(1, \bar{3}; \bar{5}, \bar{6}) \mathcal{T}^A(\bar{7}, \bar{8}; 2, \bar{4}) G^>(\bar{4}, \bar{3}) G^<(\bar{5}, \bar{7}) G^<(\bar{6}, \bar{8}).$$

The consistent treatment of gradient contributions is provided by the extended quasiclassical limit that has to be applied also to all internal space and time integrations of the scattering integral. Clearly, we have to take into account that the terms on the scattering side of the kinetic equation can have and do have gradient contributions resulting from the internal dynamics of the collision process. These gradient contributions will lead to quantum mechanical non-instant and non-local corrections to the scattering integral which allow for a classical interpretation.

The quasiclassical limit and the limit of small scattering rates explicitly determine how to evaluate the scattering integral from the self-energy $\sigma^<$. For non-degenerate systems, very similar scheme was carried through by Bärwinkel [4]. One can see in Bärwinkel's papers, that the scattering integral is troubled by a large set of gradient corrections. This formal complexity seems to be the main reason why most authors either neglect gradient corrections at all [49, 50] or provide them buried in multi-dimensional integrals [19, 51].

For a degenerate system, the set of gradient corrections to the scattering integral is even larger than for rare gases studied by Bärwinkel, see [7]. To avoid manipulations with long and obscure formulas, the gradient corrections have to be sorted and expressed in a comprehensive form. As we will see below, such a comprehensive form are Enskog-type non-instant and non-local corrections. The known physical interpretation of Enskog's corrections also provides a guide in reading formulas resulting from the algebra of quasiclassical limit.

The quasiclassical limit of with all linear gradients kept is a tedious but straightforward algebraic exercise. It results in one non gradient and nineteen gradient terms that are analogous to those found within the chemical physics [20, 23]. All these terms can be recollected into a nonlocal and noninstantaneous scattering integral that has an intuitively appealing structure of a nonlocal Boltzmann equation (1)

$$(2.14) \quad \frac{\partial f_1}{\partial t} + \frac{\partial \varepsilon_1}{\partial k} \frac{\partial f_1}{\partial r} - \frac{\partial \varepsilon_1}{\partial r} \frac{\partial f_1}{\partial k} = \sum_b \int \frac{dp dq}{(2\pi)^5} \delta(\varepsilon_1 + \varepsilon_2 - \varepsilon_3 - \varepsilon_4 + 2\Delta_E) z_1 z_2 z_3 z_4$$

$$\cdot \left| \mathcal{T}_{ab} \left(\varepsilon_1 + \varepsilon_2 - \Delta_E, k - \frac{\Delta_K}{2}, p - \frac{\Delta_K}{2}, q, r - \Delta_r, t - \frac{\Delta_t}{2} \right) \right|^2$$

$$\left(1 - \frac{1}{2} \frac{\partial \Delta_2}{\partial r} - \frac{\partial \bar{\varepsilon}_2}{\partial r} \frac{\partial \Delta_2}{\partial \omega} \right) [f_3 f_4 (1 - f_1)(1 - f_2) - (1 - f_3)(1 - f_4) f_1 f_2],$$

with Enskog-type shifts of arguments [7]: $f_1 \equiv f_a(k, r, t)$, $f_2 \equiv f_b(p, r - \Delta_2, t)$, $f_3 \equiv f_a(k - q - \Delta_K, r - \Delta_3, t - \Delta_t)$, and $f_4 \equiv f_b(p + q - \Delta_K, r - \Delta_4, t - \Delta_t)$. In agreement with [23, 20], all gradient corrections result proportional to derivatives of the

scattering phase shift $\phi = \text{Im} \ln \mathcal{T}_{ab}^R(\Omega, k, p, q, t, r)$,

$$\begin{aligned} \Delta_2 &= \left(\frac{\partial \phi}{\partial p} - \frac{\partial \phi}{\partial q} - \frac{\partial \phi}{\partial k} \right)_{\varepsilon_3 + \varepsilon_4} & \Delta_3 &= - \frac{\partial \phi}{\partial k} \Big|_{\varepsilon_3 + \varepsilon_4} & \Delta_4 &= - \left(\frac{\partial \phi}{\partial k} + \frac{\partial \phi}{\partial q} \right)_{\varepsilon_3 + \varepsilon_4} \\ \Delta_t &= \frac{\partial \phi}{\partial \Omega} \Big|_{\varepsilon_3 + \varepsilon_4} & \Delta_E &= - \frac{1}{2} \frac{\partial \phi}{\partial t} \Big|_{\varepsilon_3 + \varepsilon_4} & \Delta_K &= \frac{1}{2} \frac{\partial \phi}{\partial r} \Big|_{\varepsilon_3 + \varepsilon_4}, \end{aligned} \quad (2.15)$$

and $\Delta_r = \frac{1}{4}(\Delta_2 + \Delta_3 + \Delta_4)$. After derivatives, Δ 's are evaluated at the energy shell $\Omega \rightarrow \varepsilon_3 + \varepsilon_4$.

The Δ 's in arguments of distribution functions in (2.14) remind non-instant and non-local corrections in the scattering-in integral for classical particles. The displacements of the asymptotic states are given by $\Delta_{2,3,4}$. The time delay enters in an equal way the asymptotic states 3 and 4. The momentum gain Δ_K also appears only in states 3 and 4. Finally, there is the energy gain which is discussed in [52]. Numerical values of these shifts calculated for different potentials are presented in [53].

One has to take into account that $\bar{\varepsilon}_2$ depends on Δ_2 which depends on the energy E . This E -dependence has resulted in a norm of the singularity

$$(2.16) \quad \frac{1}{1 - \frac{\partial \bar{\varepsilon}_2}{\partial E}} \approx 1 + \frac{\partial \bar{\varepsilon}_2}{\partial E} = 1 - \frac{\partial \bar{\varepsilon}_2}{\partial r} \frac{\partial \Delta_2}{\partial E} = 1 - \frac{\partial \bar{\varepsilon}_2}{\partial r} \frac{\partial \Delta_2}{\partial \omega}.$$

In Δ 's and their derivatives the energy $\omega + E = \varepsilon_1 + \bar{\varepsilon}_2$ is substituted after all derivatives are taken. We remind that the non-localities should be viewed as a compact form of gradient corrections.

Despite its complicated form it is possible to solve this kinetic equation with standard Boltzmann numerical codes and to implement the shifts [54]. This has shown an observable effect in the dynamical particle spectra of around 10%.

3. Thermodynamic properties

The meaning of nonlocal shifts can be best seen on thermodynamic observables like density n_a of particles a , density of energy \mathcal{E} , and the stress tensor \mathcal{J}_{ij} which conserve within the nonlocal and noninstantaneous kinetic equation (2.14). Integrating (2.14) over momentum k with factors ε_1 , k and unity one finds [7] that each observable has the standard quasiparticle part following from the drift

$$\begin{aligned} \mathcal{E}^{\text{qp}} &= \sum_a \int \frac{dk}{(2\pi)^3} \frac{k^2}{2m} f_1 + \frac{1}{2} \sum_{a,b} \int \frac{dk dp}{(2\pi)^6} T_{ab}(\varepsilon_1 + \varepsilon_2, k, p, 0) f_1 f_2, \\ \mathcal{J}_{ij}^{\text{qp}} &= \sum_a \int \frac{dk}{(2\pi)^3} \left(k_j \frac{\partial \varepsilon_1}{\partial k_i} + \delta_{ij} \varepsilon_1 \right) f_1 - \delta_{ij} \mathcal{E}^{\text{qp}}, \\ (3.1) \quad n_a^{\text{qp}} &= \int \frac{dk}{(2\pi)^3} f_1, \end{aligned}$$

and the Δ -contribution following from the scattering integral

$$\begin{aligned}
 \Delta\mathcal{E} &= \frac{1}{2} \sum_{a,b} \int \frac{dkdpdq}{(2\pi)^9} P(\varepsilon_1 + \varepsilon_2) \Delta_t, \\
 \Delta\mathcal{J}_{ij} &= \frac{1}{2} \sum_{a,b} \int \frac{dkdpdq}{(2\pi)^9} P[(p+q)_i \Delta_{4j} + (k-q)_i \Delta_{3j} - p_i \Delta_{2j}], \\
 (3.2) \quad \Delta n_a &= \sum_b \int \frac{dkdpdq}{(2\pi)^9} P \Delta_t,
 \end{aligned}$$

where $P = |\mathcal{T}_{ab}|^2 2\pi \delta(\varepsilon_1 + \varepsilon_2 - \varepsilon_3 - \varepsilon_4) f_1 f_2 (1 - f_3 - f_4)$.

The density of energy $\mathcal{E} = \mathcal{E}^{\text{qp}} + \Delta\mathcal{E}$ alternatively results from Kadanoff and Baym formula, $\mathcal{E} = \sum_a \int \frac{dk}{(2\pi)^3} \int \frac{d\omega}{2\pi} \frac{1}{2} \left(\omega + \frac{k^2}{2m} \right) G_a^<(\omega, k, r, t)$, with $G^<$ in the extended quasiparticle approximation (2.8). Its complicated form, however, shows that \mathcal{E} cannot be easily inferred from an eventual experimental fit of the kinetic equation as it has been attempted in [55]. The conservation of \mathcal{E} generalizes the result of Bornath, Kremp, Kraeft and Schlages [6] restricted to non-degenerated systems. The particle density $n_a = n_a^{\text{qp}} + \Delta n_a$ is also obtained from (2.6) via the definition, $n_a = \int \frac{d\omega}{2\pi} \frac{dk}{(2\pi)^3} G^<$. This confirms that the extended quasiparticle approximation is thermodynamically consistent with the nonlocal and noninstantaneous corrections to the scattering integral.

For equilibrium distributions, formulas (3.1) and (3.2) provide equations of state. Two known cases are worth to compare. First, the particle density $n_a = n_a^{\text{qp}} + \Delta n_a$ is identical to the quantum Beth-Uhlenbeck equation of state [43, 33, 6], where n_a^{qp} is called the free density and Δn_a the correlated density. Second, the virial correction to the stress tensor has a form of the collision flux contribution known in the theory of moderately dense gases [1, 2].

4. Summary

While the short time behavior is described by off-shell transport condensed in the reduced density matrix, the later stage of evolution is described by a nonlocal Boltzmann equation. This equation is derived in the quasiclassical limit and leads to consistent thermodynamics in equilibrium including binary correlations. The latter ones represent the second virial coefficients in the low density limit. The presented kinetic equation unifies achievements of dense gases and the kinetic theory of quasiparticle transport in quantum systems. The equation has been shown applicable in recent simulation codes.

References

1. S. CHAPMAN and T.G. COWLING, *The Mathematical Theory of Non-uniform Gases* (Cambridge University Press, Cambridge, 1990), third edition Chap. 16.
2. J.O. HIRSCHFELDER, C.F. CURTISS, and R.B. BIRD, *Molecular Theory of Gases and Liquids* (Wiley, New York, 1964), chaps. 6.4a and 9.3.

3. Y.L. KLIMONTOVICH, *Kinetic Theory of Nonideal Gases and Nonideal Plasmas* (Pergamon Press, Oxford, 1982).
4. K. BARWINKEL, Z. Naturforsch, a **24**, 38, 1969, in Proceedings of the 14th International Symposium on Rarefied Gas Dynamics (University of Tokyo Press, Tokyo, 1984), Z. Naturforsch, a **24**, 22, 1969.
5. R. BALESCU, *Equilibrium and Nonequilibrium Statistical Mechanics (Russ. trans.)*, **3**, 16-20, (Wiley, New York, 1975).
6. T. BORNATH, D. KREMP, W.D. KRAEFT, and M. SCHLANGES, Phys. Rev. E **54**, 3274, 1996.
7. V. SPIČKA, P. LIPAVSKÝ, and K. MORAWETZ, Phys. Lett. A **240**, 160, 1998. P. LIPAVSKÝ, V. ŠPIČKA, and K. MORAWETZ, book (1997) sub., K. MORAWETZ, habilitation thesis (1998) University Rostock.
8. R.F. SNIDER, J. Stat. Phys., **63**, 707, 1991.
9. D. ENSKOG, in *Kinetic theory*, edited by S. Brush (Pergamon Press, New York, 1972), Vol. 3, orig.: K. Svenska Vet. Akad. Handl. **63** (4), (1921).
10. P.P.J.M. SCHRAM, *Kinetic Theory of Gases and Plasmas* (Kluwer Academic Publishers, Dordrecht, 1991).
11. J. WEINSTOCK, Phys. Rev., **132**, 454, 1963, Phys. Rev., **132**, 470, 1963, Phys. Rev. A **140**, 460, 1965.
12. L. WALDMANN, Z. Naturforsch, A **12**, 660, 1957, Z. Naturforsch, A **13**, 609, 1958, Z. Naturforsch, A **15**, 19, 1960.
13. R.F. SNIDER, J. Chem. Phys., **32**, 1051, 1960, J. Math. Phys. **5**, 1580, 1964.
14. M.W. THOMAS and R.F. SNIDER, J. Stat. Phys., **2**, 61, 1970.
15. R.F. SNIDER and B.C. SANCTUARY, J. Chem. Phys. **55**, 1555, 1971.
16. J.C. RAINWATER and R.F. SNIDER, J. Chem. Phys., **65**, 4958, 1976.
17. J.A. MCLENNAN, *Introduction to Nonequilibrium Statistical Mechanics* (Prentice-Hall, Englewood Cliffs, 1989).
18. F. LALOE, J. Phys., (Paris) **50**, 1851 (1989); G. TASTEVIN, P. NACHER, and F. LALOE, J. Phys. (Paris) **50**, 1879 (1989); P. NACHER, G. TASTEVIN, and F. LALOE, J. Phys., (Paris) **50**, 1907, 1989.
19. D. LOOS, J. Stat. Phys., **59**, 691, 1990, J. Stat. Phys., **61**, 467, 1990.
20. M. DE HAAN, Physica A **164**, 373, 1990, H. DE HAAN, Physica A **165**, 224, 1990, H. DE HAAN, Physica A **170**, 571, 1991.
21. F. LALOE and W.J. MULLIN, J. Stat. Phys., **59**, 725, 1990.
22. R.F. SNIDER, J. Stat. Phys., **61**, 443, 1990.
23. P.J. NACHER, G. TASTEVIN, and F. LALOE, Ann. Phys. (Leipzig) **48**, 149, 1991, Journal de Physique I, **1**, 181, 1991.
24. R.F. SNIDER, J. Stat. Phys. **80**, 1085, 1995, R.F. SNIDER, W.J. MULLIN, and F. LALOË, Physica A **218**, 155, 1995.
25. R.A. CRAIG, Ann. Phys., **40**, 434, 1966.
26. B. BEZZERIDES and D.F. DUBOIS, Phys. Rev., **168**, 233, 1968.
27. M. BONITZ and et al., J. Phys.: Condens. Matter **8**, 6057, 1996.
28. P. LIPAVSKÝ, F.S. KHAN, A. KALVOVÁ, and J.W. WILKINS, Phys. Rev., B **43**, 6650, 1991.
29. K. MORAWETZ, V. ŠPIČKA, and P. LIPAVSKÝ, Phys. Lett. A **246**, 311, 1998, K. MORAWETZ and H. KÖHLER, Eur. Phys. J. A **4**, 291, 1999.
30. I.B. LEVINSON, Fiz. Tverd. Tela Leningrad, **6**, 2113, 1965, Zh. Eksp. Teor. Fiz., **57**, 660 (1969), [Sov. Phys.-JETP, **30**, 362, 1970].

31. A.P. JAUHO and J.W. WILKINS, Phys. Rev., B **29**, 1919, 1984.
32. K. MORAWETZ, R. WALKE, and G. RÖPKE, Phys. Lett., A **190**, 96, 1994.
33. K. MORAWETZ and G. RÖPKE, Phys. Rev. E **51**, 4246, 1995.
34. V. ŠPIČKA and P. LIPAVSKÝ, Phys. Rev., B **52**, 14615, 1995, Phys. Rev. Lett., **73**, 3439, 1994.
35. P. DANIELEWICZ, Ann. Phys., (NY) **152**, 305, 1984.
36. H.S. KÖHLER, Phys. Rev., C **51**, 3232, 1995.
37. K. MORAWETZ, Phys. Rev., E **50**, 4625, 1994.
38. G. ZWICKNAGEL, C. TOEPFFER and P.G. REINHARD, in *Physics of strongly coupled plasmas*, edited by W. D. Kraeft and M. Schlanges (World Scientific, Singapore, 1995), p. 45.
39. W.D. KRAEFT, D. KREMP, W. EBELING, and G. RÖPKE, *Quantum Statistics of Charged Particle Systems* (Akademie Verlag, Berlin, 1986).
40. D. SEMKAT, D. KREMP, and M. BONITZ, Phys. Rev. E **59**, 1557, 1999.
41. G.E. BETH and E. UHLENBECK, Physica **4**, 915, 1937.
42. H. STOLZ and R. ZIMMERMANN, Phys. Status Solidi, B **94**, 135, 1979, R. ZIMMERMANN and H. STOLZ, Phys. Status Solidi, B **131**, 151, 1985.
43. M. SCHMIDT and G. RÖPKE, Phys. stat. sol., (b) **139**, 441, 1987, M. SCHMIDT, G. RÖPKE, and H. SCHULZ, Ann. Phys., (NY) **202**, 57, 1990.
44. D. KREMP, M. BONITZ, W. KRAEFT, and M. SCHLANGES, Ann. of Phys., **258**, 320, 1997.
45. L.P. KADANOFF and G. BAYM, *Quantum Statistical Mechanics* (Benjamin, New York, 1962).
46. D. KREMP, W. D. KRAEFT, and A. D.J. LAMBERT, Physica, A **127**, 72, 1984.
47. R.A. CRAIG, Ann. Phys., **40**, 416, 1966.
48. H.S. KÖHLER and R. MALFLIET, Phys. Rev., C **48**, 1034, 1993.
49. P. DANIELEWICZ, Ann. Phys. (NY), **152**, 239, 1984.
50. W. BOTERMANS and R. MALFLIET, Phys. Rep., **198**, 115, 1990.
51. V.G. MOROZOV and G. RÖPKE, Physica, A **221**, 511, 1995.
52. P. LIPAVSKÝ, V. ŠPIČKA, and K. MORAWETZ, Phys. Rev. E **52**, R1291, 1999.
53. K. MORAWETZ, P. LIPAVSKÝ, V. ŠPIČKA, and N. KWONG, Phys. Rev., C **59**, 3052, 1999.
54. K. MORAWETZ, Phys. Rev. Lett., **82**, 3767, 1999.
55. H. STÖCKER and W. GREINER, Phys. Rep., **137**, 277, 1986.
56. G. ZWICKNAGEL, Contrib. Plasma Phys., **39** (1999) 1-2,155, and private communications.
57. K. MORAWETZ and *et al.*, Phys. Rev., Lett., sub., physics/9905024.

ADVANCED TECHNIQUES OF PLASMA DIAGNOSTICS USING COHERENT OPTICS

T. NEGER

INSTITUT FÜR EXPERIMENTALPHYSIK, TECHNISCHE UNIVERSITÄT GRAZ
Petersgasse 16, A-8010 Graz, Austria

Coherent optics can serve as a powerful tool for particle density determination in plasma diagnostics. The paper reports on different techniques based on holographic and speckle interferometry with special emphasis of spatial resolution. While emission spectroscopy must undoubtedly be considered as the most commonly used and proven method for particle-selective diagnostics, interferometry shows its advantages in case of plasmas of significant optical thickness, when spatially resolved intensity measurements become less reliable. The article also deals with the permanently growing field of nonlinear optics with respect to plasma diagnostics and gives related examples.

1. Introduction

The investigation of plasmas by optical diagnostics can be performed using different techniques among which emission spectroscopy is still the most commonly used and important one. This method shows a large range of sensitivity and is best suited for investigations of plasmas with rather low density. Problems may arise if optical thickness reaches significant values. Since classical emission spectroscopy provides integral values of the local emission coefficients along the line of sight, the method may lose reliability in case of a required spatial resolution, the more optical thickness increases. Especially tomographic investigations of inhomogeneous and asymmetric plasmas, which are based on multidirectional observation, need correct input data from the different projections. As algorithms for the reconstruction of the local plasma parameters react very sensitive on errors, the quality of the results would be rather poor. A powerful tool to overcome this principal problem is the measurement of the refractivity of the plasma instead of spectral line intensities. Optical thickness does not affect it, as long as the plasma under investigation has a minimum transparency necessary for fringe recording. Typically in interferometry two lightwaves corresponding with two states of a plasma are compared. The related types of interferometric measurements can be classified according to the way how this comparison

is experimentally performed. If a so-called test and reference beam is realized simultaneously and spatially separated, one speaks of classical interferometry. New diagnostical possibilities arose with the invention of holographic recording and wavefront reconstruction. Thus, after recording a first plasma state, the second one maybe recorded at any favourable time and, moreover, both of them be reconstructed at another convenient time. It is obvious that this technique strongly enlarges the experimental possibilities. A completely different way, but also one which is able to compare plasma states consecutively, is based on the granulation effect of highly coherent light, the speckle effect. If laser light is incident onto a rough and diffusively reflecting surface, the reflected and incoming waves interfere, thus storing information about the surface's micro-profile. But, instead of focusing the interest to the properties of the surface, one inserts the plasma into the beam illuminating the surface. According to the plasma's refractivity it will change the phase relations of the interfering beams, resulting in a modified speckle pattern. However, instead of a direct fringe observation, characteristic speckle patterns of different states have to be treated here using image processing algorithms, finally yielding an interference pattern similar to classical or holographic interferometry. In spite of an acceptable inherent loss of resolution this method avoids any photographic technique with complicated and time consuming wet image processing like in holography, provided digital speckle interferometry is applied. The latter technique comes merely along with a suitable CCD-camera, a personal computer with a frame grabber and standard optical equipment. Plasma diagnostics using coherent optics can also be performed utilizing non-linear optical effects. It must be distinguished, whether the non-linearity happens in an optical element of the experimental arrangement or if it is really induced into the investigated medium itself. Regarding the first type, this paper will report on two-wavelength electron density determination performed by a direct optical superposition of the original testing wave and its frequency doubled one, which were faced to different refractivities of the medium due to dispersion. If the applied laser light exceeds a certain intensity, the polarisation of the plasma is not only a linear function of the involved electrical field of the highly frequent incident light wave. Actually it depends on higher powers of the electric field, too. This non-linear polarisation gives rise to a completely new class of optical effects, resulting in new experimental possibilities. By proper mixing of intense light waves in a medium even a phase conjugate signal can be extracted out of the interaction zone. Here, the superposition of light waves in the medium has some similarity with a hologram, although it acts as a transient one. The application, however, should be rather considered as non-linear spectroscopy with ultrahigh spectral resolution. This paper will present and discuss experiments according to the above mentioned methods of plasma diagnostics by coherent optics with respect to particle density determination. Advantages, disadvantages and complications will be considered in order to provide an impression of the capabilities of coherent optics in plasma research.

2. General aspects of interferometric plasma diagnostics

2.1. Refractivity of a plasma

Interferometric measurements of a plasma reveal the phase change of the wavefronts which passed the plasma due to its refractivity. Provided the illumination of the interferometer is not too intense, the refractivity of a plasma is a linear relationship of contributions from atoms a , ions i and electrons e . The total refractivity $(n - 1)_{\text{plasma}}$ of a one-component plasma, i.e., with only the first ionisation stage being reached, can be written as

$$(2.1) \quad (n - 1)_{\text{plasma}} = (n - 1)_a + (n - 1)_i + (n - 1)_e \\ = \frac{1}{2\epsilon_0} \sum_m \alpha_{a,m}(\lambda) N_{a,m} + \frac{1}{2\epsilon_0} \sum_m \alpha_{i,m}(\lambda) N_{i,m} - \frac{e^2}{8\pi^2 \epsilon_0 m_e c^2} \lambda^2 N_e .$$

The sums over the polarisabilities $\alpha_{a,m}(\lambda)$ and $\alpha_{i,m}(\lambda)$ account for the contributions of optical transitions of the atoms and ions at certain wavelengths (λ). $N_{a,m}$ and $N_{i,m}$ denote the number densities in the lower state of the transition involved of the atoms or ions, N_e is the electron density, e the elementary charge, ϵ_0 the electrical field constant, m_e the mass of the electron and c the velocity of light in vacuum.

A separation of the different refractivity contributions in order to evaluate the corresponding particle densities is mainly prepared by choosing proper wavelengths. In resonance interferometry (carried out by means of high resolution laser spectroscopy) and dispersion interferometry (performed by using hook and phase methods with classical interferometers and broad-band illumination) wavelengths close to or in the vicinity of strong optical transitions are used where the refractive index changes very strongly. Electron density measurements must be carried out at wavelengths far away from atomic resonances ("far-off resonance" interferometry) and should be performed as far in the infrared as possible because of the quadratic dependence of $(n - 1)_e$ on λ (see eq. 2.2).

2.2. Spatially resolved diagnostics

By interferometric measurements a local value of the refractive index can directly be obtained only in case of a longitudinally homogeneous plasma layer, since in this case the optical path integral across the objects extension in the expression for the phase ϕ of the lightwave experimentally determined is simply the product $(n - n_0)l$,

$$(2.2) \quad \phi = \frac{2\pi}{\lambda} \int_{\text{Obj.}} (n - n_0) dz = \frac{2\pi}{\lambda} (n - n_0) l = \Delta n l .$$

Inhomogeneous plasmas may also be analysed using a single direction of observation ("projection"), provided radial symmetry of the side-on observed plasma column may be assumed. In this case the local change of the refractive index can be calculated by an adequate ABEL-inversion as a function of the radius (for explanation of symbols see Fig. 1, left part),

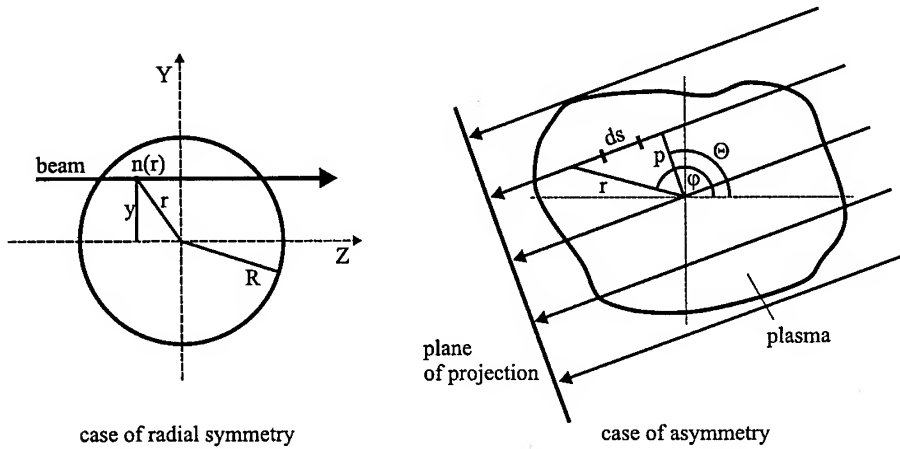


FIG. 1. Explanation of symbols for Abel-inversion (left) and tomographic reconstruction (right).

$$(2.3) \quad \Delta n(r) = -\frac{\lambda}{2\pi^2} \int_r^R \frac{d\phi(y)}{dy} \frac{dy}{\sqrt{y^2 - r^2}}.$$

Because of the sensitivity of the method due to the differential $\phi(y)/dy$ in eq. 2.3 the quality of the results strongly depends on the numerical treatment of the side-on data. A new approach prevents this problem by a special Fourier series expansion (see [1]).

However, the decision if radial symmetry is given or not is often a question of acceptable error limits. A great many of technically relevant plasmas of higher pressure are inhomogeneous and more or less asymmetric. Any quantitative analysis of the related plasma processes e.g. for optimization of the discharge's feature leads to the need of a tomographic optical setup in principle. In this case the asymmetric object has to be illuminated from different directions, the phase change produced by the plasma is separately evaluated for each projection (see e.g. [2, 3, 4, 5, 6, 7]). The change of the refractive index Δn is now position dependent as well as angularly dependent,

$$(2.4) \quad \Delta n(r, \varphi) \equiv [n(r, \varphi) - n_0],$$

the phase for a given projection direction θ then reads

$$(2.5) \quad \phi(p, \theta) = \frac{2\pi}{\lambda} \int_{Obj.} \Delta n(r, \varphi) ds + E(p, \theta),$$

($E(p, \theta)$ accounts for measurement errors). In case of exactly known projection data ($E(p, \theta) = 0$) and straight lines of integration eq. 2.5 may be considered as the RADON-transformation [8], the inversion of which is

$$(2.6) \quad \frac{2\pi}{\lambda} \Delta n(r, \varphi) = \frac{1}{2\pi^2} \int_0^\pi \int_{-\infty}^{+\infty} \frac{1}{r \cos(\theta - \varphi) - p} \frac{\partial \phi(p, \theta)}{\partial p} d\theta dp.$$

A frequently used method (especially for medical purposes), based on eq. 2.6, is called *filtered back projection* or *convolution method*. It interpretes eq. 2.6 as a differentiation, a subsequent Hilbert transformation and finally a back projection (for details see [9]). Since this method requires rather high numbers of projections, the algebraic reconstruction technique (ART) is a more convenient iterative reconstruction algorithm that works with even smaller numbers of available projections as they are usually sufficient in optical plasma diagnostics because of lower density gradients there compared to medical applications. In this case, however, the field reconstructed by the convolution method frequently serves as first approximation (see also [9]).

2.3. Evaluation of interferograms

Sophisticated reconstruction procedures strongly depend on the availability of highly resolved spatial phase profiles. Therefore, in general a fringe evaluation based on FFT-algorithms is the standard method. If smaller numbers of fringes or even not one complete single fringe is caused by the object's refractivity, spatial optical heterodyning or phase stepping methods together with Fourier-analysis allow subfringe analysis, increase the accuracy and prevent the ambiguity in the sign of the density change. In those cases the "infinite width fringes" originating from the plasma itself are superposed by a fringe system of equidistant separation, a so-called spatial carrier frequency, resulting in a 'finite width fringe system'. The intensity scans are Fourier transformed, the transform showing an intensity peak at the frequency of the carrier, however, broadened by the modulation of the phase change of the object under investigation. By proper filtering techniques and back transformation one gets rid of low-frequent background contributions to the intensity as well as of high-frequent noise. Thus, highly resolved spatial phase profiles - according to the refractivity of the plasma - can be obtained instead of only a few points of measurement in case of a mere fringe peak detection technique (for details see [10, 11]).

3. Examples for plasma diagnostics by linear coherent optics

Within this section two experimental approaches for particle density determination are presented. The first one is an investigation of an asymmetric discharge by a multidirectional and multicolor arrangement utilizing a holographic optical element as a central tool for the recording of the wavefronts, simultaneously acting as coupling device for the different projections, whereas the fringe analysis is performed through wavefront shearing interferometry. The second example demonstrates a two-wavelength end-on arrangement using digital speckle-pattern interferometry for the determination of the electron density in a wall-stabilized arc.

3.1. Interferometric single shot tomography

Beneath a spatial resolution the investigation of many discharges requires pulsed diagnostics because of their transient character. Furthermore a single wavelength

of laser light will hardly be sufficient, since the different refractive index contributions to the total refractivity may only be separable if several wavelengths are applied simultaneously. A principal solution that meets the above mentioned requirements has been demonstrated in [6, 7]. It combines holographic and classical interferometric techniques.

Firstly, through mirror galleries a multidirectional observation of the inhomogeneous object is realised (Fig. 2). The recording of the plasma states, however, is performed holographically. The special feature of the method is given by the multiple function of the hologram. The wavefronts which passed the plasma under different directions are led to the holographic plate as a system of object beams, however, vertically separated by a slight tilt of the corresponding elements of the mirror gallery. This system of stripes of object beams is coherently superposed by a single common reference beam of circular geometry with sufficient diameter (not explicitly shown in Fig. 2).

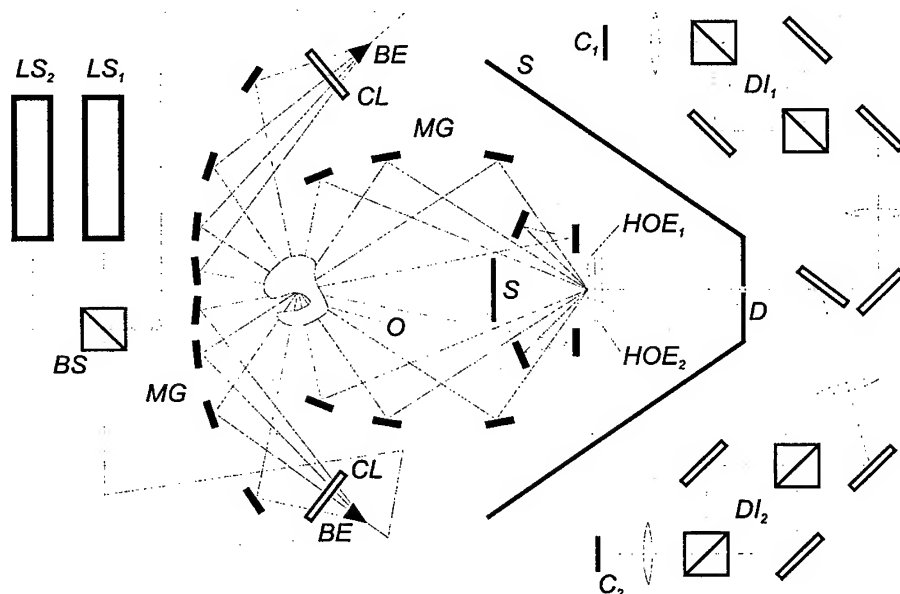


FIG. 2. Experimental setup for single-shot tomography. *LS* laser, *BS* beam splitter, *BE* beam expander, *CL* cylindrical lens, *MG* mirror gallery, *O* asymmetric, non stationary, brightly radiating object under investigation, *HOE* holographic-optical coupling element, *D* diaphragm, *S* screen, *DI* differential interferometer, *C* CCD camera. The components labelled with subscript 2 and the dashed light paths are used only when simultaneous measurements with a second wavelength of light are performed.

Thus, the hologram acts as a holographic optical element (HOE) with the following properties: (a) It stores the wavefronts after propagation through the plasma for each observation direction in horizontal stripes, which are vertically separated ("coupling element" of projections), (b) it has characteristic imaging properties for the reconstruction process realised by choosing a convergent geometry of the reference beam during the recording, and (d) it strongly reduces

the unwanted radiation of the plasma, since for the observation of the fringes the reference beam is chosen rather than the object beam. The HOE can be assumed as a grating in this mode of operation, thus the radiation is spectrally decomposed, only radiation of the same wavelength as that of the probing laser light can propagate through the spatial filter (compare also [12]) separating the recording zone (lefthand side of diaphragm D in Fig. 2) from the evaluation zone (righthand side of Fig. 2). The procedure also allows more than one wavelength to be recorded simultaneously (e.g. for two wavelengths two holographic optical elements HOE_1 and HOE_2 may be used as drawn in Fig. 2).

The next step after processing the HOE is the analysis of the holographically stored wavefronts. This task is solved by using a differential interferometer. Instead of placing the object under investigation within the arms of the interferometer, one compares the wavefronts 'distorted' by the plasma by shifting them relatively to each other, thus obtaining a measure for the gradient of the refractive index (see also [4]). Therefore this type of interferometer can be constructed in a very compact way and is easy to adjust. Fig. 2 shows a solution if two wavelengths have to be used simultaneously.

3.2. Plasma diagnostics by digital speckle pattern interferometry

The speckle effect can be observed if a coherent light source illuminates a rough and diffusely reflecting surface (see Fig. 3). Reflected and incident beams superpose coherently, the field of observation occurs "speckled". Obviously, this effect is correlated with the micro-structure of the surface. An insertion of a transparent object with different index of refraction like a plasma causes phase shifts in the superposing beams, thus changing the intensity of the speckles.

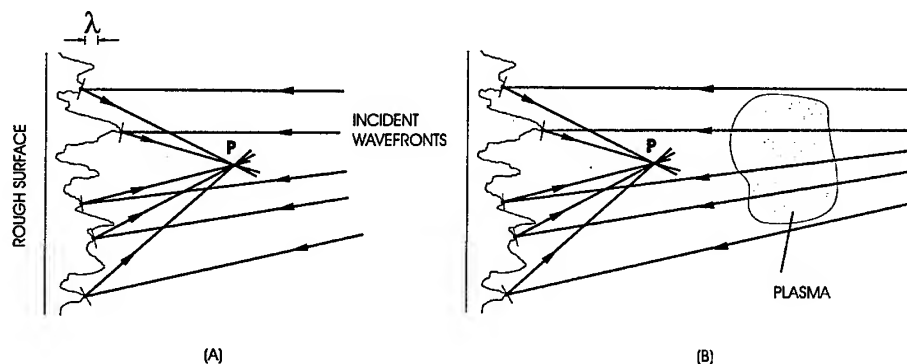


FIG. 3. The speckle effect as a superposition of incident and reflected coherent light beams (A) and its principal use for the investigation of plasmas (B).

Digital speckle pattern interferometry (DSPI) is given, if two rough surfaces are illuminated, which act similar as the mirrors of a classical interferometer, and if their patterns are superposed by a beamsplitter and are recorded by a CCD camera. One of the beams penetrates through the plasma and at least two records have to be made according to two plasma states (frequently the reference

state is simply a missing plasma).

An interference pattern similar to a classical one can be obtained if the two patterns are simply subtracted. However, a positive or negative change of the density of the plasma would cause the same pattern, therefore the effect of an external and known phase shift has to be checked in order to get rid of the before mentioned ambiguity. Related techniques refer to "phase stepping methods". In the work reported here this phase stepping is realized through a piezo-controlled mirror in the reference beam of the DSPI-arrangement within an embedded auxiliary interferometer.

In Fig. 4 a sketch of a two-wavelength digital speckle pattern interferometer is presented including the phase stepping device. As test object a MINIarc from

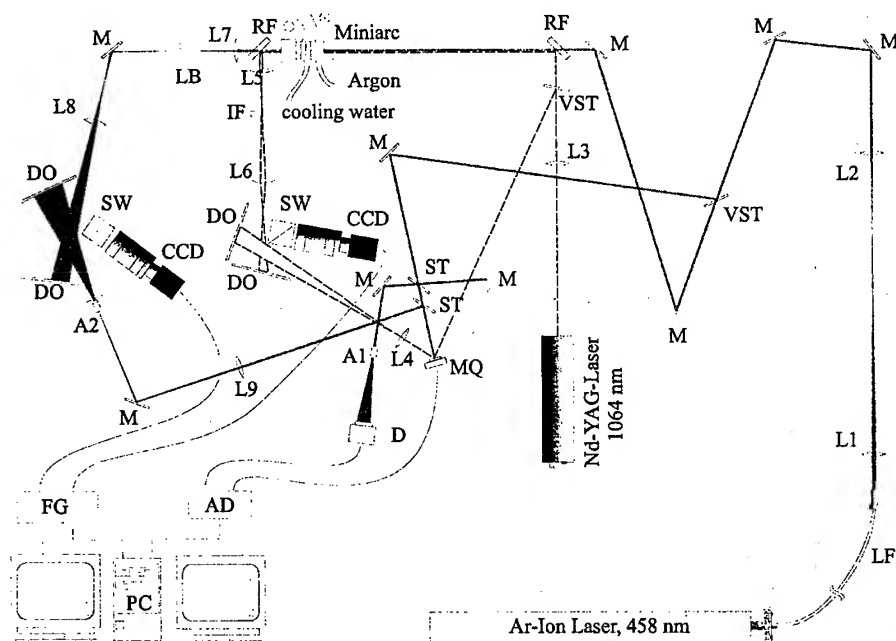


FIG. 4. End-on electron density determination using two wavelength digital speckle pattern interferometry. M mirror, L lens, LB pinhole, IF interference filter, A beam expander, DO diffusor, SW beam splitter cube, VST variable beam splitter, ST beam splitter, FG frame grabber, D detector, RF reflection filter, LF optical fibre, AD analog/digital converter, MQ piezo-controlled phase-stepping mirror.

NIST [13] was investigated end-on, which usually serves as a radiation standard for the uv spectral range. The beams of a cw argon-ion laser (458 nm) and a cw Nd:YAG-laser (1064 nm) were colinearly led end-on through the MINIarc and then to the corresponding diffusors (DO) located in the two actual speckle pattern interferometers ("object beams"). The reference beams for the two wavelengths were picked up before the laser beams reached the MINIarc using variable beam splitters VST and a reflection filter RF for separation of wavelengths.

The optical paths of both reference beams include the same piezo-controlled

mirror MQ as element in an auxiliary interferometer for phase stepping purposes as described above. Based on records taken with and without operated plasma and those from necessary phase stepping procedures one is able to obtain a fringe pattern by applying rather simple image processing techniques (e.g. subtraction of "object" and 'reference' speckle patterns) and rather sophisticated algorithms for phase evaluation. For results and further details refer to [14].

4. Examples for plasma diagnostics by non-linear coherent optics

The permanent progress in non-linear optics enables new classes of plasma diagnostic investigations. The basic requirement for the application of non-linear optics is a pulse laser system of sufficient intensity. In conventional (linear) optics the relation between polarisation P and the applied electrical field strength E of the light wave on matter is given by

$$(4.1) \quad P(t) = \chi^{(1)} E(t),$$

whereas in case of high intensities (e.g. in the focus of a high power laser) this relation must be formally expanded by higher order terms of the electrical field strength E ,

$$(4.2) \quad P(t) = \chi^{(1)} E(t) + \chi^{(2)} E^2(t) + \chi^{(3)} E^3(t) + \dots,$$

where $\chi^{(n)}$ denotes the electrical susceptibility of certain order (see [15]).

Well known are the processes of second harmonic and third harmonic generation by special non-linear crystals (SHG and THG, resp.), as they are frequently used in pulse laser systems. Beneath these standard tools in every pulse laser lab one can also use wave mixing processes in order to investigate the plasma state in situ with extreme spectral and spatial resolution. In this case one induces a non-linear polarisation into the plasma itself. Again, two examples are presented: The first one demonstrates a kind of Fizeau-type dispersion interferometry for electron density determination using a sequence of SHG-steps (" $\chi^{(2)}$ -processes"), the second one shows how plasma diagnostics in the outer regions of a wall-stabilized arc can be performed by degenerate four-wave mixing (" $\chi^{(3)}$ -process"), in order to detect molecular trace species such as nitrogen oxide in the ultraviolet spectral range at about 226 nm.

4.1. Real time end-on arc diagnostics by dispersion interferometry

Using the mini-arc [13] of the former experiment as test object, a completely different interferometric method of arc diagnostics has been demonstrated [16]. The idea is based on non-linear Fizeau interferometry [17, 18, 19, 20] (see Fig. 5). Two laser beams, one of wavelength λ and the other one of wavelength $\lambda/2$ produced by second harmonic generation (SHG) are collinearly penetrating the axis of the arc, however, each of the wavefronts is differently influenced according to the corresponding dispersion of the refractivity ($n-1$) there. After passing the arc's column longitudinally, the fundamental wavelength λ is frequency doubled and superimposed on the one which passed the column already with $\lambda/2$, other

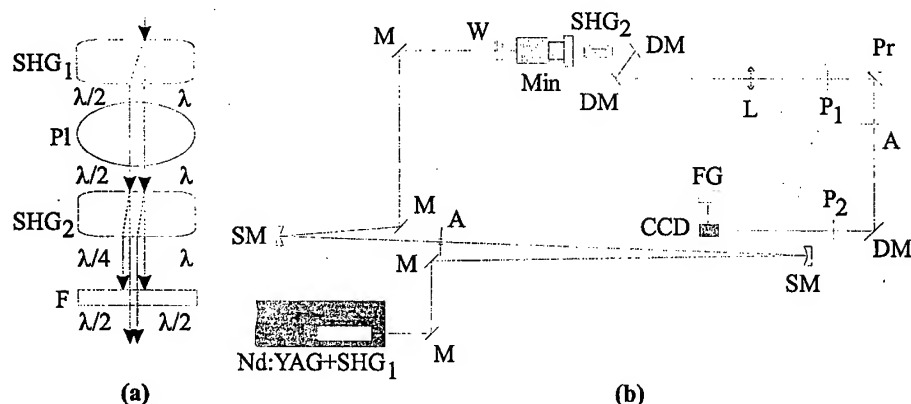


FIG. 5. (a) Principle of nonlinear dispersion interferometry. SHG₁, SHG₂ second harmonic generating crystals, PL plasma, F filter. (b) 2λ electron density measurement using real-time dispersion interferometry. Nd:YAG Nd:YAG laser, SHG₁ internal second harmonic generating crystal, M plane metallic mirror, SM spherical metallic mirror, A diaphragm, W glass wedge, Min mini-arc (end-on observed test plasma), SHG₂ external second harmonic generating crystal, DM plane dielectric mirror for 532 nm, L lens, P₁, P₂ polarizers, Pr glass prism, CCD camera, FG frame grabber.

beams are blocked (see Fig. 5(a)). Thus, the recorded interferogram is an optically obtained direct measure for the difference of the refractivities due to the discharge's dispersion.

As regards the usual methods one has to evaluate the phase changes at every wavelength from the interferograms separately and to obtain the difference numerically. Since, because of limited availability of proper laser sources, a two wavelength electron density measurement frequently suffers from only small differences of the dispersion of the refractivity, the generally error-prone phases obtained at two colours might produce very inaccurate difference values and thus electron densities. By contrast, this new method provides a direct optical approach, the obtained interferogram represents the difference of the plasma's dispersion at the two wavelenths λ and $\lambda/2$.

4.2. Trace element detection by degenerate four-wave mixing

Degenerate four-wave mixing (DFWM) utilizes three waves of equal frequency that interact in the test zone of the plasma (where the three beams are focused together), generating a fourth beam as signal beam. The wave-mixing process used in DFWM produces a coherent, highly collimated, and spectrally bright signal beam. These processes are in contrast to those of linear processes such as spontaneous Raman scattering and LIF (laser induced fluorescence), for which the signal radiates nearly isotropically in space, making signal collection and background discrimination more difficult. Although nonlinear processes are generally considered to be weak, DFWM is a complete resonant process and has very high sensitivity for detecting trace molecular species (compare [21, 22]).

Among the different configurations the phase conjugate and the forward

boxcar geometries are frequently used. The generation of a DFWM-signal in the phase conjugate geometry (pc geometry) is explained by Fig. 6 using the "grating-picture". Considering part (b) of Fig. 6, one recognizes a superposition of the forward pump beam k_f and the probe beam k_p in the test zone, thus producing a spatially strongly varying electrical field ("transient grating"), leading to a non-linear interaction with the plasma there. The backward pump beam k_b is subject to diffraction (similar to reflection here) upon this grating (compare part (c) in Fig. 6) and emerges as a signal beam out of the interaction zone, exactly opposite the incident probe beam k_p (part (a) of Fig. 6).

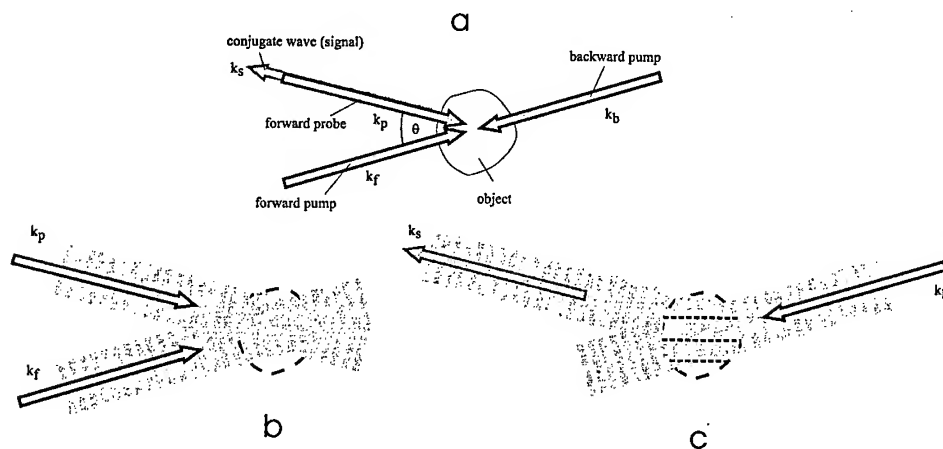


FIG. 6. The principle of DFWM in phase conjugate geometry.

As already mentioned, the signal beam is not isotropic, but rather laser beam-like. Since it is directed, it can be spatially filtered resulting in a more or less background-free signal. The most exceptional of it is, however, that it acts as phase conjugated beam with respect to the probe beam k_p . This means in particular that the path of the probe beam through the medium and its surroundings is taken exactly by the signal beam backwards. This may improve the diagnostic situation strongly, if schlieren and turbulences are given.

The object under investigation was a wall-stabilized argon arc with impurities of nitrogen oxide (NO), which should be detected at the arc axis at positions close to the electrodes. For this purpose a forward box geometry (see Fig. 7) was used instead of the pc geometry. In Fig. 8 molecular spectra of NO are presented for transitions in the vicinity of 226 nm showing an excellent spectral resolution.

An excellent DFWM-investigation of the LTE of an atmospheric argon arc plasma was reported by Musiol et al. [23], who used the ArI 696.5 nm line to obtain axial and radial profiles of temperature and electron density.

The basic requirement for a successful DFWM-measurement is an exact superposition of the pump and probe beams within the test volume. Provided this can be done, ppm-sensitivity in the detection of trace elements can be achieved without large experimental efforts using fast photomultipliers (for nanosecond rise-time) and enhanced CCD-cameras. Moreover, the detected DFWM-line

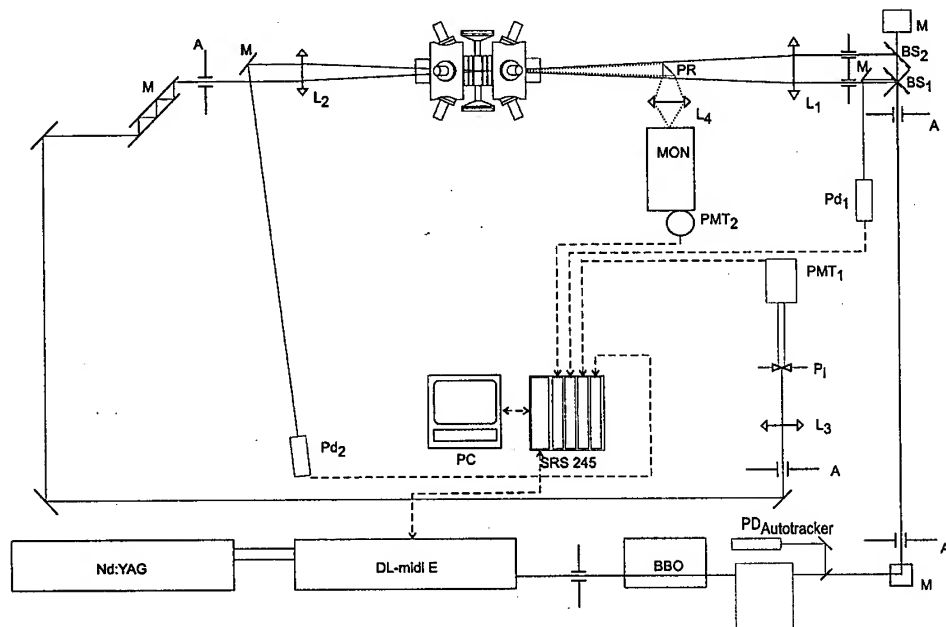


FIG. 7. DFWM with forward boxcar geometry for end-on investigations of a wall-stabilized arc. Nd:YAG neodymium-YAG pulse laser (Spectra Physics), DL-midi E dye laser (Radiant Dyes), BBO SHG-crystal, PD photodiode, M mirror, BS beam splitter, A aperture, L lens, PR prism, PMT photo multiplier tube, MON monochromator, SRS 245 box car averager.

profiles are much better resolved and background-free than those obtained in LIF-experiments because of the cubic dependence of the relevant nonlinear polarisability from the electric field instead of a linear dependence in case of laser induced fluorescence. In the special pc geometry these signals are furthermore Doppler-free. Thus, it is no question how to detect the DFWM-signal but rather one to produce it successfully.

5. Conclusions and outlook

The aim of this review about preferably own contributions to plasma diagnostics by novel techniques of coherent optics was to demonstrate the capability of interferometric measurements and spatially resolving optical arrangements in case of inhomogeneous and partially optically thick plasmas. In these cases particle density determination by refractivity measurements shows some principal advantages over pure emission spectroscopy, although the former ones are generally more complicated to be performed experimentally. The possible methods range from classical, holographic and speckle interferometry. A further development may, on the one hand, go hand in hand with more sophisticated data reduction systems and better detectors. On the other hand the continuously growing field of nonlinear optics offers new diagnostic methods with outstanding features, however, so far the interpretation of the signals turns frequently out as a difficult

problem.

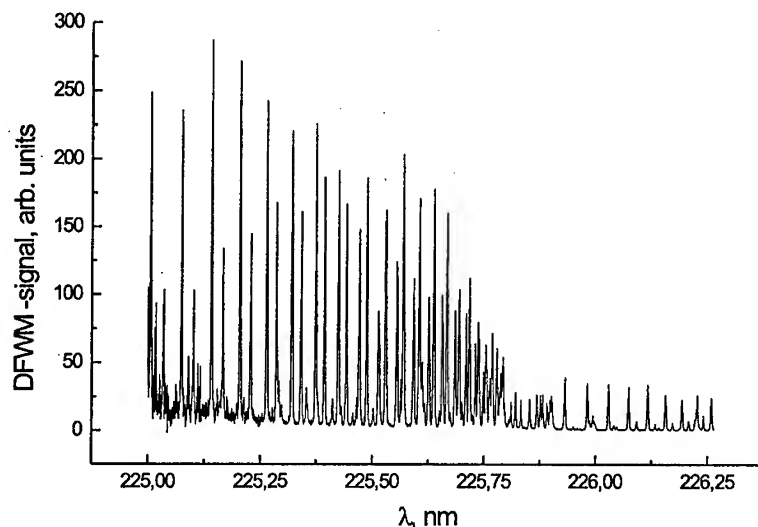


FIG. 8. Part of the rotational spectrum of the NO X-A (0,0) transition detected in situ on the axis (electrode region) of a wall-stabilized argon arc at 226 nm.

Acknowledgments

The author appreciates contributions and help of the members of his working group in the development of novel techniques of plasma diagnostics by coherent optics reported here with special thanks to G. Pretzler, W. Fließner, M. Hipp, J. Flieser, A. Morozov, K. Iskra. On the occasion of the recent retirement of Prof. Dr. H. Jäger, who has been head of the Institut für Experimentalphysik der Technischen Universität Graz for nearly 25 years, the author would like to express his deep gratitude for the permanent promotion and encouragement as well as for the innumerable discussions and suggestions that have led to a strong engagement in plasma diagnostics by coherent optics.

References

1. G. PRETZLER, H. JÄGER, T. NEGER, H. PHILIPP and J. WOISETSCHLÄGER, *Comparison of different methods of Abel inversion using computer simulated and experimental side-on data*, Z. Naturforsch., **47a**, 955, 1992.
2. J. WOISETSCHLÄGER, H. JÄGER, H. PHILIPP, G. PFEIFER and T. NEGER, *Tomographic investigation of the particle density distribution of sodium atoms in a glow discharge using resonance heterodyne holographic interferometry*, Phys. Letters A, **152**, 42, 1991.
3. H. PHILIPP, T. NEGER, H. JÄGER and J. WOISETSCHLÄGER, *Optical tomography of phase objects by holographic interferometry*, Measurement, **10**, 170, 1992.
4. G. PRETZLER, H. JÄGER and T. NEGER, *High-accuracy differential interferometry for the investigation of phase objects*, Meas. Sci. Technol., **4**, 649, 1993.
5. T. NEGER, *Optical tomography by spectral interferometry*, J. Phys. D, **28**, 47, 1995.

6. G. PRETZLER, *Single-shot tomography by differential interferometry*, Meas. Sci. Technol., **6**, 1476, 1995.
7. G. PRETZLER, C. HAAS, T. NEGER and H. JÄGER, *Spatially resolved determination of atomic particle densities and line shapes within an arc plasma by tomographic resonance interferometry*, Appl. Opt., **36**, 8806, 1997.
8. J. RADON, *Ueber die Bestimmung von Funktionen durch Integralwerte laengs gewisser Mannigfaltigkeiten*, Ber. Verh. Saechs. Akad. Wiss. Leipzig Math. Phys., **Kl. 69**, 292, 1917.
9. G. T. HERMAN, *Image reconstruction from projections*, Academic Press, London, New York, Toronto, Sydney, San Francisco, 1980.
10. M. TAKEDA, H. INA and S. KOBAYASHI, *Fourier-transform method of fringe pattern analysis for computer-based topography and interferometry*, J. Opt. Soc. Am., **72**, 156, 1981.
11. H. PHILIPP, T. NEGER and H. JÄGER, J. WOISETSCHLÄGER, *Optical tomography of phase objects by holographic interferometry*, Measurement, **10**, 170, 1992.
12. K. WIDMANN, G. PRETZLER, J. WOISETSCHLÄGER, H. PHILIPP, T. NEGER and H. JÄGER, *Interferometric determination of the electron density in a high-pressure Xe-lamp using a holographic optical element*, Appl. Opt., **35**, 5896, 1996.
13. M. BRIDGES and W. OTT, Appl. Opt., **16**, 367, 1977.
14. M. HIPPEL, W. FLIESSER, T. NEGER and H. JÄGER, *Determination of the spatial distribution of the electron density in an argon arc by digital speckle pattern interferometry*, XXIIIth ICPIG, Contributed Papers, 1997, M. C. BORDAGE and A. GLEIZES, Universite Paul Sabatier of Toulouse, Toulouse/France, **VI**, 122.
15. R. W. BOYD, *Nonlinear Optics*, Academic Press, Boston, 1992.
16. J. FLIESER, A. MOROZOV, T. NEGER and H. JÄGER, *Real-time measurements of electron density spatial distributions in a mini-arc plasma by dispersion interferometry*, J. Phys. D, **29**, 2413, 1996.
17. G. V. OSTROVSKAYA and Yu. I. OSTROVSKII, Sov. Phys.-Tech. Phys., **15**, 1890, 1971.
18. F. A. HOPF, A. TOMITA and G. AL-JUMAILY, Opt. Lett., **5**, 386, 1980.
19. Kh. P. ALUM, Yu. V. KOVAL'CHUK and G. V. OSTROVSKAYA, Sov. Phys.-Tech. Phys., **26**, 928, 1981.
20. Kh. P. ALUM, Yu. V. KOVAL'CHUK and G. V. OSTROVSKAYA, Sov. Phys.-Tech. Phys., **29**, 534, 1984.
21. R. L. RARROW and D.J. RAKESTRAW, Science, **257**, 1894, 1992.
22. J. FLIESER, K. ISKRA, A. MOROZOV, G. PICHLER and T. NEGER, *Combustion flame diagnostics using degenerate four-wave mixing: the dipole moment power law and rotational temperature for nitric oxide*, J. Phys. D: Appl. Phys., **31**, 402, 1998.
23. K. MUSIOL, K. DZIERŻĘGA, E. PAWELEC, B. POKRZYWKA, S. PELLERIN and S. LABUZ, J. Phys. D: Appl. Phys., **30**, 1, 1997.

SOLITARY WAVES IN THE EARTH'S UPPER IONOSPHERE

H. L. PÉCSELI¹, S. H. HØYMORK², B. LYBEKK¹, J. TRULSEN³ and A. ERIKSON⁴

¹PHYSICS DEPARTMENT, UNIVERSITY OF OSLO

Box 1048 Blindern N-0316 Oslo, Norway

²SWEDISH INSTITUTE OF SPACE PHYSICS

S-981 28 Kiruna, Sweden

³INSTITUTE FOR THEORETICAL ASTROPHYSICS, UNIVERSITY OF OSLO

Box 1029 Blindern, N-0315 Oslo, Norway

⁴SWEDISH INSTITUTE OF SPACE PHYSICS

S-755 91 Uppsala, Sweden

Electrostatic wave packets in the frequency range of lower hybrid waves have been detected by the instruments on the Freja satellite and earlier also by instrumented rocket payloads. These waves are often associated with local density depletions, indicating that the structures can be interpreted as wave filled cavities which are strongly elongated along the magnetic field. Frequently, the observed wave packets have the appearance of almost textbook illustrations of envelope solitons. The basic features of the observations are presented and discussed.

1. Introduction

Localized electrostatic wave packets in the lower hybrid wave frequency region have been detected by instrumented rockets MARIE as reported in [1] and on TOPAZ III described in [2], and lately by measurements from the Freja satellite [3, 4, 5, 6, 7]. Instruments on board the Freja satellite [8] measure wave bursts in the range of several hundred Hz to a few kHz. Usually, the electric field is detected in two bands; the *lf*-band is obtained with a sampling rate of 4 kHz, while the *mf*-band is sampled by 16 kHz. A characteristic feature of the observed events is a density depletion accompanied by an enhancement of the electric field fluctuations, giving the appearance of wave filled cavities in the ionospheric plasma. In Fig. 1 we show an isolated event. The observations often have the distinct appearance of an envelope soliton. The observed phenomena seem to be very persistent, thousands of such cavities have been observed distributed over a large number of orbits. It might be that the lower hybrid wave cavities described in the present study represent the example of solitary wave structures to occur most abundantly in nature.

In the present work we summarize some new results concerning the basic properties of the observed phenomena and some aspects of their interpretation.

2. Basic characteristics of wave-packets and cavities

Details of a wave-filled cavity are shown in Fig. 1. Note that the probes detecting the density variations and those measuring electric fields are separated in space, i.e. the observation times of peak density depletion and local wave envelope

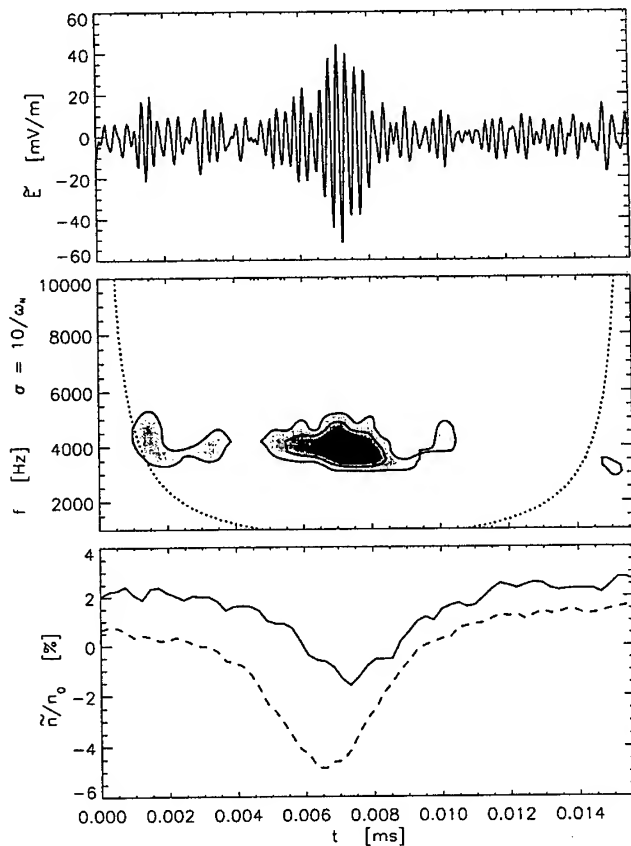


FIG. 1. An example of a lower hybrid wave cavity detected by instruments on the Freja satellite. The lower panel is the relative plasma density variations in % as detected by the two Langmuir probes, the upper panel is the electric field fluctuation in the mf -band and the middle panel shows the wavelet transform of the electric field fluctuations. The wavelet analysis is based on a Morlet wavelet. Note that the probes detecting density and electric fields are at different spatial positions on the satellite. This gives rise to a slight relative displacement in time of the respective signals.

maxima do not necessarily coincide even in the case where the shape of the spatial wave envelope closely follows the density variation.

Concerning the low frequency density variations, signals are available from *two* Langmuir probes with 11 m separation. In most cases, a density depletion is observed in *both* signals, see Fig. 1, and it is found that the depletion propagates from one probe to the other, generally with negligible change in shape, indicating that the evolution of density depletions is slow compared to the satellite cavity-transit time [5].

Wave-packets accompanying the density depletions are usually seen in the *lf* as well as *mf* data for the electric fields. Sometimes the signal can be present only in the *mf* band, as shown by an example in [9]. On the other hand there are examples where a clear density depletion was present without any local wave activity, see [9], although unmistakable examples of this type are relatively sparse. In addition, it should be mentioned that more recently we have observed lower hybrid wave activity localized at local density *maxima*. The number of these observations is limited, but the coincidence of density maxima and wave activity seems to be so clear that a simple statistical or random simultaneous occurrence may be ruled out. No definite conclusion can be made on the basis of this limited dataset.

Simultaneous measurements of electric and magnetic field components demonstrate that the fluctuations considered here are electrostatic [3, 4, 9]. By using the ionospheric data for the actual conditions, it is readily demonstrated that the observed frequencies in the spacecraft frame of reference are comparable to the lower hybrid frequency ω_{LH} , and that no other electrostatic wavetype seems to be a likely candidate.

To obtain detailed information of the frequency variation we used a wavelet transform of the electric field data, see also [9]. A typical result is shown in Fig. 1. Since the *mf*-data are usually only available during a burst mode, we can not expect *always* to have the *mf*-band activity available for a given cavity. The wave frequency is usually restricted to a relatively narrow frequency range centered at 4 kHz, and the characteristic frequency can be determined quite accurately.

Analyzing simultaneous observations of density depletions and electric fields detected in the full *mf*-bandwidth similar to that shown in Fig. 1, we obtained a scatter diagram of corresponding peak density depletions and peak electric field values, see Fig. 2. The peak electric field is obtained as the half-value of the peak to peak variations ($pp/2$). We note that the interpretation of the figure is not unambiguous, but at least it does not speak against a model which assumes a statistical relation between electric fields and density depletions. Recall that the measurements usually give only one component of the electric field, and even this may in some cases be somewhat uncertain due to probe aliasing effects.

When interpreting the satellite observations, we have to bear in mind that the cavities are spatially localized structures which are intercepted by the satellite orbit at random positions. For instance a cavity width determined from one observation is just a chord length and not necessarily the diameter of the actual cavity. Although it is not logically possible to draw any conclusion concerning the full space-time variation of the individual cavities observed, it is nevertheless meaningful to propose a physically realistic model for the space time evolution of cavities, and by simple assumption concerning the statistics on the intersection of cavities by the satellite, the relevant statistical distributions of cavity widths and

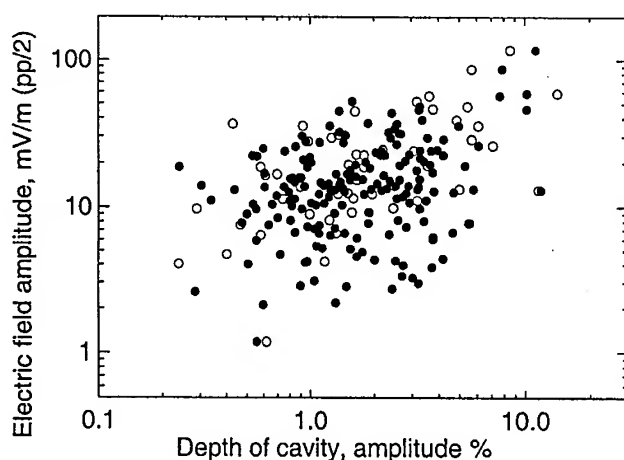


FIG. 2. Scatterdiagram, in double logarithmic presentation, of simultaneously obtained peak density depletions and corresponding electric field amplitudes in the *mf*-band.

other parameters can be determined. These analytically obtained distributions can then be compared to the experimental ones, and the model accepted or rejected according to the agreement between the two. In this way it is possible to obtain some "average" information, which in some sense pertains also to the individual cavities.

In the first analysis of this kind for the present data [9], studied the collapse model often suggested as a likely explanation for the occurrence of lower hybrid wave cavities [10]. In [9] the time evolution of the cavity width was assumed to be prescribed by the analytic results from collapsing lower hybrid waves. Assuming the collapse to be initiated at random, uniformly distributed times an expression for the cord-length distribution was obtained to be compared with experimental results. Although the study assumed a simple "inverted top hat" model for the density depletions, the results were rather unambiguously speaking against the proposed model. An alternative to the collapse model was suggested in terms of a thermal instability [9]. Here, the waves give up energy to particles predominantly in positions where a small density depletion is present due to some random irregularity. Due to the local pressure increase the plasma subsequently expands along the magnetic field lines and the process results in an enhancement of the original irregularity and an ensuing local trapping of the lower hybrid wave.

As an extension of the analysis in [9, 11] we show in Fig. 3 a scatterplot for the simultaneously measured peak amplitudes and widths, obtained from the data. The scatter in the data points in Fig. 3 can have two different origins: either the cavities are all more or less identical, and the scatter arises because of the statistical variation in the "impact parameter" of the satellite orbits with respect to a cavity. Alternatively, the scatter is predominantly reflecting the statistical distribution in the scales of the many cavities. This question can again only be resolved by postulating a model, derive its statistical properties

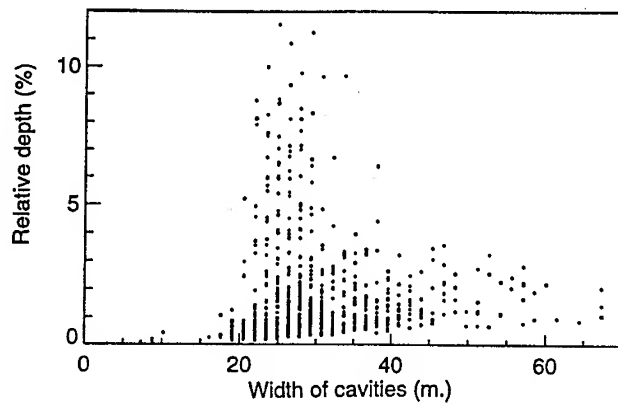


FIG. 3. Scatterdiagram for amplitudes and chord-lengths measured at half amplitude, obtained for 741 cavities found in orbit 7580. The vertical "stripes" arise because of the sampling in the data.

and compare these with observations. We here assume that the time evolution of the cavity is so slow that its variation during the transit time of the satellite can be ignored. This seems to be a good approximation since the cavities are usually found to be symmetric, see e.g. Fig. 1, i.e. the gradients on two sides of the density depletions are the same. If we "mirror" the time axis with respect to the local extremum value of the density depletions associated with the cavity, we usually find that its mirror image is usually almost indistinguishable from the original one. This property can only be explained by the assumed slow time evolution.

We postulate a relatively general analytical form for cavities

$$(2.1) \quad n = n_0 - \Delta n e^{-\frac{1}{2}[(x^2 + y^2)^m / R^{2m}]}.$$

With the adjustable parameters m , R and Δn , the model can accommodate a large variety of cavity forms. The inverted top hat model referred to before is obtained for $m \rightarrow \infty$, while a simple Gaussian density depletion is found for $m = 1$. We use the same exponent on both x and y for symmetry reasons, since the problem does not have any preferred direction perpendicular to a locally homogeneous magnetic field when large scale density gradients are of minor importance. In (2.1) we can take $y = \text{const}$ as an impact parameter defining the distance between the satellite orbit and the center of the cavity, while x is the coordinate along the satellite trajectory, which in the data is translated into a time-variable $t = x/V$ with V being the satellite velocity.

The result (2.1) offers a straight forward parametric presentation of the normalized depth-chordlength relation as

$$(2.2) \quad \left\{ e^{-\frac{1}{2}\xi^{2m}}, 2\sqrt{(2 \ln 2 + \xi^{2m})^{1/m} - \xi^2} \right\}$$

with $\xi \equiv y/R$ being the normalized impact parameter, and the density perturbation being normalized by its peak value. The chord-length in (2.2) is defined at the half-value of the peak amplitude, $\exp(-\frac{1}{2}\xi^{2m})$, along the trajectory.

When examining an actual record, the impact parameter is in general varying from cavity to cavity, with y being statistically distributed. The only acceptable assumption concerning its probability density is a uniform distribution, $P(y) = 1/L_M$ for $0 < y < L_M$, and zero otherwise, where L_M is a maximum distance of the satellite from the center of a cavity. Eventually we let $L_M \rightarrow \infty$. With this assumption we can in principle easily obtain the marginal probability densities $P(\ell)$ and $P(\tilde{n})$. For instance, using $P(\tilde{n})d\tilde{n} = P(y)dy$ we readily find

$$(2.3) \quad P\left(\frac{\tilde{n}}{\Delta n}\right) = \frac{1}{mL_M} \frac{\Delta n}{\tilde{n}} \left[2 \ln\left(\frac{\tilde{n}}{\Delta n}\right)\right]^{-1+1/(2m)},$$

with $e^{-\frac{1}{2}(L_M/R)^{2m}} < \tilde{n}/\Delta n < 1$. The probability density (2.3) is normalized for all finite L_M , but the expression may give trivial results in the limit of $L_M \rightarrow \infty$ for certain m .

We can test (2.1) by fitting the parameters m and R to the actual data, after removal of a simple linear and a quadratic trend in the data. As an illustration we show in Fig. 4 such a fit obtained for the cavity shown in Fig. 1. The data from

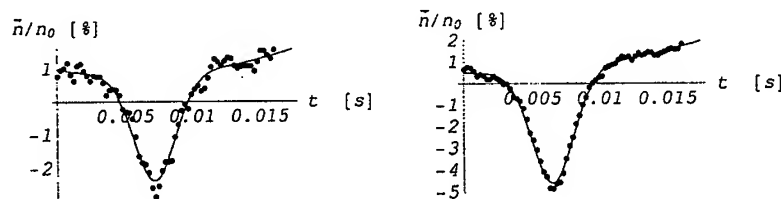


FIG. 4. Fit of a Gaussian form for a selected cavity. The two curves correspond to the two Langmuir probes which intercept the cavity at two different positions. In the curve-fitting we allowed also for two small terms proportional to t and t^2 .

the two probes are shown with black dots given by the low frequency sampling used in this case, while the full line is a Gaussian, i.e. $m = 1$, while $R = 0.0016$ s, corresponding to a length scale of 9.7 m. Note that the *same* Gaussian is used for both signals, since it is the same cavity which is intercepted at two position by the two Langmuir probes. Evidently, the fit is quite good in this case. We have examined a number of cavities, and show in Fig. 5 the normalized root-mean-square deviation between the best Gaussian fit and the individual datapoints for 130 cavities. Evidently, the fit is significantly better than 10%, and a Gaussian variation can be used as a good approximation, implying that $m \approx 1$ in (2.2) is a useful approximation when analyzing the data. In this case, however, the relation (2.2) becomes particularly simple, giving $\{e^{-\frac{1}{2}\xi^2}, 2\sqrt{2\ln 2}\}$. With y being statistically distributed, but all cavities identical, the scatterdiagram in Fig. 3 should give one vertical line with all chord-lengths being the same and

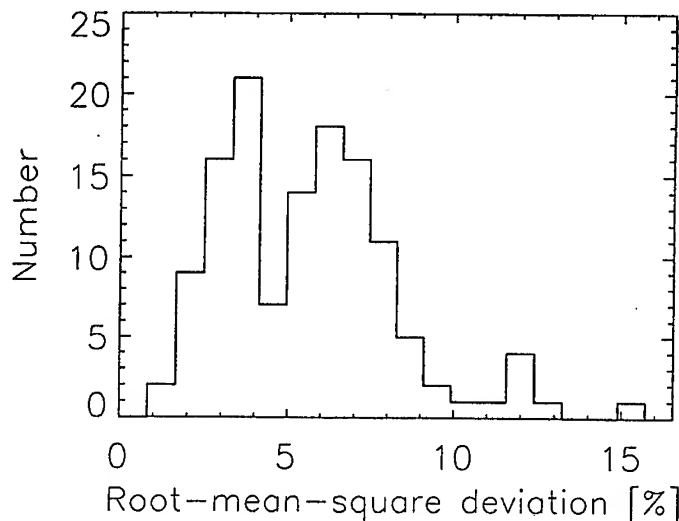


FIG. 5. Normalized mean square deviation between the best fitted Gaussian form and the datapoints for 130 cavities observed in pass 1234, 7. January 1993.

identical to the cavity half-width. Evidently this is not the case, and we can conclude that the cavity diameters are statistically distributed, with distributions as those shown e.g. in [9].

By inspection of Fig. 3 it is evident that the density depletions with the average widths are in general also those associated with the deepest density depletions. The very narrow, as well as the widest observed density depletions are generally also the most shallow ones. This seems in contradiction with a collapse model where the individual cavities are initially wide and shallow, and subsequently narrows while the density depletion gets deeper.

3. Conditions for occurrence of cavities

A large number of satellite passes were investigated [6, 7] to determine the distribution of cavities. They are observed over a large region of the polar cap, but their spatial distribution is not quite uniform, even when averaged over long times by including observations taken more than a year apart. There are regions with several orbits but with few or no cavity observations. On the other hand there are regions where cavities are present in every orbit. A summary figure in [12] give the distribution of precipitating particles in the northern hemisphere. The *drizzle-type* high energy auroral-zone precipitation seems to have a distribution reminiscent of the cavity distribution we observe. Although the statistics need to be improved, this agreement deserves a closer scrutiny.

Using the data for electron and ion energy distributions obtained on the satellite, we attempted also to correlate the occurrence of cavities with these observations. See also [5] for a similar discussion. To complete the presentation

we considered also data for magnetic fields and currents. No straightforward or evident conclusion emerged from these and similar studies. Usually we find cavities present in the vicinity, or just outside, regions of enhanced magnetospheric activity, where strong conductivity gradients are expected. (There *are* however also some observations of cavities *inside* inverted V-events; for instance [7].) A conclusion which is consistent with the observations can be made as follows; it can be argued that the active regions are characterized by excitation of many different wavetypes, which can disturb the formation of cavities *inside* these regions. It thus seems difficult to imagine formation of cavities in an environment with significant activity of ion-acoustic waves, for instance. Cavities are thus assumed to be excited in the regions with drizzle-type particle precipitation, but quenched in the active regions as argued. We expect that lower-hybrid waves can be excited as well in these active regions. All these different wavetypes are radiated out of these active regions, and most of them will be damped. Lower-hybrid waves propagating perpendicular to magnetic fields are however without any noticeable linear damping, see for instance the numerically obtained linear dispersion relation given in [9]. Outside the active regions these waves can generate cavities without the disturbance or interference from other wavetypes. By the latter argument the active regions are important for the generation of lower-hybrid waves, explaining a preference for observing waves in the vicinity of such regions. It can however not be argued that such active regions are the *only* sources of lower-hybrid waves.

3.1. Spatial distribution of cavities

Two different scenarios for the formation of cavities can be distinguished; one where they are generated with more or less regular intervals (for instance by a modulational instability) or alternatively by a random process where a cavity is formed at a spatial position independent of the presence of others. These, or other, conjectures can be tested experimentally. We propose, as a hypothesis, that the cavities are randomly distributed along the spacecraft trajectory, with the position of one cavity being statistically independent of all others [9, 11]. The consequence of the hypothesis is that cavities are to be Poisson distributed along the trajectory, i.e. the distribution of the number N of cavities in an interval of length \mathcal{L} is $P(N) = (\nu\mathcal{L})^N \exp(-\nu\mathcal{L})/N!$ with ν being the density of cavities along the trajectory. An estimate for this probability density is a measurable quantity, offering a straightforward test of the hypothesis. Here we took the time interval to be 0.375 s, corresponding to a spatial interval of $2.33 \cdot 10^3$ m. As a check we also considered other durations of the time interval, see also [11]. Results are shown by [7], based on data for plasma density, supported by *lf*-data, taking into account that not *all* cavities need to have a noticeable wave activity in the *lf*-band. The identification of cavities is not straightforward in all cases, but the uncertainty is expected to diminish in significance when a large number of events are analyzed. A Poisson distribution is found to be reasonably justified.

An alternative test of the Poisson hypothesis is to obtain the distribution of separation between cavities. For the Poisson model the distribution should follow an exponential, with the exponent determining the average distance between

cavities along the satellite trajectory. See the summary given in [7] for results.

4. Conclusions

In this paper we presented some basic properties of the localized bursts of lower-hybrid waves and associated density cavities observed by the Freja satellite. We found indications that the cavities might occur predominantly in regions where we have auroral zone (high-energy) particle precipitation (drizzle-type). There seems to be solid evidence for claiming that cavities are Poisson-distributed in the regions where they occur, and on the basis of this observation it can be argued that cavities develop independently, presumably triggered by some burst type phenomena. Our studies demonstrate that the observed distributions are surprisingly constant in time. For instance the spatial density of cavities varies by less than a factor 3 for data obtained by more than a years separation. These results indicate that lower-hybrid waves and wave cavities are common in the Earth's upper ionosphere, and not necessarily associated with violent events. The occurrence does not have any evident seasonal variation, and within the lifetime of the Freja satellite, the cavities were present at all years with equal probability.

At times where the cavity activity is significant, the data give a typical density of cavities of $\mu_c \sim 10^{-4} \text{ m}^{-2}$ in a plane perpendicular to the magnetic field (μ_c has dimensions length^{-2}). With an average diameter of 60 m, the cavities cover 10 – 20 % of the plane. The wave energy density in the cavities was found to be of the order of $10^{-2} - 10^{-4}$ % of the thermal plasma energy density. The cavities thus contribute negligibly to the overall energy budget of the plasma. On the other hand, the wave amplitude *inside* a cavity is 2-10 times that *outside*. Consequently, almost one half of the lower hybrid wave energy can be concentrated in cavities in those cases where they are a noticeable constituent in the data. It is plausible that this wave energy concentration can give rise to low density energetic particle beams. One important remaining question concerns the elongation of cavities along the magnetic field. Our expectations are that the cavities are long, probably more than several km. A complete energy-budget of the observed lower-hybrid waves is only feasible when this B-parallel scale-length is known.

Acknowledgments

This work was in part supported by the Norwegian National Science Foundation.

References

1. J. LABELLE, P.M. KINTNER, A.W. YAU and B.A. WHALEN, *Large amplitude wave packets observed in the ionosphere in association with transverse ion acceleration*. J. Geophys. Res., **91**, 7113, 1986.
2. J.L. VAGO, P.M. KINTNER, S.W. CHESNEY, R.L. ARNOLDY, K.A. LYNCH, T.E. MOORE, and C.J. POLLOCK, *Transverse ion acceleration by localized lower hybrid waves in the topside Auroral ionosphere*. J. Geophys. Res., **97**, 16935, 1992.

3. P.O. DOVNER, A.I. ERIKSSON, R. BOSTRÖM and B. HOLBACK, *Freja multiprobe observations of electrostatic solitary structures*. Geophys. Res. Lett., **21**, 1827, 1994.
4. A.I. ERIKSSON, B. HOLBACK, P.O. DOVNER, R. BOSTRÖM, G. HOLMGREN, M. ANDRÉ, L. ELIASSON and P.M. KINTNER, *Freja observations of correlated small-scale density depletions and enhanced lower-hybrid waves*. Geophys. Res. Lett., **21**, 1843, 1994.
5. P.O. DOVNER, A.I. ERIKSSON, R. BOSTRÖM, B. HOLBACK, J. WALDEMARK, L. ELIASSON, and M. BOEHM, *The occurrence of lower hybrid cavities in the upper ionosphere*. Geophys. Res. Lett., **24**, 619, 1997.
6. S.H. KJUS, L. ELIASSON, H.L. PÉCSELI, B. LYBEKK, J. HOLTET, P. NORQVIST, J. TRULSEN, and A. ERIKSSON, *Lower Hybrid Waves in the Earth's Upper Ionosphere Wave Cavitation and Ion Energization*. in *Physics of Space Plasmas (1998)*. Number 15', Eds. T. Chang and J. R. Jasperse, (MIT Center for Theoretical Geo/Cosmo Plasma Physics, Cambridge, MA, 1998), 209–214.
7. S. H. KJUS, H.L. PÉCSELI, B. LYBEKK, J. HOLTET, J. TRULSEN, H. LÜHR, and A. ERIKSSON, *Statistics of the Lower-Hybrid Wave Cavities Detected by the Freja satellite*. J. Geophys. Res., **103**, 26, 633, 1998.
8. R. LUNDIN, G. HAERENDEL and S. GRAHN, *The Freja project*. Geophys. Res. Lett., **21**, 1823, 1994.
9. H.L. PÉCSELI, K. IRANPOUR, Ø. HOLTER, B. LYBEKK, J. HOLTET, J. TRULSEN, A. ERIKSSON and B. HOLBACK, *Lower hybrid wave cavities detected by the Freja satellite*. J. Geophys. Res., **101**, 5299, 1996.
10. V.D. SHAPIRO, V.I. SHEVCHENKO, G.I. SOLOV'EV, V.P. KALININ, R. BINGHAM, R.Z. SAGDEEV, M. ASHOUR-ABDALLA, J. DAWSON and J.J. SU, *Wave collapse at the lower hybrid resonance*. Phys. Fluids, **B5**, 3148 (1993).
11. H.L. PÉCSELI, B. LYBEKK, J. TRULSEN, and A. ERIKSSON, *Lower hybrid wave cavities detected by instrumented spacecrafts*. Plasma Phys. Contr. Fusion, **39**, A227, 1997.
12. T.R. HARTZ, *The Radiating Atmosphere*, (Reichl, Dordrecht, 1971)

ELECTRON BEAMS GENERATED IN HOLLOW CATHODE LOW PRESSURE TRANSIENT DISCHARGES

A. M. POINTU¹ AND G. MODREANU¹, M. GANCIU², N. B. MANDACHE², M. NISTOR²
AND I. IOVITZ POPESCU²

¹LPGP, UNIVERSITÉ PARIS-SUD

91405 Orsay Cedex, France

²INSTITUTE OF ATOMIC PHYSICS, NILPRP, PLASMA DEPARTMENT

PO Box MG-36 Bucharest, Romania

Preionization controlled transient hollow cathode discharges operating at pulsed high voltages of some tens of kV, at gas pressure around 0.1 mbar are used to generate filamentary electron beams of some tens of A during about 10 ns. These latter are energy analyzed, with different methods, evidencing poly-energetic distribution function containing both "run away" electrons with energy equal to the total instant voltage applied to the discharge and energy distributed slower electrons extending towards some tens of eV. Specific experimental conditions allow improvement of beam propagation conditions in terms of trajectory control.

1. Introduction

Pseudospark discharges have been studied since 20 years [1] either as high power switches or as electron beam sources. A recent overview in their scientific and technological progress have been presented in [2]. The former application uses their ability to deliver high current densities within very short times; the latter one is related to an initial stage of the discharge where an intense electron beam is extracted and used for material processing, thin film deposition, semiconductor lithography.

We have developed since 1994 [3] a discharge belonging to pseudospark family but with specific configuration and operating procedure producing electron beams having the advantage of both stability and reproducibility, without the constraint of internal bore holes and correlative erosion problems. Here, we present measurements proving that the beam energy distribution function (BEDF) is poly-energetic, roughly decreasing with energy. We also describe specific experimental conditions for beam propagation allowing improvement in terms of control of its propagation conditions.

2. Basic set up, overall description

Compared to classical pseudospark, the discharge under study presents two specific characteristics consisting in an open ended cathode and a pre-ionization in the cathodic zone. In this frame, many configurations can be used, involving either internal or external electrodes, either dc or ac pre-ionization, short or long inter-electrodes region. Any gas at some 0.1 mbar can be used. Fig. 1 presents some of them, going from totally external to totally internal electrodes. They

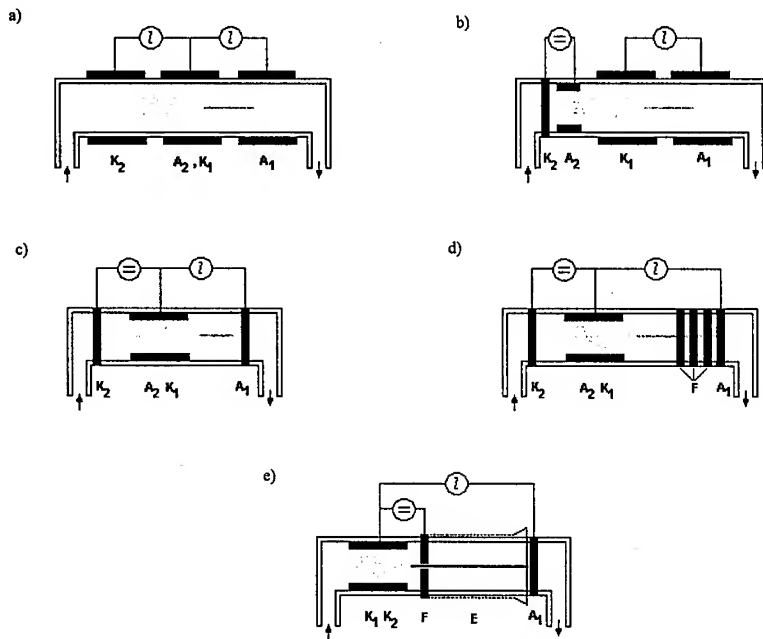


FIG. 1. Some examples of discharge configurations: K_1 , K_2 : common cathode; A_1 , A_2 : anodes for the main and the auxiliary discharges, respectively; F: floating electrodes, E: external grid; "basic" single-gap and "multigap" configuration correspond respectively to c) and d).

have in common: a glass discharge tube, 3 cm diameter, a main discharge created by a pulsed high voltage applied between a cylindrical open ended cathode K_1 with typical length of 5 to 10 cm, and an anode A_1 . In the case of external electrodes, the pre-ionization is ensured by a pulsed high voltage auxiliary discharge (electrodes A_2 and K_2), preceding the main discharge pulse with a controlled advance. In the case of internal auxiliary electrodes, the pre-ionization uses dc discharge and current adjustment. Typically, the distance between A_1 and K_1 is 2 to 3 cm. Nevertheless, when a long interelectrode region is required (up to 30 cm), a supplementary floating electrode in front of the K_1 output (cf. Fig. 1e) is related to an external grid which ensures stability and focusing of the beam, as seen in [4]. A multi-gap configuration has been also studied (cf. Fig. 1d), with several floating electrodes between A_1 et K_1 consisting in metallic plates,

with central bore holes, alike classically used in pseudospark devices [5].

In all these configurations, when adjustment of the auxiliary discharge is convenient, a beam is created and gives rise to a filamentary bright discharge, well collimated around the axis, with an apparent diameter of the order of 1 mm.

Contrary to usual pseudospark discharges, fast high voltage pulses between main electrodes are requested here to allow sufficient breakdown voltage. Although many possibilities can be used, we generally produce them by a dc high voltage supply charging in parallel two capacitors through a pulse forming line. The line is grounded via a rotary spark gap so that capacitors are discharged in series and an opposite polarity voltage, twice the initial value is applied between K_1 and A_1 with a rise time around 50 ns. Using two forming lines and four capacitors, it allows to obtain four times the initial voltage value if necessary.

Fig. 2 presents observed phenomena in the case of two external main electrodes, made of salt water, -thus transparent- cylinders. Auxiliary discharge is dc type and uses internal metallic cylindrical electrodes on the left side. Three

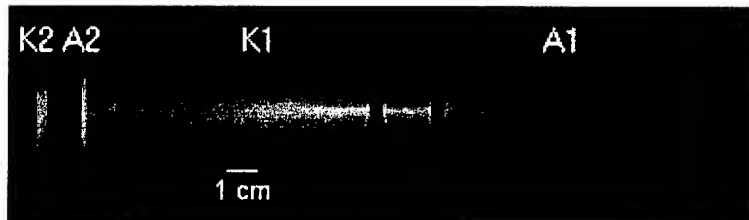


FIG. 2. Insight into the cathodic zone (on the left) and the inter-electrode bright and narrow plasma channel, using configuration with external transparent main electrodes.

successive luminescent parts of the main discharge can be observed: i) the cathodic region where a quite homogeneous brightness becomes progressively focused around the axis; ii) the inter-electrode region with an axial filamentary bright discharge; iii) the anodic region where the latter diverges towards the tube border to ensure the current return.

In fact, an axial electron beam is evidenced between K_1 and A_1 as being associated to filamentary discharge by: (i) sensitivity to a magnetic field, (ii) ability to be collected after the anode, when this latter is a perforated disc, giving a measurable current, (iii) interaction effects with the anodic collector such as X fluorescence and erosion going eventually till hole drilling if interaction time is long enough.

In order to describe the events chronology and to give an order of magnitude of some parameters, Fig. 3 presents an example of discharge parameters measured in Argon at about 0.1 mbar: inter-electrode voltage, total discharge current, filamentary discharge brightness observed by an ArII line intensity, beam current, and X-ray fluorescence of a scintillator used as a target. In an optimized geometry the beam current could rise up to 300-400 A [2, 13].

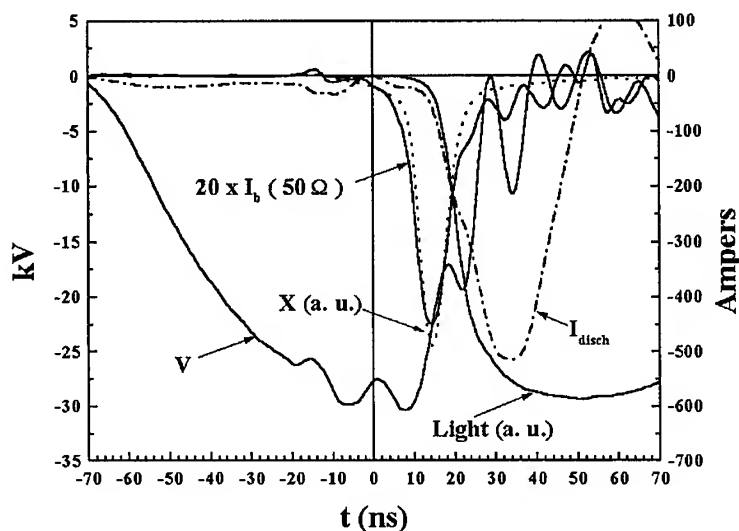


FIG. 3. Variation versus time of some electrical discharge characteristics: total discharge voltage V , beam current I_b , discharge current I_{disch} , plasma channel radiated light (427.7 nm Ar II line), scintillator X fluorescence from electron beam impact.

3. Beam Energy Distribution Function (BEDF)

Relatively few studies have been devoted to the beam energy distribution function (BEDF). Experimental evidence, however has proved that high energy electrons only exist at the beginning of the discharge, before the discharge current reaches maximum value [6, 7], consistent to the spectrum measured by Ding et al [8], which shows that electron energy equals the instantaneous chamber voltage. Such a distribution leads to a hump shaped time averaged BEDF peaked around 2/3 of voltage breakdown value, with a FWHM which is about 1/4 of this value, similar to the one measured by magnetic deflection [9] and from gas bremsstrahlung X-ray spectroscopy [5]. In fact, the magnetic measurements involved an electron detector which was not sensitive to slow electrons; moreover, in the case of bremsstrahlung measurements, it is admitted in ref [10] that the real spectrum has to be extrapolated to low energies, giving a complete distribution decreasing versus energy. This property is also predicted in a model by Pitchford [11], which, in addition to primary run-away electrons, includes a main population of lower energy electrons.

Knowledge of BEDF is essential to appreciate the pertinence of potential beam applications. We present here measurements using three different complementary methods.

3.1. Magnetic analyzer

A simple device to measure the BEDF is a magnetic analyzer. Basically, it consists of a measurement chamber behind the anode hole, in which acts a quasi-

homogeneous linear magnetic field (typically tens of Gauss). The entrance slit is placed on-axis, in order to ensure a paraxial analyzed beam. The exit slit is off-axis at a sufficient distance to ensure a good energy resolution. Behind the exit slit chamber lies the beam detector. The energy calibration in beam velocity is made in situ by using a low-intensity mono-energetic electron beam produced in a high-voltage abnormal dc discharge between the anode and a grid, mounted at the anodic end of the cathode.

First results had been presented in [9]. Results obtained with an improved analyzer are presented in [12]. Improvement consists both in the detector nature (here a Faraday cage able to collect also slow electrons) and in the measurement chamber geometrical characteristics, giving a good resolution (10%) and a relatively short chamber length (35 mm). In fact, a short beam path is necessary to reduce the effects of charge induced beam divergence and, consequently, loss of slow electrons.

Two types of configurations have been used, that we shall call basic (single gap) and multi-gap configurations, corresponding respectively to Fig. 1c and Fig. 1d.

Fig. 4 shows typical time-integrated energy spectra measured with the magnetic analyzer for the basic and multi-gap configurations, obtained at 33 kV breakdown voltage. We observe that the energy spectrum for the multi-gap configuration is enriched at all energies compared to the spectrum for the single gap. In particular we note the low energy component which is missing in the case of

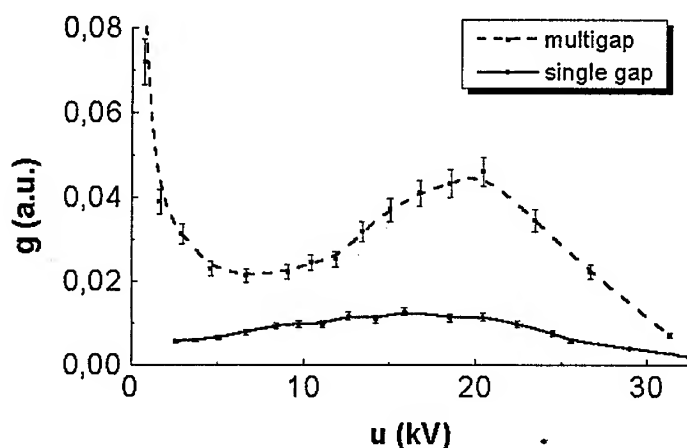


FIG. 4: Time integrated energy spectra obtained with a magnetic analyzer for the two configurations of Fig. 1c ("basic") and 1d ("multi-gap") and 33 kV breakdown voltage.

single gap configuration. These results reveal the role of multi-gap configuration in generating a relatively intense, well focused, poly-energetic electron beam, in comparison with the single gap configuration, as seen in [13].

In alternative experiments presented in the next sections the deduced electron energy spectra is qualitatively comparable with those of the spectra measured here on the multi-gap configuration (Fig. 4 dotted line): a low energy distribution function decreasing with energy and a group of high energy electrons. Quantitatively, the ratio of the fast to the low energy component appears to be different, that we attribute to the longer path of analyzed electrons until the detector in the magnetic analyzer as compared to the very compact chambers involved in the methods presented in the next section.

To underline the importance of the propagation length on the measured energy spectrum, we placed the Faraday cage axially, behind an aperture of 2 mm, at two distances: 10 mm and 42 mm, this means at the position of the entrance aperture of the magnetic analyzer and respectively at a distance corresponding to the path length of the electrons through the analyzer. The total electron beam currents measured in the two positions for the multi-gap configuration were 60 A and 7,2 A respectively. Since we know that the propagation of the lower energy electrons is more affected by the space charge effects than that of the higher energy electrons, it results that the energy spectra measured with the magnetic analyzer underestimate the low energy component in the electron beam which leaves the anode.

3.2. Bremsstrahlung X ray emission

The second method uses the bremsstrahlung X ray emission due to beam interaction with solid target, as presented in [14].

A Cu or C target has been located at a short distance d (1 - 4 cm) beyond the anodic hole. We used a Si-Li detector with a very good resolution (about 150 eV) associated to a multi-channel analyzing system. To avoid the electronic pile-up generated by the high photon rate while keeping small absorption, we use a vacuum tube of 1.5 m mounted laterally. As a result, a very long acquisition time was necessary (10^5 pulses). The expression of the bremsstrahlung emission, i.e. the energy radiated per electron and per unit of energy interval is:

$$(3.1) \quad J(h\nu) = \int_{h\nu}^{\infty} j(u, h\nu) \sqrt{u} g(u) du,$$

$j(u, h\nu)$ is the elementary emissivity, well described by the Kulenkampf empirical formula:

$$(3.2) \quad j(u, h\nu) = b \cdot (u - h\nu),$$

where b is a constant depending on the target nature.

In fact, the experimental measurable quantity is the number of photons counted per energy channel, i.e.:

$$(3.3) \quad N(h\nu) = \frac{T(h\nu) \cdot J(h\nu) \cdot \frac{d\Omega}{4\pi}}{h\nu},$$

where $T(h\nu)$ is the photon transmission coefficient due to the detector's efficiency and to the various absorbers and d the observation solid angle. From deduced

$J(h\nu)$, and inverting equation (3.1), one can obtain $g(u)$. In fact, in order to optimize the counting statistics, the experimental curve $N(h\nu)$ has to be recorded successively over several energy ranges using different absorbing screens, hence different thresholds for $T(h\nu)$ function. Fig. 5 shows $g(u)$ obtained for $d = 1$ cm and $V = 33$ kV.

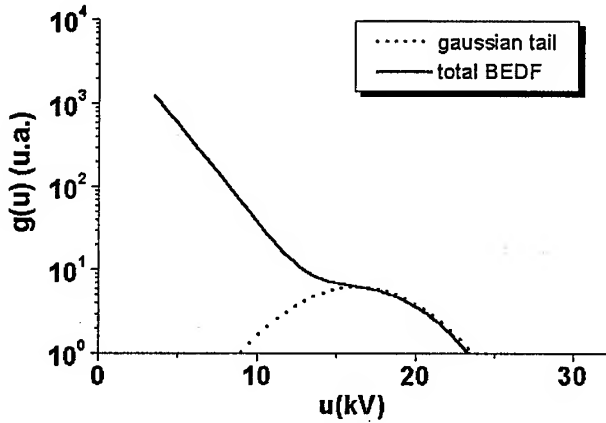


FIG. 5. BEDF from deconvolution of bremsstrahlung X ray emission (C target, 1 cm behind the anodic hole, $40 \mu\text{m}$ Al filter).

3.3. Electrostatic measurement

The last method is based on a technique starting from the classical retarding grid electrostatic analyzer but with original features allowing an access very close to the beam extraction hole. These measurements are time and space resolved. But, as we shall see, they do not analyze directly energies higher than some keV.

The method was used for the configuration presented in Fig. 1e and the diagnostic device is presented in Fig. 6. It consists of a Faraday cage analyzing the beam current extracted from an anodic hole, 1 mm diameter, with a collector C . Two positions of anodic hole (either on-axis or 1 mm off-axis) have been studied. The collector is coupled to a non-inductive grounded shunt of $R_S = 0.5\Omega$ through a serial resistor R_P , giving a total equivalent resistor $R = R_P + R_S$. The measurement principle is based on the self biasing of the collector due to the finite value of the resistor R . In fact, when passed by the beam current I_b , C is biased to a voltage RI_b making an energy selection in electrons carrying this current. So we can express I_b in function of the one dimensional BEDF, $g(u)$, which has a lower limit also dependent of I_b under the form:

$$(3.4) \quad I_b = \int_{RI_b}^{\infty} \sqrt{u} g(u, t) du,$$

where c is a constant including the anodic hole area S , given by: $c =$

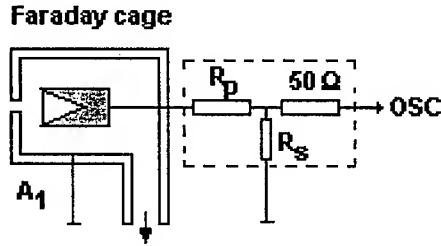


FIG. 6. Electrostatic analyzer: A₁: grounded anode; FC: Faraday Cage; C: collector; R_S: 0.5Ω shunt; R_P: variable serial resistor ($R = R_P + R_S$).

$e^{3/2} S(2/m)^{1/2}$. Varying R_p and thus the total resistance value R , several oscillograms $I_b(t)$ are recorded. Then, at fixed t , it is possible to draw the curve I_b as a function of RI_b , from which the BEDF can be deduced by the formula:

$$(3.5) \quad c \cdot g(u = RI_b) = -\frac{dI_b/d(RI_b)}{\sqrt{RI_b}}.$$

An oscillograms set corresponding to on-axis hole is presented on Fig. 7 for R values between 0.5 Ω and 450 Ω and a cathode-anode applied voltage of 25 kV. Its envelope exhibits two humps shape. At t values corresponding to these humps the extreme values of I_b evidence that the first one corresponds to fast electrons and the second one to slower electrons. The same analysis off-axis proved that the ratio between fast and slow populations appears to be higher on-axis than off-axis.

To deduce the BEDF, the calculation procedure consists first in extracting experimental points I_b versus RI_b at fixed t , then in correcting these points to take into account capacitive leaks at high R values and inductive collector biasing at low R values. A fitting curve $I_b(RI_b)$ of corrected points is then used to determine $g(u = RI_b)$ from (3.5). It is important to note that the attainable u range is limited by the two extreme values of R following:

$$(3.6) \quad R_{\min} \cdot I_b(R_{\min}) < u < R_{\max} \cdot I_b(R_{\max})$$

thus implying for every t an extrapolation both towards zero and highest energy values if macroscopic quantities are requested. We arrive finally to the relation :

$$(3.7) \quad g(u, t) = \sum_{j=1,4} a_j(t) \exp\left(-\frac{u}{\tau_j(t)}\right).$$

Fig. 8a and 8b show the deduced values of $g(u, t)$ both in the measured u ranges (bold lines) and in the extrapolated u ranges. One can show that the shape of BEDF evolves from quasi mono-exponential with low pseudo "temperature", to roughly two-exponential with a tail of high temperature at time

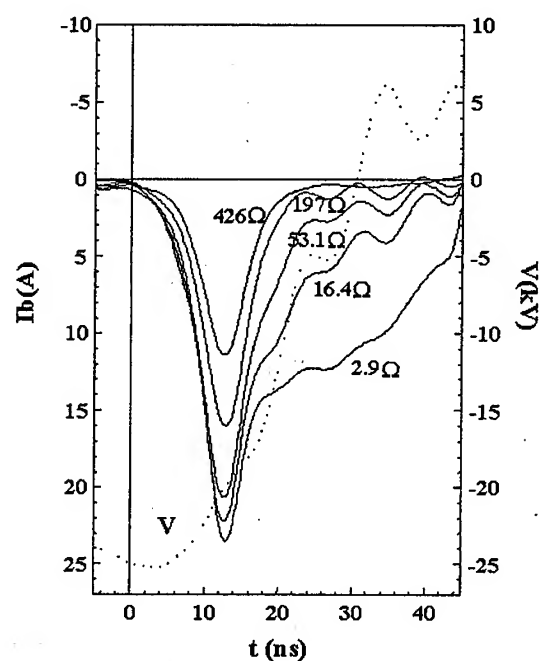


FIG. 7. Time variation of measured I_b currents with the collector for different values of R (on-axis hole).

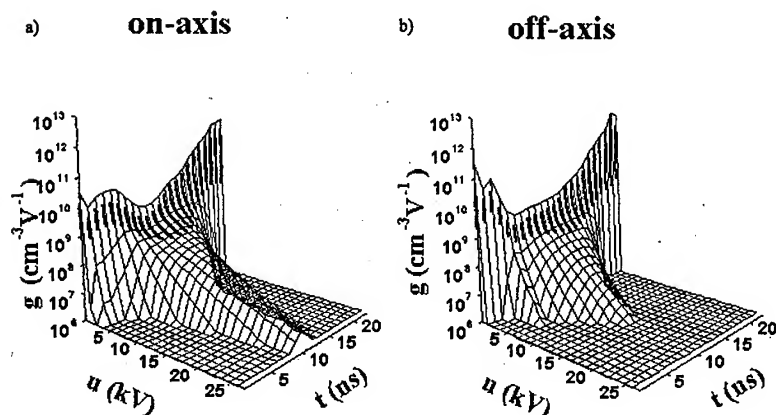


FIG. 8. Time-resolved BEDF for two positions of the anodic hole. Bold lines correspond to the measured ranges, successively for an on-axis hole and for a 1 mm off-axis hole.

around maximum beam current time. Then it evolves again to a mono-exponential, with "temperature" decreasing with increasing time. On-axis and

off-axis BEDF exhibit the same evolution with a lower mean energy in the latter case.

In order to test the extrapolation validity, the current has been calculated versus t for the minimum value of R (0.5Ω) using relation (4) and the previously deduced g , and compared to the oscillogram $I_b(R = 0.5 \Omega)$.

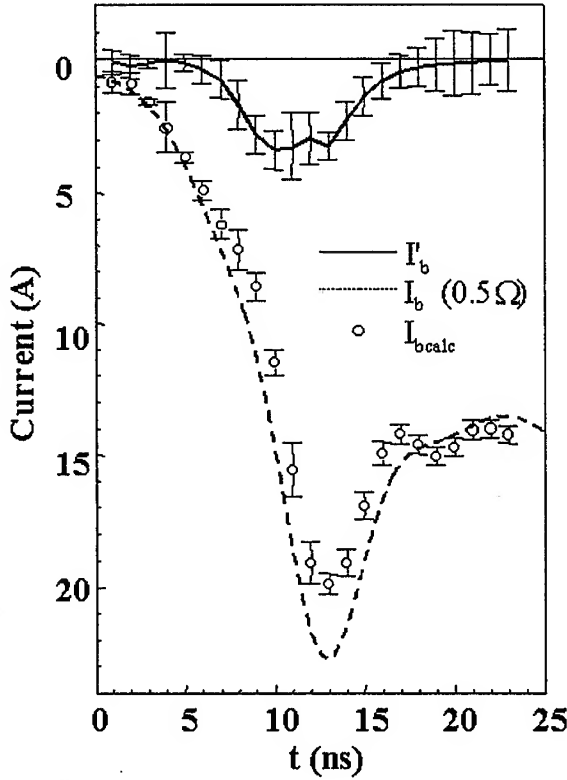


FIG. 9. Comparison between the experimental current $I_b(t)$ (for $R = 0.5 \Omega$) and the calculated one using the expansion (7), for the on-axis hole; the deduced beam current corresponding to the mono-energetic component I'_b is shown also.

Fig. 9 evidences a calculated current slightly lower than the measured one with a relative difference reaching $1/7$ at the time of maximum I_b . We assume that this difference :

$$(3.8) \quad I'_b(t) = I_{b_{meas}}(t) - I_{b_{calc}}(t),$$

is due to the "run away" (RA) electrons previously evidenced by the other BEDF measurement methods, i.e. having electron distribution function under the form of a delta function with the corresponding density $n'(t)$, such that :

$$(3.9) \quad g'(u, t) = n'(t) \cdot \delta(u - V(t)),$$

$$(3.10) \quad I'_b(t) = c \cdot n'(t) \cdot \sqrt{V(t)}.$$

Using the total BEDF $g_{tot}(u, t) = g + g'$ we shall further calculate the dependence versus time of some macroscopic quantities associated to BEDF, for the case of on-axis hole. Fig. 10 shows that the mean electron energy increases then decreases during the voltage fall-time, with a maximum value around 5 keV,

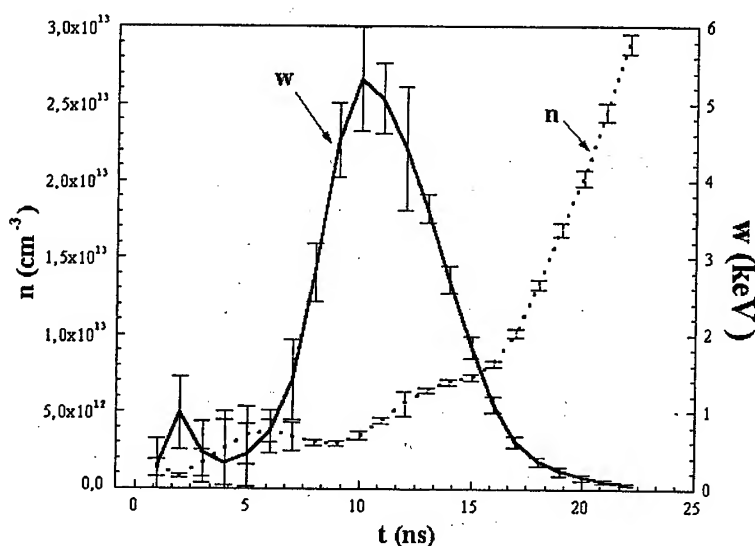


FIG. 10. Calculated time variation of on-axis beam density (n) and beam energy (w).

some ns before the time of maximum beam current, contrary to electron density which is always increasing. Note that the latest t involved in these calculations corresponds to the beginning of the filamentary discharge, i.e. to another discharge regime where the 1D BEDF becomes invalid.

The time averaged value of g_{tot} appears in Fig. 11 with a humped tail whose maximum is around one half the breakdown voltage. One can calculate that, in the time averaged value of beam current, one tenth is carried by electrons of more than 20 keV. More generally, keeping the former distinction between run-away electrons (distribution g') and slower electrons (distribution g), in table 1 are shown their time averaged relative contribution to density, current and power for axially extracted electron beam.

Table 1. Time averaged relative contributions of run-away (RA) and slower electrons to macroscopic beam characteristics

	Density (cm^{-3})	Beam current (A)	Power (W)
Total	$9.6 \cdot 10^{12}$	13	$5.5 \cdot 10^4$
% Run Away e^-	1.1	8.5	43.6
% slower electrons	98.9	91.5	56.4

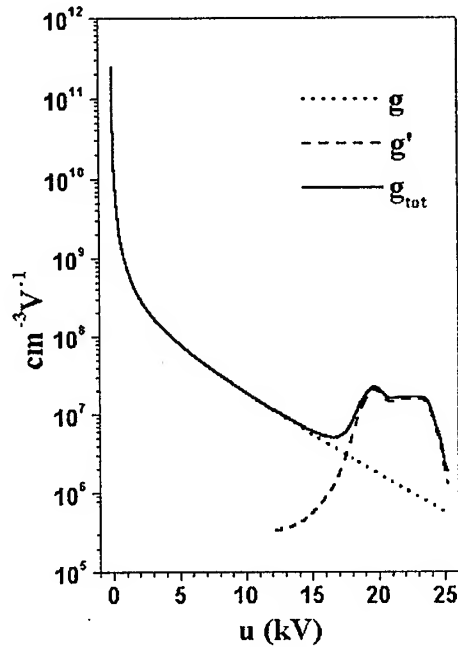


FIG. 11. Time averaged on-axis BEDF: \bar{g} : monotonically decreasing distribution; \bar{g}' : run away electrons distribution; \bar{g}_{tot} : total distribution.

3.4. Discussions

The three different methods appear to present complementary advantages and disadvantages:

- (i) The magnetic method allows measurement of time averaged BEDF in all the range of investigated energies. However, it presents the disadvantage of the analyzer length. This latter is made necessary by the request both to select a paraxial entrance beam and to have sufficient energy selectivity. Due to this length, the low energy electrons are partially eliminated from the analyzed beam under the action of the space charge force.
- (ii) The method based on bremsstrahlung X ray is, at the contrary, very local and able to test the beam at the minimum target-anode distance, i.e. about 10 mm. Nevertheless, it only concerns electrons above some keV. Moreover, it implies a very small observation solid angle with different difficulties to adjust precisely the position of observation range in the beam-target interaction spot. Finally, its main disadvantage is to make necessary a very long acquisition time, with the risk of characteristics drift.
- (iii) The electrostatic method takes advantage of the self-biasing of the collector placed very close to the anode. This means a large acceptance solid

angle, nearly equal to 180° , without risk of internal breakdown. This is a real advantage, compared to published measurements [8] which were done after several centimeters of beam propagation behind the anode, because it can be used to study interaction with the anode target, like in ref. [10]. Moreover, it allows time resolution. Its major disadvantage lies in the small accessible energy range, making necessary to extrapolate to higher energies.

All previous results evidence an energy distribution of the electron beam which is mainly poly-energetic, with some energetic electrons, and a main part composed of a monotonically decreasing distribution. This latter has first, at maximum of the beam current, a multi-exponential variation, evolving towards a mono-exponential variation later on.

Energetic hump in time averaged BEDF appears as being reasonably due to run-away electrons having an energy equal to the total instant discharge voltage. In fact, calculation with this hypothesis using electrostatic measurements, gives hump which is similar to those directly measured by magnetic or bremsstrahlung method.

Qualitatively, for the all three methods, the measured BEDF is in good agreement with the modeling of ref. [11]. This reinforces the invoked phenomenology of some electrons emitted from the cathode and accelerated at full instantaneous voltage in the cathode sheath, which then arrive on the anode without having experienced any collision, and of slower electrons composed of primaries having suffered some collisions and of resulting secondaries.

The question remains of estimating if the obtained BEDF is specific to our devices, and to point out its interest. It seems reasonable to admit that pseudospark-like devices give comparable BEDF, but with a specific ratio between run-away electrons and energy distributed electrons due to the discharge configuration and the pressure in the analysis chamber, which means different propagation conditions. The analysis distance from the anode also plays a major role. For instance, measurements presented in ref. [8] are made about 6 cm downstream on a beam extracted from a classical multi-gap pseudospark through a 0.5 mm diameter anode hole, providing only run-away electrons. In [5] it is only the fast component of the BEDF that was measured, but without the slower electrons, which was probably due to both the type of detection and the large distance from the anode, as pointed out in [10]. Recently, it has been shown [15] that in the case of multi-gap structure, the slow electrons are better collimated and that run-away and distributed electrons are less separated in time than in the case of classical pseudospark. Thus, we think that a poly-energetic distribution is a characteristic of beams produced by the pseudospark discharge family, opening perspectives for radiation source development.

4. Beam propagation conditions

4.1. Magnetic monitoring

Fig. 12 illustrates beam ability to be moved along anode diameter keeping roughly its properties if magnetic field, provided by external coils, is acting in

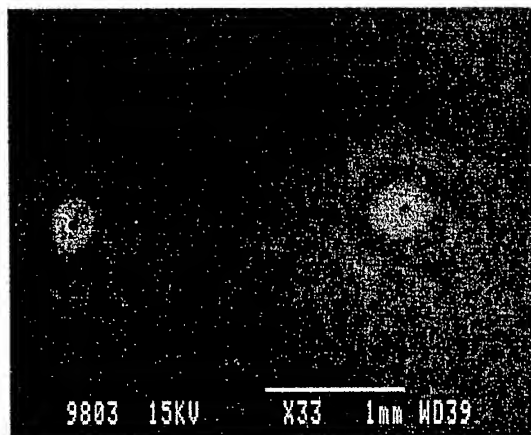


FIG. 12. Holes drilled in an anodic foil target when the beam trajectory is monitored with a magnetic coil surrounding the tube in the cathodic region.

the cathodic region. Here demonstrated by the fact that the hole characteristics remain unchanged, this ability has been also proved by the X-ray emission from point-like sources which have been measured before drilling [16]. We suppose that the electrons are deflected inside the cathode at low velocities during the beam generation, and then are accelerated to the potential applied to the cathode-anode gap. In this way it is possible to control the coupling of the beam with different targets inside the discharge tube.

4.2. Electron beam ion trap

A well known condition for a monoenergetical electron beam to propagate without any divergence is :

$$(4.1) \quad n_b \left(1 - \frac{v^2}{c^2} \right) = n_i,$$

where v is the beam velocity and c the light velocity, n_b and n_i are the respective densities of beam electrons and plasma ions. This condition ensures that electric field, created by the space charge, and the magnetic field, created by the beam current, exert counterbalanced radial forces on any beam electron. Condition (4.1) could be satisfied by the ions from auxiliary discharge inside K_1 , but outside it can only involve the ions created by the beam itself. For secondary electrons the magnetic force is small and they are expelled from the axial region. Consequently, the electron beam becomes surrounded by a thin layer of positive charge which ensures the vanishing of the electric field at the limit of the neutral plasma. The fast electrons which lose energy by collisions are still kept along the beam by the radial potential pockets due to this double layer and eventually regain energy from the axial electric field, while the secondary electrons are rapidly removed.

On the other hand, the potential seen by the ions looks similar to a simple potential well, whose characteristics were inferred in [17] and [21] as shown on

Fig. 13a under the assumption of a uniform radial ion density and a constant beam electron density. In spite of the high electron space charge in which the ions are embedded, the recombination is negligible due to the velocity mismatch between the beam electrons and the ions.

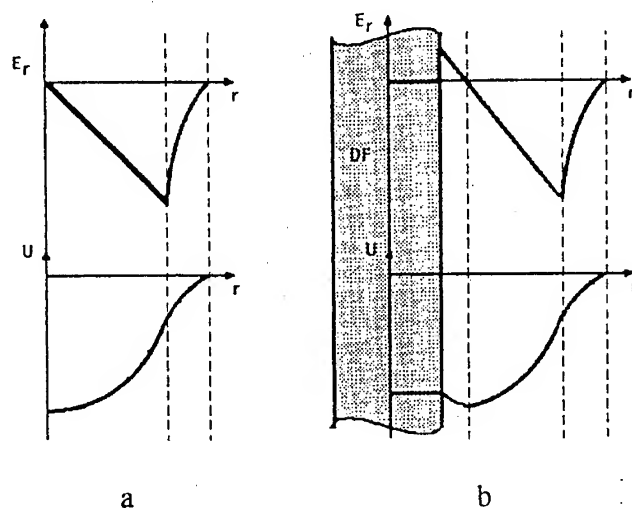


FIG. 13. Model of radial static equilibrium electric field E_r and potential U within the axial electron beam [21]: (a) free cathode-anode space (b) with an axial dielectric fiber (DF).

4.3. Cruise effect

The "cruise effect" (CE) has been evidenced in [18]. It consists in the ability of a dielectric fiber to capture and guide the beam when disposed roughly parallel to this latter, at a small distance (typically, lower than 2 mm).

The plasma brightness associated to the beam is an easy way for CE observation, as illustrated in Fig. 14a in an experiment using the configuration shown on Fig. 1c with the fiber disposed axially between K1 and A1. In contrast the effect is reversed when the dielectric fiber is replaced by a metallic wire. Fig. 15 shows a situation using configuration of Fig. 1b when the dielectric fiber is shortened and continued by a floating metallic wire exhibiting the beam successively captured by the fiber and repelled by the metallic wire, that is easily explained by the fact that charging of the wire is then negative.

CE is associated to a beam-fiber interaction which leads to a visible fiber fluorescence and to X-rays emission measured both outside and inside the fiber itself. This emission has been investigated as a function of the dielectric material, and of its geometry and size. Besides classical measurements using a scintillator mounted outside the discharge, for outwards X emission from cylindrical fiber, Fig. 14b evidences measurements of inwards X-ray emission. corresponding to experiment of Fig. 14a. In this last case, CE effect is in fact produced by a ceramic cylinder containing a scintillating fiber surrounded by a layer shielding against visible light. CE was also achieved with a quasi-planar geometry [19]

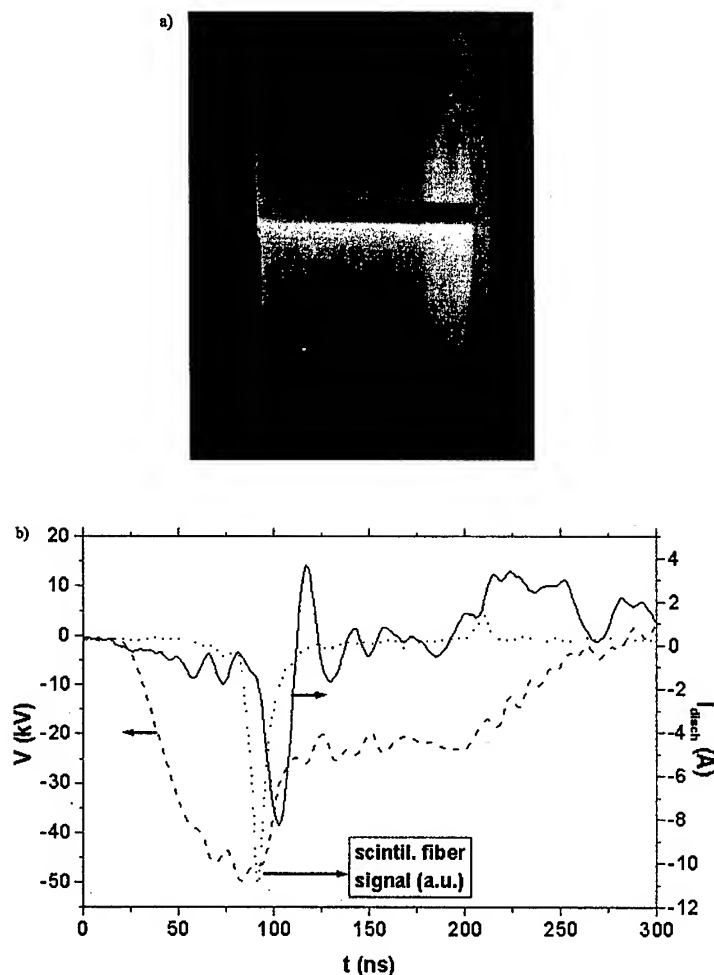


FIG. 14. Cruise effect: (a) light around a ceramic cylinder (b) corresponding X inwards emission detected with inner scintillating fiber.

consisting of a low conductivity ferrite cylinder 4 mm in diameter placed parallel to the discharge tube axis. Under proper pre-ionization conditions, a 2 cm long filamentary discharge develops along the cylinder surface, associated with X-ray emission. Since no damage of the ferrite surface was observed, the CE seems to provides a mechanism of X-ray generation, different from that proposed in [20] in which the pre-ionization of the gas adjacent to the dielectric surface plays a critical role.

The CE can be described qualitatively by extending the previous ion trap model. Due to the high secondary electron emission by the dielectric fiber, this latter is biased by superficial positive charge along its surface [21], adding to the previous potential well a small climb in a layer surrounding the fiber, which gives thus an inward force for the beam electrons (cf. Fig. 13b). As a result, the beam is captured by the fiber and is "dressing" it. The ions, although repelled

by the fiber in this layer, have gained enough kinetic energy in the potential well to be able to carry current on the fiber, in a dynamic equilibrium with the beam electron current which tends to neutralize it. Similarly, electrons emitted by the fiber undergo energizing collisions with the beam electrons, allowing them to overpass the potential barrier layer and to access the surrounding region where they are expelled, alike volume secondary electrons.

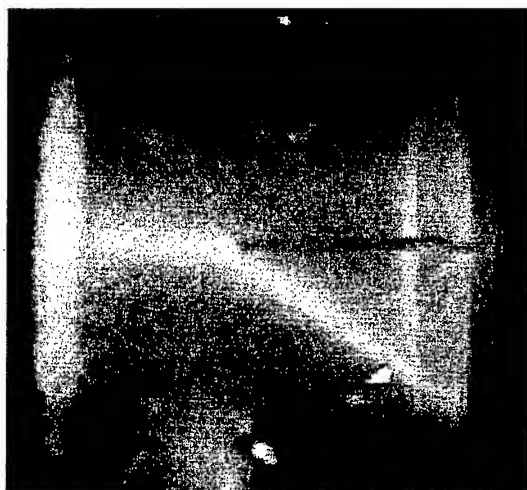


FIG. 15. Effect of an axial metallic wire following a dielectric fiber.

In reference to capillary discharges where hard X-rays emission results from the bremsstrahlung following the fast electron interaction with the walls, this system has been called "inverse capillary discharge" [21]. It presents as an important advantage the possibility to use also the ablation plasma from the fiber surface for a better cruising of the beam.

5. Conclusions

Applications of pseudospark discharges have been extensively reported in conference workshop. We shall only mention those resulting specifically from previously detailed characteristics of the produced electron beams.

In fact, we have shown that the energy distribution function of electron beams created in the studied discharge is composed of some run-away electrons with energy corresponding to the total instant discharge voltage, and of a main part composed of monotonically decreasing distribution. All pseudospark-like discharges probably have comparable BEDF, thus offering the double potential ability of thermal evaporation of solid target by the energetic part, and the excitation of extracted atoms by low energy electrons, that could be useful in elementary analysis.

Specific advantage of the presented configurations lies in its good reproducibility, due to both the auxiliary discharge and the absence of internal slits

and correlative erosion, and also in easy optical access to the complete anode-cathode interval. This allows applications as spectroscopical source of the filamentary light initiated by the electron beam, purity conditions being ensured by use of totally external electrodes.

Moreover, the possibility of monitoring the position of the beam while maintaining its properties extends the classical applications of its interactions with a solid anodic target.

In particular, it is possible to scan the target in the case of elementary analysis based on X-rays.

Preliminary tests also proved the possibility to reduce discharge tube dimensions in order to obtain pulsed X-ray sources of small size.

Finally, the easy access to the beam path allowed among others the evidence of the cruise effect and one of the first projected application of this effect is to pump nuclear isomers for gamma-ray laser studies [21]. In fact, depletion of certain K-quantum number nuclear isomers such as ^{178}Hf may be achieved by up-conversion with X-rays [22]. A successful first photon induced gamma emission experiment with this isomer has recently been reported [23], showing that the irradiation by X-ray photons with the energy of the order of some tens of keV, can induce the prompt release of the 2.5 MeV stored by the isomer into freely radiating states. Relativistic electron beams, cruising around a dielectric fiber containing such an isomer, would generate bremsstrahlung X-ray emission mainly concentrated along the dielectric fiber inside a cone with an opening angle of $2(1 - v^2/c^2)^{1/2}$, thus providing a very good coupling to the active medium [19]. A deeper understanding of the most favorable optical pumping sources and interaction mechanisms of low-energy photons with atomic nuclei, such as photon induced gamma radiation from isomeric nuclei, could pave the way to the extraordinary physics and applications of the "ultimate light" of gamma-ray lasers.

Acknowledgments

The authors acknowledge people having collaborated to presented work, in particular: E.Dewald, Dr.P.Charles, and Dr.M.Lamoureux.

References

1. J. CHRISTIANSEN and CH. SCHULTHEISS, *Production of high current beams by low pressure spark discharges*, Z. Phys. A **290**, 35, 1979.
2. K. FRANK, C. BIKES, E. DEWALD, U. ERNST, M. IBERLER, J. MEIER, U. PRUCKER, A. RAINER, M. SCHLAUG, J. SCHWAB, J. URBAN, W. WEISSER, D.H. HOFFMANN, *Scientific and Technological Progress of Pseudospark Devices*, Proc. 1998 IEEE 18th Symp. on Discharges and Electrical Insulation in Vacuum-Eindhoven 1998, p. 363.
3. M. GANCIU, G. MODREANU, A.M. POINTU, I. I. POPESCU, *Generation of intense pulsed electron beams by superposition of two discharges*, J. Phys. D: Appl. Phys., **27**, 1370, 1994.
4. M.V. UDREA, A.M. POINTU, G. MODREANU, M. GANCIU, I.I. POPESCU, N.B. MANDACHE, *Pulsed electron beams in long filamentary discharges*, J. Phys.D: Appl. Phys. **30**, L33, 1997.
5. W. BENKER, J. CHRISTIANSEN, K. FRANK, W. HARTMAN et al., *Generation of intense pulsed electron beams by the pseudospark discharge*, IEEE Trans. Plasma Sci. **17**, no. 5, 754 (1989).

6. J. WESTHEIDE, IEEE Transactions on Plasma Science, **23**, no.3, 3254, 1995.
7. K. RAMASWAMY, W.W. DESTLER, Z. SEGALOV J. RODGERS, *Characterization of electron beam generated in a high-voltage pulse-line driven pseudospark discharge*, J. Appl. Phys., **75**, 4432, 1994.
8. B.N. DING, T.J. MYERS, M.J. RHEE, *Time-resolved energy spectrum of a pseudospark-produced electron beam*, Rev. Sci. Instrum. **64**(6), 1442, 1993.
9. N. B. MANDACHE, A. M. POINTU, E. DEWALD, M. NISTOR, M. GANCIU, G. MUSA and I. I. POPESCU, *The characterization of pre-ionization-controlled electron beams produced in open-ended hollow-cathode transient discharges*, Plasma Sources Sci. Technol. **6**, p. 1, 1997.
10. R. KOWALEWICZ, T. REDEL, *Interaction of High Current Polyenergetic Electron Beam with Metal*, IEEE Transactions on Plasma Science, **23**(3), 270, 1995.
11. L.C. PITCHFORD, *Electron-beam generation during the hollow cathode phase of pseudospark operation*, J. Appl. Phys., **75**, 7227, 1994.
12. M. NISTOR, N.B. MANDACHE, E. DEAWLD, M. GANCIU, I.I. POPESCU, A.M. POINTU and Y. VITEL, *Electron energy spectra of an Open Ended Pin-Hollow Cathode Transient Discharge by magnetic analysis*, Proc. XXIVth ICPIG, Warsaw, Poland 1999, Pisarczyk et al. Ed., Vol.III, p. 29;
13. E. DEWALD, M. GANCIU, N. B. MANDACHE, G. MUSA, M. NISTOR, A.M. POINTU, I.I. POPESCU, FRANK, D.H.H. HOFFMANN, R. STARK, *The Role of Multielectrode Geometry of Pulsed Electron Beams in Preionization Controlled Open Ended Holow Cathode Transient Discharges*, IEEE Trans. Plasma Sci., **25**(2), 279, 1997.
14. P. CHARLES, M. LAMOUREUX, M. NISTOR, N.B. MANDACHE and A.M. POINTU, *A new diagnostic based on bremsstrahlung analysis for the energy distribution of hot beam electrons. Application to hollow cathode discharges*, Proc. XXIVth ICPIG, Warsaw, Poland 1999, Pisarczyk et al. Ed., Vol. II, p.1;
15. E. DEWALD, K. FRANK, D.H.H. HOFFMANN, R. STARK, M. GANCIU, N. B. MANDACHE, M. NISTOR, A.M. POINTU, I.I. POPESCU, *Pulsed Intense Electron Beams Generated in Transient Holow Cathode Discharges: Fundamentals and Applications*, IEEE Trans. Plasma Sci., Vol. 25, no. 2, 272(1997);
16. D. PENACHE, M. C. PENACHE, M. NISTOR, H. GRECU, M. GANCIU, A. M. POINTU, M. SKOVRONEK, I. I. POPESCU, V. ZORAN, *A scanning point-like X ray source using transient hollow cathode discharges*, X-ray and Inner shell processes, 9-13 September 1996, Hambourg.
17. M. GANCIU, I.I. POPESCU, V. ZORAN, A. M. POINTU, *A high density pulsed ion trap*, Nucl. Instr. and Meth. in Phys. Res., **B 98**, 541, 1995.
18. M. GANCIU, E. DEWALD, M. NISTOR, D. PENACHE, I.I. POPESCU, V. ZORAN, *Surface guided electron beams on dielectric fibers (the cruise effect)*, Rom. Journ. Phys. **39**, 787 (1994);
19. M. GANCIU, C. B. COLLINS, M. C. PENACHE, D. PENACHE, V. ZORAN, I. I. POPESCU, *Filamentary X-ray source by cruise effect*, Proceed. First Int. Workshop on Induced gamma emission, IGE'97, Predeal (Romania), 16-20 August, 1997, 198, 1999.
20. K. WATANABE, K. FURUSHO, S. KASHIWABARA, R. FUJIMOTO, *Characteristics of x-ray radiation by a nonequilibrium energetic electron flow emerged from a ferrite filament*, J. Appl. Phys., **68**, 5059, 1990.
21. V.I. ZORAN, M.GANCIU, A.M. POINTU, C.B. COLLINS, I.I. POPESCU, *X-ray generation in inverse capillary discharges for pumping*, Hyper. Inter. **107**, 415, 1997.
22. C.B. COLLINS, J.J. CARROLL, *Progress in the pumping of gamma-ray laser*, Hyper. Inter., **107**, 3, 1997.
23. C.B. COLLINS, F. DAVANLOO, M.C. IOSIF, R. DUSSART, J.M. HICKS, S.A. KARAMIAN, C.A. UR, I.I. POPESCU, V.I. KIRISCHUK, J.J. CAROL, H.E. ROBERTS, P. MCDANIEL and C.E. CRIST, *Accelerated Emission of Gamma Rays from the 31-yr Isomer of ^{178}Hf Induced by X-ray Irradiation*, Phys. Rev. Lett., **82**, 695, 1999.

TRANSITORY PHENOMENA IN REACTIVE MAGNETRON DISCHARGE

G. POPA and V. ANITA

FACULTY OF PHYSICS "A.I. CUZA" UNIVERSITY

RO-6600, Iasi, Romania

The experimental results are presented on the plasma parameters and hysteresis effect for magnetron discharge produced in reactive gas mixture as Ar/N₂ and Ar/O₂ with copper, and titanium target. Most of the primary fast electrons are trapped by local magnetic field in front of the cathode, while the electron population in the unmagnetized plasma region can be approximated as bi-Maxwellian one with their temperature in the range of about 0.5 eV to 1 eV for cold electrons and in the range of 3 eV to 12 eV for hot electrons, respectively.

The hysteresis effect was studied with the use of a method based on time variation of the potential and/or current of the discharge. Enhancing and diminishing of the hysteresis area can be obtained versus time rate of increasing and decreasing respectively of the cathode potential or of the discharge current. A qualitative description of the hysteresis is proposed starting from the symmetry breaking in the evolution of both surface and volume phenomena following the relaxation processes after rapidly increasing and decreasing, of the discharge current.

1. Introduction

Magnetron sputtering-deposition systems have wide applications especially for the high rate deposition of thin metal and/or dielectric films with good film adhesion and under fairly good control of technological parameters. Since conventional magnetron system was primarily used [1-3] it was a continue developing in both scientific knowledge of its physical properties and diversification of the magnetron type. Today a number of good review articles and chapters are available on the subject [4 - 12].

An important step forwards was made when the reactive sputtering was proposed for quite complex compound films deposition. Reactive sputtering is a non-linear process which implies rather intricate physical and chemical processes which usually exhibits hysteresis effects causing instabilities under some circumstances [13 - 23]. In the earlier stage of understanding of the mechanism of the magnetron discharge, the physical model assumed three main parts: *target*, *plasma region* and *substrate*. The experimental results have shown that each of these parts may contribute to hysteresis effect.

Target, as the cathode of the discharge, is also an origin of the sputtered material which can be a pure metal, compound or both. Reactive sputtering often switches between the metal mode and the compound mode, which may correspond to the unstable transition region. *Plasma* is the active medium which assure mainly the flux of fast particles, ions and neutrals. These particles hit the target producing both electron emission and sputtering of the target atoms. In a rather simple and convincing experiment Larsson et al. [18] have shown that, e.g., if the pumping speed is high enough a smooth transition between the different sputtering modes can be obtained. Quite recently Bretagne et al. [23] have made a modelling of a radiofrequency magnetron discharge in which the effects of atomic and molecular reactive gas species by elementary processes within the plasma volume and the getter effect of the chamber walls were considered. *Substrate* is a floating or biased electrode on which the sputtered material might be deposited as thin solid films [24]. Experiments using a reactive gas inlet laying directly on substrates have provided directly visualised insights into the mechanism of reactive sputtering of Al, Ti and Zn [25]. Thus, for materials like Al and Ti reactive gas concentration effects alone can produce fully oxidised films but for Zn the negative oxygen ions play the dominant role in oxidation. Moreover, the purpose of controlling film stoichiometry has made Affinito and Parsons [26] find the relationships between processes occurring on the target surface, substrate surface and plasma of the magnetron discharge.

Most of the experiments have shown that the mechanism of the discharge is rather complicated and a quantitative description has to consider also other phenomena such as: a gas density reduction as non-linear process with discharge current [27], a sputtering wind which is nothing but energetic particles, coming from the cathode region, colliding with the ambient gas and pumping it [28] or an effect of energetic particle bombardment on the film deposition [29, 30] and so on. Moreover, some of these phenomena appeared to be very important in the reactive discharges.

Thus, Berg's research group earlier presented a computer based model for a single target, one reactive gas sputtering process [31] which has been extended and successfully applied to multi-target reactive sputtering [32] and reactive sputtering using two reactive gases [33]. Recently, the model was applied for receptive sputter deposition of two-phase materials [34]. The model is based on simple physical relations in which the reactive gas molecule or atom is assumed to stick to the surfaces with a characteristic sticking probability (as sticking coefficient) where non-reacted metal is present. So, the compound on target surface contains more reactive gas atoms than compound alone.

In this paper, besides a short general review on the reactive magnetron discharge, with more specific discussions on hysteresis effect, new developments are proposed for plasma diagnostics and for analysis of the hysteresis effect in the reactive magnetron discharges. As plasma diagnostics is concerned a short presentation is made for a new method for processing of the probe characteristics under approximation of bi-Maxwellian electron distribution function or Maxwellian electrons and negative ions [35 - 40]. The method developed for stationary plasma can also be used for non-stationary one. The hysteresis effect is studied with the use of transitory phenomena then when the discharge current is

changed as a step function between two constant values. A direct correlation has been found between variation of the discharge voltage and the partial pressure of the reactive gas components, that may provide new information about the mechanism of the hysteresis effect.

2. Experimental set-up

The experimental apparatus is shown in Fig. 1. The magnetron - 105 mm in diameter is circular. The peak magnetic field measured at the target (cathode)

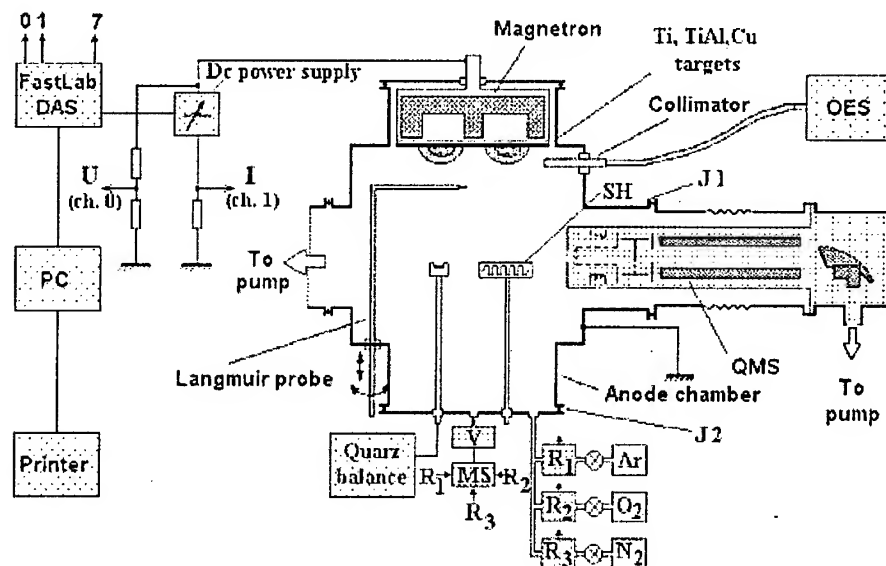


FIG. 1. Experimental set-up.

surface induced by the annular magnet assembly was in the 35 mT range. The magnetron was operated in a d.c. mode but cathode-anode potential was either linear sweep-out or pulse operation using a high voltage computer-controlled power supply. The latter was operated in a constant-current mode [41,42].

Copper and titanium targets have been used in a water-cooled system. Thin films were deposited on cleaned stainless-steel substrates that were mechanically clamped to a heater used as a sample holder. Near the substrate holder a quartz crystal microbalance was mounted in front of the target at a distance of about 5 cm from its centre.

The stainless steel discharge chamber was pumped to about 10^{-5} mbar with the use of an oil-diffusion pump equipped with a freon trap. Argon and oxygen and/or nitrogen were leaked into the system at rates controlled by three mass flow controllers (R_1 , R_2 , and R_3) and the total pressure, p , was recorded by a Scheffer Barocel gauge (V and MS). Both the neutral gas atoms and ions were pursued with the use of either a residual gas analyser or a plasma monitoring

probe (Hyden Analytical computer-controlled quadrupol mass spectrometer - QMS).

The Oriel spectrometer was also used for registration of the optical spectra (OES).

The plasma parameters such as electron number density and temperature were measured with the use of a plane Langmuir probe (tantalum plate, disk shape, of 2 mm diameter) and a data acquisition system (FASTLAB).

The properties of the thin films deposited on the sample were ex-situ analysed by different methods such as scanning electron microscopy (SEM) for surface morphology; Auger electron spectroscopy (AES) and Rutherford backscattering spectroscopy (RBS) for the film density; X-ray photoelectron spectroscopy (XPS) for chemical composition; X-ray diffraction (XRD) to confirm the XPS peak and crystal structure; low energy electron induced X-ray spectrometry (LEEIXS) [41]. The properties of the films were analysed versus plasma parameters and sample temperature. These results are not presented in this paper.

3. Plasma parameters

Characterisation of magnetron discharge plasma by Langmuir probe was made by Rossnagel and Kaufman [43]. The plasma potentials, electron temperature, and electron densities have been measured at low and intermediate discharge currents of a conventional planar magnetron in argon or helium gas. Induced drift current in circular planar magnetron was also measured with the use of a magnetic probe based on Hall effect sensor [44].

Major restrictions must be considered with respect to Langmuir probe method for plasma diagnostics in magnetron discharges. These restrictions are related to: i) possibility of the probe melting for high density of the discharge current; ii) probe contamination by deposition of the material sputtered from the target; iii) absence of a probe theory for plasma placed in inhomogeneous magnetic field; iv) presence of positive ions with different masses, charges and nature, including negative ions in the case of the reactive gases as oxygen or SF₆; v) non-Maxwellian electron distribution function, and so on.

These restrictions have been made to limit plasma diagnostics for the plasma regions rather far from the target where the presence of the magnetic field can be neglected [43]. Different methods have been used for probe cleaning by suitable probe bias either very negative, for probe sputtering by ion bombardment or more positive with respect to the plasma potential in order to heat up the probe by electron bombardment. Very recently a scanning Langmuir probe (PMT Fast Probe) [45] was used for plasma diagnostics in a HF reactive discharge. A detailed analysis of the probe in the discharge plasma was made by Godyak [46], in connection with finding of the electron distribution function.

In the following a short presentation will be made about a new development of the probe method used for plasma diagnostics under approximation of bi-Maxwellian electron distribution function [35, 36] or Maxwellian electrons and Maxwellian negative ions [37 - 39].

In the case of a bi-Maxwellian approximation of the EDF, the electron current of the probe is given by

$$(3.1) \quad I(U) = I_{01} \exp [a (U - V_1) + I_{02} [b (U - V_p)]],$$

where the new quantities associated to the electron temperatures T_1 and T_2 respectively are:

$$(3.2) \quad a = \frac{e}{kT_1}, \quad b = \frac{e}{kT_2}$$

and the electron saturation currents given by each group of electrons:

$$(3.3) \quad I_{01} = n_1 e A \sqrt{\frac{kT_1}{2\pi m}} \quad \text{and} \quad I_{02} = n_2 e A \sqrt{\frac{kT_2}{2\pi m}}$$

where n_1 and n_2 are the electron densities of each of two groups, e and m electron charge and mass, k the Boltzmann constant and A the surface area of the plane probe.

The main idea of the method starts from the general properties of the exponential functions which allow to construct two functions. The first one is called "test function" [37] and it has the expression:

$$(3.4) \quad F(U) = I'' I - (I')^2 = 0$$

where, $I' = dI/dU$ is the first and $I'' = d^2I/dU^2$ is the second derivatives of the probe current.

In the case of bi-Maxwellian EDF, given by (3.1), the "so called" the semilogarithmic characteristic of the test function shows a linear dependence on probe potential as:

$$(3.5) \quad F_1(U) = \ln [I'' I - (I')^2] = (a + b) (U - V_p) + \ln [(a - b) I_{01} I_{02}^2].$$

The linear dependence (3.5) gives two main pieces of information. First, the electron energy range in which the bi-Maxwellian approximation is valid and second, its slope B gives the sum of the quantities a and b :

$$(3.6) \quad a + b = B.$$

The second function is:

$$(3.7) \quad F_2(U) = \frac{(a + b)I' - I''}{I} = ab = C$$

With the use of 3.6 and 3.7 the analytical relation for the temperature of the two groups of electrons can be written as:

$$(3.8) \quad T_1 = \frac{e}{k} \frac{B - \sqrt{B^2 - 4C}}{2C} \quad \text{and} \quad T_2 = \frac{e}{k} \frac{B + \sqrt{B^2 - 4C}}{2C}.$$

Moreover, from the electron current of the probe at, e.g. the plasma potential, $I(V_p)$, and its derivative in the same point $I'(V_p)$, the analytical relations for the densities of the two groups of electrons can be obtained as:

$$(3.9) \quad n_1 = \frac{1}{eA} \sqrt{\frac{kT_1}{2\pi m}} \frac{I'(V_p) - bI(V_p)}{a - b}, \quad n_2 = \frac{1}{eA} \sqrt{\frac{kT_2}{2\pi m}} \frac{aI(V_p) - I'(V_p)}{a - b}.$$

The argon plasma parameters in magnetron discharge were measured with the use of this method. In Fig. 2 both radial and axial distributions of plasma parameters are presented for discharge current of 0.15 A and gas pressure $7.8 \cdot 10^{-3}$ mbar and copper cathode. In contrast with previous results reported by Rossmagel and Kaufman [43], this new method shows two Maxwellian groups of electrons with temperatures in the range of 0.5 eV (cold electrons) and 3 to about 12 eV (hot electrons) respectively, as is presented in Fig. 2a. Cold electrons have almost uniform temperature in the whole plasma volume, except cathode region where the magnetic field is present and the probe method should be reconsidered. On the contrary, hot electrons have a large gradient for both radial and axial directions with increasing temperature towards cathode region where the magnetic field is present and only hot electrons seem to be present. Spatial distributions of the electron density of these two groups of electrons are presented in Fig. 2b. Both groups of electrons show a large gradient of density for both radial and axial directions. Near the cathode, density of the hot electrons is larger than that of the cold electrons but in a distance of about 4 cm from the cathode, density of the hot electrons decrease drastically and density of cold electrons increases so they become dominant in the rest of the discharge chamber.

The origin of these two groups of electrons might be like that in the case of multipolar plasma confinement system [40, 47]. Thus, the main ionisation process is due to electron - neutral collisions, which are localised in the magnetic field region. In this region, the energetic electrons originated at the cathode, are trapped and due to inelastic collisions (ionisations and excitations) they may produce two other populations of thermalised electrons. One of them is so called "ultimate" [48] or cold electrons [49] which steam directly from ionisation process. These electrons have rather low temperature (around 1 eV) so that they are trapped in the potential well of the discharge plasma, which has a positive potential with respect to the anode potential as is presented in Fig. 2c [43, 47]. Their temperature is rather uniform across entire plasma volume and, in the most cases, it does not depend on other parameters such as gas pressure or discharge current.

The second group of thermalised electrons is composed by so called "secondary" [47, 48] or "hot" electrons [40, 48 - 50] and their temperature may range between 3 eV to more as 12 eV. Their spatial distributions of both temperature and density are, in most cases, non-uniform. Both distributions and the absolute values of these parameters depend strongly on gas pressure, discharge current and geometry of the discharge. The origin of the secondary electrons is,

mainly, the degrading process of the primaries that loose energy by inelastic collisions with neutrals. Such electrons might be also involved in some elementary processes as step ionisations by collisions with, e.g. metastables.

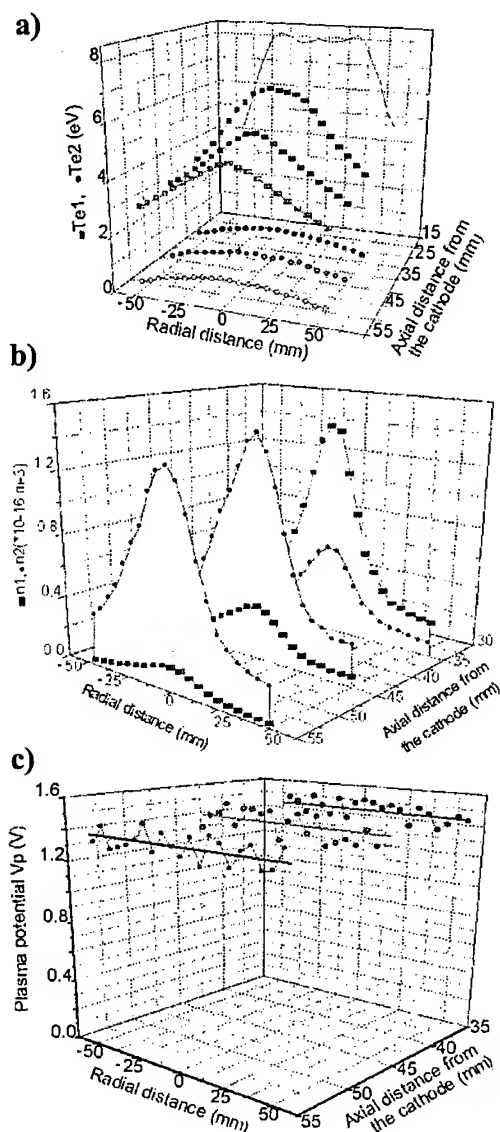


FIG. 2. Radial and axial distributions of electron temperatures (a), electron densities (b) and of the plasma potential (c) in front of the copper target. Argon pressure $7.8 \cdot 10^{-3}$ mbar and discharge current intensity of 0.15 A. Plane substrate placed at 70 mm from the target radial and axial distribution of electron temperatures.

Main difference between magnetron discharge and the multipolar confinement system is that in the former case the magnetic field is placed in front of the

cathode so that the primary electrons are trapped in that region and they cannot penetrate plasma region in a large number, while in the latter the magnetic field is in front of the anode [51, 52] so that all primary electrons cross whole the plasma volume until they are trapped by magnetic field and where they produce main part of ionisations and excitations of the gas atoms [52].

However, a small number of primary electrons can also be present in the plasma volume of a magnetron discharge because of the cathode regions where there's no magnetic field but where a cold cathode region may develop. The presence of fast primary electrons becomes important in the case of unbalanced magnetron discharge [53 - 55] where geometry of the magnetic field was changed in order to get large ion and electron fluxes at substrates and high self-bias potentials.

This new method for processing of the probe characteristics was also applied for reactive plasma where Maxwellian electron and Maxwellian negative ions more considered [38, 39]. Similar measurements are under progress also for reactive magnetron discharge in steady state system but the method can also be used for non-stationary case using box - car system [56].

4. Hysteresis and its analysis by transient processes

The second contribution in this paper is related to the hysteresis effect and a new approach is proposed. Essentially two types of experiments have been performed. In one, the cathode voltage was incremented through the range from about 200 V to about 600 V with different time rate of change between 6 V/s and 600 V/s [57] or the discharge current in the range of 0.01 A/s to 0.1 A/s. In the second type, the discharge current was pulsed as a step function between two constant values with variable of both duration and frequency of the pulses [58]. The gas flow rates of both buffer and reactive gas, the time rate of change of the discharge potential, and the current step have been used as parameters.

The experiments were performed for three combinations such as: copper target and argon-oxygen mixture, titanium target and argon-nitrogen mixture and titanium target and argon - nitrogen - oxygen mixture under experimental conditions that hysteresis is present. The typical hysteresis curves of the Cu/Ar/O₂ case are presented in Fig. 3. The relative values of the densities of the copper atoms (Fig. 3a) and of the atomic oxygen (Fig. 3b) versus oxygen mass flow rate are measured as relative intensity of the spectral lines of 521.8 nm for Cu and 777.4 nm for O, respectively. For small flux of oxygen, less than about 2.5 sccm for 1.0 A discharge current and 2.0 sccm for 0.8 A discharge current respectively, the so called metallic mode of the magnetron discharge is found, while above these limits compound mode of the discharge comes into place. The hysteresis is clearly presented at the transition between these two modes. Moreover, the limit of the oxygen flux for this transition shifts towards larger value with the increase of the discharge current intensity.

In Fig. 4 the typical hysteresis curve is presented for copper target and argon - oxygen reactive gas mixture when discharge current is constant (0.8 A) but cathode potential is measured versus oxygen mass flow rate. This result confirms the fact that electron emission at the cathode surface is larger, for

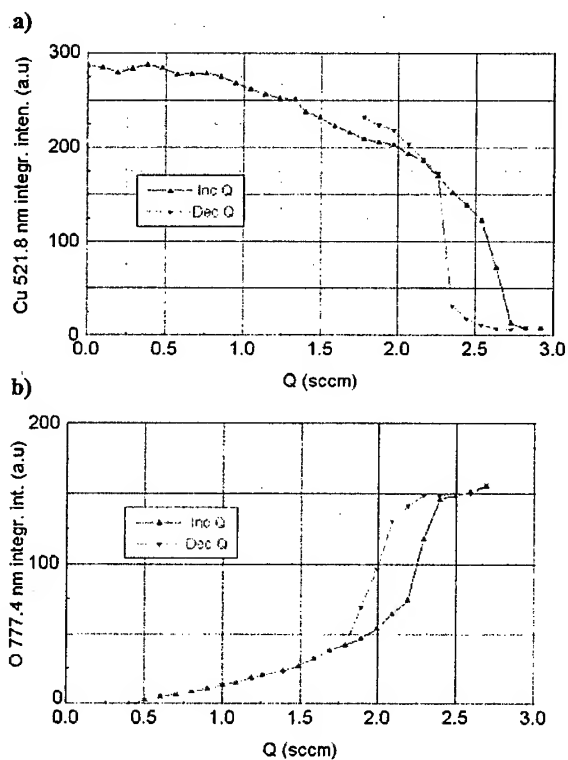


FIG. 3. Hysteresis curves presented as relative variation of the atom densities of copper (a) and oxygen (b), respectively, versus oxygen mass flow rate. The atom densities measured as intensity of the spectral lines of 521.8 nm for Cu and 777.4 nm for O, respectively.

Initial argon pressure $9.1 \cdot 10^{-4}$ mbar and discharge current intensity of 1.0 A for (a) and 0.8 A for (b).

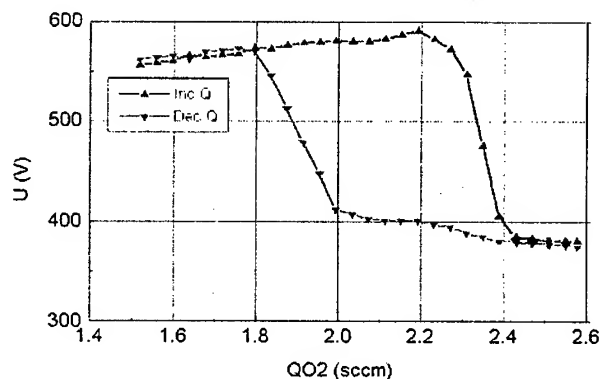


FIG. 4. Hysteresis curves as cathode potential variation versus oxygen mass flow rate. Initial argon pressure of $9.1 \cdot 10^{-4}$ mbar and constant discharge current intensity of 0.8 A.

some oxide compound as Al_2O_3 , SiO_2 , TaO or InO [59 - 62], than for the pure metal so that the discharge voltage decreases when the discharge passes from

metallic mode to the oxide mode. A detailed analysis on the drop in the cathode sputtering rate with the increase in oxygen content of the argon-oxygen flow mixture accompanied by a sharp rise in the discharge current was made by Gorganchev et al. [63] for cold cathode discharge with targets made of Al, Si, Fe, Ta or Ag.

A different result is obtained for TiN system where the secondary electron emission coefficient of TiN for Ar^+ ions is smaller than that of titanium [64]. In this case the titanium nitride compound at the target surface decreases the electron emission and increases the cathode potential in order to keep a constant discharge current. The experimental result from Fig. 5 shows clearly how the

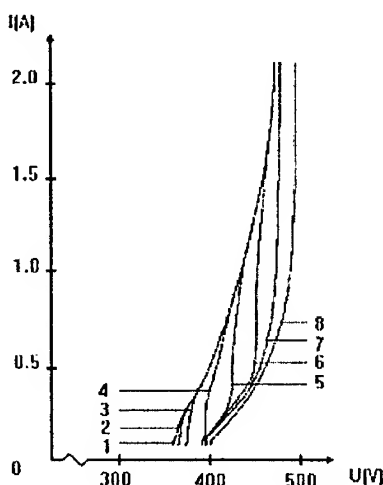


FIG. 5. Current-voltage characteristic for d.c. magnetron discharge with Ti - target and $Q(\text{Ar}) = 2.35$ sccm and different nitrogen mass flow rates $Q(\text{N}_2) = 0$ (1); 0.25 (2); 0.50 (3); 0.75 (4); 1.00 (5); 1.25 (6); 1.50 (7); 1.75 (8) sccm. Gas pressure $6.6 \cdot 10^{-3}$ mbarr.

cathode potential changes from a larger value, when the compound at the cathode surface is present, to a lower value corresponding to the metallic case. A transition is obtained with increasing of the discharge current and sputtering of the compound from the target surface [65]. Similar results were obtained in [66, 67]. Moreover, decreasing of the sputtering rate for TiN, ZrN and HfN comparing with Ti in Ar/N_2 mixture was reported [68], while fairly recently increasing of the sputtering rate of TiN compound has been found where Penning effect is present in the plasma discharge due to ternary gas mixture as: $\text{Ar}/\text{N}_2/\text{He}$ or Ne [69].

These results were obtained in a so-called classical procedure when for each experimental point the system can be considered in quasiequilibrium except for the hysteresis region where the system is unstable. In the following, the results are presented in which the variable was the discharge current which was changed relatively fast so that either the phase process can be observed or relaxation one. Other parameters like: gas flow rate, gas pressure or ratio of the flow rates of the components of the gas mixture were used as parameters.

In Fig. 6 typical hysteresis curves in the current-voltage characteristics are presented for Cu/Ar/O₂ system for a constant flow rate of both components, argon with 0.6 sccm and oxygen with 1.9 sccm, respectively. A linear and symmetric variation of the cathode potential was used between 360 V and 600 V, but with a variable frequency between 0.01 Hz and 1.0 Hz respectively. A strong change, in the hysteresis shape and area, is obtained as a function of the frequency of the cathode potential. Even two loops of hysteresis have been obtained when the sense of the loop is changing from counterclockwise to clockwise with increasing frequency of the cathode potential. Moreover, hysteresis is associated with energy stored and released in the system, according to the physical processes and the corresponding sense on the loop. As it was mentioned the processes involved are very complex including both surface and volume phenomena but also external circuit of the discharge may contribute in hysteresis mechanism. In the following both experiments and results are presented referring to the time evolution of composition and density of the plasma particles and of the surface-plasma impedance. The results allow at least a qualitative understanding of the hysteresis effect.

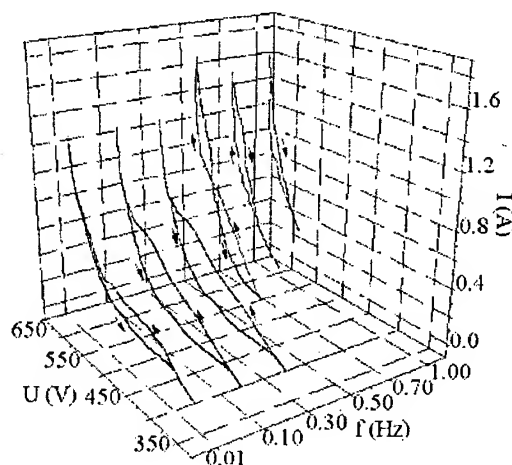


FIG. 6. Hysteresis in the current-voltage characteristics of the magnetron discharge. Copper target, $Q(\text{Ar}) = 0.6$ sccm and $Q(\text{O}_2) = 1.9$ sccm and gas pressure $6.6 \cdot 10^{-3}$ mbarr. Frequency of the symmetrical ramp voltage applied on the cathodes as parameter.

The hysteresis curve in the current-voltage characteristic for Ti/Ar/N₂ system is presented in Fig. 7a. The corresponding dependencies of the relative values of the densities of the main ions as (Ti^+ , Ar^+ , N^+ and N^{+2}), measured by mass spectrometer, versus discharge current in the hysteresis region are presented in Fig. 7b and c. The ions were measured by mass spectrometer placed in the J_2 position of Fig. 1, with the plasma probe placed at 70 mm from the target. The initial gas pressure was $6.5 \cdot 10^{-3}$ mbar and the mass flow rates were: $Q(\text{Ar}) = 2.7$ sccm and $Q(\text{N}_2) = 1.1$ sccm. During linear increment of the discharge current from about 50 mA to about 0.5 A in about 10 s followed by

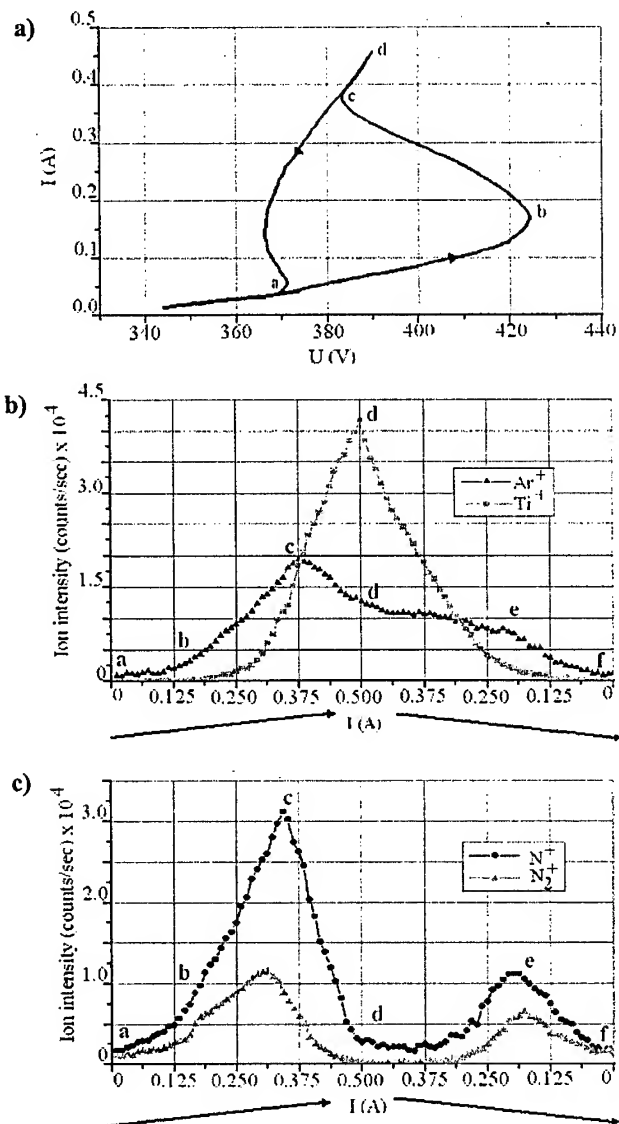


FIG. 7. Current-voltage characteristic (a) of a magnetron discharge with titanium target and $Q(Ar) = 2.7$ sccm and $Q(N_2) = 1.1$ sccm and total pressure of $6.6 \cdot 10^{-3}$ mbar. (b) and (c) the dependence of the ion flux of Ti^+ and Ar^+ (b) and N_2^+ and N^+ respectively (c) versus linear increasing and symmetrical decreasing of the discharge current in 10 s.

symmetric decrement to the initial value, the densities of all ions components have a nonlinear evolution which can be associated to the hysteresis of the Fig. 7a. Thus, the initial increase of the discharge current from 50 mA (point a Fig. 7a) to about 0.15 A (point b Fig. 7a) corresponds to the compound mode of the

magnetron discharge when the target surface is covered mainly by $Ti_x N_y$. In this regime the ion densities of Ar^+ , N^{+2} and N^+ increase with discharge current almost linearly but Ti^+ is not present. Above the limit of about 0.15 A strong change in all characteristics of Fig. 7 can be registered which corresponds to the appearance of titanium ions (Fig. 7b, point b). That means that the compound from the target surface was partly removed and the pure metal surface starts to be involved in the mechanism of the discharge. But, as it was already mentioned, the secondary electron emission of Ti metal is larger than that of the compound [64] so that the cathode voltage can decrease and a negative slope of the I-V characteristic is registered (Fig. 7a, region bc). This part lasts until compound from all target surface involved in the magnetic region is removed. In the domain the ion densities of the gas components (Ar^+ , N^{+2} and N^+) continue to increase but with higher rate because of the increase of the number of primary electrons, at the cathode region (Fig. 7b and c, regions bc). The upper limit of this regime is about 0.375 A. Above this limit the metallic regime is dominant so that the discharge current increases with the discharge potential but with a higher slope (Fig. 7a, region cd) because of the higher secondary electron emission at the cathode, but the ion densities of the gas components start to decrease. This decrease can be explained by two processes. One, probably the most important, is the fact that ionisation potential of Ti ($=6.84$ eV) is smaller than that of any gas components (15.76 eV for Ar, 15.7 eV for N_2 and 14.54 eV for N) so the sputtered titanium atoms and their positive ions become the main population in the plasma region in front of the target. This mechanism might explain, primarily, the decrease of the Ar^+ ion density, while the decrease of the N^{+2} and N^+ ions can also be explained by the second mechanism which involves the reaction at the substrate where the pure Ti metal is deposited as a result of the cathode sputtering. Actually, the decreasing rate of both N^{+2} and N^+ ion density (Fig. 7c, region cd) is larger than that for Ar^+ ions (Fig. 7b, region cd).

With decreasing of the discharge current back to about 50 mA the hysteresis is obtained. The hysteresis depends on the time rate of the change of the discharge current (or potential as in Fig. 6) being related to the chemical reactions in both plasma volume and active surfaces. The symmetry breaking the dependencies of both neutrals and ions' densities with respect to the increasing and decreasing of the discharge current show that both surface and volume processes are not fully reversible. Their time rates are different when the time rate of the discharge current changes its sign. This asymmetry may qualitatively explain the hysteresis.

Some additional information can be obtained by measuring time evolution of the partial pressures or the relative value of the densities of both ions and neutrals after step change of the discharge current. Taking into account the fact that at the constant discharge current, at least the ion flux at the cathode should be almost constant, the cathode potential will be fixed by the impedance of the discharge. Moreover, the discharge impedance depends on the plasma parameters and the electrical properties of the thin layers on the cathode (target), anode (usually wall of the discharge chamber) and sample surface (in some cases).

A typical example is presented in Fig.8. The pulse of the discharge current

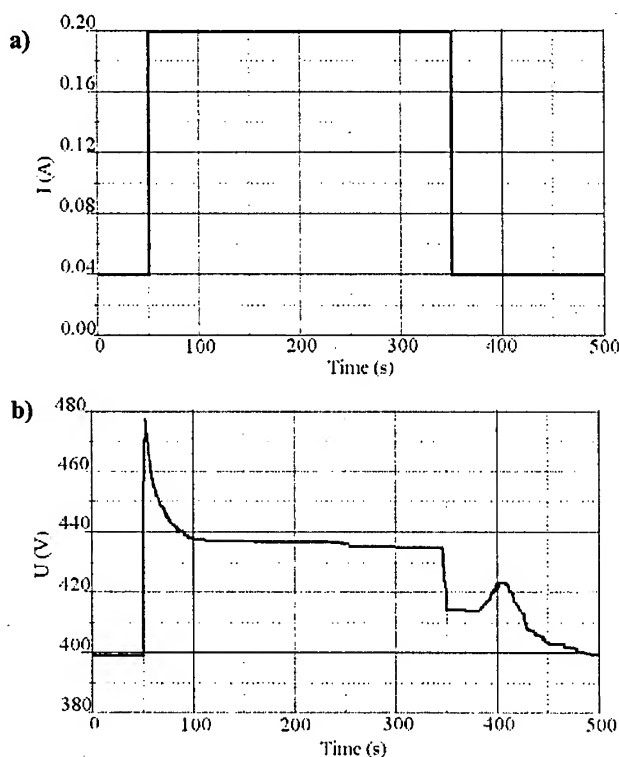


FIG. 8. Time variation of the discharge currents (a), as step function and (b) corresponding time variation of the cathode potential Ti - target $Q(Ar) = 1.7$ sccm, $Q(O_2) = 0.3$ sccm, $Q(N_2) \simeq 0.1$ sccm. Gas pressure $6.1 \cdot 10^{-3}$ mbarr.

(Fig. 8a) for $Ti/Ar/O_2/N_2$ mixture is presented together with the time evolution of the cathode potential (initial pressure of $6.1 \cdot 10^{-3}$ mbar, $Q(Ar) = 1.7$ sccm and $Q(O_2) = 0.3$ sccm). Again there is a large difference between the relaxation processes after increasing of the discharge current with respect to the relaxation after its decreasing to the initial value (Fig. 8b). Each of these parts depends on both gas pressure and composition and discharge current respectively. Moreover, the time evolution of the both N_2 and O_2 partial pressure measured with mass spectrometer placed laterally on J_1 port (Fig. 1) show that the cathode potential follows the N_2 time evolution after increasing of the discharge current (Fig. 9a) while after decreasing of the discharge current to the initial value the cathode potential follows mainly the evolution of the O_2 partial pressure (Fig. 9b). Thus, in the former case, both N_2 partial pressure (Fig. 9a) and the cathode potential (as in Fig. 8b), increase with increasing of the discharge current intensity as a step function from 40 mA to about 200 mA. But then, a typical exponential relaxation process takes place in which the N_2 partial pressure decreases 4 to 5 times (Fig. 9b), while the cathode potential decreases to a value which is about 10% less than the peak value (Fig. 8b). There is no particular behaviour of the oxygen partial pressure in this case (Fig. 9b). Increasing of the discharge

current is followed by a decrease of the partial pressure of the molecular oxygen towards a value which depends on the oxygen flux and on the discharge current. Because of the chemical reaction with titanium metal.

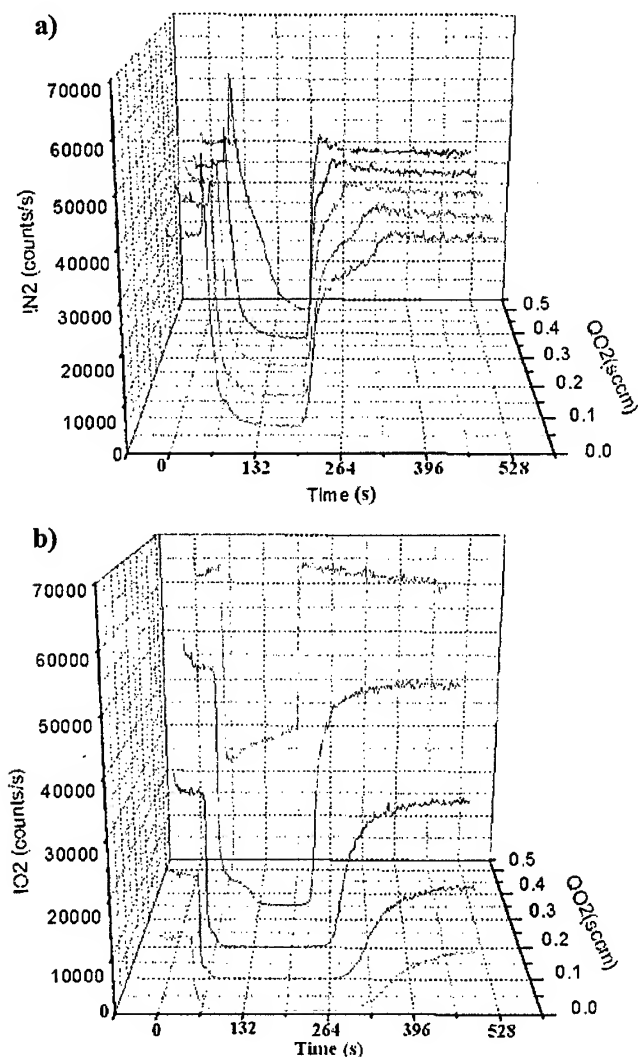


FIG. 9. Time variation of both partial pressures for molecular nitrogen (a) and molecular oxygen (b) and oxygen flux as parameter. Ti-target.

The relaxation constant time of the molecular nitrogen increases with increasing value of the step discharge current. Decreasing of partial pressures of both molecular components, O₂ and N₂ show that the sputtered titanium metal react with both gases and the difference in their reactivity can be observed at decreasing of the discharge current from the higher value to the initial one. The partial pressure of N₂ follows almost instantly the discharge current while the oxygen

partial pressure increases more slowly (Fig. 9b). This fact can be explained by higher reactivity of the oxygen with respect to nitrogen. The analysis of the phenomena related to the relaxation processes which follow the step transitions between two regimes, each of them being characterized by constant discharge current intensity are under investigations. The analysis of the phenomena related to the relaxation phenomena which follow the step transition between two stages, characterised by constant discharge current intensities, is under investigation.

5. Conclusions

- The electron distribution function of a non-reactive magnetron discharge can be approximated as a bi-Maxwellian one. The origin of these two Maxwellian groups of electrons can be explained by ionisation processes and by degrading of the primary fast electrons.
- The hysteresis effect can be explained mainly as the result of the competition between sputtering process and formation of the compounds at the target surface related with changing of the plasma parameters in front of the cathode.

Acknowledgement

This paper was supported by Ministry of National Education (Grant nr. 39.702).

References

1. T. VAN VOROUS, *Solid State Technol.*, **19**, 62, 1976.
2. R.W. WILSON and L.E. TERRY, *J. Vac. Sci. Technol.*, **13**, 157, 1976.
3. F.A. GREEN and B.N. CHAPMAN, *J. Vac. Sci. Technol.*, **13**, 165, 1976.
4. A. Grill, *Cold Plasma in Material Fabrication. From Fundamentals to Applications*, IEEE Press, 1994.
5. B.C. DANILIN and V.K. SIRCHIN, *Magnetronie raspilitenie sistemi*, Radio i Sviazi, 1982.
6. B. CHAPMAN, *Glow Discharge processes*, N.Y. Wiley, 1980.
7. J.A. THORNTON and A.S. PENFOLD, in *Thin Film Processes*, edited by J.L. Vossen and W. Kern Academic, N.Y., p. 75, 1978.
8. J.A. THORNTON, *Thin Solid Films*, **80**, 1, 1980.
9. M.A. LIEBERMAN and A.J. LICHTENBERG, *Principles of Plasma Discharges and Materials Processing*, John Wiley & Sons Inc. 1994.
10. R.K. WAITS, *J. Vac. Sci. Technol.*, **15**, 179, 1978.
11. S.M. ROSSNAGEL, in *Handbook of Plasma Processing Technology*, edited by S.M. Rossnagel, J.J. Cuomo and W.D. Westwood, Noyes Publications, Park Ridge, N.J., p. 160, 1990.
12. R.A. POWELL and S.M. ROSSNOGEL, *Thin Films, PVD for Microelectronics: Sputter deposition Applied to Semiconductor Manufacturing*, Academic Press. N.Y., 1999.
13. S. KADLEC, J. MUSIL and H. VYSKOCIL, *J. Phys. D: Appl. Phys.*, **19**, L189, 1986.
14. S. MANIV and W.D. WESTWOOD, *J. Vac. Sci. Technol.*, **17**, 743, 1980.
15. S. SCHILLER, E. BEISTER and W. Sieber, *Thin Solid Films*, **111**, 259, 1984.

16. M.J. BRETT, R.W. MCMAHON, J. AFFINITO and R.R. PARSONS, *J. Vac. Sci. Technol.*, **A1**, 352, 1983.
17. A.F. HMIEL, *J. Vac. Sci. Technol.*, **A3**, 592, 1985.
18. T. LARSSON, H.O. BLOM, C. NENDER and S. BERG, *J. Vac. Sci. Technol.*, **A6**, 1832, 1988.
19. S. BERG, H.O. BLOM, T. LARSSON and C. NENDER, *J. Vac. Sci. Technol.*, **A5**, 202, 1987.
20. M. WAUTELET, F.F. DEBAL, S. EDART and M. HECQ, *Surf. Coat. Technol.*, **74-75**, 238, 1995.
21. A. BILLARD, C. FRANTZ, *Surf. Coat. Technol.*, **59**, 41, 1993.
22. M. TOUZEAU, D. PAGNON and J. BRETAGNE, *Vacuum*, **52**, 33, 1999.
23. J. BRETAGNE, T.M. MINEA, G. GOUSSET, L. MAGNE, D. PAGNON and M. TOUZEAU, *Proc. X-th Conf. on Plasma Phys. and Applications*, Iasi, July 1998.
24. N. SAVVIDES and B. WINDOW, *J. Vac. Sci. Technol.*, **A4**, 504, 1986.
25. J.L. VOSSEN, S. KROMMENHOEK and V.A. KOSS, *J. Vac. Sci. Technol.*, **A9**, 600, 1991.
26. J. AFFINITO and R.R. PARSONS, *J. Vac. Sci. Technol.*, **A2**, 1275, 1984.
27. S.M. ROSSNAGEL, *J. Vac. Sci. Technol.*, **A6**, 19, 1988.
28. D.W. HOFFMAN, *J. Vac. Sci. Technol.*, **A3**, 561, 1985.
29. S. BERG, C. NENDER, B. GELIN and M. OSTLING, *J. Vac. Sci. Technol.*, **A4**, 448, 1986.
30. S.M. ROSSNAGEL, *J. Vac. Sci. Technol.*, **A7**, 1025, 1989.
31. S. BERG, T. LARSSON, C. NENDER and H.O. BLOM, *J. Appl. Phys.*, **63**, 887, 1988.
32. M. MORADI, C. NENDER, S. BERG, H.O. BLOM, A. BELKIND and Z. ORBAN, *J. Vac. Sci. Technol.*, **A9**, 619, 1991.
33. P. CARLSSON, C. NENDER, H. BARANKOVA and S. BERG, *J. Vac. Sci. Technol.*, **A11**, 1534, 1993.
34. T. NYBERG, P. SKYTT, B. GALNANDER, C. NENDER, J. NORDGREN and S. BERG, *J. Vac. Sci. Technol.*, **A15**, 248, 1997.
35. D. RUSCANU, G. POPA AND, E. STAMATE, in *Proc. Int. Conf. on Plasma Physics*, edited by W. Freysinger, K. Lockner, R. Schrittwieser and W. Lindinger Innsbruck II, 1179, 1992.
36. D. RUSCANU, G. POPA, V. ANITA and V.D. HODOROABA, *Romanian Rep. Phys.*, **49**, 491, 1997.
37. E. STAMATE and G. POPA, in *Proc. Intern. Conf. on Plasma Phys.*, Nagoya, edited by H. Sugai and T. Hayashi, **2**, 1518, 1997.
38. E. STAMATE and K. OHE, *J. Appl. Phys.*, **32**, 671, 1998.
39. E. STAMATE, G. POPA and K. OHE, *Rev. Sci. Instrum.*, **70**, 58, 1999.
40. E. STAMATE, K. INOGOKI, K. OHE and G. POPA, *J. Phys. D: Appl. Phys.*, **32**, 671, 1999.
41. D. LUCA, A.W. DENIER VAN DER GON, R.F.G.C. SCHRAUWEN, M.W.G. PONJEE, V. ANITA, H.H. BRONGERSMA and G. POPA, *Balkan Phys. Lett.*, **5**, 2298, 1997.
42. V. ANITA, G. POPA and D. LUCA, in *Proc. of International Congress on Plasma Physics*, edited by J. Babalec, J. Stockel, P. Sunka and M. Tendler, Prague, **2**, 701, 1998.
43. S.M. ROSSNAGEL and H.R. KAUFMAN, *J. Vac. Sci. Technol.*, **A4**, 1822, 1986.
44. S.M. ROSSNAGEL and H.R. KAUFMAN, *J. Vac. Sci. Technol.*, **A5**, 88, 1987.
45. M.V. MALYSHEV, V.M. DONNELLY, A. KORNBLIT, N.A. CIAMPA, J.I. COLONELL and J.T.C. LEE, *J. Vac. Sci. Technol.*, **A17**, 480, 1999.
46. V.A. GODYAK, in *Plasma- Surface Interactions and Processing of Materials*, edited by O. Auciello, A. Gras-Marti, J.A. Valles-Abarca and D.L. Flamm, Kluwer Acad. Publishers, London, 1990.
47. D. RUSCANU, G. POPA and V. ANITA, *European J. Phys.* (accepted)
48. J.H. MERILL and H.W. WEBB, *Phys. Rev.*, **55**, 1191, 1939.

49. T. YAMAZUMI and S. IKEZAWA, *Jpn. J. Appl. Phys.*, **29**, 1807, 1990.
50. G. HASSALL and J.E. ALLEN, *J. Phys. D: Appl. Phys.*, **30**, 381, 1997.
51. R. LIMPAECHER and K.R. MAC KENZIE, *Rev. Sci. Instrum.*, **44**, 726, 1973.
52. C. GAUTHEREAU and G. MATTHIEUSSENT, *Phys. Lett.*, **A102**, 231, 1984.
53. B. WINDOW and N. SAVVIDES, *J. Vac. Sci. Technol.*, **A4**, 196, 1986.
54. B. WINDOW and N. SAVVIDES, *J. Vac. Sci. Technol.*, **A4**, 453, 1986.
55. N. SAVVIDES and B. WINDOW, *J. Vac. Sci. Technol.*, **A4**, 504, 1986.
56. G. POPA, R. SCHRITTWIESER and E. MRAVLAV, *Plasma Phys. Contr. Fusion*, **31**, 1963, 1989.
57. V. ANITA, G. POPA, J. BRETAGNE, D. PAGNON, D. VERDES and D. RUSCANU, in *Proc. Int. Conf. on Plasma Phys.*, Nagoya, edited by H. Sugai and T. Hayashi, **2**, 14, 1996.
58. G. POPA and V. ANITA, *An.st.Univ. "Al. I. Cuza" Iasi*, submitted
59. J. HELLER, *Thin Solid Films*, **17**, 163, 1973.
60. S. MANIV and W.D. WESTWOOD, *Surface Sci.*, **100**, 108, 1980.
61. S. MANIV and W.D. WESTWOOD, *J. Appl. Phys.*, **51**, 718, 1980.
62. G. ESTE and W.D. WESTWOOD, *J. Vac. Sci. Technol.*, **A2**, 1238, 1984.
63. B. GORGANCHEV, V. ORLINOV and V. POPOVA, *Thin Solid Films*, **33**, 173, 1976.
64. Y. GUOQING, C. JINGSHENG, S. YING, P. HAOCHANG, Z. DEZHANG, X. HONJIE and Z. ZHIHAO, *Thin Solid Films*, **335**, 59, 1998.
65. V. ANITA, D. LUCA, V. HODOROABA and G. POPA, *Vacuum*, **47**, 1103, 1996.
66. J.P. NOEL, D.C. HOUGHTON, G. ESTE, F.R. SHEPHERD and H. PLATTNER, *J. Vac. Sci. Technol.*, **A2**, 284, 1984.
67. K. TOMINAGA, S. INOUE, R.P. HOWSON, K. KUSAKA and T. HANABUSA, *Thin Solid Films*, **281-282**, 182, 1996.
68. W.D. SPROUL, *J. Vac. Sci. Technol.*, **A3**, 580, 1985.
69. C.P. LUNGU, M. FUTSUHARA, O. TAKAI, M. BRAIC and G. MUSA, *Vacuum*, **51**, 635, 1998.

PLASMA CONTROL FOR NEXT-STAGE PLASMA PROCESSING

N. SATO and S. IIZUKA

DEPARTMENT OF ELECTRIC ENGINEERING, GRADUATE SCHOOL OF ENGINEERING,
TOHOKU UNIVERSITY
Sendai 980-8579, Japan

A short review is presented of our experiments on plasma controls for next-stage material and device manufacturings, which are concerned with uniform large-diameter plasma production, electron-temperature control, and dust-particle behaviors. We can provide uniform high-density ECR and rf plasmas, the diameters of which are larger than several ten centimeters. The electron temperature is controlled in the range of one or two orders of magnitude in a region separated from a discharge region. Basing on investigations of dust-particle behaviors in low-pressure discharge plasmas, we can now establish a simple method of dust-particle removal from dusty plasmas.

1. Introduction

Weakly-ionized plasmas have been widely used for various kinds of material and device manufacturings. In order to promote further progresses in these plasma processings, new methods have to be established for plasma production and control. In next-stage large-scaled processings, it is of crucial importance to have unmagnetized large-diameter plasmas providing sufficient ion flux uniform within a few percents in front of substrates. It is also required to control the electron temperature (or electron energy distribution function) in weakly-ionized plasmas. This control is necessary to find the best conditions for various plasma processings because reactive processes occurred strongly depend on the electron temperature. In addition, the electron temperature is closely related to the plasma property and structure including sheath regions in front of the substrates. A removal of dust-particles, which are generated in reactive plasmas, is also quite important for next-stage dust-free plasma processings.

Here we report our experiments carried out at Tohoku University from these points of view. In Section 2, the experiments on uniform-plasma production are presented. Section 3 presents the experiments on electron-temperature control. Section 4 contains active controls of dust-particle behaviors in plasmas. The results are summarized in Section 5.

2. Uniform-plasma production

Here, two simple methods are presented of uniform-plasma production. One of the method is based on the electron cyclotron resonance (ECR). For the other method, we employ the magnetron-typed rf discharge. In the both methods, weakly-ionized plasmas can be produced by low-pressure discharges in a vacuum chamber, the wall of which is separated into two parts. The one part is electrically grounded. The other part is used as an antenna or rf electrode. Therefore, in principle, we need no additional electrode for plasma production in the vacuum chamber. Radial profiles of the plasmas are nonuniform in a region of plasma production. But, radial plasma diffusion makes the plasmas uniform at an axial position a little away from the production region. We employ a magnetic field to provide efficient plasma production and to control plasma flow toward the wall (or electrode) which is closely connected with plasma loss and particle sputtering. The magnetic field, which is generated by permanent magnets, modifies electron motions and is used for plasma-profile control, although there is no direct magnetic effect on ions in front of substrates.

2.1. Plane-slotted antenna with magnets

A main feature of the antenna used is shown in Fig. 1. Details of the antenna system have already been described in Refs. [1, 2, 3]. The antenna, which is

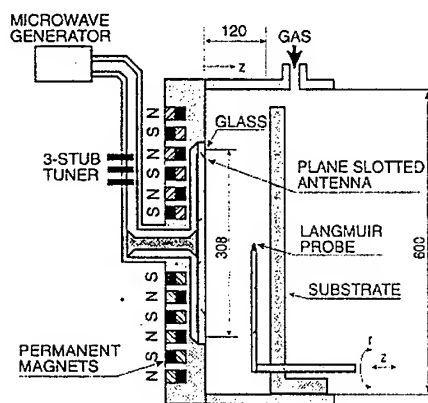


FIG. 1. Plane slotted ECR antenna with magnets.

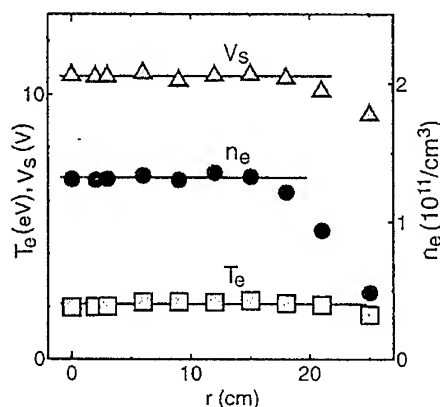


FIG. 2. Radial profiles of plasma density n_e , electron temperature T_e , and space potential V_s of ECR plasma produced.

situated at one end of a vacuum chamber, consists of a back plate with permanent magnets behind and a slotted plate separated from the back plate. A microwave of 2.45 GHz is fed through a coaxial waveguide to satisfy the ECR condition (≈ 875 G) in a region near the magnet surfaces in front of the antenna. The slotted plate can be covered with a thin glass plate. The plasma produced is nonuniform radially in front of the antenna, depending on the positions of the slots and magnets. But, with an increase in z (distance from antenna front),

inward plasma diffusion makes the plasma profile flat in the radial direction. Typical results are presented in Fig. 2, where argon pressure $\approx 1.5 \cdot 10^{-2}$ Torr and microwave power ≈ 1 kW. The plasma of density $n_p \approx 1.3 \cdot 10^{11} \text{ cm}^{-3}$ and electron temperature $T_e \approx 2.1$ eV is found to be uniform within 3% in the radial region of 35 cm in diameter at $z=10$ cm. The plasma density is almost proportional to the microwave power.

A reactive plasma produced by this method was confirmed to yield uniform etching of polysilicon [4]. Changing the magnetic configuration in front of the antenna, we can vary the axial position for the uniform plasma profile in the radial direction [2].

2.2. Modified magnetron-typed rf discharge

A typical setup used for the modified magnetron-typed discharge is shown in Fig. 3. A rf power of 13.56 MHz is fed to a ring electrode [A] of 55 cm in

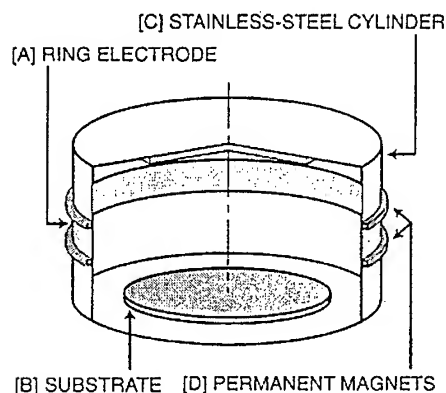


FIG. 3. Setup for modified magnetron-typed rf discharge.

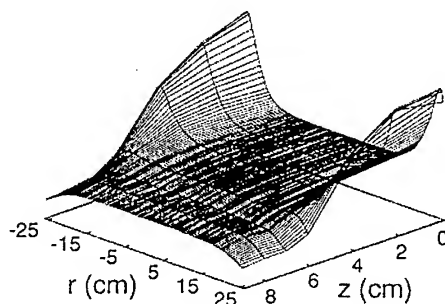


FIG. 4. Density profile of rf plasma produced.

diameter and 7 cm long, which is a central part of a cylindrical vacuum chamber of 55 cm in diameter and 15 cm long. A discharge is triggered between this powered electrode and the other parts [C] of the vacuum chamber, which are electrically grounded, in the range of argon pressure $5.0 \cdot 10^{-4} \sim 5.0 \cdot 10^{-2}$ Torr. Permanent magnets [D], which are situated just outside the cylinder to construct azimuthal magnet rings, provide magnetic mirrors axially near the inner surface of the ring electrode. This magnetic configuration enhances plasma production because high-energy electrons responsible for ionization move in the azimuthal direction, being well trapped in the magnetic mirrors inside the ring electrode. This motion of electrons reduces a potential drop in front of the electrode, which is closely connected with an interaction of ions with the electrode. The plasma density is found to have a peak near the electrode and decrease in the direction toward the radial center. But, with an increase in z (axial distance from machine center), the plasma diffuses toward the radial center, flattening the radial density profile. This modified magnetron-typed rf discharge [5] yields an almost uniform

plasma in the radial region of 40 cm in diameter at $z = \pm 6.0$ cm where substrates [B] can be situated, as shown for argon pressure of $1.0 \cdot 10^{-3}$ Torr and rf power of 200 W in Fig. 4. Now we can produce a uniform plasma of density around 10^{10} cm^{-3} , the diameter of which is larger than 100 cm [6, 7]. For production of such a large uniform plasma, a weak additional discharge near the radial center is useful for the profile control.

The potential drop in front of the ring electrode is changed by varying the magnetic strength and configuration. Therefore we can control energies of ions toward substrates [8] and particle sputtering due to high-energy ions accelerated by the potential drop. In fact, we could find the condition where there is no appreciable sputtering from the electrode [9].

3. Electron-temperature control

Generally speaking, it is quite difficult to change the electron temperature in weakly-ionized plasmas. In this Section, we demonstrate two methods used for electron-temperature control, which might be useful in next-stage plasma processings. One of them is accomplished by using a pin-hollow cathode while the other employs a mesh grid. The both methods are based on trapping of electrons ionized in discharge-free region, which is provided by varying a local discharge structure. Therefore, in the both methods, there appears a region of low-electron temperature in addition to the discharge region of high electron temperature. Our methods suggest a general principle of electron-temperature control in low-pressure discharge plasmas.

3.1. Control by pin-hollow cathode

Here, the pin-hollow cathode is employed for low-pressure dc discharges. In a typical setup shown in Fig. 5, the cathode used consists of 20 cm-diam stainless-steel cylinder with 17 cm-diam hole at the front edge and 0.2 cm-diam pointed stainless-steel pins installed inside [10]. The 48 pins, connected electrically with the cylinder, are set with an equal separation on a 16 cm-diam circle. The pin length δ is varied from 0 to 7 cm. A low-pressure gas discharge is triggered between this pin-hollow cathode and a 30 cm-diam anode with 10 cm-diam hole under a weak axial magnetic field of $100 \sim 150$ G.

As found in Fig. 6, for $\delta = 0$ cm, there appears a glowing plasma column, the diameter of which is determined by the cathode front hole in the region up to the anode. With an increase in δ , the glow becomes weak gradually in the radial core part of the plasma. For $\delta = 6 \sim 7$ cm, the glow is limited only in the radial edge region. The core plasma passes through the anode hole, being terminated by a target. As δ is increased, the electron temperature T_e is observed to decrease drastically, being accompanied by a slight increase in the plasma density n_p (from $4 \cdot 10^9 \text{ cm}^{-3}$ to $6 \cdot 10^9 \text{ cm}^{-3}$) in this core plasma. For argon gas pressure $\approx 1.0 \cdot 10^{-2}$ Torr, $T_e (= 2 \sim 3 \text{ eV for } \delta = 0 \text{ cm})$ decreases by an almost one order of magnitude as δ is increased up to 7 cm. This result is ascribed to enhanced trapping of primary electrons in the potential-hill structure formed by the pins in the cathode.

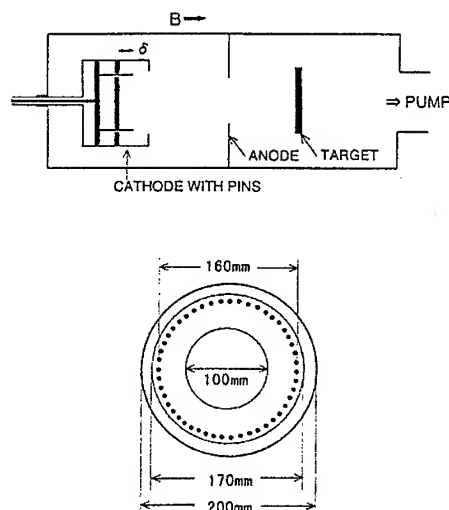


FIG. 5. Setup for electron temperature control using pins installed in a hollow cathode.

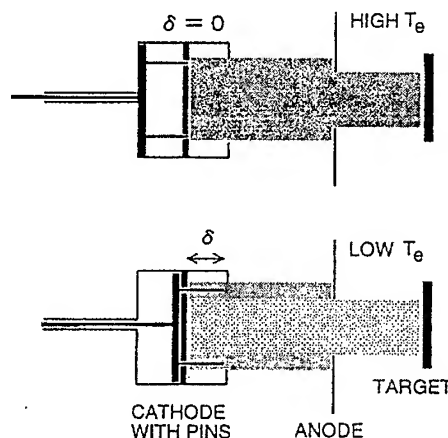


FIG. 6. Plasma structures changed by pin position.

With a decrease in T_e , there appear drastic changes in the densities of ion and radical species in reactive plasmas. Typical effects of the electron temperature on reactive processes have been described in Refs. [11, 12].

3.2. Control by mesh grid

A typical setup for the electron-temperature control by a mesh grid is shown in Fig. 7. A plasma of $n_p = 10^9 \sim 10^{10} \text{ cm}^{-3}$ and T_e of a few eV is produced by a low-pressure argon discharge in a region (I), diffusing through a coarse mesh grid into a region (II). As shown also in Fig. 7, at z (distance from grid) = 0.2 cm, we can recognize high-energy electrons passed through the grid. At $z = 0.4$ cm, however, there appear low-energy electrons. As z is increased, their density increases while high-energy electrons disappear gradually. At $z \geq 2.0$ cm, there are only low-energy electrons with density higher than that in the region (I), where we can neglect effects of the grid potential V_G . In Fig. 8, T_e at $z = 7.0$ cm in the region (II) is plotted against V_G for various grid mesh sizes [mesh size: 0.25(open circles) - 6.8(closed squares)mm]. There is a quite drastic effect of V_G on T_e . We can obtain $T_e = 0.035$ eV, lower by almost two orders of magnitude than that in the region (I) [13]. The result is understood by taking account of ionization in the region (II). Since the space potential is lower in the region (II) than in the region (I), higher-energy electrons passing through the grid lose their kinetic energy. But, some of them have the energy still large enough to ionize atoms in the region (II). Electrons produced there are not responsible for maintaining the discharge. Therefore, there is no reason for these electrons to have such a high energy as in the region (I).

In this example of the electron-temperature control, the plasmas are produced

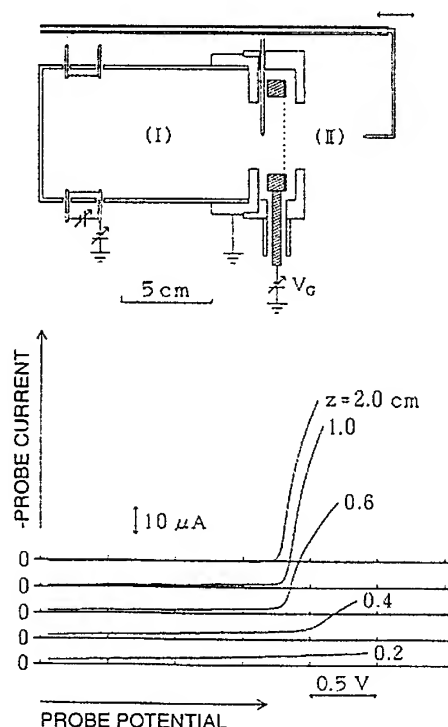


FIG. 7. Setup (upper) for electron temperature control using mesh grid and typical probe characteristics (lower) at different positions z from the grid.

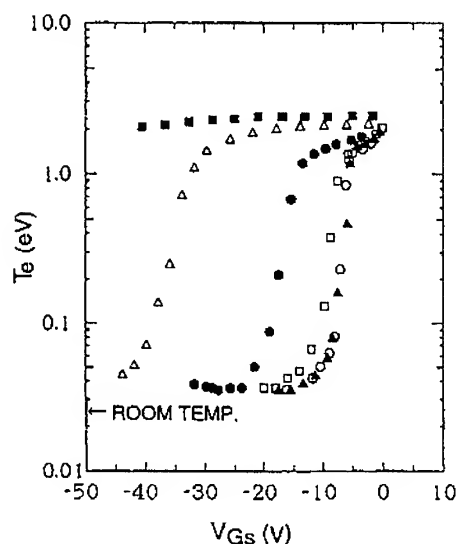


FIG. 8. Electron temperature T_e in the region (II) against grid bias V_{Gs} (with respect to plasma potential).

by dc discharges. But, our method was confirmed to work also for low-pressure discharge plasmas produced by different methods. In fact, this method was used for plasmas produced by the ECR and rf discharges mentioned in the previous section [14, 15].

The electron temperature can also be controlled by varying a mesh size of the grid at a fixed bias potential. Even if there is no external potential applied to the grid, the electron temperature depends on the mesh size. In general, however, it is difficult to vary the mesh size during the machine operation. It is better to make a hole (or slit) in the grid, the size of which is much larger than the mesh size. Varying the hole (or slit) size mechanically, we can control the electron temperature [16]. An example of the grids used is shown in Fig. 9, where we can vary the azimuthal slit length L_s . As demonstrated in Fig. 10, the electron temperature is well controlled by the slit length. This mechanical method might be quite useful for the electron-temperature control in reactive plasmas, where the grid is often covered by thin films of insulator.

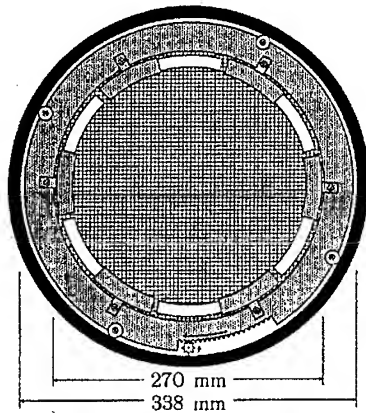


FIG. 9. Grid with slit for electron temperature control.

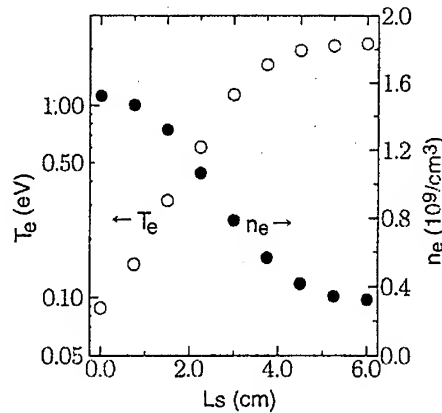


FIG. 10. Electron temperature T_e and plasma density n_e against slit length L_s .

4. Control of dust particle behaviors

As a series of our experiments on fine-particle clouds in plasmas, we have carried out many kinds of experiments on structure controls of the fine-particle clouds in low-pressure dc discharge plasmas. They include controls of vertical and radial profiles, phase transition, vortices driven electrostatically, azimuthal rotations driven by a vertical magnetic field, vertical spread of particle clouds, and vertical strings of periodic alignment of particles. Essential points of the results are found in Ref. [17].

A standard situation used in our experiments is schematically described in Fig. 11. A plasma is produced at argon gas pressure around 0.2 Torr by applying a negative dc potential to a cathode (stainless steel 6 mesh/inch grid) of 8.5 cm in diameter with respect to a ring anode (outer and inner diameters are 80 and 9.5 cm, respectively) which is separated 1 cm downward from the cathode, being electrically grounded. The discharge current is in the range 0.2 ~ 2 mA, yielding $n_p = 10^7 \sim 10^8 \text{ cm}^{-3}$ and $T_e = 1 \sim 3 \text{ eV}$, respectively.

Mono-dispersive methylmethacrylate-polymer particles (specific gravity: $1.17 \sim 1.20 \text{ g/cm}^3$) of $10 \mu\text{m}$ in diameter are injected through the mesh cathode. There are stainless steel plates for vertical levitation and radial confinement of the particles in the experimental region below the anode. The 2 cm-diam plate (LE) for the levitation is set at a position of 1.5 cm downward from the anode. The plate (CE) for the confinement with a 2.0 cm-diam hole at its center is set at a position of 0.1 cm upward from the LE. The particles are observed by a CCD camera detecting Mie-scattering of He-Ne laser light spread with horizontal width of 0.5 cm.

When the CE is biased more negatively than the LE, there appears a hill-shaped radial potential profile above the LE. Then, the particles levitate, being confined radially above the LE, as shown schematically in Fig. 11. The electric charge on each particle is estimated to be $10^4 \sim 10^5 e$ (e : electronic charge).

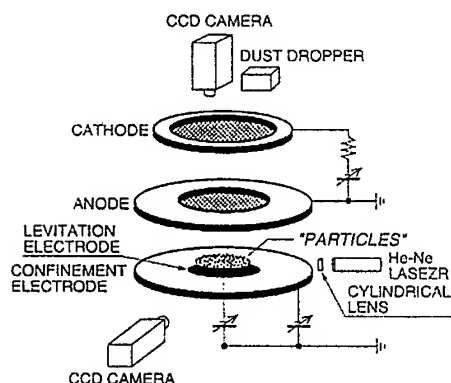


FIG. 11. Setup for experiments on controls of fine-particle clouds.

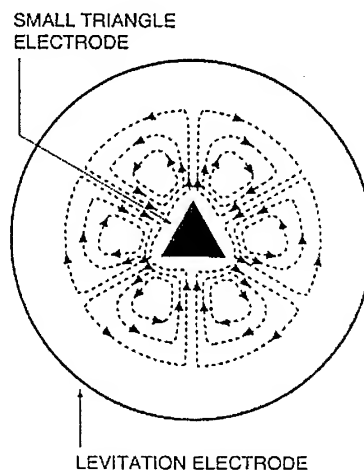


FIG. 12. Vortices generated by applying a negative potential to a small triangle electrode on a levitation electrode.

The particle clouds has an almost hexagonal lattice structure with interparticle distance of a few hundred μm , although the particle positions fluctuate.

Among the various features of the fine-particle clouds, the vortex formation is closely related to a removal of dust particles from dusty plasmas. In order to generate vortices in the horizontal plane, a small electrode (SE) with sharp edges is situated just on the LE [18]. When the SE is biased, there appear large potential gradients around the sharp edges, which give rise to forces acting on the particles and generate particle flows in the particle clouds.

An example of the particle flows is described in Fig. 12, where the SE with triangle shape is biased negatively. The sharp edges push away fine particles, generating vortices with velocity shear in the horizontal plane above the LE, just as in case of usual liquids. In general, one edge drives two vortices, generating six vortices in this case. The speeds of the vortices are in the range up to a few mm/s, depending on the position. The measurements for different shapes of the SE with n (integer) edges show that there appear $2n$ vortices in the particle clouds.

When the SE is biased positively, fine particles move toward the sharp edges, being also accompanied by generation of vortices. The size of the vortices is smaller than that in case of the negative bias. On the basis of this dynamics of the fine-particle clouds, we can establish a simple method of dust removal from dusty plasmas. In the measurements, fine particles of 0.1 to 10 μm in diameter are observed to be completely removed from low-pressure discharge plasmas. This method could be used for dust-free plasma processings for various purposes.

5. Summary

Plasmas produced by the ECR discharges using a plane-slotted antenna with permanent magnets and by the modified magnetron-typed rf discharges are uniform within a few percent in a region of several ten centimeters in diameter at a position where substrates might be situated. A direct magnetic effect on ions is negligible there, although the magnetic configuration is of crucial importance to obtain such a uniformity. We can produce much larger uniform plasmas if necessary. In our methods, there could be no powered electrode for plasma production in the vacuum chamber because the part of the chamber wall could be used as the powered electrode. Our results could be applied to large-scaled plasma processings at the next stage.

In order to control the electron temperature, a local discharge structure is modified to provide a region where electrons are not responsible for the discharges. One of the methods employed, which is mechanical, is to use pins installed in a hollow cathode. With an increase in the pin length, the temperature decreases by almost one order of magnitude. A more drastic electron temperature decrease by almost two orders of magnitude down to 0.035 eV is accomplished in a plasma separated by a coarse negatively-biased grid from the discharge region. The electron temperature is also controlled by varying the size of the hole (or slit) made in the grid. Our methods of the electron temperature are based on local modification of the discharge structure.

The experiments on fine-particle behaviors in low-pressure discharge plasmas have clarified many characteristic features of fine-particle clouds in plasmas. On the basis of the particle motions observed, we can now establish a simple method for removal of dust particles from dusty plasmas, which might be of practical importance for dust-free plasma processings.

Acknowledgements

We thank our many collaborators for their contributions to the experiments presented here, whose names are found in References. The work was partly supported by Grant-in-Aid for Scientific Research from the Ministry of Education, Science, Sports, and Culture, Japan, ANELVA Corporation, and KOKUSAI ELECTRIC Co., Ltd.

References

1. N. SATO, S. IIZUKA, Y. NAKAGAWA and T. TSUKADA, *Uniform Plasma Produced by a Plane Slotted Antenna with Magnets for ECR*, Appl. Phys. Lett., **62**, 13, 1469, 1993.
2. S. IIZUKA and N. SATO, *ECR Devices with Permanent Magnets for Production of Large-Diameter Uniform Plasmas*, Jpn. J. Appl. Phys., **33**, 1, 7B, 4221, 1994.
3. K. HORIUCHI, S. DOWAKI, S. IIZUKA and N. SATO, *Compact ECR Plasma Apparatus*, Proc. of 15th Symp. on Plasma Processing, Hamamatsu, January 21-23, p.148 - 151, 1998.
4. T. ISHIDA, Y. NAKAGAWA, T. ONO, S. IIZUKA and N. SATO, *Large-Diameter Reactive Plasma Produced by a Plane ECR Antenna*, Jpn. J. Appl. Phys., **33**, 1, 7B, 4236, 1994.
5. Y. LI, S. IIZUKA and N. SATO, *Production of Uniform Large-Diameter Radio-Frequency Discharge Plasma*, Appl. Phys. Lett., **65**, 1, 28, 1994.

6. Y. LI, S. IIZUKA and N. SATO, *Production of a Large-Diameter Uniform Plasma by Modified Magnetron-Typed Radio Frequency Discharge*, Jpn. J. Appl. Phys., **36**, 1, 7B, 4554, 1997.
7. Y. URANO, Y. LI, K. KANNO, S. IIZUKA and N. SATO, *Production of 1-m Size Uniform Plasma by Modified Magnetron-Typed RF Discharge with a Subsidiary Electrode for Resonance*, Thin Solid Films, **316**, 60, 1998.
8. T. SHIMIZU, Y. LI, S. IIZUKA and N. SATO, *Ion-Energy Control by Magnetic Field near an RF Electrode in Modified Magnetron-Typed RF Discharge*, Proc. of 15th Symp. on Plasma Processing, Hamamatsu, January 21-23, , p.593 - 596, 1998.
9. Y. LI, S. IIZUKA and N. SATO, *Control of Sputtering in a Modified Magnetron-Typed Radio-Frequency discharge*, Nuclear Instrum. Methods in Phys. Res., **B 132**, 585, 1997.
10. N. SATO, S. IIZUKA, T. KOIZUMI and T. TAKADA, *Electron-Temperature Control by Movable Pins Installed in a Hollow Cathode for Discharge Plasmas*, Appl. Phys. Lett., **62**, 6, 567, 1993.
11. S. IIZUKA, T. KOIZUMI, T. TAKADA and N. SATO, *Effect of Electron Temperature on Negative Hydrogen Ion Production in a Low-Pressure Ar Discharge Plasma with Methane*, Appl. Phys. Lett., **63**, 12, 1619, 1993.
12. S. IIZUKA, T. TAKADA and N. SATO, *Enhanced Methyl-Radical Production in an Ar-CH₄ Pin-Hollow Cathode Discharge*, Appl. Phys. Lett., **64**, 14, 1786, 1994.
13. K. KATO, S. IIZUKA and N. SATO, *Electron-Temperature Control for Plasmas Passing through a Negatively Biased Grid*, Appl. Phys. Lett., **65**, 7, 816, 1994.
14. K. KATO, S. IIZUKA, G. GANGULY, T. IKEDA, A. MATSUDA and N. SATO, *Electron and Ion Energy Controls in a Radio Frequency Discharge Plasmas with Silane*, Jpn. J. Appl. Phys., **36**, 1, 7B, 4547, 1997.
15. S. IIZUKA, K. KATO, A. TAKAHASHI, K. NAKAGOMI and N. SATO, *Negative Hydrogen Ions Produced by Electron Temperature Control in an RF Plasma*, Jpn. J. Appl. Phys., **36**, 1, 7B, 4551, 1997.
16. K. KATO, S. IIZUKA and N. SATO, *Electron Temperature Control by Varying Length of Slots on a Grid*, Abstracts of 12th Symp. on Plasma Science for Materials, Tokyo, June 16-17, p.76, 1999.
17. N. SATO, G. UCHIDA, R. OZAKI and S. IIZUKA, *Fine-Particle Coulomb Lattices Formed and Controlled in DC Discharge Plasmas*, *Physics of Dusty Plasmas* (edited by M. Horanyi, S. Robertson, and B. Walch, American Institute of Physics, New York), p.239 - 246, 1998.
18. S. IIZUKA, G. UCHIDA, T. KAMIMURA and N. SATO, *Potential-Driven Vortices of Strongly-Coupled Fine Particles in a Plasma*, *Physics of Dusty Plasmas* (edited by M. Horanyi, S. Robertson, and B. Walch, American Institute of Physics, New York), p.175-178, 1998.

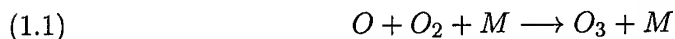
THE ROLE OF ELECTRONEGATIVE IMPURITIES IN OZONE GENERATION BY HIGH PRESSURE DISCHARGES

J. SKALNÝ

DEPARTMENT OF PLASMA PHYSICS, COMENIUS UNIVERSITY
Mlynská dolina F-2 842 15 Bratislava, Slovakia

1. Introduction

The high pressure discharges (pulsed or DC corona, barrier, gliding and the others), have been intensively studied both experimentally and theoretically as sources of low temperature plasma for pollution control technologies. The potential of electrical discharge methods has been demonstrated for the decomposition of many types of VOC [1]. Mostly air or oxygen are used as a feed gas in which pollutant is diluted. It is well known that ozone is efficiently produced if air or oxygen are exposed in such discharges [2, 3, 4]. Hence the ozone production is a phenomenon which more or less accompanies a depletion of pollutants from exhaust gaseous mixtures with air or oxygen. Some of the processes to be active in ozone formation mechanism are partially competitive with the decomposition of pollutant molecules, hence the ozone production, under certain conditions, must be taken into account. Especially a consumption of a portion of oxygen atoms in the three-body ozone formation process



which otherwise could participate in removal of pollutant molecules from treated mixture [5], tends to reduce the decomposition efficiency.

The effect of impurities in air or in oxygen is also considered to be important in respect to variations in the energy yield of ozone generation in various types of ozonators. The earlier investigations [6, 7, 8] were seldom conducted in such a way that of quantitative comparison of obtained results with currently published data could be done [9, 10]. The systematic study of ozone generation from oxygen mixtures with various gases carried out in Siemens ozonator has shown a gradual reduction in the energy yield if H₂, H₂O, CCl₂F₂, Ar and CO₂ were added into oxygen, while an apparent maximum in the energy yield

of ozone was registered if N_2 or CO impurities were used [9]. A similar tendency in the energy yield of ozone was reported by Filippov et al. in case of $N_2 + O_2$ mixtures processed in the ozonator [11]. Only the inhibition action of hydrocarbons (Cyclohexane, n-Hexane and n-Heptane) was observed in ozonator feed with mixtures of oxygen containing one of the mentioned substances [10]. The rate of ozone formation varied linearly down with the increasing hydrocarbon concentration. The ozone formation was practically stopped if the concentration of each of the tested impurities was higher than 1% by volume [10]. The authors presumed that a consumption of oxygen atoms by hydrocarbon molecules is the main reason for reduction in the rate of ozone generation.

Many of pollutants are electron attaching gases. The effect of some of them on the mechanism of ozone generation was already mentioned [9], but the activity of a lot of them in various discharges was investigated only recently. We have shown that a production of ozone from mixtures of air with CCl_2F_2 is substantially reduced with increasing concentration of Freon-12 in the mixture if this is treated in negative corona discharge [12]. Lately the inhibition effects of CCl_4 [13], Trichloroethylene [14] and Freon-113 [15] were described and theoretically analysed [15, 16]. Various high pressure discharges were used in experiments for removal of the mentioned additives from air.

In contrast to the mentioned inhibition effect of several impurities on ozone production, a simultaneous increase in the energy yield of ozone production was observed as the SF_6 impurity concentration was varied within the range of (0.08–0.8)% [17], however any apparent changes in ozone production was registered if $O_2 + 0.01\%$ SF_6 mixture was treated in the same ozonator. The recently published self-consistent model also predicts a substantial increase in the relative ozone formation rate in $O_2 + SF_6$ mixtures [18]. Moreover it was shown that a tiny admixture [SF_6] < 0.1% in air can have an appreciable effect on the characteristics of ozonator [18]. The increase in ozone production, due to the addition of SF_6 traces was also noticeable if ozone was produced from $O_2 + SF_6$ mixtures by irradiation with energetic particles from the $^{10}B(n, \alpha)^7Li$ reaction [19] at SF_6 concentrations below 10%. In contrast to the experiments mentioned above, any measurable increase in the ozone concentration was observed if air + SF_6 mixture was exposed in negative corona discharge at atmospheric pressure, but the decrease of ozone concentration has occurred for higher SF_6 concentration (5%) [20, 21].

The identification of the mechanisms responsible for the inhibition effect of pollutants in air on ozone production is complicated by the well known deleterious effect of NO_x molecules produced very efficiently by high pressure discharges in air [22]. Therefore mixtures of oxygen with tested substances are more appropriate for understanding kinetics of reactions to be responsible for their inhibition effect on ozone generation.

Hence in this paper we report on results of several studies that have been carried out to understand ozone generation in mixtures of oxygen with various impurities processed in the negative corona discharge. The effect of an electronegativity of added molecules was investigated. Three representative groups of compounds were selected (weakly attached CO_2 , strongly attached SF_6 and the set of chloro- and chlorofluorocarbons having a considerably different rate

constants for an electron attachment) to illustrate how the electron attachment as well as the other electron impact processes contribute to the inhibition of ozone generation.

2. Experimental

Two different experimental apparatuses, used for the study of inhibition effect of several compounds on ozone production in the negative corona discharge, have been described earlier [21, 23]. In flow-through configuration [21] a gaseous mixture was passed through the one meter long cylindrical corona reactor. Two coaxially placed cylindrical electrodes, the inner one, diameter 0.1 mm and the outer, diameter one of 15 mm, were used. The ozone concentration in the gas mixture was determined at the reactor outlet by a UV light absorption spectrometer. The flow-stopped glass reactor [23] was placed directly in the UV absorption spectrometer so that the ozone concentration was determined directly in the reactor, without losses in manifold transporting usually the gaseous mixture after treatment from the reactor into the UV spectrometer [21]. The diameters and materials of the inner and the outer electrodes were identical with those used in the flow-through arrangement except for the outer electrode length which was 40 mm only. The simultaneous measurement of corona parameters (current and applied voltage) and ozone concentration is described elsewhere [23].

3. Experimental results and discussion

The experimental results shown in Figs 1, 2 and 3 have been obtained in experiments carried out in the flow-through regime at atmospheric pressure. The

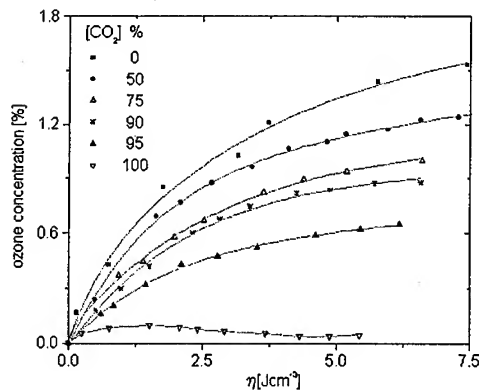


FIG. 1. Dependence of relative ozone concentration on the input energy density η in $O_2 + CO_2$. (Flow-through regime, $p=1$ bar).

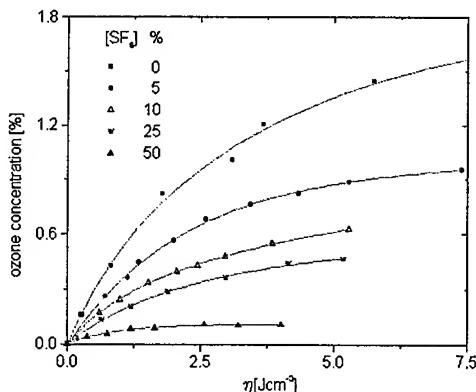


FIG. 2. Dependence of relative ozone concentration on the input energy density η in $O_2 + SF_6$. (Flow-through regime, $p=1$ bar).

dependencies of the relative ozone concentration $[O_3]_R$ on the input energy density η are plotted for three different impurities. The input energy density is the ratio of the power UI (U voltage on electrodes, I mean discharge current) deposited into the gas to the gas flow rate Q at standard conditions. The results achieved in the flow-stopped regime at the pressure $p=900$ mbar, are shown in Figs 4, 5, 6, and 7. The input density η was calculated as a ratio of the total en-

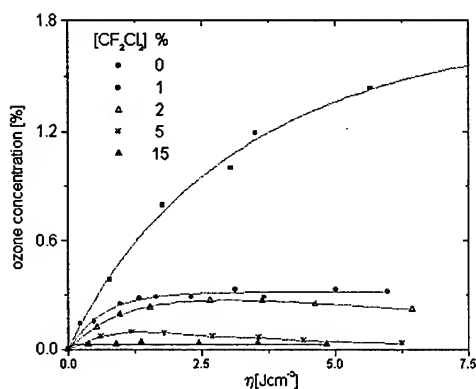


FIG. 3. Dependence of relative ozone concentration on the input energy density η in $O_2 + CF_2Cl_2$. (Flow - through regime, $p=1$ bar).

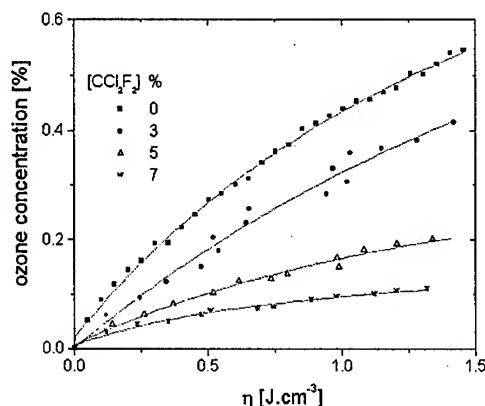


FIG. 4. Dependence of relative ozone concentration on the input energy density η in $O_2 + CCl_2F_2$. (Flow - stopped regime, $p=900$ mbar).

ergy consumed in the discharge UIt (t is the time of processing) to the pressure $p_0 = 1$ bar reduced volume of the reactor Vp/p_0 . There are apparent differences in the inhibition effect on ozone production in regard both to the concentration as well as to gaseous impurity. In order to understand the mechanism responsible for the observed deleterious effect of individual gases, the processes to be active in ozone formation and ozone destruction must be analysed. There are three main groups of processes contributing to ozone formation and destruction which could be affected by the added impurity into oxygen:

- electron impact processes (excitation, ionisation, dissociation and attachment),
- ion-molecule reactions,
- reactions of radicals produced in dissociative processes either with parental molecules or between themselves.

If in the negative corona discharge a mixture of oxygen with traces of gaseous impurity is processed, the input energy is dissipated by primary electrons mostly in interactions with oxygen molecules [24]. At the elevated impurity concentration also interactions of electrons with impurity molecules become to be important, however the threshold concentration value, from which this effect starts to be

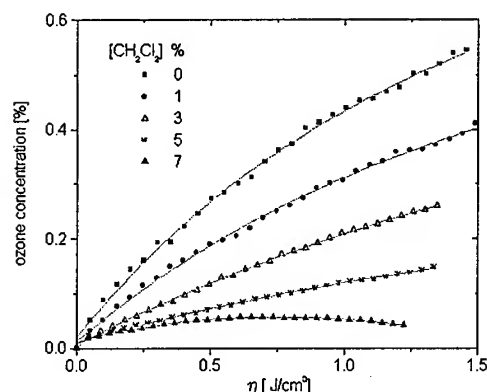


FIG. 5. Dependence of relative ozone concentration on the input energy density η in $O_2 + CH_2Cl_2$. (Flow - stopped regime, $p=900$ mbar).

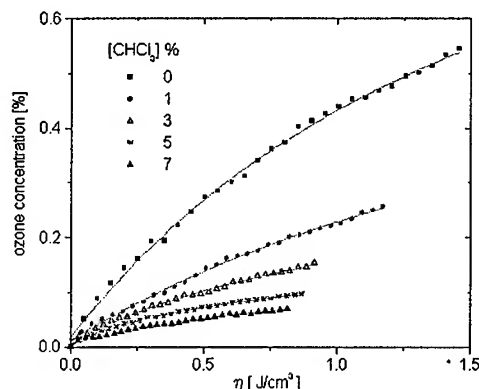


FIG. 6. Dependence of relative ozone concentration on the input energy density η in $O_2 + CHCl_3$. (Flow - stopped regime, $p=900$ mbar).

significant, is different for the different impurity and also is specific in regard to the electron impact process. Except for SF_6 , there was not observed a noticeable effect of tested impurities on the corona onset potential U_0 if the concentration of these was below 5%. In $O_2 + SF_6$ mixtures an apparent increase of U_0 was registered with the increasing SF_6 concentration in oxygen. From the experimentally observed constancy of the onset corona voltage against variations in concentration of the most of tested compounds follows the constancy of reduced electric field E/N in the ionising region (sometimes named glow region [25]) of negative corona discharge. Within the glow region, the electron concentration is much greater than outside this zone. The reduced electric field E/N within this region is assumed to be constant and close to $(E/N)_c$, where the letter is the critical value of reduced electric field at which the rate of ionisation and the rate of electron attachment are in equilibrium [24, 25, 26]. As noted by Morrow (see in ref. [25]), the electron density in the ionising part will drop by more than an order of magnitude as E/N is reduced from $1.03(E/N)_c$ to $0.97(E/N)_c$. Hence we can presume, that conditions in the glow region for the most of electron impact processes are not substantially influenced by the presence of a small amount of tested impurities. Presuming that the rate of electron impact ionisation, producing secondary electrons required for the other electron impact processes, is not considerably influenced by a presence of impurities in oxygen, the explanation for the observed inhibition phenomena can not be looked out in the ionisation of added molecules.

Before examining the experimental results obtained from the present investigation, the specific character of DC corona discharges must be pointed out. All processes requiring a high energy of electrons (ionisation, excitation, dissociation and several dissociative attachment processes) are confined to the mentioned small active region (glow or ionising), its volume being much smaller in

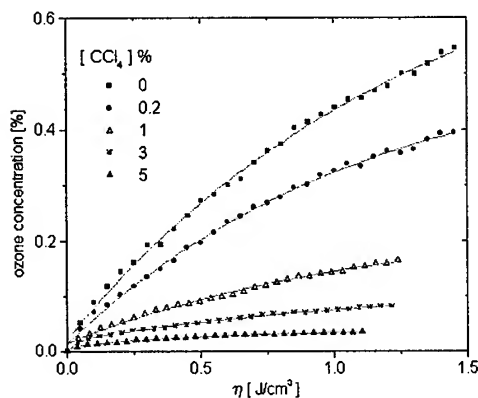


FIG. 7. Dependence of relative ozone concentration on the input energy density η in $O_2 + CCl_4$. (Flow - stopped regime, $p=900$ mbar).

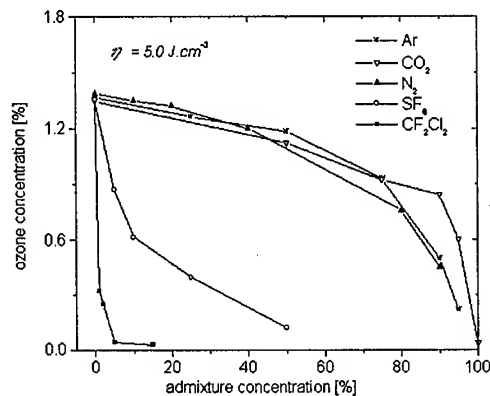


FIG. 8. Dependence of relative ozone concentration at the impurity concentration at $\eta = 0.5 \text{ J cm}^{-3}$.

comparison with that of the rest of the discharge gap, so called drift region, or the rest of the total volume of the discharge reactor. In the drift region only the processes requiring low energy of interacting electrons (dissociative attachment to several halocarbons or ozone), or ion-molecule reactions and chemical reactions of neutral particles are proceeded. Due to the very efficient dissociative electron attachment in the glow region



($k_2 = 4.3 \cdot 10^{-11} \text{ cm}^3 \text{ s}^{-1}$ at $E/N \approx 110 \text{ Td}$, [27]), corresponding to conditions in flow-trough experiments, $U_0 \approx 4.1 \text{ kV}$ and atmospheric pressure), the concentration of free electrons in the drift region of the negative corona discharge in pure oxygen is low [26]. Hence, most likely the interactions of electrons with the impurity molecules do not contribute substantially to the reduction in ozone generation the presence of impurity in oxygen.

In regard to electron attachment efficiencies of the tested substances, the results can be divided into three groups:

- CO_2 represents a weakly electron attaching gas not containing chlorine atoms,
- SF_6 represents a strongly attaching gas not containing chlorine atoms,
- CH_2-Cl_2 , $CHCl_3$, CCl_4 and CCl_2F_2 differ both in the number of substituted chlorine atoms and the electron attachment rate constant, which substantially increases in the case of chloromethanes with a number of chlorine atoms in parent molecule.

Therefore the results will be discussed in respect to the foregoing classification of tested compounds.

4. CO₂

The reduction in ozone concentration at the constant input energy density η is shown over a whole range of CO₂ concentrations of (0 - 100)% in Fig. 1. The decrease in ozone concentration observed at high [CO₂] concentrations is comparable to or even smaller than that reported earlier in O₂ + Ar and O₂ + N₂ mixtures treated in negative corona discharge [28], which is evident from Fig. 8, where the ozone concentration at $\eta = 5 \text{ Jcm}^{-3}$ is presented as a function of impurity concentration for various added gasses. If we consider a two step process of ozone generation in pure oxygen, electron impact dissociation



($k_3 = 2.4 \cdot 10^{-9} \text{ cm}^3\text{s}^{-1}$, at $E/N \approx 110 \text{ Td}$, [27]) together with the three-body associative process (1.1), then the observed reduction in ozone concentration fairly well corresponds to the decrease of oxygen concentration. At low impurity concentration the linear decrease in ozone concentration is in a fairly good accordance with predictions followed from Vasiljev-Eremin formula discussed recently [29, 30, 31]. The formula describes forward and backward processes of ozone formation and decomposition

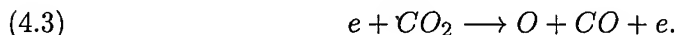


and can be expressed in a formula

$$[O_3]_R = \frac{2k_G(1-\zeta)}{3(k_G + k_D)} \{ (1 - \exp[-(k_G + k_D)\eta]) \}$$

where $[O_3]_R$ and ζ are the relative ozone and impurity concentrations respectively (0 - 1.0). The rate constants k_G and k_D correspond to ozone generation and destruction processes of ozone. It must be noted that in an accordance with the Eremin's theory, the introduced rate constants k_G and k_D are expressed in $[\text{cm}^3\text{J}^{-1}]$ units. At low oxygen concentration Eremin's theory failed.

The apparent differences in the ozone concentration produced from mixtures of oxygen with Ar, N₂ and CO₂ at low O₂ concentration can be explained by a generation of ozone directly from CO₂ molecules. The electron impact dissociation of carbon dioxide molecules is proceeded in the glow region, where electrons have energies sufficient to dissociate CO₂



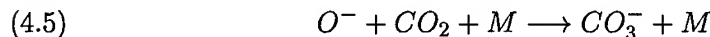
The rate constant k_5 strongly depends on E/N [32, 33]. Under the conditions of our experiments $E/N \approx 110 \text{ Td}$, the value $6 \cdot 10^{-10} \text{ cm}^3\text{s}^{-1}$ was estimated for k_5 from plotted $k_5 = f(E/N)$ dependence [32]. At sufficiently high concentration

of CO₂ (more than 80% by volume in mixture), the contribution of reactions (4.1) and (4.3) to production of oxygen atoms are comparable, hence the oxygen atoms formed through (4.3) from ozone via reaction (1.1) or in the associative process



($k_6 = 7.1 \cdot 10^{-33} \text{ cm}^6 \text{ s}^{-1}$ [32], $k_6 = 1.0 \cdot 10^{-32} \text{ cm}^6 \text{ s}^{-1}$ [33], at $T = 300 \text{ K}$) form molecular oxygen required for further ozone formation via (1.1). The importance of the described pathway increases with increasing content of CO₂. The mentioned sequence of reactions can explain the relatively high concentration of ozone (< 500 ppm) found in carbon dioxide treated in negative corona discharge [34, 35].

After an addition of even a low amount of CO₂ into pure oxygen, the spectrum of negative ions in the discharge gap is substantially changed [37]. The ions O⁻, which are precursors of O₂⁻ and especially O₃⁻ (in pure oxygen predominantly abundant ion [36, 37]) are scavenged by CO₂ molecules through the very fast process



($k_7 = 9.0 \cdot 10^{-29} \text{ cm}^6 \text{ s}^{-1}$ for $M = CO_2$, $k_7 = 3.0 \cdot 10^{-28} \text{ cm}^6 \text{ s}^{-1}$ for $M = O_2$, [33]). Therefore the ions O⁻, O₂⁻ and O₃⁻, which otherwise could partially participate in ozone formation processes [26, 27], are converted to a very stable ion CO₃⁻. Therefore the contribution of parent O⁻ ions in ozone formation is excluded. It must be noted however, that this suppression is only marginally significant in comparison with much more efficient decrease in oxygen concentration, which much likely is the most important reason for the inhibition of the ozone generation at increasing content of carbon dioxide in oxygen.

5. SF₆

Besides theoretical [18] and experimental [17, 19] studies reporting on an increase in the energy efficiency of ozone production at low SF₆ concentrations in mixtures with air, there are many papers devoted to the chemistry of SF₆⁻ decomposition in various high pressure discharges [25, 38, 39, 40, 41, 42, 43, 44]. Considerable work has been done recently for understanding primary oxidation mechanisms associated with the dissociation of SF₆ in its mixtures with traces of water or oxygen molecules. Several results of such studies have been reviewed by Brunt [25, 40]. It must be noted however, that in all of the mentioned papers, the concentration of oxygen impurities was much lower in the comparison with the content of oxygen in mixtures studied in our experiments. That is an explanation why processes participating in ozone formation were not considered [25, 40]. Moreover, the gas chromatography method used for analysis of gaseous products in treated mixtures is not very appropriate for detection of ozone. That is why no ozone traces were detected in the mentioned experiments. It was noted recently by V. Brunt [25], that at higher oxygen content in the mixture with

sulfur hexafluoride it may be necessary to consider processes omitted usually from the reaction scheme of SF_6 decomposition, such as these involving formation and destruction of O_3 . Despite the fact, that most of the mentioned experiments have been carried out at minimal content of oxygen in mixture, (less than 25% by volume [41]), the results discussed in [25, 40] can be partially used for the explanation of our experimental results.

The dependence of relative ozone concentration on the input energy density η found at various sulfur hexafluoride concentration in oxygen is shown in Fig. 2. Remarkable decrease in ozone concentration associated with the increasing content of SF_6 in oxygen is evident both from Fig. 2 as well as from Fig. 8, where the inhibition action of various compounds is demonstrated. As it was already noted, the increase in SF_6 concentration leads to the noticeable increase of the corona onset voltage U_0 . This effect is in accordance with the theoretically predicted variations in the effective ionization coefficient α' due to the SF_6 admixture in oxygen [45]. Therefore in such mixtures the critical value of reduced electric field $(E/N)_c$ at which $\alpha'/N \approx 0$ increases with increasing SF_6 concentration. So the rate of electron generation through ionization collisions of electrons with oxygen molecules is enhanced. Moreover due to the increase of E/N value in the glow region, the efficiency of electron impact dissociation of oxygen (4.1) in this zone is also enhanced because of the higher mean electron energy.

The increase in the rate of ionization is however compensated by an increase in the total rate of electron attachment processes, due to the very efficient attachment of electrons to added SF_6 molecules. The substantial decrease of the corona discharge current induced by an increase in the SF_6 concentration is a tangible evidence for the reduction of free electrons density in the discharge gap. Numerous studies on electron attachment to SF_6 have been conducted, especially in pure sulfur hexafluoride (see references in [46]). It was concluded that predominantly SF_6^- negative ions occur at thermal energy of electrons via



($k_8 = 3.1 \cdot 10^{-7} \text{ cm}^3 \text{ s}^{-1}$ at $T = 300 \text{ K}$, [47]). There is a variety of other ions, which can be created in collisions of an electron with sulfur hexafluoride molecules. Among them, especially SF_5^- ions are interesting from a point of view the processes in a negative corona discharge. The mentioned ions are formed via the dissociative electron attachment



($k_9 = 2.3 \cdot 10^{-10} \text{ cm}^3 \text{ s}^{-1}$, unspecified E/N , [40]), having the maximum in the cross section at relatively low electron energy of 0.35 eV, while the fragment ions F⁻ are formed predominately by electrons having energies higher than 4 eV



($k_{10} = 1.5 \cdot 10^{-10} \text{ cm}^3 \text{ s}^{-1}$, unspecified E/N , [40]). Under the negative corona discharge conditions F^- is produced mainly in glow region whilst SF_5^- and SF_6^-

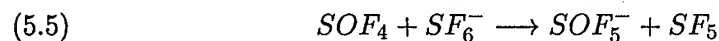
are produced near, but outside this zone [43]. The F^- ions undergo an efficient charge transfer process



($k_{11} = 1.4 \cdot 10^{-12} \text{ cm}^3\text{s}^{-1}$, [40]). The characteristic time for a charge exchange (5.4) is at atmospheric pressure and SF_6 concentration only 3 microseconds, what is much less in comparison with the average transport time of fluoride ions F^- the drift region. Hence the charge transfer ([11]) can sufficiently explain the low signal of F^- ions in spectrum of ions extracted from the drift region of discharge [43, 44].

The mass spectrometric studies of ions directly extracted from the drift region of negative corona discharge in pure SF_6 confirmed the dominance of two mentioned negative ions [43, 44]. It must be noted however, that the mass spectrometric studies have been carried out at relatively low SF_6 pressures, below 20 kPa. By the author's knowledge there are no experimental results available to be completed at pressures close to the atmospheric one. Moreover, there is a lack of mass spectrometric studies performed in $O_2 + SF_6$ mixtures, especially those in which the oxygen content in the mixture would be close to values typical for our experimental conditions. There is only one known study of negative ions extracted from negative corona discharge in mixtures of sulfur hexafluoride with oxygen and water traces suggested that the abundance of ions in spectra is dramatically changed even if only a small amount of oxygen molecules is added into pure SF_6 , probably due to the formation of oxyfluorides [41, 44].

To confirm a foregoing presumption, the 0.5% SOF_4 was added into SF_6 . The only ion observed in the mass spectra of ions extracted from the drift region of negative corona was SOF_5^- created predominantly from the prominent ions SF_6^- via F^- exchange reaction



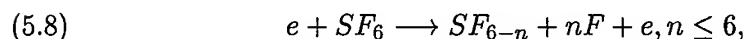
($k_{12} = 4.0 \cdot 10^{-10} \text{ cm}^3\text{s}^{-1}$, [25]). The reaction (5.5) is very effective due to the high F^- affinity to SOF_4 (2.59 eV, [44]). The temporal variations in the SOF_5^- signal, observed by Sauers [44] in flow-stopped experiments carried out in SF_6 containing traces oxygen or water, is the further evidence for high efficiency of F^- exchange. The production of SOF_4 was experimentally confirmed by gas chromatography measurements of by-products of oxidation mechanisms in mixtures $SF_6 + O_2 + H_2O$ processed in high pressure discharges [38, 39, 41]. If we presume that there are no traces of water present in mixture of O_2 with SF_6 , then SOF_4 is predominantly generated via reaction of SF_5 radicals with oxygen atoms



($k_{13} = 2.0 \cdot 10^{-11} \text{ cm}^3\text{s}^{-1}$, [41]). The rate constant of the last reaction is comparable with the rate constant corresponding to the recombination



($k_{14} = 1.7 \cdot 10^{-11} \text{ cm}^3\text{s}^{-1}$, [38]). The reaction (5.7) is one of those, determining the equilibrium value of the SF_6 dissociation level in the glow region of negative corona discharge in studied mixtures. The electron impact dissociation



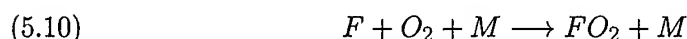
is the initial rate-controlling step in the decomposition of pure SF_6 [40]. In general, the rate constant k_{15} depends on E/N and can be calculated if there exist information about the electron energy dependencies corresponding to all electron-impact processes determining the electron energy distribution function. Unfortunately to far there have been no direct measurements of dissociative excitation cross section for SF_6 which could be used to compute k_{15} [40]. Moreover, there is no experimental data in literature on the total electron induced dissociation rate of SF_6 . Hence only the upper limit on the SF_6 decomposition rate constant was estimated of $7.4 \cdot 10^{-9} \text{ cm}^3\text{s}^{-1}$ at $(E/N)_c \approx 360 \text{ Td}$, [25]. If ion formation processes are completely excluded then $k_{15}(\text{min}) = 5.7 \cdot 10^{-9} \text{ cm}^3\text{s}^{-1}$. This value decreases apparently with decreasing reduced electric field E/N [40] and reaches the value of $1.0 \cdot 10^{-9} \text{ cm}^3\text{s}^{-1}$ at $(E/N) \approx 110 \text{ Td}$, typical of conditions in pure oxygen in our discharge reactor. The value was assessed from calculated $k_{15} = f(E/N)$ dependence [40].

From all theoretically possible dissociation channels, it is presumed that the pathway leading to the SF_5



predominates and accounts for more than 90% of the electron impact induced dissociation collisions [25]. The reaction (5.6) is a sink of a portion of oxygen atoms generated by the dissociation process (4.1). Therefore the formation of SOF_4 could be the process active in the experimentally observed inhibition effect of SF_6 on ozone generation if $k_{13}[\text{SF}_5] \approx k_1[\text{O}_2]^2$. Using the data for $k_1 = 6.9 \cdot 10^{-34} \text{ cm}^6\text{s}^{-1}$ [25] at $p = 1 \text{ bar}$ for the critical value of $[\text{SF}_5]$ concentration it follows $[\text{SF}_5] = 1.95 \cdot 10^{16} \text{ cm}^{-3}$. If we presume that 10% (or less) of added SF_6 molecules is dissociated in the glow region of discharge, then the reaction (5.6) could be significant even at $[\text{SF}_6] \approx 0.5\%$. The assumed 10% level of dissociation in the glow region is a fairly realistic assessment because the rate constant of the associative process in which SF_5 radicals are scavenged (5.7) is smaller by two-orders of magnitude than the rate constant corresponding to the dissociation process (5.9). The effect of SOF_4 formation is amplified by the reaction of SOF_4 with the dominant SF_6^- ions (5.5), through which SF_5 radicals are released again into cyclic process.

Besides the recombination (5.7), the most likely fate of fluoride atoms produced via (5.9) is the formation of stable FO_2 through the three body process, especially effective at high pressures



($k_{17} = 5.8 \cdot 10^{-33} \text{ cm}^6\text{s}^{-1}$, for $\text{M} = \text{N}_2$, [48]), although the formation of FO_2 is slightly an endothermic process (formation enthalpy 12 kJmol^{-1}) [40].

Some parts of fluoride atoms can participate in the catalytic removing cycle in which the molecules of ozone are decomposed

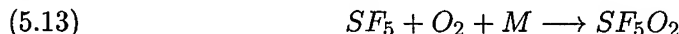


$$(k_{18} = 1.0 \cdot 10^{-11} \text{ cm}^3 \text{ s}^{-1}, [48]),$$

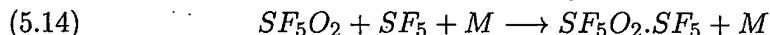


($k_{19} = 2.7 \cdot 10^{-11}$, [48]) The cycle of reactions (5.10) and (5.11) is similar to the well known Cl mechanisms for removal of ozone in the stratosphere [49].

At the high content of O_2 in the mixture it may be necessary in V. Brunt's opinion [25] to consider relatively slow as well it



followed by further clustering



The rate constant for pseudo two-body process



is by Sauers small $k_{22} < 5.0 \cdot 10^{-16} \text{ cm}^3 \text{ s}^{-1}$ [38]. Therefore O_2 reactions are only marginally significant in comparison to the effect of SOF_4 formation (5.6) if the SF_6 concentrations is higher than 1% and minimally 1% of all molecules in the glow region is dissociate, which is, under the conditions of our experiments a fairly well fulfilled presumption.

A conclusion can be drawn from the above discussion. There are three groups of processes which most likely contribute considerably to the inhibition effect of SF_6 on ozone production from mixtures $SF_6 + O_2$ in negative corona discharges:

- decrease of the electron density due to the electron attachment (5.1), (5.2) and (5.3),
- consumption of the significant portion of oxygen atoms in sequence of cyclic reactions (5.6) and (5.5), initiated by the electron impact dissociation of SF_6 (5.9).
- decrease in oxygen atoms production due to the reduction of oxygen content in the mixture and due to the competitive electron impact dissociation of SF_6 molecules (5.8).

6. Halomethanes

The influence of the presence of several halomethanes (X) in oxygen on the relative ozone concentration in mixtures $O_2 + X$ is demonstrated in Fig. 3-7. While the results shown in Fig. 3 were obtained in flow-through experiments at atmospheric pressure, the rest of experiments were performed in the already described

flow-stopped reactor at $p = 900$ mbar. There was not observed any noticeable effect of all tested compounds on the corona onset voltage U_0 within the whole range of halomethane concentrations. Also the effect of added halomethane impurities on the discharge current was much less impressive [12, 23] to be compared with the conspicuous current reduction in case of SF_6 [20, 21]. Based on the obtained experimental results we dare to presume that two group of processes are not significantly influenced by added impurities, or better to say, these two do not play an important role in the inhibition of ozone formation. Because of the experimentally observed constancy of the corona onset voltage, we can presume that the ionization of added halocarbon molecules is not significant. The drop in the ozone concentration can be hardly contributed to the dissociative attachment of electron to tested molecules



because of following reasons.

The electron attachment to the most of tested molecules is at its maximum at thermal energy of incidental electron [50] or slightly higher (≈ 0.5 eV for CHCl_3 , [51]). Hence the best conditions for the dissociative attachment of electrons are in the drift region, but the density of free electrons in the drift region is low, as it was already mentioned above [26]. The electron attachment rate constant for all tested substances is reduced considerably with increasing electron energy [51] or reduced electric field [52], however also at higher electron energies the differences in the absolute values of individual rate constants corresponding to the tested compounds are more than four-orders in magnitude [52]. At thermal electron energy these are even larger [50]. The observed decrease in the relative ozone concentration at the constant energy density does not correspond to a such conspicuous differences in the rate of the dissociative electron attachment. Moreover, a much more efficiently electron attaching impurity CCl_2F_2 ($k = 1.77 \cdot 10^{-9} \text{ cm}^3\text{s}^{-1}$ at thermal electron energy and $7.7 \cdot 10^{-10} \text{ cm}^3\text{s}^{-1}$ at $\varepsilon = 4$ eV, recommended by Christophorou [53]) is even noticeably less effective in the inhibition effect on ozone production, than very weakly attaching gas CH_2Cl_2 ($k = 4.7 \cdot 10^{-12} \text{ cm}^3\text{s}^{-1}$, see references in [50]) as it can be seen in Fig. 9. Also conspicuously more effective deleterious effect of CCl_2F_2 in comparison with strongly attaching SF_6 , evident from Fig. 8, supports our assumption that the electron attachment may be excluded from the potential reasons of the reduction in ozone concentration.

The analysis of processes probably responsible for the observed inhibition effect will be done for the most representative CCl_2F_2 for which a lot of important data was published recently [53]. Before examining the experimental results in oxygen + Freon-12 mixtures in the flow-stopped regime, it must be noted that there is one important difference between SF_6 and tested halomethanes in affinity to atomic oxygen. Due to its high chemical inertness, no direct reaction of SF_6 molecules with oxygen atoms $\text{O}(^3\text{P})$ or even not with $\text{O}(^1\text{D})$ is mentioned [25, 40, 41, 54]. The ground state oxygen atom, $\text{O}(^3\text{P})$, and the excited state oxygen atom, $\text{O}(^1\text{D})$, are produced via two channels of reaction (4.1)

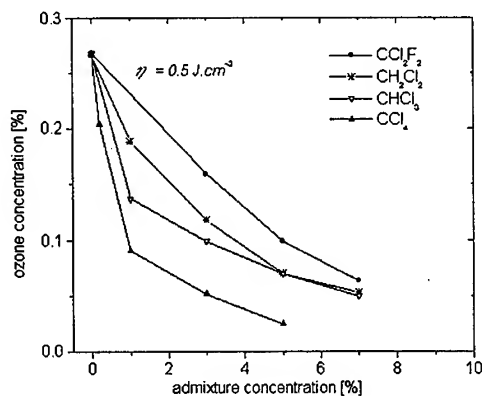
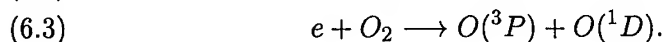
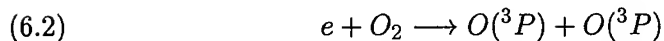
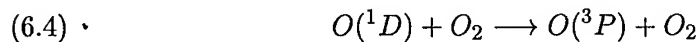


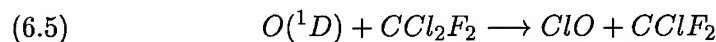
FIG. 9. Dependence of relative ozone concentration at the impurity concentration at $\eta = 0.5 \text{ J cm}^{-3}$.



The rate constant for the process (6.3) is more than double of that for (6.2), however the excited oxygen atoms $O(^1D)$, which otherwise are very efficient in chemical reactions, are lost preferentially to quenching by oxygen molecules [55]



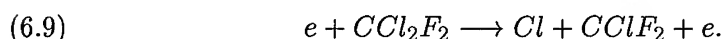
($k_{24} = 4.0 \cdot 10^{-11} \text{ cm}^3 \text{ s}^{-1}$, [25]). Anyway, in contrast to SF_6 some part of $O(^1D)$ atoms can interact directly with added CCl_2F_2 molecules [48]



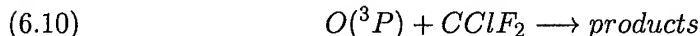
The total rate constant for all four processes $k_{25} = 1.4 \cdot 10^{-10} \text{ cm}^3 \text{ s}^{-1}$, [48], is relatively very high. For the process of $O(^1D)$ quenching $k_{25b} = 0.15k_{25}$ thus the part of $O(^1D)$ atoms is not lost for ozone generation via (1.1). The consumption of a half of created $O(^1D)$ via (6.5 - 6.8) leads approximately to the 35% reduction of created ozone molecules due to differences in rates of oxygen dissociation through the reactions (6.2) and (6.3). If the competition of reactions (6.5 - 6.8) with (6.4) is considered, then the following condition $k_{24}[\text{O}_2] \approx k_{25}[\text{CCl}_2\text{F}_2]$ for

half reduction in $O(^1D)$ concentration must be fulfilled. From this, the relative concentration of $[CCl_2F_2]_R \approx 20\%$ follows. The assessed value is much higher than the value found in experiments. Similar reactions of $O(^1D)$ were studied in some other halocarbons, however only data for CCl_4 ($k_{25} = 3.3 \cdot 10^{-10} \text{ cm}^3\text{s}^{-1}$, [48]) from all compounds tested in our experiments are available. There are no directly measured data for $O(^3P)$ reactions with chloromethane molecules. These are mostly endothermic under normal conditions, however in the glow region the chloromethane molecules could be excited vibrationally and hence under certain conditions the scavenging of oxygen atoms in a ground state could be possible. The active role of $O(^3P)$ oxygen atoms in the decomposition of Freon-12 was presumed and discussed recently [16]. Using the experimental data obtained in a nanosecond corona discharge the authors assessed the rate constant for the reaction of $O(^3P)$ with Freon-113 ($k = 0.5 - 1.0 \cdot 10^{-12} \text{ cm}^3\text{s}^{-1}$, [16]). Under the experimental conditions the dominant product determined by UV light absorption was molecular chlorine, which suggests that most likely the channel similar to (25d) predominates.

Besides already concluded problem with the endothermic character of $O(^3P)$ reactions with chloromethanes, the model did not take into account some other processes. In case of Freon-12, as well as in case of the other chloromethanes, the direct electron impact dissociation can be efficient at sufficiently high electron energies. As it was concluded by Stoffels et al. [55] however, there is an absolute lack of data for such processes in halomethanes. Stoffels et al. developed a model allowing the determination of rate constant $k_{26} = 8.0 \cdot 10^{-9} \text{ cm}^3\text{s}^{-1}$ for the electron impact dissociation

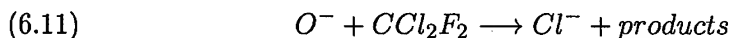


Comparing the values k_3 and k_{26} we presume that under our experimental condition the production of oxygen atoms is accompanied by the production of chlorine atoms and reactive radicals $CClF_2$. It was shown earlier that radical CH_2Cl reacts efficiently with oxygen atom in the ground state, $O(^3P)$, ($k = 2.67 \cdot 10^{-10} \text{ cm}^3\text{s}^{-1}$ [56, 57]). Also the reaction of CCl_3 was experimentally investigated giving the $k = 4.38 \cdot 10^{-11} \text{ cm}^3\text{s}^{-1}$ [58]. Recently calculated data for the reaction



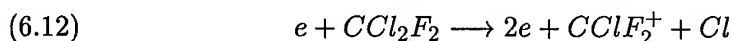
($k_{27} = 4.38 \cdot 10^{-11} \text{ cm}^3\text{s}^{-1}$, [59]) are identical with these valid for the CCl_3 reaction. If we presume that a portion of oxygen atoms in the ground state is scavenged in reactions with radicals formed from chloromethanes by the electron impact dissociation, then the higher value of k for the reaction of oxygen atom $O(^3P)$ with CH_2Cl radicals to be compared to that of k_{27} could explain surprisingly more efficient inhibition effect of CH_2Cl_2 on ozone formation (see Fig. 9).

There are the other pathways of direct decomposition of halomethanes in the glow region of negative corona discharge. Very efficient is the reaction of primary ions O^- , generated within the glow region via the dissociative electron attachment (3.1) [60]. In case of CCl_2F_2 the reaction



($k_{28} = 1.5 \cdot 10^{-9} \text{ cm}^3\text{s}^{-1}$, [60]), the most likely products are stable COF_2 and high reactive chlorine atom Cl . As it was shown by mass spectrometric study, due to the very fast conversion the precursor ions O^- , generated in pure oxygen, are very effectively converted into negative chlorine ions Cl^- or into the various clusters containing this ion in mixtures with Trichlorethylene [61]. The fate of Cl^- is the neutralization on the outer electrode, where either can react with the metal surface [62], or can form Cl_2 . Unfortunately, the mass spectrometric study relevant to conditions in our experiments are not available in literature.

Both the process of electron impact dissociation (6.9) and the negative oxygen ion O^- stimulated decomposition of Freon-12 (and similar compounds), (6.11), are sources of chlorine atoms which could enter into the catalytic cyclic destruction of ozone molecules, well known in stratospheric ozone chemistry [49, 63]. The third source of Cl atoms, dissociative ionization [64]



is not effective because of low values of E/N in the glow region of discharge under our conditions. The rate constant calculated by using electron energy distribution function in pure oxygen [65] and the ionization cross section for (6.12), [64], at $E/N = 100 \text{ Td}$, is negligible in comparison with the value corresponding to oxygen ionization [27].

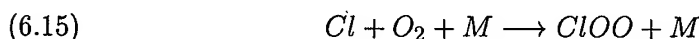
The reaction



($k_{30} = 1.2 \cdot 10^{-11} \text{ cm}^3\text{s}^{-1}$, at $T = 300 \text{ K}$, [48]) is of fundamental importance in stratospheric chemistry. It plays a key role in catalytic ozone destruction cycle because in the second reaction.



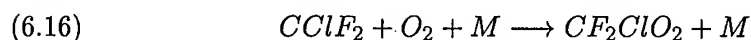
($k_{31} = 3.8 \cdot 10^{-11} \text{ cm}^3\text{s}^{-1}$, at $T = 300 \text{ K}$, [48]) chlorine atom is again released. Under the conditions of the glow region of negative corona discharge both the chlorine atoms and ClO radicals can contribute to reduction in ozone concentration, because Cl atoms are active in the destruction of already formed ozone molecules and ClO by-product can reduce the concentration of atomic oxygen needed for ozone formation. Hence, the described scheme may be active in the inhibition of the observed ozone formation by chlorine containing halometanes. The efficiency of reactions (6.13), (6.14) is limited by the three body process



($k_{32} = 1.6 \cdot 10^{-33} \text{ cm}^6\text{s}^{-1}$, [48]) which is competitive with (6.13). The rates of reactions (6.13) and (6.15) are equal if relative ozone concentration in the glow region reaches the value of 0.3%, which is well fulfilled conditions, because the values of ozone concentration in the glow region of the discharge are larger by

two-orders of magnitude to that of measured in the discharge reactor volume [23, 26]. Moreover, the by-product ClOO is a part of ClO dimer mechanism described recently, releasing again chlorine atoms [66].

Molecular oxygen is even a more efficient inhibitor of CClF₂ radical reaction (6.10) due to the very effective three body process



($k_{33} = 1.4 \cdot 10^{-29} \text{ cm}^6\text{s}^{-1}$, $M = \text{N}_2$, [48]). The frequency of the reaction (6.16), $\nu_{33} = k_{33}[\text{O}_2]^2$ at atmospheric pressure is much higher than that corresponding to (6.10) $\nu_{27} = k_{27}[\text{O}]$ even if we presume not realistic $[\text{O}] = 0.1[\text{O}_2]$ in the glow region. Therefore, the earlier presumed reaction of radicals are probably not responsible for the inhibition effect.

The experiments in mixtures of oxygen with halomethanes lead us to the conclusion that in contrast to SF₆, the direct reactions of oxygen atoms with halomethane molecules contribute to the decrease in number of formed ozone molecules. Moreover, due to the efficient electron impact dissociation of halomethane molecules chlorine atoms released in various processes destroy a portion of ozone molecules which were already formed in the glow region of negative corona discharge. Hence, both the processes leading to ozone formation as well as processes of ozone destruction are influenced by the presence of halomethane impurity in oxygen.

7. Conclusions

In this paper we have presented the results from experimental studies aimed at identifying the mechanisms responsible for the inhibition effect of several representative compounds, which can be divided into three groups:

- CO₂ a weak electron attaching gas not containing chlorine atoms,
- SF₆ a strong electron attaching gas not containing chlorine atoms,
- CH₂Cl₂, CHCl₃, CCl₄ and CCl₂F₂ having different number of substituted chlorine atoms and conspicuously different electron attachment rate constants.

Each of these three groups was shown to inhibit ozone production by a different mechanisms including decrease of oxygen content in the mixture (CO₂, SF₆, halomethanes), reduction of the free electron density (SF₆), reactions of oxygen atoms with radicals (SF₆) or impurity molecules (halomethanes), decrease in oxygen atoms production due to the competitive electron impact dissociation of added impurity molecules (SF₆, halomethanes) and the decomposition of ozone in the catalytic destruction cycle with chlorine atoms (halomethanes). The further experiments, especially mass spectrometric studies of ions extracted from the discharge and GMS, IR and UV absorption spectrometry for analysis of by-products of processes, are needed for better understanding of the processes to be responsible for the inhibition effect of impurities on ozone production in high pressure discharges.

Acknowledgment

Technical support and useful discussion with my colleagues Jozef Ráhel, Viktor Foltin, L. Holubčík and Stefan Matejčík are gratefully acknowledged. The research was supported by Slovak Grant Agency under project 1/5184/98 and partially supported by Austria-Slovakia project 25s19.

References

1. NATO ASI Series, *Non-Thermal Plasma Techniques for Pollution Control*, (Edit. by M. Penetrante and S. E. Schultheis), Springer-Verlag, Berlin, Heidelberg, 1993.
2. J.F. LOISEAU, F. LACASSIE, C. MONGE, R. PEYROUS, B. HELD and C. COSTE, *J. Phys D: Appl. Phys.*, **27**, 63-73, 1994.
3. C. MONGE, P. PIGNOLET, R. PEYROUS, J.F. LOISEAU, B. HELD, C. COSTE, *Proc. 10th Gas Discharges and Their Appl.*, Swansea 13 - 18 September 1992, (Ed. W. Terry Williams), University College of Swansea, Wales, 340-344, 1992.
4. S. HADJ-ZIANE, B. HELD, P. PIGNOLET, R. PEYROUS, and C. COSTE, *J. Phys. D: Appl. Phys.*, **25**, 677-685, 1992.
5. S. FUTAMURA, A. ZHANG and H. EINAGA, *Proc. of The Asia-Pacific Workshop on Water and Air Treatment by Advanced Oxidation Technologies: Innovation and Commercial Applications*, AIST Tsukuba Research Centre (Japan), 87-90, 1998.
6. E. BRINER, B. BEVER, *Helv. Chim. Acta*, **25**, 900-906, 1942.
7. G. GLOCKNER, S.C. LIND, *Electrochemistry of Gases and Other Dielectrics*, Wiley, New York, 1939.
8. A.M. JULIARD, *Bull. Acad. Roy. Belg.*, **12**, 914-920, 1926.
9. W.E. CROMWELL and T.C. MANLEY, *Ozone Chemistry and Technology*, Publish. American Chemical Society, Washington, 304- 312, 1959.
10. E. INOUE, K. SUGINO, *Ozone Chemistry and Technology*, Publish. American Chemical Society, Washington, 313-316, 1959.
11. Yu.V. FILIPPOV and V.P. VENDILLO, *Zhurnal. Tech. Chim.*, **36**, 1987-1992, 1962.
12. V. SOBEK, J.D. SKALNÝ, P. LUKAC, *Le Vide, Les Couches Minces-Supplement*, No-256, 73-75, 1991.
13. J.S. CHANG, T.A. MYINT, A. CHAKRABARTI and A. MIZIOLEK, *Proc. 3rd Int. Conf. on Reactive Plasmas*, Nara (Japan), 369-370, 1997.
14. T. ODA, T. TAKAHASHI, K. TADA, *Proc. of IEEE IA Soc. Annual Meet.*, New Orleans, 165-173, 1997.
15. R.A. AKHMEDZHANOV, A.L. VIKHAREV, A.M. GORBACHEV, O.A. IVANOV and A.L. KOLYSKO, *Tech. Phys. Lett.*, **22**, 104-106, 1996.
16. R.A. AKHMEDZHANOV, A.L. VIKHAREV, A.M. GORBACHEV, O.A. IVANOV and A.L. KOLYSKO, *Teplofizika vysokokorych temperatur*, **35**, 524-537, 1997.
17. S. OKAZAKI, H. NIWA, H. SUGIMITSU, M. KOGOMA, T. INOMATA, *Contributed Papers of HAKONE V*, Milovy (Czech Republic), 26-30, 1996.
18. V.V. RYZHOV and A.I. SUSLOV, *Tech. Phys.*, **44**, 44-47, 1999.
19. H.E. ELSAYED-ALI and G.H. MILEY, *J. Appl. Phys.*, **60**, 1189-1205, 1986.
20. J.D. SKALNY, *Acta Phys. Univ. Comen.*, **33**, 71-75, 1992.
21. J.D. SKALNY, P. LUKAC, *Acta Phys. Univ. Comen.*, **33**, 61-70, 1992.

22. A. DERYUGIN, A. NAPARTOVICH, C. GORSE, F. PANICCIA and M. CAPITELLI, *Plasma Chem. and Plasma Processing*, **17**, 79-91, 1997.
23. J.D. SKALNÝ, J. RAHEL, L. HOLUBCK, *Czech. J. Phys.*, **49**, 335-348, 1999.
24. M.B. PENETRANTE, M.C. HSIAO, J.N. BARDSLEY, B.T. MERRITT, G.E. VOGTLIN, A. KUTHI, C.P. BURKHART, and J.R. BAYLESS, *Plasma Sources Sci. Technol.*, **6**, 251-259, 1997.
25. R. J. VAN BRUNT and J.T. HERRON, *Physica Scripta*, **T53**, 9-29, 1994.
26. F. PONTIGA, C. SORIA, A. CASTELLANOS, *Journal of Electrostat.*, **40&41** 115-120, 1997.
27. B. ELLIASSON, *Brown Boveri Forschungsbericht*, No. KLR 83-40C, 1985.
28. J.D. SKALNÝ, V. SOBEK, *Proc. 3rd HÁKONE*, Strasbourg, 185-190, 1991.
29. C. MONGE, R. PEYROUS, and B. HELD, *Ozone Science & Engineer.*, **19**, 533-547, 1997.
30. R. PEYROUS, C. MONGE, and B. HELD, *Ozone Science & Engineer.*, **20**, 317-342, 1998.
31. B. HELD and R. PEYROUS, *Eur. Phys. J. AP*, **4**, 73-86, 1998.
32. H. HOKAZONO, M. OBARA, K. MIDORIKAWA and H. TASHIRO, *J. Appl. Phys.*, **69**, 6850-6868, 1991.
33. A. CENIAN, A. CHERNUKHO and V. BORODIN, *Contrib. Plasma Phys.*, **35**, 273-296, 1995.
34. S. STREKOVA, L. HOLUBCK and J.D. SKALNÝ, *Contrib. Paper of 24th ICPIG*, Warsaw, accepted, 1999.
35. S. MATEJCK, S. STREKOVA, L. HOLUBCK and J. D. SKALNÝ, *Contrib. Paper of 14th ICPIG*, Prague, accepted, 1999.
36. P.S. GARDINER, J.L. MOROZZI and J.D. CRAGGS, *J. Phys. D: Appl. Phys.*, **11**, 237-244, 1978.
37. M.M. SHAHIN, *Applied Optics*, Supplement on Electrophotography, 106-110, 1969.
38. I. SAUERS, *Plasma Chem. and Plasma Process.*, **8**, 247-262, 1988.
39. C. BOUDENE, J.L. CLUET, G. KREIB and G. WIND, *Rev. Gen. Electr.*, 45-78, 1978.
40. R.J. VAN BRUNT, J.T. HERRON, *IEEE Trans. on EI*, **25**, 75-94, 1990.
41. R. J. VAN BRUNT, M.C. SIDDAGANGAPPA, *Plasma Chem. and Plasma Process.*, **8**, 207-223, 1988.
42. A.M. CASANOVAS, J. CASANOVAS, F. LAGARDE and A. BELARBI, *J. Appl. Phys.*, **72**, 3344-3354, 1992.
43. I. SAUERS, G. HARTMAN, *J. Phys. D: Appl. Phys.*, **25**, 761-773, 1992.
44. I. SAUERS, G. HARTMAN, *J. Phys. D: Appl. Phys.*, **25**, 774-782, 1992.
45. L. LÁSKA, K. MAEK, J. KRASA, V. PERINA, *Czech. J. Phys*, **B34**, 1038-1047, 1984.
46. D. SMITH, P. SPANEL, S. MATEJCK, A. STAMATOVIC, T. D. MARK, *Chem. Phys. Lett.*, **240**, 481-488, 1995.
47. D. SMITH, N.G. ADAMS, E. ALGE, *J. Phys B: At. Mol. Phys.*, **17**, 461-472, 1984.
48. R. ATKINSON, D.L. BAULCH, R.M. HAMPSON Jr., J.A. KERR, M.J. ROSSI and J. TROE, *J. Phys. Chem. Ref. Data*, **26**, 521-1011, 1997.
49. S. BAUMGARTEL, R.F. DELMDAHL, K.H. GERICKE and A. TRIBUKAIT, *Eur. Phys. J. D*, **4**, 199-205, 1998.
50. S.J. BURNS, J.M. MATTHEWS and D.L. MCFADDEN, *J. Phys. Chem.*, **100**, 19436-19440, 1996.
51. H. SHIMAMORI, Y. TATSUMI, Y. OGAWA and T. SUNAGAWA, *J. Chem. Phys.*, **97**, 6335-6247, 1992.
52. T.G. LEE, *J. Phys. Chem.*, **67**, 360-366, 1963.
53. L.G. CHRISTOPHOROU, J.K. OLTHOFF and Y. WANG, *J. Phys. Chem. Ref. Data*, **26**, 1205-1238, 1997.

54. K.R. RYAN, *Plasma Chem. and Plasma Process.*, **9**, 483-496, 1989.
55. W.W. STOFFELS, E. STOFFELS, M. HAVERLAG, M.W. KROESEN and F.J. DEHOOG, *J. Vac. Sci. Technol. A*, **13**, 2058-2066, 1995.
56. J.A. SEETULA, I.R. SLAGLE, *Chem. Phys. Lett.*, **227**, 381-386, 1997.
57. B. WANG, H. HOU and Y. GU, *J. Phys. Chem. A*, **103**, 2060-2065, 1999.
58. J.A. SEETULA, I.R. SLAGLE, D. GUTMAN, S.M. SENKAN, *Chem. Phys. Lett.*, **252**, 299-303, 1996.
59. B. WANG, private communication, 1999.
60. C.A. MAYHEW, R. PEVERALL, P. WATTS, *Int. J. Mass Spectrom. Ion. Processes*, **125**, 81-93, 1993.
61. A. DONO, C. PARADISI, G. SCORRANO, *Rapid Com. in Mass Spectrom.*, **11**, 1687-1694, 1997.
62. M. LUKNÁROVA, J.D. SKALNY, D. DINDOSOVA, P. VARGA, *Acta Phys. Univ. Comen.*, **33**, 83-94, 1992.
63. N.J. MASON and S.K. PATHAK, *Contemporary Physics*, **38**, 289-299, 1997.
64. K. LEITER, P. SCHEIER, G. WALDER and T.D. MARK, *Int. J. Mass Spectrom. and Ion Processes*, **87**, 209-224, 1989.
65. M. KUZUMOTO, J. KITAYAMA and Y. TABATA, *Proceedings of 13th Ozone World Congress, Kyoto (Japan)*, Vol. **2**, 815-820, 1997.
66. J. ZHANG and Y.T. LEE, *J. Phys. Chem. A* **101**, 6485-6495, 1997.

PLASMA HIGH-POWER MICROWAVE SOURCES DRIVEN BY RELATIVISTIC ELECTRON BEAMS

P. S. STRELKOV

GENERAL PHYSICS INSTITUTE, RUSSIAN ACADEMY OF SCIENCES
Vavilova str. 38, Moscow, 117942 Russia

The presence of plasma affects drastically the operation of microwave devices driven by high-current relativistic electron beams. Loading vacuum relativistic microwave oscillators with plasma changes the power and frequency band of the radiation. The Cherenkov plasma maser, operates only with plasma inside and is based on exciting the eigenmodes of the plasma waveguide. Changing the plasma density in a Cherenkov plasma maser allows the radiation frequency to be varied from 4 to 28 GHz, which is impossible in vacuum microwave electronics. The results of experiments are presented, and the bases of theory are briefly outlined.

1. Introduction

Vacuum relativistic high-power microwave (HPM) electronics studies devices comprising high-current relativistic electron beam (REB) and a vacuum electrodynamic structure. At present, a microwave power of 10^{10} W is achievable in the X-band of oscillations and 10^9 W in the Ka-band. In vacuum relativistic microwave electronics, the efficiency of devices varies from several percent in the Ka-band to about 30% in the X-band. Plasma relativistic microwave electronics deals with the problem of the conversion of the energy of high-current REBs propagating in electrodynamic structures filled with plasma into the energy of electromagnetic radiation. From the scientific standpoint, a study is made of the interaction of electron beams and powerful electromagnetic radiation with a bounded plasma. From the standpoint of practical applications, these studies are intended to develop powerful microwave oscillators and amplifiers. Therefore, we will concentrate on experiments in which a significant fraction of the electron beam energy (no less than several percent) is converted into microwave energy. The present paper consists of two parts. In the first one, we discuss the experiments in which the plasma is created so as to improve the parameters of a vacuum microwave oscillator, e.g., to increase its power and efficiency. The second part presents the studies in which an electron beam excites the eigenmodes of the plasma waveguide. Unlike the previous case, the device cannot

emit microwaves in the absence of plasma. Plasma microwave electronics makes it possible to transport high-current beams, to tune frequency by varying the plasma density, etc. We introduce the following notation, which will be used throughout this paper:

1. *general parameters*: p is background gas pressure, z is direction along the axis, R is the waveguide radius, B is external magnetic field; e is the electron charge, m is the electron mass, and c is the speed of light;
2. *plasma parameters*: n_p is the electron plasma density, $\omega_p = \sqrt{\frac{4\pi n_p e^2}{m}}$ is the electron plasma frequency, $\Omega_e = \frac{eB}{mc}$ is the electron cyclotron frequency, R_p is the radius of the plasma column, Δ_p is the thickness of the annular plasma column, and L_p is the length of the plasma column;
3. *REB parameters*: W_e is the electron energy, γ is the relativistic factor, u is the electron velocity, n_b is the beam-electron density, I_b is the beam current, R_b is the beam radius, Δ_b is the thickness of the annular beam, and L_b is the beam length;
4. *parameters of microwaves*: P is the microwave power, $f = \omega/2\pi$ is the microwave frequency, E is the microwave electric field, v_{ph} is the phase velocity, v_{gr} is the group velocity, k_z is the longitudinal (with respect to the axis of the system) wavenumber, and k_\perp is the transverse wavenumber.

2. Plasma-induced performance enhancement of relativistic oscillator

Loading an electrodynamic structure of a microwave oscillator with plasma changes the distribution of microwave field over the cross section of the structure. This may cause the efficiency increase of the microwave device. First this effect was found in a carcinotron (BWO) in [1], and then was observed in other studies [2, 3]. Electrodynamic structure of a carcinotron was made as a corrugated waveguide. In such a waveguide a slow wave exists in which longitudinal component of electric field $E_z \neq 0$. If the phase velocity of this wave is equal to the beam electrons speed, microwave radiation appears on the basis of Vavilov-Cherenkov effect. In a vacuum carcinotron the amplitude of E_z -component of the slow wave is the highest on the wall of the rippled waveguide and drops towards the axis. Loading the waveguide with plasma causes an increase of the E_z -field far from the wall, and a change of the efficiency. In the experiments [1, 2, 3] plasma inside a carcinotron was created by means of the residual gas ionization by the REB itself. In paper [1], an REB (30-ns pulse duration, 15-kA current, 1-MeV electron energy) was injected into a diaphragmed waveguide at the range of a gas pressures from 10^{-5} to 5 Torr. The radiation power increased from practically zero to maximum as the gas pressure increased from 10^{-5} to $2 \cdot 10^{-2}$ Torr. A further increase in the gas pressure culminated in a strong decrease in the radiation power

Plasma changes the dispersion of a microwave oscillator's electrodynamic structure. As a result a possibility appears to tune microwave radiation frequency

by means of plasma density variation. This effect was observed in many studies. The most significant changes of the frequency were obtained in [4]. At beam currents of 500 and 800 A (the electron energy being $W_e = 550$ (600 keV), the radiation frequency upshift was found to increase from 8.5 GHz in the absence of a plasma to 11 GHz in the presence of a high-density ($n_p \geq 10^{12} \text{ cm}^{-3}$) plasma. Also, filling up of the REB transport channel with a plasma provides the charge neutralization of the beam [5], which, in turn, causes the beam potential and the REB electron momentum spread to decrease. As a result, the plasma either improves the beam quality in comparison with that in the absence of plasma or makes it possible to transport beams with higher currents. In turn, improving the REB quality raises the efficiency of the device.

The influence of the plasma on the beam transport in the interaction region as well as the microwave power enhancement were demonstrated in [6]. In this paper, an annular plasma was created in the resonator of a relativistic gyrotron by an external source. As a result of a partial neutralization of the beam space charge by a plasma of concentration up to $3 \cdot 10^{11} \text{ cm}^{-3}$, it was possible to increase the optimum beam current in vacuum from 0.4 kA up to 1.2 kA in plasma and the microwave radiation power from 25 MW up to 60 MW. The vacuum gyrotron efficiency was 20% and gyrotron with plasma efficiency was approximately the same - 17%. It is necessary to emphasize that, with plasma loading, the optimum current was almost twice the limiting vacuum current, whereas, in the absence of a plasma, this current was lower than the vacuum limit by a factor of 2. Note that only the TE_{13} mode was generated both in vacuum and with plasma.

3. Relativistic Cherenkov plasma maser (CPM)

It is well known that an electron beam in plasma may be unstable. If the density of the plasma is much higher than that of the beam, the beam instability is governed by the Cherenkov effect, and plasma eigenmodes with a phase velocity close to the velocity of the beam electrons are excited. The beam instability can occur in both infinite and bounded plasmas, with and without an external magnetic field. If the transverse (with respect to the magnetic field lines) component of the electron-beam velocity is equal to zero, $u_{\perp} = 0$, then only Cherenkov instability is excited. If this component is nonzero, $u_{\perp} \neq 0$, the cyclotron mechanism for wave excitation may come into play. We will focus on experiments on the excitation of plasma waves by beams having only the longitudinal velocity component. The main properties of the beam-plasma instability, which was first predicted in [7, 8], were investigated in quite a number of experiments with nonrelativistic electron beams in 1960-70s. These experiments were carried out in three directions. First, the experimental conditions provided the generation of strong and weakly damped electric fields in a plasma, and a study was made of the possibility for particle acceleration. Second, the problem of whether it is possible to dissipate the energy of the excited waves in order to heat the plasma was analyzed. Finally, experiments of the third group were carried out to study the efficiency with which the energy of the plasma waves can be converted into electromagnetic radiation. These experiments, as applied to nonrelativistic plasma microwave electronics, are reviewed in [9, 10]. In studying

Cherenkov plasma masers, two main problems arise, namely, the excitation of intense waves in plasma and the efficiency with which the wave energy is converted into electromagnetic radiation. In the presence of high-current REBs, the approaches to solving these problems change radically, because powerful REBs maintain intense waves in a plasma. Additionally, in the course of Cherenkov interaction, relativistic beams excite waves whose phase velocity is about the speed of light. The efficiency of the wave transformation is very high because the phase velocities in plasma and vacuum are approximately the same. It is important to note that the group velocity of the waves excited by a relativistic beam in a bounded plasma may also be close to the speed of light.

For the first time a relativistic Cherenkov plasma maser was investigated in experiment [11]. The scheme of this CPM is presented in Fig. 1. A REB (1) was

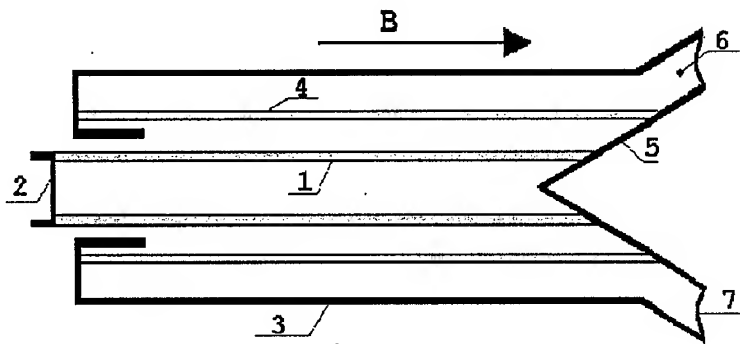


FIG. 1. Scheme of the relativistic CPM: (1) REB, (2) cathode, (3) metallic waveguide, (4) plasma, (5) collector, (6) coaxial waveguide, and (7) window.

produced by the cathode (2) and injected along the axis of the circular metal waveguide (3) pre-filled with an annular plasma (4) [12]. Both the plasma and the REB were immersed in an external longitudinal uniform magnetic field. The electron beam terminated on the central conductor of the coaxial outlet emitting facility (5). Microwaves generated in the plasma waveguide propagated along the vacuum coaxial waveguide (6) and were emitted from the window (7). The main ideas embedded in this scheme are as follows:

1. The annular plasma has a diameter larger than that of the beam and does not penetrate into the diode of the high-current accelerator. This makes it possible to perform experiments without using a foil that separates the plasma-filled area from the diode and to generate beams with zero transverse electron velocities $u_{\perp} = 0$.
2. All transverse dimensions of the beam, plasma, and waveguide, the densities of the plasma and REB, and the magnitude of the magnetic field are all constant along the axis of the system. This significantly simplifies the theoretical analysis. Also, since the magnetic field does not change in space, there is no resonant absorbing layer in which $\omega = \sqrt{\omega_p^2 + \Omega_e^2}$, be-

cause the condition $\omega < \omega_p < \Omega_e$ holds everywhere. Such a layer might appear if the plasma were terminated on the walls of the waveguide in a weak magnetic field.

3. The major portion of the energy of the excited plasma wave is deposited in the vacuum gap between the plasma and the waveguide wall, rather than in the plasma. High efficiency of the conversion of the plasma wave energy into the outlet microwave energy is provided by two factors: the structure of the "vacuum" part of the plasma wave is close to that of the TEM wave in a coaxial outlet facility and the phase velocity of the plasma wave is high (close to the speed of light).
4. The fact that the outlet facility is a coaxial system makes it an effective radiation source in a broad frequency band.

The theoretical foundations of plasma relativistic microwave electronics were formulated by A.A. Rukhadze and his collaborators [13, 14, 15]. To better understand the experimental results discussed below, we briefly describe the theoretical results obtained in the linear approximation. Fig. 2 (curve 1) presents the dependence of the frequency (of a slow plasma wave on the longitudinal

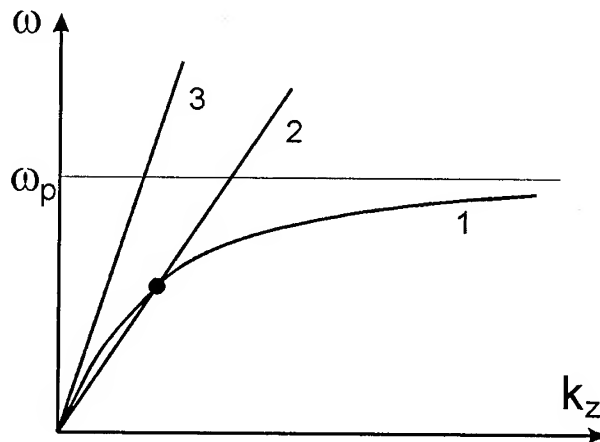


FIG. 2. Dependence of the frequency (on the longitudinal wavenumber of (1) the plasma wave, (2) the beam wave $\omega = k_z u$ (for $n_b \ll n_p$), and (3) $\omega = k_z c$.

wavenumber k_z . For large k_z ($k_z \gg k_\perp$), the frequency ω approaches ω_p , the wave becomes purely longitudinal, and the microwave field is concentrated inside the plasma. When $k_z < k_\perp$ and $\omega < \omega_p$, the electric field is mainly generated in a gap between the plasma and the waveguide wall (the pattern of the force lines of the electric field of the plasma wave is shown in Fig. 3). Curve 2 in Fig. 2 corresponds to the dispersion relation for the beam wave, $\omega = k_z u$, in the limit $n_b \ll n_p$. At the point of intersection of curves 1 and 2, the Cherenkov condition $u \approx v_{ph}$ is satisfied, which corresponds to the onset of the beam-plasma instability. The phase velocity of the plasma wave is maximum at the point $k_z = 0$.

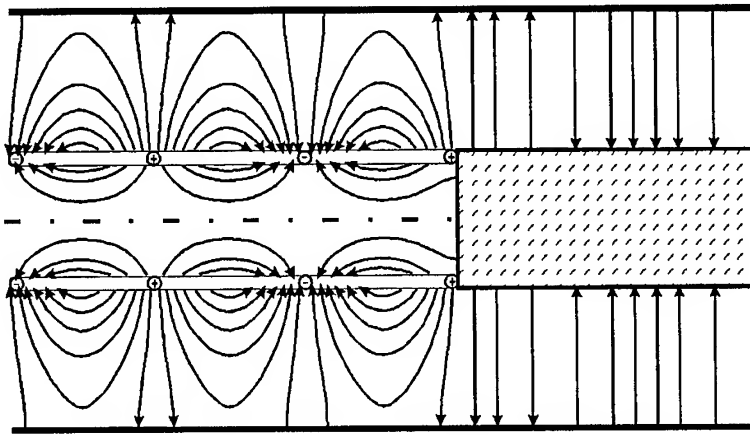


FIG. 3. The pattern of the force lines of the electric field of the plasma wave. $R = 1.8$ cm, $R_p = 0.9$ cm, and $\omega = 0.36 \omega_p$.

$$(3.1) \quad v_{ph} = c \left(1 + \frac{c^2}{\omega_p^2 R_p \Delta_p \ln \frac{R}{R_p}} \right)^{-1/2}$$

Therefore, the condition $v_{ph} < c$ always holds, which is demonstrated in Fig. 2 in which curve 3 corresponds to the equation $\omega = kc$. It is shown that v_{ph} depends on the plasma density and on the transverse dimensions of the plasma and of the waveguide. If the plasma density is lower than a certain critical value,

$$(3.2) \quad n_{cr} = \frac{u^2 \gamma^2}{3.18 \cdot 10^9 R_p \Delta_p \ln \frac{R}{R_p}}$$

we have $v_{ph} < u$, and no beam-plasma instability is observed. The latter relationship holds for $n_b \ll n_p$, and actually the critical plasma density n_{cr} depends on n_b , namely, n_{cr} decreases with the rise of n_b . From Fig. 2 we can see that, in the resonance region, the group velocity v_{gr} of the plasma wave is high enough, whereas, at $\omega \approx \omega_p$, we have $v_{gr} \approx 0$. The output radiation power is $P \sim E^2 v_{gr}$. To obtain the maximum values of P , the parameters of the CPM should be chosen so that the group velocity in the resonance region is high and the electric field in the plasma could attain the maximum value, which is governed by the nonlinearity of the beam. Fig. 3 indicates that the axial field E_z is maximum in the plasma and falls off toward the waveguide axis. This makes it possible to control the coupling between the beam and the plasma wave by changing the gap between the beam and the plasma. REB excites oscillations in the plasma not only at the resonant frequency, indicated in Fig. 2, but in a rather broad range of frequencies. In the linear stage of the instability development the microwave electrical field increases along the length of the beam according to the

law $E = E_0 e^{\delta k z}$. Dependence of the amplification coefficient δk on frequency for different values of plasma density is shown in Fig. 4. The frequency range where the amplification coefficient $\delta k > 0.15$ changes from 5 - 10 GHz to 33 - 37 GHz with the plasma density increase. The nonlinear problem of wave amplification in plasma waveguides (in particular, for the experimental layout shown in Fig. 1) was solved. The magnetic field is assumed to be infinite: $\omega < \omega_p < \Omega_e$. In this steady-state approach, the plasma waveguide is fed with TEM mode in a broad frequency band. The transverse structure of the microwave field, the spectrum and the field amplitudes along the waveguide were determined. Usually, the maximum width of the spectrum was observed in the region of the wave amplitude saturation. The problem was considered to be solved when the maximum spectrum bandwidth of the plasma waves turned out to be shorter than the radiation-frequency bandwidth at the input. It was shown that, for the attainable parameters of a REB, the length of the region over which the microwave field amplitude saturates for the frequency band 10 - 30 GHz may be of the order of several tens of centimeters, and the maximum conversion efficiency can reach 20%.

As shown, the linear theory predicts the instability in a broad frequency range with fixed plasma density. Calculation in the non-linear approach shows that the spectrum width of the outlet radiation is much less than the frequency range according to the linear theory. In Fig. 4 frequency bands where the spectrum density of the plasma radiation exceeds 0.3 of its maximum are shown by the

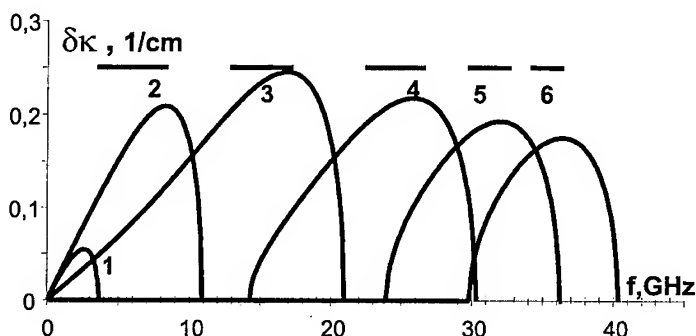


FIG. 4. Microwave electric field amplification coefficient for $\gamma = 2$, $I_b = 2$ kA, $R = 1.8$ cm, $R_p = 0.9$ cm, $R_b = 0.6$ cm, and $n_p = (1) 3 \cdot 10^{12}$, (2) $8 \cdot 10^{12}$, (3) $2.3 \cdot 10^{13}$, (4) $4.4 \cdot 10^{13}$, and (5) $6 \cdot 10^{13}$, (6) $7 \cdot 10^{13}$ cm $^{-3}$. Horizontal boldface lines indicate frequency bands where according to the nonlinear theory the microwave radiation spectral power exceeds the level of 0.3 of its maximum.

lines 2, 3, 4, 5, 6. It is shown that in the particular conditions the spectrum width is in the limits of 2.5-5 GHz, and the relative width changes from 100% to 7%.

Calculation of the generation regime is not yet performed. Starting conditions of turning on the generator are defined from the condition $\kappa_1 \kappa_2 e^{\delta k L} > 1$, where κ_1 and κ_2 are the reflection coefficients of a wave for the reflection from the left and right borders of the plasma waveguide, and L is the length of the plasma

waveguide.

Now we present the results of experimental investigation of the relativistic CPMs with the installation, which is schematically presented in Fig. 1 (General Physics Institute, Moscow, since 1982 up to this time) In [11], it was shown that, for a certain set of parameters (i.e., the beam parameters, the radial distribution of the beam and plasma densities, and the waveguide radius), there is a critical length L_{cr} , defined as follows: if the length L of the setup is less than L_{cr} , then the beam-plasma system does not emit microwaves, regardless of the value of the plasma density.

Dependencies of the total energy of the radiation on plasma density for several lengths of the plasma waveguide $L = 10, 12.5, 15, 20$ cm are shown in Fig. 5. Full energy of the REB in one pulse ≈ 30 J (500 keV, 2 C, 30 ns). So Fig. 5

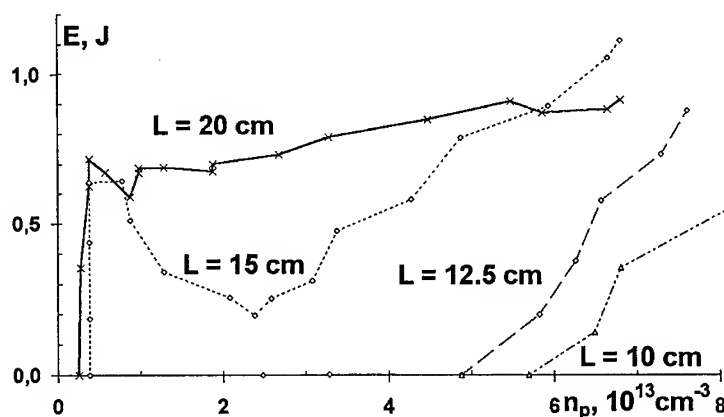


FIG. 5. Microwave pulse energy E vs plasma density n_p for different interaction lengths L of plasma waveguide. $B = 2.2$ T, $R_p = 0.9$ cm, $R_b = 0.6$ cm, $p = 4.5 \cdot 10^{-4}$ Torr (Xenon).

shows that the CPM efficiency in energy is 3%. Microwave pulse duration is 20 ns, so the power of ~ 50 MW are reached, and the efficiency in power is 5%. The radiation at $L = 20$ cm (curve 1) appears at a threshold value of plasma density $2.5 \cdot 10^{12} \text{ cm}^{-3}$. This value is close to the calculated value of plasma density, for which in the given conditions the amplification coefficient $\delta k > 0$. Since for small values of plasma density the maximum value of the amplification coefficient (k_{max} increases with the rise of plasma density (Fig. 4), the CPM at $L = 15$ cm is switched on with greater values of plasma density $n_p = 4 \cdot 10^{12} \text{ cm}^{-3}$, Fig. 5, in accordance with the formula $\kappa_1 \kappa_2 \cdot e^{\delta k L} > 1$. The increase of the threshold value of plasma density under a further shortening of the plasma waveguide length ($L = 12.5, 10$ cm) has no a simple explanation because δk_{max} at the values $n_p = 5 - 6 \cdot 10^{13} \text{ cm}^{-3}$ (curves 5, 6, Fig. 5) are less than the maximum value, which is reached at $n_p = 2 \cdot 10^{13} \text{ cm}^{-3}$ (curved 3, 4, Fig. 5). It may be explained by increasing reflection coefficient $\kappa_1 \kappa_2$, when plasma density increases.

As the spread angle of the electrons increases up to $\sqrt{\Theta^2} = 12^\circ$ and 21° , the radiation intensity decreases by a factor of three and 20, respectively [11]. This

does not contradict the fact that the Cherenkov mechanism for wave excitation has come into play.

The spectra of CPM were investigated in [16, 17]. In [17], the spectra were measured with the help of cut-off filters and a calorimeter [18], which made it possible to perform direct measurements of the total radiation power in a certain frequency band.

Radiation spectrums of the CPM for different values of plasma density at the length of plasma waveguide $L = 20$ cm are shown in Fig. 6. In each of the

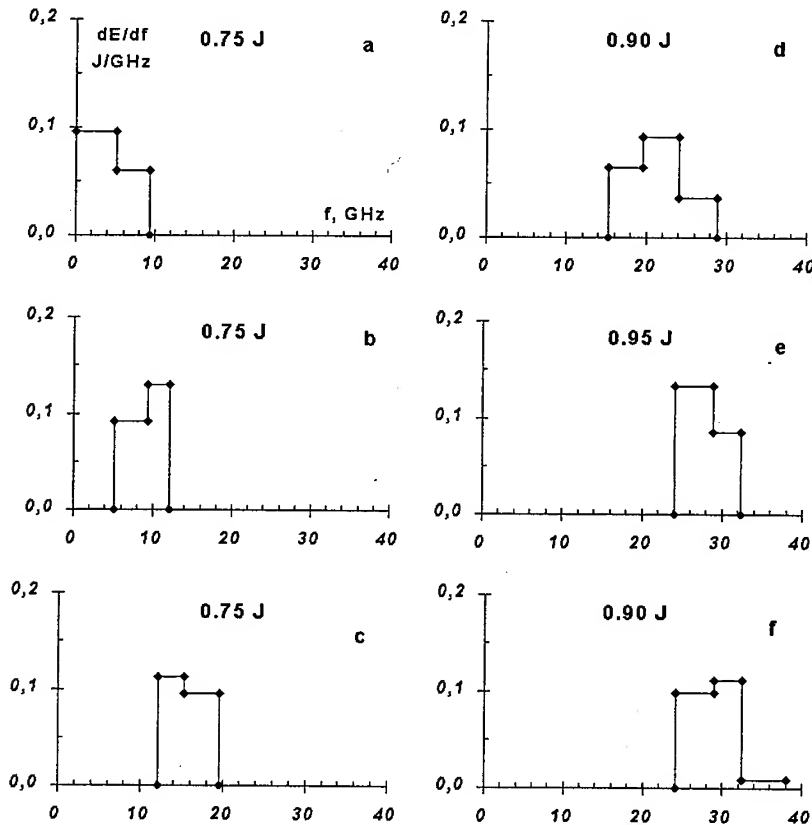


FIG. 6. Experimental spectra of microwaves for different plasma densities: a) $- 0.4 \cdot 10^{13} \text{ cm}^{-3}$, b) $- 0.8 \cdot 10^{13} \text{ cm}^{-3}$, c) $- 2.3 \cdot 10^{13} \text{ cm}^{-3}$, d) $- 4.4 \cdot 10^{13} \text{ cm}^{-3}$, e) $- 6 \cdot 10^{13} \text{ cm}^{-3}$, f) $- 7 \cdot 10^{13} \text{ cm}^{-3}$.

six graphs the total energy of microwave radiation pulse in J is indicated. It is shown that the mean radiation frequency increases from 4 to 28 GHz when plasma density changes from $4 \cdot 10^{12}$ to $7 \cdot 10^{13} \text{ cm}^{-3}$. Measurement accuracy of spectrum width is not high. From our measurements it follows that the spectrum width exceeds the width of the spectrometer bands, i.e. $\Delta f > 3 \text{ GHz}$. This can be inferred from the fact that microwave radiation frequency monotonically depends on plasma density, and the measured spectrum for any plasma density

is never located inside one band of the spectrometer. The greatest possible spectrum width is defined by the borders, indicated in Fig. 6, i.e. exceeds 2 or 3 times the bands of the spectrometer. Calculated dependence of the mean radiation frequency on plasma density for microwave amplifier in the suggestion $B \rightarrow \infty$ with experimental dependencies for CPM for two values of the magnetic field $B = 1.3$ T and $B = 2.2$ T are compared in Fig. 7. Hatching denotes the area, where according to the calculation $dP/df > 0.3(dP/df)_{max}$. It is seen that in the field of small values of plasma density (small radiation frequencies) the results of the experiment coincide with those of calculations. For greater values of plasma density a discrepancy appears between the calculation and experiment. For instance, in the experiment for $n_p = 6 \cdot 10^{13} \text{ cm}^{-3}$ at $\Omega_e = 0.5\omega_p$ radiation frequency $f = 21$ GHz, and with an increase of the magnetic field $\Omega_e = 0.9\omega_p$ the radiation frequency rises up to $f = 27$ GHz. According to the calculation for $n_p = 6 \cdot 10^{13} \text{ cm}^{-3}$ under $\Omega_e \gg \omega_p$ the frequency $f = 32$ GHz. Thereby, the discrepancy between the calculation and experiment can be explained by the fact that in the experiment with great values of plasma density the condition $\Omega_e \gg \omega_p$ is not valid.

In Fig. 7 (vertical line cuts on the curve 1) the greatest possible widths of experimental spectra are shown. As it was mentioned above, the spectrum width

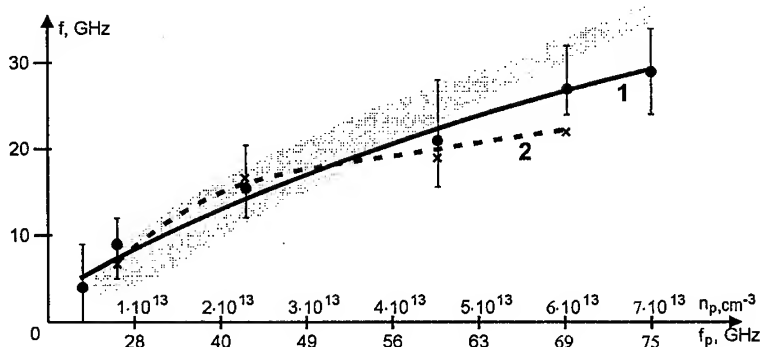


FIG. 7. Microwave radiation mean frequency vs plasma density (plasma frequency $f_p/2\pi$). Curves: 1 - $B = 1.3$ T, 2 - $B = 2.2$ T were obtained in experiment, hatching area - calculation according to the nonlinear theory. The vertical lines on the graph denote the measurement bandwidth.

is measured roughly. However, it is possible to affirm that for small values of plasma density the width of experimental spectrum is approximately equal to the calculated one, but for greater values the width of experimental spectrum exceeds the calculated values. The coincidence of the experimental and calculated dependencies of the radiation frequency on plasma density $f(n_p)$ is the most reliable proof of the fact that the lowest on the radial index azimuthally-symmetrical mode of the slow plasma wave is really excited. Constant level of the radiation power when changing plasma density (Fig. 5, curve 1) related to the fact that the maximum value of the growth rate (k is approximately on the same level for different values of plasma density, Fig. 4. Besides, the constant

level of the radiation power demonstrates that the reflection coefficient of a wave from the transition of the plasma waveguide in vacuum coaxial waveguide remains approximately constant under simultaneous change of plasma density and excited waves frequencies. It is common knowledge that loading a waveguide with plasma allows currents to be transported exceeding the value of the limiting vacuum current [5], so it is worth researching a dependence of microwave radiation power on the current value. All results were obtained at the current 2 kA, whereas the limiting vacuum current was 3.5 kA. Increase of the beam current to 3 kA did not cause a rise of the microwave generation power. This is related to the reduction of the amplifier efficiency obtained in the theory [15], when the beam current approached the value of the limiting vacuum current. Hence, it is experimentally proved that in the plasma relativistic microwave oscillator in a broad range of values of plasma densities the lowest on the radial index azimuthally-symmetrical slow eigenmode of the plasma waveguide is excited. For the first time a frequency tuning was obtained by a factor of 7 from 4 to 28 GHz at the power level 30 - 50 MW due to the varying of one parameter: plasma density. From application standpoint it is important that such a frequency tuning can be implemented during $\sim 30 \mu\text{s}$, which is defined by the plasma density variation rate. In some applications, it is convenient to possess the H_{11} mode of a circular waveguide on the exit side of the device. In [19], a unit that converted the TEM mode into the H_{11} mode was installed between the coaxial outlet waveguide and the conical horn. It was shown that, for a 570-keV, 3-kA beam, only the radiation corresponding to the H_{11} mode was observed, the radiation power being 100 MW. In that paper, the possibility of increasing the beam current was studied. In the previous work, the beam was injected into the plasma cylinder, i.e., the beam diameter was small (11 mm). The vacuum limiting current determined by the ratio of the waveguide to beam radius was not high,

$$(3.3) \quad I = 8.5kA \cdot \frac{(\gamma^{2/3} - 1)^{3/2}}{\ln \frac{R}{R_b}} \approx 3.5kA.$$

The plasma around the beam leads to an increase in the maximum possible beam current; this effect becomes more pronounced as the plasma density grows. Another way to increase the beam current is to use beams with $R_p < R_b < R$. In [19], for the beam diameters $2R_b = 20$ and 25.5 mm, the limiting currents were found to be 10.5 and 30 kA, respectively. In the presence of a plasma, these currents can be further increased, but even the vacuum limiting current of about 30 kA is sufficient to eliminate all the problems associated with the beam space charge for $I_b < 10$ kA (note that, in previous experiments, the beam current was equal to 1 - 3 kA). In [19], it was found that the start current of the oscillator rises with increasing beam diameter. This corresponds to the situation when the longitudinal microwave field E_z decreases with increasing the radial coordinate in the gap between the plasma and the waveguide wall (see Fig. 3). Hence, the interaction between the beam electrons and the wave field weakens. For $2R_p = 25.5$ mm and the beam current 6 kA, the electron energy 420 keV and the

microwave power 300 MW were achieved, the conversion efficiency being 12%. A further increase in the current leads to a decrease in the microwave power. Besides other advantages, the principle of operation of the CPM makes it possible to avoid the problem of microwave pulse shortening, which is inherent to vacuum devices of relativistic high-current microwave electronics. In any high-current microwave oscillator driven by a REB, pulse shortening of microwave radiation is determined by the process of plasma formation in the device. Although there are many factors leading to the undesirable plasma formation, most of them can be successfully eliminated. Nevertheless, in any vacuum high-current microwave device, in which a REB propagates near the slow-wave structure surface because of its significant space charge, there is one mechanism [20] for intense plasma accumulation that is difficult to overcome. First, a strong microwave field causes the destruction of a REB, and a certain fraction of the beam electrons are ejected to the wall under the action of this field. The electron bombardment results in the formation of a plasma layer on the wall surface. Then, a microwave discharge develops, and the amount of plasma increases until the process of microwave radiation comes to an end.

In order to avoid microwave pulse shortening, we propose to use plasma microwave oscillators. In these devices, the space charge of an electron beam is neutralized by that of the plasma, so that the REB may propagate far from the waveguide surface. Besides, the microwave field on the wall is low, and the probability of the development of a microwave discharge on the wall is also low. Of course, all the available means must be engaged in eliminating the influence of the plasma on the collector, cathode, etc. over the entire device. Our experiment with a CPM of microsecond pulse duration is described in [21].

The CPM was driven by a REB with peak electron energy of 500 keV and beam current of 2 kA. This current was approximately equal to the vacuum limiting current in the drift tube. The annular REB of microsecond pulse duration had the geometry completely stabilized according to the technology described in [22], so neither beam radius, nor its thickness changed in the course of the pulse. The waveforms of the cathode voltage and of the microwave pulse are shown in Fig. 8. Microwaves are emitted over 800 ns, and the radiation does not terminate abruptly, as it usually does in the case of microwave breakdown. The radiation pulse energy was measured with a broadband calorimeter [18] and, in the shot under consideration, was found to be 21 J, being the value corresponding to the average microwave power ~ 25 MW (and, accordingly, the peak power ~ 40 MW) and the peak efficiency 4%. Fig. 9 displays the experimental spectra of microwaves for comparatively low and high plasma densities (the ratio being about 2) measured by a calorimetric spectrometer. Therefore, our experiments demonstrated that the features of the Cherenkov plasma maser enable the effect of microwave pulse shortening to be eliminated, and we think that this result is very encouraging. First experiments were carried out on the creation of plasma relativistic microwave amplifier [23]. Successful experiments on plasma relativistic microwave oscillator give hope to design the amplifier with broad-band frequency tuning, e.g., from 4 GHz to 28 GHz. The scheme of the amplifier

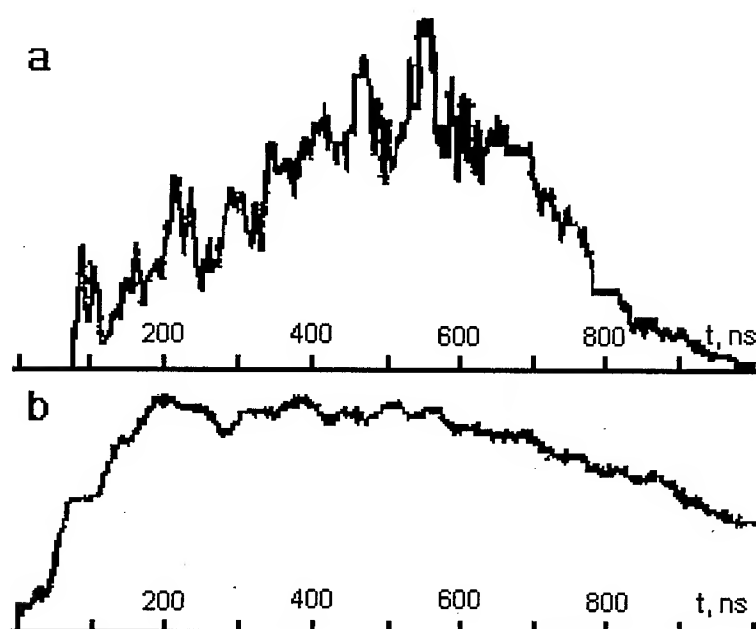


FIG. 8. Waveforms of: a) - microwave power; b) - cathode voltage.

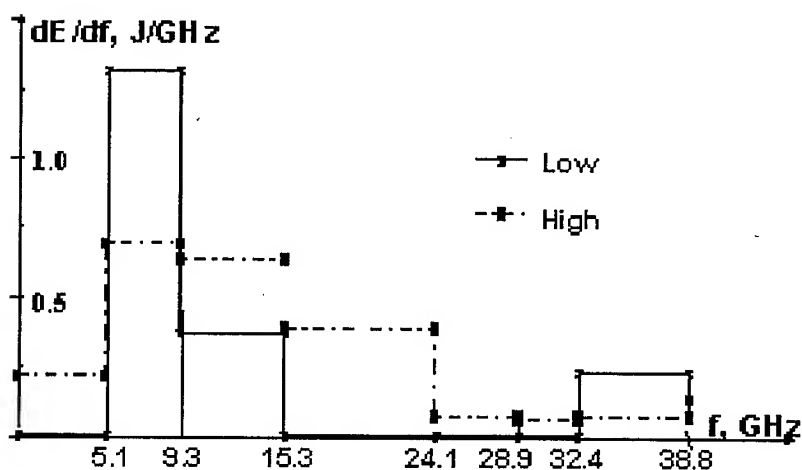


FIG. 9. Spectra of the microsecond CPM microwave radiation for *low* and *high* plasma densities.

is mostly similar to that of the oscillator. It differs by the presence of a microwave absorber for a feedback damping and by an additional waveguide, through which the entrance is supplied by microwave power (~ 100 kW) at the frequencies ~ 9 and 13 GHz. A part of the amplifier radiation (~ 100 kW) was received with a horn and divided further in a waveguide in two equal parts. One part went

directly to a detector, and the other one was directed through a microwave filter with the passband of 4%. Denote the signal from the first detector as A_1 and from the second one as A_2 . In the range of plasma densities $\frac{n_p^{max}}{n_p^{min}} = 3$ an amplification was observed. In this range of plasma densities microwave generation was almost absent. The signal A_1 was equal to 1 V, and $A_2 = 0$. With the power $P = 100$ kW at the entrance the signal $A_1 = 7.5$ V, and $A_2 \approx A_1$. The equality $A_1 \approx A_2$ means that the bandwidth of the amplified signal is less than 4%. The outlet radiation power $P = 20$ MW with the electron beam power 750 MW (500 keV, 1.5 kA). Hence, the possibility of experimental implementation of the amplifier is proved. Its efficiency 3% is low, nevertheless calculations show a possibility of efficiency increase to 20%.

The design of the plasma amplifier will allow to have a source of narrow band microwave radiation with broad frequency tuning, whereas the plasma microwave oscillator gives broad-band radiation $\frac{\Delta f}{f} \approx 1 - 0.3$ with the same wide tuning of the mean frequency.

4. Conclusion

Thus, it was checked experimentally that three physical effects due to loading a vacuum relativistic oscillator with plasma, namely, the change of microwave field spatial distribution, REB space charge neutralization, and the change of electrodynamic structure dispersion, can improve the parameters of vacuum relativistic microwave oscillators. The plasma relativistic microwave oscillator was created. High electron energy plays a decisive role, the proposed scheme of the CPM is effective only if relativistic electrons are in use. The main features of the interaction between a REB with bounded plasma were studied theoretically and experimentally. The unprecedented microwave broad-band oscillator, which is tunable in a wide frequency range, was designed. This oscillator has no analogues in vacuum relativistic microwave electronics. Seven-fold frequency variation can be performed during $\sim 30 \mu s$. First results in the study of plasma relativistic microwave amplifier were obtained. This study is aimed at the creation of a source of monochromatic radiation tunable in a wide frequency band similar to that of the CPM.

References

1. Yu.V. TKACH, Ya.B. FAINBERG, I.I. MAGDA, N.I. GAPONENKO, G.V. SKACHEK, S. S. Science, *Seventh special issue on high power microwave generation*, IEEE Trans. on. Pushkarev, N. P. Gadetskii and A. A. Belukha, *Microwave emission in the interaction of a high-current relativistic beam with a plasma-filled slow wave structure*, Sov. J. Plasma Phys., **1**, 43-46, 1975.
2. K. MINAMI, W.R. LOU, W.W. DESTLER, R.A. KEHS, V.L. GRANATSTEIN and Y. CARMEL, *Observation of a resonant enhancement of a microwave radiation from a gas-filled backward wave oscillator*, Appl. Phys. Lett., **53**, 559-561, 1988.
3. X. ZHAI, E. GARATE, R. PRÓHASKA, A. FISHER and G. BENFORD, *Experimental study of a plasma-filled backward wave oscillator*, Proc. of 9-th Int. Conference on High Power Particle Beams, Beams-92, Washington, pp.1631-1636, 1992.

4. A.G. SHKVARUNETS, S. KOBAYASHI, Y. CARMEL, J. RODGERS, T.M. ANTONSEN, JR., V.L. GRANATSTEIN, *Operation of a relativistic backward wave oscillator filled with a pre-ionized, high density, radially inhomogeneous plasma*, IEEE, Trans. on plasma science, Special Issue on high power microwave generation, 9, Vol. 26, 3, pp. 646-652, June 1998.
5. V.I. KREMENTSOV, P.S. STRELKOV and A.G. SHKVARUNETS, *Neutralization of the space charge and magnetic field of a relativistic electron beam upon injection into a plasma in a homogeneous magnetic field*, Sov. J. Plasma Phys., 2, 519-522, 1976.
6. V.I. KREMENTSOV, M.I. PETELIN, M.S. RABINOVICH, A.A. RUKHADZE, P.S. STRELKOV and A.G. SHKVARUNETS, *Plasma filled gyrotron with a relativistic supervacuum electron beam*, Sov. Phys., JETP, 48, 1978.
7. A.I. AKHIEZER, Ya.B. FAINBERG, *On the interaction of charged particles with electron plasma*, Dokl. Akad. Nauk USSR [in Russian], 69, 3, 551-561, 1949.
8. D. BOHM, E.P. GROSS, *Theory of plasma oscillations*, Phys. Rev., 75, 1851-1861, 1949.
9. G.A. BERNASHEVSKII, E.B. BOGDANOV and Z.S. CHERNOV, *Plasma and electron accelerators and microwave generators*, Sov. Radio [in Russian], 1965.
10. D.I. TRUBETSKOV, L.A. PISHCHIK, *Nonrelativistic Cerenkov-radiation microwave plasma devices*, Sov. J. Plasma Phys., 15, 3, 200-207, 1989.
11. M.V. KUZELEV, F.KH. MUKHAMETZANOV, M.S. RABINOVICH, A.A. RUKHADZE, P.S. STRELKOV and A.G. SHKVARUNETS, *Relativistic plasma UHF generator*, Sov. Phys. JETP, 54, 780, 1982.
12. O.T. LOZA, A.V. PONOMAREV, P.S. STRELKOV, D.K. ULYANOV and A.G. SHKVARUNETS, *Source of an annular controlled-radius plasma for a plasma relativistic microwave oscillator*, Plasma Phys. Reports, 23, 3, 201-208, 1997.
13. L.S. BOGDANKEVICH, M.V. KUZELEV, A.A. RUKHADZE, *Plasma microwave electronics*, Sov. Phys. Usp., 24, 1, 1-16, Jan, 1981.
14. M. BIRAU, M.A. KRASILNIKOV, M.V. KUZELEV and A.A. RUKHADZE, *Problems in the theory of relativistic microwave plasma electronics*, Sov. Phys. Usp., 40, 1997.
15. M.V. KUZELEV, A.A. RUKHADZE, *Plasma free electron lasers*, Paris: Frontier, 1995.
16. A.G. SHKVARUNETS, A.A. RUKHADZE and P.S. STRELKOV, *Wide-band relativistic plasma microwave oscillator*, Plasma Phys. Rep., 20, 7, 613-616, 1994.
17. M.V. KUZELEV, O.T. LOZA, A.V. PONOMAREV, A.A. RUKHADZE, P.S. STRELKOV, A.G. SHKVARUNETS and D.K. ULYANOV, *Spectral characteristics of a relativistic plasma microwave generator*, Sov. Phys. JETP, 82, 6, 1102-1111, 1996.
18. A.G. SHKVARUNETS, *A broadband microwave calorimeter of large cross section*, Instruments and Experimental Techniques, 39, 4, 535-538, 1996.
19. I.A. SELIVANOV, P.S. STRELKOV, A.V. FEDOTOV and A.G. SHKVARUNETS, *Single-mode relativistic microwave oscillator*, Sov. J. Plasma Phys., 15, 11, 744-748, 1989.
20. O.T. LOZA, P.S. STRELKOV and S.N. VORONKOV, *Causes of Microwave Generation Disruption in Vacuum Relativistic Microwave Generators*, Plasma Phys. Rpts., 20, 7, 617-619, 1994.
21. O.T. LOZA, P.S. STRELKOV and I.E. IVANOV, *Relativistic Cherenkov plasma maser of microsecond pulse duration*, IEEE Trans. on plasma science, Special Issue on high power microwave generation, 26, 3, 336-339, 1998.
22. O.T. LOZA, P.S. STRELKOV, *Generation of an annular REB of microsecond pulse duration and stabilized transverse dimensions in a diode with a field-emission cathode*, Proc. of 12-th Int. Conference on High Power Particle Beams (Beams'96), Haifa, Israel, June 7 - 12, 1998.
23. A. V. PONOMAREV, P.S. STRELKOV and A.G. SHKVARUNETS, *Relativistic plasma-beam microwave amplifier*, Plasma Phys. Reports, 24, 1, 48-52, 1998.

GAS DISCHARGE PRODUCED BY STRONG MICROWAVES OF NANOSECOND DURATION

A. L. VIKHAREV

INSTITUTE OF APPLIED PHYSICS, RUSSIAN ACADEMY OF SCIENCE
46 Ulyanov st., Nizhny Novgorod 603600, Russia

The results of the investigation of nanosecond microwave discharge are reviewed. Nanosecond microwave discharge is a new branch of gas discharge physics. The paper lists base types of microwave generators used to produce nanosecond discharge and classifies the discharges relative to their base parameters: the way the discharge gets localized in a limited space, amplitude and frequency of microwave field, gas pressure, duration of microwave pulses. The laboratory experiments performed and the new effects which appear in nanosecond microwave discharge are briefly summarized. Different applications of such a discharge are analyzed on the basis of the experimental modelling.

1. Introduction

Microwave discharges attract much attention as sources of non-equilibrium plasma. High chemical activity of the excited particles (vibrationally and electronically excited molecules; radicals formed in the process of dissociation of molecules) explain the interest in application of non-equilibrium plasma for production of novel materials, surface treatment, film deposition, etc. Microwave discharges have a number of attractive features in terms of the mentioned applications, as compared, e.g., with dc discharges. Among these features are technological ease of transportation of microwave energy to the plasma reactor; efficiency of absorption of electromagnetic energy in the discharge plasma; long time during which purity of the gas mixture is retained due to the absence of electrodes; ease of producing large volumes of plasma; high specific energy contributions that can be achieved; selective character of application of electron energy to internal degrees of freedom of molecules.

The simplest classification of microwave discharges is based on the difference in regimes of operation of microwave generators, i.e. they can be pulsed or continuous. A microwave breakdown in the pulsed regime requires stronger electric fields than that in the continuous wave regime and the threshold field depends on pulse duration. The thing is that for a gas breakdown to occur the value of

the field should be such as to provide evolution of the electron avalanche during the pulse.

The performed experiments employed microwave pulses of different duration: from several nanoseconds to hundreds of microseconds. During a microwave gas breakdown various physical situations are possible. At longer duration of microwave pulses (tens of microseconds or longer) electromagnetic fields with moderate intensity are needed for gas breakdown, in which the oscillatory electron energy $\epsilon_{\sim} = e^2 E^2 / 2m(\omega^2 + \nu^2)$, where e and m are the charge and the mass of electron, ω is the field frequency, ν is the effective collision frequency of electrons, is much less than the average electron energy $\bar{\epsilon}$ and the atomic ionization potential I_i : $\epsilon_{\sim} \ll \bar{\epsilon} < I_i$.

Gas breakdowns by microwave pulses with short nanosecond duration require strong microwave fields. In such a strong field in the region of low and moderate gas pressures the oscillatory electron energy is equal to or more than the ionization potential of the gas: $\epsilon_{\sim} > I_i$. Under these conditions the development of discharge is accompanied by some effects absent at gas breakdown in moderate intensity fields, where $\epsilon_{\sim} \ll \bar{\epsilon} < I_i$. These effects are due to the high rate of ionization of molecules by electron impact, short pulse duration and high electron energies [1-4].

2. Microwave sources

Currently pulsed discharges produced by microwave radiation in the frequency range $f = 2.45 - 40$ GHz are studied intensively. In these experiments the discharge was produced by means of different generators: magnetrons, powerful gyrotrons and generators on relativistic electron beams. Table 1 lists characteristic parameters of these generators.

Table 1. Lists characteristic parameters of pulsed microwave generators

Microwave source	Pulse duration	Peak power
Magnetron	0.1 - 10 μ s	100 kW
Gyrotron	100 - 1000 μ s	0.1 - 1 MW
Relativistic BWO	10 - 100 ns	0.1 - 1 GW

At present there is a great progress in development of microwave generators on relativistic electron beams [5]. These generators have a high peak power $P = (3 - 5) \cdot 10^9$ W at pulse duration $\tau = 10 - 100$ ns [6] and can operate with a high repetition frequency up to $F = 100$ Hz [7]. These sources are widely used in laboratory experiments [8, 9].

Note that recently significant progress has been made in obtaining powerful nanosecond microwave pulses by the method of pulse compression. When this method is used, a low-power (and, hence, inexpensive) pulsed magnetron combined with a microwave compressor can easily compete with generators on relativistic electron beams in production and application of powerful nanosecond microwave pulses in technology.

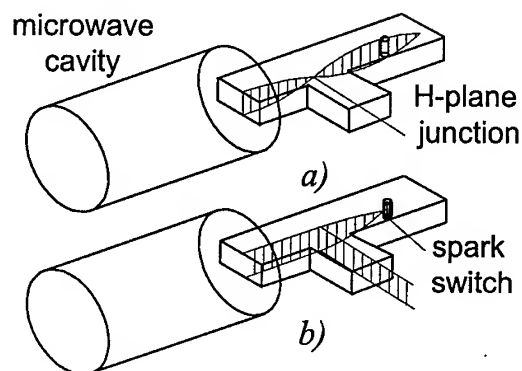


FIG. 1. Switched energy storage and spatial distribution of the electric field during the energy storage cycle (a) and the energy extraction cycle (b).

The most widely studied system is a microwave pulse compressor based on a storage of microwave energy in cavity and subsequent quick extraction of the energy to a load by a rapid change in the coupling to the load by the use of gas switches. The best results obtained so far are presented in Table 2. Some results were obtained with cavities based on oversized waveguides, switches were based on the H-plane junction [10-12]. The most widely studied compressor is shown in Fig. 1.

Table 2. Single stage compressors

Frequency GHz	Power gain	Output power MW	Pulse duration ns	Reference
3	44	70	15	[10]
3	70	100	20	[12]
2.85	23	160	20	[11]
10	50	2.5	8	[12]
9.4	20	1.8	25	[14]
11.4	12	100	50	[15]

It is seen from Table 2 that using such a compressor, researchers obtained powerful microwave pulses at large wavelength ($f = 3$ GHz) owing to the successful design of the energy outlet based on the H-plane junction. Unfortunately, at the shorter wavelength, such compressor operates much worse. Primarily, this is because the single-mode H-plane junction has a small cross-section and therefore limits the extracted power.

For the operation in the X-band a new type of the compressor has been proposed [13-15]. The idea consists of the using Bragg resonators for storage microwave energy. A schematic diagram of the compressor is shown in Fig. 2. The compressor is a cylindrical cavity limited by Bragg reflectors at both ends. The microwave radiation of the generator is put into the cavity through one of

the Bragg reflector and put out through the other. The plasma switch placed into the second Bragg reflector is used for switching from the regime of energy storage to the regime of energy extraction. The use of Bragg reflectors makes it possible to employ oversized waveguide resonators with diameters much greater than the wavelength, at the same time retaining the control of the spatial structure of the microwave radiation. Since the compressor operates in the low-loss TE_{0n} mode, the primary microwave generator is coupled to the compressor via a mode converter.

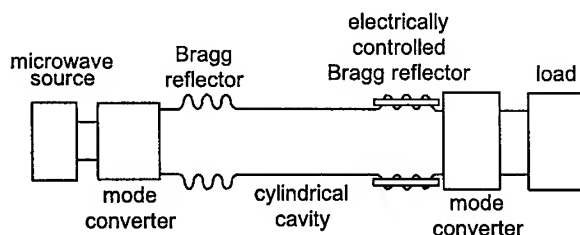


FIG. 2. Schematic layout of microwave pulse compressor with Bragg reflectors.

The schematic diagrams of the output reflectors with a plasma switches which have been used in experiments are shown in Fig. 3. In the first case (Fig. 3a) the plasma switch is made of gas-discharge tubes placed along a periodic structure of the Bragg reflector. The plasma in the tubes is produced by supplying a high-voltage pulse to one electrode of the tubes. The tubes are not switched in the energy storage regime. When the plasma is produced simultaneously in the tubes, the wave constant in the Bragg reflector is changed at the reflector length, the Bragg reflection conditions are not satisfied and the reflector becomes transparent.

In the second case (Fig. 3b) the output reflector is based on a step-wise widening of a circular waveguide. This stepped widening section comprises a cylindrical TE_{311} mode resonator containing a quartz ring-shaped gas-discharge tube. The discharge tube is used for switching from the regime of energy storage to the regime to energy extraction. The testing of prototype designs of such a compressor using 100 kW-level microwaves ($f = 9.4$ GHz) showed that a compressor of this design is able to provide power gains up to 20 [14]. Recently an active pulse compressor has been developed that is able to provide output pulses of at least 100 MW power with pulse duration of 100 ns at X band and with a power gain of 12 - 15 and compression efficiency of 50 - 60% [15].

Thus, modern microwave sources, such as generators on relativistic electron beams and magnetrons combined with microwave compressors can generate pulses of power $10^7 - 10^9$ W, duration $10^{-8} - 10^{-7}$ s, and mean power 1 - 2 kW. Such parameters of radiation make it possible to consider nanosecond microwave discharges for different applications.

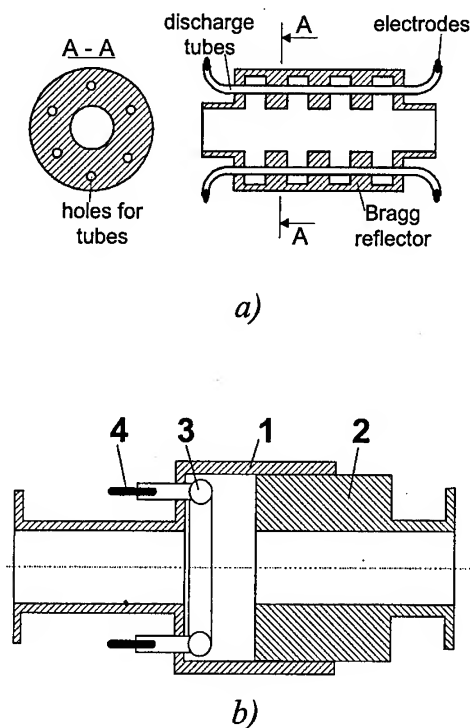


FIG. 3. Output reflector based on electrically controlled Bragg reflector (a); on the stepwise widening of the circular waveguide (b) (1 - waveguide, 2 - movable waveguide, 3 - gas discharge tube, 4 - electrode).

3. Experimental schemes

Up to now a number of various experiments have been performed, in which the nanosecond microwave discharge has been studied. First of all one can divide microwave discharges into two groups according to schemes of producing them. The first group includes discharges with free space localization. The localization of the discharge is produced by geometry of the electromagnetic field. In the experiments different structures of the wave field were created [9, 16]. The main schemes for producing freely localized discharges are shown in Fig. 4. It should be noted that the microwave gas breakdown in the conditions of free field localization has the following specific features [17]. The discharge evolves under a strong perturbing action of the forming plasma upon the field. The main processes that determine limitation of the field in plasma are electrodynamic effects: refraction, absorption and reflection of electromagnetic waves. These processes limit the growth of the electron avalanche during the gas breakdown at a lower level than the critical density.

The second group includes discharges in which plasma gets localized by means of a vacuum chamber or a tube. The main schemes for producing such discharges

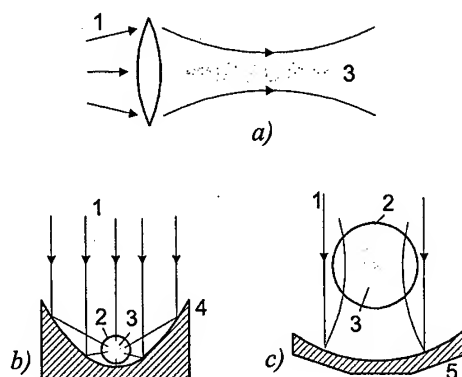


FIG. 4. Schemes for creation of pulsed microwave discharges: in a focused wave beam (a), in the field of a converging cylindrical wave (b), in two opposite wave beams (c): 1 - microwave radiation, 2 - quartz retort, 3 - discharge plasma, 4 - parabolic cylinder, 5 - spherical mirror.

are shown in Fig. 5. The discharge was produced in tubes in a waveguide [18]. Discharges of the second group also have their specific features. In such discharges the nonlinearity, which leads to field variation in plasma, is a field displacement out of the plasma due to the skin-effect. The electron density in such discharges is higher than the critical one.

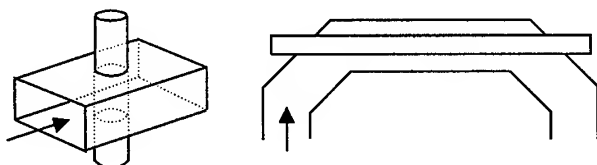


FIG. 5. Schemes for creation of microwave discharges with plasma localization by means of tubes in waveguide.

4. Ionization rate measurements

Measurements of the ionization frequency in a wide range of microwave fields is an important problem for gas discharge physics. Many experiments were concerned with measurements of ν_i [1, 9, 19]. The gas ionization rate in the experiments [1, 9] was determined through measurements of the breakdown time τ_b by the cutoff of the post-focus microwave pulse. For a nanosecond gas breakdown the electron losses during the pulse are absent, therefore ν_i coincides with the avalanche constant in the expression for the electron concentration. The ionization frequency ν_i was calculated by the formula

$$(4.1) \quad \nu_i = \ln(N_{ek}/N_{eo})/\tau_b$$

where N_{ek} and N_{eo} are the final and initial electron densities. At a low pressure ($\nu \ll \omega$), ν_i can be represented as the dependence of the ratio ν_i/p on another the parameter E/ω . This law of similarity follows from the kinetic equation. Fig. 6 presents results of measurements obtained by different researchers. It was found out that in the parameter region $5 \cdot 10^{-7} < E/\omega < 2 \cdot 10^{-6}$ Vs/cm the ionization frequency ν_i does not change with increasing E and can be approximated by the expression $\nu_{im} = A \cdot 10^9 p \text{ s}^{-1}$, where $A = 1.2$ for helium, $A = 7$ for nitrogen and gas pressure in Torr.

For these conditions the gas ionization rate can be calculated by using the results of the investigation of the energy electron distribution function in the strong fields [20, 21]. If the ionization capacity does not depend on the electron translational velocity the electron distribution function can be regarded as the function of uniform electron distribution over initial phases of their motion in the wave field [20]:

$$(4.2) \quad f(v, t) = N_e(t) / \pi \sqrt{v_0^2 - u^2},$$

where $v_0 = eE/m\omega$, u is translational velocity and $v = u - v_0 \cos \omega t$. Computations and some analytical estimations taking into account the dependence of the ionization rate on the translational velocity u were done in [1].

Calculations of ν_i in a wide region of the parameter E/ω , taking into account the function of uniform electron distribution over initial phases (formula (4.2)), are in satisfactory agreement with the experimental data, Fig. 6.

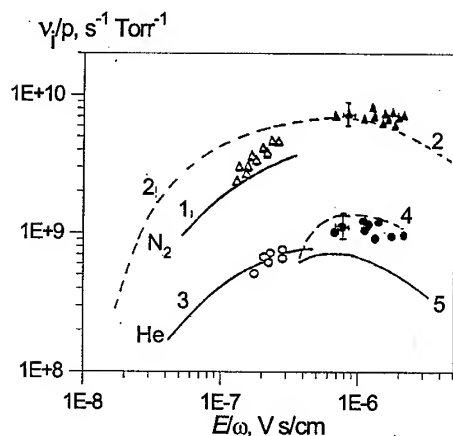


FIG. 6. Ionization frequency for nitrogen (1), (2) and helium (3) - (5): D, O - our experiment; 1, 3 - data of [19]; 4, 5 - calculation of [20, 21].

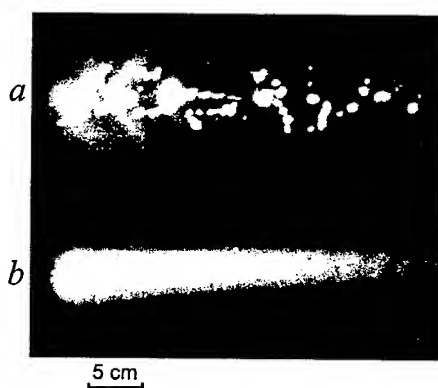


FIG. 7. Open-shutter photographs of the discharge at different initial electron densities: a - 1 cm^{-3} , b - 10^5 cm^{-3} . The microwave beam propagates from left to right.

5. Discharge dynamics and structure

In comparison with microwave discharge in weak electric field where $\epsilon \ll \bar{\epsilon} < I_i$ some new effects appear in nanosecond microwave discharge [1-4].

5.1. Discrete structure of discharge

At gas pressures from 1 to 100 Torr two types of structures of a nanosecond discharge in wave beam were observed, depending on the level of initial (pre-breakdown) electron density [9]. Time-integrated photographs of the discharge in helium at the pressure of $p = 50$ Torr and at the electric field intensity in beam focus $E_F = 15$ kV/cm is given in Fig. 7. The first discrete multiplasmoid structure occurred as a result of gas breakdown on separate initial electrons. The initial electron avalanches formed around every primary electron did not merge because of short duration of the microwave pulse. The second homogeneous structure was observed under the increase of the initial level of electron density.

The densities of primary electrons were changed by an external ionizer. When the spark discharge was put into the vacuum chamber and its ultraviolet radiation increased the electron density in the breakdown region before the microwave pulse up to $10^3 - 10^5$ cm $^{-3}$, then the light emission of the discharge was always homogeneous, Fig. 7.

The development of the discharge on separate electrons can be observed only in strong microwave field. This conclusion is confirmed by the following estimation. The average interval between the initial electrons equals $r_0 = N_{eo}^{-1/3}$ and the electron avalanche around every primary electron expands due to diffusion. During the breakdown time τ_b its dimension will be approximately equal to the characteristic diffusion length for electrons $L_e = (D\tau_b)^{1/2}$. Taking into account the formula (4.1) for the breakdown time, one obtains the expression at which the electron avalanches do not overlap and the discharge is discrete:

$$(5.1) \quad D \cdot \tau_b < N_{eo}^{-2/3}$$

or

$$(5.2) \quad \nu_i > D \cdot N_{eo}^{2/3} \cdot \ln(N_{ek}/N_{eo}).$$

Thus, there is a limitation for the ionization frequency when the discrete structure of the discharge is being observed.

5.2. Delay of the optical radiation relative to microwave pulse

High electron energies obtained in a nanosecond discharge can influence greatly the dynamics of its light radiation. The experiment [22] demonstrated that at low nitrogen pressures the light radiation of the discharge produced in the focal region of the beam reached its maximum after the microwave pulse, Fig. 8. The observed delay of the light pulse is explained by high electron energy during the microwave pulse. According to calculations this electron energy substantially exceeds the energy corresponding to the maximum of the excitation cross-sections

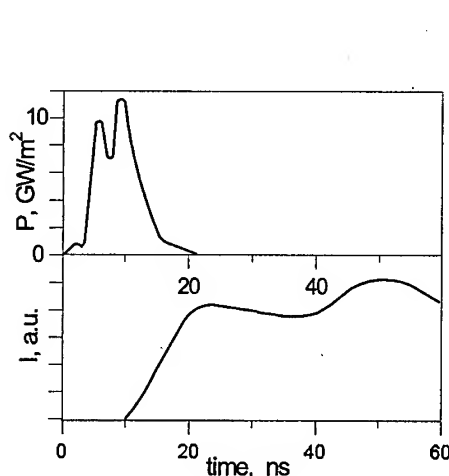


FIG. 8. Oscillograms of the microwave pulse and optical radiation of the discharge at nitrogen pressure $p = 0.6$ Torr, as presented in [22].

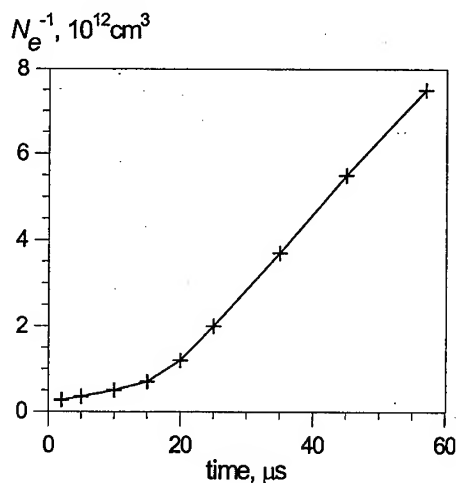


FIG. 9. Inverse electron density N_e^{-1} at nitrogen pressure $p = 0.6$ Torr.

of the electronic levels responsible for light emission ($\epsilon_e = 10 - 20$ eV). Therefore, the main excitation of the nitrogen molecules takes place after cessation of the microwave pulse, when the electron energy drops appreciably.

5.3. Effect of slow plasma decay in nitrogen-oxygen mixture

The plasma decay of the nanosecond microwave discharge also has specific features. The dynamics of electron density was investigated with the help of microwave interferometer [1] at a wavelength of $\lambda = 8$ mm. Fig. 9 presents the time dependence of the inverse electron density at nitrogen pressure $p = 0.6$ Torr. We can see that at $t \leq 10$ μs the plasma decay goes on slowly. A linear dependence of N_e^{-1} on time characterizes the plasma decay due to dissociative recombination with the coefficient $\alpha_{ei} \simeq 2 \cdot 10^{-8}$ cm^3/s at $p = 0.6$ Torr.

Such a recombination coefficient indicates an appreciable electron temperature at times $t \leq 10$ μs after cessation of microwave pulse. By approximating the dependence of recombination coefficient on the electron temperature by the power-law expression $\alpha_{ei} = \alpha_0 \cdot (300/T_e)^{0.5}$ where $\alpha_0 = 2.7 \cdot 10^{-7}$ cm^3/s [23] we obtain $T_e \approx 5$ eV. The expression used for the electron recombination rate is correct for the electrons having temperature which does not exceed $T_e = 1$ eV [23]. Nevertheless this estimation gives the order of magnitude of electron temperature.

The prolonged relaxation of electron energy after a microwave discharge is apparently due to the influence of collisions between electrons and electronically excited nitrogen molecules. The population of the electronic levels of nitrogen after a nanosecond microwave discharge can be appreciable, since a major portion of the microwave energy absorbed by the discharge, at a high value of

the parameter E/N , is expanded in ionization and excitation of the electronic levels of the molecules. A calculation of the electron distribution function in the decaying plasma, carried out in [24], shows that the electron distribution function is enriched with high-energy electrons due to superelastic collisions of electrons with electronically excited molecules $N_2(A^3\Sigma_u^+)$. After cessation of the microwave pulse the share of excited molecules (their influence) is decreasing with time. It influences the change of the recombination coefficient at times $t > 10\mu\text{s}$ (Fig. 9) and the gradual transfer to the recombination decay with the coefficient $\alpha_{ei} \simeq 1.6 \cdot 10^{-7} \text{ cm}^3/\text{s}$, close to the value at the electron temperature equal to gas temperature ($T_e = T$). Consequently, the rate of plasma decay depends greatly on the density of electronically excited molecules.

5.4. Additional ionization effect after low-pressure discharge

The discharge was studied at low pressure ($p = 3 \cdot 10^{-3} - 1$) Torr with the use of pulse gas injection into the focal region of the wave beam [1]. This scheme was used for the localization of the discharge in a small focal region. The electric field intensity in the focus was $E_F = 70 - 120 \text{ kV/cm}$, and the oscillatory energy in this field was $\epsilon \sim 1.2 - 3.5 \text{ keV}$. It was found that the electron density after the microwave pulse was 5 to 10 times larger than the critical density for the microwave radiation, $N_c = 10^{12} \text{ cm}^{-3}$. The electron density was also measured with the use of an interferometer at a wavelength of $\lambda = 8 \text{ mm}$. Fig. 10 is the dependence of the maximal electron concentration after the microwave pulse on gas pressure. Fig. 11 is an interferogram of the discharge in nitrogen at the pressure $p = 0.4 \text{ Torr}$ and the initial density $N_{e0} = 10^6 \text{ cm}^{-3}$. One can see a $2 \mu\text{s}$ cutoff of the probing signal, then plasma starts to decay. For the pressure $p = 10^{-2} - 10^{-1} \text{ Torr}$ no cutoff was observed but the sign of the signal changed in $0.5 \mu\text{s}$ after the microwave pulse. It means that the electron density was increasing for about $0.5 \mu\text{s}$.

These results can be explained in the following way. After the field switches off, the plasma contains electrons whose energy is much higher than the ionization potential. These electrons lose their energy in ionizing collisions, because $\nu_i > \nu$. Therefore N_e can increase considerably due to the continuing ionization process. Assuming that the energy loss of electrons due to the ionizing collisions is of the order of $2I_i$, we find that after the passage of the pulse the electron density increases ($\epsilon/2I_i$) times over the electron cooling time. The electron cooling time can be approximated by the relation:

$$(5.3) \quad \tau_{di} = \int_{I_i}^{\epsilon} d\epsilon / 2I_i \nu_i(\epsilon) = \epsilon / 2I_i \nu_{im}.$$

For example, in nitrogen at pressure $p = 5 \cdot 10^{-2} \text{ Torr}$ and $\epsilon = 2 \text{ keV}$ according to the formula (5.3) value τ_{di} equals $\tau_{di} = 0.5 \mu\text{s}$. This estimated value of electron cooling time is as in experiment.

Additional gas ionization was also observed at a higher initial density of electrons: $N_{e0} = 3 \cdot 10^{10} \text{ cm}^{-3}$. For example in helium we achieved N_e of the

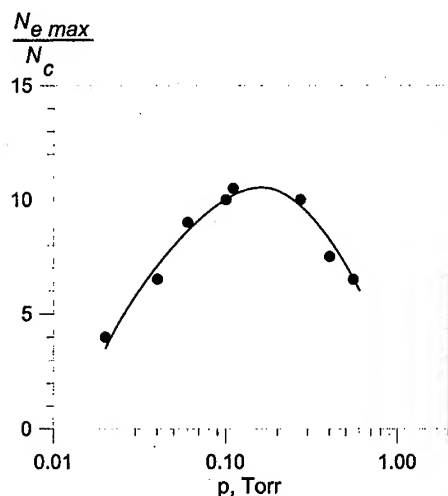


FIG. 10. Dependence of maximal electron density after the microwave pulse on gas pressure.

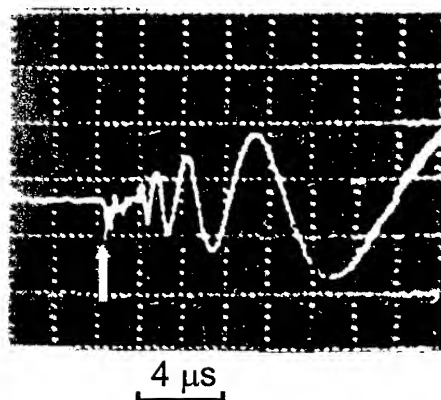


FIG. 11. Interferogram of the discharge in nitrogen at pressure $p = 0.4$ Torr and initial density $N_{e0} = 10^6 \text{ cm}^{-3}$. Arrow shows cessation of the microwave pulse.

order of six times the critical density ($N_{em} = 6 \cdot 10^{12} \text{ cm}^{-3}$) at the pressure of $p = 3 \cdot 10^{-2}$ Torr after the microwave pulse which passed through the ionized region undistorted. The fact is that N_e increases 2 or 3 times during the microwave pulse:

$$(5.4) \quad N_k = N_{e0} \cdot \exp(\nu_{im}\tau) = e^1 N_{e0}.$$

These newly-born electrons getting cold after the microwave pulse induce additional ionization:

$$(5.5) \quad N_{em} = N_k \cdot \epsilon / 2I_i = 5 \cdot 10^{12} \text{ cm}^{-3}.$$

The estimation is made for $\epsilon = 2 \text{ keV}$. Thus, a low pressure discharge in a superstrong field is followed by a considerable additional ionization process.

Thus, these effects, as well as the appearance of accelerated ions [1], prove that when the gas is broken down in a super-strong microwave field in a wave beam, the conditions characteristic for gas breakdown by intense short-pulse laser radiation are achieved [36].

6. Applications of the nanosecond microwave discharge

The nanosecond microwave discharge is interesting for various applications. Such discharge can be used successfully for pumping the nitrogen and excimer lasers and ozone generation.

6.1. Generation of UV radiation

At gas breakdown by nanosecond microwave pulses a strongly nonequilibrium medium is created, since the major part of the microwave energy absorbed in the plasma is spent on ionization and excitation of the molecule electronic states. Therefore a nanosecond microwave discharge can be successfully used for pumping excimer lasers and lasers based on electronic transitions of molecules, namely those lasers that require high energy contributions in a short period of time [25, 26]. The schematic diagram of the nitrogen laser with a microwave pumping is shown in Fig. 12. The microwave radiation was produced by a relativistic 3-cm

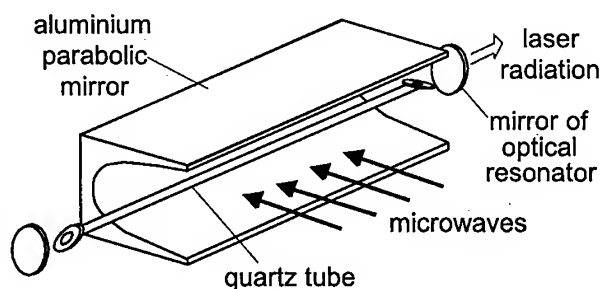


FIG. 12. Schematic diagram of the nitrogen laser: $l = 3$ cm, $t = 40$ ns, $E = 10 - 100$ kV/cm, nitrogen $p = 10 - 760$ Torr.

wavelength band generator. The pulse duration was $\tau = 40$ ns. The radiation of circular or linear polarization was converted into a quasi-Gaussian beam and turned upon an aluminium mirror (parabolic cylinder) by a conical horn. As the result, all microwave radiation was reflected by the mirror. The focus line of the mirror was coupled with the optical axis of the laser. The scheme of the transverse freely localized microwave discharge was realized. We used a short-focus parabolic mirror (with its focal length of 8 cm) that formed a steeply converging wave beam (a converging cylindrical wave). The intensity of the electric field in the breakdown region, in dependence on the incident power was 10 - 100 kV/cm. The tube was pumped out and then filled with nitrogen, the pressure of which was changed in the range $p = 10 - 760$ Torr.

The discharge tube (we used a quartz tube with its diameter 0.8 - 2.5 cm and length 85 cm) had quartz windows situated at the Brewster angle to its axis. The optical 90 cm long resonator consisted of an aluminum mirror and plane-parallel quartz plate. Laser radiation was detected by means of an absolutely calibrated photo-electron converter and a fast oscilloscope.

In the experiment laser generation was obtained in all the pressure range under investigation. The characteristic oscillograms of microwave and laser pulses are shown in Fig. 13. The highest intensity of radiation was observed in the band 0-0 ($\lambda = 337.1$ nm) of the second positive nitrogen; it exceeded the power of radiation in the bands 0-1 ($\lambda = 357.7$ nm) and 1-0 ($\lambda = 315.9$ nm). The duration of laser radiation was weakly dependent on the gas pressure and was growing as the diameter of the discharge tube was made larger and actually coincided with the

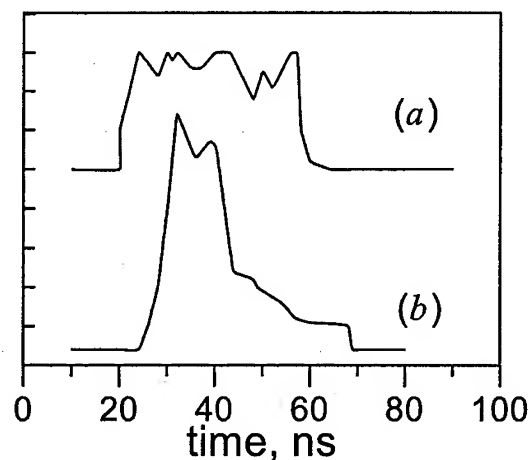


FIG. 13. Oscillograms of microwave pulse (a) and laser radiation pulse (b).

duration of the microwave pulse. When the level of microwave power was high, spatial distribution of UV radiation intensity over the tube cross-section was a 2-4 mm thick ring with its external radius equal to the radius of the tube. The amplitude of the laser pulse had an optimum with respect to the incident microwave power. It was revealed that under a low level of pumping the generation was formed initially at the center of the tube, and then moved towards its wall. The radiation from the central region was shorter than the general duration of the laser generation.

Thus, when the described way of excitation is used, laser radiation is generated consequently by plasma layers situated at different distances from the axis, and that makes the generation pulse longer. The power of laser generation grew in proportion to the plasma volume, and under optimal pressure it was 60 - 70 kW for the tube 2 cm in diameter. Specific energy removal equalled $0.5 - 1 \text{ J atm}^{-1} \text{ l}^{-1}$. The efficiency of the laser was $10^{-4} - 10^{-3}$ and was defined as the ratio of laser power to the incident microwave power.

6.2. Ozone generation

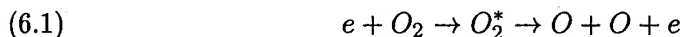
A whole series of laboratory experiments [4, 16, 27-29] have been carried out in which the ozone generation in the repetitive nanosecond microwave discharge was observed. The schemes of these experiments are shown in Fig. 4. The discharge was ignited in two basically different electrodynamic systems. In the first case the microwave radiation was focused with a parabolic cylinder, so that the electromagnetic field in the breakdown region was close to a standing cylindrical TE mode. The discharge was shaped as a cylinder several millimeters in diameter and about 30 cm long. In the second case a quasi-planar standing electromagnetic wave was formed by means of a spherical mirror. Then the discharge was a set of plasmoids about 3 cm in diameter localized at the antinodes of the standing wave.

In the experiments the following factors varied: air density (pressure $p = 10-250$ Torr) and temperature ($T = 200-300$ K), radiation parameters, namely, pulse duration ($\tau = 5, 6$ and 500 ns), repetition rate ($F = 1-1000$ Hz), power ($P = 1-20$ MW) and the discharge structure, Fig. 4. The experiments were performed with the use of different sources of microwaves. In the first experiment the relativistic carcinotron of 8-mm wavelength band was used. The second experiment was performed with use of 3-cm wavelength band magnetron with a microwave pulse compressor.

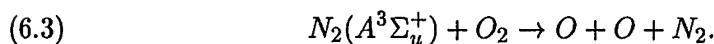
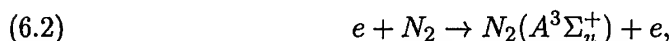
Densities of ozone and nitrogen dioxide were measured by means of observing absorption of hydrogen lamp radiation at wavelengths $\lambda \approx 260$ nm and $\lambda \approx 360$ nm, respectively, which was based on the known relation: $I(\lambda) = I_0(\lambda) \cdot \exp(-\sigma N_a L)$, where $I(\lambda)$ and $I_0(\lambda)$ are transient and incident intensities of the diagnostic radiation at wavelength λ , L is length of the optical path, σ is absorption cross-section for O_3 or NO_2 , and N_a is density of the absorber.

An important parameter that makes the nanosecond microwave discharge rather advantageous for generation of ozone is the amount of energy going into production of one ozone molecule. The energy cost was determined by means of basing on the total energy of the microwave pulse, $W = P \cdot \tau$, and with the use of the following formula: $\delta = P \cdot \tau \cdot n_p / [O_3] \cdot V_k$, where n_p is number of microwave pulses, $[O_3]$ is ozone density after n_p pulses and V_k is the volume of the vacuum chamber. The results of measuring the energy cost of ozone production for two different types of the microwave discharge are shown in Fig. 14 [16]. The energy cost was 2-3 times lower in a discharge created by standing waves than in a discharge formed by a converging cylindrical TE-mode. This shows that efficiency of ozone formation depends essentially on the electrodynamic system producing the discharge. For systems operating with standing waves or crossing wave beams efficiency turns out to be higher.

These experiments showed that the energy cost of production of one ozone molecule is lower in that type of the microwave discharge, in which the maximum of its energy goes into dissociation of oxygen molecules. Oxygen atoms are produced and then converted into ozone mainly in dissociation of O_2 molecules by an electron impact:



and in collisions of O_2 with metastable N_2 molecules:



The velocity constants for processes (6.1) and (6.2) are determined by the function of electron distribution over energies and depend on intensity of the electric field in plasma. The value of O_2 dissociation rate for process (6.1) in air, k_d , is rather well known for a constant electric field. Using it we can estimate the energy cost of production of one ozone molecule in the microwave discharge. We assume that all oxygen atoms are formed in the process of direct dissociation

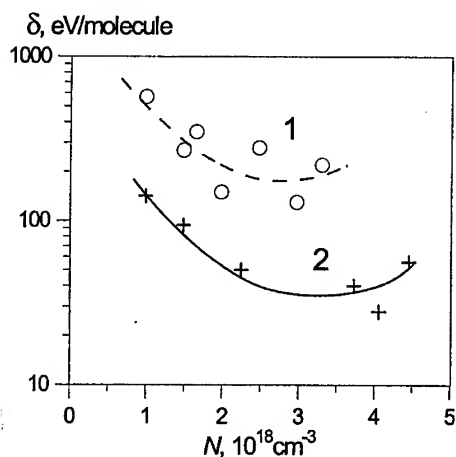


FIG. 14. Experimental dependence of energy cost of ozone formation on air density for discharges created by a converging cylindrical TE-mode (1) and by standing wave (2).

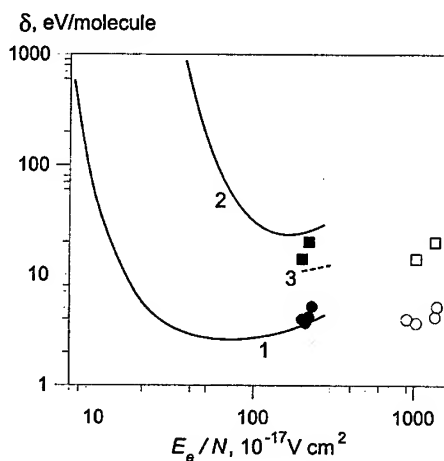


FIG. 15. Dependence of energy cost of ozone formation on the reduced electric field: data of calculation in oxygen (1), in air (2, 3); data of experiment ($t = 6$ ns): \circ, \bullet - oxygen, \square, \square - air.

of oxygen (6.1), and then they enter the reaction of ozone synthesis taking place in the after discharge period [30, 31]:



where $k_1 = 6.2 \cdot 10^{-34}(T/300)^{-2} \text{ cm}^6/\text{s}$ for $M = O_2$ and $k_1 = 5.7 \cdot 10^{-34}(T/300)^{-2.8} \text{ cm}^6/\text{s}$ for $M = N_2$. For ozone density produced in one microwave pulse we find:

$$(6.5) \quad [O_3] = [O] = 2 \cdot k_d(E_e/N) \cdot [O_2] \cdot N_e \cdot \tau.$$

The energy cost of one ozone molecule is found from the ratio of the microwave energy absorbed in plasma to ozone density:

$$(6.6) \quad \delta = \sigma \cdot E^2 \cdot \tau / 2 \cdot k_d \cdot [O_2] \cdot N_e \cdot \tau = 5/2 \cdot (e^2/m) \cdot (\nu/N)^{-1} \cdot (E_e/N)^2 / k_d,$$

where $\sigma = e^2 N_e \nu / m(\nu^2 + \omega^2)$ is specific plasma conductivity, ν is the rate of electron-molecule collisions, and ω is the wave frequency, $E_e = E \cdot \nu / (\nu^2 + \omega^2)^{1/2}$ is the efficient electric field. Using equation (6.6) it is easy to determine optimal conditions, when at the preset energy of the microwave pulse the number of oxygen atoms produced in the ionized region is maximal. The value of $(E_e/N)^2 / k_d$ is minimal when the value of the reduced efficient electric field E_e/N is determined by the following expression:

$$(6.7) \quad E_e/N = 2 \cdot k_d / dk_d/d(E_e/N).$$

Fig. 15 shows the dependence of δ on the reduced electric field, E_e/N determined by calculation (curve 2) and by experiment [29]. The calculations employed the constants of O_2 dissociation rates for process (6.1) in air from paper [32]. It was taken into account that dissociation of ozone molecules in reaction (6.1) goes on from three electronic levels. For calculation of δ the total constant k_d was used. The experimental value of efficient field E_e was determined from intensity of the electric field in the discharge region before the breakdown starts, and the rate of electron collisions in air was assumed equal to $\nu = 5.3 \cdot 10^9 p$ (s^{-1}) [33]. Using the results of [34], we added curve 3 to Fig. 15 to represent the results of calculating the energy cost of ozone formation with account for indirect channel of O_2 dissociation due to processes (6.2) and (6.3).

Thus, there are optimal conditions for oxygen dissociation in oxygen and air. The above estimates dealt with determination of optimal conditions for production of oxygen atoms. In the case of a discharge produced by a single nanosecond pulse (or a short series of microwave pulses) they are valid also for ozone, since the process of accumulation of ozone destroying particles is too low, and gas is heated insignificantly. By that, the energy cost of ozone formation is determined by electrodynamics of the discharge and depends on how fast the optimal conditions for oxygen dissociation are achieved and for how long they will be sustained in the discharge region.

The results of the performed experiments make it possible to conclude that a nanosecond microwave discharge can efficiently generate ozone. The laboratory experiments demonstrated sufficiently low energy costs of producing one ozone molecule: $\delta = 15 - 20$ eV/molecule, which corresponds to the production of 100 g of O_3 per 1 kWh of consumed energy.

6.3. Atmospheric ozonizer

Laboratory experiments show that the nanosecond microwave discharge can be used for the replenishment of ozone in the region of the ozone "holes". The scheme of the way we propose to realize this idea is shown in Fig. 16. Using ground-based antennas two beams of high-power microwaves at frequencies 10 - 40 GHz are transmitted into the atmosphere. At the region where they cross at heights of 20 - 30 km, where the electric field is especially high, a nanosecond microwave discharge occurs, which will be an efficient source of ozone. The estimation shows that the production of air breakdown at the height of $H = 30$ km by the transmitting antennas of diameter $d = 100$ m, put at the distance of 30 km, requires the pulse microwave power (the radiation of 3-cm band, pulse duration $\tau = 50$ ns) $P \approx 4$ GW in every beam. This level of microwave power has already been achieved by modern generators in laboratory experiments [6]. So the advance of microwave electronics in development of the powerful generations on the relativistic electron beams (for instance, back-wave oscillator [5]) makes real the idea of creation of an atmospheric ozonizer.

The nanosecond microwave discharge in the stratosphere is advantageous for solving environmental problems due to the following reasons: 1) it is easy and highly efficient to deliver energy to the atmosphere by wave beams; 2) by using intersecting beams it is easy to single out the required region in the stratosphere,

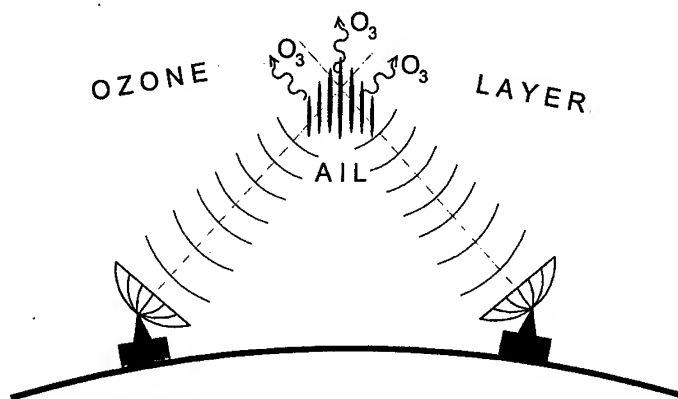


FIG. 16. Scheme of atmospheric ozonizer creation.

and scanning the beams, to process large air volume; 3) moreover, the efficiency of plasma-chemical reactions in the nanosecond discharge is among the highest of all those known for non-equilibrium low-temperature plasma. The majority of the plasma chemical reactions are strongly dependent on the gas temperature T . Therefore, in order to predict the effect of the nanosecond microwave discharge upon the stratosphere in the series of experiments the ozone generation was investigated at pressures and temperatures of the air that correspond to the conditions of the stratosphere. The schematic of the experimental set-up is shown in Fig. 4. Fig. 17 shows time dependence of ozone density at fixed density of neutrals, $N = 2 \cdot 10^{18} \text{ cm}^{-3}$, for various gas temperatures. The maximum ozone density under the studied pressures was growing in proportion to the air pressure.

The analysis show that a decrease in T leads to higher velocities of ozone production in reaction (6.4) and, at the same time, reduces strongly the efficiency of nitrogen oxides production in reaction:



where $k_3 = 4.4 \cdot 10^{-12} \cdot \exp(-3200/T) \text{ cm}^3/\text{s}$. Estimations of ozone and nitrogen dioxide production at the stage of linear ozone growth show that the density produced in the retort during one pulse under the pressure $p = 90 \text{ Torr}$ is in experiment for $O_3 \approx (2-3) \cdot 10^{12} \text{ cm}^{-3}$, and for $NO_2 < 10^{10} \text{ cm}^{-3}$. Thus, when the microwave discharge in the stratosphere is generated, such conditions may be achieved, under which nitrogen dioxide density will not exceed the natural level of NO_2 [35], and O_3 density will correspond to or exceed the density at the maximum of the ozone layer.

This conclusion is also proved by calculating the ratio of O_3 and NO_x in the ionized region in the stratosphere. Fig. 18 shows the results of calculating ratio $[O_3]/[NO + NO_2]$ in dependence on specific energy contribution into the discharge. The energy contribution varied in the discharge changing duration of the microwave pulse and leaving the initial electric field in the ionized region

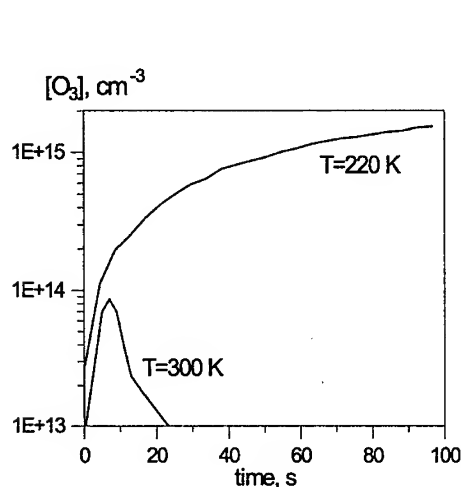


FIG. 17. Dependence of ozone density on time at density of neutrals $N = 2 \cdot 10^{18} \text{ cm}^{-3}$, $F = 3 \text{ Hz}$ and various gas temperature.

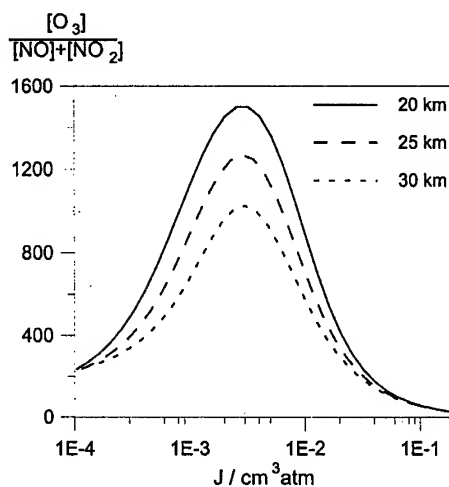


FIG. 18. Ratio of O_3 and NO_x in dependence on specific energy contribution into the discharge.

intact. The calculations were performed for the microwave radiation in the 3-cm wavelength band, which was sent to the stratosphere by two ground-based antennas 100 m in diameter each and distanced to 30 km from each other. As it is seen from the figure, the maximum ratio of $[O_3]$ to $[NO + NO_2]$ equal to 10^3 can be achieved. Thus, there is the regime for creation of an atmospheric ozonizer, at which the ratio of densities of ozone and nitrides in the ionized region will be the same as in the non-perturbed natural stratosphere [35].

References

1. M.P. BRIZHINEV, A.L. VIKHAREV, G.YU. GOLUBYATNIKOV et al., *Sov. Phys. JETP*, **71**, 2, 242-248, 1990.
2. A.L. VIKHAREV, in *Proc. Intern. Workshop on "Strong Microwave in Plasmas"*, Ed. by A.G. Litvak, Nizhny Novgorod: IAP Press, , 306-323, 1991.
3. A.L. VIKHAREV, A.M. GORBACHEV, O.A. IVANOV et al., *J. Geoph. Res.*, **99**, D10, 21097-21108, 1994.
4. A.L. VIKHAREV, O.A. IVANOV, A.G. LITVAK, *IEEE Trans. on Plasma Science*, **24**, N2, 460-477, 1996.
5. A.V. GAPONOV-GREKHOV and M.I. PETELIN, *Vestnik Akad. Nauk SSSR*, **4**, 11-23, 1979.
6. S.P. BUGAEV, A.N. VLASOV, V.I. KANAVETS et al., *Radioeng. Electron.*, **35**, 2346, 1990.
7. V.I. BELOUSOV, B.V. BUNKIN, A.V. GAPONOV-GREKHOV et al., *Pis'ma v Zh. Tech. Fiz.*, **4**, 1443, 1978.
8. C.A. SULLIVAN, W.W. DESTLER, J. RODGERS et al., *J. Appl. Phys.*, **63**, 5228-5232, 1988.
9. A.L. VIKHAREV, V.B. GILDENBURG, O.A. IVANOV et al., *Sov. J. Plasma Phys.*, **12**, 2, 870-872, 1986.
10. N.D. DEVIATKOV, A.N. DIDENKO, L.Y. ZAMYATIN et al., *Radioeng. Electron.*, **25**, 87-91, 1980.

11. R.A. ALVAREZ, D. BIRX, D.P. BYRNE et al., Particle Accelerators, **11**, 125-130, 1981.
12. V.A. AVGUSTINOVICH, S.A. NOVIKOV, S.A. RAZIN et al., Radiophys. Quantum Electron., **28**, 10, 1347-1348, 1985.
13. A.L. VIKHAREV, N.F. KOVALEV, M.I. PETELIN, Pis'ma v Zh. Tekh. Fiz., **22**, 19, 41-46, 1996.
14. A.L. VIKHAREV, A.M. GORBACHEV O.A. IVANOV et al., Pis'ma v Zh. Tech. Fiz., **24**, 20, 6-11, 1998.
15. A.L. VIKHAREV, A.M. GORBACHEV, O.A. IVANOV et al., in Proc. Int. Particle Accelerator Conf., NY, 1999.
16. R.A. AKHMEDZHANOV, A.L. VIKHAREV, A.M. GORBACHEV et al., Plasma Physics Reports, **23**, 1, 53-61, 1997.
17. V.B. GILDENBURG, Sov. Phys. JETP, **51**, 480-482, 1980.
18. A.N. DIDENKO, V.M. PETROV, V.N. SLINKO et al., Sov. Phys. Tech. Phys., **33**, 363-365, 1988.
19. D.M. KARFIDOV, Fizika Plazmy, **5**, 929-930, 1979.
20. S.G. ARUTYUNYAN and A.A. RUKHADZE, Sov. J. Plasma Phys., **5**, 702-704, 1979.
21. L.G. GLAZOV and A.A. RUKHADZE, Sov. J. Plasma Phys., **15**, 1484-1490, 1989.
22. W.T. ARMSTRONG, R.A. ROUSSEL-DUPRE, R. KARL et al., in Proc. of the 18th Intern. Conf. on Phenomena in Ionized Gases, (Swansea, UK), 4, 850-851, 1987.
23. A.V. ELETSKII and B.M. SMIRNOV, Sov. Phys. Usp., **136**, 25-59, 1982.
24. N.A. DYATKO, I.V. KOCHETOV and A.P. NAPARTOVICH, J. Phys.D: Appl. Phys., **26**, 418-423, 1993.
25. A.L. VIKHAREV, A.M. GORBACHEV, O.A. IVANOV et al., Quantum Electronics, **24**, 7, 595-598, 1994.
26. A.L. VIKHAREV, A.M. GORBACHEV, O.A. IVANOV et al., J.Phys. D: Appl. Phys., **28**, 523-529, 1995.
27. R.A. AKHMEDZHANOV, A.L. VIKHAREV, A.M. GORBACHEV et al., Pis'ma v Zh. Tech. Fiz., **21**, 9, 26-31, 1995.
28. R.A. AKHMEDZHANOV, A.L. VIKHAREV, A.M. GORBACHEV et al., Phys. Lett. A, **207**, 3-4, 209-213, 1995.
29. R.A. AKHMEDZHANOV, A.L. VIKHAREV, A.M. GORBACHEV et al., Zh. Tekh. Fiz., **67**, 3, 9-18, 1997.
30. D. BAULCH, R. COX, P. CRUTZEN et al., J. Phys. Chem. Ref. Data, **11**, 327, 1982.
31. P. ATKINSON, D. BAULCH, R. COX et al., J. Phys. Chem. Ref. Data, **18**, 881, 1989.
32. N.L. ALEKSANDROV, F.P. VYSIKAILO, R.SH. ISLAMOV et al., Teplofiz. Vys. Temp., **19**, 485-490, 1981.
33. A. MACDONALD, *Microwave breakdown in gases*. New York: Wiley, 1966.
34. N.L. ALEKSANDROV et al., Pis'ma v Zh. Tech. Fiz., **16**, 6, 4-7, 1990.
35. G. BRASSEUR, S. SOLOMON, *Aeronomy of the Middle Atmosphere*, Dordrecht, Holland: D.Reidel Publishing Company, 1984.
36. B. LUTHER-DAVIES, E.G. GAMALY, Y. WANG et al., Laser Physics, **1**, 4, 325-365, 1991.

GROWTH PROCESSES OF PARTICLES UP TO NANOMETER IN HIGH-FREQUENCY SiH_4 PLASMAS

Y. WATANABE, M. SHIRATANI, T. FUKUZAWA AND K. KOGA

GRADUATE SCHOOL OF INFORMATION SCIENCE AND ELECTRICAL ENGINEERING
Kyushu University, Japan

Growth processes of particles in high-frequency SiH_4 discharges have been understood fairly well in a size range above 10 nm. Recently, we have developed two in situ particle detection methods to study those of particles (clusters) in a size range below ~ 10 nm. The studies have clarified time evolution of their density and size and revealed the following facts: the cluster density amounts to $\sim 10^{11} \text{ cm}^{-3}$ under the device quality low-power and low-pressure conditions: the discharge modulation, substrate heating and H_2 dilution are quite effective in suppressing the cluster growth. We have proposed the cluster growth model explaining reasonably the obtained results.

1. Introduction

Silane (SiH_4) discharges are used to fabricate devices such as amorphous silicon (a-Si:H) solar cells and thin film transistors for flat-panel display and to deposit films such as SiC and SiN. Germane (GeH_4) discharges are also used to prepare a-SiGe:H layer for improving output efficiency of a-Si:H solar cells. In such discharges, particles are generated due to gas phase reactions, leading to serious contamination into the films and devices. Thus, many studies on particle formation have been carried out mainly using high-frequency (HF) SiH_4 discharges in the last decade.

To study particle formation processes in the discharges, it is important to reproduce the processes precisely and to measure important parameters related to them quantitatively. From such viewpoint, we have developed a pulse discharge method and *in situ* laser-light-scattering methods to observe time evolution of particle size and density [1, 2, 3]. Using these methods, we have revealed the following six facts concerning the particle growth in HF SiH_4 discharges, while the supplied power is in a range high compared to that for the so-called device quality conditions: 1) the particles grow through the initial growth phase in a size range below a few-10 nm, the rapid growth phase in a size range from a few-10 nm to a few 10's-100 nm, and the subsequent growth saturation phase

[4]; 2) the particles initially nucleate around the plasma/sheath (P/S) boundary where radicals are generated actively [5]; 3) time evolution of spatial distribution of particle amount is very similar to those of short-lifetime SiH_2 radicals and their generation rates, and different from those of negatively charged species and SiH_3 's [5 - 7]; 4) the SiH_2 density is a low value of $\sim 10^9 \text{ cm}^{-3}$ in spite that they are considered to be generated at almost the same rate as that of SiH_3 's [5]; 5) a considerable proportion of particles of $\sim 10 \text{ nm}$ in size are electrically neutral; 6) with increasing the discharge frequency, the size growth rate of particles in the rapid growth phase decreases, while their density increases [4]. Based on a series of the results, we have proposed a coagulation model explaining reasonably the growth of particles above $\sim 10 \text{ nm}$ [2].

When we started to study particle formation in GeH_4 discharges, there were no reliable rate coefficients regarding dissociation of parent gas and reactions of generated radicals, while particles have been known to be generated in the discharges. We have employed the same methods for the particle growth observation as those for SiH_4 discharges and revealed the following facts [8, 9, 10]: the particles grow through the three growth phases similar to those for SiH_4 discharges, while its growth rate is rather fast compared to that for the SiH_4 ; the time evolution of spatial distributions of GeH_2 radicals are very similar to those of radical generation rate and particle amount and the GeH_2 density is a low value of $\sim 10^9 \text{ cm}^{-3}$, which is almost the same value as the SiH_2 density in SiH_4 discharges. From these studies, we have found that the growth processes for GeH_4 discharges are essentially similar to those for SiH_4 discharges.

While our studies on particle formation in SiH_4 and GeH_4 discharges are carried out fairly systematically, their focus has been placed mainly on the growth of particles above $\sim 10 \text{ nm}$ in size, because there is no method applicable in a size range below $\sim 10 \text{ nm}$. Recently, we have newly developed two *in situ* methods for observing the growth of such small particles (hereafter, the particles in the size range below $\sim 10 \text{ nm}$ are referred to as clusters) [11, 12, 13, 14]. These methods have made it possible to study the growth processes under the device quality low-power and low-pressure conditions and also to clarify which of short lifetime radicals (especially SiH_2 's) or SiH_3 's is important as key precursors for cluster nucleation [15].

Recently it has been pointed out that the decrease in output power of a-Si:H solar cells with time due to light soaking is closely related to polymerized species in HF SiH_4 discharges, which are considered to grow up to clusters. For commercial use of a-Si:H solar cells, the films must be deposited at a deposition rate high at least by one order of magnitude compared to the present one. Such high deposition rate is likely to generate many clusters. And also, it has been reported that the clusters may be applicable to various uses including fabrication of good quality solar cells [16, 17]. Thus, it is extremely important to develop a method for controlling the cluster growth.

We showed the periodical modulation of HF discharge was useful for suppressing particle growth, while the size range of detected particles was above a few 10 's nm and its suppression mechanism was not clear at that time [18]. Recently, we have studied the effect of discharge modulation on cluster growth and its growth suppression mechanism using the developed two methods. Further-

more, by using these methods, we have studied effects of substrate heating and hydrogen dilution, which are conventionally employed for making good-quality films, on the cluster growth [19].

In this paper, we present recent experimental results regarding the growth processes of clusters under the device quality low-power and low-pressure conditions and effects of discharge modulation, electrode heating and H_2 dilution on their growth, and then propose a cluster growth model for explaining reasonably a series of their results.

2. Experimental

A photon-counting laser-light-scattering (PLLS) method and a method combined threshold-photoemission method with microwave interferometry (TPE+MI method) have been developed for in situ observation of time evolution of cluster size and density in HF SiH_4 discharges. Since their principles have already been described in detail elsewhere, [10, 11, 12, 13] only brief explanation of them is given here.

For the PLLS method, the intensity signal of light scattered by laser-irradiated clusters (LLS intensity) is detected using a photon-counter. Just after the discharge is turned off (HF-off), the clusters which grow being localized around the P/S boundary diffuse and coagulate. When the increase in LLS intensity due to coagulation is dominant compared to the decrease in that due to diffusion, being true in a size range from a few nm to ~ 10 nm under our experimental conditions, the LLS intensity increases linearly with time. The density is deduced using this linear characteristic and the size deduced using this density value and an LLS intensity calibrated by Rayleigh scattering of nitrogen gas. This detection system is shown in Fig. 1(a) together with the HF discharge reactor. An Ar^+ laser of wavelength 488 nm was used as the light source for PLLS. The LLS intensity was detected with the system composed of a lens, monochromator with a photomultiplier, photon-counter and computer. In a stainless steel (SUS) vessel of 300 mm diameter, SUS electrodes of 100 mm diameter, the lower one of which was grounded, were placed at a separation of 45 mm. Discharge frequency and supplied power were 13.56 MHz and 8W (0.1 W/cm^{-2}) respectively.

For the TPE+MI method, the following two properties just after HF-off are utilized: the temperature of plasma electrons, T_e , is rapidly cooled down due to their collisions with neutral molecules and their attachment to clusters grown during the discharge period T_{on} is enhanced; the diffusion rate of clusters being localized around the P/S boundary depends on their size. The decay of electron density, n_e , due to the attachment is related to the cluster density by giving the attachment cross-section as a function of cluster size and T_e and also the change of T_e after HF-off as a function of time. Thus, if the n_e decay rate and the time evolution of T_e are given, the cluster density can be deduced. In our case, the time evolution of T_e was estimated assuming that electrons lose their energy due to elastic collisions with gas molecules and the n_e decay rate was measured experimentally. This method is applicable in a size range below a few nm, in which the diffusion is dominant compared to coagulation. The detection system

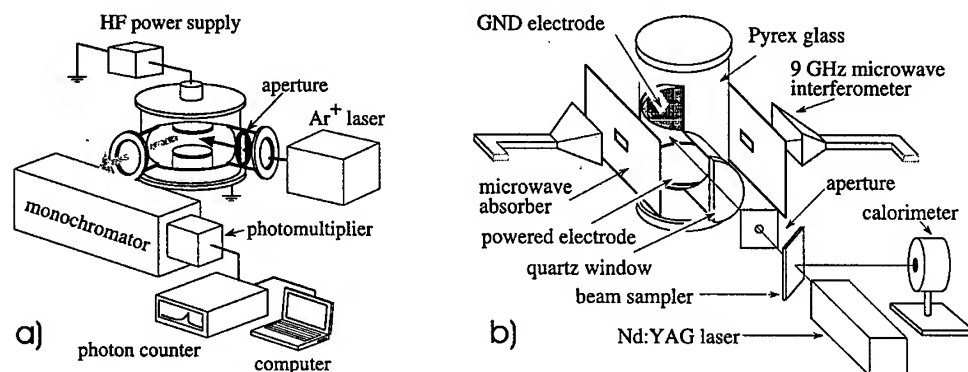


FIG. 1. Systems for observing time evolution of cluster size and density and HF discharge reactors: (a) PLLS method; (b) TPE+MI method.

is shown in Fig. 1(b) together with the HF discharge reactor. The third harmonics (355 nm) of Nd:YAG laser light (pulse energy 230 mJ and pulse duration 9 ns) was used as the light source to ionize clusters by two-photon process. The n_e decay due to the attachment and electrons emitted due to photo-ionization of clusters were detected using a 9 GHz microwave interferometer. The laser beam of 6 mm diameter was propagated parallel to electrode surfaces at 15 mm above the powered electrode, the position of which is in the cluster growth region around the P/S boundary. The microwave beam was also propagated, parallel to electrode surfaces and perpendicular to the laser beam, so that the cluster growth region was included inside the microwave beam. Discharge frequency and supplied power were 14 MHz and 10 - 40 W ($0.18 - 0.72 \text{ W/cm}^2$) respectively. SUS electrodes of 85 mm diameter were placed at a separation of 50 mm in a Pyrex glass vessel of 94.5 mm diameter. The lower electrode was grounded and the upper one was of mesh type.

3. Growth observation of clusters

The time evolution of cluster size and density in a size range below a few nm has been observed using the TPE+MI method. The result is shown as a function of discharge period T_{on} in Fig. 2 together with the volume fraction, which is defined as the volume occupied by clusters in unit volume [12, 13]. From our studies carried out until now, this T_{on} dependence of cluster size and density is found to correspond to their time evolution after the discharge initiation. The conditions for 10W are close to those of the device quality ones except that the grounded (GND) electrode is not heated. For this method, clusters above $\text{Si}_{5-6}\text{H}_x$ are detectable. In the figure, their growth below $\text{Si}_{5-6}\text{H}_x$ is assumed as shown by broken lines, taking into account that Si_2H_x 's are produced within an extremely short time by the fast reaction of SiH_2 with SiH_4 . The solid circle shows a size obtained using TEM observation. The clusters are found to grow to $\text{Si}_{5-6}\text{H}_x$ by 50 ~ 100 ms after the discharge initiation and to a few nm by ~ 0.5 s. The density of clusters increases up to a high value of $\sim 10^{11} \text{ cm}^{-3}$.

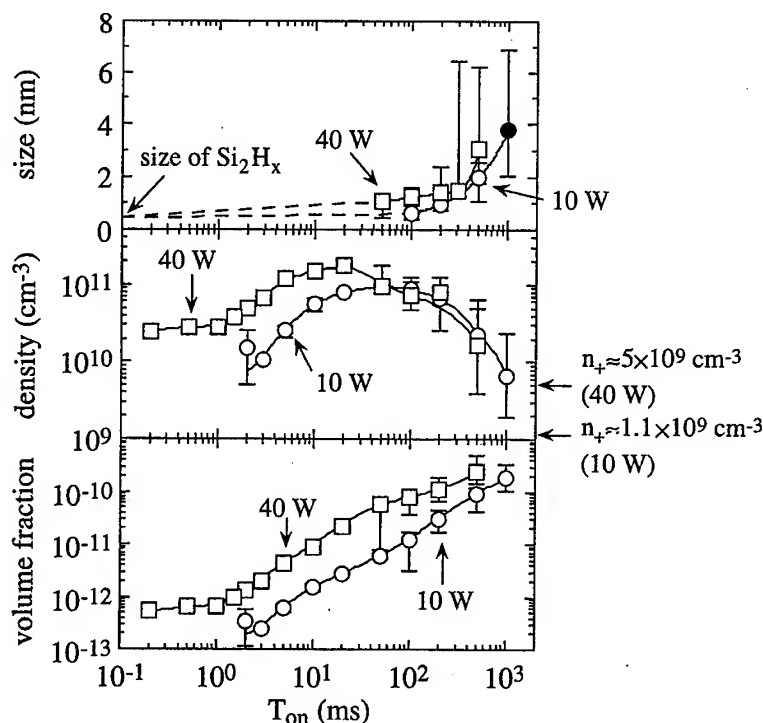


FIG. 2. Discharge period T_{on} dependence of size, density and volume fraction of clusters as parameter of supplied power under conditions of 100% SiH_4 , flow rates of 20 sccm (10 W) and 5 sccm (40 W), and pressure 13 Pa. Circles and squares show mean values for 10 and 40 W respectively. Solid circle for 10 W is mean size measured by TEM. Cluster densities for $T_{on} < 100$ ms (10 W) and $T_{on} < 50$ ms (40 W) are deduced assuming that sizes increase with T_{on} as shown by broken lines.

within 20 ~ 50 ms and then decreases due to coagulation between them. The volume fraction however increases monotonously during this period. This implies that, in the size range of interest, clusters mainly grow due to influxes of radicals and polymerized species (and/or smaller clusters) generated later than a time when they nucleated. The density value at a few nm size has been found to be consistent with that obtained by the PLLS method.

The result in Fig. 2 indicates that many neutral clusters exist around the P/S boundary even under the device quality low-power and low-pressure conditions, and hence a fraction of them may arrive at the substrate on the GND electrode. This suggests that the better quality a-Si:H films may be obtained by suppressing the cluster growth.

4. Growth model of clusters

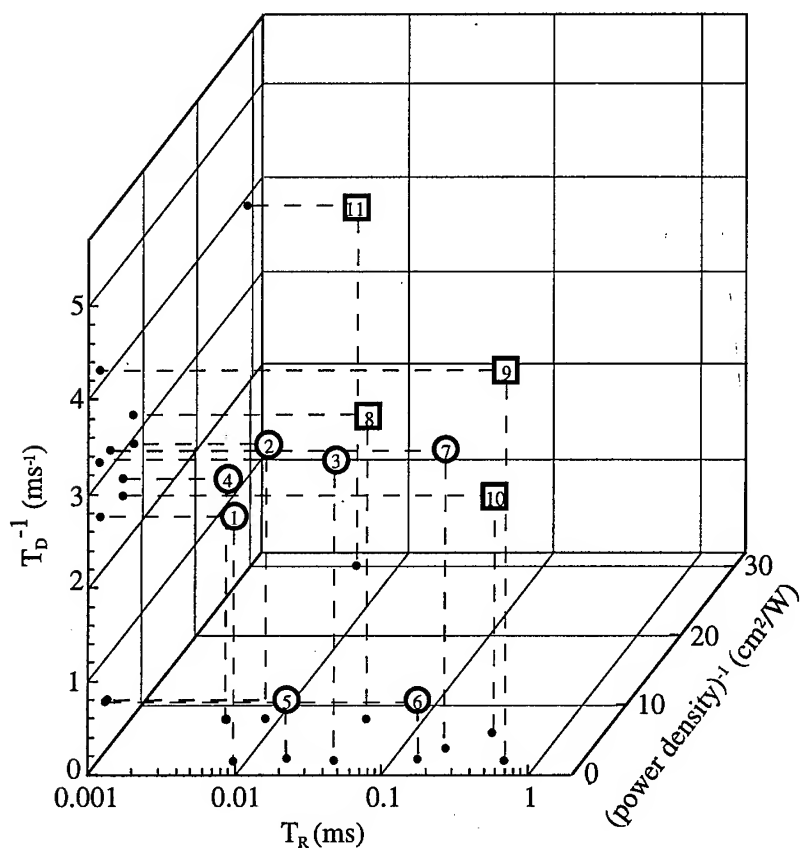
All the results described above and reported regarding the particle growth until now can be systematically understood using three parameters in the radical

generation region: generation rate of short lifetime SiH_2 's proportional to the supplied power; reaction rate for cluster growth initiated by SiH_2 's; loss rate of clusters due to diffusion. If SiH_2 's are supplied sufficiently and growth time of clusters is shorter than their diffusion time, then rapid cluster growth is observed in the radical generation region. If the supply of SiH_2 's is not sufficient or the growth time of clusters is longer than their diffusion time, then the growth of clusters becomes slow and, if a fraction of clusters diffused into plasma bulk are negatively charged, their growth would be observed even in there.

This model is supported by the experimental fact that there are two cases regarding particle growth. In one case, the growth of particles is observed only around the P/S boundary and the rapid growth phase begins at a short time of ~ 1 s after the discharge initiation. In the other case, their growth is observed in the plasma bulk as well as around the P/S boundary and the rapid growth phase begins at a time considerably long compared to ~ 1 s after the discharge initiation. We have classified these results using three parameters of supplied-power density, reaction time T_R of SiH_2 with SiH_4 , and diffusion time T_D of SiH_2 , which are important at the initial stage of cluster nucleation [20]. The result is shown in Fig. 3. In the case of high supplied power, short T_R and long T_D (shown by circles), the growth is observed only around the P/S boundary. On the other hand, when one of these parameter conditions is not satisfied (shown by squares), the growth is observed even in the plasma bulk. While negatively charged clusters are necessary for their growth in the bulk, they may originate not from negative SiH_3^- ions but from clusters diffused out of the radical generation region.

As described above, clusters grow rapidly in the radical generation region due to fast reactions such as the SiH_2 insertion reactions [21] initiated by that of SiH_2 with SiH_4 . Since SiH_4 's participate mainly in the initial reaction, their contribution to cluster growth is considered to be small compared to that of SiH_2 's. This suggests that the total number of SiH_2 's, $[\text{SiH}_2^{\text{total}}]$ generated until a time t after the discharge initiation should be close to the total number of atoms in all of clusters existing at the time t in the radical generation region. Hence, $[\text{SiH}_2^{\text{total}}]$ was calculated using rate equations concerning SiH_2 , SiH_3 and SiH_4 . In the calculation, the branching ratio for SiH_4 to be dissociated to SiH_2 and SiH_3 is necessary. This value was deduced using a reaction rate of SiH_2 with SiH_4 reported [22] and giving steady-state density values of SiH_2 and SiH_3 in their rate equations by those measured by the intra-cavity laser absorption method and estimated from a deposition rate of film on the substrate placed on the GND electrode, respectively [5]. The calculation result is shown in Fig. 4 [14]. As expected, the total number of Si atoms incorporated into clusters in the radical generation region is very close to the total SiH_2 's generated there.

While time evolution of their size and density is elucidated and clusters are found to grow due to fast successive reactions initiated by that of SiH_2 with SiH_4 and then due to influxes of radicals and polymerized species (and/or smaller clusters) generated later than a time when they nucleated, such successive reactions themselves are not clear yet.



- ① 10%SiH₄+Ar, 13 Pa, 0.51 W/cm².
- ② 10%SiH₄+Ar, 13 Pa, 0.13 W/cm².
- ③ 5%SiH₄+He, 80 Pa, 0.51 W/cm².
- ④ 50%SiH₄+Ar, 13 Pa, 0.13 W/cm².
- ⑤ 3%SiH₄+He, 80 Pa, 1.1 W/cm².
- ⑥ 0.5%SiH₄+He, 80 Pa, 1.1 W/cm².
- ⑦ 50%SiH₄+He, 10 Pa, 0.25 W/cm².
- ⑧ 1%SiH₄+Ar, 9 Pa, 0.51 W/cm².
- ⑨ 100%SiH₄, 13 Pa, 0.13 W/cm².
- ⑩ 1%SiH₄+Ar, 24 Pa, 0.015 W/cm².
- ⑪ 100%SiH₄, 13 Pa, 0.03 W/cm².

FIG. 3. Classification of particle growth region with parameters of supplied power density, reaction time of SiH₂ with SiH₄, T_R , and diffusion time of SiH₂, T_D . Open-circles and -squares show cases for which particles are observed around P/S boundary and in plasma bulk as well as around P/S boundary respectively.

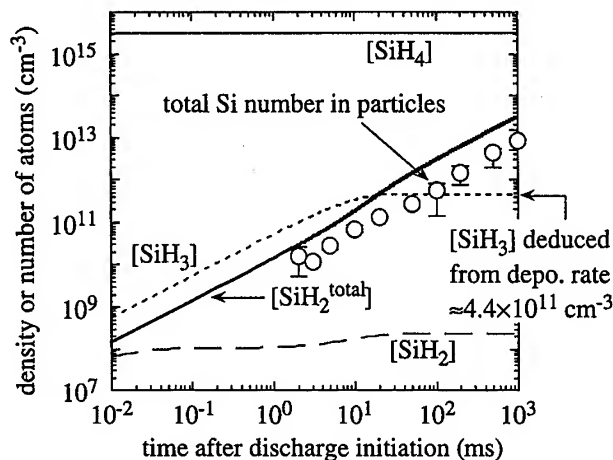


FIG. 4. Time evolution of SiH_x ($x = 2 - 4$) density, $[\text{SiH}_x]$, total number of SiH_2 's generated in radical generation region, $[\text{SiH}_2^{\text{total}}]$, and total number of Si atoms (circles) in clusters in unit volume under conditions of 100% SiH_4 , flow rate 20 sccm, pressure 13 Pa, and supplied power 10 W. Broken, dotted, thin solid and thick solid lines show $[\text{SiH}_2]$, $[\text{SiH}_3]$, $[\text{SiH}_4]$ and $[\text{SiH}_2^{\text{total}}]$ respectively.

5. Growth suppression of clusters

According to our proposed model, the growth suppression of clusters can be obtained by interruption of radical supply, transport of clusters by some force out of the radical generation region, and suppression of their growth reactions.

5.1. Modulation of HF discharge

For the discharge modulation of HF-on period, t_{on} , and HF-off period, t_{off} , the radical supply is stopped and the density of clusters in the radical generation region decreases due to diffusion during t_{off} . Their size becomes smaller with a shorter t_{on} , leading to their faster diffusion out of the radical generation region. We have studied the effect of discharge modulation on cluster growth as a function of t_{on} and a parameter of t_{on} using the TPE+MI method. The results are shown in Fig. 5 [13, 14]. In the experiments, the total discharge duration $\sum t_{\text{on}}$ was 100 ms independent of t_{on} . The density was measured just after the end of the last t_{on} period. For $t_{\text{off}} < 0.3$ ms, the densities for all t_{on} 's are close to that of the non-modulated discharge of $T_{\text{on}} = 100$ ms. For $0.3 \text{ ms} < t_{\text{off}} < 50$ ms, the density for a shorter t_{on} decreases more rapidly with t_{off} . For $t_{\text{off}} > 50$ ms, the density decreases to a smaller constant value for a shorter t_{on} , which is almost the same value as that for single discharge of duration t_{on} . This result suggests that for the discharge modulation, the density becomes low by one order of magnitude compared to that for the non-modulated discharge. This density decrease due to discharge modulation can be reasonably explained by the proposed model in the previous section. Fig. 6 shows the time evolution of the peak density

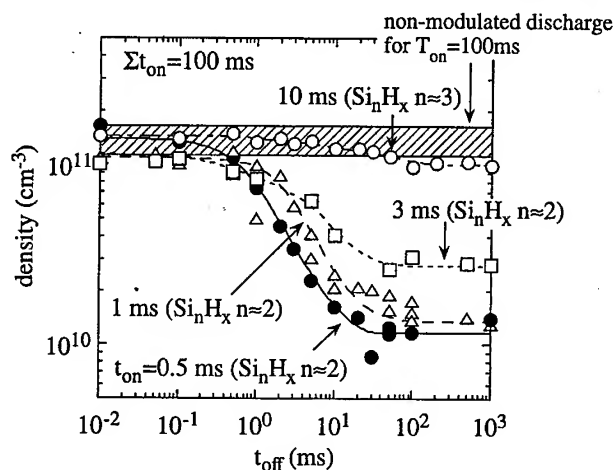


FIG. 5. Dependence of cluster density on t_{off} for $t_{\text{on}} = 0.5$ ms (solid circle), 1 ms (open triangle), 3 ms (open square), and 10 ms (open circle) under conditions of 100% SiH_4 , flow rate 5 sccm, and pressure 13 Pa. Shaded area indicates range of cluster density for non-modulated discharge of $T_{\text{on}} = 100$ ms.

values of Si_2H_4 , Si_3H_8 and Si_{10} species in the radical generation region due to their diffusion after the HF-off (From the results in Fig. 2, for a discharge duration below 50 ms, the cluster size is estimated to be smaller than Si_{10}H_x). In the calculation, a FWHM of radical generation region was assumed to be 10 mm, which is equal to that of the spatial profile of SiH-emission intensity. As can be seen, a time after HF-off when the density decreases appreciably (for example, decreases to one third of the density at the end of HF-on) is quite close to a time when the density decreases greatly with t_{off} in Fig. 5.

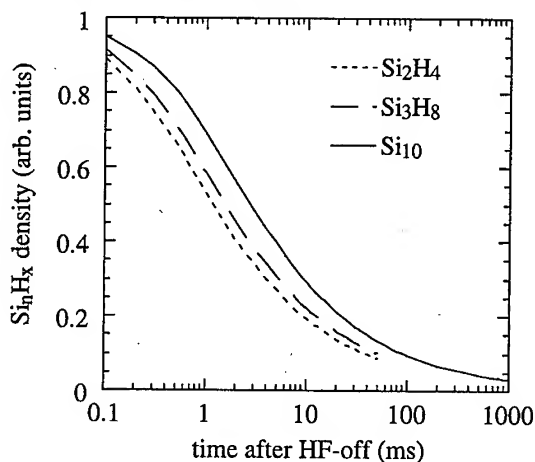


FIG. 6. Time evolution of peak densities of Si_2H_4 , Si_3H_8 and Si_{10} in radical generation region after HF-off under conditions of 100% SiH_4 and pressure 13 Pa.

5.2. Heating of GND electrode

When preparing the device-quality a-Si:H films, the substrate on the GND electrode is usually heated to about 250°C . In our experiments, the effect of substrate heating on the cluster growth was studied by heating the SUS GND electrode without the substrate (the powered electrode was also made of SUS). Fig. 7 shows spatial distributions of LLS intensities (number of photons per second) be-

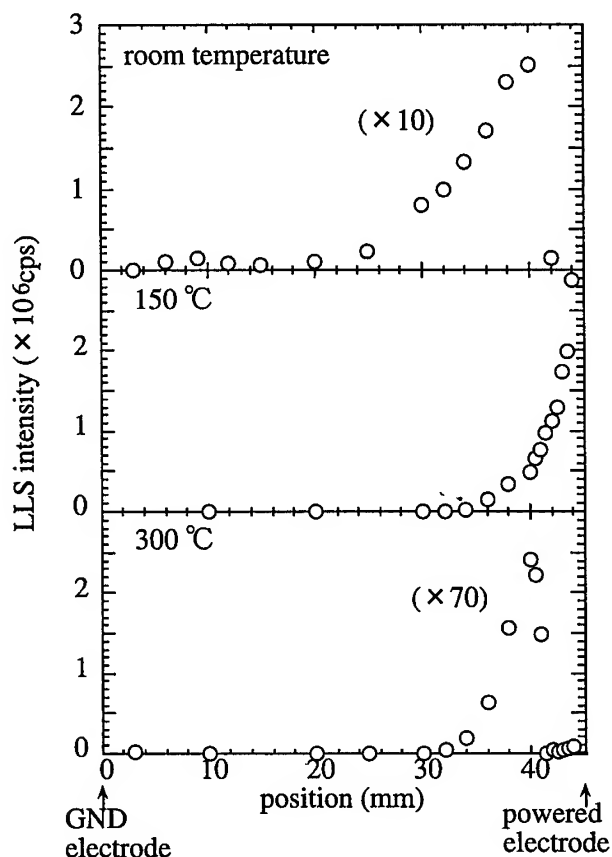


FIG. 7. Spatial distributions of LLS intensity for T_G = room temperature, 150°C and 300°C under conditions of 100% SiH_4 , flow rate 5 sccm, pressure 13 Pa, supplied power density 0.1 W/cm^2 (8 W), and $T_{on} = 0.8 \text{ s}$.

tween electrodes as a parameter of GND electrode temperature T_G [19]. A size of clusters of interest is in a few to several nm range. For T_G = room temperature, the LLS intensity is the highest around the P/S boundary near the powered electrode. For $T_G = 150^{\circ}\text{C}$, its peak position shifts toward the powered electrode. For $T_G = 300^{\circ}\text{C}$, the intensity is very low compared to those for the other two cases and its peak is located again around the P/S boundary. This means that a large proportion of clusters are driven toward the powered electrode and the rest exist around the P/S boundary. While not shown here, the result similar to

that for $T_G = 300^\circ\text{C}$ has been obtained for $T_G > 200^\circ\text{C}$ [19].

When gas between the electrodes is heated, the growth of clusters has been known to be suppressed due to the decreases in SiH_4 density and/or in rates of reactions related to cluster growth [23]. However, the result in Fig. 7 can not be explained by these effects, because the sharp change in LLS intensity is observed only around the cold powered electrode. The phenomenon of interest can be explained taking into account the thermophoresis [24]. As has been shown, the clusters, a large proportion of which are neutral, tend to grow being localized around the P/S boundary and hence to diffuse out of the P/S boundary region due to their pressure. Since the thermophoretic force due to GND electrode heating is proportional to the second power of cluster size and to the temperature gradient, and acts toward the powered electrode, it can drive the clusters above a critical size toward the powered electrode for a given temperature gradient. To see this, the thermophoretic forces for $20^\circ\text{C}/\text{cm}$ ($T_G = 90$) and $50^\circ\text{C}/\text{cm}$ ($T_G = 225^\circ\text{C}$) were compared with the pressure gradient of clusters existing in the radical generation region of 10 mm in width. The calculation result is shown in Fig. 8. As can be seen, the thermophoretic force dominates the pressure

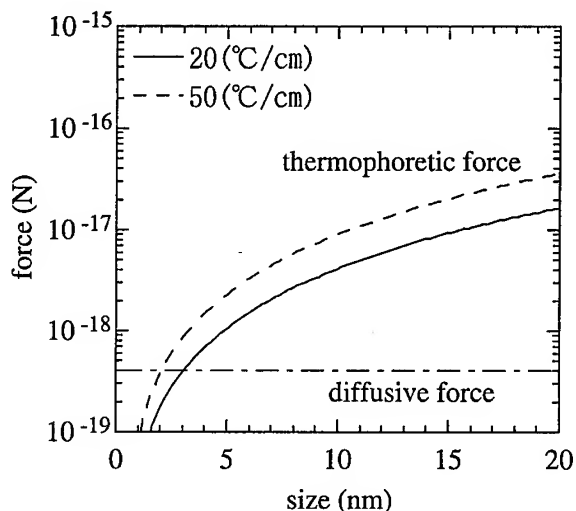


FIG. 8. Comparison of thermophoretic force with pressure gradient of clusters (diffusive force) as function of size for temperature gradients of 20 and 50 $^\circ\text{C}/\text{cm}$.

gradient in a size range above a few nm. Electrically neutral clusters above a few nm in size can be driven toward the powered electrode through the sheath due to the thermophoresis, leading to the shift of peak-density position as shown in Fig. 7. The clusters around the P/S boundary for $T_G = 300^\circ\text{C}$ are a fraction of negatively charged ones being trapping there, because a density of clusters at the peak intensity is estimated to be 10^{8-9}cm^{-3} , almost equal to that of plasma ions. As shown in Fig. 7, the LLS peak intensity for $T_G = 150^\circ\text{C}$ is high compared to that for $T_G = \text{room temperature}$. This phenomenon can be explained taking into account both the suppression of cluster diffusion toward the plasma bulk due to the thermophoresis and coagulation enhancement due to

ionization of clusters by high energy electrons in the sheath region [19].

Combination of this electrode heating with the discharge modulation is extremely effective in suppressing cluster growth. Fig. 9 shows the cluster growth time, which is defined as a time when the photons detected by the PLLS method becomes 10^3 cps, as a function of t_{off} for $t_{on} = 5\text{ ms}$ and $T_G = 200^\circ\text{C}$ under low-power and low-pressure conditions [19]. The value of 10^3 cps correspond to a density of $\sim 10^8\text{ cm}^{-3}$ for clusters of several nm in size. As can be seen, any clusters can not be detected over one hour for $t_{off} = 3\text{ ms}$, that is, a duty cycle of 63%.

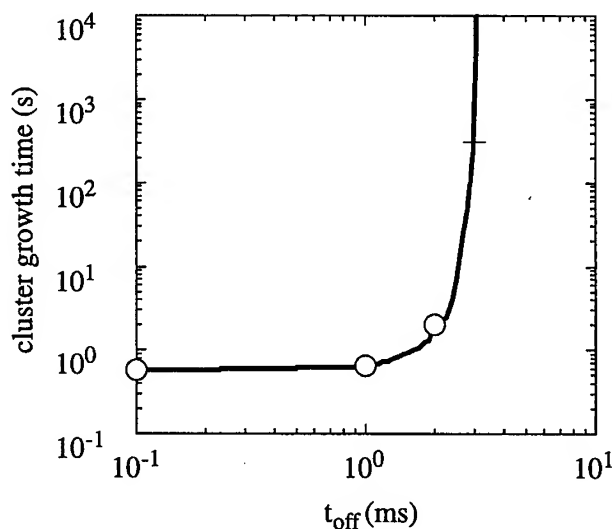


FIG. 9. Cluster growth time as function of t_{off} for discharge modulation under conditions of $T_G = 200^\circ\text{C}$, $t_{on} = 5\text{ ms}$ 100% SiH_4 , flow rate 5 sccm, pressure 13 Pa, and supplied power density 0.1 W/cm^2 (8 W).

5.3. H_2 dilution of SiH_4

Dilution of H_2 gas has been employed to prepare high-quality a-Si:H films. We studied its effect on cluster growth as a parameter of H_2 partial pressure. The result for $T_G = \text{room temperature}$ and a SiH_4 partial pressure of 13 Pa is shown in Fig. 10 [19]. With increasing the H_2 partial pressure, the ratio between LLS intensities near the GND and powered electrodes becomes large. Especially, the LLS signal is observed only on the GND electrode side for a 80% H_2 . While this phenomenon is not understood yet, it is hard to explained by contribution of non-excited H_2 molecules to suppression of cluster growth reactions and also by the change of discharge parameters due to H_2 dilution. The spatial profile of light intensity of SiH radicals indicating that of radical generation rate has a peak at around the P/S boundary near the powered electrode. The species such as H atoms and/or excited H_2 molecules, which are generated more actively around the P/S boundary near the powered electrode rather than the GND

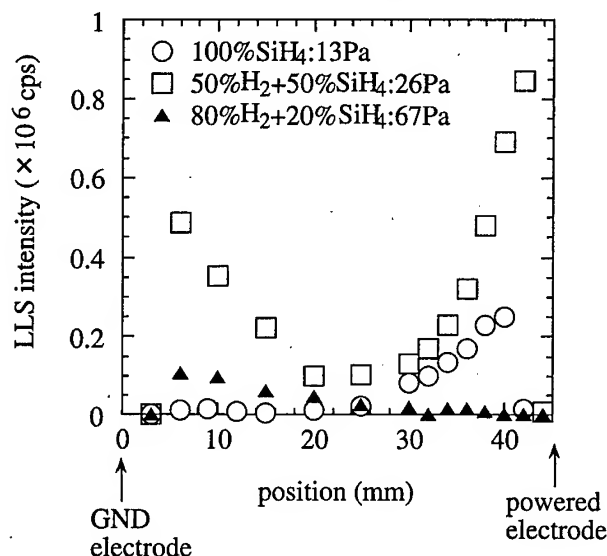


FIG. 10. Spatial distributions of LLS intensity as parameter of H_2 dilution rate under conditions of flow rate 25 sccm, pressure 67 Pa, and supplied power density 0.1 W/cm^2 (8 W).

electrode, are considered to play an important role in this phenomenon. The GND electrode heating is also quite effective in transporting clusters toward the powered electrode. For $T_G > 200^\circ\text{C}$, the growth of clusters around the GND electrode are effectively suppressed and only a small amount of clusters are observed around the P/S boundary near the powered electrode for the 80% H_2 dilution case (not shown here).

6. Conclusions

The two methods recently developed for in situ observation of cluster growth processes in HF discharges have brought about great progress in understanding their overall growth kinetics. The clusters initiated by the fast reactions of short lifetime SiH_2 's grow due to influxes of radicals and polymerized species (and/or smaller clusters), generated later than a time when they nucleated, and then do due to their coagulation. The density of clusters amounts to $\sim 10^{11} \text{ cm}^{-3}$ within $\sim 50 \text{ ms}$ after the discharge initiation and their size grows to a few nm within $\sim 0.5 \text{ s}$ after the discharge initiation even under the device quality low-power and low-pressure conditions. The proposed cluster growth model explains reasonably the results obtained in our present experiments. While our present studies have been carried out using SiH_4 discharges, the knowledge on cluster growth obtained here is considered to be applicable for GeH_4 discharges.

The growth of clusters can be controlled by interruption of SiH_2 supply, suppression of their growth reaction and enhancement of their loss due to diffusion and some driving force. The modulation of HF discharges is useful to decrease

their density by about one order of magnitude. The substrate heating is considerably effective in driving particles above a few nm toward the cold powered electrode. The dilution of H₂ gas is also quite effective in suppressing cluster growth reactions, while its detailed mechanism is not clear yet.

Acknowledgments

Our research was partly supported by a grant-in-aid for Scientific Research from the Ministry of Education, Science, Sports and Culture. We would like to acknowledge the assistance of Messrs. T. Kinoshita, S. Maeda, and Y. Matsuoka who contributed greatly to the execution of experiments.

References

1. Y. WATANABE, M. SHIRATANI and M. YAMASHITA, *Appl. Phys. Lett.*, **61**, 91, 1992.
2. M. SHIRATANI, H. KAWASAKI, T. FUKUZAWA, T. YOSHIOKA, Y. UEDA, S. SINGH and Y. WATANABE, *J. Appl. Phys.*, **79**, 104, 1996.
3. M. SHIRATANI, H. KAWASAKI, T. FUKUZAWA and Y. WATANABE, *J. Vac. Sci. Technol.*, **A14**, 603, 1996.
4. Y. WATANABE, M. SHIRATANI, H. KAWASAKI, S. SINGH, T. FUKUZAWA, Y. UEDA and H. OKURA, *J. Vac. Sci. Technol.*, **A14**, 540, 1996.
5. Y. WATANABE, M. SHIRATANI, T. FUKUZAWA, H. KAWASAKI, Y. UEDA, S. SINGH and H. OKURA, *J. Vac. Sci. Technol.*, **A14**, 995, 1996.
6. T. FUKUZAWA, H. KAWASAKI, M. SHIRATANI and Y. WATANABE, *Jpn. J. Appl. Phys.*, **33**, 4212, 1994.
7. H. KAWASAKI, H. OKURA, T. FUKUZAWA, M. SHIRATANI, Y. YAMAMOTO, S. SUGANUMA, M. HORI and T. GOTO, *Jpn. J. Appl. Phys.*, **36**, 4985, 1997.
8. H. KAWASAKI, J. KIDO, K. SAKAMOTO, T. FUKUZAWA, M. SHIRATANI and Y. WATANABE, *J. Appl. Phys.*, **83**, 5665, 1998.
9. H. KAWASAKI, J. KIDO, K. AKAMOTO, T. FUKUZAWA, M. SHIRATANI and Y. WATANABE, *Jpn. J. Appl. Phys.*, **37**, L475, 1998.
10. H. KAWASAKI, K. SAKAMOTO, S. MAEDA, T. FUKUZAWA, M. SHIRATANI and Y. WATANABE, *Jpn. J. Appl. Phys.*, **37**, L1264, 1998.
11. H. KAWASAKI, K. SAKAMOTO, S. MAEDA, T. FUKUZAWA, M. SHIRATANI and Y. WATANABE, *Proc. 4th Int. Conf. on Reactive Plasmas*, Maui, Hawaii, 59, 1998.
12. M. SHIRATANI, T. FUKUZAWA and Y. WATANABE, *Jpn. J. Appl. Phys.*, **38**, No.7B, 1999 (in press).
13. T. FUKUZAWA, S. KUSHIMA, Y. MATSUOKA, M. SHIRATANI and Y. WATANABE, *Proc. 4th Int. Conf. on Reactive Plasmas*, Maui, Hawaii, 67, 1998.
14. T. FUKUZAWA, S. KUSHIMA, Y. MATSUOKA, M. SHIRATANI and Y. WATANABE, to be published in *J. Appl. Phys.*
15. Ch. HOLLENSTEIN, J.-L. DORIER, J. DUTTA, L. SANSONNENS and A. A. HOWLLING, *Plasma Sources Sci. Technol.*, **3**, 278, 1994.
16. E. BERTRAN, S. N. SHARMA, G. VIERA, J. COSTA, P. ST'ACHEL and P. R. I. CABARROCAS, *J. Materials Res.*, **13**, 2476, 1998.
17. Y. WATANABE, *Plasma Phys. Control. Fusion*, **39**, A59, 1997.
18. Y. WATANABE, M. SHIRATANI, Y. KUBO, I. OGAWA and S. OGI, *Appl. Phys. Lett.*, **53**, 67, 1988.

19. M. SHIRATANI, K. SAKAMOTO, S. MAEDA, K. KOGA and Y. WATANABE, to be submitted to Jpn. J. Appl. Phys.
20. H. KAWASAKI, K. SAKAMOTO, S. MAEDA, T. FUKUZAWA, M. SHIRATANI and Y. WATANABE, Jpn. J. Appl. Phys., **37**, 5757, 1998.
21. A. MATSUDA, J. Vac. Sci. Technol. A, **16**, 365, 1998.
22. H. NOMURA, K. AKIMOTO, A. KONO and T. GOTO, J. Phys. D: Appl. Phys., **28**, 1977, 1995.
23. L. BOUFENDI, J. HERMANN, A. BOUCHOUL, B. DUBREUIL, E. STOFFELS, W. W. STOFFELS and M. L. DE GIORGI, J. Appl. Phys., **76**, 148, 1994.
24. G. M. JELLUM, J. E. DAUGHERTY and D. B. GRAVES, J. Appl. Phys., **69**, 6923, 1991.

LASER-PRODUCED PLASMA AS AN EFFECTIVE SOURCE OF MULTICHARGED IONS

E. WORYNA¹, J. KRÁSA², L. LÁSKA², K. MAŠEK², P. PARYS¹, K. ROHLENA²,
J. WOŁOWSKI¹

¹INSTITUTE OF PLASMA PHYSICS AND LASER MICROFUSION

00-908 Warsaw, P.O. Box 49, 23 Hery St., Poland

²INSTITUTE OF PHYSICS, ACADEMY OF SCIENCES OF THE CZECH REPUBLIC

182 21 Prague 8, Na Slovance 2, Czech Republic

Properties of expanding laser plasma as a source of highly charged, energetic ions are discussed. A possibility to use sub-nanosecond near-infrared systems as driving lasers of the ion source is highlighted. Experimental data characterising the laser driven ion source performance are presented. A physical interpretation of experimental findings is outlined.

1. Introduction

Studies and applications of ion sources have a long history. To name but a few application fields e.g. high energy physics, nuclear and atomic physics, heavy ion fusion, probe beams for analytical purposes (Rutherford back-scattering, RBS or secondary ion mass spectrometry, SIMS), laser mass spectrometry, nanometer structure fabrication, ion beam lithography, semiconductor doping, ion implantation, surface treatment, neutral beam injection, radiation therapy etc. are worth mentioning. All of these applications are dependent on the use of an ion beam and, consequently, on its technology, which may vary widely in complexity, in dependence on the method used to produce the beam of desired ion composition with a required intensity and energy. There is a broad variety of ion sources, the most prominent among them being electron beam ion source (EBIS), electron cyclotron resonance source (ECR) or laser ion source (LIS), [1].

Since the first experiments on laser interaction with matter it has become clear that the expanding laser plasma is a very efficient source of ions. Construction of new accelerators of heavy ions and the demand for new ion implantation techniques have in recent years revived interest in production of multiply charged ions [2]. It has been demonstrated [3, 4] and generally accepted that the LIS can produce by one to two orders of magnitude higher ion current densities as well

as higher ion charge states than the ECR ion source, which is presently favoured for its technological standard.

Besides the necessity for high yield ion sources to inject the modern accelerators a small scale application of laser ion sources covers the field of ion implantation. The ions emanating from an expanding laser plasma are both highly charged and accelerated, which favours their interaction with the solid substrate. An additional acceleration is also possible and plans are underway to implement this new technological method for a friction control in steels [2] or for a treatment of textile tissue materials. Conversely, the implanted substrate, if analysed by the methods of material analysis such as RBS, can render an independent evidence about the properties of the ion source itself.

The paper summarizes the results of investigations of physical properties of ion streams emitted from the plasma of medium and high atomic number elements produced with the short wavelength ($\leq 1 \mu\text{m}$) and short pulse ($\leq 1 \text{ ns}$) lasers at power densities of $10^{13} \div 10^{15} \text{ W/cm}^2$. The main goal of our studies was to find optimum conditions in which the laser produced plasma can be used as a stable pulsed source of highly ionised ions for various applications.

2. Experimental

2.1. Ion diagnostics for laser produced plasma

The principal diagnostic techniques for studying the laser produced ions are based on the time-of-flight method (TOF) [5]. This method is correct in the case when $t \gg \tau$ and $L \gg r$, where: t is the time of flight of the ions passing the distance L from the laser focal spot (target) to the detector, τ is the laser pulse duration and r is the radius of the laser focal spot. In our experiments we used ion collectors, a cylindrical electrostatic ion energy analyser (IEA) and a Thomson mass-spectrograph (TS). The collectors utilize the TOF effect only, the IEA combine the TOF with the action of imposed electric field, the TS utilise the action of parallel electric and magnetic fields on the ions passing through them, respectively.

For the case of IEA the relation connecting the measured voltage on the load resistance, U_z for given charge state z , and the ion rate reaching the detector (windowless electron multiplier EM) input slit dN_z/dt is:

$$(2.1) \quad i_z = ez dN_z/dt = U_z(t)/\delta \mathcal{G}_c(z, t) R_{load}$$

where δ ($\delta = 10^{-2}$) is the transmittance of the IEA used, \mathcal{G}_c is the current gain of EM, R_{load} is the load resistance. By repeating the shots with the analyser voltage changing the dual charge-energy spectrum can be found. The knowledge of the current gain \mathcal{G}_c makes possible absolute measurements of ion currents of different ion species for which the EM is calibrated. Calibration of multipliers used in our experiments, namely determination of their current gains as a function of ion kinetic energy and charge, was performed by using beams of Ta ions generated by the Kansas State University Cryogenic Electron Beam Ion Source (KSU-CRYEBIS) [6].

The ion probes are plane collectors or Faraday cups with a wire mesh at the entrance for ion and electron component separation. The ion current measured by the collector is affected by the secondary ion-electron emission. The ion current, I_{coll} or the time derivative of the ion charge, dQ/dt at the entrance aperture mesh for a given moment of time t is [5]:

$$(2.2) \quad I_{coll} = dQ/dt = U_c(t)/\mathcal{E}R_{load}[1 + \bar{\gamma}(t)/\bar{z}(t)]$$

where U_c is the voltage amplitude of collector signal, \mathcal{E} is the transparency of the entrance mesh, $\bar{\gamma}$ and \bar{z} are the average secondary ion-electron emission coefficient and average charge state of ions.

From equation (2.2) the velocity, dQ/dv and energy, dQ/dE , distributions of the ion charge can be obtained; and by integrating them it is possible to calculate the total charge (or the total number of ions) and the total energy carried by the ions as well as the mean ion energy, \bar{E} . Taking into account the average charge state of ions from the IEA measurements and the mean ion energy of plasma from the ion collector measurements, the electron temperature $T_{e,0}$ and the average charge state \bar{z}_0 in the region of interaction of laser radiation with the plasma can be estimated. From the relation connecting the mean energy of the arriving ions with $T_{e,0}$ and \bar{z}_0 , $\bar{E} = C(\bar{z}_0 + \alpha)T_{e,0}$ and the relation $\bar{z}_0 = \bar{z}_0(T_{e,0})$ [7, 8, 9] one can estimate $T_{e,0}$ and \bar{z}_0 . The C factor ($C = 3.33 \div 5$) depends on the accepted model of plasma expansion and $\alpha = T_i/T_e$ is the temperature ratio.

Another important tool of ion diagnostics is the Thomson mass spectrograph (TS), which supplies information on both the ion charge as well as the energy distribution in a single shot. This is achieved, however, partially at the cost of resolution, especially, in the interesting region of high charge states and high energies of ions [10, 11].

2.2. Experimental

The experiments used the laser systems at the Institute of Physics ASCR in Prague and at the Institute of Plasma Physics and Laser Microfusion in Warsaw. The photodissociation iodine laser PERUN in Prague operates at the wavelength $\lambda = 1.315 \mu m$ and with the maximum output energy $E_L = 50$ J in 500 ps laser pulses [12]. The diameter of the focal spot was about $100 \mu m$, the power density on the target was thus $\leq 10^{15}$ W/cm². Frequency conversion by DKDP crystals to 2ω and 3ω is available with about 50% efficiency. The chamber was fitted either with an aspherical ($f = 20$ cm) lens or alternatively with a parabolic mirror ($f = 28.5$ cm) having a 14 mm hole in the centre to allow access to the part of the plasma expanding directly against the laser beam (Fig. 1).

The Nd:glass laser in Warsaw gives a maximum energy of 15 J at $1.06 \mu m$ in 1 ns pulses. The spot size with lens optics is about $100 \mu m$ with the power density on the target $\leq 10^{14}$ W/cm². Besides the aspherical focusing lens a combination of an aspherical lens with an ellipsoidal mirror also with a central hole was used [13].

Two types of ion collectors of different construction were used: the standard flat circular collectors and the ring ion collector. The last one allowed to measure the ion stream close to the axis of the IEA.

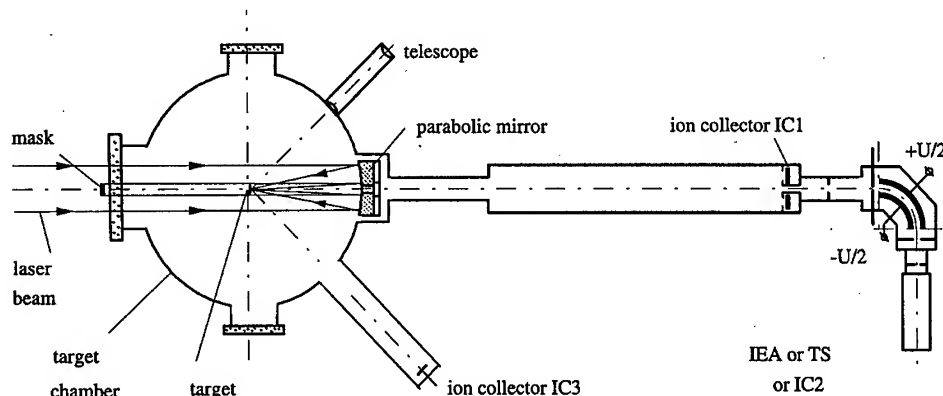


FIG. 1. Scheme of the experiment with the mirror focusing system.

The IEA had a bending radius of $R_0 = 10$ cm, the deflection angle $\Psi = 90^\circ$ and the gap between the cylindrical electrodes was $\Delta R = 0.5$ cm. The width of input and output slits of the IEA were $150 \mu\text{m}$ (or $200 \mu\text{m}$) and 1 mm, respectively. The path of ion flight L was typically varied from 94 cm to 210 cm for the IC. In the experimental system in Prague both the IEA and one of the ion collector (IC1) were positioned at 40° with respect to the incident laser beam. As the tilt angle of the target was 30° , ion signals were registered at 10° with respect to the target normal. Thick slabs of medium and high- Z metals (Co, Ni, Cu, Ag, Sn, Ta, W, Pt, Au, Pb and Bi) were used as targets. To make the evaluation of the experimental spectra easier and to help further data processing a computer code WELAN was developed [14].

3. Results

The IC measures the time resolved signal of the ions, from which the charge carried by ions as well as the ion energy can be derived. The IEA helps to identify the ion species produced, their energy and abundance. An ion collector signal with the record of IEA spectra in two different time-scales is presented in Fig. 2. In general, the structure of collector signals points to the existence of two

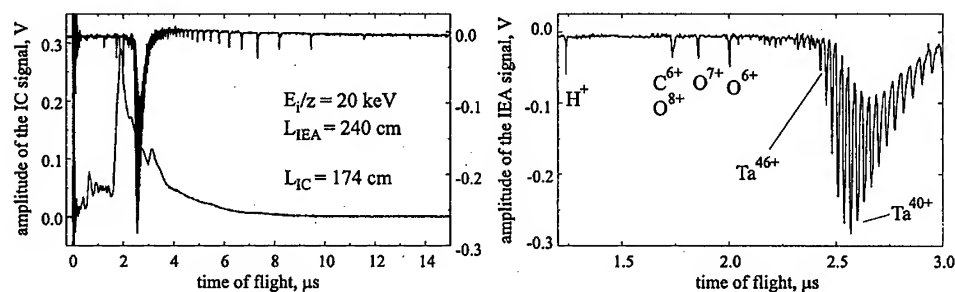


FIG. 2. IC and IEA records for Ta.

or, in some cases, of more ion groups. The faster one, if analysed by the IEA, is found to be composed of high charge state Ta ions and of light contamination ions (H, C and O). The ion collector signal if combined with the record of ion spectra from the IEA opens the possibility of calculating the total number of highly charged ions with $z = 35 - 44$ in the fast group. The mean current density of this group of ions is 6.4 mA/cm^2 at a distance of 94 cm from the target. The peak current density was about 12.8 mA/cm^2 . With an ion pulse duration of about $1.4 \mu\text{s}$, the number of particles arriving at the collector aperture of 1 cm^2 is $N_i \sim 1.4 \times 10^9$ per one laser shot. The latest experiments confirmed the presence of ions with charge states up to $55+$. The estimates of electron temperature $T_{e,0} = 1.7 \text{ keV}$ and of average charge state of ions $\bar{z}_0 \sim 50$ in the focal spot were derived from these data. The charge state-ion energy diagrams (Fig. 3), abundance of ion species (Fig. 4), and average charge state of ions as a function of ion energy (Fig. 5) were determined from a set of measurements for different values of IEA voltage.

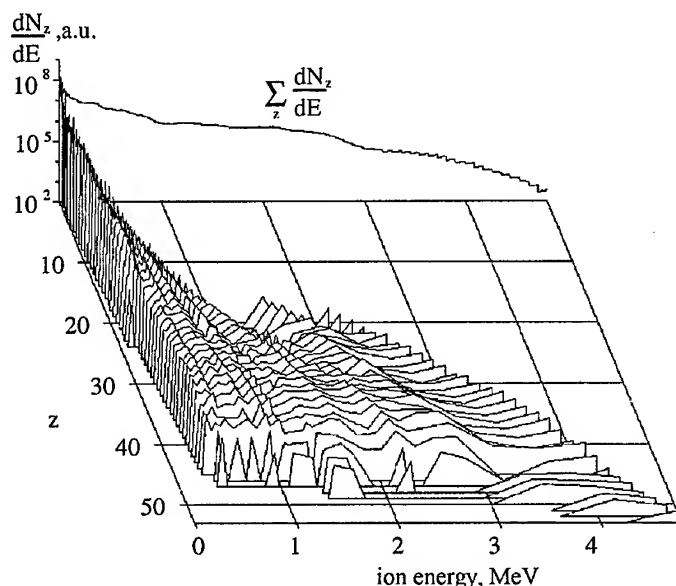


FIG. 3. Charge-energy spectrum of Ta ions. Iodine laser, 1ω , 29.1 J, distance of 205 cm from the target, 10° with respect to the target normal.

The experiments were performed at three laser frequencies 1ω (fundamental frequency), 2ω and 3ω , with the laser pulse energy from about 5 to 40 J. Owing to the varying laser pulse lengths and different focal positions the reduced power density, $I\lambda^2$, varied from $5 \cdot 10^{13} \text{ W}\mu\text{m}^2/\text{cm}^2$ to $1.5 \cdot 10^{15} \text{ W}\mu\text{m}^2/\text{cm}^2$.

The charge state, the ion energy, the ion current density together with its angular distribution in space were the basic parameters of our interest. The generation of the Ta ions with the charge states higher than $45+$ were found to be independent of laser wavelength within a relatively broad range of laser energies. Maximum charge state z_{max} as well as the maximum ion energy E_{max} ,

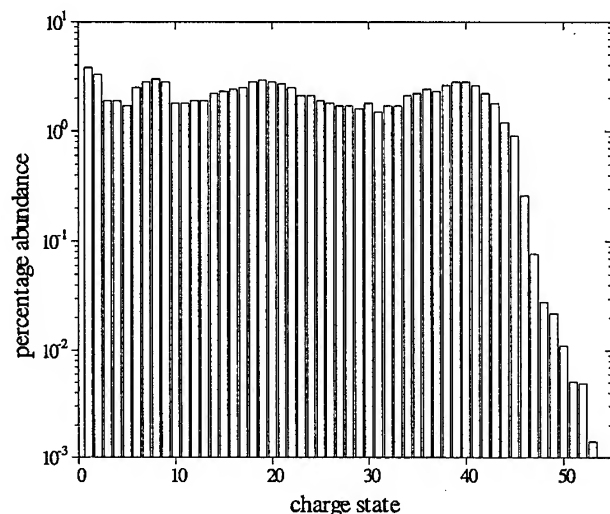


FIG. 4. Relative abundances of Ta ion species (parameters of Fig. 3).

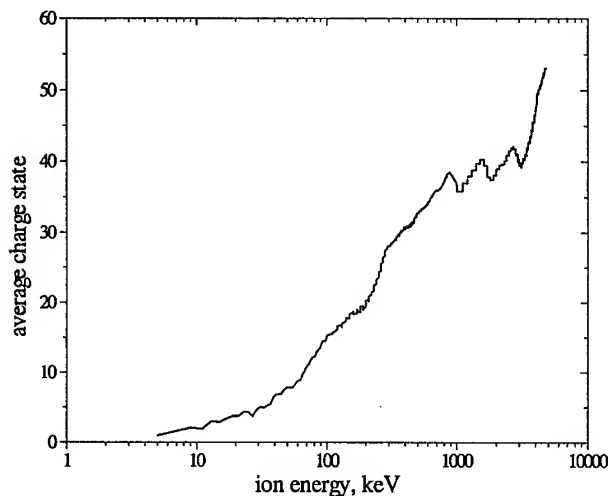


FIG. 5. Average charge of Ta ion species versus ion energy (parameters of Fig. 3).

increases with laser power density, however, the former dependence is less pronounced, Fig. 6. We varied the focal position versus the target surface, the target tilt angle with respect to the laser beam, the laser energy and wavelengths to achieve the maximum current of the highly charged ions. The ion yield depends strongly on the focus position with respect to the target surface. The maximum charge state of ions is less dependent on the focus setting than the IC current. The Ta ions with the charge states above 45+ were registered even with the focus position in a range of about $\pm 500 \mu\text{m}$ from the optimum one (for maximum ion current), but the maximum amplitude of the IC signal decreased several times over that range. The optimum focus position means that the laser focus is to be

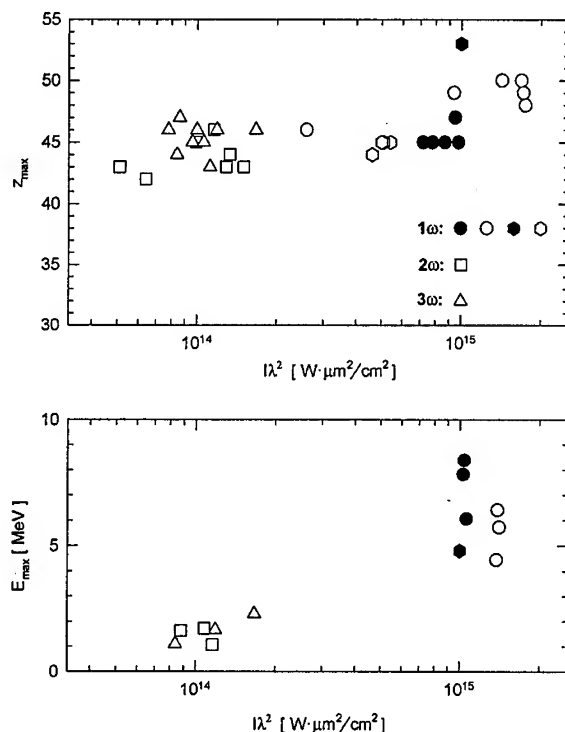


FIG. 6. The dependence of maximum attainable charge and of maximum ion kinetic energy on a reduced intensity for Ta ions.

about 125 μm in front of the target surface (Fig. 7). A brief physical characterization of the fast ion group for the iodine laser case and for different target materials is given by Table 1. M and L stands for the mirror or lens focusing system. The second column gives the average (maximum) charge states of the fast ion group. $\langle E_{\text{fast}} \rangle$ is the average energy of the fast ion group, A is the atomic mass, [u] is the atomic mass unit.

Table 1. Characteristics of the fast ion group for the 1 ω iodine laser case and for different target materials.

Elem.	$\langle z_{\text{fast}} \rangle$	$\langle E_{\text{fast}}/A \rangle [\text{keV}/u]$	$j [\text{mA}/\text{cm}^2]$
Co (M)	22 (25)	32.7	14.2
Ni (M)	20 (26)	15.7	18.5
Cu (L)	(25)		
Ta (L)	(55)		12.8
Ta (M)	42 (48)	12.7	22.8
W (M)	45 (49)	10.9	22.8
Pt (M)	40 (50)	15.9	12.8
Au (M)	38 (49)	15.7	7.0
Pb (M)	40 (51)	15.9	8.5
Bi (M)	40 (51)	12.9	10.0

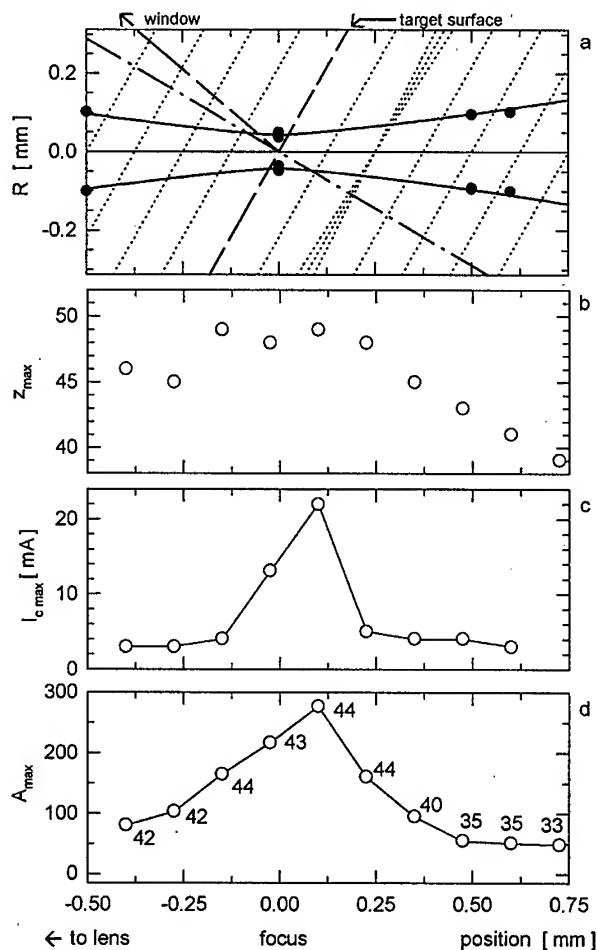


FIG. 7. The caustic of the laser beam (a), the maximum charge state (b), ion current from IC (c) as well as the maximum amplitude of ions (registered by means of the IEA) (d), as a functions of the focus position with the respect to the Ta target surface.

4. Discussion

4.1. Physical processes

The laser radiation is absorbed mainly in the vicinity of the critical surface either due to the classical absorption (inverse Bremsstrahlung) or due to a non-classical absorption (resonant absorption, parametric instabilities). It is well known that in the plasma the non-classical absorption gives birth to a population of suprathermal hot electrons. As a result of this at least two groups of ions (thermal and fast) are emitted from the plasma. The ions are gaining their energy during the heating stage of the plasma formation (isothermal expansion), which is followed by a large scale adiabatic expansion into the vacuum. More

energetic fast ions are accelerated in the space charge field set up by the hot electrons leaving the plasma corona and pulling the ions behind them.

A part of the X-ray radiation emitted by the hot plasma is once again re-absorbed by the target surface in the immediate vicinity of the primary laser focus where it together with the hot electrons and the outward propagating shockwave creates a dense, but colder plasma emitting, in addition, a slow groups of ions. The experimental investigations [15] have shown that the amount of slow ions registered from the plasma heated by X-rays increases with the increase of the target Z number. The charge of the escaping ions is determined by the ionization processes in the hot plasma and a subsequent three-body recombination during the adiabatic expansion - the so called charge freezing. The depletion of vulnerable highly charged ion states in the expanding cooling plasma due to the recombination processes ($\sim z^3 n_e T_e^{-9/2}$) was already recognized in the early proposals for the design of LIS [16]. Consequently, according to the conventional hydrodynamic theory [17, 18, 19], the highly charged ions produced by a sub-nanosecond laser pulse should not occur in the far expansion zone. These predictions, however, do not agree with our experiments.

A possible way of explanation of the occurrence of high state in the far expansion zone is offered by the existence of the fast ion group seen on the collector signals, which invariably contains the high charge states. The existence of the fast group means that the plasma time evolution follows the mechanism of two-temperature isothermal expansion [20]. During the expansion phase, first the hot electrons leave the plasma pulling the ions behind. The thermal electrons follow, guiding the thermal group. In some cases, besides the mentioned process of emission from the secondary focus, adds even a third maximum to the collector signal corresponding to the late arrival of slow ions. To support this notion a series of model calculations was performed assuming that the energy deposition process renders a two-temperature electron energy distribution, which, in turn, leads to a two-temperature exponential electron density profile [21]. Simulated collector signals and ion charge distribution calculated on the basis of this simplified model are in a good agreement with the experimental results.

4.2. Characteristics of laser ion sources

The practical reasons like an easy commercial availability, a high repetition rate and a robust construction dictated as the first choice the CO_2 laser as driver. Nevertheless, the laser ion source based on CO_2 laser may also suffer from serious setbacks. It is the long ($10.6 \mu m$) wavelength of the CO_2 laser, the badly controllable pulse length and a poor focusability. Also, the electron density in the corona of the plasma produced by a CO_2 laser is low and, hence, the ionization is slow. Under these conditions the presence of high charge states of ions produced from a target of heavy elements (such as lead) is not expected to exceed 30+. A complementary region of high power densities and shorter wavelengths, though perhaps at present less practical than that dominated by the CO_2 lasers, is thus worth exploring at least from a purely physical point of view. It may well happen that the newly available high repetition rate, medium energy systems in the near-infrared region will soon become drivers for the next generation of LIS.

5. Conclusion

Laser ion sources are distinguished by high yields of ions which can be delivered to various substrates, elements of ion optics to be subsequently formed into ion beams or ion sensors by plasma expansion to a large distance from the laser focus. Their main disadvantage is the inherent final charge and energy spread of the ions produced. With a near infrared sub-nanosecond laser, such as the iodine or the Nd:glass laser as drivers, the attainable charge states of the ions are generally much higher than in a case when a more conventional CO_2 laser driver is used. The resulting ion charge composition in a far expansion zone results from a complicated interplay between the ionization in the laser focal spot and the recombination occurring during the adiabatic expansion of the plasma, which follows the active heating stage of plasma formation. For the diagnostics ion collectors as well as the electrostatic ion analyser proved to be indispensable tools. On the collector signal generally several maxima can be identified, pointing to the existence of several ion groups. Among these fast ions driven by hot electrons, thermal ions and slow ions emitted from a secondary focus heated by X-rays and hot electrons from the primary focus are usually recorded. Although still in the early stages of development the laser ions sources are finding numerous applications such as the accelerator injection or the ion implantation.

References

1. H. HASEROTH and H. HORA, *Advances of Accelerator Physics and Technologies* (Ed. H. Schopper), World Scientific, Singapore, 446, 1993.
2. F.P. BOODY et al., 13th Int. Conf. on Laser Interactions and Related Plasma Phenomena, LIRPP'97, Monterey, April 13-18, 1997, AIP Conference Proceedings (Eds. G.H. Miley, E.M. Campbell), Woodbury, New York, p. 539, 1997.
3. G. KORSCHINEK and J. SELLMAIR, *Nucl. Instr. Meth.* **A268**, 473, 1988.
4. Y. AMDIDOUCE et al., *Rev. Sci. Instrum.* **63**, 2838, 1992.
5. E. WORYNA et al., *Laser and Particle Beams*, **14**, 293, 1996.
6. J. KRÁSA et al., *Rev. Sci. Instrum.* **69**, 95, 1998.
7. J. W. SHEARER and W. S. BARNES, *Laser Interaction*, **1**, 307, 1972.
8. M. BUSQUET, *Phys. Rev.*, **B25**, 2302, 1982.
9. J. FARNY and E. WORYNA, 18th European Conference on Laser Interaction with Matter, Prague, Czechoslovakia, May 4-8, 1987.
10. W. MRÓZ et al., *Rev. Sci. Instrum.*, **67**, 1272, 1996.
11. M. PFEIFER et al., *Proc. Int. Symp. PLASMA'97*, Jarnołtówek (Poland), June 10-12, 1997, (Eds. M. Sadowski, H. Rothkaehl), Space Research Center PAS, Warsaw, Vol.1, p. 425, 1997.
12. M. CHVOJKA, et al., *Czech. J. Phys.*, **42**, 899, 1992.
13. E. WORYNA et al., 24th European Conference on Laser Interaction with Matter, Oxford, UK, September 19-23, 1987, (Ed. S.J. Rose), IOP Conference Series 140, Inst. of Physics Publishing, Bristol, p. 463, 1987.
14. M. PFEIFER et al., *Proceedings of the 2nd National Symposium PLASMA'95*, 1995, Warsaw Vol. 1. p. 77, 1995.

15. W. MRÓZ et al., *Laser and Particle Beams*, **10**, 689, 1992.
16. T.R. SHERWOOD, *Rev. Sci. Instrum.*, **63**, 2789, 1992.
17. A.V. GUREVICH, L.V. PARIISKAYA and L.P. PITAEVSKII, *ZhETF*, **22**, 449, 1966.
18. J.E. ALLEN and J.G. ANDREWS, *J. Plasma Phys.*, **4**, 187, 1970.
19. J.E. CROW, P.L. AUER and J.E. ALLEN, *J. Plasma Phys.*, **14**, 65, 1975.
20. J. WOŁOWSKI et al., 12th Int. Conf. Laser Interaction and Related Plasma Phenomena, (Editors Sadao Nakai and George H. Miley), Osaka, Japan, April 1995.
21. L.M. WICKENS, J.E. ALLEN, *J. Plasma Physics*, **22**, 167, 1979.

Appendix

**Lectures presented at
the Conference Workshop**

SUPERSONIC PLASMA FLOWS AND THEIR INFLUENCE ON AERODYNAMICS OF FLIGHT

A. F. ALEXANDROV, N. V. ARDELYAN, S. N. CHUVASHEV, A. P. ERSHOV,
A. A. RUKHADZE, I. B. TIMOFEEV, B. I. TIMOFEEV, V. M. SHIBKOV

M. V. LOMONOSOV MOSCOW STATE UNIVERSITY, PHYSICS FACULTY
Moscow, Russia

1. Introduction

Different types of gas discharges were considered repeatedly from the point of view of plasma technique applications for aerodynamic problem solutions. They are: the longitudinal one (when electric current j is parallel to airflow's velocity v) and the transverse one (when electric current j is perpendicular to v) stationary discharges, high frequency discharges, microwave and optical discharges [1, 2, 3, 4].

It is necessary to note that plasma aerodynamics nowadays is in a state of formation as an independent area of plasma physics. There is a small number of experimental and theoretical works confirming the efficiency of plasma technique applications in aerodynamics.

Supersonic shockless motion of a dense plasma jet was observed in ionized air created by the optical discharge [4, 5]. In such a case plasma body motion in the atmosphere with the velocity of 1 - 3 km/s was detected, i.e. with the velocity 3 - 10 times greater than the sound velocity in undisturbed air. On the other hand the anomalous strong interaction of shock waves with low temperature plasmas was observed in a number of experiments [6, 7, 8, 9]. The results of several experiments are well explained by the refraction effects [10 - 18].

Generation of gas discharges directly before an airplane or on its surface could be the possible means of plasma affect the supersonic airflow. It could lead to the substantial improvement of its aerodynamic characteristics, and particularly to a considerable decrease of the head drag coefficient [2].

The most convenient methods for the practical application still stay unclear. They concern methods of the discharge forming, energy expenses necessary for the plasma generation, a discharge type and its optimal geometric form, etc. Besides, plasma diagnostic methods in the supersonic flows are undeveloped,

and as a result of this characteristics of the discharge plasma in the supersonic flow are practically uninvestigated.

In connection with this investigations of gas discharges in supersonic airflows and studies of plasma application possibility in the aerodynamics have been carried out on installations of TsAGI, MSU, TsNIIMash, MRTI, IVTAN during the last decade.

The purposes of this work were as follows: the experimental and theoretical investigation of free-burning and surface gas discharges generation in supersonic airflows, the detection of plasma characteristics at different values of electric power put into the discharge, and the demonstration of the possibility of aerodynamic characteristic improvement of a flying vehicle (FV).

2. Free-burning transverse gas discharges in the supersonic airflow

A high-pressure chamber was used for investigation of discharges in the supersonic airflows. It represented the cylinder of the stainless-steel 3 m long and 1 m diameter. Its vacuum system allowed to achieve the back pressure of about $\sim 10^{-5}$ Torr (see Fig. 1). A supersonic airflow was created at the filling of the

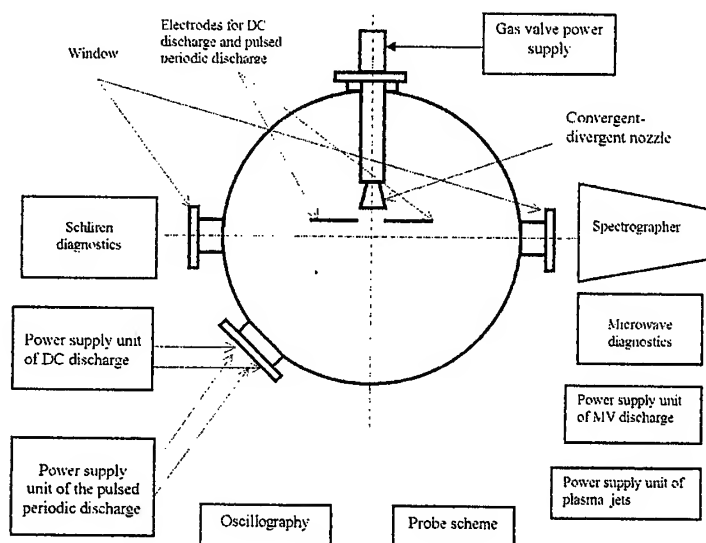


FIG. 1. Schematic design of the experimental diagnostic installation.

chamber by the atmospheric air through a hydraulic valve. On the outlet tube of the latter a profiled cylindrical Laval nozzle calculated for the Mach number $M = 2$ [12] was then located.

Free-burning transverse gas discharges in the supersonic flow were formed by means of two electrodes, located at a distance of 0.5 - 1 cm down the nozzle's cut, in the plane perpendicular to the supersonic flow axis.

A modulator of power up to 0.5 MW with the controlled voltage up to 30 kV (and maximal electric current 40 A) was used for the creation of transverse pulse-periodic discharge. The modulator allowed varying the duration of microwave pulses from 1 to 300 μ s and their repetition frequency from 1 to 1000 Hz.

The transverse steady with current discharge was created by means of a power source with the working voltage of 5 kV (and current up to 3 A).

A discharge current value was adjusted with a help of a ballast resistors set. The synchronizing scheme ensured necessary time delay between opening of the valve and switching-on and shut-down of the discharge.

The visualization of discharges in the supersonic flow was realized by means of photo and video cameras. The shadow set up with the pulse lamp-flash of 1 μ s duration was used for the detection of gasdynamic structure of the supersonic flows.

The detection of temporal dependencies of the discharge current and voltage, floating potential and electric field in the plasma was carried out by means of the C8-17 two-beam oscilloscope.

Three independent methods were applied for measuring an electron concentration: the double-probe method, especially elaborated for plasma diagnostics in a supersonic flow, an 8 mm microwave interferometer, and the spectral method of electron concentration's detection by the Stark broadening of the hydrogen line H_β ($\lambda = 486.1$ nm). In the last case a small amount of hydrogen was added into the supersonic flow. Undoubted advantage of the probe method over the others ones consists in the local character of measured characteristics. In so doing two problems are added to those of diagnostics of a classical arc discharge. They are connected with high values of the probe current and gas temperature. They show high (kV) values of the space potential in respect to the earth and an extremely high (kV) level of its oscillations. Thorough mathematical modelling in the two-dimensional and non-stationary formulation was carried out for clarifying the interaction between the supersonic air flows and the probe in strong electric fields.

A gas temperature was measured with spectral methods, taking relative intensities of lines of the rotational structure of the band (0; 2) with the quantum wave length $\lambda = 380.5$ nm of the second positive system of nitrogen molecule, and that of the band (0;0) with quantum wave length $\lambda = 388.3$ nm of the CN molecule. A vibrational temperature was evaluated from the relative intensity of the molecular bands of the second between positive system of nitrogen [13].

In Fig. 2 there are presented typical pictures of the transverse pulse-periodic discharge and of the steady current discharge for the supersonic airflow with the Mach number $M = 2$, at the initial air pressure in the chamber 40 Torr and the discharge current 4.5 A. Repetition frequency of the microwave pulse was 70 Hz. The Laval nozzle cut was to the right in the presented picture. The outside view of the transverse discharge in the supersonic airflow was the following: The discharge consisted of two bright current channels with distinct boundaries, then a weakly glowing diffuse region was observed. The discharge current was shorting through this region. The length of channels increased with the increase of the current's pulse, approximately proportionally to the pulse duration. It reached 12 cm length at the current's duration $\tau = 500$ μ s. This size was close

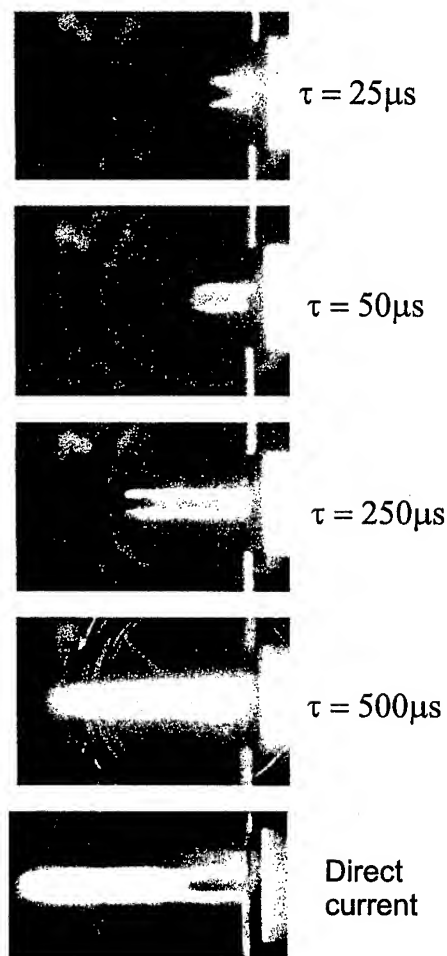


FIG. 2. Transversal pulsed-periodical discharge in supersonic airflow: $M = 2$, $p = 40$ Torr, $I = 4.5$ A, $f = 70$ Hz.

to the length of the plasma jet at the steady current discharge. This discharge consisted of two bright long ($l \sim 15$ cm) with distinct boundaries plasma jets going from electrodes. Considerably less bright region of jet's shorting started at some distance (about $\sim 4 - 5$ cm) from the electrodes. It was spread over the remained length of the discharge.

Analogous pictures of the discharge were obtained in TsAGI experiments [21] in an airflow at $M = 3$ within a wind tunnel at values of discharge currents and pressure close to ours, and also in experiments at GAU of the MSU Institute of Mechanics at $M = 6$ [1].

The high value of the potential difference is the distinctive feature of the discharge in the supersonic airflow. The voltage on the discharge is several of kV at the pressure of several tens of Torr, in spite of a small inter-electrode

distance (about ~ 1 cm). The obtained distribution of the floating potential in the steady current discharge is represented in Fig. 3.

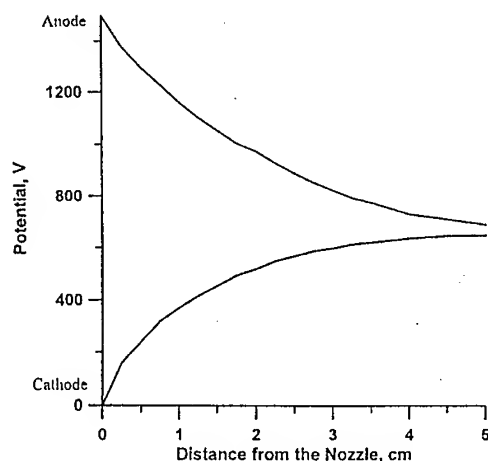


FIG. 3. Potential distribution averaged over the oscillations.

It is seen that the distribution of the potential in both channels was close to the mirror-symmetrical one in respect to the direction of the supersonic flow. The maximal value of the field, about 1.5 kV/cm, was achieved near the electrode surfaces and decreased monotonously down the flow.

The investigation of the ampere-volt discharge characteristics shows that the current and voltage have distinctive pulse character, and their modulation depth can reach 80%. The pulsation frequency proves to be about tens of kHz and it is significantly dependent on the initial air pressure in the discharge chamber and the discharge current. The frequency decreases with the increase in the initial gas pressure and with the increase in the discharge current.

Measurements of gas temperatures stream down the flow in the steady current discharge showed that it was in the range 1000 - 2000 K at the variation of the discharge current from 0.5 to 4 A, and it changed weakly in the axial direction. The vibrational temperature was in the range 5000 - 10000 K at the same values of the current. These data show that the produced plasma was characterized by a strong vibrationally-translation nonequilibrium in the studied range of plasma characteristics.

A dependence of an electron concentration on the discharge current in plasma with the steady current discharge, and in plasma of the pulse-periodic discharge, is represented in Fig. 4. The data were obtained by three independent methods. Values of concentrations measured by the probe and spectral methods, corresponded to the region located at the distance $z \approx 30 - 40$ mm from the electrodes, down the flow (outside the region of shorting of plasma jets). The microwave probing was carried out for the region of shorting of plasma jets ($z \approx 40 - 50$ mm). One can see the satisfactory agreement between the results of measurement performed with different methods. From Fig. 4 it follows that the

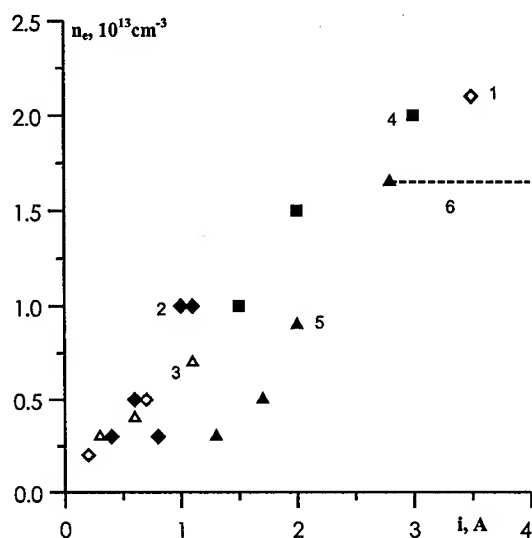


FIG. 4. Electron density versus the discharge current at measured with different methods at $p = 40 \text{ Torr}$. 1 - probe $\phi 0.2 \text{ mm}$; 2 - probe $\phi 0.5 \text{ mm}$; 3 - microwave interferometer; 4 - spectral method; 5 - microwave interferometer in pulsed periodic discharge; 6- cutoff level.

electron concentration increases practically linearly with the discharge current's increase, and it is of the order of 10^{13} cm^{-3} at currents of about $\sim 1 \text{ A}$ and the pressure of tens Torr.

3. Surface gas discharges in plasma aerodynamic experiment

The experiments on forming discharges on model surfaces in the supersonic airflows were carried out in TsAGI at the Mach number $M = 4$ in the wind tunnel T-113 and in MRTI at $M = 2$ [2]. The models had a cylindrical form. Head parts of the models were made as cones or half-spheres. A copper electrode placed into a ceramic tube of 4 mm diameter was fastened to the head part of each of the model. A conical end part of the electrode was 27 mm long. Another, sectionalized electrode (consisted of 8 sections) was located on the side surface of the model's head part. Models were made mainly of kaprolon, but also ceramic models were used in some experiments.

Two types of discharges between the frontal and sectionalized electrodes were used in the experiments. The first type corresponded to a direct current discharge (0.5-2.6 A) at power up to 1.5 kW. The direction of the current was either parallel or anti-parallel to the velocity of the supersonic flow. The second type corresponded to the discharge of the alternative current with a frequency $f = 50 \text{ Hz}$. The discharge current value could be changed from 0.5 to 5 A at the maximal discharge power input being about $\sim 0.9 \text{ kW}$.

The discharge studies were carried out at the following airflow characteristics: the pressure $p_0 = 1 \text{ atm}$, the static pressure $p_{st} = 30 \text{ Torr}$, Mach number $M =$

2.3, the static gas temperature $T_{st} = 160$ K (MRTI); $p_0 = 6$ atm, $p_{st} = 29$ Torr, $M = 3.98$, the static gas temperature $T_{st} = 68$ K (the TsAGI wind tunnel).

The voltage-current characteristics of the surface discharge proved to be practically the same for both of the Mach number values. The oscillogram fragments of the alternative current discharge in the air (without a flow) are presented in Fig. 5a for voltage (the upper curve) and for current (the lower curve). One

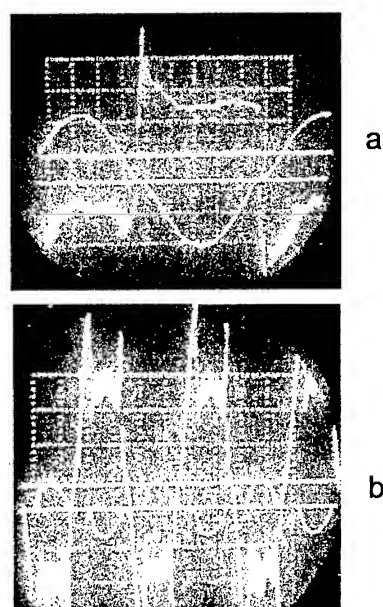


FIG. 5.

can see that the discharge current looks like a disturbed sinusoid with extent (1.5 - 2 ms) temporal regions of nil current values. A quick rise of the voltage on the discharge gap is observed during this time, for example, at $U_0 = 7$ kV, $\frac{\partial U}{\partial t}|_{t=0} = 2.2$ MV/s. After reaching the breakdown value the voltage on the discharge gap sharply falls down and then stays practically constant (about 1 kV) during the next 7-7.5 ms. The maximal discharge current in this case was 2.6 A.

The oscillograms of the voltage (the upper curve) and of the current (the lower curve) for the alternative current discharge in the supersonic airflow at $M = 4$ are presented in Fig. 5b. Their general view is like the oscillogram view in a steady air, but the duration of the nil current value is greater, the breakdown voltage is higher, one can see the high frequency noise on the voltage curve.

In Fig. 6a the typical view of the longitudinal direct current discharge for the model with the spherical head part made of kaprolon is represented. The flow was quasi-stationary with a slow velocity decrease (from $M = 2.3$ to $M = 1$). The maximal discharge current was 1.6 A, and the maximal voltage on the discharge gap was 4 kV. One can see that the plasma fills the whole discharge gap and the discharge is axially symmetric. The plasma layer thickness on the model's

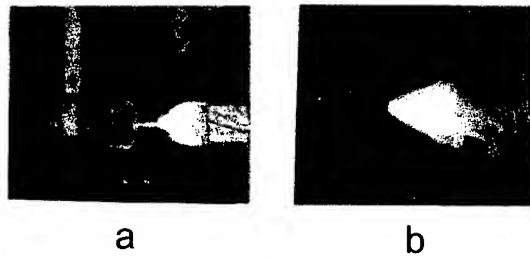


FIG. 6. Appearance of the discharges over the models with the spherical (a) and conic (b) frontal parts.

frontal part is about 1-2 mm, the plasma boundaries are distinct enough. The discharge's radiation is significantly non-uniform; it is the most bright near the sectionalized electrode.

An appearance of the longitudinal alternative current discharge in a quasi-stationary airflow with a slow velocity decrease (from $M = 2.3$ to $M = 1$) and the conical form of the frontal part is represented in the Fig. 6b. It corresponds to the maximal current 1.6 A, maximal voltage value $U_1 = 5$ kV and the discharge duration $\tau = 5$ s. One can see that the plasma covers the whole frontal part of the model, but the plasma boundaries are not so sharp in contrast to the previous case; some part of the plasma has drifted from the discharge area. The discharge's radiation is significantly non-uniform; the discharge is most bright near the back edge of the frontal spike electrode and near the sectionalized electrode.

Photo frames of the transverse discharge on the ceramic model in the airflow at $M = 4$ are presented in Fig. 7. One can see that the discharge is axially

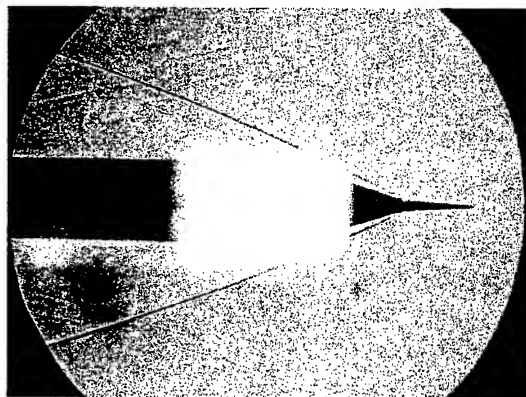


FIG. 7. Shadow photo frame of the transversal discharge.

symmetric and it is formed on the spherical frontal part of the model along the circle going through the sectionalized electrode.

Notice that the most successful experiments on the forming of the surface discharges on the models were carried out with the models made of refractory

ceramics. The discharge formed on the surfaces of the ceramic models in the flow with $M = 4$ is usually uniform and covers practically the whole side surfaces of the models.

Let us consider the effect of the surface discharge on the aerodynamic drag of the model in the airflow at $M = 4$.

The most considerable decrease of the head drag was observed for the model with the spherical frontal part at a generation of the longitudinal discharge between the nose electrode-spike and the sectionalized electrode located on the side surface of the model. During the time of the discharge burning the coefficient of the head drag C_x decreased by 14 - 15% (it means that $C_{x1} = 0.85 - 0.86$; C_{x0}). A temporal dependence of the head drag coefficient in the course of one experiment with the application of the aerodynamic balances is presented in Fig. 8. The 6 - 7% decrease of the head drag was observed in the experiments with

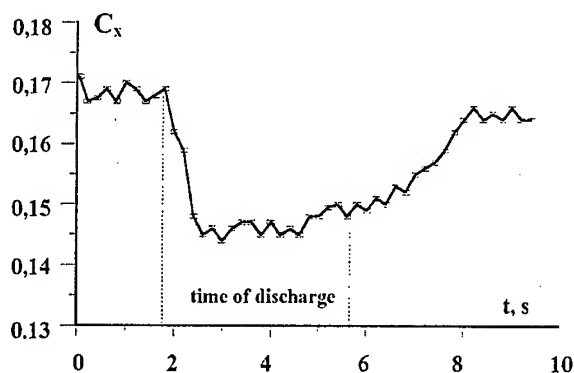


FIG. 8. Drag coefficient temporal dependence.

the model with the conical frontal part; it is also an extremely good result from the point of view of aerodynamics.

The next fact was absolutely unexpected. During the experiments with the models with the ring transverse discharge the value of C_x also decreased considerably. Here the effect was weaker than that in the experiments with the longitudinal discharges, C_x decreased by 2.5 - 4% (in respect of the power input to the discharge). It was observed in numerous experiments with both of the models and it was independent of the model's frontal part form. It seems quite understandable: in these cases the discharge is formed on the side surface of the model's frontal part and it is drifted far down the flow. The decrease of the drag here can be a result of the existence of the considerably extended plasma region on the models, and it shifts the coordinate at the beginning of the laminar-turbulent transfer, and this effect leads to the decrease of the viscous friction.

An analysis of the radiation spectra of the surface discharges shows that the gas temperature is high enough $T_g = 1500 - 2500$ K at $M = 2.3$. Its longitudinal dependence is not monotonous. The vibrational temperature ($T_v = 8000 - 10000$ K) is 3 - 5 times greater than the translational one in these conditions.

The gas temperature axial distributions for the case $M = 4$ and the longitudinal discharge show that the gas temperature increases with the current increase. It stays practically constant in the gap between the electrodes and it drops down the flow (in the place of plasma's exit). The vibrational temperature reaches $T_v = 10000$ K in this case.

The electron density in the surface discharges in the supersonic flows at $M = 2$ and $M = 4$ reaches the value about $\sim 10^{14} \text{ cm}^{-3}$ at the discharge current 3 A. It is close to the electron concentration in the arc discharges.

4. Computer simulation of plasma aerodynamic processes

As the experiments provide a data set, which is far from being complete for a description of the main processes in the nonequilibrium plasma, they should be complemented by a computer simulation. An adequate theoretical model of the phenomenon should consider, on the one hand, the gas-plasma dynamics with the Maxwell equations, and on the other hand, the plasma kinetics. In the present study they were considered separately, in two complementary models (implementation of the summary model is difficult).

The kinetic approach to a modelling of the longitudinal discharge was applied. The gas dynamics and field blocks have been simplified according to the following:

This model considers a plasma channel formed by the longitudinal discharge along the supersonic airflow. It is supposed that the gas longitudinal speeds inside and outside the channel are close to each other and to the speed of the unperturbed airflow v_∞ . It is also supposed that the weakly ionized plasma static pressure equals to that of the unperturbed airflow p_∞ , thus gas concentration n_g in the plasma channel is determined as $n_g = p_\infty / (k_B T_g)$, here k_B is the Boltzmann constant. These altogether substitute for the gas dynamic block at the studies of the main plasma parameters' distributions along the axis, for the gas temperature T_g is obtained from the plasma kinetics simulation.

The electric current density j distribution across the channel is known to be close to a Π -shape as a rule. If the current channel cross section A and the total current $I = jA$ are known, say, from experimental data, and the plasma conductivity σ is obtained on the base of the plasma kinetics, then the electric field E distribution along the channel can be calculated as $E = I / (\sigma A)$. Thus, the field block is also simplified radically.

A steady one-dimensional approximation is used to describe the main kinetic processes in the weakly ionized plasma near the channel axis. The main equations of the model include the following.

4.1. The balance of the translational and rotational gas temperature T_g

$$\partial T_g / \partial z = (2/7)(S_{exT} + S_{VT} + S_{V'T} + S_{xT} + S_{DT} + S_{RT} + S_{ii} + S_{eT}) \cdot T_g / (p_\infty v_\infty),$$

here S_{exT} is the power of gas heating at quenching of excited electronic states, primarily $N_2(A^3\Sigma_u^+)$, at their collisions with each other, as well as with molecules

on high vibration levels N_2^V ; S_{VT} and $S_{V'T}$ are the powers of gas heating due to the quenching of the lower and higher vibration levels, S_{xT} , S_{DT} , S_{RT} , S_{ii} correspond to the gas heating at the reactions of VV exchange, dissociation, dissociative and ion-ion recombination, S_{eT} is the power of e-T heating at elastic collisions. The corresponding formulae and cross sections of these and other reactions are listed, e.g., in [21, 22, 23].

4.2. The balance of the electron mean energy

$$S_F = S_I + S_D + S_{ex} + S_{eV},$$

$S_F = \sigma E^2$ is the electric field energy input, S_I , S_D , S_{ex} , S_{eV} are the electron energy losses for ionization, dissociation and excitation of the electron and vibration states, respectively.

4.3. The balances of vibration quanta q_T , positive n_i and negative n_- ions, neutral atoms n_a and electronically excited molecules n_{ex}

$$\begin{aligned}\partial q_T / \partial z &= (K_{eV} - K_{VT} - K_\alpha - (q_T/n_g)\Delta r)/v_\infty, \\ \partial(n_i v_i) / \partial z &= K_I - K_{DR} - (n_i/n_g)\Delta r, \\ \partial(n_- v_-) / \partial z &= K_a - K_{ii} - K_d - (n_-/n_g)\Delta r, \\ \partial n_a / \partial z &= [K_a + K_{ii} + 2(K_D + K_{DR}) - (n_a/n_g)\Delta r]/v_\infty, \\ \partial n_{ex} / \partial z &= [K_{ex} - K_q - (n_{ex}/n_g)\Delta r]/v_\infty,\end{aligned}$$

here $q_T = \Sigma V n_V \cong n_g / [\exp(\hbar\omega/T_V) - 1]$, n_V is a number of molecules on V-th vibration level, T_V is the vibration temperature, $\hbar\omega$ is the vibration quantum, K_{eV} is the frequency of pumping due to the eV excitation processes, K_α accounts for the processes of V-V excitation and VT transfer at high vibration excitation levels, K_{VT} - VT transfer at low levels; K_I , K_{DR} are the rates of ionization and dissociative recombination; K_a , K_d , K_{ii} are the rates of dissociative attachment, associative detachment and ion-ion recombination at pair collisions; K_D is the total rate of electronic excitations that result in dissociation, K_{ex} and K_q are the rates of excitation and quenching of the metastable molecules. The terms with $\Delta r = v_\infty p_\infty / (k_B T_g^2) \partial T_g / \partial z$ result from the radial expansion at the plasma heating;

4.4. The dynamics of the positive and negative ions,

$$v_i = v_\infty + E\mu_I, \quad v_- = v_\infty - E\mu_I,$$

here μ_I is the ion mobility.

4.5. The stationary kinetic equation for the local electron distribution function f

$$\partial f / \partial t = \delta_F + \delta_{ee} + \delta_{eV} + \delta_{ex} = 0,$$

here δ_F , δ_{ee} , δ_{eV} , δ_{ex} correspond to the field pumping, the electron-electron collisions, excitation of electronic and vibration energy levels, respectively:

$$\delta_F = 2/(3W^{1/2}m_e)(eE)^2 \partial[(W^{3/2}/\nu_{em})\partial f / \partial W] / \partial W,$$

$$\delta_{ee} = (2/W^{1/2})\partial[W^{3/2}\nu_{ee}(f + T_e\partial f / \partial W)] / \partial W,$$

$$\delta_{ex} = \Sigma_l[f(W + W_{vl})\nu_{vl}(W + W_{vl})(1 + W_{vl}/W)^{1/2} - \nu_{vl}(W)f(W)],$$

$$\delta_{eV} = \Sigma_{v'}[f(W + W_{vv'})\nu_{vv'}(W + W_{vv'})(1 + W_{vv'}/W)^{1/2} - \nu_{vv'}(W)f(W)].$$

Here W and T_e are the electron energy and the effective electron temperature (as a measure of the mean energy), ν_{em} is the frequency of elastic electron-molecule scattering, the summarizing is produced for all the final vibration v , v' and excited electron l energy levels (the basic energy level v was taken as an initial), ν_{vl} and $\nu_{vv'}$ are the frequencies of the l -th electron (for transitions with a change of the electron and possibly vibration quantum numbers) and the v' -th vibration level excitation (for the transitions with a change of the only vibration quantum number), W_{vl} and $W_{vv'}$ are the corresponding threshold energies. The electron distribution function is necessary at the spectral integration of the cross sections for a calculation of the local reaction rates. Deviations from the equilibrium distribution function take place due to the energy losses of electrons at inelastic collisions, namely, at the vibration and electron excitation of molecules. The number of electrons with energies corresponding to high cross sections of the inelastic collisions (as well as the rates of these collisions) is F_1 times less than at equilibrium; F_1 can be estimated as [23].

$$F_1 \approx [(1 + 4C)^{1/2} - 1]/[(1 + 4C)^{1/2} + 1]/C,$$

here $2C$ is the ratio of frequencies of the inelastic and the elastic collisions at the electron energy W being about T_e higher than the threshold ΔW of the corresponding inelastic process, $W = \Delta W + T_e$. The following boundary conditions were applied. Ion concentration at $z = 0$ point (near the frontal electrode) $n_i(z = 0) = n_{i0}$, $n_{i0} > 0$ is small in comparison with a characteristic value of plasma concentration n'_l (results do not depend on n_{i0} because of a very fast growth of n_i value, and its further stabilization at $z \approx 0$ on the same level n'_l). The rest boundary conditions are: $T_g(z = 0) = T_\infty$, $q_T(z = 0) = n_a(z = 0) = n_-(z = 0) = n_{ex}(z = 0) = 0$. The listed above set of implicit algebraic and differential equations is two-dimensional (spatial z and electron energy W variables). It was solved numerically with use of the Newton and Runge-Kutta methods. Spatial intervals at the vicinity of $z = 0$ point were 30...300 times smaller than a couple of millimeters below (to provide the calculation stability at an extremely fast alteration of most of the variables). For calculation of the electron distribution function f in spatial point z_i , the

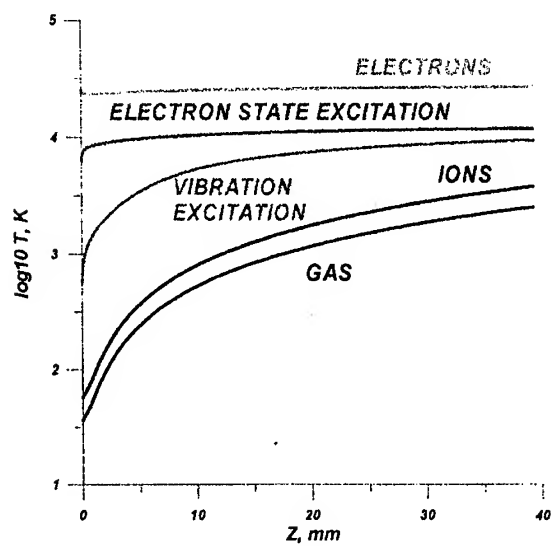
parameters in the previous point z_{i-1} were used. In a part of the calculations the approximate equations for F_1 (see above) have been also used instead of the kinetic equation; it did not result in a considerable deviation of the magnitudes of the main plasma parameters, and it did not affect the qualitative results at all, but a considerable acceleration of the computations was observed.

The model was verified by a comparison of the computer simulation and the experimental results for the longitudinal gas discharge with the geometry [8] which provided a practically free plasma channel, with an absence of its contact with the body on its major part, instead of a flow over a body with a complicated shape. The experiments [8] in a wind tunnel at $I = 1.5$ A, $M = 6$, $T_\infty = 36$ K, $p_\infty = 30$ Torr, the current channel length $L = 40$ mm, and the diameter $2R = 2.5 \dots 3$ mm were taken. At computation these experimental data for I , T_∞ , p_∞ , R , L were used as initial conditions. The model thus contained no degrees of freedom for fitting. A good agreement has been obtained for the gas temperature ($\cong 20 \dots 30\%$) and the total discharge voltage (experimental voltage is about 30 - 50% higher, but it includes electrode layers, which have not been taken into account in the present model). The same calculations have been produced also for the conditions of the plasma aerodynamic experiments with the flow over the model. The regime corresponded to $M = 2.3$, $T = 160$ K, $p = 70$ Torr. Some results are presented on Fig. 9.

Two different regions are observed in the discharge column. Most of the events (electric energy absorption, ionisation, vibration excitation, generation of metastable molecules, gas heating, etc.) take place primarily at $0 < z < 2$ mm. Downstream the flow relative rates of change of all the plasma parameters are much smaller. The speed of ion drift is about an order of magnitude smaller than the speed of airflow. Considerable gas heating takes place. The local Mach number changes from $M = 2.3$ to $M < 1$. There takes place a multiple growth of the plasma viscosity, that can cause a considerable delay of the turbulent transition and a reduction of viscous component of drag. The ratio of field to gas concentration F/n_m is approximately a constant at $0 < z < 6$ mm. The electron concentration also changes rather weakly. It means that if one neglects the variations of electron concentration, it is possible to consider the plasma conductivity to be in an inverse proportion to the gas concentration. The influence of the deviations of the electron distribution functions from equilibrium due to the excitation of vibration and electron states is considerable in the frontal part of the channel (here the mean cross sections are 2...5 times smaller than at equilibrium) and vanishes downstream, while F/n_m is approximately the same. It is a result of the fact that the plasma parameters deviate from those characteristic ones for the steady state at given F/n_m . The plasma contains a great number of molecules with the vibration and electron excitation. Another model considered the plasma dynamics and the current distribution in the discharge in flow over the body. According to the results of the first model, the plasma concentration and the electron temperature were considered to be constant, i.e. the conductivity was in an inverse proportion to the gas density. The delay in energy transport to the gas temperature was neglected. The simultaneous equations of plasma dynamics and electromagnetic field,

Air flow temperature 36K, pressure 30 Torr

Temperatures



Particles concentrations

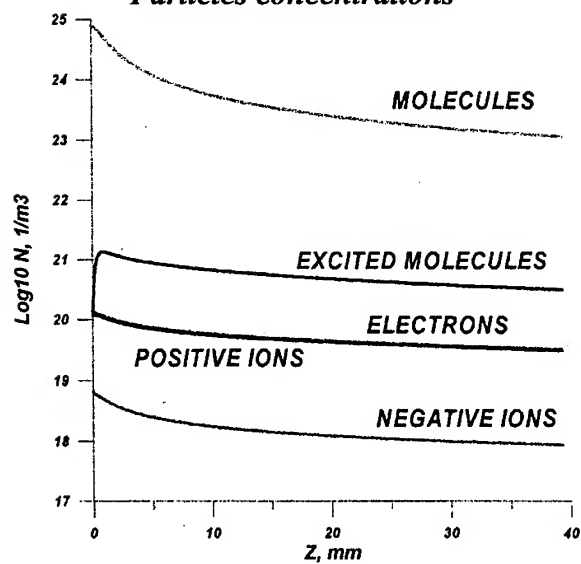


FIG. 9.

$$\begin{aligned}
\partial \rho_g / \partial t + \operatorname{div}(\rho_g v_g) &= 0, & \rho_g dv_g / dt &= -\nabla p_g, \\
\rho_g dE_g / dt &= -p_g \nabla \mathbf{v}_g + j^2 / \sigma, \\
\partial \mathbf{B} / \partial t &= \nabla[1/(\mu_0 \sigma) \nabla \mathbf{B}] + [\nabla[\mathbf{v}_g, \mathbf{B}]], \\
\mathbf{j} &= [\nabla \mathbf{B}] / \mu_0, & \mathbf{E} &= \mathbf{j} / \sigma,
\end{aligned}$$

were solved in the axially symmetric approximation (here ρ_g , v_g , p_g , E_g are the gas density, velocity, pressure, and specific energy, correspondingly; \mathbf{B} is the magnetic induction, \mathbf{j} is the current density, \mathbf{E} is the electric field, μ_0 is the magnetic constant) with use of the free Lagrangian method on the base of the completely conservative difference schemes on adaptive triangular grids [24].

The wave drag was computed as an integral over the model's surface of the axial components of the overpressure forces. Boundary conditions corresponded to a gliding on the walls and the axis, a free entry and exit upstream and downstream the body, zero tangent components of \mathbf{E} near the metallic surfaces, and a zero \mathbf{B} on all the other boundaries but the wall between the electrodes, where $B = 2\mu_0 I/r$ (here I is the total current). The experimental data for I and the energy input were applied. The regime corresponded to that examined experimentally and at the plasma kinetic computations, see above.

The modelling has shown the following (Fig. 10). A long and narrow current channel filled with the plasma is formed. The gas temperature is about 2000 K there. Practically all the energy input takes place at the channel's frontal end, primarily near the hind end of the spike electrode: the air that enters the current channel is cold and dense, its conductivity is comparatively small, the joule heating power j^2/σ is high. As the air is heated, its density falls downstream together with the electric field and the heating power. The local speed of sound in the plasma channel due to the gas heating becomes higher than the local velocity. An additional shock wave is formed before the region of energy release; it results in local growth of pressure, and in additional acceleration of the plasma towards the model. As the surface near this region is parallel to the axis, this pressure gain gives no additional drag. Due to the flow modification by the discharge the main shock wave before the model becomes somewhat weaker than at the flow without the discharge (compare Fig. 2a and 2b). It results in a total wave drag reduction of about 5 - 10%. Note that the experiments have shown a close or a somewhat higher total drag reduction.

5. General consideration of results

A unanimous analysis of all the experimental and theoretical data with respect to their accuracy has resulted in the following reliable conclusions.

Under the conditions of the plasma aerodynamic experiments, the plasma state is very far from equilibrium: the vibration is excited in a major part of the molecules, a considerable number of electronically excited molecules is generated, the electron energy distribution function deviates from the equilibrium one (especially in the region of the major energy input). It results from the spectral measurements of T_V and T_g and from the plasma computations.

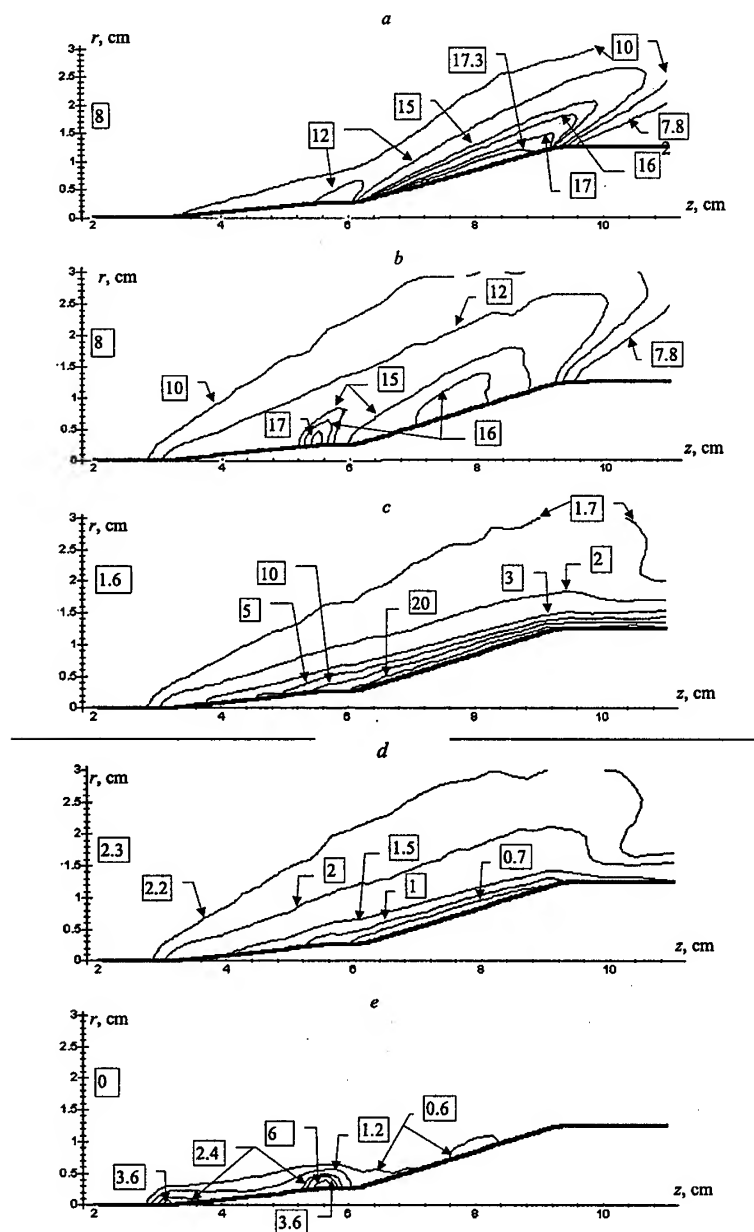


FIG. 10. Spatial distribution of pressure, kPa(a, b), temperature, 100 K(c), Mach number (d), Joule heating power distribution, GW/m^3 (e), without (a) and with (b-e) the discharge. The initial parameters: airflow Mach number 2.3, pressure 8 kPa, temperature 160 K, current 2 A.

The plasma processes of energy distribution from the electric field to various energy reservoirs are non-linear and change the whole flow over the model considerably. The energy input into plasma at the longitudinal discharges takes place in

a small quasi spherical region. It results from the both numerical researches (the plasma and gas/field approaches), and corresponds to the measured temperature longitudinal distributions (T_g quickly rises from the initial cryogenic temperature to ~ 1000 K, the further relative changes of the measured and computed temperature is much weaker).

A considerable gas heating is observed, the molecular translation temperature rises up to $1 \dots 2$ kK. The high values of the gas temperature are present in the both numerical approaches and in the experimental results.

The best registered drag reduction in these experiments is rather considerable (15% for the model with the spherical frontal part, and 10% for the conic model). Note that the MHD computations also show 5 - 10% wave drag reduction for the conic model.

Thus, the experimental and theoretical investigations of the gas discharge interaction with the supersonic airflows in the plasma aerodynamic experiment, carried out lately, open prospects for the development and application of plasma technologies in aerodynamics for a substantial improvement of the aerodynamic characteristics of flying vehicles.

References

1. A. ERSHOV, B. LIAGUSHIN, S. CHUVASHEV, B. TIMOFEEV, I. TIMOFEEV, *Ambient Air Modification for Drag Reduction: DC Discharges in Rarefied Supersonic Air Flow*, Proceedings, USAF Academy, Colorado 9-13 June 1997, Section M, p.M-3 - M-13.
2. S. CHUVASHEV, A. ERSHOV, A. KLIMOV, S. LEONOV, W. SHIBKOV, I. TIMOFEEV, *Flow around body and characteristics of AC/DC discharges in plasma aerodynamic experiment*, Proceedings 2-nd Weakly Ionized Gases Workshop, AIAA 8-th International Planes and Hypersonic Systems and Technologies Conference, April 24-30, 1998, Norfolk, Virginia, USA, p.59-67.
3. A.V. KRASILNIKOV et al., *Experimental and theoretical study of the possibility of reducing aerodynamic drag by employing plasma injection*, Proceedings 2-nd Weakly Ionized Gases Workshop, AIAA 8-th International Planes and Hypersonic Systems and Technologies Conference, April 24-30, 1998, Norfolk, Virginia, USA, p. 68-92.
4. A.F. ALEXANDROV, S. CHUVASHEV, A.P. ERSHOV, I. IMAD, I.B. TIMOFEEV, V.M. SHIBKOV, *High speed plasma jets in air, III Non laser continuous optical discharge in the atmosphere*, *Teplofizika Vysokikh Temperatur*, **31**, 5, 850-851, 1993.
5. A.P. ERSHOV, I.B. TIMOFEEV, S.N. CHUVASHEV, V.M. SHIBKOV, *Experimental realization of forming of the hot channel and supersonic motion of the plasma flow in the atmosphere without shock wave excitation*, IV International symposium on radiative plasmadynamics, Report thesis, Moscow, 1997, pp. 124-125.
6. E.M. BARKHUDAROV, V.P. BEREZOVSKII, M.O. MDINASHVILI et al., *Dissipation of the weak shock wave in the laser plasma in air*, *Pis'ma v Zhurnal Tekhnicheskoi Fiziki*, **10**, 10, 1178-1181, 1984.
7. A.M. GALKIN, N.N. SYSOEV, F.V. SHUGAEV, *Interaction of shock waves with the carbon torch. Collection of works: Kinetic and gasdynamic processes in nonequilibrium media*, Moscow, MSU publishers, 1984, p. 134.
8. A.I. KLIMOV, A.N. KOBLOV, G.I. MISHIN et al., *Propagation of shock waves in the glow discharge plasma*, *Pis'ma v Zhurnal Tekhnicheskoi Fiziki*, **8**, 7, 439-443, 1982.
9. G.I. MISHIN, *Shock waves in low ionized and low temperature plasma*, *Pis'ma v Zhurnal Tekhnicheskoi Fiziki*, **11**, 5, 274-278, 1985.
10. H. EDELS, D. NITTEIKER, *Detection of the arc temperature by the shock wave velocity. Collection of works: Optical pyrometry of plasmas*, Moscow, IL, 1960, p. 381.

11. A.F. ALEXANDROV, N.G. VIDYAKIN, V.A. LAKUTIN, M.G. SKVORTSOV, I.B. TIMOFEEV, V.A. CHERNIKOV, *Interaction of shock waves with the decaying plasma of the laser spark in air*, Zhurnal Tekhnicheskoi Fiziki, **56**, 4, 771-774, 1986.
12. A.F. ALEXANDROV, A.P. ERSHOV, A.A. KUZOVNIKOV, A.A. RUHADZE, S.F. TESELKIN, I.B. TIMOFEEV, *Shock Wave Interaction with Spatial-limited Low-temperature Plasma [in Russian]*, Fundamental Problems of Physics of Shock Waves, Chernogolovka, USSR, 1987, vol.2, pp.78-80.
13. P.A. VOINOVICH, A.P. ERSHOV, A.A. KUZOVNIKOV, S.E. PONOMAREVA, V.M. SHIBKOV, *About mechanisms of acceleration of shock waves in plasma of glow discharge in air [in Russian]*, Proc. III Conference on Physics and Gasdynamics of Shock Waves, Vladivostok, Russia, 1989, vol.2, pp.12-19.
14. A.P. ERSHOV, S.V. KLISHIN, A.A. KUZOVNIKOV, S.E. PONOMAREVA and YU.P. PYT'EV, *Interpretation of MW interferometer measurement of shock wave in a weakly ionized plasma*, Proc. XIX ICPIG, Belgrad, 1989, vol.4, pp. 846-847.
15. P.A. VOINOVICH, A.P. ERSHOV, S.E. PONOMAREVA, V.M. SHIBKOV, *Shock Wave Propagation on Glow Discharge Plasma in Air [in Russian]*, Preprint 1453, A.F.Ioffe Physicotechnical Institute, Academy of Sciences of the USSR, Leningrad, 1990.
16. A.P. ERSHOV, S.V. KLISHIN, A.A. KUZOVNIKOV, S.E. PONOMAREVA and YU.P. PYT'EV, *Analysis and interpretation of experiments on microwave interferometry of shock wave in a weakly ionized plasma*, High Temperature, **28**, 6, 779-785, 1990.
17. P.A. VOINOVICH, A.P. ERSHOV, S.E. PONOMAREVA and V.M. SHIBKOV, *Propagation of weak shock waves in plasma of longitudinal glow discharge in air*, High Temperature, **29**, 3, 468-476, 1990.
18. O.G. VASIL'EV, A.P. ERSHOV and S.E. PONOMAREVA, *Heat conduction precursor in the blast wave propagating in a weakly ionized plasma*, Moscow University Physics Bulletin, **49**, 2, 84-87, 1994.
19. A.P. ERSHOV, I.B. TIMOFEEV, V.A. CHERNIKOV, V.M. SHIBKOV, *Gas discharges in the supersonic airflows*, XXVI Zvenigorod conference on plasma physics and CTS.5-9 April, 1999. Report thesis.
20. A.S. ZARIN, A.A. KUZOVNIKOV, V.M. SHIBKOV, *Free localized microwave discharge in air*, Moscow, Neft i gas, 1996, p.204.
21. V.I. ALFEROV, A.S. BUSHMIN, B.V. KALACHEV, Zhurnal Exp. Teor. Fiz., **51**, 5 (11), 1281-1287, 1966.
22. YU.S. PROTASOV, S.N. CHUVASHEV, *Physical Electronics of gas discharge devices [in Russian]*, V2. Moscow. Vysshata Shkola, 1993, p.736.
23. L.M. BIBERMAN, V.S. VOROBIEV, I.T. YAKUBOV, *Kinetics of Non-equilibrium Low Temperature Plasma [in Russian]*, Moscow: Nauka, 1982.
24. N.V. ARDELYAN, K.V. KOSMACHEVSKII, S.N. CHUVASHEV et al, in: *Radiating Plasma Dynamics*, Moscow [in Russian], Energoatomizdat, 1991, pp.191-249.

INDUSTRIAL APPLICATIONS OF E-BEAM PLASMA TO AIR POLLUTION CONTROL

A. G. CHMIELEWSKI¹, Z. ZIMEK¹, E. ILLER¹, B. TYMIŃSKI¹, J. LICKI²

¹INSTITUTE OF NUCLEAR CHEMISTRY AND TECHNOLOGY

Warsaw, Poland

²INSTITUTE OF ATOMIC ENERGY

Otwock, Poland

Fossil fuel combustion creates a threat to environment. Waste quantities of SO₂, NO_x and VOC (volatile organic compounds) are emitted into atmosphere. Municipal wastes incineration is another air pollution potential problem. New technologies for simultaneous removal of different pollutants are searched for. Electron beam process is among the most promising advanced technologies of new generation. The laboratory unit (400 Nm³/h) and industrial pilot plant (20000 Nm³/h) have been constructed in Poland. Full scale industrial project is under development (270000 Nm³/h). New developments, connected mostly with energy consumption reduction, made this process very competitive in comparison with conventional technologies.

1. Introduction

The most important source of air pollution is the combustion of fossil fuels. Among the processes in which fuel is used for energy (electricity and heat) production coal burning plays a leading role. Burning fossil fuel is and will be the main source of energy for a long time. In the year 1995 the power installed based on the coal fired boilers was equal to 870 GW, oil fired boilers 435 GW, while the total world power installed was equal to 2900 GW. According to predictions the total number will increase to 5400 GW by the year 2020, including 1836 GW installed in power stations using coal and 648 GW in oil fired power stations [1].

When burning fossil fuels air polluting substances, in particular, SO₂, NO_x, volatile organic compounds (VOC) and other are generated. Flue gas compositions vary from one fuel to another [2, 3, 4], e.g. for lignite emissions of SO₂ as high as 5500 ppm are observed. Even though the concentration of pollutants is low the global emission is very high for the volume of flue gases emitted. In the case of hard coal the volumetric rate of gas flow (per MW of heat capacity) is in the range 1000 - 1500 m³/h (gas temperature 393 - 473 K), lignite - 1550 - 2200 m³/h (gas temperature 393 - 473 K). Combustion of one ton of municipal solid waste incineration creates 4200 m³ (505 K).

The worldwide emission of SO_2 only from coal fired power stations reaches about 55 million metric tons annually: 17.5 in the US, 7 in China, 6.6 in CIS, 3.6 in Germany, 1.9 in Poland, 2.2 in Bulgaria and 1.3 in Turkey. Emission from domestic and industrial furnaces which use coal as an energy carrier must be added to these numbers. It is necessary to remember that the total emission is much higher and, for example, in the case of China is equal to 22000 kt/year.

Emission of NO_x (recalculated as nitrogen) created by fossil fuel combustion including engines is equal to 21 million tons (N) annually [5].

VOC emissions from combustion (not including traffic) reach almost 0.2 million tons annually in the US only [6]. The total emission of this pollutant in GB was equal to 1.8 million tons and 2 million tons in France in 1989 [7].

Air pollution caused by particulate matter and other pollutants not only directly affect the environment but by contamination of waters and soil leads to their degradation. Wet and dry deposition of inorganic pollutants leads to acidification of the environment.

These phenomena affect people's health, increase corrosion, destroy cultivated soil and forests. Most of the plants, especially coniferous trees are not resistant to the influence of sulfur and nitrogen oxides. Following longer exposition leaves become yellow and fall down. Wide spread forest damage has been reported in most Central and Eastern European countries, as well as in the northeastern USA and Canada. Many cultivated plants are not resistant to these pollutants especially in the early period of vegetation.

The scheme, of the called "acid rains" formation, is presented in Fig. 1 [8]. Transportation distance of the pollutants, before being transferred to the acids and deposited, is equal to hundreds or thousands kilometers. In many cases pollutants are deposited over the territory of another country. Therefore, this is a global problem and subject of international treaties. This is the reason why in most countries all over the world emission standards have been introduced [9].

The mechanisms of pollutants transformation in atmosphere are described by environmental chemistry. The processes are rather complicated, some not very well clear so the reactions scheme differs from source to source. The pathways depends on many conditions (e.g. darkness, sunshine, air humidity or presence of dust or water droplets, presence of other pollutants). An important role in process mechanism is played by photochemistry. These reactions concern molecules which absorb highly energetic light in the region 300 - 700 nm.

Another problem discussed recently is the combustion of municipal solid waste. Waste incineration leads to volume and weight reduction, destruction of some components and detoxification of others, destruction of biodegradable compounds which emit methane to the atmosphere in an uncontrolled manner, energy recovery from organic compounds with adequate calorific value that leads to fossil fuel consumption reduction [4].

The public concern over incineration is connected with the identification of chlorinated dibenzo-p-dioxins and dibenzofurans in incinerator emission. These emissions are observed when incomplete combustion may occur when the incinerator is improperly operated, for example, operation at excessively low temperatures (below 800°C) or overloading of the plant.

Different technologies have been applied for air pollution control, e.g. coal

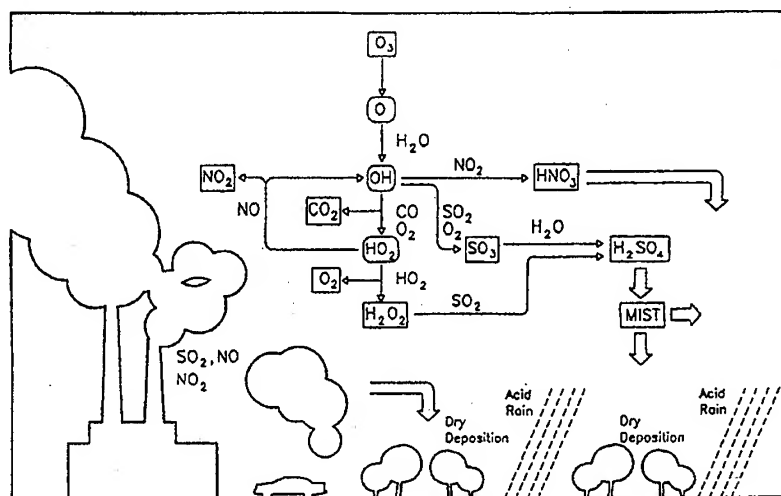


FIG. 1. Scheme of acidic rain formation [8].

and oil desulfurization, combustion modification or flue gas purification. The most widely applied system for coal fired boilers are wet flue gas desulfurization (FGD) using lime or limestone as reagent and selective catalytic reduction (SCR) for NO_x reduction. In the first case commercial or throw away gypsum is generated as a byproduct and in the second case NO_x are reduced to nitrogen using ammonia over a catalyst. Electron beam process is among the most promising advanced technologies of new generation where usable by product is also obtained during a gas purification process.

2. Electrons interaction with gas

Fast electrons which have a limited penetration range in matter are a good tool for processing of gases of low density (three orders of magnitude lower than that of liquids or solids). During the movement of electrons through a medium which consists mostly of light nuclei its energy is dissipated mainly through interactions with the orbital electrons, and ionization or excitation occurs. The average energy of an ion pair formation (ω) in gaseous material lies between 25 and 40 eV. The ionization potentials j of the gases are lower than the ω - values and the rest of energy $\omega - j$ must be used for excitation. For air ω is equal to 34 eV, ionization potential $j = 15$ eV, so $\omega - j = 19$ eV. The differences for the air components are not very large, $\omega = 34.9$ eV for N₂, 30.8 eV for O₂ and 32.8 eV for CO₂. Since the excitation energies per atom are ≤ 5 eV, several excited atoms are formed for each ion pair. Along the electron track excited and ionized molecules are formed and secondary electrons are liberated. The penetration range of electrons depends on their energy i.e. in air for 1 MeV electrons is equal

to 405 cm, for 3 MeV - 1400 cm and for 10 MeV - 4200 cm.

The energy is transferred to unit mass components as an absorbed dose. In the absence of chemical reactions, the ions recombine, excited species return to their ground states, and energy will appear as thermal energy (heat) that will cause the temperature to increase. This is a very useful dosimetric method often applied in gas treatment research systems.

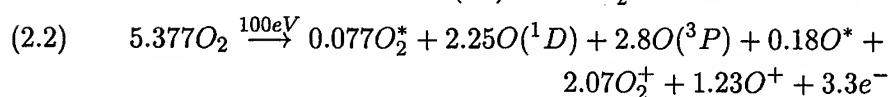
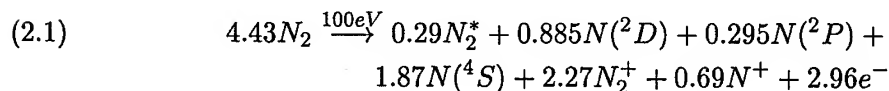
There is no possibility of photonuclear reactions which may induce radioactivity in materials for photons with energies below 10 MeV. Practically, in the case of flue gas treatment accelerators with electron beam energy less than 1 MeV are applied so these phenomena do not occur. Accelerators with electron energy up to 10 MeV are used commercially for radiation processing, sterilization and food irradiation.

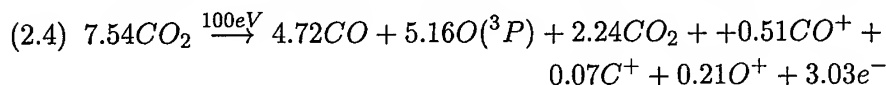
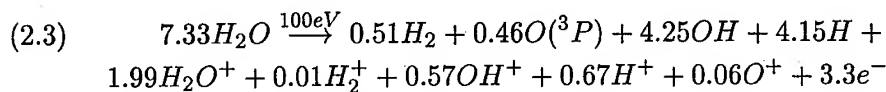
Energy of electrons is absorbed by the components of gaseous mixture proportionally to their mass fraction. In the case of air or flue gases a matrix consists of nitrogen, oxygen, water and carbon dioxide. In the case of electron beam irradiation only 6% or less of the absorbed energy is dissipated in vibrational excitation of molecules. Most of it is consumed in dissociation and ionization of molecules which is illustrated by data given in Table 1 [10].

Table 1. Energy dissipation in the plasma produced by electron beam irradiation of dry air (80%N₂ + 20%O₂)

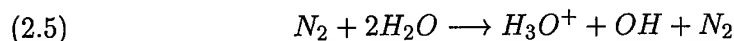
Process	Energy dissipation (% of input power)
N ₂ vibrational	5.3
N ₂ (A ³ Σ _u ⁺)	1.1
N ₂ (B ³ Π _g)	1.8
N ₂ dissociation	24.0
N ₂ dissociative ionization	13.9
N ₂ molecular ionization	28.3
O ₂ vibrational	0.6
O ₂ (a ¹ Δ _g)	0.7
O ₂ dissociation	8.3
O ₂ dissociative ionization	2.9
O ₂ molecular ionization	2.8
Others	10.3

The radiolytic yield of primary reactive species is given in the literature [11, 12]:

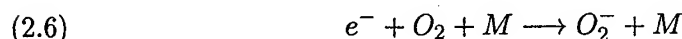




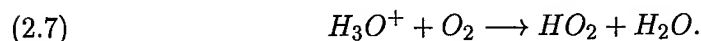
The G-values for the reactions presented in equations (2.1 - 2.4) are 6 ± 2 that corresponds to the radiolysis of 25 ± 10 of gas molecules per kGy. Some of the excited molecules react rapidly with the background molecules to produce additional dissociation. E.g. excited oxygen atoms $O(^1D)$ react rapidly with H_2O to form additional OH radicals. Ions react with H_2O to decompose it through a charge transfer



electrons react mainly with O_2 to produce O_2^- or its cluster ion



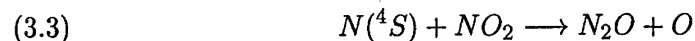
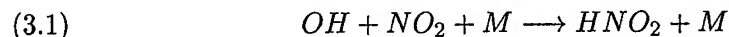
These ions neutralize to form HO_2



Therefore, one pair of ions produces one OH and one HO_2 radicals. The radicals produced initially through direct and ionic decomposition processes are OH, N, H_2O , O and H. These radicals react with NO and SO_2 which are good radical scavengers.

3. Nitrogen oxides and sulfur dioxide removal pathways

The biggest amount of nitrogen oxides is emitted by power plants which burn coal. In such a case 95% of the oxides is monoxide (NO) and NO_2 is the rest. NO is unsoluble, and a little reactive. Therefore in most cases it is necessary to oxidize it to NO_2 before the removal or reduce to gaseous nitrogen. In the case of electron beam treatment the most effective removal pathways are as follows:



SO_2 removal is based on two different pathways: thermochemical oxidation and radiation induced reaction. SO_2 oxidation in the gas phase is possible through direct photooxidation or oxidation through photochemically formed components (e.g. radicals) [6]. Even in the absence of light, SO_2 in air is oxidized in the presence of several metal oxides (aluminum, calcium, and iron).

However, conversion of SO_2 within liquid droplets, dew and on solid particles surfaces is of special significance for oxidation of SO_2 . This is a heterogeneous oxidation. The process is based on two steps ab(ad) sorption and chemical oxidation.

For small droplets and pH values below 6 the equilibrium between SO_2 in the gaseous phase and hydrogen sulfite or hydrate in the liquid phase is quickly reached. With decreasing pH values it shifts towards the gaseous phase. The factor determining the SO_2 transformation is the oxidation stage and not the SO_2 absorption in water [6]. The process of oxidation of SO_2 in droplets depends on many different factors and is not fully known. The oxidation of SO_2 by O_2 can be accelerated in polluted air by catalysts, in particular by magnesia and ferrous ions.

The reaction with OH radicals, as it is seen from this reaction, plays the most important role in SO_2 transformation. The rate constant of the first reaction (with OH) depends on temperature, pressure and water vapor content. A remarkable increase in process efficiency is observed in humid air or water droplets. The decrease of initial absolute humidity from 7 to 2% causes an increase of oxidation energy from 2 to 15 eV/molecule.

In the case of water droplets spray present in irradiation region, the observed chain reaction in the liquid phase leads to a significant energy consumption reduction for the SO_2 removal in a heterophaseous air stream. Firstly, this is connected with a well-known, from environmental chemistry, liquid-phase chain mechanism and secondly with a specially proposed ionic chain oxidation mechanism in a cluster [13].

SO_2 is converted to sulfuric acid which reacts with ammonia to form ammonium sulfate. The pathways of NO_x and SO_2 removal are presented in Fig. 2 [14]. It should be noted that SO_2 , besides the radical reactions, is removed via a thermochemical reaction. The mechanism of the second reaction is not fully known and some differences in the results obtained by different investigators were reported.

According to the observations in the environmental chemistry [15], the presence of ammonia in the air polluted by SO_2 does not lead to the formation of particles. But it has been realized that air photolytic particles, enriched in SO_2 , are of larger size when NH_3 is added. SO_2 dissolved in atmospheric water droplets form H_2SO_3 which is then oxidized by oxygen dissolved in droplets to sulfuric acid.

When an electron beam is applied, the oxidation of SO_2 is much faster due to the radical reactions. The formed SO_3 condensates in the presence of water vapor even at high temperatures. The role of water vapor was proven [16, 17], the reaction practically stops at temperatures below the dew point.

The positive role of increasing oxygen and nitrogen oxide concentration on the removal efficiency was observed [18]. However, in these investigations gas mixtures containing pure SO_2 were studied and the dew point temperature is characteristic for a given content of water vapor. Quite a different case concerns real flue gases from a power plant where SO_3 is always present. The understanding of the physico-chemical mechanism of the process allows the optimization of the removal process to achieve the highest SO_2 removal efficiency at the lowest

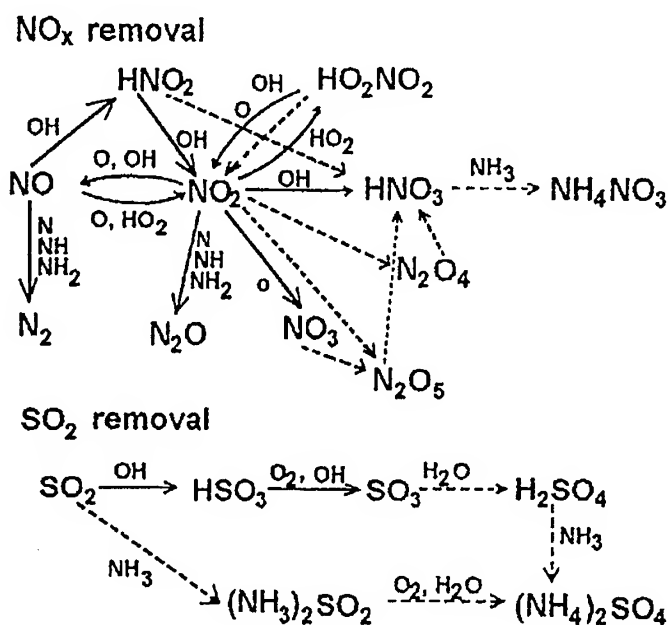


FIG. 2. Simplified pathways of SO₂ and NO_x removal in ammonia presence [14].

power (beam) consumption.

Sulfuric and nitric acids formed during flue gas treatment easily react with other than ammonia neutralizing reagents as well. Ca(OH)₂, KOH or NaOH can be used. Sulfates and nitrates result as products of these reactions.

Nitrous oxide (N₂O) occurs in the troposphere at the background concentration of about 300 ppb and measurement over the past two decades has shown that its concentration is rising at a rate of about 0.2 - 0.4% per year. The molecules, being chemically stable in the troposphere (the life time of approximately 150 years) if transported to the stratosphere undergo conversion to NO, which subsequently reacts with O₃. Hence an increase in N₂O emission is followed by further O₃ depletion in the stratosphere.

4. Volatile organic compounds reduction

Volatile organic compounds (VOC) are mostly toxic substances affecting human beings or the environment directly or as an ozone precursor. Ozone is formed as a product of the reaction of VOC with NO_x. VOC react in troposphere with hydroxyl radicals to form organic radicals which, through the reaction with oxygen, form peroxy radicals oxidizing NO. As a result of the photochemically induced reaction of NO₂ with oxygen ozone is formed.

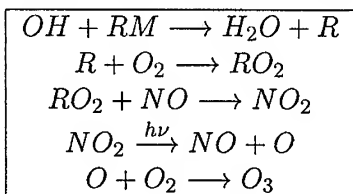
Different processes have been introduced for VOC removal from industrial gases. Adsorption, thermal catalytic and non catalytic combustion, biofiltration,

etc. Thermal combustion for low VOC concentrations is not very economical because the whole stream of flue gas has to be heated.

Electron beam application for the VOC destruction is advantageous due to the fact that the energy is directed preferentially toward pollutant molecules which act as scavengers of formed radicals. A carrier gas is heated slightly. A fast electron creates up to 3000 secondary electrons which slow down very quickly on the neutral species to the energy 0.025 - 1 eV.

Mechanism of energy transfer on the example of chloroorganic compounds destruction is given in Table 2 [19].

Table 2. Ozone formation in troposphere



The oxygen and chlorine radicals produced will react with other VOC molecules. Even in the case when the concentration of halogenated organic compounds is low in comparison with nitrogen or oxygen the attachment of slow electrons to them is much more probable.

The reactions of OH radicals with aromatic hydrocarbons occur via the addition of OH radicals to the aromatic ring (at temperature below 320°K). Two possible reaction pathways, namely the hydrogen diminishing and oxygen addition can be considered for reactions of the intermediate radicals with oxygen. The oxygen addition reaction may give a ring cleavage, which leads to the production of various organic compounds through the reactions with NO and/or oxygen. The predominant primary products of the ring opening reactions are simple aldehydes under tropospheric reaction conditions. These opening reactions are of minor importance compared with aerosol formation. The aerosol formation proceeds via retainment of the aromatic structure which is favorable from the energetic point of view. Such pathways may be a combination of oxidation and substitution reactions which would lead to the substituted xylene, toluene and benzene of low vapor pressure. Parallel to such reactions, coagulation of the molecules may take place to produce polymeric particles. With aliphatic hydrocarbons like butylacetate, no comparable reactions are possible, hence aromatic hydrocarbons like xylene are much more favorable for aerosol formation upon electron beam treatment [20].

The electron-generated plasma is used to decompose different chlorinated hydrocarbons. These compounds with more chlorine molecules are more easily decomposed. The electron-capture cross section is a measure of how readily a molecule captures a slow secondary electron. Molecules that have electronegative elements such as chlorine or fluorine are more likely to attach to free electrons, and these molecules have higher electron-capture cross sections. Consequently, the rate constant of their dissociation reactions will be higher.

For example CCl₄, which has four chlorine atoms per one carbon atom, has the highest electron-capture cross section of any chlorinated molecule. Therefore,

its rate constant for dissociative electron attachment is high and, as a result, the molecule will decompose more easily in the plasma than a VOC with a similar decomposition mechanism but of lower electron-capture cross section.

The energy efficiency for CCl_4 is insensitive to the gas temperature, at least up to 300°C . The mechanism of the process is discussed in [20]. The chain reactions may play a role in the decomposition of VOC (e.g. TCE) as well. The mechanisms of most of the reactions are still not very clear.

5. Electrical discharge process for pollution control

Electrostatic precipitation and pulsed corona discharge processes have a capability, as well as electron beam, to reduce SO_2 and NO_x concentration in treated flue gas. These non-thermal plasma discharge processes may produce electrons with the energy sufficient to form active radicals and initiate chemical reactions described in previous chapters.

Electrostatic precipitation has been practically implemented at the beginning of the century. This method is being now applied to collect the solid particles (ashes) in filters commonly installed in power stations. The typical configuration of such an instrument is composed of two electrodes where high voltage is applied to the wire against the grounded plate to form corona discharge region consisting of electrons and ions. These charged particles interact with particulates which are driven latter to the collecting plates. The radical formation in such equipment depends on the electric field strength. The radicals' formation process can be optimized by the use of the pulse power technology where fast rising, short length high voltage pulses are applied.

Pulse corona discharge process provides the benefit of better control of the process and lower retrofit cost to compare with electrostatic precipitators. The significant advantage of corona discharge process to compare with electron beam treatment is related to less expensive apparatus needed to perform this process. The high voltage generators are usually simpler and cheaper than electron accelerators. On the other hand the high power, high voltage pulse generators with sufficient electrical efficiency are not yet commercially available.

An even more important fact is related to the cost of implementation of certain technology. Both pulse corona discharge and electron beam methods were found to be competitive to conventional SO_2/NO_x removal processes [21]. Having in mind the best experimental results achieved in pilot plant tests with application of pulse corona discharge and electron beam treatment the power requirement and cost estimates were performed by Penetrante [22, 23]. In accordance with the process mechanism discussed in chapter 3 the main part of energy provided by ionizing radiation is consumed by NO_x removal process. SO_2 is mostly removed in thermal reaction processes. Therefore the comparison of the pollution removal processes can be done on the base of NO_x removal efficiency.

The best value of specific energy consumption for NO_x achieved by the electron beam process is found to be $14 \text{ eV}/\text{NO}_x$ molecule whereas the same value for pulse corona discharge process is $50 \text{ eV}/\text{NO}_x$ molecule. This experimental results provide necessary information to calculate the total energy consumption for SO_2/NO_x removal process for certain initial NO_x concentration. It was found

that for 350 ppm of NO_x initial concentration the power requirements for electron beam process is 1.5% of the total power output of the plant whereas the same value for pulse corona discharge process is 5.3%.

The experimental data are based on laboratory and pilot plant tests already performed. At the moment three industrial installations for EB treatment are under construction/operation. The full cost and process cost effectiveness will be known in the year 2000. As soon as corona discharge industrial plant is constructed the final comparison could be done.

6. Laboratory and pilot installations

6.1. Laboratory installation at INCT

A laboratory unit with a gas flow capacity of up to $400 \text{ Nm}^3/\text{h}$ has been constructed at the INCT [24]. The composition of flue gases from two natural gas fired boilers can be adjusted by the dosage of different gaseous pollutants (SO_2 , NO_x , VOC). An irradiator, accelerator ILU-6 is used with an electron beam energy in the range 600 - 1000 keV. The installation is completed with two independent microwave generators. This allows to investigate a combined removal concept based on the simultaneous use of electron beam and streams of microwave energy to produce free radicals in the reaction vessel [25]. The simultaneous use of the electron beam and microwave energy increase the total removal efficiency at the same power consumption [26].

The system has been used for the investigation of SO_2 removal from off-gases with high SO_2 concentration (up to 15%). This range of SO_2 concentration is observed in the case of off-gases emitted in the processes applied in the copper industry [27].

Flue gas with high SO_2 content can be effectively cleaned by NH_3 and electron beam treatment, even at higher than optimal, temperatures. 90-95% of the efficiency the SO_2 removal was obtained in specific conditions (10 - 15% SO_2 content). The ammonia stoichiometry, humidity and a dose up to 7 kGy have a strong influence on the SO_2 removal efficiency. The product formed in the process is ammonium sulfate.

The other problem investigated was electron beam induced destruction of VOC. A very resistant to radiation benzene vapor was investigated. The doses were established by using foil (PCV) dosimeters in accordance with the standard procedures. Simulated gases were composed of air, 10% water vapor and two initial concentrations of benzene $3.48 \cdot 10^{-6} \text{ g/cm}^3$ and $3.5 \cdot 10^{-5} \text{ g/cm}^3$. A large number of unidentified organic products obtained by irradiation was detected by gas chromatography. A Perkin Elmer 8700 gas chromatography was used for the determination of radiolysis products. The chromatography was equipped with a flame ionization detector (FID) and a capillary column of 12.5 m in length. Temperature of the oven was kept at 110°C (isothermal) and the gas flow was 40 ml He/min. These conditions assured the measurement of phenol with an accuracy of $3.48 \cdot 10^{-12} \text{ g/cm}^3$. Phenol constituted the main product of benzene radiolysis. The removal efficiency amounted to ca. 45% for benzene under the dose 40 kGy. The relatively low efficiency is caused by exceptionally

high resistivity of benzene to radiation.

The described laboratory installation can be used for the development of new electron beam based processes and for the investigation of optimal physico-chemical parameters. However, this unit, and other units of this size used in different laboratories all over the world, cannot be used for process upscaling. Dimensions of laboratory irradiation chambers do not allow to study the effect of electron (with limited range of penetration) interaction with separate fragments of flue gas streams flowing inside large ducts. Industrial pilot plants (size of 20000 Nm³/h and bigger) are necessary to be constructed to investigate these phenomena.

6.2. Pilot plant at EPS Kawęczyn

Two modern pilot plants based on the multistage gas irradiation principle were constructed in Poland (INCT-EPS Kawęczyn) [28] and in Japan (Ebara-JAERI-Chubu Electric) [29] at the same time. The first pilot plant is still operational [30]. The Polish pilot plant was constructed at the Electropower Station Kawęczyn [31]. It was installed on a bypass of the main flue gas stream from a boiler WP-120. A scheme of the installation is given in Fig. 3. Two accelerators ELV-3a (50 kW, 500 - 800 keV) were installed in series on the reaction vessel. For the first time in an industrial pilot installation, a cascade double gas irradiation was applied.

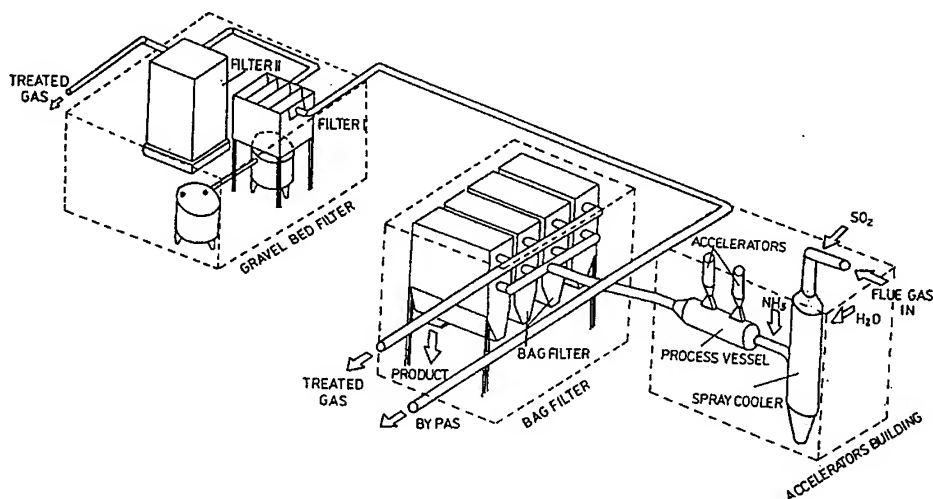


FIG. 3. Industrial pilot plant for flue gas treatment at EPS Kawęczyn.

Flue gases are cooled down in a spray cooler working in "dry-bottom" conditions and then irradiated in two steps in the reaction vessel which is a cylinder 7 m long and 1.6 m in diameter [32]. The double window system was employed, with the windows made of 50 μ m thick titanium foil. An "air curtain" was used

to separate the secondary window from the corrosive flue gas. Gaseous ammonia is injected by nozzles upstream of the flue gas irradiation. Aerosols formed in the process (ammonium sulfate and nitrate) are captured in filters. The particles formed are small of diameter lower than $1\text{ }\mu\text{m}$ and sticky. Two types of filters were applied - a bag filter and a gravel bed filter [33, 34]. The bag filter consists of four compartments with a total filtration area of 600 m^2 (512 bags). An "off line" regeneration mode was used (one compartment in regeneration, three others in operation). The bag filter system is equipped with two lines for filtration aid dosage. One of them could be used for precoating, while the other one allowed the introduction of additional powder during the continuous operation. Another system for filter preheating and air conditioning was designed and applied. Filter walls are insulated and bottom heated. Different types of bag fabrics were investigated and cages construction modified to obtain good bag regeneration (cleaning from the product). The continuous 30 day test of the installation, equipped with the filter described, has been performed. Very high aerosol removal efficiencies have been achieved (over 99.8%). However, to obtain the stable operation of the filter (constant pressure drop) it is necessary to apply filtration aid (silica, fly ash, dolomite etc.) and to keep a filter temperature in the range $70 - 80^\circ\text{C}$.

The wet gravel bed filter was designed together with Forschungszentrum, Karlsruhe where this type (dry and wet) of equipment was developed for the process. In this case the byproduct (soluble) can be easily separated from fly-ash (unsoluble). The off-line cleaning of the gravel from fly ash was applied in the system. The experiments have proved that the fly ash presence in the flue gas do not affect SO_2 and NO_x removal efficiency (investigated range 100 - 700 mg of solid particles/ Nm^3 at the inlet). An additional SO_2/NO_x removal was obtained in the wet filter. However, the product in this case is obtained in the form of aqueous solution (liquid fertilizer or crystallization). The concentration of the nitrogen salts cannot be higher than 40%wt.

The pilot plant is equipped with a modern monitoring and control system [35, 36]. The manual sample grab methods were used for their verification.

The first experiments were performed with gas humidity of 7 - 8% vol. and its temperature (at the irradiation vessel inlet) being $70 - 80^\circ\text{C}$. The SO_2 removal efficiencies, depending on the inlet concentration, were 70 - 90%, while the NO_x removal efficiencies, depending on the dose, process parameters and inlet concentration, were 70 - 90%.

The fact that the NO_x removal efficiency depends mostly on the dose and, on the other hand SO_2 is mostly removed via a thermal reaction, impose an interesting observation concerning the ammonia consumption in both reactions. The thermal reaction efficiency for SO_2 removal decreases with temperature. Thus, at higher temperatures more ammonia (at constant stoichiometric ratio) is available for concurrence of NO_x reductive processes. However, there are not the only phenomena which affect the process, that is well illustrated by the further described experiment (the influence of ammonia stoichiometry). SO_2 is more reactive with ammonia, at a given dose, SO_2 removal efficiency is strongly dependent on ammonia stoichiometry. There is not a big influence of ammonia stoichiometry (at a given dose) on NO removal efficiency; this is well illustrated

by the fact that the reaction yields (NO reduction and oxidation path ways) depend mostly on the dose.

The first set of experiments, as has been already mentioned, was performed for low gas humidity and at rather high temperatures. For the second set of experiments the humidification system of the Kawęczyn pilot plant was upgraded. The high enthalpy water was used, packing was introduced into the column and water recirculation was applied. The humidity of flue gases can be increased up to 15% vol. and the inlet temperature reduced down to 45°C. In these conditions the SO₂ removal efficiency as high as 98% can be achieved (Fig. 4). Due

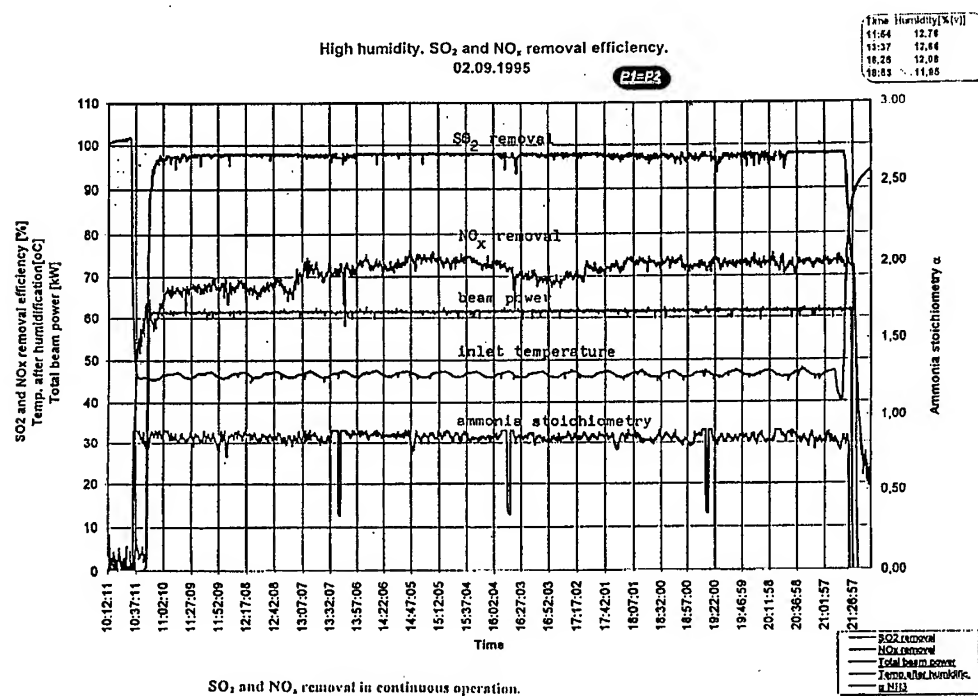


FIG. 4. Record of pilot plant parameters during continuous operation.

to the thermal reaction a very low dose is required to obtain a high removal efficiency. It is important to note that an adequate dose is necessary to obtain the oxidized byproducts (sulfate and nitrate). In the case when a moderate NO_x removal efficiency is required, the economical competitiveness of the EB process with conventional technologies further increases.

A high removal efficiency was obtained with the use of a bag filter. The other methods of filtration, gravel bed [37] and wet gravel bed filters were investigated. However, all these experiments proved that no special methods of filtration should be developed; the most adequate ones are already offered by equipment manufactures e.g. dry and wet ESP's.

The most important problem to be solved in the upscaling process is the irradiation vessel construction. In the Kawęczyn's pilot plant longitudinal, double

irradiation of the flue gases has been applied.

Because of the limited electrons penetration the adequate beam energy is required [38]. A marker seen on the photographs presented in Fig. 5 has been installed in the horizontal axis of the irradiation vessel. The glowing ionized gas

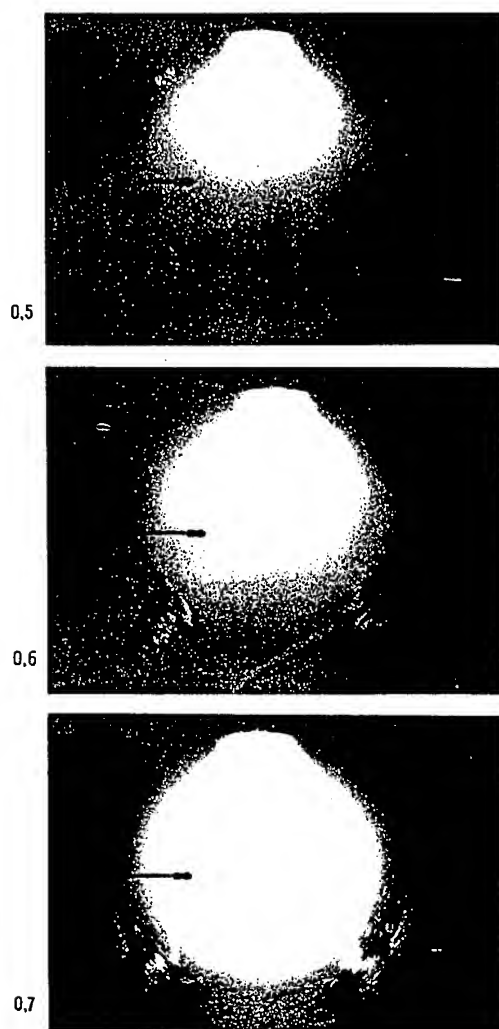


FIG. 5. Photographs illustrating electrons penetration range (ionisation plume).

plum only in the case of electrons energy 0.7 MeV covers the whole irradiation vessel intersection. The losses in the beam energy delivered to the gas consist of two components; the stopping power of two titanium foil windows and the air in the gap between them and the absorption in the walls of the irradiation chamber. Of course losses connected with gas heat dissipation are not discussed here. For electrons with lower energy the losses of power in the windows system

are higher. On the other hand for higher energy electrons the energy absorbed by the vessel walls (and losses) are higher. Therefore, an optimum energy of electrons for a given vessel design exists. For an optimum energy the highest NO_x removal efficiency can be achieved.

The improvement of removal efficiency due to the limited electron penetration through the flowing gas can be achieved by a multistage irradiation. The gas mixing between irradiation stages is favorable for the process. The further optimization can be achieved by an adequate dose distribution between irradiation stages [39].

A comparison of the experimental data for a single-stage and two-stage irradiation indicates agreement with theoretical assumption. The case of three-stage irradiation concerns only the data theoretically calculated because at the pilot plant only the cases of single-stage and two-stage irradiation can be studied. A deeper analysis of the multistage process of the flue gases exposition by an electron beam revealed that in the case of NO_x removal a non-uniform power distribution of the accelerators at the successive stages will provide further energy savings.

An optimal distribution of the electron energy dose supplied to the gas has been calculated with the use of the dependence for NO_x removal after its two-stage and three-stage exposition by an electron beam of a given energy. The experiments have confirmed theoretical computations. However, the energy savings in the case of non equal stage irradiation are not so significant as in the case of the substitution of the single-stage irradiation by the two-stage one.

7. Comparison of solutions applied in different pilot plants

Four industrial pilot plants for the flue gases from coal fired boiler have been built all over the world (Indianapolis, USA; Karlsruhe, Germany; Kawęczyn, Poland and Nagoya, Japan). Most of the technological solutions were similar and the main differences concerned the irradiation vessel construction. The process vessel applied in the four earlier mentioned cases is presented in Fig. 6 [40].

A dose distribution must be considered during the design of the process vessel. It is worth mentioning that only in the case of the Polish pilot plant the longitudinal gas irradiation was applied which is favorable for optimum vessel geometry solution. The dose distribution which is non uniform due to the physical properties of electron radiation, is the reason why the multistage gas irradiation gives a better NO_x removal efficiency in comparison with a single step process. Mixing between the stages causes a better energy distribution to volumes control of the gas flowing through the vessel [41]. A similar result can be obtained through both sided irradiation which was proved in the Nagoya experiment [42, 43].

A comparison of the SO_2 and NO_x removal efficiency obtained at the different pilot plants is given in Fig. 7 and Fig. 8. The tendencies in changes of the curves representing the above functions are similar; differences in the results obtained were connected with different test conditions.

A higher removal efficiency of NO_x (at least at higher process temperatures) is observed for higher SO_2 inlet concentrations (at a given dose). The phenomenon can be caused by the NO_2 (oxidized NO) absorption in sulfuric acid mist (formed

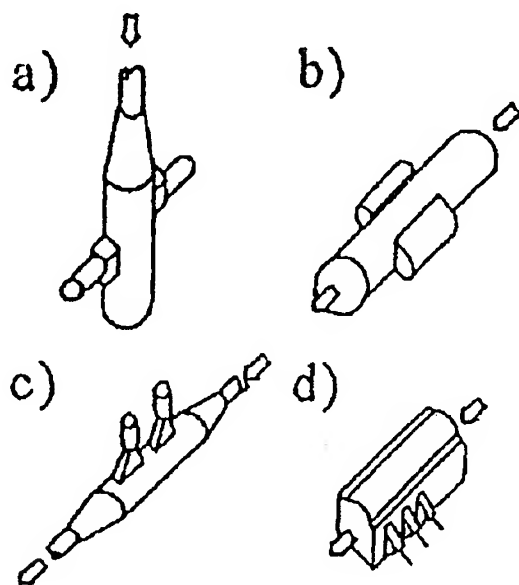


FIG. 6. Process vessel geometry for different pilot plans: a) Indianapolis, b) Karlsruhe, c) Kawęczyn, d) Nagoya.

by SO_3 increased concentration). However, this phenomenon was not proved in another experiment [44]. It is important to mention that temperature conditions in the second case were quite different from those in the first reported case. However, reports from Indianapolis, USA and Badenwerk, Germany pilot plants operation noticed a similar, as the EPS Kawęczyn pilot, positive influence of the SO_2 inlet increased concentration on the NO_x removal efficiency [41].

An exemplary composition of a byproduct for the coal fired boiler flue gases is given in Table 3. In principle, the byproduct with a small fly ash content (less than 2%) is equivalent to a commercial fertilizer - ammonium sulfate. The granulated form has more valuable and can be sold at higher price, so dry granulators are proposed for the byproduct final treatment.

Table 3. Byproduct composition (coal fired boilers), wt %

Pilot plany	$N(\text{total})$	$N(\text{NH}_4^+)$	$N(\text{NO}_3^-)$	$S(\text{total})$	$S(\text{SO}_4^{2-})$
Kawęczyn	19.5-21.6	19.4-20.7	0.74-1.9		
Badenwerk	19.5	19.4	0.74	25.5	24.5
		NH_4^+	NO_3^-	SO_4^{2-}	
Nagoya		25.4	5.45	65.6	
			NH_4NO_3	$(\text{NH}_4)_2\text{SO}_4$	
Indianapolis			5	95	

Another possibility is to use the byproduct as a component of the NPK fertilizer. A test performed in Poland has proved that a blend obtained with

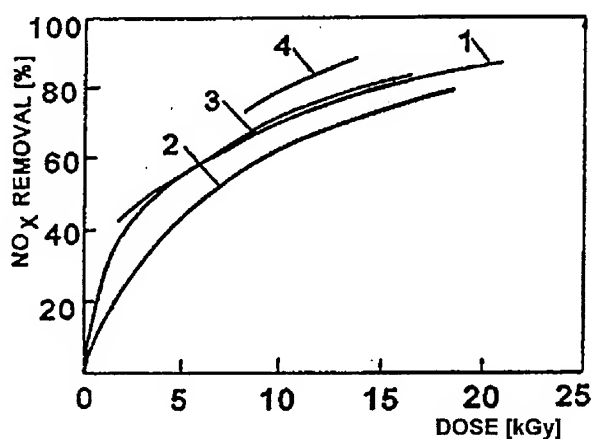


FIG. 7. Nitrogen oxides removal vs. dose. 1 - Indianapolis; $\text{NO}_x = 270\text{--}390$ ppm, $\text{SO}_2 = 800\text{--}1500$ ppm, $T_{\text{out}} = 80\text{--}85^\circ\text{C}$, $R_{\text{NH}_3} = 0.8\text{--}1.17$, 2 - Badenwerk, $\text{NO}_x = 250\text{--}450$ ppm, desulfurized gaz, $T = 70^\circ\text{C}$, $R_{\text{NH}_3} = 0.7\text{--}1.5$, 3 - Kawęczyn, $\text{NO}_x = 150$ ppm, $\text{SO}_2 = 300$ ppm, $T = 70^\circ\text{C}$, $R_{\text{NH}_3} = 0.8$, 4 - Nagoya; $\text{NO}_x = 200\text{--}220$ ppm, $\text{SO}_2 = 650\text{--}950$ ppm, $T_{\text{out}} = 63\text{--}72^\circ\text{C}$.

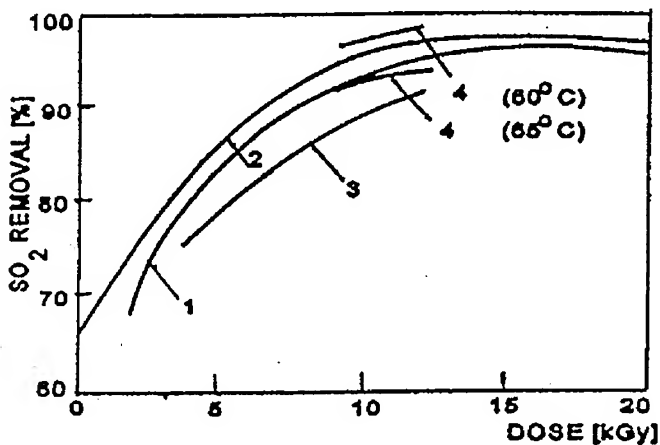


FIG. 8. Sulphur dioxide removal vs. dose. 1 - Indianapolis; $\text{SO}_2 = 800\text{--}1500$ ppm, $T_{\text{out}} = 74\text{--}77^\circ\text{C}$, $R_{\text{NH}_3} = 0.84\text{--}1.17$, 2 - Badenwerk, $\text{SO}_2 = 300$ ppm, $T = 70^\circ\text{C}$, $R_{\text{NH}_3} = 1$, $\text{H}_2\text{O} = 7\text{--}12\%$, 3 - Kawęczyn, $\text{SO}_2 = 1000$ ppm, $T = 70^\circ\text{C}$, $R_{\text{NH}_3} = 0.75$, $\text{H}_2\text{O} = 5\text{vol}\%$, 4 - Nagoya; $\text{SO}_2 = 700\text{--}850$ ppm, $T_{\text{out}} = 60\text{--}65^\circ\text{C}$.

the application of this byproduct meets the standards established for this kind of fertilizers.

Agriculture tests have been performed with a pure byproduct and a byproduct with different fly-ash content. Results are very positive. The byproduct was registered as a fertilizer in Japanese Fertilizer Act as well.

The content of heavy metals, e.g. [ppm]:

Pb	Cd	Cr	Hg	As
< 5	0.5 - 0.6	1.24	0.025 - 0.05	0.025 - 0.39

is much lower than the values allowable for commercial fertilizers which are:

As - 50 ppm, Cd - 140 ppm, Pb - 140 ppm, Hg - 2 ppm.

The worldwide consumption of ammonium sulfate is estimated to be approximately 15 million tons/year; in the US - 2 million tons/year. It is interesting to note that the demand for fertilizers containing sulfur will increase in the future.

Researchers used to believe that S deficiencies could not exist in the industrial countries and, as a result, few scientists conducted research on the S nutrition of arable crops. Special attention needs to be given to Brassica crops because of their considerable importance for agriculture in the northern Europe and their high demand for S. The reason for increasing S deficiency symptoms in Brassica species is based predominantly on the significant reduction of atmospheric S deposition to agricultural ecosystems during the last decade. The reduction of the S supply has also caused increased ecological problems because of the reduction of fertilizer N efficiency in S-deficient crops, resulting in increased leaching of nitrate into groundwater and probably increased accumulation of surface ozone [43].

8. Industrial projects

Three industrial projects are under development (China, Japan, Poland). The others are planned, for example in the US [45]. The last project will apply a modern technology based upon the high-power transformer accelerator (HPTA).

Ebara Corporation, Japan constructed an electron beam desulfurization plant at Seito Electrical Plant, Sichuan Electric Power Administration [46]. The installation treats flue gases from a 100 MW coal (2% S) fired boiler. Flue gas throughput is 300000 Nm³/h and is treated with a 3.2 kGy dose, assuring the 80% SO₂ and 10% NO_x removal. The inlet concentrations of SO₂ are 2000 ppm. Two sets of accelerators, 800 keV and 400 mA, are applied. The byproduct fertilizer production rate is approximately 2470 kg/h.

A construction of another plant has started in Nishi-Nagoya Thermal Power Plant which belongs to Chubu Electric Power Company, Inc. The installation will treat 620000 Nm³/h flue gases emitted from a 220 MW_e boiler [46].

The experience gathered during laboratory and pilot plant tests has allowed the preparation of a full scale industrial plant design. The plant will be built in the Electropower Station Pomorzany ("Dolna Odra" Group). The flow rate of the gas will be 270 000 Nm³/h [475]. The flue gas purification will treat flue gases from the block which consists of two Benson type boilers of power 56 MW_e each supplying additional steam for heating purposes up to 40 MW each. The boilers will be reconstructed during the flue gas treatment plant construction, to reach the power of 60 MW_e and 100 MW_{th} each. The annual operating time is 6500

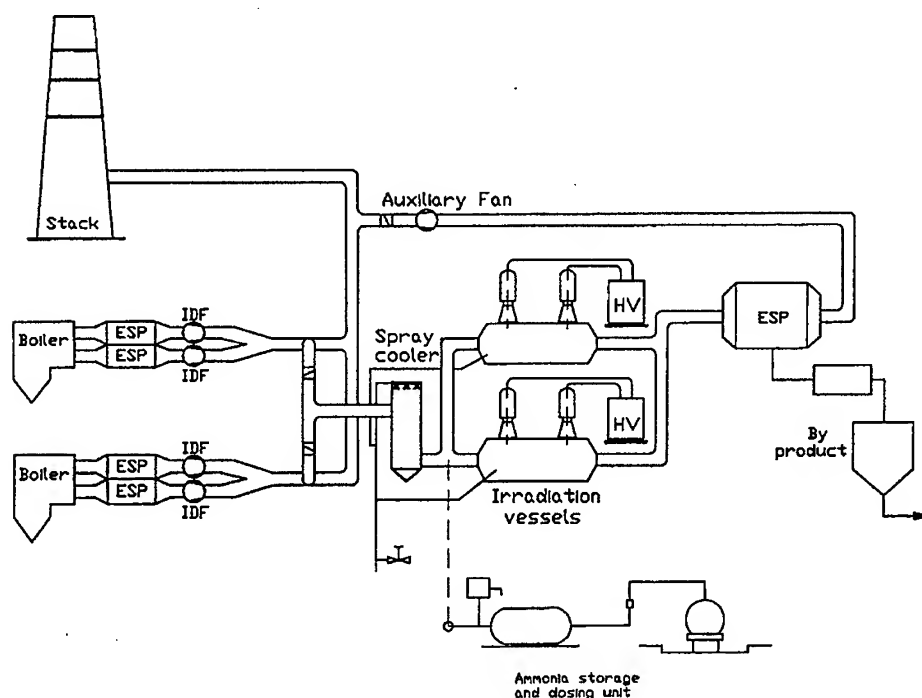


FIG. 9. Scheme of industrial plant at EPS Pomorzany, Szczecin.

h/year of equivalent to full-load operation. A scheme of the industrial electron beam plant is presented in Fig. 9. The boilers fire pulverized bituminous coal that has the following characteristics: caloric value 22820 kJ/kg, sulfur content 0.72 - 0.8%, ash content 21.8%, moisture content 7.8%. The boilers are equipped with modern four zone electrostatic precipitators with a fly-ash removal efficiency of 99.8%. The emission of SO_2 and NO_x has to meet the Polish standards which will be 870 g/GJ and 170 g/GJ, respectively. The local ambient air standards must be observed as well. The guaranteed removal efficiency must be equal to a minimum of 80% for NO_x and 70% for SO_2 . However, the efficiencies possible to obtain are 80 and 95%, respectively. This range allows to operate the installation at a quite high (over 100°C) stack temperature.

The flue gas will be humidified up to 10% by volume, in a dry bottom spray cooler. Then ammonia will be injected before two parallel irradiation vessels equipped with two 300 kW, 800 kV accelerators installed in the series (Kawęczyn pilot plant's solution). The longitudinal gas irradiation will be applied. The finally formed aerosol will be collected in a dry ESP with a flat heated bottom furnished in the scraping device. The manufacturers guarantee a high removal efficiency (particulate at the outlet less than 20 mg/Nm^3) and corrosion resistivity of the equipment. The product will be granulated.

The ammonia consumption is estimated to be 180 - 200 kg/h and the byprod-

uct yield ca. 800 kg/h. High power accelerators have to be applied in such big systems [48]. Two accelerators $2 \times 2 \times 300$ kW (two HVS plus two heads each) with 800 keV electrons energy will be applied.

9. Conclusions

The tests performed on laboratory installations and pilot plants resulted in the preparation of industrial plants design. All the technical and economical analyses proved the advantages of this technology over the conventional technologies nowadays used. The designed flue gas treatment plant with the 1.2 MW beam power will be one of the biggest radiation processing unit in the world.

References

1. H.R. WOLK, *Electric power supplies - the next 25 years*, 5th World Congress of Chemical Engineering, San Diego, USA, 15-18 July 1996.
2. H. MICHELE, *Purification of flue gases by dry sorbents - possibilities and limits*, Intern. Chem. Eng., **27**, 2, 183-196, 1987.
3. J.R. JORDAN, *The feasibility of wet scrubbing for treating waste-to-energy flue gases*, APCA Journal, **37**, 4, 422-430, 1987.
4. *Waste incineration and the environment*, in: *Environmental science and technology*, Eds. R.E. Hester, R.M. Harrison. The Royal Society of Chemistry, Cambridge 1994.
5. *Emission standards handbook*, IEACR/43, IEA Coal Research, London 1991.
6. G. Baumbach, *Air quality control*, Springer Verlag, Berlin 1996.
7. *Volatile organic compounds in the atmosphere*, in: *Environmental Science and Technology*, Eds. R.E. Hester, R.M. Harrison, The Royal Society of Chemistry, Cambridge 1994.
8. H. NAMBA, *Collecting of by-products by ESP and bag filter*, in: *Regional training course on electron beam technology for purification of flue gases*, UNDP/IAEA/RCA. Takasaki, Japan 5-9 February 1996, pp. 17-21.
9. W. ELLISON, *Limiting of SO₂ and NO_x emissions in worldwide coal - power production*, Rad. Phys. Chem., **45**, 6, 1003-1011, 1995.
10. B.M. PENETRANTE, *Economics of electron beam and electrical discharge processing for post-combustion NO_x control in internal combustion engines*, in: 6th SDIO/ONR Pulse Power Meeting, Chicago, USA. 9-11 August 1993, pp. 1-8.
11. J.C. PERSON, D.O. HAM, *Removal of SO₂ and NO_x from stack gases by electron beam irradiation*, Radiat. Phys. Chem., **31**, 1-3, 1-8, 1988.
12. H. MATZING, *Model studies of flue gas treatment by electron beams*, in: *Application of isotopes and radiation in conservation of the environment*, IAEA-SM-325/186, International Atomic Energy Agency, Vienna 1995, pp. 115-124.
13. E.J. BARANCHICOV et al., *Investigation of SO₂ oxidation in humid air stream by high current density pulsed electron beam*, Radiat. Phys. Chem., **45**, 6, 1063-1066, 1995.
14. S. HASHIMOTO, H. NAMBA, O. TOKUNAGA, *Factors affecting removal of NO_x and SO₂*, in: *Electron beam flue gas treatment - research cooperation among JEARI, IAEA and INCT*, JAERI-Research 96-053, JAERI, Takasaki 1996, pp. 7-16.
15. *Environmental chemistry*, Ed. J.O'M. Bockris, Plenum Press, NY-London 1978.
16. H. BAI, P. BISWAS, T.C. KEENER, *Particle formation by NH₃-SO₂ reactions at trace water conditions*, Ind. Eng. Chem., **31**, 88-94, 1992.

17. K. HIROTA et al., *Reactions of sulfur dioxide with ammonia*, Env. Sci. (Japan), **6**, 2, 143-150, 1993.
18. K. HIROTA, J. MAKELA, O. TOKUNAGA, *Reactions of sulphur dioxide with ammonia: dependence on oxygen and nitric oxide*, Ind. Eng. Chem. Res., **35**, 3362-3368, 1996.
19. K. HIROTA, H. MATZING, H.R. PAUR, *Removal of gaseous xylene by electron beam irradiation*, in: Proceedings of the 6th Japan - China Bilateral Symposium on Radiation Chemistry, Tokyo, Japan, 1994.
20. S.A. VITALE et al., *Decomposing VOCs with an electron-beam accelerator*, CHEMITECH, **4**, 58-63, 1996.
21. D. BHASAVANICH, S. ASHBY, C. DEENEY, L. SCHLITT, *Flue gas irradiation using pulsed corona and pulsed electron beam technology*, Proceedings of 9th IEEE International Pulsed Power Conference, Albuquerque, New Mexico, 1993.
22. B.M. PENETRANTE, *Pollution control application of pused power technology*, Proceedings of 9th IEEE International Pulsed Power Conference, Albuquerque, New Mexico, 1993.
23. B.M. PENETRANTE, *Economics of electron beam and electrical discharge processing for post-combustion NO_x control in internal combustion engines*, 6th SDIO/ONR Pulse Power Meeting, Chicago, 9-11 August, 1993.
24. A.G. CHMIELEWSKI et al., *Laboratory and industrial research installations for electron beam flue gas treatment*, in: *Application of isotopes and radiation in conservation of environment*, IAEA-SM-325/124. International Atomic Energy Agency, Vienna, 1992, pp. 8-92.
25. Z. ZIMEK et al., *Flue gas treatment by simulataneous use of electron beam and streams of microwave energy*, Rad. Phys. Chem., **46**, 4-6, 1159-1162, 1995.
26. Z. ZIMEK et al., US Patent **5**, 397, 444, 1995.
27. L. VILLANUEVA, L. AHUMADA, J. LICKI, *Possible use of electron beam treatment for removal SO₂ in off-gases from copper smelters*, in: *Clean technology for the mining industry*, University of Concepcion, Concepcion-Chile 1996, pp.165-174.
28. A.G. CHMIELEWSKI, E. ILLER, Z. ZIMEK, J. LICKI, *Pilot plant for electron beam flue gas treatment*, Radiat Phys. Chem., **40**, 4, 321-325, 1992.
29. H. NAMBA et al., *The study on electron beam flue gas treatment for coal-fired thermal plant in Japan*, Radiat. Phys. Chem., **42**, 4-6, 669-672, 1993.
30. A.G. CHMIELEWSKI et al., *Pilot plant for flue gas treatment - continuous operation test*, Radiat. Phys. Chem., **46**, 4-6, 1067-1070, 1995.
31. A.G. CHMIELEWSKI, E. ILLER, M. ROMANOWSKI, *Pilot plant for electron beam SO₂ and NO_x removal*, Report INCT-2125/VI, Institute of Nuclear Chemistry and Technology, Warszawa, 1991.
32. A.G. CHMIELEWSKI et al., *The double window for electron beam injection into the flue gas process vessel*, Radiat. Phys. Chem., **45**, 6, 1029-1033, 1995.
33. A.G. CHMIELEWSKI, B. TYMINSKI, G. ZAKRZEWSKA-TRZNADEL, *Separation of aerosols from irradiated flue gas in bag filter*, in: Proceedings of International Symposium on Filtration and Separation of Fine Dust, Wirtschaftskammer Osterreich, Vienna, 1996, pp. 140-150.
34. A.G. CHMIELEWSKI et al., *Separation of fine aerosols from irradiated flue gas in wet granular bed filter*, *ibid*, pp. 30-41.
35. J. LICKI et al., *Monitoring and control systems for an EB flue gas treatment pilot plant - part I. Analytical system and methods*, Rad. Phys. Chem., **40**, 4, 331-340, 1992.
36. J. SZLACHCIAK et al., *Monitoring and control systems of an EB flue gas treatment*, Part 2. Radiat. Phys. Chem., **40**, 4, 341-346, 1992.
37. Z.Z. HULEWICZ, A.G. CHMIELEWSKI, *On dry granular bed filtration of aerosols induced by irradiation*, Radiat. Phys. Chem., **45**, 6, 1039-1047, 1995.
38. P. PANTA, W. GLUSZEWSKI, S. BULKA, *Dosimetry for process vessel for flue gas treatment pilot plant*. *Raporty IChTJ*, Seria A nr. 1/97, Institute of Nuclear Chemistry and Technology, Warszawa, 1991.

39. A.G. CHMIELEWSKI et al., *Optimization of energy consumption for NO_x removal in multistage gas irradiation process*, Radiat. Phys. Chem., **45**, 6, 1077-1079, 1995.
40. A.G. CHMIELEWSKI, *Technological development of EB flue gas treatment based on physics and chemistry of the process*, Radiat. Phys. Chem., **46**, 4-6, 1057-1062, 1995.
41. A.G. CHMIELEWSKI et al., *Influence of gas flow patterns on NO_x removal efficiency*, Radiat. Phys. Chem., **52**, 1-6, 339-341, 1998.
42. N.W. FRANK, A. MAEZAWA, *Simultaneous SO₂ and NO_x removal system for burning all grades of coal*, in: Materials of 20th International Conference on Coal Utilization and Fuel Systems, Clearwater, USA, 1995.
43. H. NAMBA, O. TOKUNAGA et al., *Pilot scale test for electron beam purification of flue gas from coal-combustion boiler*, Radiat. Phys. Chem., **46**, 4-6, 1103-1106, 1995.
44. E. SCHUNG, S. HANEKLAUS, *Sulphur deficiency in Brassica Napus*, Landbauforschung Volkenrode, Sonderheft 144, 1994.
45. R.D. GENUARIO, *Electron scrubbing of flue gases to remove unwanted by-products*, in: *Plasma science for environment*, eds. W. Manheimer, L.E. Sugiyama, Th.H. Stix. AIP Press, Woodbury, 1997.
46. O. TOKUNAGA, *A technique for desulfurization and denitration of exhaust gases using an electron beam*, Sci. Techn. in Japan, **16**, 64, 47-50, 1998.
47. A.G. CHMIELEWSKI, et al., *Industrial demonstration plant for electron beam flue gas treatment*, Radiat. Phys. Chem., **46**, 4-6, 1063-1066, 1995.
48. Z. ZIMEK, A.G. CHMIELEWSKI, *Present tendencies in construction of industrial electron accelerators applied in radiation processing*, Nukleonika, **38**, 2, 3-20, 1993.

A REVIEW OF EXPERIMENTAL AND THEORETICAL INVESTIGATIONS OF STABLE ISOTOPE SEPARATION BY PLASMA METHODS

D. A. DOLGOLENKO, N. M. GORSHUNOV, A. I. KARCHEVSKY¹, V. S. LAZKO,
Yu. A. MUROMKIN, V. G. PASHKOVSKY, A. T. PESHKOV, E. P. POTANIN, G. E. ZOTIN

MOLECULAR PHYSICS INSTITUTE, RRC KURCHATOV INSTITUTE

Moscow, 123182, Russia

Here is given a review of experimental and theoretical investigations of isotope separation processes in different plasma separation devices: plasma centrifuges, RF-systems with traveling magnetic field, DC arc discharges, nonequilibrium plasmachemical reactions (diffusion methods), and also in ICR-installations, performing isotopically selective ion-cyclotron resonance heating of the target component in magnetized collisionless plasma (selective collisionless method). Applied to separation installations, with the use of diffusion processes, various cardinal mechanisms are considered, leading to separation phenomena in plasma: centrifuging, thermodiffusion, ion wind, difference of isotope ionization degree, etc. Comparison is performed with the results of experiments. Problems of metal isotope separation by method of isotopically selective ion cyclotron resonance (ICR) are considered. Estimations of energetic consumption in all plasma methods of isotope separation and possibility of their industrial use are given.

1. Introduction

Existing industrial methods of stable isotope separation (ionic exchange, gas centrifuges, electromagnetic separators) do not meet all demands of societies (nuclear industry, medicine, fundamental physics). Usage of gas centrifuges for separation of stable isotopes is limited to elements which have gaseous compounds. A universal electromagnetic method is not cheap or productive enough. The investigation and development of new methods of stable isotope separation are required not only by necessity of increasing of volume and extension of variety of isotopic production, but in some cases by increased ecology requirements. All this has given an impetus to development of alternative methods of isotope separation and, particularly, of plasma methods. Below a review is given of the most important results of investigations of separation of stable isotopes in plasma: 1) in plasma centrifuges, 2) in plasma of RF discharge with traveling magnetic field, 3) in DC arc discharge, 4) in nonequilibrium plasmachemical reactions in glow and microwave discharges, 5) at isotopically selective ion-cyclotron

¹Kurchatov sq. 1, Moscow, Russia

resonance (ICR) heating. The first four separation processes listed above are principally collisional processes, having diffusional character, and only the last one (ICR-method) is purely collisionless process of heating (acceleration) of the target isotope in a flow of low-temperature plasma. Several reviews on isotope separation by plasma methods are already known, and among them the review on SPLG-2 [1], a book, issued in Russia in the series "Science results" [2], as well as the report on SPLG-4 [3] are worth to mentioning.

2. Plasma centrifuges

In the 70 s and of the beginning of the 80 s a widespread attention of specialists was attracted to the idea of usage of rotating plasma for isotope separation [4 - 20]. The possibility of achievement of high velocities of rotation of ionized gas (is tens times higher than in mechanical centrifuge) gave hope for realization of high productivity and high separation coefficients in one stage. Attractive, of course, was the simplicity of construction and the absence of mechanical moving parts. The rotation of ionized gas mixture is performed by means of interaction of radial electric current I_r and axial magnetic field B_z . The separation of isotopes in rotating plasma was undertaken both in continuous, and in pulsed devices. However the most complete physical results on isotope separation had been obtained in pulsed installations, which made it possible to realize significant energy inputs by relatively simple means and to reduce requirements to heat resistance of construction materials. Redistribution of pressure in rotating mixture is described by the following relation:

$$(2.1) \quad P(R_2) = P(R_1) \exp \int_{R_1}^{R_2} \frac{\bar{m} V_\varphi^2}{r k T} dr$$

where V_φ - velocity of plasma rotation, T - temperature of the mixture, R_2 and R_1 are radii of the outer and inner electrodes, \bar{m} - mean mass of atoms, k - Boltzmann constant. The separation coefficient α for binary mixture of the isotopes in the centrifuge is defined as a ratio of relative concentrations C of the target isotope in peripheral and axial regions

$$(2.2) \quad \alpha = \frac{\left(\frac{C}{1-C}\right)_{R_2}}{\left(\frac{C}{1-C}\right)_{R_1}} = \exp \left\{ \int_{R_1}^{R_2} \frac{\Delta m V_\varphi^2}{r k T} dr \right\},$$

where Δm - mass difference of the isotopes. From the relation (2.2) it is seen that the separation coefficient α is rapidly diminishing with temperature, therefore a relatively cold plasma must be more preferable for performing the isotope separation process [6]. The layout of the pulsed partially ionized plasma centrifuge, used in the Kurchatov Institute [10, 11, 21] is shown in Fig. 1.

A cylindrical chamber of full length 40 cm or 60 cm and inner diameter 25 cm had insulators on each side. Quasi-stationary longitudinal magnetic field $B_z \approx 0.04 - 0.6$ T was created by coils. Maximum power, dissipated in discharge reached 1 MW. Duration of discharge current was 6 ms. For taking gas samples

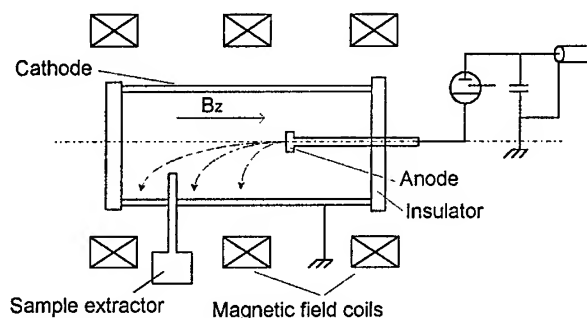


FIG. 1. Layout of the pulsed plasma centrifuge

at different areas of discharge and for estimation gas pressure in various moments of the current pulse a high-speed (0.15 ms) valve was used. In experiments with the use of different noble gases it was found that in a discharge at high velocities of gas rotation a radial pressure gradient is established which increases rapidly with the atomic mass (see Table 1).

Table 1.

Gas	He	Ne	H ₂ + Ne mixture	Xe
$P(R_2)/P(R_1)$	3	30	3000 Ne density	400

These results confirm the redistribution of pressure under influence of centrifugal force, resulted from relation (2.1). Radial separation coefficients α for isotopes H-D, ^3He - ^4He , ^{20}Ne - ^{22}Ne , ^{129}Xe - ^{136}Xe in a discharge in each gas and also in mixture with hydrogen are presented in Table 2.

Table 2.

Mixture	Separation factor α
H ₂ - D ₂	25
H ₂ - ^3He - ^4He	6
^{20}Ne - ^{22}Ne	1.2
H ₂ - ^{20}Ne - ^{22}Ne	1.5
^{129}Xe - ^{136}Xe	1.1
H ₂ - ^{129}Xe - ^{136}Xe	1.25

For plasma parameters, achieved in [10, 11, 13, 21], the observed separation coefficient of isotopic mixtures (Table 2) is of the same order as a radial centrifugal effect, calculated from the relation (2.2). It is also obviously that the increase of separation coefficient of isotopic mixtures in discharges with addition of hydrogen (Table 2) can be explained by the decrease of ionized gas temperature due to higher value of thermal conductivity of a lighter component

(H₂). Electromagnetic force, resulting in rotation in partially ionized plasma centrifuge, is equilibrated by viscous friction of gas with a side surface of the discharge chamber, and heating of plasma due to viscous losses becomes determining with the increase of rotation velocity. The temperature of rotating gas becomes proportional to its squared rotation velocity. This proportionality in fact limits the maximum coefficient of isotope separation in plasma centrifuge [14]. For a monoatomic gas this limiting separation coefficient depends only on atomic weight [15] and it is small enough in centrifuge for elements with medium and heavy mass

$$(2.3) \quad \alpha_{lim} \approx \exp \left(\frac{15}{4} \cdot \frac{\Delta m}{m} \right).$$

In this context experiments with addition of light gases (H₂) in isotopic mixture to be separated [7, 11, 21] represent an attempt to partially overcome the limit [14], which is set by viscous losses in the rotating gas. From the relation (2.3) it is seen, that plasma centrifuge is more appropriate for separation of the light gases than for heavy elements. Experiments were actively carried out with so-called vacuum arc centrifuge, in which a cloud of metal vapour was created in the working chamber from the surface of the electrode by a laser radiation pulse [16]. After putting plasma into rotation by pulsed current in the short discharge zone, the rotating plasma column freely flowed in longitudinal magnetic field to the opposite end of the chamber. As being cleaned from neutral gas, the flow gained high ionization degree, and therefore was regarded as a rotating highly ionized plasma. It must be taken into account that the main period of preparation and acceleration of the plasma by current pulse in such installations was carried out similarly to the described above pulsed plasma centrifuges, and, as a result of this, isotope separation effect also did not exceed 20% (⁶⁵Cu - ⁶³Cu: $\alpha = 1.18$, ²⁵Mg - ²⁴Mg: $\alpha = 1.15$). Investigations in this field were continued by several groups [22, 23]. Some progress in plasma rotation speed was achieved by [24, 25]. Nevertheless, no significant results in isotope separation have been achieved so far. Investigations of isotope separation in steady-state plasma centrifuges confirmed the result, that separation coefficient of isotopes achieved in one stage is rather small and it increases with the decrease of mass. Steady-state rotating plasma was created in Kurchatov Institute [12, 17] in the working chamber with heated walls ($T > 1100^\circ \text{ K}$), which also allows to use lithium vapours in experiments. In all experiments the longitudinal separation effect was observed, while the near cathode area was enriched by heavy isotopes. The results obtained in [12, 17] testify the existence of circular flows in the discharge chamber volume which transform the radial centrifugal effect of isotope separation into longitudinal one. An attempts were also made to realize separation of uranium isotopes in a steady-state plasma centrifuge [18, 19, 20].

3. Isotope separation in RF discharge with travelling magnetic field

Isotope separation in positive column of RF discharge with traveling magnetic field is described in a series of works [26 - 33]. The layout of one of the installa-

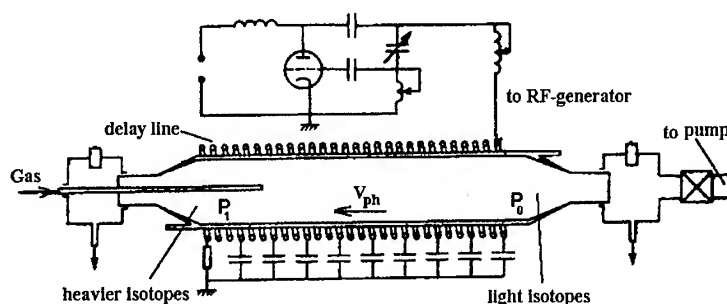


FIG. 2. Layout of the installation with traveling magnetic field.

tions, operated at the Kurchatov Institute, is presented in Fig. 2.

The discharge was initiated in a water-cooled quartz chamber which was 110 cm in length and 6.5 cm in diameter. The wave phase velocity V_{ph} , obtained with the use of a 90 cm delay line was $(5 - 9) \cdot 10^6$ cm/s. RF generator up to 15 kW power operated on frequency 100 - 460 kHz. The used gases were of Ne, Kr, Xe and their mixtures at pressures from $2 \cdot 10^{-2}$ Torr to 2 Torr. A longitudinal separation effect was observed: the gas was enriched by heavy isotopes at the end of the delay line (P_1) and by light isotopes at the beginning of the delay line (P_0). In RF discharge of such type the gas pressure at the end of the delay line P_1 always exceeded the pressure P_0 at the beginning of the delay line: $P_1 > P_0$, with value of $\ln(P_1/P_0)$ dependent on the power dissipated in plasma and from initial pressure of the gas P . The value of $\ln(P_1/P_0)$ is changed in experiments from 1 to 5. For isotopic mixture ^{129}Xe - ^{136}Xe separation coefficient up to 1.3 (enrichment coefficient $\epsilon_{Xe} \approx 30\%$) was achieved.

Measured values of the enrichment coefficient ϵ_{Xe} reduced to one unit of mass difference $\Delta\mu = 1$ in dependence on initial gas pressure P are presented by black squares in Fig. 3. Effects of longitudinal isotope separation observed experimentally in RF discharge with a traveling wave can be explained by several physical processes, realized in the positive column. At initial pressures higher than 10^{-1} Torr the separation effect is determined, principally, by ordinary thermodiffusion in the neutral gas of RF discharge: radial thermodiffusion effect transforms into longitudinal effect of isotope separation due to forced convection, caused by the radial nonuniformity of the electromagnetic force of the traveling wave. The second process, which can lead to the longitudinal isotope separation in the plasma of RF-discharge is a friction forces, influencing the neutral component of the isotopic mixture from the ion flow (ion wind) with predominant transfer of momentum to heavier particles in binary elastic ion-neutral collisions. This process resembles mass-diffusion effect of isotope separation [34, 35, 36]. But as it is seen from Fig. 3, this effect has an insignificant role in experiment due to the low density of the ionic current, excited by the traveling wave. At low initial pressures ($P = 10^{-2} - 10^{-1}$ Torr) large pressure ratios P_1/P_0 are realized, reaching in this experiment the value of about 30. Under these conditions in

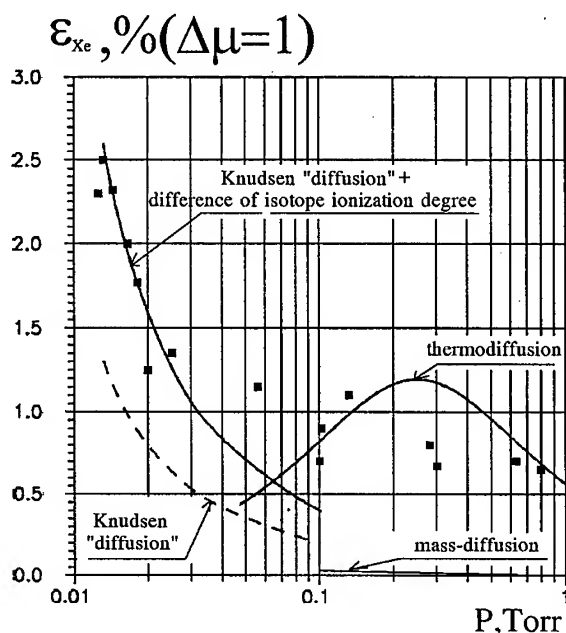


FIG. 3. Dependence of the enrichment coefficient ε_{Xe} from initial pressure P ([32]).

most part of the working chamber a low pressure of neutral gas is maintained, when the length of the free path of the particles is comparable or higher than transverse dimensions of the vessel. A flow of neutral atoms from zone of high pressure, supported by ion transfer, results in the occurrence of usual mechanism of so-called Knudsen diffusion and in enriching by heavy isotope the zone of higher pressure with enrichment coefficient proportional to the logarithm of pressures ratio

$$(3.4) \quad \varepsilon = \frac{\Delta\mu}{2\mu} \cdot \ln \frac{P_1}{P_0}.$$

The dependence (3.4) is shown in Fig. 3 by the dashed line. The mechanism of Knudsen diffusion is not sufficient for explanation of the observed separation effect at low pressures (Fig. 3). That is why one more mechanism of isotope separation, which is caused by increased degree of ionization β of heavy isotopes relative to ionization degree of light isotopes in the positive column of RF discharge [37] is considered. This difference in ionization degrees $\Delta\beta$ is determined by radial ambipolar diffusion in plasma column, when light isotopes, having higher mobility, recombine on the camera walls faster. Longitudinal transfer of ions (cataphoresis), due to the difference in ionization degrees of isotopes in plasma, results in an additional enrichment effect in longitudinal direction with $\varepsilon_{cat} \approx (\Delta\beta/\beta) \cdot \ln(P_1/P_0)$. In the Knudsen regime the ions did not collide with neutral atoms, and their rate of recombination is determined only by the frequency of collisions with the walls. This also leads to the relative difference in

ionization degrees of isotopes $\Delta\beta/\beta = \Delta\mu/2\mu$. In this case the dependence of the longitudinal separation effect, caused by a difference in ionization degree of isotopical ions, on the logarithm of pressure ratio, is the same as (4), and overall separation effect is shown for the low pressure region by continuous line (Fig. 3).

4. Isotope separation in DC arc discharge

The first successful work in such a system was presented in [38]: the mixture ^{20}Ne - ^{22}Ne had been separated in DC discharge with current 5 A, initial pressure 3 Torr and with the length of the water-cooled capillary 10 cm tube. Longitudinal separation coefficient α for Ne isotopes reached $\alpha = 1.45$. The mass diffusion mechanism caused by friction forces of ionic wind was proposed to explain the separation effect. Later these experiments were continued on isotopes of Ne, Kr, Xe and also on their mixtures [39, 40, 41, 42]. Experimental installation does not differ significantly from that realized in [38], and its layout is presented in Fig. 4. DC discharge was initiated in a water-cooled 100 -190 mm quartz tube

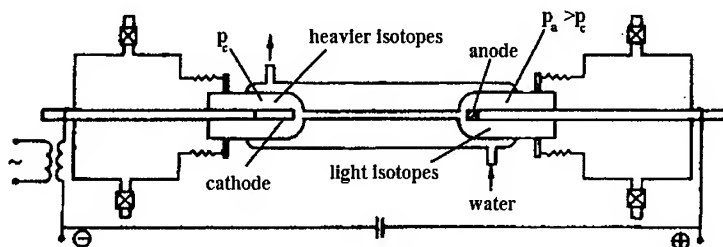


FIG. 4. Layout of the installation with DC discharge [40].

of a diameter 3 - 9 mm. Discharge current was 5 - 10 A, initial pressure of gas (Ne, Kr, Xe and their mixtures) 1 - 10 Torr. Gas pressure P near the anode is higher than near the cathode $P_A > P_C$. Longitudinal isotope separation effect is observed, cathode zone is enriched by heavy isotopes.

The value of enrichment coefficient ε is proportional to the discharge current I , to the length of the narrow part of the discharge tube l and inversely proportional to the cross section area of discharge: $\varepsilon \sim \frac{I \cdot l}{d^2}$; The dependence of the enrichment coefficient ε for Kr isotopes reduced to one unit of mass difference [40] on the initial pressure value in the discharge chamber is presented in Fig. 5. The same mass-diffusion mechanism (ionic wind) as in the work of [38], was considered to understand these experiments [43]. The result of contribution of this effect into the experimentally observed on shown in Fig. 5. It seems that the contribution of the difference of ionization degrees of isotopes in the positive column [43] is not less significant. The relation between these two principal processes in real conditions of the DC discharge are considered in the recent works of [42].

In experiments with DC discharge, placed into longitudinal magnetic field up to 0.1 T an attempt was made [40, 44] to influence on created in discharge the

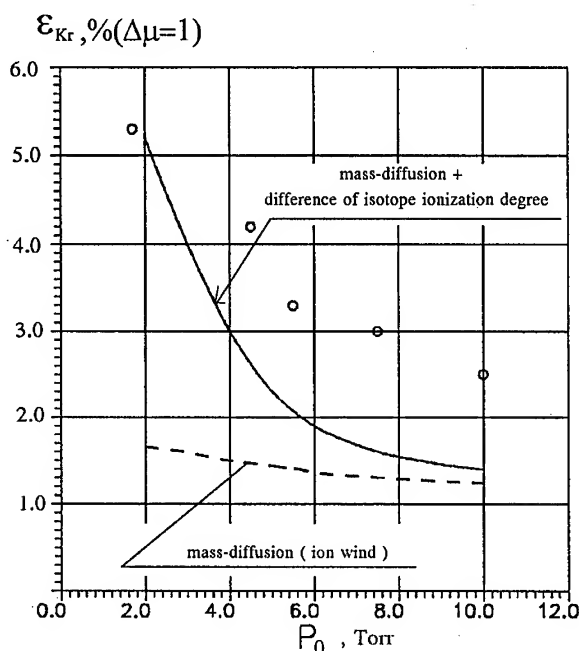


FIG. 5. Dependence of the enrichment coefficient Kr isotopes in DC discharge on the initial pressure.

longitudinal pressure differences and find out in experimentally what the role of the pressure difference in DC discharge on isotope separation process. Magnetic field results in significant diminishing of the pressure difference, but does not have influence on the separation effect in DC discharge (Fig. 6). This indicates that multiplication of the radial effect (for example, thermodiffusion) can not have a significant influence on the observed longitudinal separation of isotopes.

5. Isotope separation in nonequilibrium plasmachemical reactions in glow and microwave discharges

The principle idea lies in the usage of nonequilibrium vibration-vibrational (V-V) energy exchange in a gas of two-atomic molecules, when vibrational and transitional temperatures are not equal [45]. The proposal refers first to two-atomic CO and N₂ molecules. Nonequilibrium vibrational excitation is performed either with the use of laser radiation, or by electron impact in gas discharge plasma. At collisions of such excited molecules, predominant transfer of the quanta of the vibrational energy from molecules with light isotope (¹⁴N¹⁴N) to molecules with heavy isotope (¹⁵N¹⁴N) takes place, and therefore vibrationally excited states of molecules with heavy isotope become overpopulated. It can be expected that the molecules with heavier isotopes, having higher vibrational energy, can predominantly react with the formation of chemical products, enriched with heavier isotope.

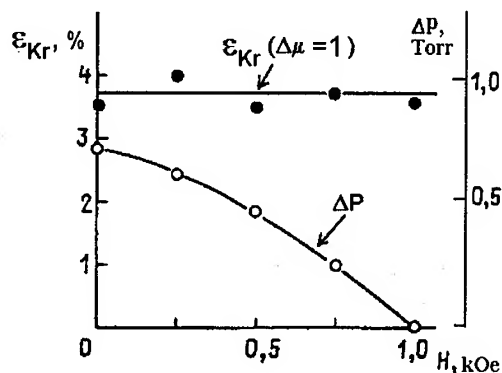


FIG. 6. Dependence of enrichment coefficient of Kr isotopes and of pressure difference on the value of longitudinal magnetic field.

Conditions of the different vibrational and transitional temperatures can be realized in cold glow discharges. Enrichment of nitrogen monoxide NO by isotope ^{15}N in reaction products of the glow discharge in air with separation coefficient $\alpha = 20$ was reported by N. Basov et al., 1974 [45]. The same authors obtained enrichment in NO by ^{15}N up to $\alpha = 130$ with cooling of the walls of the discharge chamber by liquid nitrogen [46].

Such high results were not confirmed in experiments of other groups [47, 48] where the value α for isotope ^{15}N was only 1.05 - 1.2. The authors [47, 48] connected the observed in [46, 49] enrichment effects with the mistakes at mass-spectroscopy analysis of NO.

The excitation of CO molecules for producing nonequilibrium plasmachemical reactions was carried out by optical way [50, 51] and by electron impact in the glow discharge [52]. But in the final chemical products of the CO dissociation (CC_2O_2 and CO_2) enrichment by isotope ^{13}C was practically absent ($\alpha \approx 1.15$).

Despite the fact that experiments on two-atomic molecules CO and N_2 did not give positive results on enrichment of the products of nonequilibrium plasmachemical reactions by heavy isotopes ^{13}C and ^{15}N , interest in these investigations was aroused by the series of works, where high enrichment by carbon ^{13}C in the products of dissociation of three-atomic molecules CO_2 was experimentally observed [53, 54].

In the works [53, 54] the dissociation of CO_2 was performed in a microwave (2.4 GHz) plasmachemical reactor. In the region of high energy inputs into plasma ($\sim 7 \text{ J/cm}^3$) these authors observed that the value of conversion of molecules $^{12}\text{C}^{16}\text{O}_2$ is 2.5 times higher than the value of conversion of molecules $^{13}\text{C}^{16}\text{O}_2$.

In the next work the same group of authors [54] reported spectacular isotopic effects not only in the process of the dissociation of CO_2 in the microwave discharge, but also at the excitation and dissociation of CO_2 in glow discharges. Without going into mechanisms, by which the authors [53, 54] try to explain the observed large isotopic effects in conditions described above, let us note that

such a significant enrichment by ^{13}C of the products of dissociation of CO_2 in the microwave discharge and such a depletion by ^{13}C of the products of dissociation of CO_2 in the glow discharge were not confirmed in the investigations at the Kurchatov Institute [55].

The dissociation of CO_2 in the microwave discharge with the purpose of observation isotopic effects in the products of dissociation was also carried out at the Tokyo Institute of Technology [67], and in much more wider range of energy inputs and initial pressures, than in [53, 54, 38]. These investigations, as well as investigations made by [58], did not reveal any noticeable isotopic effects at dissociation of CO_2 molecule in microwave discharge.

Taking into account earlier vain efforts to observe isotopic effects on two-atomic molecules CO and N_2 [47, 48, 59] in dissociation products of nonequilibrium plasmachemical reactions, it must be accepted that nowadays chances of obtaining noticeable isotopic effects are very poor at dissociation of such complicated (also from vibrational point of view) three-atomic molecule as CO_2 . It must be taken into account that in the discharge conditions a high rate of exchange isotopic reactions must exist. This leads to diminishing of the isotope separation effect in the dissociation products.

6. Isotope separation with the use of isotopically selective ion cyclotron heating

Method of isotope separation, by means of isotopically selective ion cyclotron resonance (ICR) heating, has a particular place in the series of plasma methods of isotope separation, since it can provide a product with high degree of enrichment in one-stage process. Contrary to the described above plasma methods of separation, which are defined principally by collisional processes (diffusion, ion wind, V-V exchange etc.), the ICR method of separation is collisionless.

In this method the following operations are performed consequently: 1) ionization of vapour of the element, whose isotopes are to be separated, and generation of plasma flow along the uniform magnetic field; 2) selective ICR heating of ions of the extracted isotope; 3) deposition of the heated particles on collectors.

Isotope effects in the ICR resonance were observed experimentally by [60], and proposals of ICR heating for isotope separation had been made by [61]. First results of the successful experiments in the USA on ICR separation of potassium isotopes with separation coefficient $\alpha \approx 40$ were published at the end of 1976 [62]. A principal scheme of the ICR method of isotope separation in plasma is presented in Fig. 7.

For isotopically selective ICR heating of ions with the mass of M_i and mass difference, related to neighbour isotopes ΔM_i , in the magnetic field B on the cyclotron frequency ω_{ci} ($\omega_{ci} = eB/M_i$) fulfilment of a set of conditions is required for uniformity of magnetic field $\delta B/B < \Delta M_i/M_i$; for frequency of ion-ion collisions $nu_{ii}/\omega_{ci} < \delta M_i/M_i$. Resonance condition for ion traveling along the magnetic field with velocity V_z is $\omega - k_z V_z = \omega_{ci}$, where $k_z = 2\pi/\lambda$ - wave vector of the antenna. Due to spreading of longitudinal velocities of ions ΔV_z , whose value is about the thermal velocity of ions V_T , Doppler broadening of the ICR heating line exists: $\Delta\omega_D = k_z \Delta V_z$, which also must be small enough: $\omega_D/\omega_{ci} < \Delta M_i/M$. Besides the Doppler broadening of the ICR heating line also the time-of-flight

broadening $\Delta\omega_\tau$ of the ICR heating line exists, connected with the finite time τ of the ion flight through the heating zone length L : $\Delta\omega_\tau = \pi V_z/L$ and fulfilment of the following condition is necessary: $\Delta\omega_\tau/\omega_{ci} < \Delta M_i/M$.

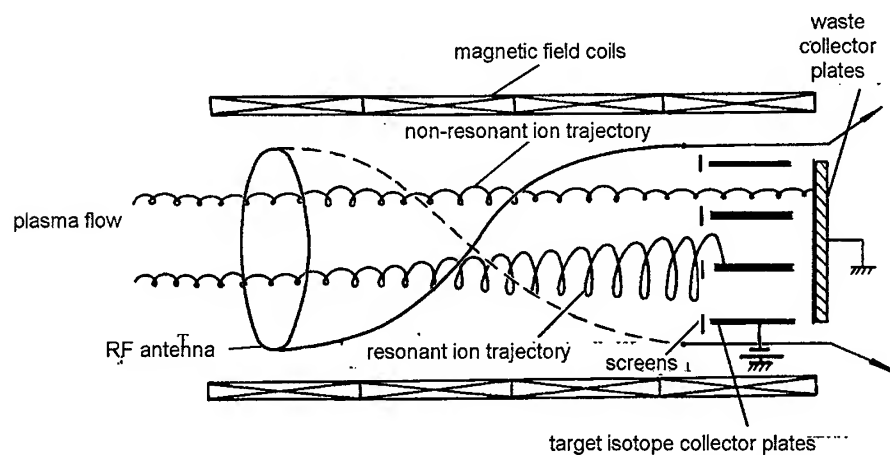


FIG. 7. Scheme of the ICR installation

To fulfill all these conditions it is necessary to have a sufficiently uniform ($\Delta B/B \leq 10^{-3}$) and strong ($B \geq 3T$) magnetic field of length of about $L = 4 - 6$ m, where inductive ICR-antenna is placed. Plasma must be not very dense ($n \leq 10^{12} \text{ cm}^{-3}$) with low initial temperature.

Separated flow Q in ICR installation is determined by the plasma cross section S , plasma density n and by longitudinal ion velocity in the flow V_z : $Q = M_i n V_z S$.

Production of steady state uniform plasma flow with large cross section in strong magnetic field for metal elements is a rather complicated task. In experiments in the USA [63, 64] the plasma flow was created by ECR-discharge. Atomic vapour of Ni was produced by cathode sputtering.

Isotopically selective ICR heating can be performed by various types of antennae. To obtain effective heating of isotope ions in overall plasma cross section, antennae producing RF-fields with azimuthal wave number $m=1$ are needed. The most suitable F-antenna in this case appears to be the helical one. It is used now in most experiments on ICR isotope separation.

Collector system in ICR-installation presents a set of equidistantly placed, parallel to magnetic field plates, cutting the plasma flow (Fig. 7). The distance between the plates is about two Larmor radii r_L for heated particles, where $r_L = M_i V_\perp / eB$, and V_\perp - transverse velocity of the heated ions of the target isotope. Separation coefficient of isotopes in ICR system can depend not only on the distance between the collector plates but also on the value of positive retarding potential at the collecting plates.

In large-scale experiments in the USA on ICR separation of isotopes significant success was demonstrated on isotopes Ni, In, Pb. Nickel was enriched by isotope ^{58}Ni up to 97% [63, 64]. Productivity of the installation at production

of Ni, enriched by ^{62}Ni isotope up to 40% was about 13 g/day.

Isotopes of ^{132}Ba , ^{176}Yb , ^{157}Gd and ^{48}Ca were obtained on the ERIC installation (France) [65, 66], where ^{48}Ca isotope was extracted with separation coefficient $\alpha = 130$. Isotopes of ^6Li with separation coefficient $\alpha = 90$ was obtained in Russia [67]. Fundamental processes at ICR heating for separation are investigated in Japan [68, 56, 57, 69].

A good resolution of isotopic Zn-ion current peaks in the ERIC installation [66] is shown in Fig. 8.

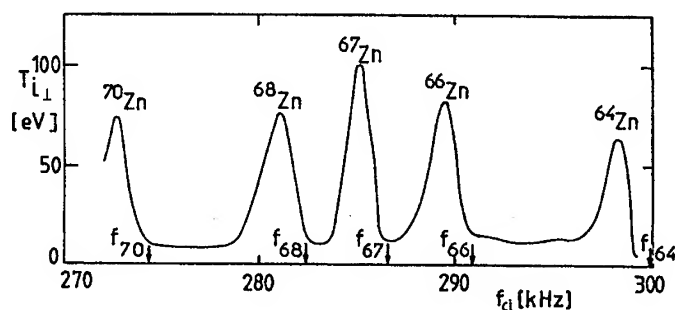


FIG. 8. Heating of Zn isotopes, $n \simeq 10^{12} \text{ cm}^{-3}$, $B = 1.25 \text{ T}$.

To obtain high selectivity of the process of isotope separation in one stage of ICR installation it is necessary to have a possibility of maintaining sufficiently high strength of the magnetic field in the working area of heating. This was shown on ^6Li and ^7Li isotopes in the work [67], and presented in Fig. 9.

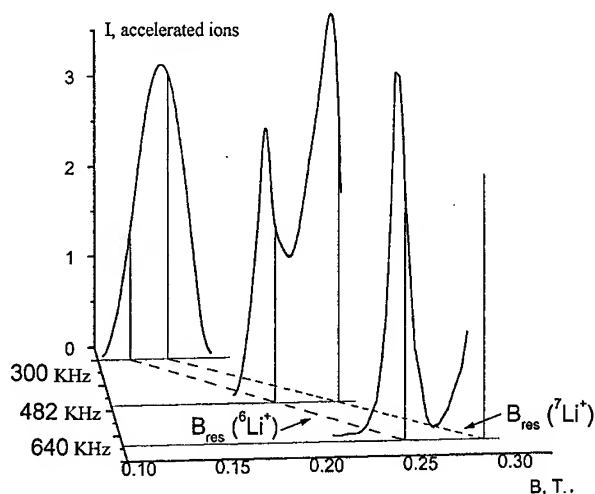


FIG. 9. Dependence of ionic current of the heated particles on collector versus the value of magnetic field at different frequencies of RF generator.

All stages of ICR isotope separation in lithium plasma were investigated at the Kurchatov Institute. A set of experiments with full-scale collector system aimed at measuring the separation coefficient α and the extraction factor of desired isotope γ was made recently.

At present at the Kurchatov Institute a project of semi-industrial ICR installation MCIRI (Magnetic Cyclotron Ion Resonance of Isotopes) is under development with feed of ECR plasma source up to some kg/day, superconducting solenoid with of length of 7 m and clear bore diameter of 1 m, with magnetic field 3 - 4 T and uniformity better than 10^{-3} in the region with length 5 m and diameter 0.5 m.

Advantages of this method have to be estimated, firstly, by the possibility of extension of production of such isotopes as Gd, Ca, Tl, Yb and others, which are required in amounts much higher than it can be provided by electromagnetic separators.

7. Some comparative estimations of energy consumption for separation of isotopes by different methods

In the Table 3 estimations of energy consumption per Separation Work Unit (SWU) are presented, where W - energy consumption of installation and δU - separation power of installation (single step).

Table 3.

Separation method	Gas centrifuges	Gas diffusion	Electromagnetic method [70]	Plasma centrifuge	RF systems with travelling wave	DC discharge	ICR [70] for vanadium isotope
Energy consumption							
$\frac{W}{\delta U} \left(\frac{\Delta m}{m} \right)^2$, [$\frac{kW \cdot hour}{SWU}$]	10^{-2}	0.2	$2.7 \cdot 10^3$	40	200	1200	1.0

8. Conclusion

Let us evaluate the methods of isotope separation in plasma. Investigations of the isotope separation in the plasma centrifuges showed existence of intrinsic limit for separation coefficient in one step. This limit prohibits this method for

possible industrial use. Excitation of DC discharge or RF discharge leads to development different physical processes (ion wind, difference in ionization degrees of isotopes, thermodiffusion, etc.) in plasma, which can result in observation of spatial separation of isotopes. But these systems (RF discharge with traveling wave, or DC discharge) have high energy consumption per SWU. From all of plasma methods the ICR method can be most advanced for possible industrial usage, as it has moderate energy consumption and is competitive with electromagnetic method for elements, that not have any volatile compounds. Highly perspective for separation of rare isotopes is a combination of the ICR method with the electromagnetic method, where the ICR method, as more productive one, can perform preliminary enrichment. Investigations of isotope separation processes in plasma undoubtedly allow us to broaden our fundamental knowledge in the field of plasma physics and its applications.

References

1. P. LOUVET, *Separation Phenomena in Liquids and Gases (SPLG)*, 2-nd Workshop, Versailles, Proc., 1, p. 5-104, 1989.
2. Itogi nauki i tehniki. Plasma physics., [in Russian], Moscow, 12, p. 3-111. VINITI, edited by Karchevsky A.I., 1991.
3. J.V. WHICHELO, P.J. EVANS, S.W. SIMPSON, *A review of recent plasma centrifuge and vacuum arc centrifuge development*, SPLG-4, 4-th Workshop, Beijing, p. 215-230, 1994.
4. B BONNEVIER, Ark. Fys., 33, 15, p. 255-269, 1966.
5. B BONNEVIER, Plasma Physics, 13, 763-774, 1971.
6. B. LEHNERT, Physica Scripta, 7, 102-106, 1973.
7. B.W. JAMES, S.W. SIMPSON, Phys. Lett., A, 46, 5, p. 347-348, 1974, Plasma Phys., 18, 289-300, 1976.
8. J.B.S CAIRNS, Int. Conf. on Uranium Isotope Separation, London, Proc. N, 9, 1-6, 1975.
9. A.V. BELORUSOV, E.F. GORBUNOVA, A.I. KARCHEVSKY, YU.A. MUROMKIN, A.I. MYACHIKOV, A.L. USTINOV, XVII-th ICPIG, Budapest, Contr. Papers p. 765-767, 1985.
10. A.V. BIELOROUSOV, A.I. KARCHEVSKII, YU.A. MUROMKIN, E.P. POTANIN, Sov. Tech. Phys. Letters, p. 260-261, 1976.
11. A.V. BIELOROUSOV, A.I. KARCHEVSKII, YU.A. MUROMKIN, E.P. POTANIN, A.L. USTINOV and A.P. BABICHEV, Sov. J. Plasma Phys., 5, 6, 693-699, 1979.
12. A.V. BIELOROUSOV, E.F. GORBUNOVA., A.I. KARCHEVSKY., YU.A. MUROMKIN, A.I. MYACHIKOV, A.L. USTINOV, Sov. Phys. Tech. Phys., 30, 5, 550-551, 1985.
13. S.V. KOROBTSSEV, T.A. KOSINOVA, J.R. RAHIMBABAEV, Dokladi A.N. SSR, [in Russian], 270, 876-878, 1983.
14. M.M.B. WIJNAKKER, E.H.A. GRANNEMAN, Z. Naturforsch., 35A, 883-893, 1980.
15. E.P. POTANIN, A.L. USTINOV, Sov. J. Plasma Phys., 10, 5, 599-602, 1984.
16. M.GEVA, M. KRISHNAN, J.L. HIRSHFIELD, J. Appl. Phys., 56, 5, 1398-1413, 1984.
17. YU.A. MUROMKIN, A.I. MYACHIKOV, A.L. USTINOV, A.V. CHEPKASOV, XIX-th ICPIG, Belgrade, Contr. Papers, 1, p. 246-247, 1989.
18. N. NATHRATH, XIII-th ICPIG, Berlin, Contr. Papers, p. 697-698, 1977.
19. J.J. McCLURE, N. NATHRATH, XIII-th ICPIG, Berlin, Contr. Papers, p. 693-694, 1977.

20. G. MUCK, M. SIMON, XIII-th ICPIG, Berlin, Contr.papers, p. 695-696, 1977.
21. A.V. BIELOROUSOV, E.F. GORBUNOVA, A.I. KARCHEVSKII, YU.A. MUROMKIN and A.L. USTINOV, Sov. Tech. Phys. Letters, **6**, 3, 154-155, 1980.
22. E. DEL BOSCO, S.W. SIMPSON, R.S. DALLAQUA, A. MONTES, J.Phys. D: Appl.Phys., **24**, 2008, 1991.
23. P.J. EVANS, F.J. PAOLONI, J.T. NOORMAN, J.W. WHICHELLO, J. Appl. Phys., **66**, 115, 1989.
24. T. IKEHATA, K. OOHASHI, N.Y. SATO, T. TANABE, H. MASE, Nucl. Instrum. Methods in Phys. Research B, **70**, 26, 1992.
25. T. IKEHATA, K. HASEGAWA, N.Y. SATO, T. TANABE, H. MASE, Trans. IEE Japan **114-A**, 135, 1994.
26. R.A.DEMIRKHANOV, A.N.DOROSHENKO, V.N. ZHARIKOV, I.J. KADYSH, A.G. KIROV, V.P. MINENKO, 3-rd USSR-Conf. on Plasma Accelerators, Minsk, Collection of annotations, [in Russian], p. 198, 1976.
27. R.A. DEMIRKHANOV, A.N. DOROSHENKO, V.N. ZHARIKOV, I.J.KADYSH, A.G. KIROV, V.P. MINENKO, 13th ICPIG, Berlin, Contr. papers, Part II, p. 699, 1977.
28. A.I. KARCHEVSKY, V.L. MARTSYNKYAN, I.A. POPOV, E.P. POTANIN, 3-rd USSR-conf. on Plasma Accelerators, Minsk, Collection of annotations, [in Russian], p. 201, 1976.
29. A.I. KARCHEVSKY, V.L. MARTSYNKYAN, I.A. POPOV, E.P. POTANIN, Fizika plazmy, [in Russian], **3**, 2, 409-417, 1977.
30. E.F. GORBUNOVA, A.N. EZUBCHENKO, A.I. KARCHEVSKY, YU.A. MUROMKIN, A.P. BABICHEV, Pisma v Zhur.Tech.Fiz., [in Russian], **3**, 4, 154-157, 1977.
31. E.F. GORBUNOVA, A.N. EZUBCHENKO, A.I. KARCHEVSKY, YU.A. MUROMKIN, A.P. BABICHEV, Pisma v Zhur.Tech.Fiz., [in Russian], **3**, 13, 598-601, 1977.
32. E.F. GORBUNOVA, A.N. EZUBCHENKO, A.I. KARCHEVSKY, YU.A. MUROMKIN, A.P. BABICHEV, Sov. Phys. Tech. Phys., **24**, 9, 1053-1056, 1979.
33. A.P. BABICHEV, E.F. GORBUNOVA, A.N. EZUBCHENKO, A.I. KARCHEVSKY, YU.A. MUROMKIN, Sov. Tech. Physics Letters, **5**, 9, 480 - 481, 1979.
34. A.I. KARCHEVSKY and E.P. POTANIN, Sov. Phys. Tech. Phys., **23**, 10, 1197-1200, 1978.
35. A.I. KARCHEVSKII and E.P. POTANIN, Journal de Physique, Colloque C7, **40**, 7, C7-213-214, 1979.
36. A.I. KARCHEVSKY and E.P. POTANIN, Zhur.Tech.Fiz., [in Russian], **50**, 2, 433-435, 1980.
37. A.I. KARCHEVSKY and E.P. POTANIN, Sov. J. Plasma Phys., **7**, 2, 171-174, 1981.
38. Y. MATSUMURA, T. ABE, Jap. J. Appl. Phys., **19**, L457-L459, 1980.
39. E.F. GORBUNOVA, A.N. EZUBCHENKO, A.I. KARCHEVSKY, YU.A. MUROMKIN, Pisma v Zhur. Tech. Fiz., [in Russian], **7**, 12, 763-766, 1981.
40. E.F. GORBUNOVA, A.I. KARCHEVSKY, YU.A. MUROMKIN, Sov. J. Plasma Physics, **12**, 9, 625-630, 1986.
41. T. SONE, H. AKATSUKA, M. SUZUKI, Journ. Nucl. Science and Technology, **33**, 5, 414-422, 1996.
42. H. AKATSUKA, A.N. EZOUBTCHENKO, M. SUZUKI, Proc. of SPLG-6, 6 - th Workshop, Nagoya, Japan, p. 359-370, 1998.
43. A.I. KARCHEVSKII and E.P. POTANIN, Pisma v Zhur. Tech. Fiz., [in Russian], **8**, 21, 1285-1289, 1982.
44. E.F. GORBUNOVA, A.N. EZUBCHENKO, A.I. KARCHEVSKY, YU.A. MUROMKIN, 16th ICPIG, Dusseldorf, Contr.papers, **4**, 492- 493, 1983.
45. E.M. BELENOV, E.P. MARKIN, A.N. ORAEVSKII, V.I. ROMANENKO, JETP Lett., **18**, 116, 1973.
46. N.G. BASOV, E.M. BELENOV, V.A. ISAKOV, E.P. MARKIN, A.N. ORAEVSKII, V.I. ROMANENKO, N.B. FERAPONTOV, Sov. Phys. -JETP, **41**, 1017, 1975.

47. T.J. MANUCCIA, M.D. CLARK, Appl. Phys. Lett., **28**, p. 372, 1976.
48. V.M. AKULINTSEV, N.M. GORSHUNOV, S.E. KUPRIYANOV, YU.P. NESHCHIMENKO, A.A. PEROV, A.N. STEPANOV, Khimiya Vysokikh Energiy (Sov. High Energy Chemistry), [in Russian], **12**, 461, 1978.
49. N.G. BASOV, E.M. BELENOV, L.K. GAVRILINA, V.A. ISAKOV, E.P. MARKIN, A.N. ORAEVSKII, V.I. ROMANENKO, N.B. FERAPONTOV, JETP Lett., **19**, 190, 1974.
50. J.W. RICH, R.C. BERGMAN, Chem. Phys., **44**, 53, 1979.
51. R.C. BERGMAN, G.F. HOMICZ, J.W. RICH, G.L. WOLK, J. Chem. Phys., **78**, 1281, 1983.
52. T.G. ABZIANIDZE, V.A. ANDRYUSHCHENKO, A.B. BAKHTADZE, A.S. ELIZAROV, G.I. TKESHELASHVILI, Stable Isotopes in the Life Science, IAEA, Vienna, p. 69-74, 1977.
53. M.A. KERIMKULOV, V.N. OCHKIN, S.YU. SAVINOV, M.V. SPIRIDONOV, S.N. TSKHAI, JETP Lett., [in Russian], **54**, 4, p. 212-215, 1991.
54. S.N. ANDREEV, A.A. MAZURENKO, M.A. KERIMKULOV, V.N. OCHKIN, S.YU. SAVINOV, S.N. TSKHAI, Sov. J. Tech. Phys., [in Russian], **64**, 5, 22-29, 1994.
55. N.M. GORSHUNOV, G.E. ZOTIN, A.I. KARCHEVSKY, A.T. PESHKOV, Abstracts of Third All Russian Science Conference "Physical-chemistry processes at atoms and molecules separation", Oct. 5-9, Zvenigorod, p. 33, 1998.
56. M. SUZUKI, Private communication, 1998.
57. T. SUZUKI, S. KUGAI, N. FUJITA, Y. KAWAI, H. IWABUCHI, M. NOMURA, Y. FUJII, Fall Meeting of the Atomic Energy Society of Japan, Paper L67, 1997.
58. J.W. RICH, R.C. BERGMAN, M.J. WILLIAMS, *Gas-Flow and Chemical Lasers*, Hemisphere, New York, p. 181-190, 1979.
59. J.P.M. SCHMITT, Phys.Rev.Lett., **31**, 982, 1973.
60. G.A. ASKARYAN, V.A. NAMIOT, A.A. RUKHADZE, Pisma v Zhur. Tech. Fiz., [in Russian], **1**, 820, 1975.
61. J.M. DAWSON, H.KIM, D. ARNUSH, ? D. FRIED, R.W. GOULD, L.O. HEFLINGER, C.F. KENNEL, T.E. ROMESSER, R.L. STENZEL, ? Y. WONG, R. F. WUERKER, Phys. Rev. Lett., **37**, 1547-1550, 1976.
62. M. MUSSETTO, T.E. ROMESSER, D. DIXON, C. STRAWITCH, J. TANG, IEEE Int. Conf. on Plasma Science, San Diego, Calif., 1983; IEEE Conf. Records, Abstracts, p. 70, 1983.
63. M. MUSSETTO, Bull. American Phys. Soc., **28**, 1029, 1983.
64. A.C. La FONTAINE, C. GIL, P. LOUVET, Compt. Rend., **308**, 821-825, 1989.
65. A. PAILLOUX, A.C. LA FONTAINE, P. LOUVET, Proc. *Separation Phenomena in Liquids and Gases*, Nagoya, Japan, 332, 1998.
66. A.C. La FONTAINE, P. LOUVET, *Les isotopes stable applications-production*, Comptes rendus des Journees., 24-25 Novembre 1993, Saclay, France, p. 332-336, 1994.
67. A.I. KARCHEVSKII, V.S. LAZKO, YU.A. MUROMKIN, A.I. MJACHIKOV, V.G. PASHKOVSKII, A.L. USTINOV, A.V. CHEPKASOV, Preprint No. 5239/7, RRC Kurchatov Institute, p. 1-16, Moscow, 1990; Plasma Phys. Rep., **19**, 3, p. 214-218, 1993.
68. Y. KAWAI, T. SUZUKI, M. NOMURA, Y. FUJII, *Fall Meeting of the Atomic Energy Society of Japan*, Paper, L66, 1997.
69. K. NANRI, K. ARAI, A. MATSUBARA, K. SUNAKO, T. TANIKAWA, E. YABE, K. KAWAMURA, K. TAKAYAMA, 12th Intern. Conf. on Electromagnetic Isotope Separators and Techniques Related to their Applications, CYRIC, Tohoku University, Japan. Paper, A-P6, 1991.
70. J.G. TRACY, J.W. TERRY, Nucl. Instrum. and Meth. in Phys. Research, **B10/11**, 972-975, 1985.

Late contributed papers

ON THE THEORY OF NON-RECIPROCAL SURFACE ELECTROMAGNETIC WAVES IN SEMI-BOUNDED MAGNETIZED ELECTRON PLASMA

E. ABU ASSALI

DEPARTMENT OF PHYSICS - FACULTY OF SCIENCES, DAMASCUS INIVERSITY
 Damascus - Syria

Propagation of non-reciprocal surface electromagnetic waves perpendicular to external magnetic field \vec{B}_0 , parallel to plane surface of purely electron plasma, is investigated. It's shown that for small phase velocities the waves are potential and can be excited by transverse drift of electrons, which flow in the plasma.

In monograph [1], it was shown that in semi-bounded purely electron plasma, confined by external magnetic field \vec{B}_0 which is parallel to the surface of plasma, could develop non-reciprocal potential waves. These waves propagate along the plasma surface normal to the magnetic field. Ignoring thermal motion of electrons (cold plasma), we can get the frequency spectrum of the waves from the dispersion equation:

$$(1) \quad \varepsilon_{\perp} + 1 + \frac{k_y}{|k_y|}g = 2 - \frac{\omega_{Le}}{\omega(\omega + \frac{k_y}{|k_y|}\Omega_e)}$$

where ε_{\perp} and g are the components of dielectric permittivity tensor for a cold electron plasma

$$(2) \quad \varepsilon_{ij} = \begin{pmatrix} \varepsilon_{\perp} & ig & 0 \\ -ig & \varepsilon_{\perp} & 0 \\ 0 & 0 & \varepsilon_{\parallel} \end{pmatrix}$$

$$\varepsilon_{\parallel} = 1 - \frac{\omega_{Le}^2}{\omega^2}, \quad g = \frac{\omega_{Le}^2}{\omega(\omega^2 - \Omega_e^2)},$$

$$\varepsilon_{\perp} = 1 - \frac{\omega_{Le}^2}{\omega^2 - \Omega_e^2},$$

$$\omega_{Le} = \left(\frac{4\pi e^2 N_e}{m} \right)^{1/2}, \quad \text{and} \quad \Omega_e = \frac{eB_0}{mc}$$

are Longmuir and Larmor frequencies, N_e density of electrons and ω is the wave frequency. We assumed that the magnetic field is along the z-axis, parallel to the plasma surface [plane YZ] and $k_y \neq 0$, $k_z \neq 0$ are the components of the wave vector.

The waves described by equation (1) are important for two reasons: First, they can exist in the range of helical frequency, where $\omega \ll \Omega_e$. In this range, we obtain

$$(3) \quad \omega = \frac{k_y \omega_{Le}^2}{|k_y| 2\Omega_e}.$$

It is obvious that this wave frequency depends on the ratio $\frac{n_0}{B_0}$ and such waves can exist as distinct from helicon, in rare, strongly magnetized plasma, $\omega_{Le}^2 \ll \Omega_e^2$.

Secondly they are one directional, i.e. non-reciprocal $\omega(k_y) \neq \omega(-k_y)$. For this reason it is easy to detect them. The latter situation makes the waves have good prospects in diagnosis of the density of plasma near its surface. Such waves are very interesting for astrophysical and laboratory applications (solid state plasma).

It must be noticed that in obtaining equation (1) and (3) we assumed that field oscillations are potential, i.e. $\vec{E} = -\nabla\Phi$ and this will narrow the range of their applications. Below we will generalize these relations for the arbitrary non-potential electro-magnetic case. In the considered geometry of the problem, the non-zero components of fields are E_x , E_y and B_z (TE - wave). From Maxwell's equations, taking into account the dielectric permittivity tensor (2), we obtain

$$(4) \quad \begin{aligned} \frac{\partial^2 B_z}{\partial x^2} - k_y^2 B_z + \frac{\omega^2}{c^2} \cdot \frac{\epsilon_{\perp}^2 - g^2}{\epsilon_{\perp}} B_z &= 0 \\ E_x &= -\frac{1}{\epsilon_{\perp}^2 - g^2} \left(\frac{k_y c}{\omega} \epsilon_{\perp} B_z + g \frac{c}{\omega} \frac{\partial B_z}{\partial x} \right) \\ E_y &= -\frac{1}{\epsilon_{\perp}^2 - g^2} \left(\frac{k_y c}{\omega} g B_z + \epsilon_{\perp} \frac{c}{\omega} \frac{\partial B_z}{\partial x} \right) \end{aligned}$$

These equations are valid in all regions of x-coordinate, inside the plasma, where $x \leq 0$ as well as outside it $x \geq 0$ where $\epsilon_{ij} \rightarrow \delta_{ij}$. So we will solve them separately in these two regions, and match the two solutions at surface $x = 0$, satisfying the boundary conditions for B_{1z} , B_{2z} and E_{1y} , E_{2y} at the surface $x = 0$.

$$(5) \quad \{B_z\}_{x=0} = 0, \quad \{E_y\}_{x=0} = 0$$

$$E_y = -\frac{1}{\epsilon_{\perp}^2 - g^2} \left(\frac{k_y c}{\omega} g B_z + \epsilon_{\perp} \frac{c}{\omega} \frac{\partial B_z}{\partial x} \right).$$

Symbol $\{A\}_{x=0}$ means a jump of quantity A , when crossing the surface of plasma-vacuum at $x = 0$.

Assuming the solution of the first equation of (4) to have the form

$$(6) \quad B_z = \begin{cases} C_1 e^{k_p x} & , \quad x \leq 0 \\ C_2 e^{-k_0 x} & , \quad x \geq 0 \end{cases}$$

we obtain

$$(7) \quad \begin{aligned} k_p^2 &= k_y^2 \frac{\omega^2 \varepsilon_{\perp}^2 - g^2}{c^2 \varepsilon_{\perp}}, \\ k_0^2 &= k_y^2 - \frac{\omega^2}{c^2}. \end{aligned}$$

Substituting these solutions in the boundary conditions, we find the following dispersion relation

$$(8) \quad \frac{k_y + \varepsilon_{\perp} k_p}{\varepsilon_{\perp}^2 - g^2} + |k_y| = 0.$$

This relation is more general than (1) and in the limit

$$(9) \quad \omega^2 \ll k_y^2 c^2 \frac{\varepsilon_{\perp}}{\varepsilon_{\perp}^2 - g^2} \cong k_y^2 c^2.$$

goes over to (1). So we can consider this condition as a condition for potential approximation. Also we notice that in the absence of magnetic field, i.e. when $B_0 = 0$ equation (1) goes over to the well-known equation of surface waves in semi-bounded isotropic plasma [1].

As an application of potential approximation, we will discuss the problem of wave excitations by drift of electrons. Such drift or more accurately the beam in low density plasma can appear in the magnetosphere of Earth as a result of solar wind [2]. The density of the beam in magnetospheric plasma is $n_b \approx 1 \text{ cm}^{-3}$, with energy $\approx 1 - 3 \text{ keV}$ together with the assumption of a semi-bounded magnetosphere plasma with a density up to $n_p \approx 5 - 10 \text{ cm}^{-3}$. So it can accordingly explain the extended radio-frequency radiation detected by Sputniks of the Earth at altitude 500 - 800 km. Below, we will show that the transverse beam of electrons can excite these kinds of non-reciprocal surface waves, which we discussed above. For this aim we assumed the beam is non-relativistic, and moving with velocity $u \ll c$ along the y-axis, parallel to plasma surface. In this case equation (1) becomes more complicate and take the form

$$(10) \quad \varepsilon_{\perp b} + \varepsilon_{\perp p} + \frac{k_y}{|k_y|} (g_b + g_p) = 2 - \frac{\omega_p^2}{\omega \Omega_e} \cdot \frac{k_y}{|k_y|} - \frac{\omega_b^2}{(\omega - k_y u) \Omega_e} \frac{k_y}{|k_y|}.$$

Here the indexes "p" and "b" refer to plasma and beam respectively.

Equation (10) was obtained in the range of low frequencies for which (3) is valid. The influence of the beam, which modified equation (1) and appears in equation (10), will lead to correction in ω .

Assuming $\omega \rightarrow \omega + \delta = k_y u + \delta$, we will get for δ the relation

$$(11) \quad \delta^2 = -\frac{\omega_b^2}{\omega_p^2} \omega^2 = -\frac{n_b}{n_p} \omega^2$$

where $\frac{n_b}{n_p}$ is the ratio of densities of electrons in beam and plasma. We notice that $\delta^2 < 0$. Consequently the surface non-reciprocal waves will be excited in magnetized plasma by transverse electron beam. It is easy to show that these waves can be developed in rare plasma with $\omega_{Le}^2 \ll \Omega_e^2$ which is satisfied in magnetosphere of the Earth. Remembering that in magnetosphere $B_0 \cong 0.3$ Gs, for the frequency of the surface wave we obtain $\omega \cong 5 \cdot 10^3 \text{ s}^{-1}$, which is three orders of magnitude less than Larmor frequency, $\Omega_e \cong 5 \cdot 10^6 \text{ s}^{-1}$.

References

1. A.F. ALEXANDROV, L.S. BAGDANKEVICH, A.A. RUKCHADZE, *Principles of Plasma Electrodynamics*, Springer-Verlag, 1984.
2. A. HILGERS, A. ROUX, R. LIUDIN, *Characteristics of AKR sources, A. Statistical description geophysic research letters*, Vol. 18, pp. 1493-1496, 1991.

PERIODIC STRUCTURES IN THERMAL DUSTY PLASMAS

D. N. GERASIMOV¹, O. A. SINKEVICH¹ AND V. F. CHINNOV²

¹MOSCOW POWER ENGINEERING INSTITUTE (TECHNICAL UNIVERSITY),

HEAT PHYS. DEPT.

Krasnokazarmennaja, 14, Moscow, 111250, Russia,

fax (095)3611620, e-mail: oleg.sinkevich@mpei.ac.ru

²ASSOCIATE INSTITUTE FOR HIGH TEMPERATURE, RUSSIAN ACADEMY OF SCIENCE

Izhorskaya 13/19, Moscow, Russia

1. Introduction

The periodical structures or particle crystals in dusty plasma were found experimentally in rf and dc discharges [1, 2]. Often the following criterion for the dust crystal formation is used $\Gamma = \frac{(eZ)^2}{\langle r \rangle kT}$, where T is the temperature, k is Boltzman constant, e is the charge of electron, Z is electric charge of a drop, $\langle r \rangle$ is the mean distance between dust grains. In this work we derive the another criterion for the dust crystal formation.

2. Formulation of the problem

Here the thermal dusty plasma is considered when temperatures of all plasma components are equal to T_g . Let the spherical charged dust particle is surrounded by similar particles. In this case the distribution of an electric potential is obtained from the Poisson equation:

$$(2.1) \quad \Delta\varphi \equiv \frac{d^2\varphi}{dr^2} + \frac{2}{r} \frac{d\varphi}{dr} = \frac{en_0}{\varepsilon_0} \left[\exp\left(\frac{e\varphi}{kT_g}\right) - \exp\left(-\frac{e\varphi}{kT_g}\right) \right].$$

Here n_0 is the plasma density when $r \rightarrow \infty$. Using the non-dimensional variables we write the equation (2.1) in the form:

$$(2.2) \quad \frac{d^2\Phi}{dx^2} + \frac{2}{x} \frac{d\Phi}{dx} = sh\Phi$$

Here we use the next designations:

$$\Phi = \frac{e\varphi}{kT_g}, \quad x = \frac{r}{r_d} = r \sqrt{\frac{2n_0 e^2}{\varepsilon_0 kT_g}}.$$

3. The potential of the dust particles

In two important cases: a) $\Phi \ll 1$, or b) $x \ll \frac{1 + \sqrt{1 + 2(sh\Phi - \Phi)/\Phi}}{(sh\Phi - \Phi)/\Phi}$ the analytical solution of the equation (2.1) may be presented in the well known form:

$$(3.1) \quad \Phi = \Phi_s \frac{x_s}{x} \exp(x_s - x)$$

Here x_s is the non-dimensional radius of a dust, Φ_s is the dust surface potential.

This solution is valid for dust particles when $\Phi_s \sim 3$ and $x_s \sin 0.1$ so we use it for all r .

The electrostatic energy of two charged dust particles is represented in the form:

$$(3.2) \quad K(s) = \varphi(s)eZ + \int \varphi(s; x, y, z) \rho(x, y, z) dx dy dz$$

where s is non-dimensional distance between the particles.

Here the first term in the right side of the equation (3.2) describes the repulsion of particles, the second one describes attraction between charged clouds and particles.

Using the solution (3.1) we calculate the integral (3.2)

$$(3.3) \quad K(s) = K_0 \left[2 \left(1 + x_s + x_s^2 \right) \frac{e^{-s}}{s} - e^{-s} \right]$$

where $K_0 = 4\pi k T_g n_0 r_d^3 \Phi_s^2 x_s^2$.

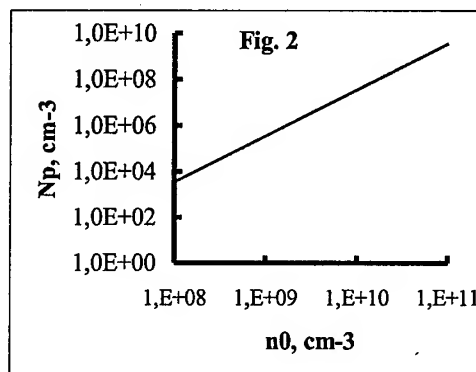
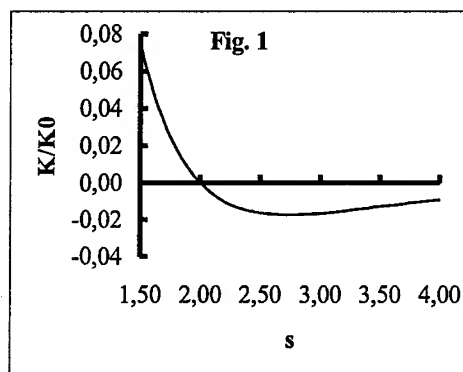
The electrostatic energy $K(s)$ as a function of distance is presented on Fig. 1. From this graph it is clear that the electrostatic energy has the classic form: the repulsion for the small radii and attraction for the big ones.

4. The criterion for the dust crystal formation

The Vlasov's kinetic equations are widely used in collisionless plasma physics. Because of very rare collisions between dust particles in plasma we may use the Vlasov's kinetic equations for charged dusts that interact through the collective electric field.

A. Vlasov has suggested the criterion of periodical structure formation [3] that for the charged dust has the form:

$$(4.1) \quad -\frac{4\pi N_p r_d^3}{kT} \int_{2x_s}^{\infty} K(s) s^2 ds = 1$$



where N_p is the dust density.

In (4.1) we should integrate for $x_s \ll 1$ from 0 to ∞ without taking into account the boundaries. The criterion (4.1) predicts infinite period crystal formation.

Incorporate (3.3) into the equation (4.1) we find the dust density that is needed for dust crystal formation. This dust density depends from plasma and dust parameters in the form:

$$(4.2) \quad N_p = \frac{1}{48\pi^2 n_0 \Phi_s^2 x_s^4 r_d^6}.$$

Dependence of dust density on plasma density n_0 for $\Phi_s = 3$, $x_s = 0.05$, $T_g = 2000$ K is presented on Fig. 2.

5. Conclusion

Using the electrostatic interaction between charged dust particles and the Vlasov's criterion periodical structure formation we derived the condition of dust crystal formation.

References

1. A.V. CHERNYSHEV, V.E. FORTOV, A.P. NEFEDOV, and O.F. PETROV, Proc. of XXIII ICPIG, Vol. 1, p. 176.
2. V.E. FORTOV, A.M. LIPAEV, V.I. MOLOTKOV, A.P. NEFEDOV, O.F. PETROV, V.M. TORCHINSKII, ibid, p. 178.
3. A.A. VLASOV, *The statistical functions*, Moscow: Nauka, 1966 (in Russian).
4. P.P.J. SCHRAM, S.A. TRIGGER, Contrib. Plasma Phys., **37**, 251-264, (1997).

ELECTROSTATIC PROBE MEASUREMENTS IN THE OUTER REGION OF A NITROGEN OPERATED PULSED LOW PRESSURE ARC

D. GRONDONA, H. KELLY¹, A. MÁRQUEZ AND F. MINOTTI¹

**INSTITUTO DE FÍSICA DEL PLASMA (CONICET), DEPARTAMENTO DE FÍSICA, FACULTAD
DE CIENCIAS EXACTAS Y NATURALES (UBA)**

Ciudad Universitaria Pab. I, (1428) Buenos Aires, Argentina,

kelly@tinfiplfp.uba.ar

1. Introduction

Vacuum or low pressure plasma arcs are attractive because they produce an intense metallic ion flux emerging from the cathode surface [1]. Although the angular distribution of the ion flux is peaked towards the anode, the ions are emitted within broad angles (measured with respect to the normal to the cathode plane), so that depending on the electrode geometry a considerable fraction of the ion yield flies away from the inter-electrode region, penetrating into the otherwise empty outer space. Usual gas neutral pressures employed with d-c arcs are in the range 0.01-0.1 mbar, but in some works gas neutral pressures in the range 1-10 mbar were used, either with the purpose of studying the attenuation of the metallic ion flux through the absorption by the neutral gas [2], or because in some pulsed high current experiments [3] with currents in the range 500 - 1200 A, and with faced electrodes separated by a small gap (2 - 5 mm), the above quoted high pressure range resulted in good reactive coating production. The study of the outer region of the discharge when the arc is operated with neutral gas filling is important because in this region the ions lose their kinetic energy by elastic collisions with the neutral particles and some of them are recombined through inelastic processes. Recently, a stationary fluid model with spherical symmetry to describe the interaction between metallic plasma ions with neutral gas in the outer region of a multi-cathode spot low pressure arc was presented [4]. It was found that the neutrals interpenetrate the metallic plasma with density values small with respect to the initial gas filling density value, but comparable to the metallic plasma density. The neutrals resulted also strongly heated during the

¹Member of the CONICET.

transient expansion of the metallic plasma. The model predicts the plasma-neutral gas structure up to the radial position at which the ions have completely lost its kinetic energy (r^*), while for $r > r^*$ only the neutral gas temperature and density can be obtained. In this work we present results from electrostatic probe measurements in the outer region of a pulsed low pressure arc with faced electrodes operated with Nitrogen gas, with the purpose of obtaining information on the plasma structure in the outer region of the arc channel of a vacuum arc operated at relatively high neutral gas pressures. Since a key point necessary to interpret the probe signals is the knowledge of the collision mean free path of the charged particles (which in turn requires some information about the plasma-neutral gas structure), the plasma and neutral gas parameters are inferred using the model of Ref [4].

2. Experimental apparatus and procedure

The arc was produced by discharging an electrolytic capacitor bank with $C = 0.075$ F, connected to a series inductor-resistor ($L = 2$ mH, $R = 0.33$ W) which critically damped the discharge. The vacuum chamber was a 25 cm long and 10 cm diameter stainless steel cylinder, through whose bases two faced electrodes were introduced. The Ti cathode was 15 mm in diameter and contained a central trigger electrode (1 mm diameter Titanium wire) for arc ignition. The anode was made of Copper, with the same diameter than that of the cathode. The gap d between anode and cathode was set at 2 mm. The arcs were performed in N_2 gas, at pressure values (p) of = 0.6, 2 and 10 mbar. An electrostatic probe was inserted into the discharge chamber in the radial direction (perpendicular to the electrode axis), and located at an axial position approximately in the middle of both electrodes. The probe radial positions (r_p) investigated were: $r_p = 1.25$, 2.75 and 9.5 cm. The probe electrode consisted of a spherical Copper tip (0.9 mm of diameter), which was made by melting (and then quenching) a Cu wire 0.5 mm thick. The arc was ignited by applying a short ($\sim \mu s$) high voltage pulse to the trigger electrode. The operating voltage was 180 V (≈ 1.2 kJ of stored energy), giving a current pulse with an amplitude of 320 A, and half-amplitude-full-width duration of 35 ms. The arc current was measured by employing a small series resistance (0.01 W), and the arc voltage by means of a high impedance resistive voltage divider. The probe was biased by connecting it to a regulated d-c power source (± 50 V, 2 A) through a calibrated series resistor (R_p). The probe voltage (V_p), the voltage drop on R_p (which in turn is proportional to the probe current i_p), the voltage between the electrodes (V_{ac}) and the total discharge current were simultaneously registered using a four-channel digitizing oscilloscope. In order to study the dependence of the plasma floating potential (V_f) on the radial position of the probe (for fixed p), a series of shots with the probe simply connected to a high impedance resistive voltage divider was also performed. In general, the probe was operated at V_p values corresponding to the ion branch of the V-I characteristic, but for the case $p = 0.6$ mbar, $r_p = 9.5$ cm a complete V-I characteristic was obtained.

3. Results

The probe signals were very noisy, with a shot-to-shot reproducibility of only 20%. In Table 1 average values (over ten shots) of V_f and the ion probe current (i_p^+) for different p and radial probe positions values are presented. The theoretical values [4] of the neutral gas density (n_N), the plasma potential (V_{pl}), the ion kinetic energy (E_i), and the non-dimensional parameter l/r_p (being l the mean free path of the charged particles) are also included in the Table 1. In this experiment l is mainly controlled by elastic collisions with the neutrals ($\sigma_{ei} \sim 5 \cdot 10^{-15} \text{ cm}^2$).

Table 1. Average values of V_f and the ion probe current (i_p^+) for different p and radial probe positions, together with several parameters of the plasma-gas system obtained from [4].

$p(\text{mbar})$ (mbr)	r^* (cm)	r_p (cm)	V_f (V)	i_p^+ (mA)	n_N (10^{15} cm^{-3})	V_{pl} (V)	E_i (eV)	l/r_p
0.6	3.3	1.25	13.9	7.2	1.4	17.2	34	3.1
0.6		2.75	14.7	1.9	2.3	14.9	5.9	1.9
0.6		9.5	10.8	0.002	25.6			0.17
2	1.7	1.25	14.7	7.8	4.3	17.5	14.6	1.0
2		2.75	14.6	0.37	8.1			0.54
2		9.5	6.3	0.0007	86.3			0.05
10	0.95	1.25	13.9	3.7	21.5			0.2
10		2.75	13.7	0.026	41.1			0.1
10		9.5	3.7	$< 10^{-5}$	428			0.01

For all the shots, it was found $V_{ac} = 20 \pm 1 \text{ V}$. The of the probe signals were interpreted according to the value of l/r_p . For $l/r_p > 1$, Lam's generalization of the classical Langmuir theory [5] (which includes the case of ions with arbitrary energy) was used; for $l/r_p < 1$, a simplified diffusive theory [6] (valid for probe potentials close to V_f) was employed; while for $l/r_p \ll 1$ Cohen's theory [7] (which includes a collisional sheath) was used. The electron temperature (T_e) was obtained from the difference between V_f and V_{pl} . For the cases in which V_{pl} was not available from the theoretical model, V_{pl} was extrapolated according to the relationship: $V_{pl} \approx V_{ac} - T_e \ln(n_{i0}/n_i)$, where n_{i0} is the ion density in the arc channel (this relationship is predicted from [4]). In spite of the different collisional regimes, for all the cases it was obtained $T_e \approx \text{const} = 0.6 \pm 0.2 \text{ eV}$. This value was confirmed from the slope of the probe characteristic (for small electron currents) in the case $p = 0.6 \text{ mbar}$, $r_p = 9.5 \text{ cm}$. In Table 2 the ion density (n_i) values obtained from the probe signals are given, together with the corresponding theoretical ones (n_i^{th}) obtained from [4]. The best fitting between n_i and n_i^{th} was obtained for the following parameters of the model: ion current into the outer part of the arc: 20 A, ion absorption cross section $\sigma_{abs} = 10^{-16} \text{ cm}^2$.

4. Final remarks

For $r_p < r^*$ the measured values of n_i are in good agreement with those predicted by the model of Ref. [4]. The measured T_e values are considerably smaller than the theoretical one. This fact can be attributed to the anchoring of T_e due to atomic dissociation processes of the N_2 molecule. Since the number of N atoms in this discharge is quite high (due to the thermal dissociation of the strongly heated N_2 gas), the molecular dissociation by electron impact produces a depletion of the thermal electron energy, until an equilibrium state is reached by the microscopic balance with the atomic recombination in the presence of an electron. The equilibrium T_e value is quite close to that experimentally determined.

Another interesting result is the absorption cross section for the metallic ions with the neutral gas, which results very similar to that previously determined in an ion absorption experiment [8].

Table 2. Ion density obtained from the probe, together with the corresponding theoretical values (for $r_p < r^*$) obtained from Ref. [4].

p (mbar)	r_p (cm)	$n_i(10^{12} \text{ cm}^{-3})$	$n_i^{th}(10^{12} \text{ cm}^{-3})$
0.6	1.25	3 ± 0.5	3.0
0.6	2.75	1.6 ± 0.2	1.2
0.6	9.5	0.006 ± 0.001	
2	1.25	3.9 ± 0.6	4.2
2	2.75	0.64 ± 0.1	
2	9.5	0.0016 ± 0.0002	
10	1.25	5.9 ± 0.9	
10	2.75	0.054 ± 0.09	
10	9.5	$< 10^{-5}$	

Acknowledgements

Work supported by Grants of the Buenos Aires University and CONICET.

References

1. R. L. BOXMAN, D. M. SANDERS and P. J. MARTIN, *Handbook of Vacuum Arc Science and Technology, Fundamentals and Applications*, Noyes Publ (Park Ridge, New Jersey, 1995).
2. C. W. KIMBLIN: J. Appl. Phys., **45**, 5235, 1974; J. L. MEUNIER and M. DOUYON DE ACEVEDO, IEEE Trans. Plasma Sci. **PS 20**, 1053, 1992.
3. R. L. BOXMAN, S. GOLDSMITH, S. SHALEV, H. YALAZ and N. BROSH: Thin Solid Films **139**, 41, 1986; H. BRUZZONE, H. KELLY, A. MÁRQUEZ, D. LAMAS, A. ANSALDI and C. OVIEDO: Plasma Sources Sci. Technol, **5**, 582, 1996.
4. H. KELLY, A. MÁRQUEZ and F. MINOTTI; IEEE Trans. Plasma Science, **PS 26**, 1322, 1998.
5. S. H. LAM, Phys. Fluids, **8**, 73, 1965.
6. Y. P. RAIZER, *Gas Discharge Physics*, (Springer Verlag), Berlin, 1991.

7. I. COHEN, Phys. Fluids, **6**, 1492, 1963.
8. H. KELLY, A. MÁRQUEZ, F. MINOTTI, D. GRONDONA and A. LEPONE; Proc. VIII Latin-American Workshop on Plasma Physics; Vol. Invited Papers, p. 110 (1998).

Author Index:

- | | | | |
|------------------------|--------|------------------------------|--------|
| ALEXANDROV A. F. | p. 533 | HEIL B. | p. 325 |
| ANITA V. | p. 421 | VAN HEESCH E. J. M. | p. 273 |
| ARDELYAN N. V. | p. 533 | HUIJBRECHTS P. A. H. J. | p. 273 |
| ARMENISE I. | p. 203 | HØYMORK S.H. | p. 391 |
| ABU ASSALI E. | p. 589 | | |
| | | IIZUKA S. | p. 439 |
| BADIE P.J. M. | p. 239 | ILLER E. | p. 551 |
| BALAKIREV V. A. | p. 293 | IOVITZ POPESCU I. | p. 401 |
| BALESCU R. | p. 015 | | |
| BLOM P. P. M. | p. 273 | JOUBERT O. | p. 035 |
| BLUNDELL R. E. | p. 227 | JOVANOVIC M. | p. 147 |
| BERTRAND PH. | p. 239 | | |
| BOGAERTS A. | p. 183 | KARAS' I. V. | p. 293 |
| BOLLANTI S. | p. 051 | KARAS' V. I. | p. 293 |
| | | KARCHEVSKY A. I. | p. 573 |
| CAPITELLI M. | p. 203 | KELLY H. | p. 597 |
| CATELLA M. | p. 203 | KLINGER T. | p. 307 |
| CHINNOV V. F. | p. 593 | KOGA K. | p. 505 |
| CHUVASHEV S. N. | p. 533 | KORNILOV E. A. | p. 293 |
| CHMIELEWSKI A. G. | p. 551 | KORTSHAGEN U. | p. 325 |
| COLONNA G. | p. 203 | KRAHNSTÖVER N. O. | p. 307 |
| CZUPRYNSKI P. | p. 035 | KRÁSA J. | p. 521 |
| | | | |
| DALGARNO A. | p. 023 | VAN DER LAAN P. C. T. | p. 273 |
| DESVOIVRES L. | p. 035 | LAZKO V. S. | p. 573 |
| DOLGOLENKO D. A. | p. 573 | LAZZARO P. DI | p. 051 |
| | | LÁSKA L. | p. 521 |
| ELIEZER S. | p. 215 | LETARDI T. | p. 051 |
| ERIKSON A. | p. 391 | LEVCHENKO V. D. | p. 293 |
| ERSHOV A. P. | p. 533 | LICKI J. | p. 551 |
| | | LIPAVSKÝ P. | p. 361 |
| FANG M. T. C. | p. 227 | LYBEKK B. | p. 391 |
| FAINBERG YA. B. | p. 293 | | |
| FLAMANT G. | p. 239 | MALUCKOV A. | p. 147 |
| FLORA F. | p. 051 | MAKABE T. | p. 345 |
| FUARD D. | p. 035 | MANDACHE N. B. | p. 401 |
| FUKUZAWA T. | p. 505 | MAUSBACH T. | p. 307 |
| FRANKLIN R. | p. 013 | MAŠEK K. | p. 521 |
| | | MÁRQUEZ A. | p. 597 |
| GANCIU M. | p. 401 | MINOTTI F. | p. 597 |
| GERASIMOV D. N. | p. 593 | MODREANU G. | p. 401 |
| GIJBELS R. | p. 183 | MONGET C. | p. 035 |
| GOURAUD P. | p. 035 | MORAWETZ K. | p. 361 |
| GRONDONA D. | p. 597 | MUROMKIN Yu. A. | p. 573 |
| GORSHUNOV N. M. | p. 573 | | |
| | | NEGER T. | p. 377 |
| Haidar J. | p. 257 | NISTOR M. | p. 401 |
| | | | |
| | | PARYS P. | p. 521 |
| | | PASHKOVSKY V. G. | p. 573 |

PEMEN A. J. M.	p. 273
PESHKOV A. T.	p. 573
PÉCSELI H. L.	p. 391
PHELPS A. D. R.	p. 073
PIEL A.	p. 307
POINTU A. M.	p. 401
POPA G.	p. 421
POTANIN E. P.	p. 573

RIEMANN K. U.	p. 089
ROHLENA K.	p. 521
RUKHADZE A. A.	p. 533

SADOWSKI M.	p. 123
SATO N.	p. 439
SATO T.	p. 147
SCHIAVONE P.	p. 035
SHIBKOV V. M.	p. 533
SIGOV YU. S.	p. 293
SINKEVICH O. A.	p. 593
SHIRATANI M.	p. 505
SKALNY J.	p. 449
SOTNIKOV G. V.	p. 293
STRELKOV P. S.	p. 469
ŠKORIĆ M.	p. 147
ŠPIČKA V.	p. 361

TIMOFEEV B. I.	p. 533
TIMOFEEV I. B.	p. 533
TORVÉN S.	p. 165
TRULSEN J.	p. 391
TYMIŃSKI B.	p. 551

VALLIER L.	p. 035
VIKHAREV A. L.	p. 485

WATANABE Y.	p. 505
WOŁOWSKI J.	p. 521
WORYNA E.	p. 521

YAN J. D.	p. 227
YAN K.	p. 273

ZHENG C. E.	p. 051
ZIMEK Z.	p. 551
ZOTIN G. E.	p. 573